Biomechanics of the Ankle Joint Complex using a Muscle Model Assisted Optimisation Model

Thomas R Jenkyn

THE
UNIVERSITY OF
STRATHCLYDE
IN GLASGOW

A THESIS SUBMITTED IN FULFILMENT OF
THE REQUIREMENTS FOR THE DEGREE OF
DOCTOR OF PHILOSOPHY

BIOENGINEERING UNIT
UNIVERSITY OF STRATHCLYDE

Supervisor: Dr. A.C. Nicol

February, 2001

ABSTRACT

A seven segment model of the right leg and foot was developed with segments: thigh, lower leg, talus, hindfoot, midfoot and lateral and medial forefoot. Three-dimensional mapping of internal structures was made from CT scans and anatomical photographs (Visible Human Project). Twelve healthy subjects performed level walking and medial walking turns at slow, preferred and fast speed.

Equilibrium about the two joints of the ankle complex (ankle and subtalar), was solved using Muscle Model Assisted Optimisation (MMAO). A three component, Hill-type muscle model determined tensions in eight muscles of the lower leg using EMG. Linear optimisation then corrected muscle tensions and solved for ligament tensions and articular surface compression.

MMAO was successful in modeling ankle complex equilibrium during walking and walking turn. External forces acting on the right foot were similar for all subjects. Despite similar external loading, subjects employed different muscle tension strategies to produce equilibrium about the ankle and subtalar joints. For all subjects, triceps surae muscle tensions were largest. Peak tension in achilles tendon was 7.9×BW during walking and 8.0×BW during walking turn. The two heads of gastrocnemius behaved as distinct muscles performing different roles during stance. Peroneus brevis produced movement about the subtalar joint while peroneus longus had a stabilising role. The dorsi-flexors were significantly active during stance phase, antagonistic to triceps surae muscle group. This antagonism has not been predicted by previous models.

Ligaments acted in an *all-or-nothing* manner when constraining the ankle complex. Ligaments were either slack or tensed at constant tension. Maximum ligament tension was 1.75×BW in the lateral ligaments of the ankle joint during walking turn. No difference between the walking and walking turn was seen in compressive loading of articular surfaces. Maximum compression of ankle joint was 10.0×BW and of subtalar joint was 8.0×BW.

ACKNOWLEDGEMENTS

I wish to thank my supervisor, Dr. Sandy Nicol, for his support and guidance. It was he who introduced this outsider to the grey area that exists between the disciplines of engineering and medicine and it was he who suggested that the ankle could use some looking in to.

I must also thank the Visible Human Project for supplying the medical images on which the model was based. Thank you also to the Over-seas Research Scheme that allowed me to follow the path of most resistance and study in the United Kingdom as a financially-disadvantaged Canadian who was a long way from home.

Finally I must thank the person to whom I owe everything, Krista Bray. You made many sacrifices to join me in the Old World, not the least of which was leaving the New World. It is unlikely that I would have finished this without you propping me up, unseen, from behind. You have earned an equal share in this accomplishment and we make a good team.

TABLE OF CONTENTS

NOMENCLATURE

Template: $\overset{Superscript-left}{Subscript-left}X\overset{-right}{-right}$

A, B, C -landmarks defined in Internal Map (chapter 4)
A, B -velocity-tension curve shape constants (6)
a -muscle activation level (6)
b -point (4)
C -surface compression optimisation variable (7)
c -muscle tension correction variable (6, 7)
CSA -cross sectional area (6)
d -lever arm (6, 7)
dl -moment potential (6, 7)
e -example sample (4),
EMG signal (6)
F -ground reaction force (3),
force (6, 7)
f -velocity-tension (Hill) factor (6)
h -general sample (4, 6 ,7)
k -SEC stiffness coefficient (6)
L -ligament tension optimisation variable (7)
l -point (4),
length (6),
line of action (6, 7)
M -moment (6, 7)
N -number of sarcomeres (6),
scaling factor for PEC length-tension curve (6)
O -origin (4)
p -point (4)
PCSA -physiological cross sectional area
q -proportionality factor (6)
r -vector (4)
R -rotational matrix (4)
S -anthropometric scaling factor (6)
s -muscle model calibration factor (6)
SF -muscle specific tension (6)
T -translation matrix (4),
tension (6, 7)
x,y,z -frame of reference axes (4)
x -point (6 ,7)
v -vector (4),
velocity (6)
z -objective function (6, 7)
1,2,3 -frame of reference axes (4)
θ -muscle pennation angle (6)

τ -muscle twitch time constant (6)
$\hat{\tau}$ -specific muscle twitch time constant (6)

Subscript-right

A,B,C -anthropometric landmarks (4)
a→b -transformation from frame a to frame b (4)
CC -contractile component (muscle model) (6)
cp -centre of pressure (4, 6, 7)
f -final entity (4),
missing entity (with gap-filling) (4),
of the fibre (muscle model) (6)
GRF -of the ground reaction force (7)
i -the i^{th} entity (4)
lig -of the ligaments (7)
max -maximum value (6)
mus -of the muscle (7)
muscle -of the muscle (6, 7)
muscle-tendon -of the muscle-tendon unit (6)
[opt] -optimal value (6)
PEC -parallel elastic component (muscle model) (6)
[rest] -resting value (6)
sarc -of the sarcomere (6)
SEC -series elastic component (muscle model) (6)
s -starting entity (4)
surf -of the articular surfaces (7)
tendon -of the tendon (6, 7)
total -total value (6)
trans -transitional value (6)
x,y,z -directional components (3)
x -cross-product vector (3, 4, 6)
1,2,3,4 -force plate pillar number (3)
1,2,3 -entity number (4)
β -rotation of θ degrees (with gap-filling) (4)
θ -rotation of θ degrees (with rotational matrix) (4)

Subscript-left (Frames of Reference)

bone -bone-fixed frame (4)
cluster -marker cluster frame (4)
example -example frame (4)
g -VICON/ ground frame (3, 4)
h_s-2 -frame defined at field h_s-2 (4)
joint -joint-fixed frame (Ankle or Subtalar) (4)
Kistler -force plate frame (3)
MI -medical image frame (4)
VICON -VICON/ ground frame (3)

Superscript-right

T	-transpose (4)
‘	-derivative with respect to time (4), altered frame of reference (4), altered length (6)
*	-estimated value (6)

Superscript-left

$\hat{1},\hat{2},\hat{3}$	-component of the vector or matrix (4)
$\hat{1},\hat{3} and \hat{2}$	-axis of scale factor, S (4)

Tops

$\vec{x}$	-vectors (4, 6, 7)
$\hat{x}$	-unit vectors (4, 6)
$\bar{x}$	-average or rectified signal (6)

Bases

$\underline{x}$	-point or matrix (4, 6, 7)

AIM OF THE CURRENT MODEL

The aim in the current study was to develop mathematical a model which would determine the loads acting on the internal structures of the Ankle Complex during the stance phases of walking and walking turns. The structures which were modelled were the muscles, tendons, ligaments and articular surfaces. The Model was intended to minimally simplify the internal structure and to be as representative of the anatomy of the Ankle Complex as possible.

To mathematically represent the internal structure of the Ankle Complex an Internal Map was constructed from medical images. The Internal Map defined the positions, orientations and geometries of the structures within the joint complex.

Kinematic data formed the input for the model. A VICON Motion Analysis System was used to collect the kinematic data. The kinematic data aimed to capture not only the large relative motion of the segments of the leg but also the smaller relative motion of the segments of the foot which has been often ignored in past locomotion studies.

The Model finally aimed to demonstrate to effectiveness of the Muscle Model Assisted Optimisation (MMAO) method for solving indeterminate joint systems of highly mobile joints during gait.

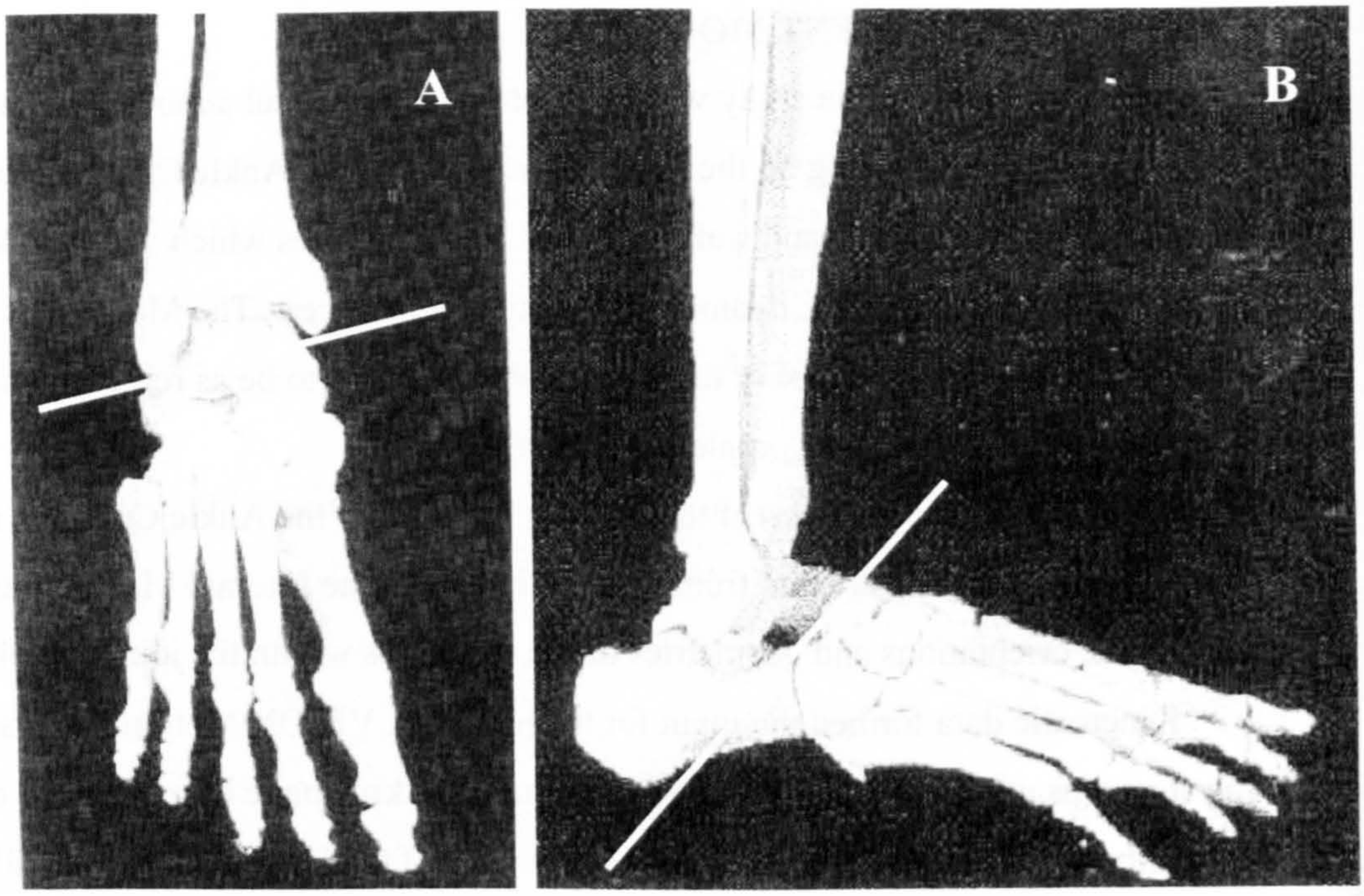

Figure 1.1.1-1 The positions of the Ankle Joint (A) and Subtalar Joint (B) axes with respect to the bones of the lower leg and foot (Gosling, et al, 1993).

CHAPTER 1 ANATOMY AND FUNCTION

1.1 ANATOMY OF THE ANKLE COMPLEX

1.1.1 The Joints of the Ankle Complex

There are two joints that compose the Ankle Complex: the *Ankle Joint* and the *Subtalar Joint*. The Ankle Joint has also been called the *Talocrural Joint* in the literature. This joint is formed by the Talus articulating with the Tibia and Fibula. The axis of rotation is directed generally medial to lateral with the axis running postero-laterally and distally. Figure 1.1.1-1 shows the location and orientation of the Ankle Joint axis with respect to the bones of the leg and foot. The motions allowed by the Ankle Joint joint are *dorsi-flexion* and *plantar-flexion*. If the axis is considered to point laterally, then a positive rotation of the foot about the axis is dorsi-flexion, where the angle formed by the anterior surface of the tibia and the dorsum of the forefoot becomes smaller. A negative rotation is plantar-flexion where this angle becomes larger.

The Subtalar Joint is also known as the *Talocalcaneonavicular Joint*. While this second name is useful in indicating the bones that are involved in the joint, the name is otherwise cumbersome, and therefore Subtalar will be used for the remainder of this study. This joint is composed of two separate joints which function together as a unit. The first subjoint is formed by articulations between the Calcaneous and the Talus, and the second between the Navicular and the Talus. The axis of this joint runs generally posterior to anterior with the axis moving anteriorly, proximally and medially. The axis for the Subtalar Joint is also plotted in Figure 1.1.1-1. The motions allowed by this joint are *inversion* and *eversion*. If the axis of the joint is considered to run anteriorly, then a positive rotation of the *right* foot about the axis produces inversion where the angle formed between the medial surface of the tibia and the medial aspect of the midfoot becomes smaller. A negative rotation produces eversion where this angle is increased.

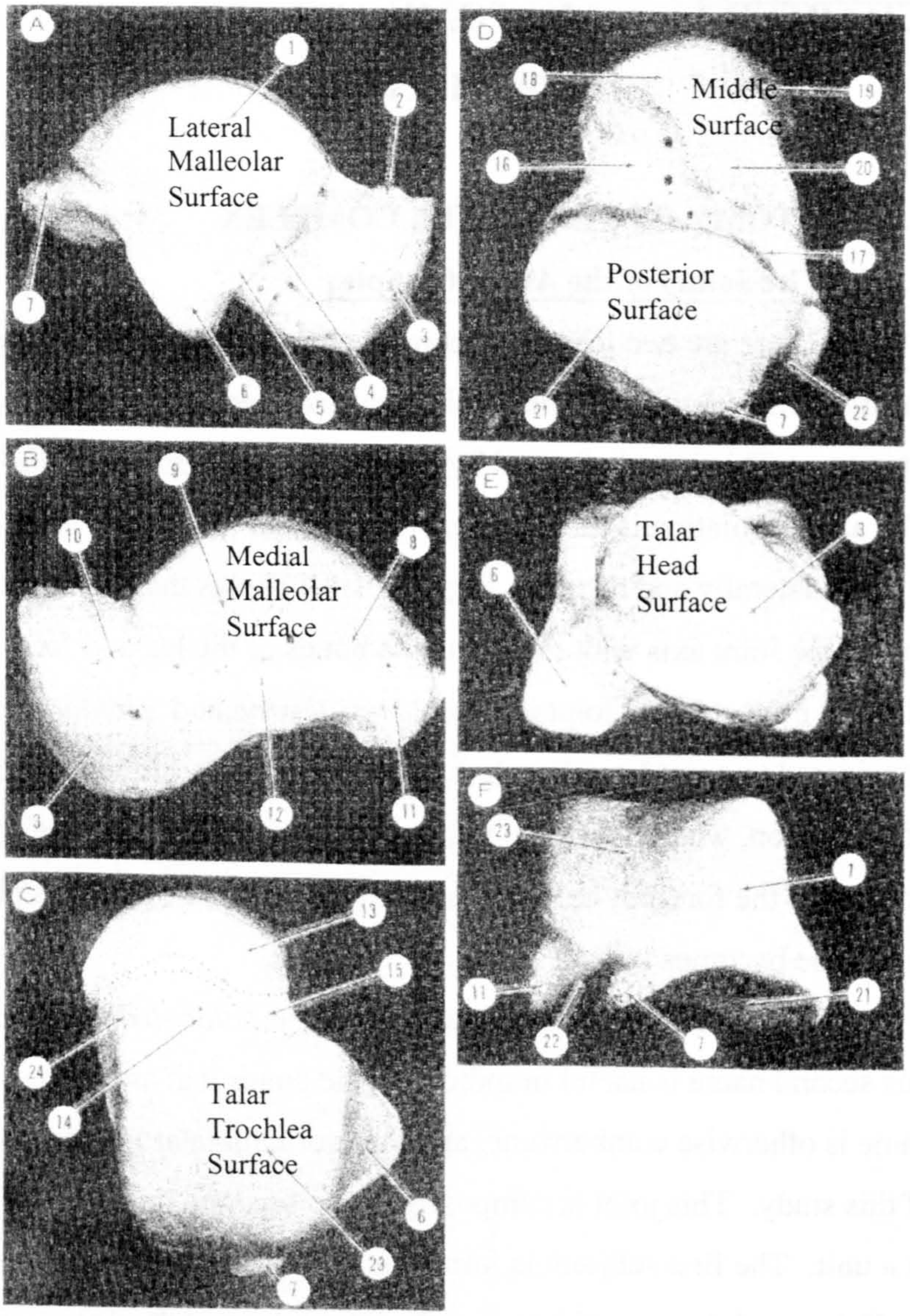

Figure 1.1.2-1 Views of the Talus bone: Lateral (A), Medial (B), Superior (C), Inferior (D), Anterior (E), Posterior (F) (Sarrafian, 1983).

1.1.2 The Bones of the Ankle Complex

The bones that make up the Ankle Complex can be subdivided functionally and anatomically into five different groups: the Lower Leg, Talus, Hindfoot, Midfoot and the Forefoot plus Phalanges.

Talus

The Talus is central to the function of the Ankle Complex and possesses articulations for both the Ankle and the Subtalar Joints, however, it is not palpable from the skin surface. Figure 1.1.2-1 shows the Talus bone. The Talus is composed of three portions: the body, neck and head. The body is the largest portion of the Talus and is secured within the bimalleolar fork by strong ligaments. The superior surface of the body is pulley shaped and covered by the Talar Trochlear surface of the Ankle Joint. The lateral and medial surfaces are covered by the Lateral Malleolar surface, which is the larger, and the Medial Malleolar surface. These two surfaces are also involved in the Ankle Joint.

The Inferior surface of the body is covered by the Posterior Talocalcaneal surface of the Subtalar Joint. The long axis of this surface is directed antero-laterally. The surface is strongly concave in its long axis and either flat, or minimally concave in its short axis. The posterior surface of the Talar body has two tubercles. The sulcus between these tubercles forms a pulley surface for the Flexor Hallucis Longus tendon.

The neck of the Talus is attached to the anterior of the body. The long axis of the neck is directed antero-medially and inferiorly with respect to the body. The inferior surface of the neck forms the *sinus tarsi* laterally and the *canalis tarsi* medially. These concave surfaces form a cavity between the Talus and the Calcaneus, which is the bone lying inferiorly to the Talus. Anterior to the canalis tarsi, lies the Middle Talacalcaneal articular surface. This surface is also involved in the Subtalar Joint. The sinus and canalis tarsi are both strongly concave and serve to separate the Posterior and Middle Talocalcaneal surfaces.

The neck of the Talus connects the body portion to the head portion. The head of the Talus articulates with the Navicular and is dominated by an articular

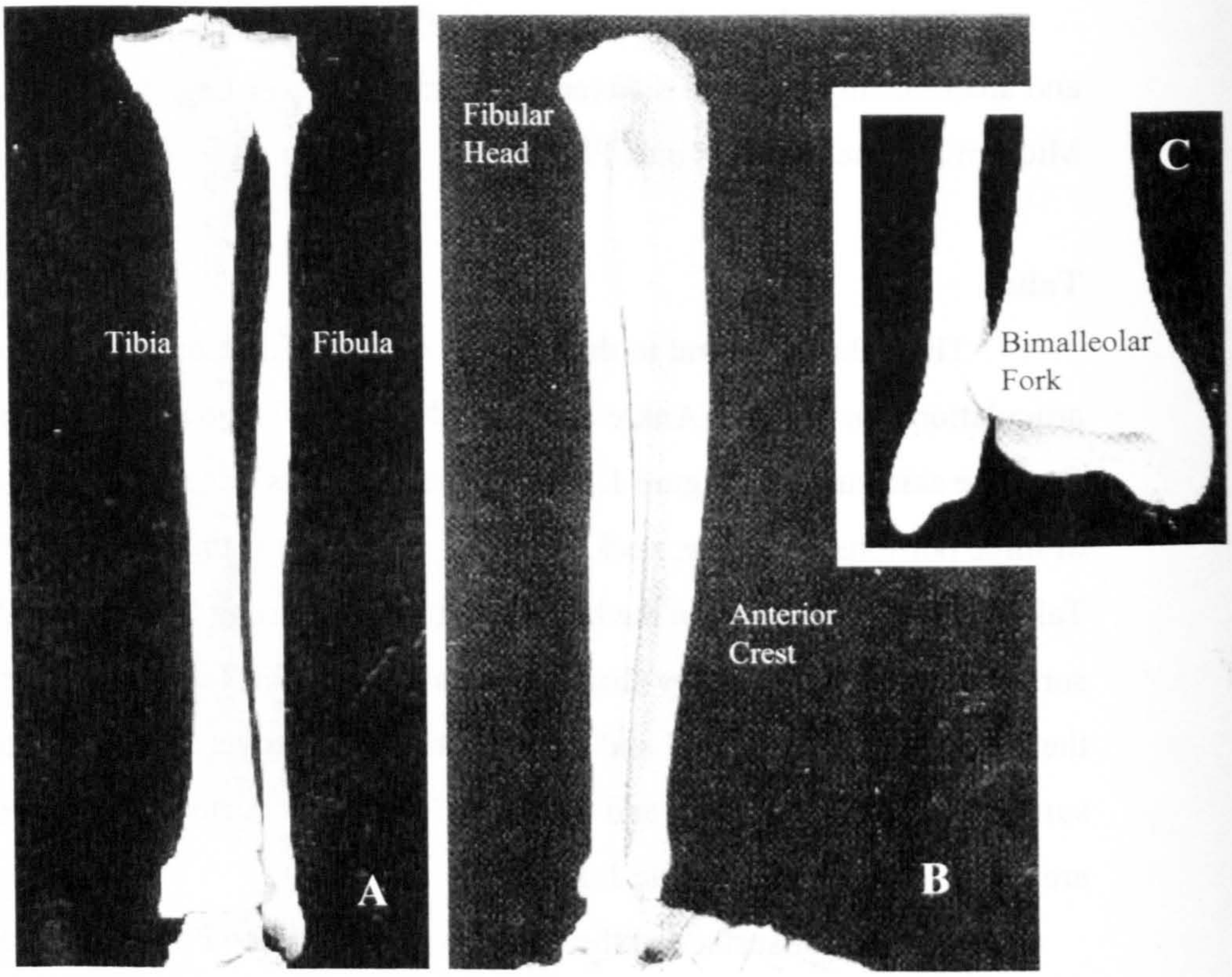

Figure 1.1.2-2 Bones of the lower leg: Tibia and Fibula. Anterior view (A), Lateral view (B) and Distal end (C) (Gosling, et al. 1993).

surface. The long axis of this surface is directed supero-laterally and is convex along both its long axis and short axis.

Lower Leg

There are two bones in the lower leg: the Tibia and the Fibula. These bones span from the Knee Joint down to the Ankle Joint in the Ankle Complex. Both of these bones are long bones, with the long axes of the two running parallel to one another. They are illustrated in Figure 1.1.2-2. The Tibia is the larger of the two. The anterior surface of the Tibia is dominated by the tibial anterior crest. Distally, the medial Tibia forms the Medial Malleolus which is palpable from the skin surface and forms one side of the bimalleolar fork which holds the Talus body. The inside of the malleolus holds the Medial Malleolar surface of the Tibia. The inferior surface of the Tibia is covered by the concave Mortice surface. These two surfaces articular with the Talus in the Ankle Joint.

The Fibula is the smaller of the two lower leg bones. The Fibula is positioned laterally to the Tibia and joined to it very strongly by an interosseus membrane which allows very little relative motion. The proximal end of the Fibula, the head, is knob-like and is palpable from the skin surface. The distal end forms the Lateral Malleolus which is also palpable and which is the other tong in the bimalleolar fork. The inside surface of this is covered by the Lateral Malleolar surface.

The Lateral and Medial Malleolar surfaces and the Mortice surface at the distal ends of the Tibia and Fibula articular with the Talus surfaces, forming the Ankle Joint.

Hindfoot

The Hindfoot group is composed solely of the Calcaneus bone which is the largest bone of the foot. This bone lies inferior to the Talus and forms the plantar heel surface of the foot. The Calcaneus is shown in Figure 1.1.2-3. The superior surface of the Calcaneus is divided into three portions. The posterior third is non-articular. The middle third is covered by the Posterior Talocalcaneal surface which

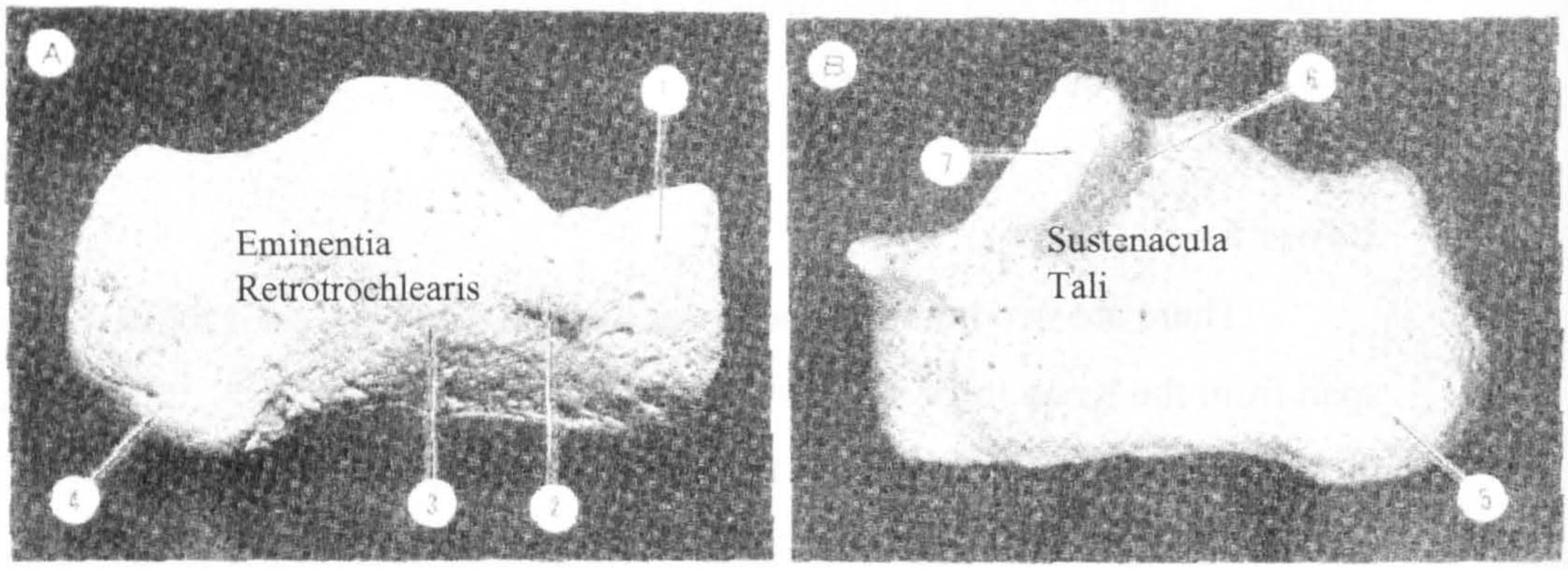

Figure 1.1.2-3 Views of the Calcaneus: Lateral (A), Medial (B), Superior (C) and Inferior (D) (Sarrafian, 1983).

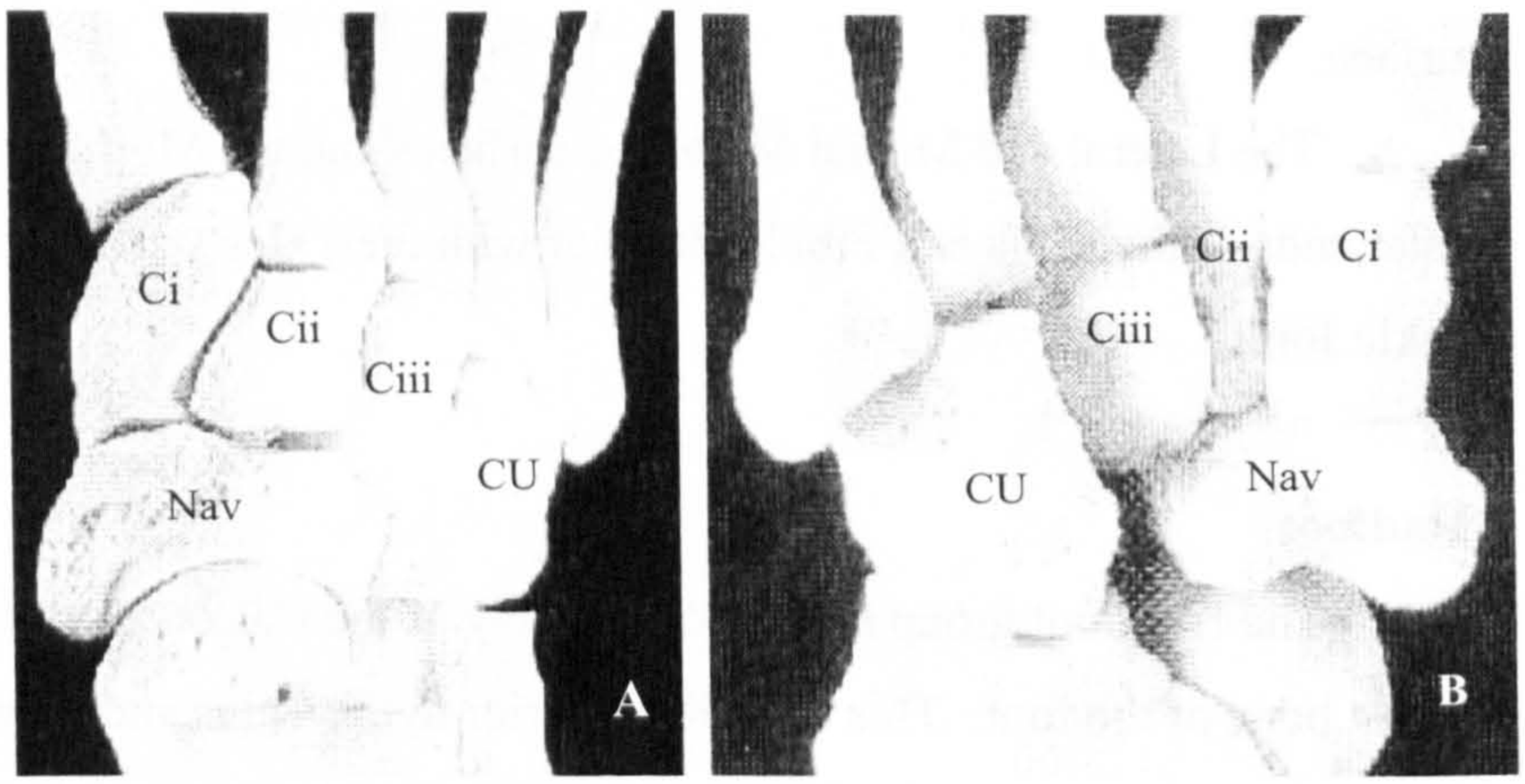

Figure 1.1.2-4 Bones of the Midfoot: Navicular (Nav), First to Third Cuneiforms (Ci to Ciii) and Cuboid (CU). Superior (A) and Inferior (B) views (Gosling, et al, 1993).

articulates with the Talus. The anterior third holds the sulcus calcanei and the Middle Talocalcaneal surface. The sulcus calcanei is the floor of the cavity between the Talus and Calcaneus formed by the sinus and canalis tarsi.

The posterior surface of the Calcaneus forms the insertion for the Achilles tendon. To either side of the tendon attachment are tuberosities, lateral and medial, which are palpable from the skin surface. The lateral surface of Calcaneus is flat apart from a broad tubercle, the *eminentia retrotrochlearis* which is also palpable from the skin surface. The medial surface of Calcaneus is flat except for a large projection from the superior middle third, the *sustenaculum tali* which supports the medial aspect of the Posterior Talocalcaneal surface. Anteriorly, the Calcaneus is entirely articular where it meets the Cuboid bone of the midfoot group of bones.

Midfoot

Five bones make up the midfoot group. These are: Navicular, Cuboid, and the First, Second and Third Cuneiforms. These bones are tightly joined together by strong ligaments and there is very little relative movement between the five. For this reason, they can be considered to operate as a single rigid segment. The midfoot bones are illustrated in Figure 1.1.2-4.

The Navicular lies at the medial, proximal corner of the midfoot group. The posterior surface of the Navicular articulates with the head of the Talus. The long axis of this surface runs in the supero-lateral direction similarly to the corresponding Talar Head surface. The long axis of the surface is strongly concave while the short axis is slightly concave or even flat and the Navicular surface is not entirely congruent with the corresponding Talar surface. The medial edge of the Navicular is dominated by a large tuberosity which is palpable from the skin surface.

The lateral edge of the Navicular meets the Cuboid at an inflexible joint. The Cuboid lies in the posterial lateral corner of the midfoot group where it articulates with the anterior surface of the Calcaneus. The lateral border of Cuboid holds a groove which serves as a pulley point for the Peroneus Longus muscle. The Cuboid extends anteriorly to the bases of the Fourth and Fifth Metatarsal bones and borders the Third Cuneiform medially.

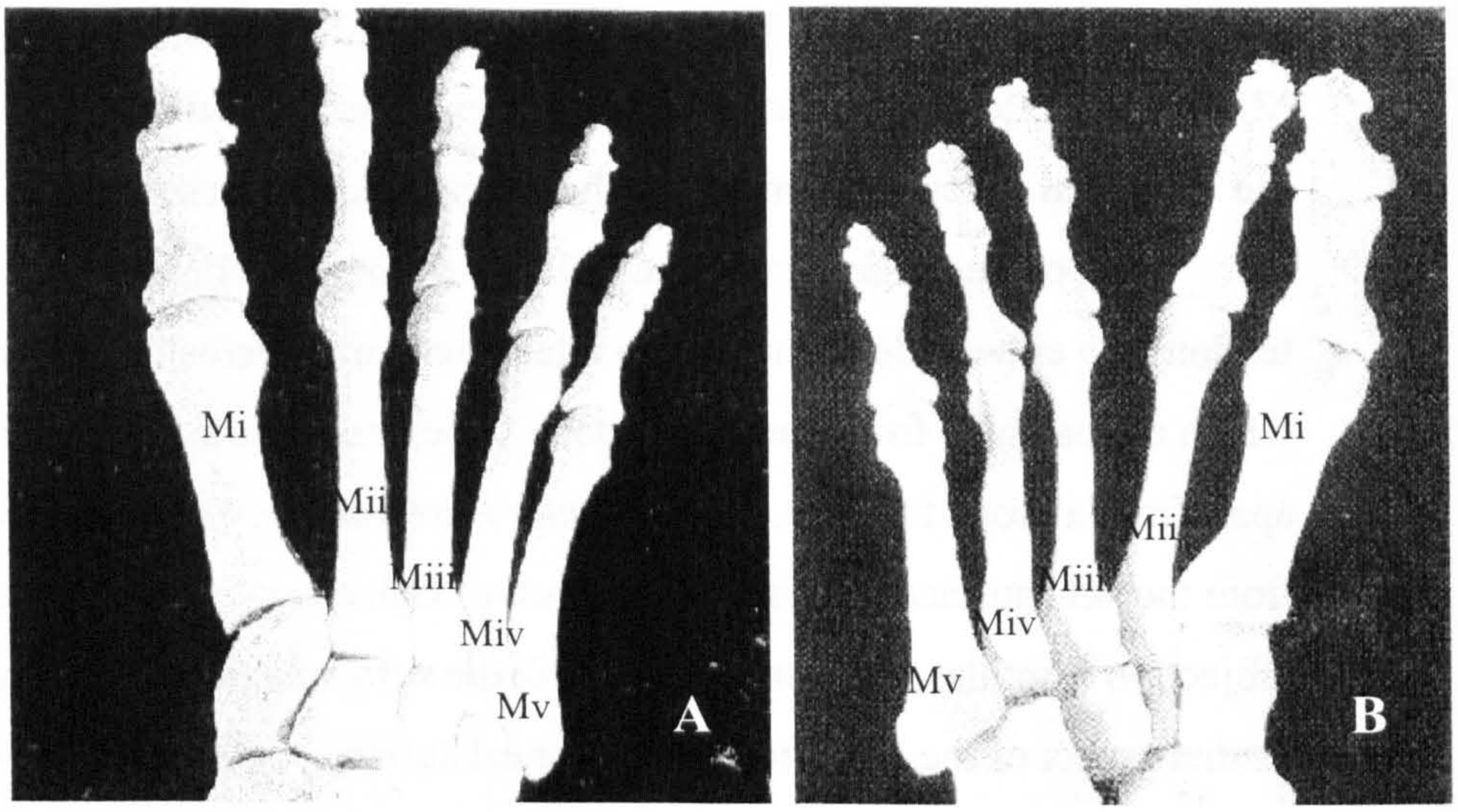

Figure 1.1.2-5 Metatarsals of the Forefoot: First to Fifth (Mi to Mv) and the Phalanges. Superior (A) and Inferior (B) views (Gosling,et al 1993).

The three Cuneiform bones form the anterior medial corner of the midfoot group. The First Cuneiform is most medial and lies on the medial edge of the foot. Its dorsal surface bears a ridge which is palpable from the skin surface. The Second Cuneiform lies lateral to the First and medial to the Third Cuneiform. The lateral border of the Third Cuneiform meets the Cuboid. The three Cuneiforms with the Cuboid form the transverse arch of the foot which is dorsally convex. The anterior surfaces of the Cuneiforms atriculate with the bases of the First to Third Metatarsals in a zig-zag patten. This pattern of articulations forms the Tarsometatarsal Joint (or Lisfranc's Joint) and determines its behaviour.

Forefoot and Phalanges

There are five Metatarsal bones within the forefoot group of bones. These articulate with the three Cuneiforms and the Cuboid proximally at the Tarsometatarsal Joint and with the Phalanges distally. The five Metatarsal are all long bones with their long axes running parallel, proximal to distal, from base to head. The First Metatarsal is the most medial and is the shortest and thickest of the five. The other four Metatarsal rays are all thinner than the First and are of similar cross-section (Figure 1.1.2-5).

The base and head of the First Metatarsal each possess dorsal ridges which are palpable from the skin surface. The head of the Fifth Metatarsal bears a similar dorsal ridge. The base of the Fifth Metatarsal however possesses a large palpable prominence which extends postero-laterally from the lateral border of the foot.

The remaining bones of the foot are the fourteen Phalanges, which make up the five toes, and the two sesamoid bones of the great toe. The great toe is composed of only two Phalanges while the other four toes have three each.

1.1.3 The Ligaments of the Ankle Complex

The ligaments of the Ankle Complex can be divided into three groups based on location: the Lateral, Medial and Subtalar groups. The Lateral and Medial ligaments are all attached to the Tibia or Fibula and act primarily about the Ankle

Joint. The Subtalar ligaments each attach to the Talus and exclusively act about the Subtalar Joint.

Lateral Ligaments

The Lateral ligament group comprises three distinct ligaments: the Anterior and Posterior Talofibular and the Calcaneofibular ligaments. All of these attach to the Fibula on the lateral malleolus. The three Lateral ligaments are illustrated in Figure 1.1.3-1. The Anterior Talofibular is a flat, strong ligament which runs anteriorly from anterior surface of the lateral malleolus and attaches to the body of the Talus just anterior to the Lateral Malleolar surface. The ligament is composed of two distinct bands of fibres, the upper and lower, which work as a single functional unit. This ligament constrains the motion of the Talus about the Ankle Joint so that it is unable to internally rotate or to invert.

The Calcaneofibular ligament is a strong cord-like bundle of fibres which runs from the anterior lateral malleolus and attaches to a small tubercle on the posterior lateral surface of the Calcaneus. This ligament therefore acts to constrain the motion of the Calcaneus and Talus about both the Ankle and Subtalar Joints. This ligament restricts the Calcaneus and Talus from externally rotating at the Ankle Joint and limits the amount of inversion of the Calcaneus about the Subtalar Joint.

The Posterior Talofibular ligament is the strongest ligament of the three. It is trapezoidal in shape and attaches to the medial, inside surface of the lateral malleolus, just inferior to the Lateral Malleolar articulation of the Fibula. The ligament runs posteriorly and attaches to the posterior surface of the Talus body. This ligament constrains motion of the Talus about the Ankle Joint so that it is unable to externally rotate or invert.

Medial (Deltoid) Ligaments

The division of the Medial group into individual ligaments is not as obvious as with the Lateral group. Figure 1.1.3-2 illustrates the Medial or *Deltoid* group. The majority of the fibres of the Deltoid group are directed posteriorly and laterally from the medial malleolus. A smaller number of fibres extend anteriorly.

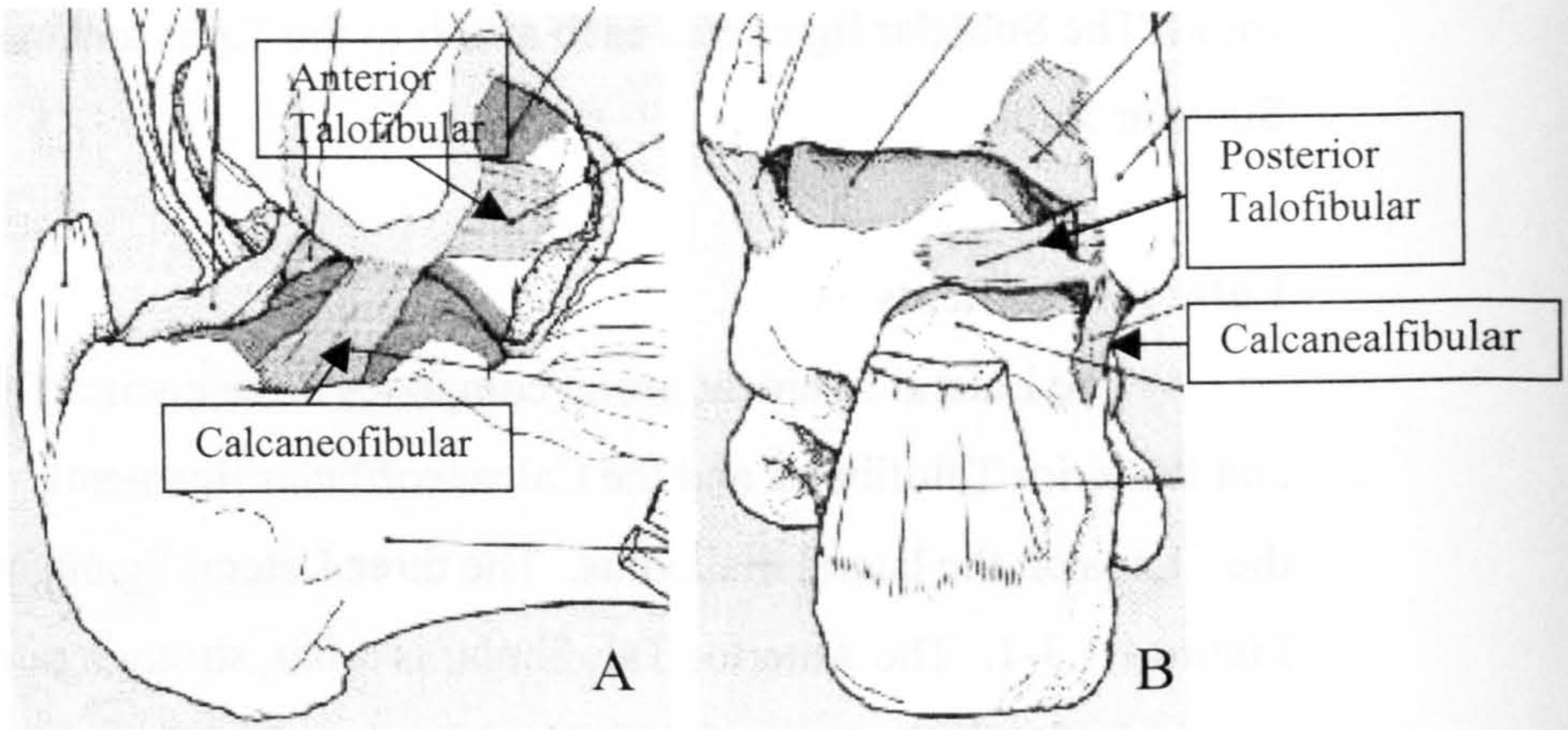

Figure 1.1.3-1 Lateral ligaments in lateral view (A) and posterior view (B) (Gosling, et al., 1993).

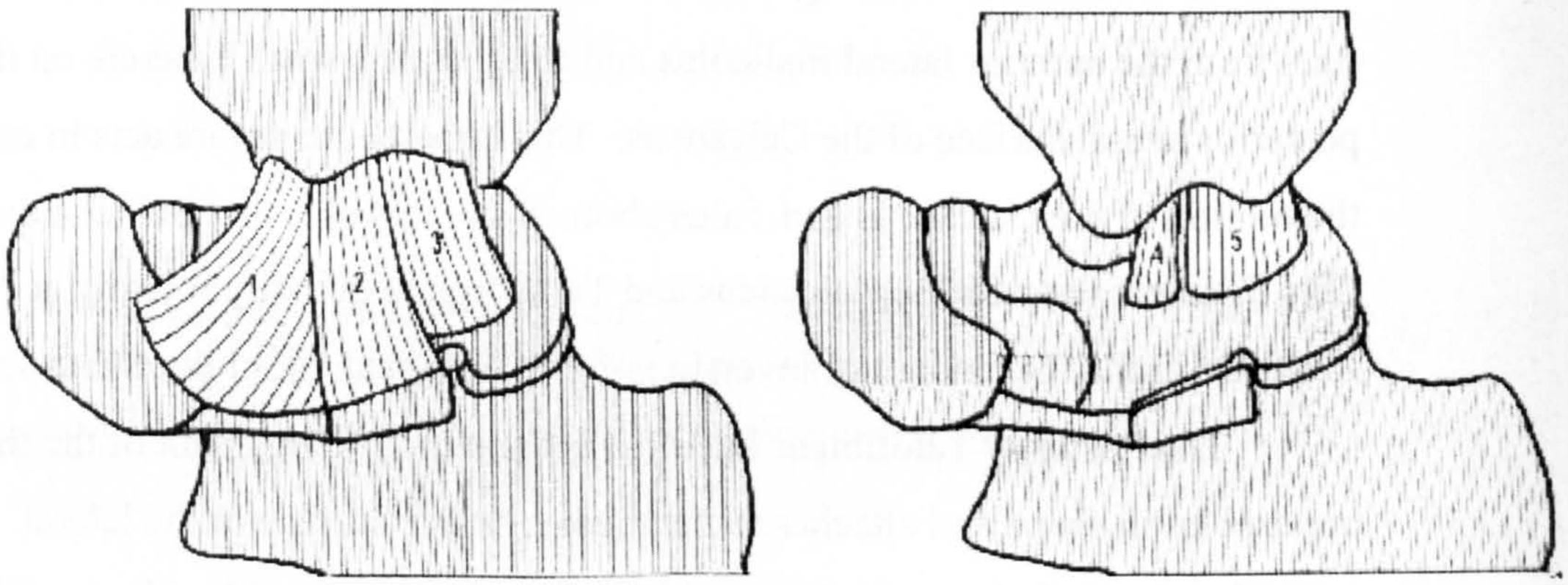

Figure 1.1.3-2 Medial (Deltoid) ligaments: Tibionavicular and Anterior Talotibial (1), Tibiocalcaneal, superficial (2) and deep (4) and Posterior Talotibial, superficial (3) and deep (5)
(Pankovich & Shivaram, 1979)

The division of the Deltoid group will be described according to Pankovich & Shivaram (1979) which defines four separate ligaments, each attached to the medial malleolus. The Posterior Talotibial ligament attaches at the posterior distal surface of the medial malleolus near the groove for the Peroneus Brevis tendon. This ligament runs to the posterio-medial surface of the Talus near the border of the posterior third of the Talar Trochlear surface. This ligament possesses two thick bundles, the superficial and deep, which function as a single unit to constrain the Talus within the Ankle Joint. This ligaments stops the Talus from internally rotating at the Ankle Joint or from everting.

The Tibiocalcaneal ligament runs from the anterior surface of the distal tip of the medial malleolus to the sustenaculum tali of the Calcaneus. This ligament is flat in geometry and constrains the Calcaneus and Talus within the Ankle and Subtalar Joints. The Talus is contrained from internally rotating and the Calcaneus is limited in the amount of eversion it is allowed at the Subtalar Joint.

The Anterior Talotibial ligament is thinner and weaker that the preceding two. This ligament runs from the anterior surface of the distal tip of the medial malleolus to the medial surface of the Talar neck. This ligament constrains the Talus in the Ankle Joint from externally rotating.

The final ligament of the Deltoid group is the Tibionavicular ligament, which shares an attachment with the Anterior Talotibial ligament on the medial malleolus. This ligament runs in the same direction as the Anterior Talotibial and lies superficially to it. This ligament, however, is thicker and stronger than the Anterior Talotibial and is attached to the dorso-medial aspect of the Navicular bone of the midfoot. This ligament therefore constrains Talus about the Ankle Joint and the tarsal bones about the Subtalar Joint. As with the Anterior Talotibial ligament, the Talus is constained from externally rotating within the Ankle Joint. The ligament also stops the tarsal bones of the foot from externally rotating about the Subtalar Joint and from dislocating the Talar Head-Navicular Socket articulating of the Subtalar Joint.

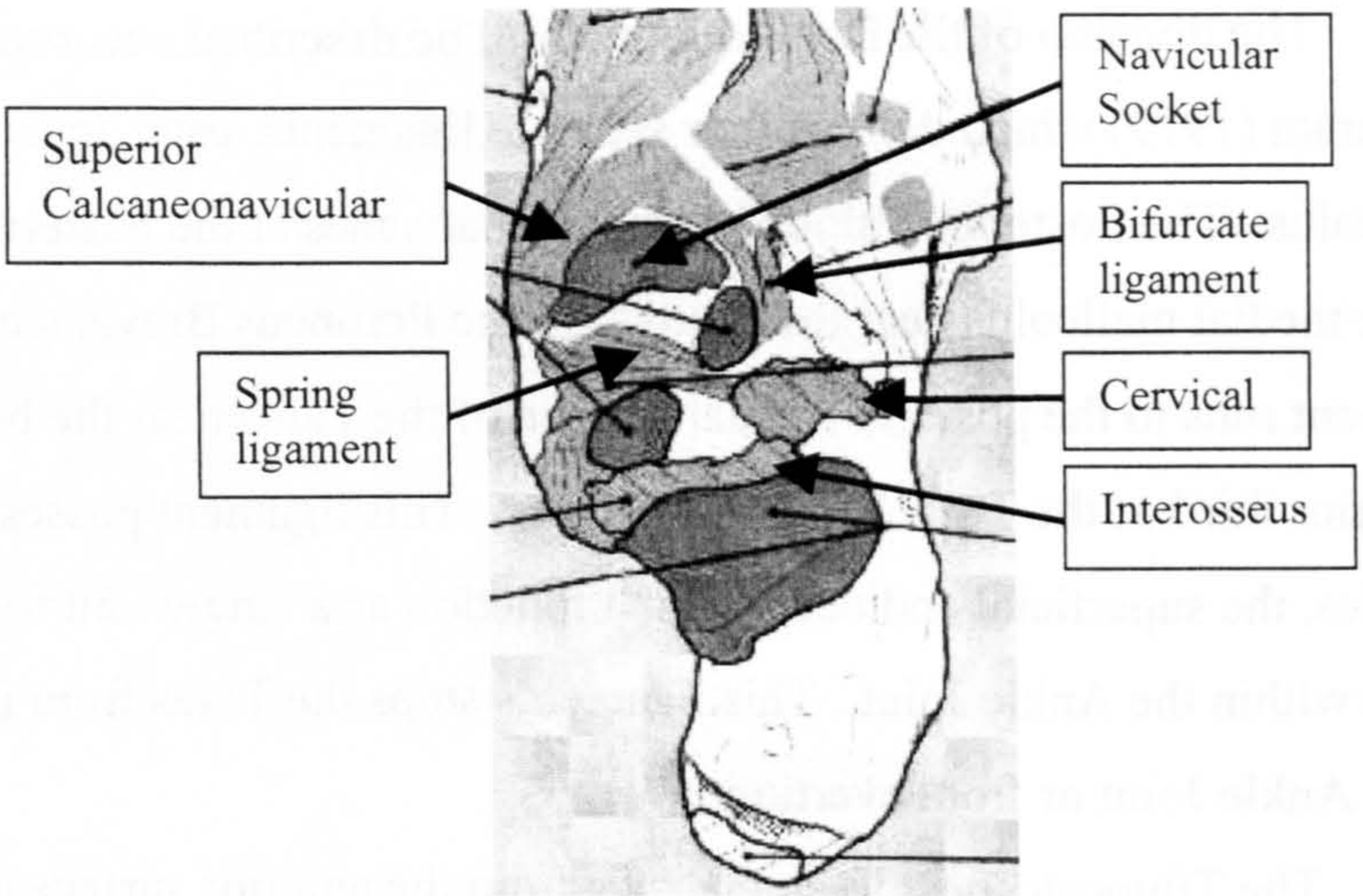

Figure 1.1.3-3 Superior view of the Subtalar ligaments (Gosling, et al. 1993).

Subtalar Ligaments

There are a large number of ligaments which attach the Talus, Calcaneus, Navicular and Cuboid. These ligaments range in size and strength from minor thickenings of the subtalar joint capsules to large distinct cord and band-like ligaments. Four ligaments are particularly important in the constraint of Subtalar Joint motion: the Cervical, the Inter-osseus, and the Posterior and Medial Talocalcaneal ligaments.

The Cervical ligament is the strongest of the ligaments joining the Talus to the Calcaneus. This ligament runs from the anterio-medial aspect of the floor of the sinus tarsi on the Calcaneus to the inferior aspect of the Talar neck. The Cervical ligament is shaped like a narrow rectangular band. The wide and flat Interosseus ligament is located medially to the Cervical ligament in the canalis tarsi. The ligament is oblique in its orientation as it runs from the sulcus calcanei of the Calcaneus to the sulcus tali. The medial fibres of this ligament are shorter than the lateral fibres, and the ligament fills the width of the canalis tarsi. Figure 1.1.3-3 shows the Cervical and Interosseus ligaments.

The Posterior and Medial Talocalcaneal ligaments are located at the posterior aspect of the Subtalar Joint. The Posterior Talocalcaneal ligment is broad and flat and attaches to the apex of the lateral posterior tubercle of the Talus. It runs inferiorly and posteriorly down to the posterior third of the superior surface of the Calcaneus. The Medial Talocalcaneal ligament attaches to the apex of the medial posterior tubercle of the Talus and runs to the sustenaculum tali on the Calcaneus. This ligament is thick, short and very strong.

Three other ligaments are involved in the Subtalar Joint. While they do not act to constrain its motion, they do complete the concave shape of the Navicular Socket surface with which the Talar head articulates. These ligaments are the Calcaneonavicular component of the Bifurcate ligament and the Superior and Plantar Calcaneonavicular ligaments. The Bifurcate ligament runs in a V-shape from the anterio-medial aspect of the sinus tarsi of the Calcaneus. The ligament has two components: the Calcaneonavicular and the Calcanealcuboidal. The

Calcaneonavicular component attaches to the lateral and plantar aspects of the Navicular Socket surface. This fibres of this ligament component form part of the floor of the concave Socket surface.

The Superior Calcaneonavicular ligament runs from the the anterior and medial aspects of the sustenaculum tali of the Calcaneus. It is directed upward and around the Talar head and attaches to the supero-medial aspect of the Socket surface. This ligament forms the medial aspect of the Navicular Socket. The Plantar Calcaneonavicular ligament, or *Spring ligament* is the strongest of the three. It also plays a large role in the maintenance of the longitudinal arch of the foot. This ligament runs from the inferior surface of the Calcaneus, anterior to the sustenaculum tali and is direct upward to its attachment on the plantar aspect of the Socket surface. This ligament forms the plantar aspect of the Navicular Socket.

1.1.4 The Retaining Structures of the Ankle Complex

Very few of the muscles acting about the Ankle and Subtalar Joints of the Ankle Complex exert tension along a straight line from origin to insertion. Most of the muscles possess one or two pulley points where the tendon of the muscle changes direction as it passes over a bone surface or under a retaining structure. There are four retaining structures in the Ankle Complex: the Superior and Inferior Extensor Retinacula and the Superior and Inferior Peroneal Retinacula.

Extensor Retinacula

The Extensor Retinacula changes the direction of the extrinsic ankle and toe extensor tendons. The extrinsic muscles are those that originate on the leg but insert on the foot. The Superior Extensor Retinaculum is continuous with the superficial aponeurosis of the lower leg and can be considered a thickening of this aponeurosis rather than a completely separate ligament. This structure runs transversely across the anterior surface of the distal lower leg. It attaches laterally to the lateral crest of

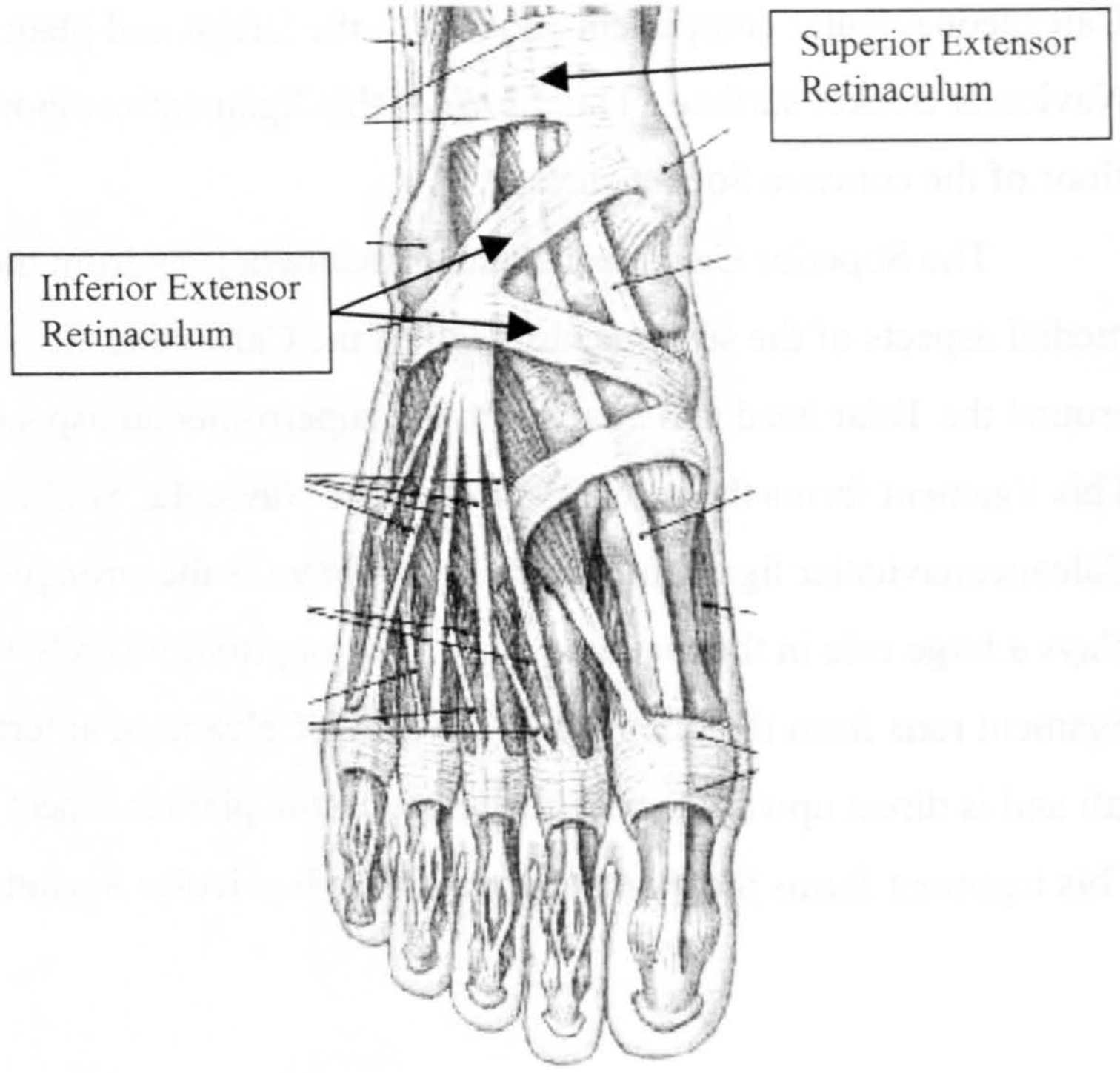

Figure 1.1.4-1 Dorsal view of the Superior and Inferior Extensor Retinacula (Martini, 1995).

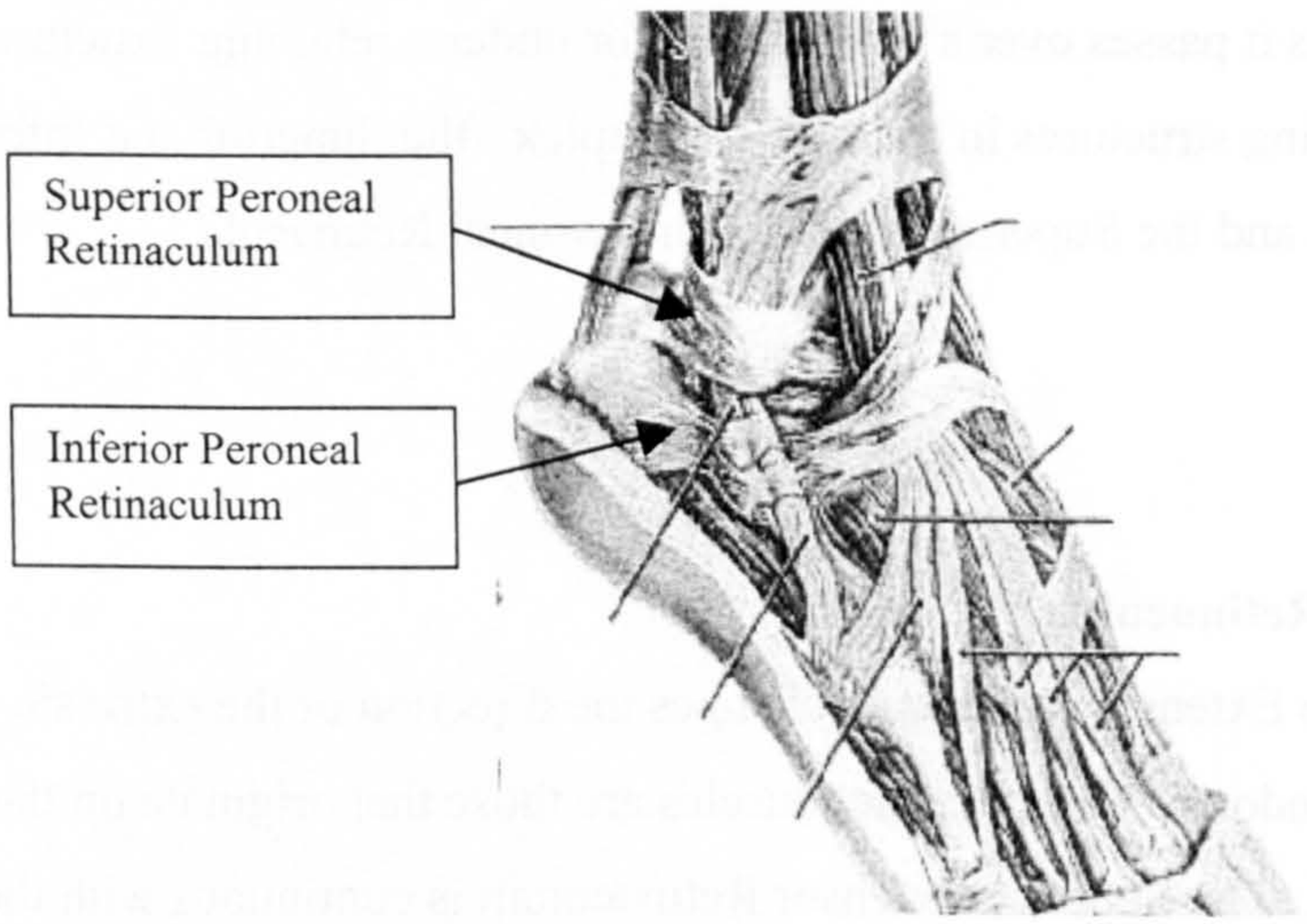

Figure 1.1.4-2 Lateral view of the Superior and Inferior Peroneal Retinacula (Moore, 1992).

the Fibula and the lateral aspect of the lateral malleolus. The medial attachment is the anterior crest of the Tibia and the medial malleolus. The Superior Extensor Retinaculum is illustrated in Figure 1.1.4-1. This retaining structure acts as a pulley point for four muscle tendons: Tibialis Anterior, Peroneus Tertius, Extensor Digitorum Longus and Extensor Hallucis Longus.

The Inferior Extensor Retinaculum is distinct from the surrounding dorsal foot aponeurosis. This retaining structure is Y-shaped and covers the dorsal surface of the midfoot and Talus. The Inferior Extensor Retinaculum is attached medially at the anterior surface of the medial malleolus and the medial aspect of the Navicular-First Cuneiform joint in the midfoot. The single lateral attachment runs from the lateral surface of the lateral malleolus to the floor surface of the sinus tarsi on the Calcaneus. This provides pulley points for the two extrinsic toe extensors: Extensor Digitorum Longus and Extensor Hallucis Longus.

Peroneal Retinacula

The two Peroneal Retinacula both act as retaining structures for the Peroneal Longus and Brevis tendons. While the pulley points for these tendons are supplied by a shallow groove in the posterior surface of the lateral malleolus, the Retinacula ensure that the tendons remain in position. The Superior Peroneal Retinaculum is the shorter and more distinct of the two. It attaches at the lateral border of the posterior malleolar groove for the Peroneal tendons on the Fibula and extends down to the posterior edge of the lateral surface of the Calcaneus, close to the insertion of the Achilles tendon.

The Inferior Peroneal Retinaculum is a continuation of the lateral, inferior branch of the Inferior Extensor Retinaculum. Its medial attachment is in the sinus tarsi, on the superior surface of the Calcaneus, where the Inferior Extensor Retinaculum attaches. It extends inferiorly to the lateral malleolus and attaches to the lateral surface of the Calcaneus, anterior to the attachment of the Superior Peroneal Retinaculum. These two retaining structures are shown in Figure 1.1.4-2.

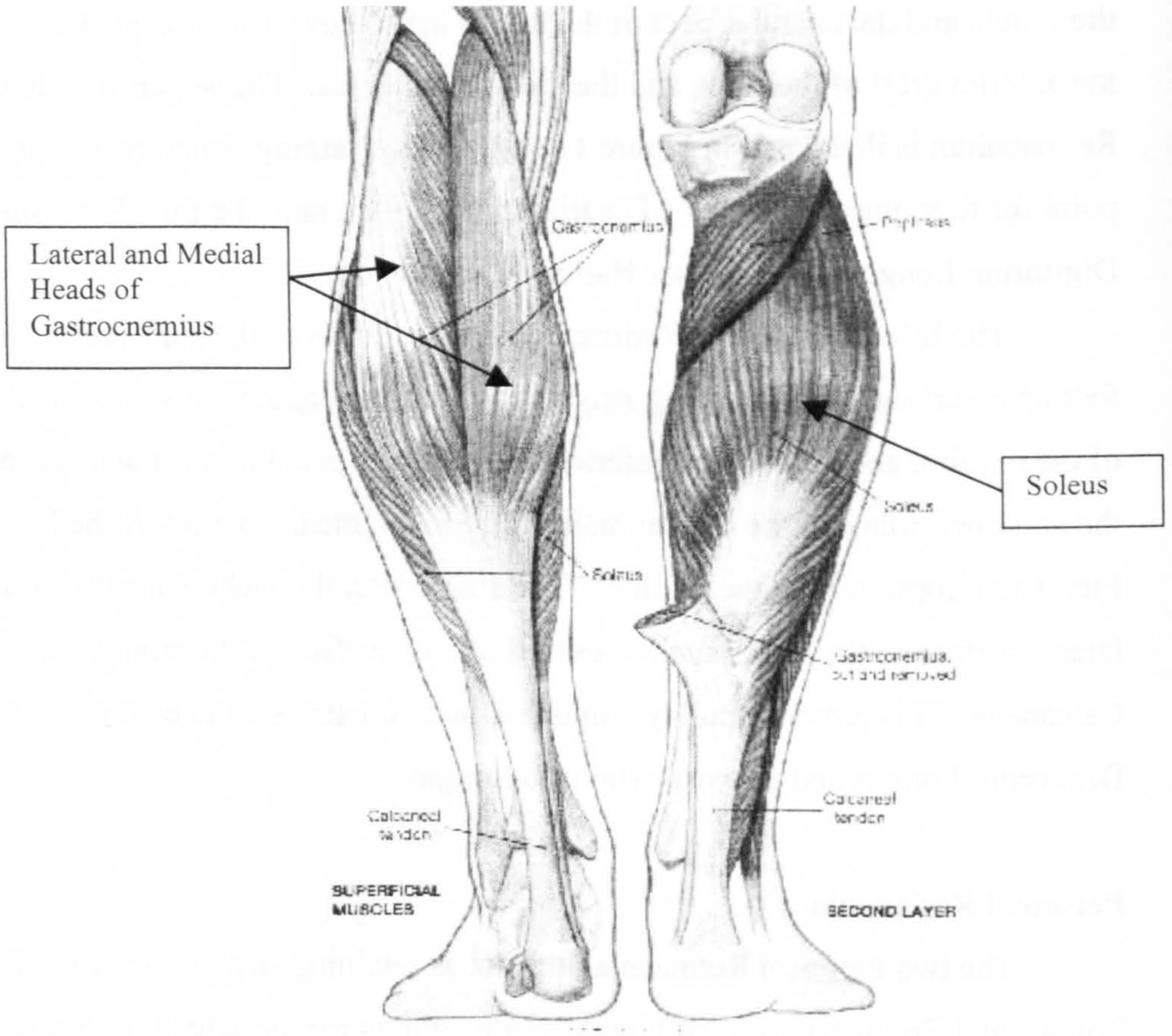

Figure 1.1.5-1 Posterior view of the Triceps Surae muscles: Gastrocnemius and Soleus (Martini, 1995).

1.1.5 Muscles and Tendons of the Ankle Complex

The muscles of the ankle and foot are classified as either intrinsic or extrinsic. The intrinsic muscles are those that both originate and insert on the foot. These muscles therefore do not exert any influence over the Ankle or Subtalar Joints. The extrinsic muscles insert on the foot but originate on the leg. These are the muscles which actuate the Ankle Complex joints. The eleven extrinsic muscles are subdivided into four groups based on location: the Triceps Surae, the Peroneal and the Anterior and Posterior Tibial groups.

Triceps Surae Group

This group contains the two largest muscles of the Ankle Complex: the Gastrocnemius and the Soleus. These muscles are unique in that they share a common tendon, the Achilles tendon, which inserts on the posterior edge of the anterior surface of the Calcaneus. They also have no pulley points and their lines of action run straight from insertion to origin. These muscles are located superficially on the posterior side of the lower leg. The two are illustrated in Figure 1.1.5-1.

The Gastrocnemius muscle has two distinct heads and lies superficially to the Soleus. This muscle crosses the Knee Joint as well as the Ankle Complex and originates on the posterior surface of the distal Femur. Soleus lies deep to Gastrocnemius and originates on the posterior aspect of the proximal third of the Tibia and Fibula.

The Triceps Surae muscles are both strong plantar-flexors and weak invertors. The effects of the Triceps Surae muscles are listed in Table 1.1.5-1, along with the effects of the other extrinsic muscles. The Gastrocnemius muscle is a propulsive muscle and contibutes greatly to the plantar-flexing moment of the foot required during the push-off phase of walking. The Soleus fulfils a propulsive role like the Gastrocnemius, but it is also influential in the maintenance of posture.

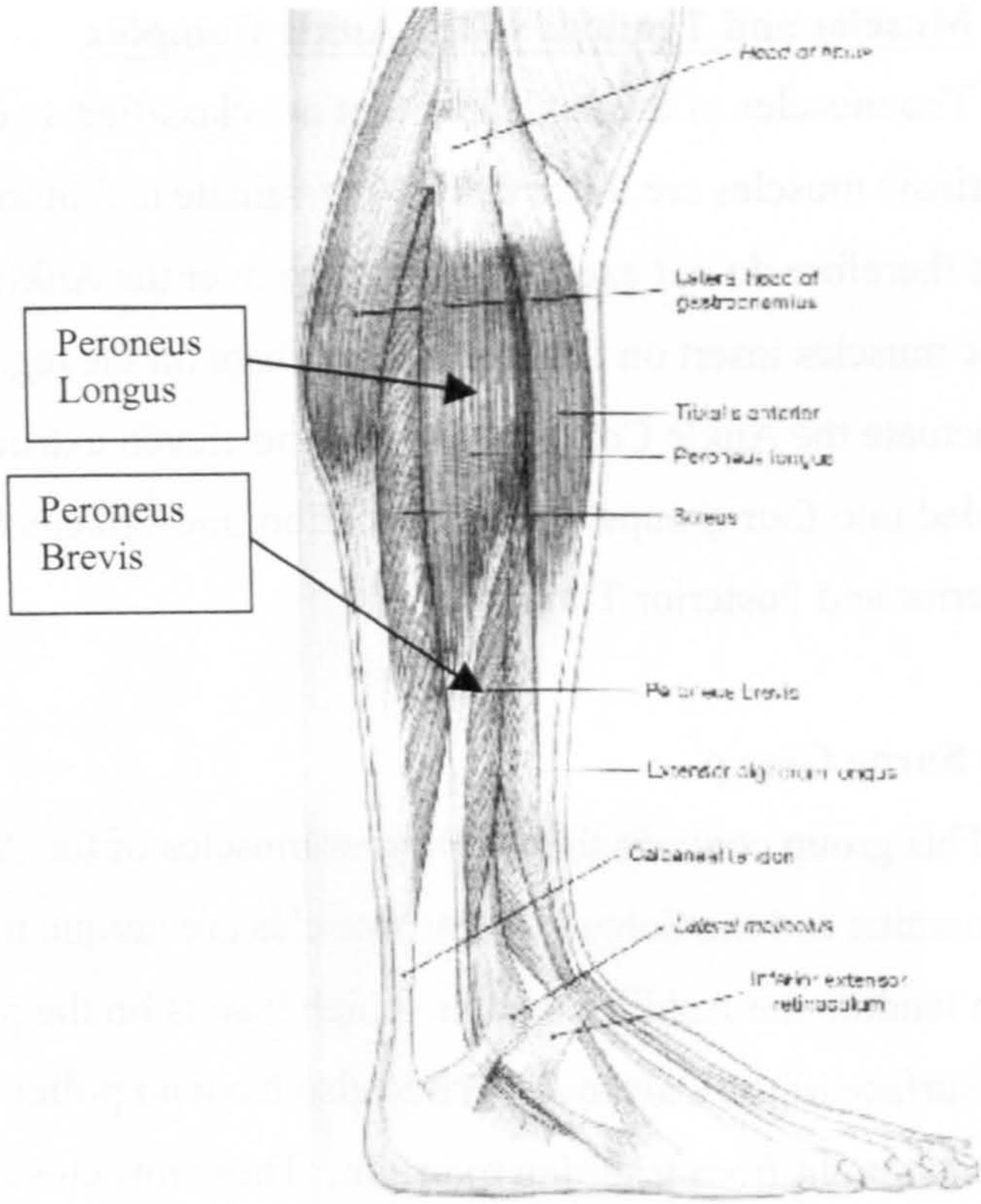

Figure 1.1.5-2 Lateral view of the Peroneal muscles: Peroneus Longus and Peroneus Brevis (Martini, 1995).

Group	Muscle	Ankle Joint	Subtalar Joint
Triceps Surae	Gastrocnemius	Plantar-flex	Invertor
	Soleus	Plantar-flex	Invertor
Peroneal	Peroneus Longus	Plantar-flex	Evertor
	Peroneus Brevis	Plantar-flex	Evertor
	Peroneus Tertius	Plantar-flex	Evertor
Anterior Tibial	Tibialis Anterior	Dorsi-flex	Invertor
	Extensor Digitorum Longus	Dorsi-flex	Evertor
	Extensor Hallucis Longus	Dorsi-flex	Evertor
Posterior Tibial	Tibialis Posterior	Plantar-flex	Invertor
	Flexor Digitorum Longus	Plantar-flex	Invertor
	Flexor Hallucis Longus	Plantar-flex	Invertor

Table 1.1.5-1 The Muscles of the Ankle Complex and their effects about the Ankle and Subtalar Joints.

Peroneal Group

Three muscles make up the Peroneal group: the Peroneus Longus, Brevis and Tertius. The Longus and Brevis are the two largest of the group. These are shown in Figure 1.1.5-2. The Peroneus Longus and Brevis originate on the lateral surface of the Fibula, with the Longus originating more posteriorly and proximally than Brevis. The Peroneus Brevis lies deep to Longus and runs along the long shaft of the Fibula from its origin to a groove on the posterior surface of the lateral malleolus. From this pulley point, the tendon of Brevis is directed anteriorly and distally to the lateral prominence on the base of the Fifth Metatarsal were it inserts. The Peroneus Longus, from its origin, runs down the down the long shaft of the Fibula, superficially to Brevis, and has a pulley point *on* the Brevis tendon at the posterior

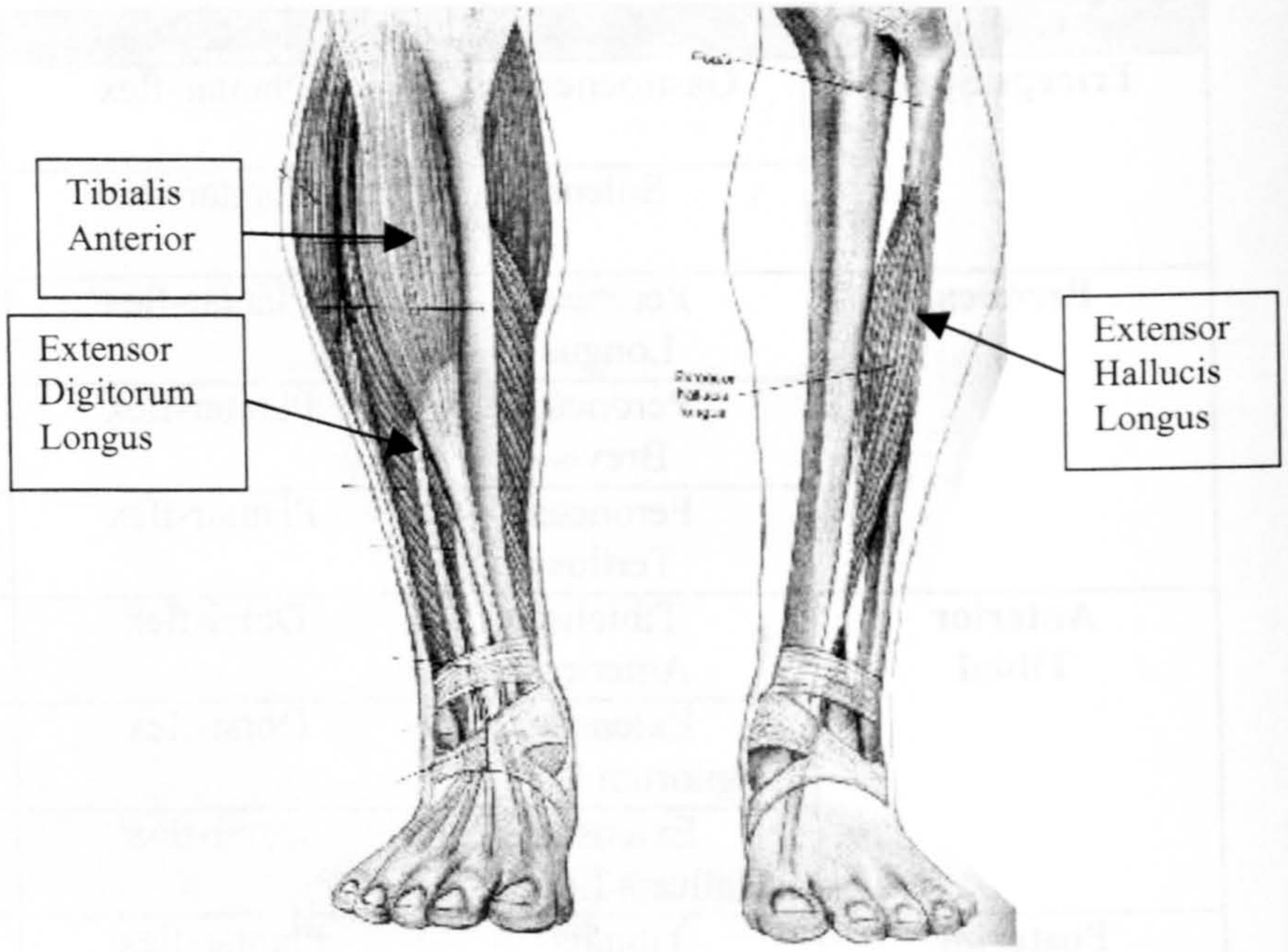

Figure 1.1.5-3 Anterior view of the Anterior Tibial muscles: Tibialis Anterior, Extensor Digitorum Longus and Extensor Hallucis Longus (Martini, 1995).

lateral malleolus. The tendon is then directed anteriorly and distally to a groove on the lateral border of the Cuboid were the tendon turns again and passes under the plantar surface of the midfoot. The Peroneus Longus tendon then inserts on the medial, plantar aspect of the First Cuneiform and the base of the First Metatarsal. The Peroneus Longus and Brevis muscles are both strong evertors and weak plantar-flexors. The Peroneus Longus has a propulsive role during locomotion and the Brevis is more of a postural muscle (Moore, 1992).

The Peroneus Tertius is distinct from the Lonus and Brevis since it originates on the distal third of the anterior surface of the Fibula. It is sometimes considered to be a part of the Extensor Digitorum Longus muscle. The Tertius runs down the anterior surface of the Fibula lateral to the Extensor Digitorum Longus and passes under the Superior Extensor Retinaculum. From this pulley point, the tendon is directed anteriorly and distally where it inserts on the dorsal aspect of the Fifth Metatarsal base. Since the Peroneus Tertius runs anterior to the lateral malleolus, this muscle primarily a dorsi-flexor and a weak evertor. Due to the size of the Peroneus Tertius muscle belly and the effective lever arm of the tendon about the two joints of the Ankle Complex, this muscle has only a weak influence. The effects of all the muscles about the Ankle Complex is summarised in Table 1.1.5-1.

Anterior Tibial Group

There are three muscles in the Anterior Tibial group: Tibialis Anterior, and the two toe extensors, Extensor Digitorum Longus and Extensor Hallucis Longus. These three muscles are shown in Figure 1.1.5-3. The Tibialis Anterior originates on the lateral, anterior surface of the Tibia. It runs down the long shaft of the Tibia from its origin and passes under the Superior Extensor Retinaculum. The tendon is then directed from this pulley point to its insertion on a tubercle on the inferior, medial surface of the First Metatarsal base. This muscle is the strongest of the dorsi-flexors and an invertor.

The Extensor Hallucis Longus originates on the medial, anterior surface of the Fibula and on the Interosseus Membrane. This muscle runs deep to the Tibialis Anterior and Extensor Digitorum Longus. The tendon passes under the Superior and

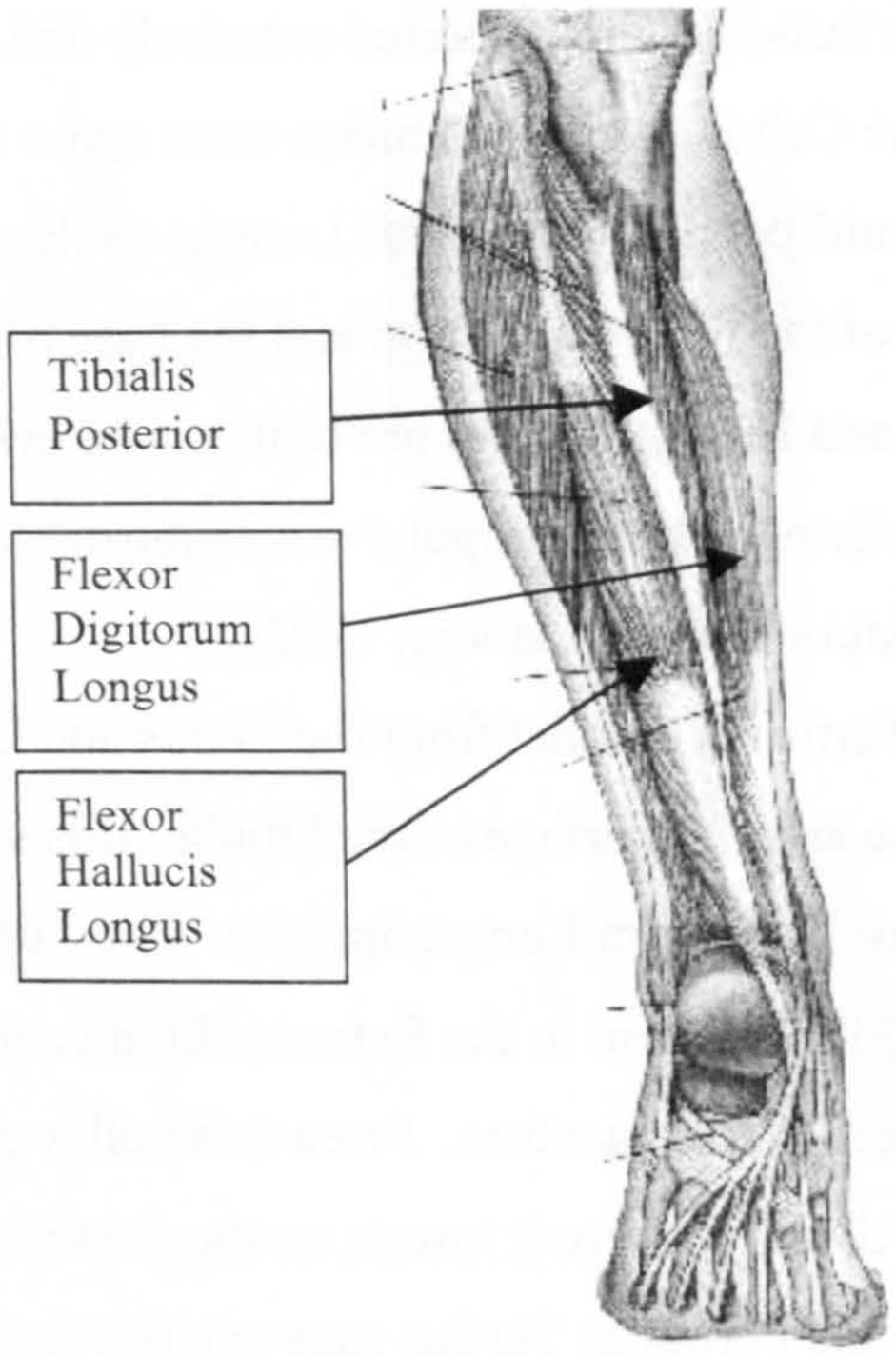

Figure 1.1.5-4 Posterior view of the Posterior Tibial muscles: Tibialis Posterior, Flexor Digitorum Longus and Flexor Hallucis Longus (Martini, 1995).

Inferior Retinacula and runs along the medial side of the First Metatarsal until it inserts on the dorsal surface of the Distal Hallucal Phalanx. In addition to extending the great toe, this muscle also acts as a relatively strong dorsi-flexor and a very weak evertor.

The Extensor Digitorum originates on the proximal third of the lateral, anterior surface of the Fibula. It passes down the long shaft of the Fibula, lateral to Tibialis Anterior and medial to Peroneus Brevis, and passes under both the Superior and Inferior Extensor Retinacula. Under the Inferior Extensor Retinaculum, the tendon splits into four separate tendons which travel down the rays of the Second to Fifth Metatarsals and each inserts variously on the dorsal surfaces of the Phalanges of the lesser toes. In addition to extending the lesser toes, this muscle is a strong dorsi-flexor and a weak evertor. The effects of each of these muscles are listed in Table 1.1.5-1. Each of the muscles of this group is active both during locomotion and in the maintenance of posture.

Posterior Tibial Group

The three muscle of the Posterior Tibial group all lie deep to the Triceps Surae group and are much smaller than the Gastrocnemius and Soleus muscles. The muscles of this group are: Tibialis Posterior, and the two toe flexors, Flexor Digitorum Longus and Flexor Hallucis Longus. Figure 1.1.5-4 illustrates these three muscles. The Flexor Hallucis Longus lies deep to the other two muscles of this group and originates on the posterior surface of the distal third of the Interosseus Membrane. It runs down the posterior surface of the Interosseus Membrane and over a groove on the posterior surface of the Talus, between the lateral and medial posterior tubercles. From this pulley point, the tendon runs inferior to the sustenaculum tali and along the plantar surfaces of the midfoot and forefoot bones. The tendon inserts on the plantar aspect of Distal Hallucal Phalanx. This muscle, in addition to flexing the great toe, is a weak plantar-flexor and invertor.

The Flexor Digitorum Longus originates on the medial aspect of the middle third of the posterior Tibial surface. It runs parallel and medial to the Hallucis Longus tendon and passes over a groove in the posterior surface of the medial

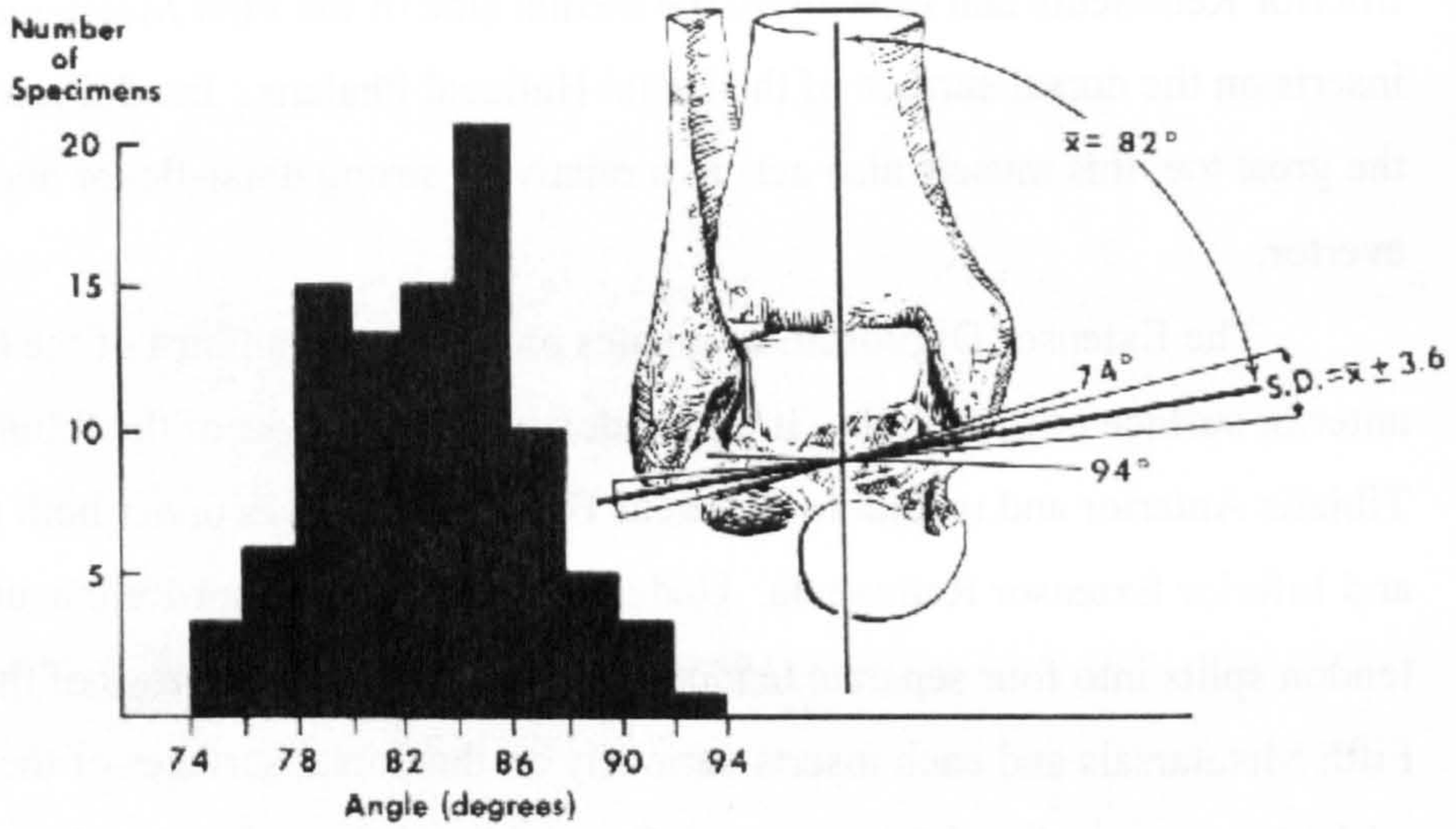

Figure 1.2.1-1 Variability between individuals of the orientation of the Ankle Joint Rotational Axis in the normal population (Inman, 1976).

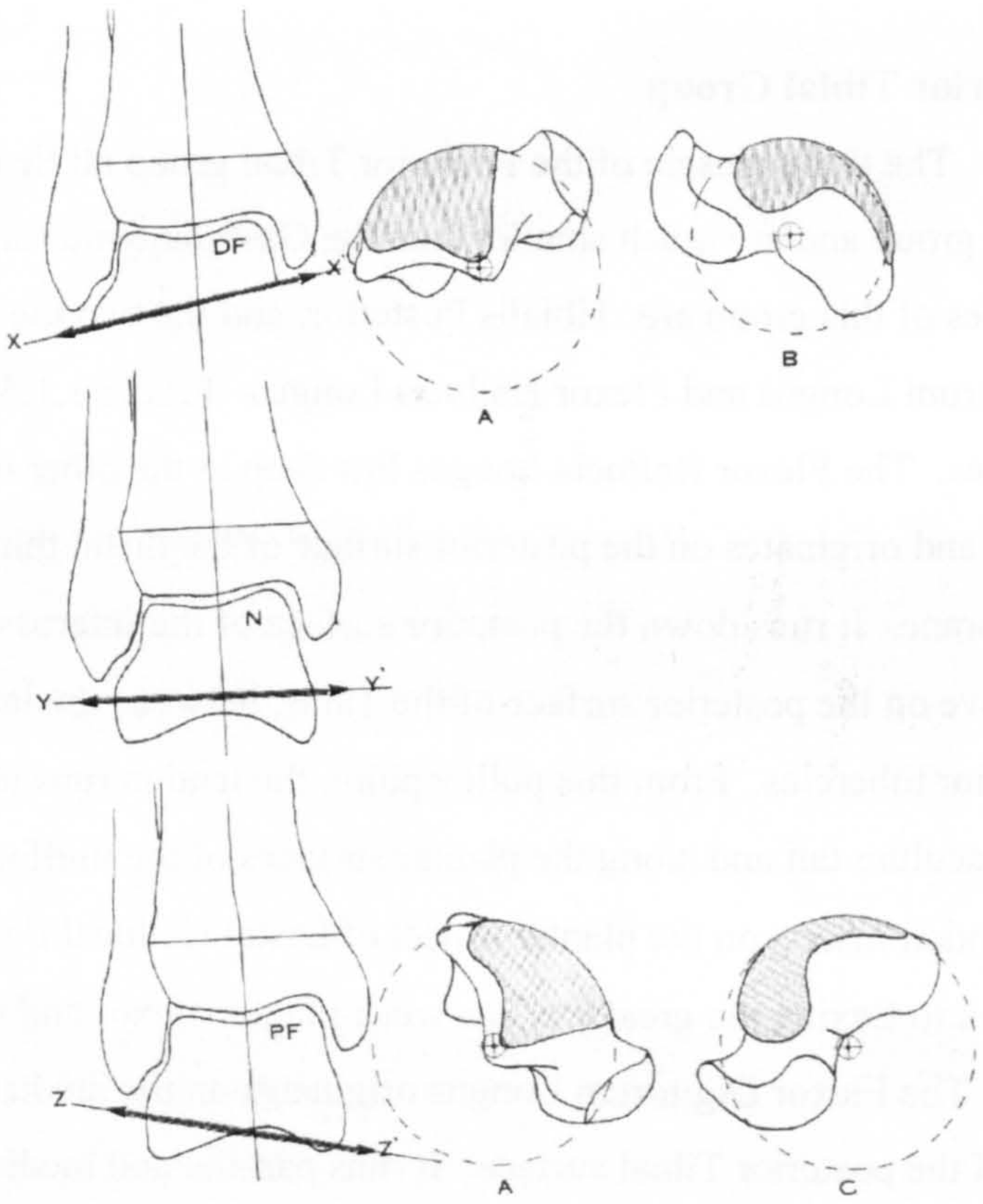

Figure 1.2.1-2 Migration of the Ankle Joint Rotational Axis as the Talus moves through its Range of Motion (Barnett, et al. 1952 in Sarrafian, 1983).

malleolus and under the sustenaculum tali. From here, the tendon splits into four which each travel along the plantar surfaces of the rays of the Second to Fifth Metatarsals. The tendons each insert on the plantar aspects of the Phalanges of the lesser toes. This muscle primarily flexes the four lesser toes. Secondarily, it is a weak plantar-flexor and very weak invertor.

The third muscle of the group is the Tibialis Posterior. This muscle originates on the proximal and middle thirds of the posterior surface of the Interosseus Membrane. It runs superficially to the Flexor Hallucis Longus down the posterior Tibia and passes over a groove in the posterior surface of the medial malleolus and under the sustenaculum tali of the Calcaneus. The tendon then splits into three components which variously insert on the plantar surfaces of the tuberosity of the Navicular, the Second and Third Cunieforms and the Cuboid bones. This muscle is a weak plantar-flexors and a very weak invertor. Each of the three muscles of the Posterior Tibial group are active in the maintenance of standing posture. However, due to the size of the three muscle bellies and the small lever arms that each possess about the joints of the Ankle Complex, they exert very little influence during the propulsive phase of locomotion (Moore, 1992).

1.2 FUNCTIONAL ANATOMY OF THE ANKLE COMPLEX

1.2.1 Motion of the Ankle Joint

The Ankle Joint is formed by the articulations between the Tibial Mortice surface and the Talar Trochlear surface and between the Medial and Lateral Malleolar surfaces of the Tibia-Fibula and Talus. The two malleoli form a fork within which the Talus is tightly held. The Mortice surface is concave and the Trochlea convex, so the Talus tends to rotate about an axis that runs generally medial to lateral. The axis of the Ankle Joint has been located in various cadaver studies performed on fresh and unfixed tissue (Inman, 1976, Sammarco et al., 1973).

Inman showed the axis of rotation for the Ankle Joint to run just distal to the tip of the medial malleolus at 5±3 mm below and just lateral and anterior to the tip of

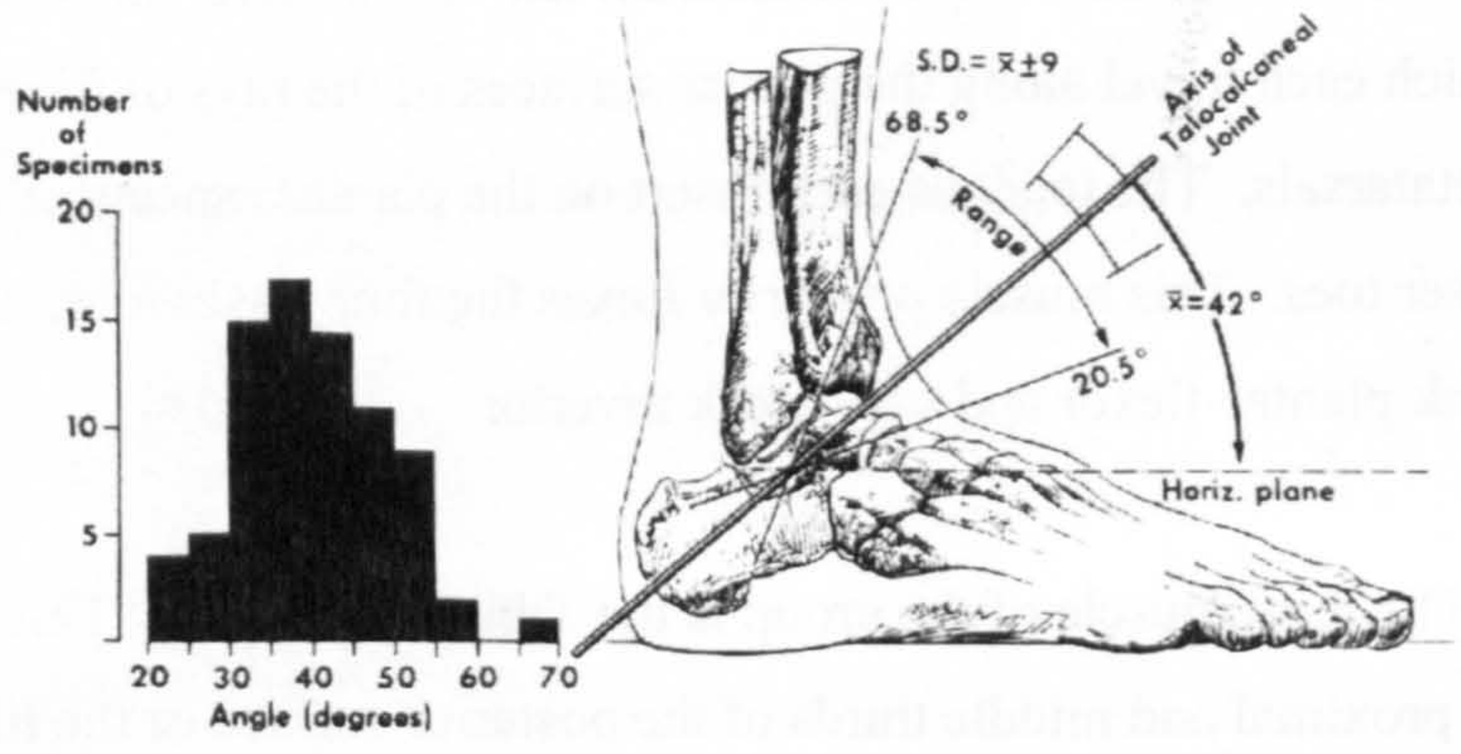

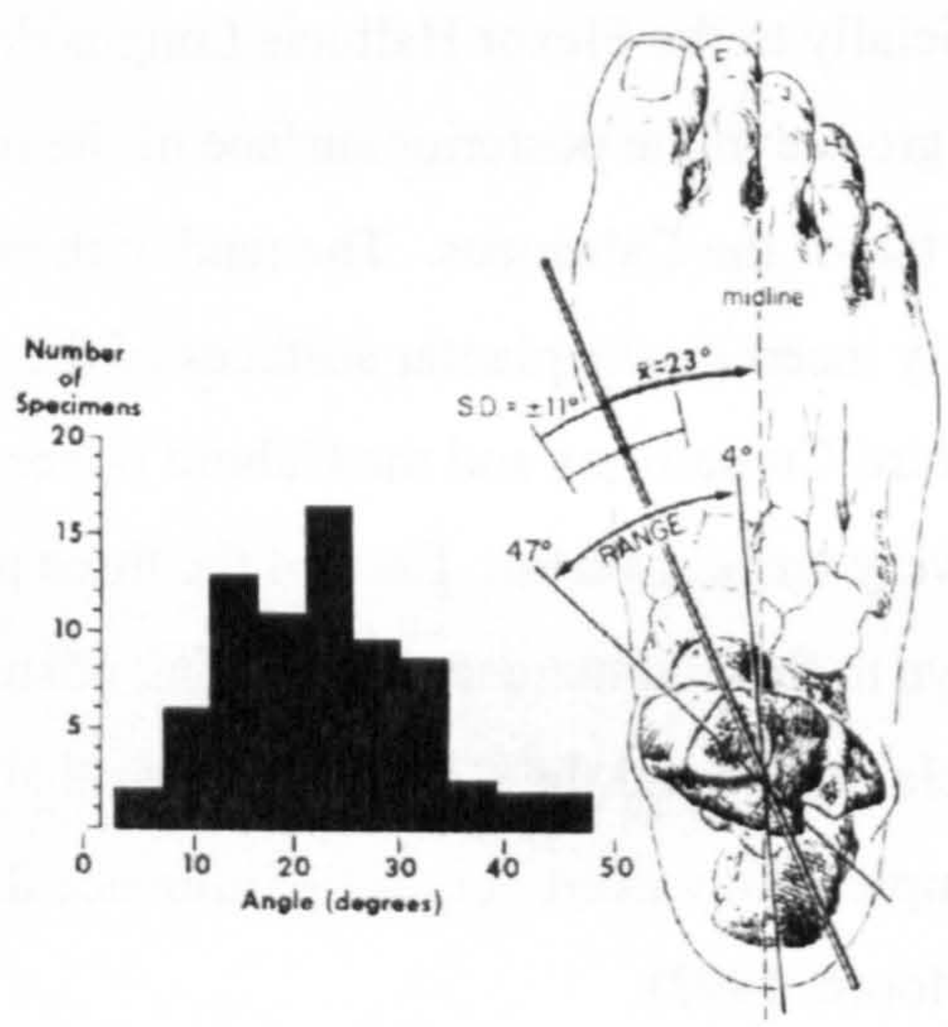

Figure 1.2.2-1 Variability between individuals of the orientation of the Subtalar Joint Rotational Axis in the normal population (Inman, 1976).

the lateral malleolus at 3±2 mm below and 8±5 mm to the anterior. The axis is therefore oriented distally and laterally in the frontal plane and postero-laterally in the transverse plane. This orientation of the axis is plotted in Figure 1.2.1-1. Note the variation in the position of the axis from the Inman study. The angle of the axis with respect to vertical in the frontal plane was on average 82.7° with a range from 74° to 94°. The major motion allowed by the Ankle Joint is dorsi- and plantar-flexion of the foot. However, since the rotational axis is not horizontal and transverse, there are small amounts of foot abduction and adduction coupled to dorsi-flexion and plantar-flexion.

In a cadaveric study done by Barnett, et al. (1952), this axis was shown to migrate as the Ankle Joint moved through its range of motion. This is illustrated in Figure 1.2.1-2. When in a dorsi-flexed position, the axis is oriented downward laterally. As the foot moves into neutral, the axis migrates into a more horizontal position and in full plantar-flexion the axis is oriented upward laterally in the frontal plane. The reason for this was identified in the Barnett study as being anatomical. The radius of curvature of the lateral border of the Talar Trochlea surface in the sagittal plane is larger than that of the medial border. The surface of the lateral border is almost circular through all of its arch in the sagittal plane. However, the curvature of the medial border of the surface is not circular. The radius of curvature of the anterior portion of the medial border is smaller than the posterior portion. The radius of curvature of the medial border goes from being smaller than the lateral and its anterior portion to being almost equal in its posterior portion. Therefore, as the Talus moves through its range of motion and the radius of curvature of the portion of surface in contact with the Mortice changes, the axis of rotation migrates.

Mathematical models of the migration of the Ankle Joint rotational axis have shown that the behaviour of the axis in the sagittal plane is well predicted in an unloaded state when the surfaces are considered to be held together by a multi-bar linkage (Leardini et al, 1999a, Glitsch and Baumann, 1997).

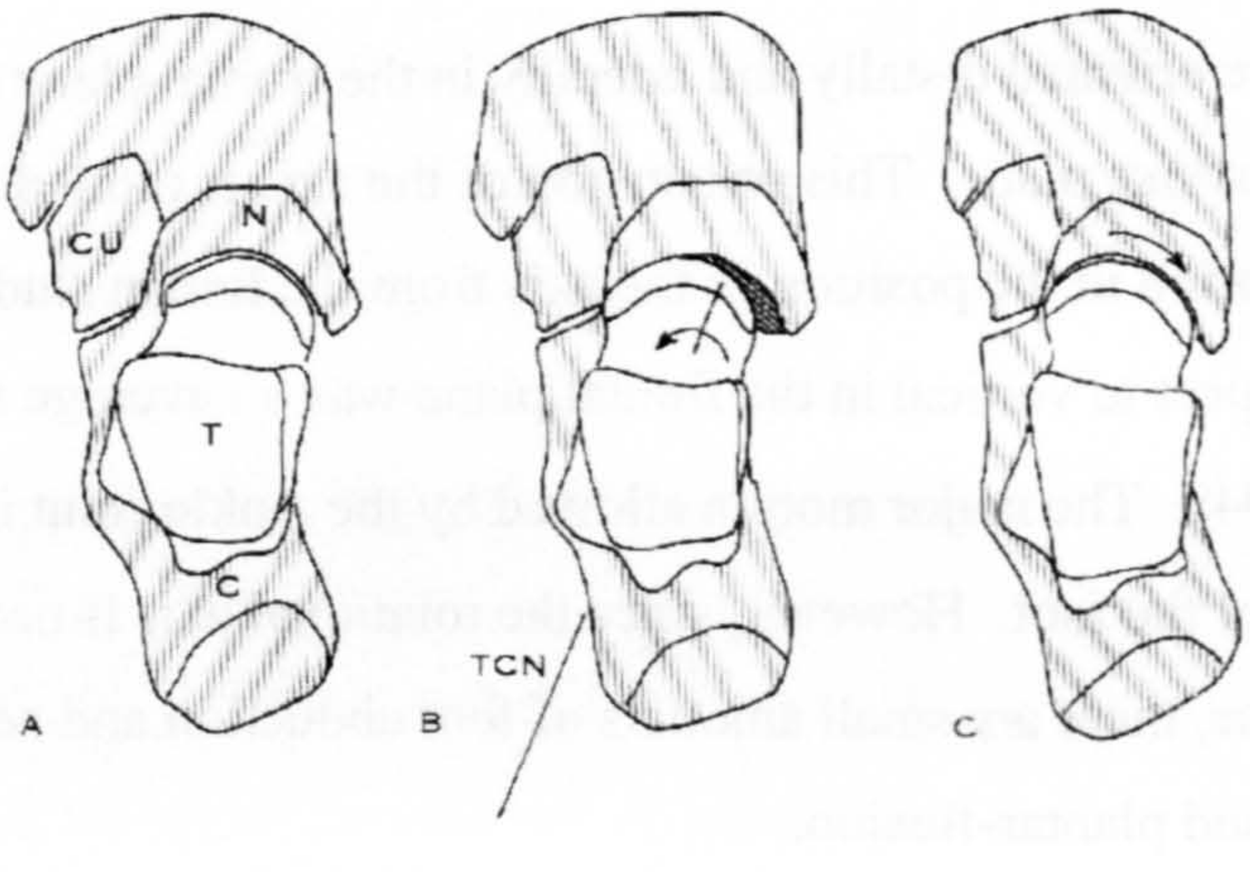

Figure 1.2.2-2 Movement of the Navicular with respect to the Talar Head as the foot moves from eversion (A) into inversion (C). Dislocation of Talus-Navicular articulation resulting this movement is not allowed (Huson, 1961).

1.2.2 Motion of the Subtalar Joint

The Subtalar Joint is composed of the articulations between the Posterior and Middle Talocalcaneal surfaces and between the Talar Head and Navicular Socket. The axis of rotation is oriented generally posterior to anterior, moving supero-medially as it travels anteriorly. Cadaver studies by Inman (1976) demonstrated the variability in the orientation of the axis in normal populations. This is plotted in Figure 1.2.2-1. The angle of the axis from horizontal in the sagittal plane was on average 42° with a range of 20.5° to 68.5°. The angle of the axis with respect to the midline of the foot in the transverse plane was an average 23° with a range of 4° to 47°. The axis passed through the anterio-medial border of the Posterior Talocalcaneal surface of the Calcaneus and through the medial border of the superior surface of the Talar neck. The motions allowed by the joint are inversion and evertion. Unlike the Ankle Joint rotational axis, the axis of the Subtalar Joint does not seem to migrate as the joint moves through its range of motion.

The geometry of the Navicular Socket surface is not congruent with the Talar Head surface. Therefore, as the Subtalar Joint moves through its range of motion, the midfoot bones, the Navicular and Cuboid, rotate with respect to the Calcaneus and Talus to avoid dislocation of the Socket-Head articulation (Huson, 1961). This is demonstrated in Figure 1.2.2-2. This subtle motion between the hindfoot and midfoot can be considered as a part of the overall motion of the Subtalar Joint.

1.2.3 Motion of the Tarsometatarsal (Lisfranc's) Joint

The Tarsometatarsal Joint or *Lisfranc's Joint* of the foot is not part of the Ankle Complex. However, its motion has interesting influence on the loading of the Ankle and Subtalar Joints and on the positions and movements of the bones of these joints during locomotion. Lisfranc's Joint is formed by the zig-zag pattern of articulations between the distal surfaces of the three Cuneiforms and the Cuboid in the midfoot and the proximal surfaces of the bases of the five Metatarsals of the forefoot. The axis of this joint is generally directed medial to lateral across the foot at the level of these articulations. The type of movement that the joint allows the five

rays of the Metatarsal bones is rather interesting. This joint allows a pronation and a supination *twist* of the foot.

During a supination twist, the ray of the First Metatarsal is extended and the Fifth Metatarsal is flexed with respect to the midfoot. A pronation twist sees the First Metatarsal flexing and the Fifth Metatarsal extending with respect to the midfoot. Therefore, the forefoot group of bones, composed of the five Metatarsal *cannot* be treated as a rigid segment the way that the midfoot can. This forefoot twisting motion is crucial for the foot to change from a compliant, flexible structure during the landing portion of stance phase in locomotion into a rigid structure during the propulsive portion of stance.

CHAPTER 2 REVIEW OF PREVIOUS MODELS

2.1 MUSCLE MODELS AND EQUILIBRIUM MODELS

The model in the current study combines two different classes of model when determining the loading in the Ankle Joint Complex: a Muscle Model and an Equilibrium Model.

Muscle models are concerned with simulating tension production within individual muscles and groups of muscles. Modeled is the dependence of this tension on various external factors such as the level of neurological stimulation applied to the muscle, the instantaneous length and velocity of the muscle and the mechanisms of fatigue and different muscle pathologies.

Equilibrium models attempt to balance the external and internal forces and moments within a system of joint(s). The forces and moments arise externally from the loading environment of the system. The internal forces and moments arise from the load-bearing structures of the system, such as the muscles, ligaments and articular surfaces. These models are less interested in how each structure produces force or how each structure force is distributed within the structures, than they are interested in the relative force contributions of each of the structures necessary to produce equilibrium between internal and external loading.

2.2 PREVIOUS MUSCLE MODELS

The range of methods that have been devised to model the behaviour of skeletal muscle is wide and varied. The variety of models that have been used in the past reflects the enormous range of aspects of the behaviour of muscle that exist to be studied. This arises from the fact that the ability of skeletal muscle to produce tension is determined by its composition both microscopically and macroscopically. Skeletal muscle is composed of microscopic muscle cells which are able to collectively produce tensions at the macroscopic scale. The behaviour of muscle is

therefore governed by a variety of parameters which exist and exert influence at different scales from macroscopic down to microscopic.

The microscopic muscle cells are themselves composed of the basic functional unit of skeletal muscle, the *sarcomere*. The sarcomere is the smallest component of skeletal muscle that can produce tension when stimulated. The sarcomeres are composed of protein filaments, *myosin* and *actin* which are arranged in parallel running longitudinally along the sarcomere. The filaments are arranged in a regular three-dimensional geometry with the actin filaments overlapping the myosin. When stimulated, crossbridges on the myosin filaments attach to, flex and detach from the actin filaments. This cycle of actions walk the actin along the myosin, thereby shortening the sarcomere. When stimulated, the actin filaments attach to the myosin filaments with crossbridges and pull the actin past the myosin, thereby shortening the sarcomere. The microscopic process of sarcomere contraction is explained in more detail in McComas (1996). The microscopic physiology of the contracting sarcomere was not modelled in the present study. This description served only to introduce some of the aspects of muscle behaviour at the microscopic level.

Several thousand sarcomeres are arranged in series in each of the muscle fibres in the muscle belly. The muscle fibres are held together in position by fascicles, which are composed of elastic tissue. These fascicles maintain the relative positions of the muscle fibres during muscle contraction and also serve to attach the muscle to its tendon. The number of sarcomeres arranged in series has great influence over the behaviour of the individual fibres (Wickiewicz, et al., 1983, Wilkie, 1950). The greater the number of sarcomeres, the longer the muscle fibres and the faster the fibres are able to contract. The arrangement of the fibres within the muscle belly and the number of fibres arranged in parallel has great influence over the behaviour of the muscle belly (Wickiewicz, et al., 1983). The more fibres arranged in parallel, the greater the force that the muscle can produce. The orientation of the muscle fibres is defined by its *pennation angle* which is the angle between the direction of the fibres and the direction of the tendon. The geometry of the muscle attachment to its tendon defined by the pennation angle, influences the

behaviour of the entire muscle-tendon (Alexander and Ker, 1990, Lieber el al., 1992, Otten, 1988, Zajac, 1992).

The type of muscle model used is therefore decided by the *scale* of behaviour that is to be modelled. Models of individual sarcomeres and isolated muscle fibres would examine the function of the sliding filaments within the sarcomeres (Huxley, 1974). Parameters that would be involved in such sarcomere and fibre models would include the crossbridge behaviour, Ca^{2+} concentrations and the histological composition of the muscle fibres (Hatze, 1981). The modelling of muscle at this scale is dominated by the classic model developed by Huxley (1974), the *Sliding Filament Theory*. While this sort of model is well suited to examining the behaviour of sarcomeres and individual muscle fibres, it is far too complex and singularly unsuited to modelling muscle during locomotion and movement.

When modelling the behaviour of skeletal muscle at the scale of gross body movement, the muscle plus its tendon is usually modelled as a system of functional components. The primary component is the *contractile* component which represents the behaviour of all the muscle fibres of the muscle belly lumped together into a single unit. Other components have been added to the contractile component in various configurations. These additional components model the elastic tissue of the muscle belly and of the tendon. Depending on their arrangement, these are variously called *series* and *parallel elastic* components. Modelling the collection of muscle fibres as a single component was first devised by Hill (1938) and these type of lumped component muscle models are therefore often referred to as *Hill-type* models.

Hill-type models have been used to model the joint angle to moment relationship in a number of joints (Hof & van den Berg, 1981a, Winters and Stark, 1985) and more complex activities such as locomotion (Pandy and Anderson, 1999, White and Winter, 1993), reaching tasks (Winters and Van der Helm, 1994, Buchanan et al., 1993) and jumping (Pandy, et al, 1990). The arrangement of components used by various models has ranged from a single contractile component (White and Winter, 1993), two components: a contractile and series elastic component (Caldwell, 1995), three components: a contractile component, series

elastic and parallel elastic in various configurations (Winters and Stark, 1995, Durfee and Palmer, 1994, Hof and Van den Berg, 1981a) to four components: with two series elastic components, a contractile and parallel elastic component (Pandy and Anderson, 1999).

The common practice is to model the tension produced by the contractile component as being a function of three inputs: the level of muscle activation, the muscle length and the muscle velocity. The muscle activation level represents the amount of neurological stimulation coming from the central nervous system or from external electrical stimulation. Extra complexity has been added to the contractile component in order to model various other additional aspects of muscle behaviour. The dependence of activation level on neurone firing rate (Crago, 1992), muscle load history (van Zandwijk, et al, 1990), and eccentric loading behaviour (Krylow and Sandercock, 1997) have all been examined with Hill-type models. A good overview of the interdependence of the basic three contractile component parameters and the various additional parameters is given in Huijing (1995).

The complexity of a muscle model and the number and arrangement of components is decided by the aspect of the muscle behaviour that is of greatest importance and the tasks which the muscles are performing. The model should not be so simple that it is unable to demonstrate the aspect of behaviour that is of interest, yet the model should not be so complex as to hide the behaviour amongst others of lesser importance. Finally, the arrangement of components and the parameters governing their behaviour should be specific to the tasks being modelled (Winters, 1995, Winters and Stark, 1987).

2.3 JOINT EQUILIBRIUM MODELS

While the Knee and Hip Joints of the lower limb have both received much attention in terms of biomechanical modelling in the last thirty years, the Ankle Complex has been relatively neglected. After the seminal paper by Paul (1967) which demonstrated that the tensions in the muscles acting about a joint could create compression forces on the joint articulations that were several times body weight,

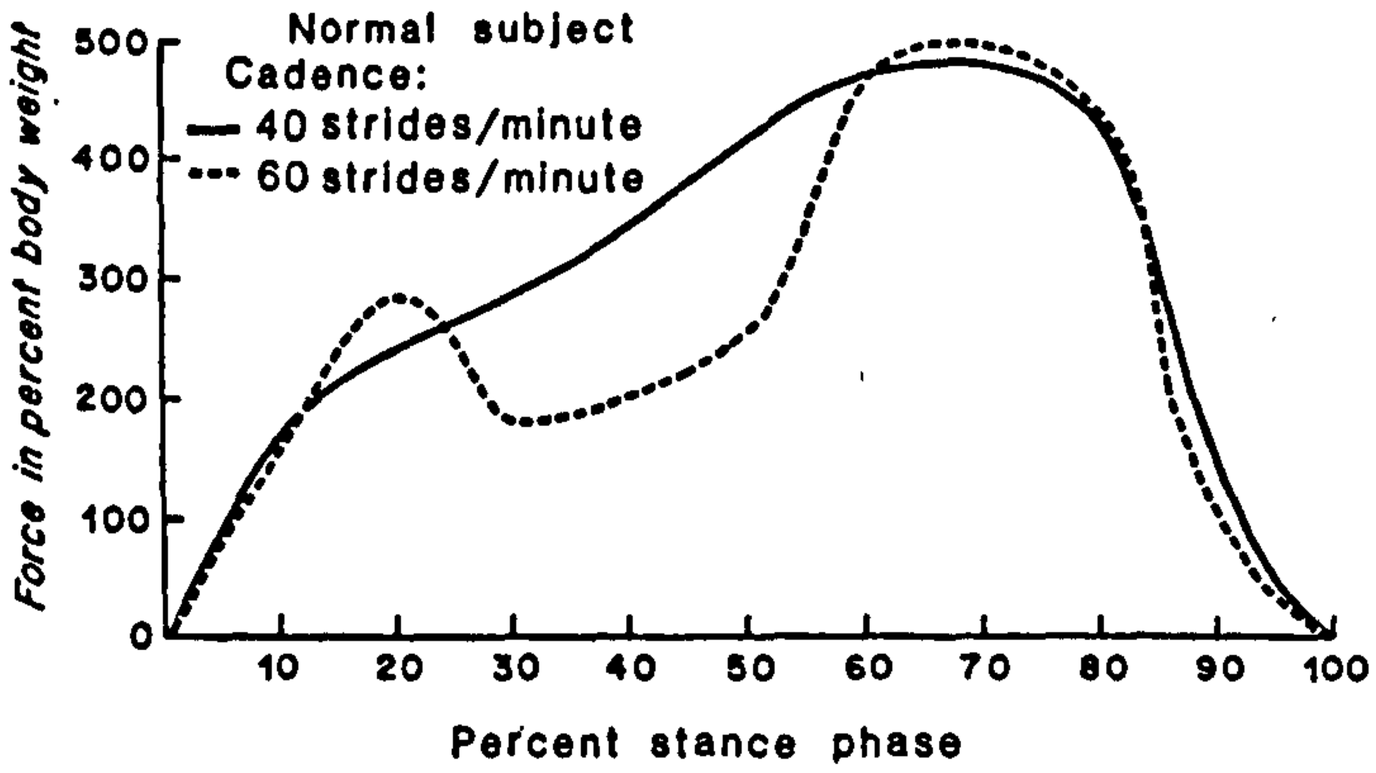

Figure 2.3-1 Joint compression forces at two different walking speeds as reported by Stauffer, et al, 1977.

only a handful of models were developed to examine the equilibrium of the Ankle Complex. The first attempts were two-dimensional models of the Ankle Joint in the sagittal plane (Brewster et al., 1974, Stauffer et al., 1977, Wynarsky and Greenwald, 1983). These models confined themselves to predicting the joint contact forces anterio-posteriorly and vertically and assumed a fixed rotational axis for the Ankle Joint that was perpendicular to the sagittal plane.

As was similar with each of these two-dimensional Ankle Joint models, the Stauffer model treated the foot as a single rigid segment in the sagittal plane. Since the model was confined to the sagittal plane, the Subtalar Joint could not be modelled. Only two groups of muscles were considered to act about the Ankle Joint, the calf muscles on the posterior side and the anterior tibial group on the anterior side, which acted as antagonists. No ligaments were included in the model and the Ankle Joint itself was assumed to be a simple hinge joint running perpendicular to the sagittal plane.

The input to the model was motion data taken from five normal males and nine subjects with ankle pathologies. The stance phase was subdivided into three sections: heel strike to heel raise, heel raise to toe strike, and toe strike to toe raise. The lines of action of the ground reaction force and the muscle tensions were defined separately for each of these stance sections. The solution for ankle loading equilibrium was *quasi-static*, meaning that the inertial effects of the foot segment were ignored as the foot was effectively consider massless.

The Stauffer model assumed nearly no antagonism about the Ankle Joint during stance phase. Therefore the anterior tibial group of muscles alone were actively tensed initially in stance phase during the application of an external, plantar-flexing moment. As stance phase progressed, the calf group of muscles became active and the anterior tibial group inactive, as the external ankle moment became dorsi-flexing. The model predicted peak joint compressive forces of as high as 5.5 times body weight (BW) occuring around 0.75 of stance phase. This joint loading was found to be independent of walking gait cadence, which ranged from 40 to 60 strides/minute. These results are plotted in Figure 2.3-1. The author noted that this joint compressive loading was larger than that predicted for the hip and knee joints in

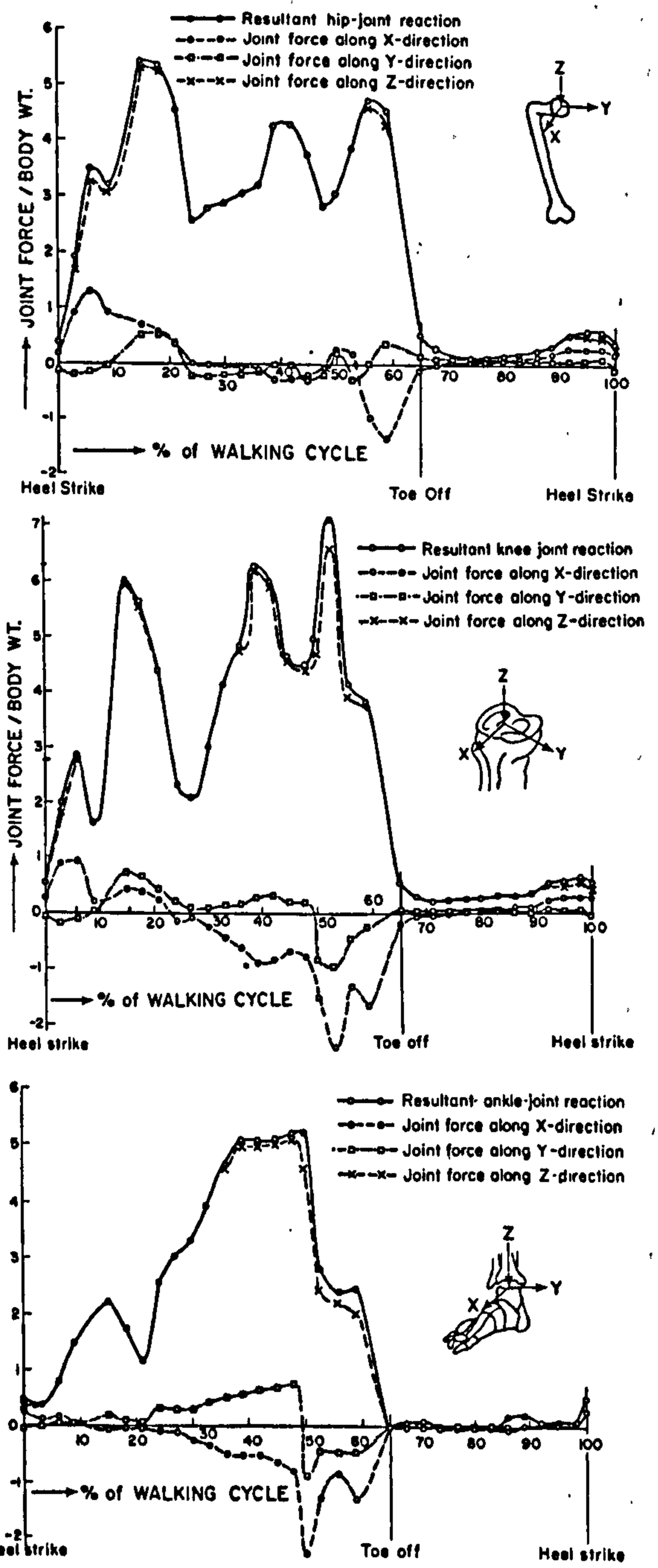

Figure 2.3-2 Joint compressive loading at the hip (top), knee (middle) and ankle (bottom) as calculated by the Seireg model (Seireg and Arvikar, 1975).

other biomechanical models and that this perhaps reflects the more robust role that the ankle plays in gait and the sensitivity of normal gait to pathologies of the ankle. Stauffer at el. also speculated that the Ankle Joint is able to bear this magnitude of compression due to the larger articular surface area of the ankle compared to the knee and hip. A larger surface area would mean that the pressures on each of the lower limb joints would therefore be similar.

A model of more complexity was developed by Seireg and Arvikar, 1975, which was a three-dimensional model of the entire lower limb from the hip to the foot. The Ankle and Subtalar Joints were modelled as simple hinges with the Ankle rotational axis running horizontally in the frontal plane and the Subtalar rotational axis running in the sagittal plane. Thirty-one muscles of the lower limb were defined in the model including twelve of the Ankle Complex. These muscles were defined as lines of action between origin and insertion with appropriate wrapping of the muscles around anatomical structures. No ligaments were included in the model.

The indeterminate system was solved using a global optimisation routine, which used EMG data from the University of California (1953) as input. The segment positioning was based on assumed kinematic data from a representative walking gait. The solution was quasi-static, assuming no inertial effects from any of the rigid segments of the lower limb.

The Seireg model predicted no antagonism at the Ankle Complex but some antagonism about the knee. This pattern was sensitive to the objective function chosen by the author and the author noted that in order to minimise the compressive loading at the Ankle Joint there could be no antagonism. However, he was uncertain if this muscle pattern was physiological. The joint compression predicted had a maximum of 5.2 time body weight at 0.8 of stance phase. Figure 2.3-2 illustrates the joint compression loading at the hip, knee and ankle as predicted by the Seireg model during walking. Note that Seireg predicts similar loads at hip and ankle (around 5.5×BW) with a higher load at the knee (around 7.2×BW). Interestingly, the combined muscle load passing posterior to the Ankle Joint was predicted to be 8.6×BW at late stance.

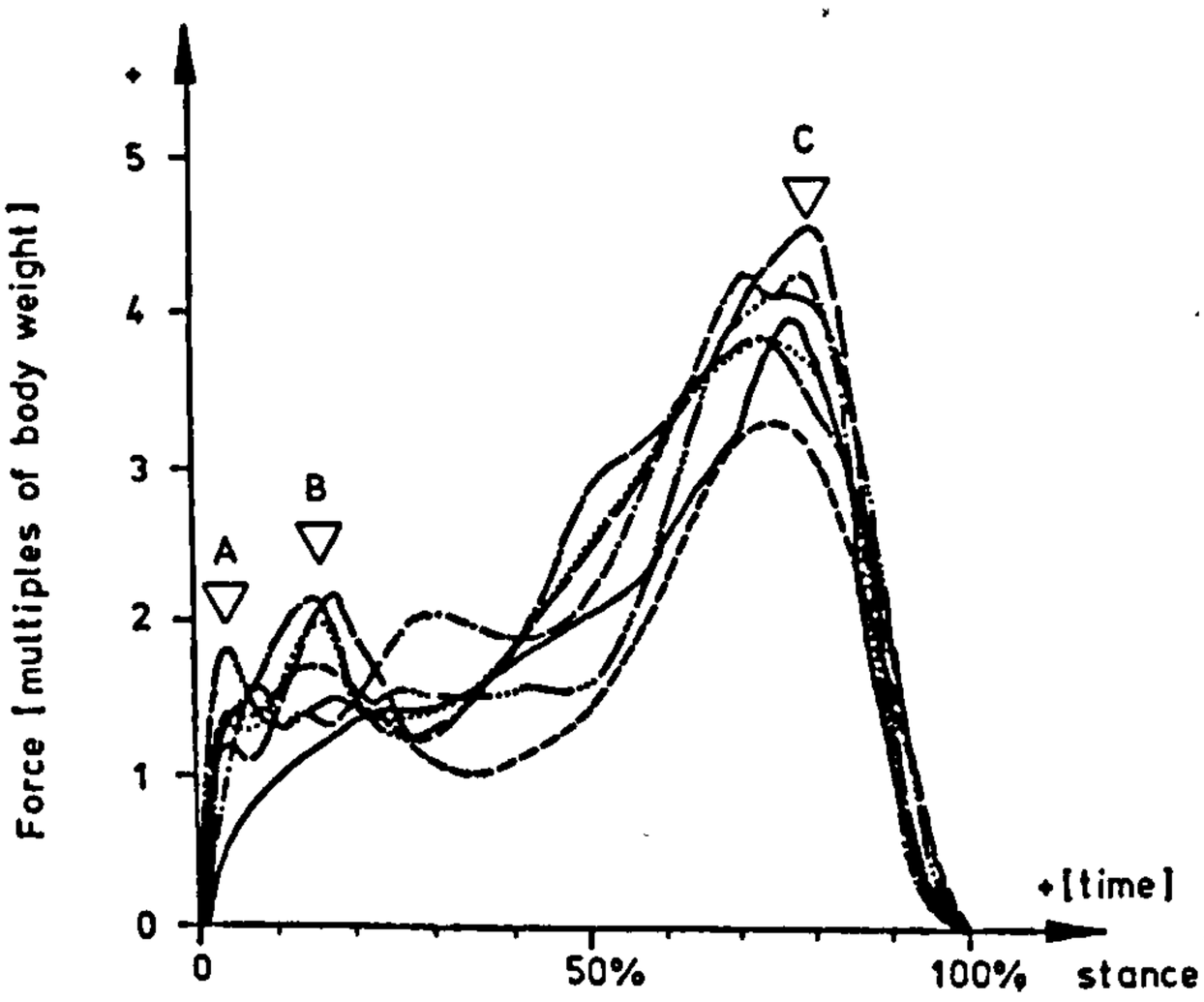

Figure 2.3-3 Joint compressive loading in the Ankle Joint as calculated by the Procter model (Procter, 1980).

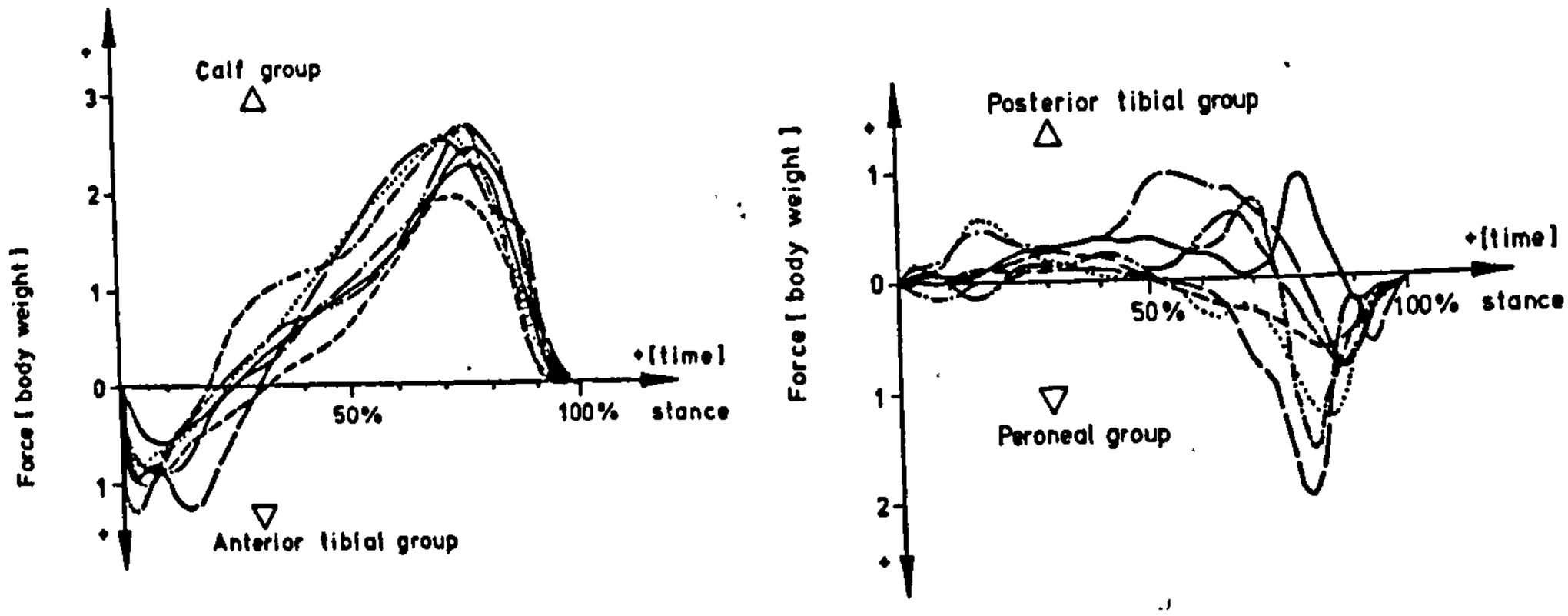

Figure 2.3-4 Muscle loads in the four functional muscle groups: Calf, Anterior Tibial, Posterior Tibial and Peroneal, as predicted by the Procter model (Procter, 1980).

The first and only three-dimensional model of the biomechanics of just the Ankle Complex was developed by Procter (Procter, 1980, Procter and Paul, 1983). The Procter model considered the two joints of the Ankle Complex to be fixed, ideal hinges with rotational axes which were attached to the Talus bone. The joint contact forces were given three degrees of freedom at the Subtalar Joint and five at the Ankle Joint where two separate vertical and anterio-posterior force components were defined. This splitting of the compressive loading at the Ankle Joint was based on the anatomical observation that the Talar Trochlea possessed two broad, longitudinal ridges at the medial and lateral borders of the articular surface. The Ankle Joint was therefore able to oppose inverting-everting and internally-externally rotating moments. Procter overcame the indeterminacy of the Ankle Complex equilibrium system by *functional grouping* of the muscles crossing the joint complex. Positionally similar muscles were assumed to function as a single unit and no antagonism was allowed dorsi-flexing and plantarflexing muscle groups. The Procter model also did not include the ligaments of the Ankle Complex within the loading solution at equilibrium. Some results from Procter are plotted in Figures 2.3-3 and 2.3-4.

The Procter model predicted a maximum compressive joint load of 5.0×BW to occur at 0.8 of stance phase. The tension passing through the Achilles tendon at this point was 3.0×BW and the tension passing posterior to the Ankle Joint in total was 4.0×BW. The author noted that since no antagonism was allowed by the model, the joint contact loading and the muscle tension loading predicted by the model were likely minimum values required for equilibrium. The presence of antagonism would therefore increase the equilibrium tension in the calf group of muscle and increase the compression in the joint.

2.4 KINEMATIC MODELS

Since Procter, modelling of the Ankle Complex has occurred in three general areas: modelling the kinematics using cadaver ankles (Sharkey and Hamel, 1998, Hashimoto and Inokuchi, 1997) and determining the areas of contact using cadavers (Ward and Soames, 1997, Thordarson et al., 1997), inverse dynamics modelling of

the whole lower limb in various tasks. The lower limb would include a simple, hinged ankle complex (Glitsch and Baumann, 1997, Pandy and Anderson, 1999), and kinematic models of the isolated Ankle Joint which model the migrating rotational axis (Leardini et al., 1999a, 1999b, Udupa et al, 1998, Thoma, 1993).

This final group of models which examined the kinematics of the Ankle Complex were all, with the exception of Udupa (1998), two-dimensional models which modelled the Ankle Complex in unloaded, passive motion. These models did well to predict the migration of the Ankle Joint rotational axis by modelling the joint as a multi-rigid-bar mechanism. This provides useful insight into some possible roles for the ligaments, which would anatomically correspond to these rigid bars. However, since these models exist in the sagittal plane, they are completely unable to usefully model the behaviour of the Subtalar Joint and its interaction with the Ankle Joint. Also, these models are all restricted to unloaded conditions. For this reason, they are of little use in understanding the loading of the internal structures of the Ankle Complex during common activities such as walking, walking turns, standing or jumping.

A new aspect of kinematic and equilibrium modelling has been examined by Lu and O'Connor (1999). One drawback of joint models (not limited to the Ankle Joint) which use stereophotogrammetric motion data as input was that when the trajectories of the rigid segments of a system were reconstructed from the reflective marker trajectories, adjacent segments would often experience *virtual dislocations*. For instance, the shank segment during stance phase may be reconstructed so that it moves away from the thigh segment; dislocating the knee. These dislocations arose from errors in the marker trajectories which were unavoidable and inherent in the motion analysis equipment. During segment reconstruction, these errors were magnified to produce gross segment dislocations. Lu and O'Connor developed a global correction method which corrected the marker trajectory errors during segment reconstruction and constrained the adjacent segments of the system from dislocating.

This technique is a new introduction to kinematic models and has yet to be applied to models simulating internal joint loading at equilibrium, such as the current model. But this technique will be an important component of future models.

2.5 OPTIMISATION MODELS

Most of the joints of the human body are mathematically indeterminate systems and the Ankle Complex is no exception. This means that when the system of equations governing load equilibrium about the joint are formulated, there are more unknowns defined in the system than there are equations to solve for them. The unknowns defined by the system are the loads in each of the distinct structures of the joint. In the indeterminate joint system then, a unique solution for the loading of each of the structures of the joint in equilibrium does not exist. One technique for overcoming the indeterminacy of the joint system and determining a unique equilibrium solution is *optimisation*.

2.5.1 Linear and Non-linear Optimisation

The indeterminate joint system will possess a number of possible solutions that satisfy equilibrium. The number of possible solutions to the system depends on how the system is constrained, and a relatively unconstrained system may possess an infinite number of possible solutions. The optimisation method defines an *objective function* which is added to the system of equations. The aim of optimisation is to select from the set of possible solutions the one that maximises (or minimises) the objective function. Therefore the solution which is eventually chosen as the unique solution to the joint system is somewhat dependent on the choice of objective function.

There are two aspects of the objective function which are important: what aspect of the system it represents and whether the function is linear or non-linear. Past models of indeterminate joints have optimised various aspects of the joint system: muscle stress (Crowninshield, 1978), muscle force or activation level of muscles (Happee and Van der Helm, 1995, Kaufman, 1991a, 1991b), the muscle

moments (Herzog, 1987a, Herzog and Binding, 1993), or the overall dynamics of the system (Happee and Van der Helm, 1995, Happee, 1994). By choosing differing objectives and optimising different aspects of the system, the loading is assigned to each of the loaded structures with different priorities, and therefore the ultimate solution chosen will differ.

The form of the function is equally important. Linear objective functions are the more popular option since the process of optimising linear functions is simpler (Bean et al., 1988, Crowninshield, 1978, Seireg and Arvikar, 1973). However, linear optimisation has the drawback that it is ill-suited to assigning an antagonistic pattern of tensions to the muscles about the joint. Nonlinear objective functions behave more physiologically when assigning the loading to synergistic muscles and ligaments but they are more complex to implement (An, et al., 1984, Happee and Van der Helm, 1995, Herzog and Leonard, 1991).

Evaluating the solutions produced by the various forms of optimisation is commonly done with surface electromyography (EMG) studies. EMG measured from the superficial muscles of the joint system is an effective, non-invasive way of observing muscle *activity*. However, the amplitudes of the EMG signals are not linearly related to the tensions in the muscle and therefore EMG can really only be used to validate the *patterns* of muscle tensions and not the magnitudes of muscle tensions. EMG studies also give no indication as to the loading in the ligaments and retaining structures of the joint or the loading on the articular surfaces. The EMG evaluation process therefore leaves much uncertainty about the physiological appropriateness of the optimisedequilibrium solutions.

2.5.2 EMG Assisted Optimisation (EMGAO)

During static tasks where the muscles of the joint can all be assumed to be contracting isometrically, the tension in each of the muscles *can* be estimated from the EMG signals. The EMG signals are each smoothed and the amplitude of the smoothed signals are then each multiplied by a gain to produce the muscle tensions. This process, however, requires a separate calibration procedure to determine the appropriate gain for each muscle. This method has the drawback that it is unlikely to

produce a pattern of muscle tensions that gives equilibrium about the joint (Choi and Vanderby, 1999, Cholewicki et al., 1995). However a hybrid of this EMG method and the optimisation method has the advantage of matching the pattern of activation in the muscles of the joint plus producing equilibrium about the joint. The name for this hybrid technique has been coined as *EMG Assisted Optimisation (EMGAO)* (Cholewicki and McGill, 1994). With the EMGAO technique, the EMG signals from each of the muscles of the joint are smoothed and then multiplied by separate gains to give estimates of the muscle tensions. A linear or nonlinear optimisation routine is then applied which assigns loading to the ligaments and articular surfaces and alters the muscle tension estimates so that equilibrium about the joint is achieved. The EMGAO method, however, is best applied to static loading conditions since the EMG portion of the technique still relies on the isometric relationship between smoothed EMG and muscle tension. This technique has been applied to the static loading of the joints of the thorax and neck with great success (Choi and Vanderby, 1999, Cholewicki et al., 1995, Cholewicki and McGill, 1994, Sparto, et al., 1998) but has not been applied to biomechanics of joints involved in locomotion.

2.5.3 Muscle Model Assisted Optimisation (MMAO)

Since the EMGAO technique is restricted to the equilibrium solutions of static loading situations it is clearly unsuitable for use on the joints of the lower limb during gait or of the upper limb during goal directed movements. The EMGAO technique is only restricted due to its reliance on the linear isometric EMG to muscle tension relationship. However, if this reliance is removed from the EMGAO technique, and the muscle tensions could instead be estimated with a more robust, EMG to tension relationship that was valid for non-isometric conditions, then the advantages of the EMGAO technique could be applied to the joints of the upper and lower limbs, and to the Ankle Complex in particular.

Such a robust, movement valid, EMG to tension relationship does exist, and it was developed in the field of physiology concerned with modelling the behaviour of isolated muscles. These EMG-based Muscle Models were originally developed to

model the contraction behaviour and energy usage of skeletal muscle (Hill, 1938, Hof and Van den Berg, 1981a, Winters, 1995). By replacing the isometric EMG to tension relationship of EMGAO with an EMG-based Muscle Model, a new hybrid technique for solving equilibrium about highly mobile, indeterminate joints has been developed in this study: Muscle Model Assisted Optimisation (MMAO).

As has been described in the three different models; Stauffer et al. (1977), Seireg and Arvikar (1975) and Procter and Paul (1982), no models of the ankle have been published which can predict antagonism about the joints of the Ankle Complex. The previous models have not include antagonism and have noted their results of the internal loading therefore represent minimum equilibrium solutions. The current model is able to examine antagonism and to predict whether or not its presence is variable between individuals. If antagonism is indeed predicted to be present, the internal loading determined by the model well therefore likely be of greater magnitude than that of the previous models.

The current model also includes ligaments in the equilibrium solution. The previous models have either been unable of include ligaments or have ignored their contribution, assuming them not to be involved. Since in vitro kinematic studies of the cadaver ankles have shown the segments of the Ankle Complex to be constrained to move about only two discrete rotational axes, rather than the six possible degrees of freedom, the loading in the ligaments is likely quite important.

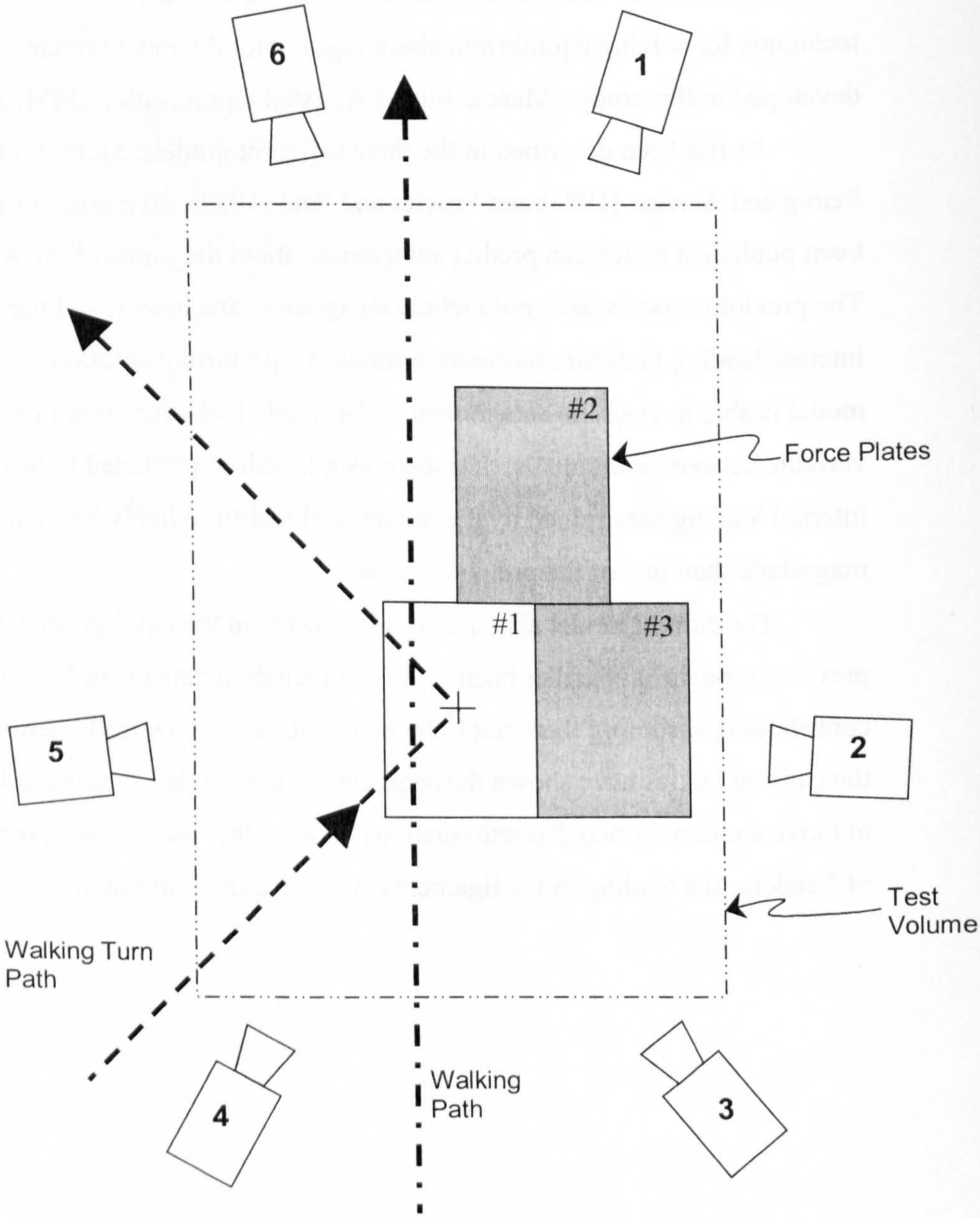

Figure 3.1.1-1 Plan of Camera Positions and Test Volume with respect to Walking and Walking Turn paths of motion.

CHAPTER 3 COLLECTION OF KINEMATIC DATA

3.1 MOTION ANALYSIS EQUIPMENT

3.1.1 VICON

A six camera VICON 370 Motion Analysis System was used for the collection of Kinematic Data from subject motion. The VICON worked in conjunction with three floor-mounted Kistler Force Plates and an 8-channel Electromyography (EMG) Amplifier. The VICON cameras actively strobed infra-red light into the test volume through which the subject moved and then sampled the reflected light at a rate of 50 Hz. The test volume was symmetrical around Force Plate #1. The dimensions of the volume were 2.0 m along the direction of walking, 1.1 m vertically up from the floor and 1.0 m medio-laterally. The cameras were focused on the centroid of this volume.

Figure 3.1.1-1 shows the planform view of the camera positions and the test volume. Cameras 1 and 6 faced the walking subject, cameras 2 and 5 looking on the subject in profile and 3 and 4 viewed from behind. The cameras were numbered clockwise when looking from above. In order to maximise the angle between adjacent cameras with respect to the test volume centroid, Cameras 2 and 5 were placed nearer to the floor than the others. The higher cameras were approximately 1.2 m from the floor and the lower ones 0.5 m. Figure 3.1.1-2 shows a photograph of the camera arrangement.

Since the cameras were all pointed generally downward into the test volume and since they each actively emitted light, reflection of light off the floor and into other cameras was a concern. Reflected light from the floor could either be misinterpreted by the VICON System as non-existent markers or the glare could mask the reflections from actual markers. To minimise this occurring, a dark blue sheet of fabric covered the floor on either side of the subject path of motion. The fabric absorbed, rather than reflected, the emitted infra-red light.

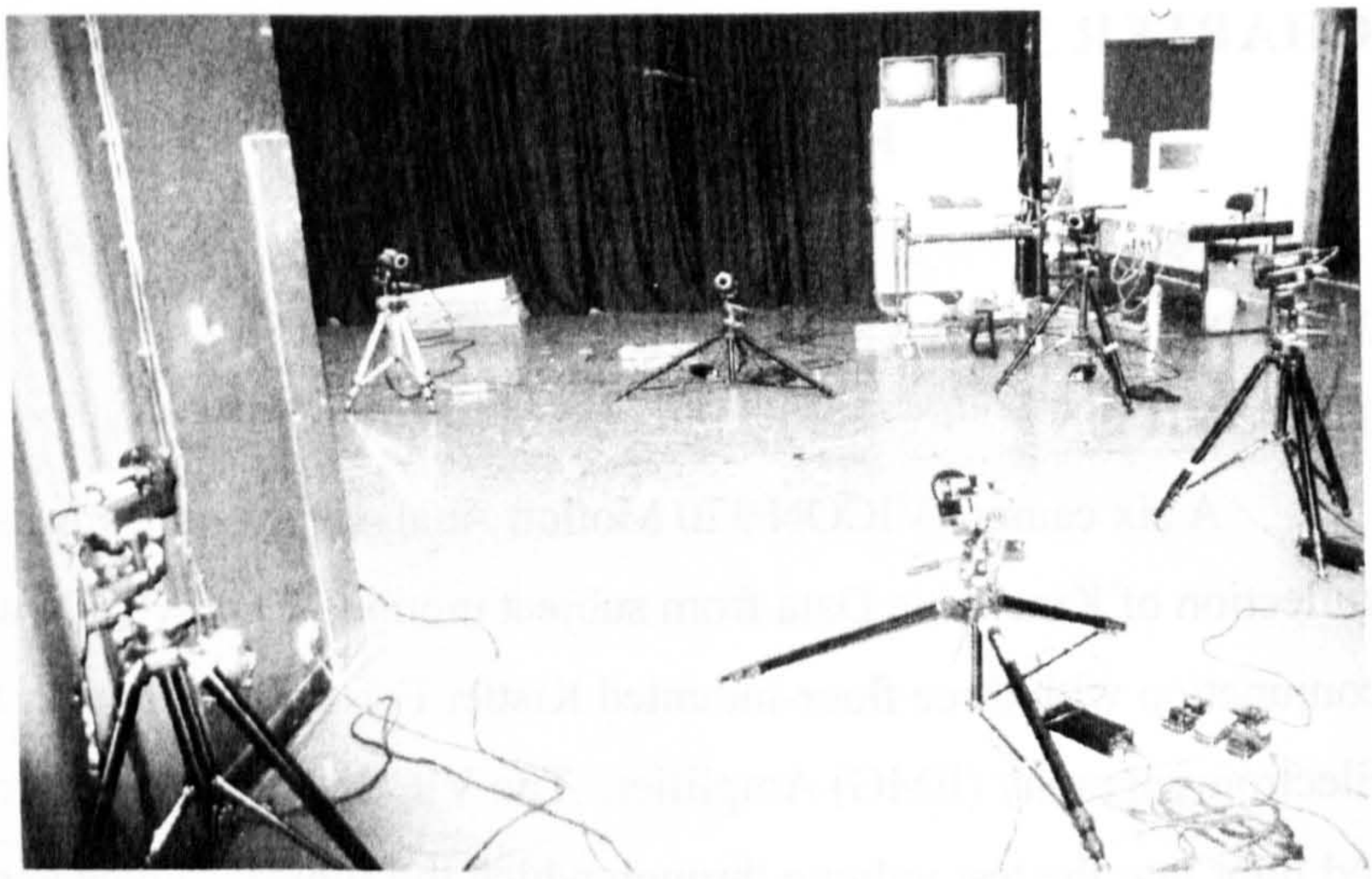

Figure 3.1.1-2 Photograph of the camera set-up. Cameras 2 and 3 are in the foreground and Camera 5 is facing.

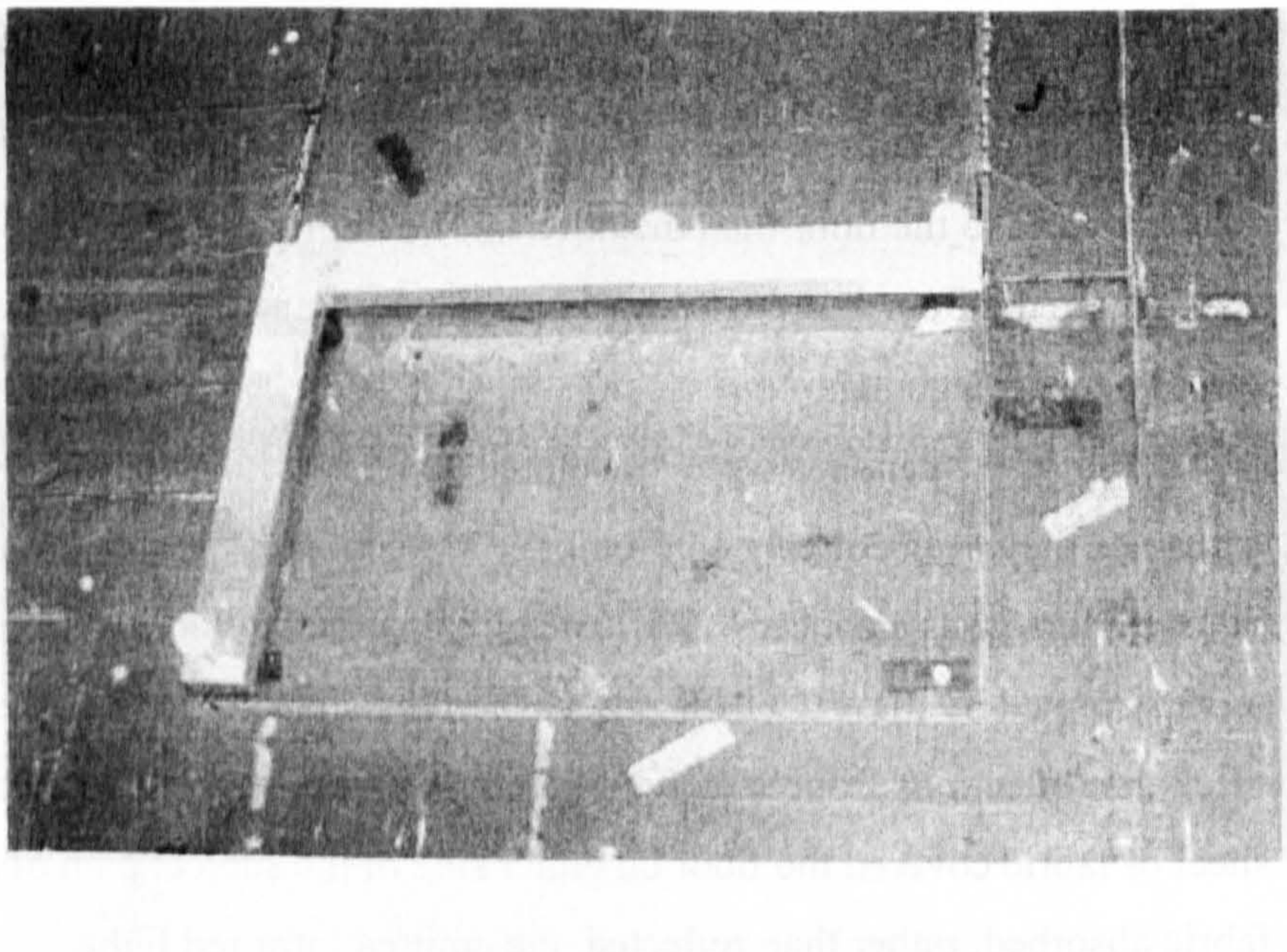

Figure 3.1.2-1 The L-frame device in position on Force Plate #1.

3.1.2 Dynamic Calibration

Since the cameras in the laboratory were placed and removed before and after each movement analysis session, the test volume had to be calibrated before each session. The calibration enabled the computer to determine the relative positions of each of the cameras. Once this was known, the reflected light from the markers seen by each of the six cameras in two dimensions could then be reconstructed into three-dimensional positions within the test volume.

Until recently, the test volume was calibrated using *static* hanging calibration rods. These rods held reflective markers of known positions in three-dimensions. These positions had been previously surveyed by theodolite. The rods were hung within the test volume and the cameras set in position for the session. The VICON System then used the static rod markers to determine the relative camera positions and to calibrate the test volume. The static method yielded *calibration error residuals* of between 1.5 and 2.5. These error residuals represented the discrepancy between the reconstructed position of a marker and its actual position in the test volume. Given the size of the test volume this corresponded to a spatial error of ±1.5 to 2.5 mm.

Due to the size and relative proximity of the reflective markers used in this study and the degree of motion between rigid segments that was being observed (i.e. movement between the Midfoot and Forefoot segments), the spatial error arising from static calibration was deemed to be too large. Lower calibration residuals could be achieved using the *dynamic* method of calibration. The VICON system could be calibrated in a two step, dynamic procedure given the appropriate calibrating objects. Required were a right-angle *L-frame* and *marker wand* which were designed and constructed in-house for this purpose.

In the first step of the two-step calibration process, the L-frame was secured to Force Plate #1. Figure 3.1.2-1 shows the L-frame in position. The long arm of the L-frame held three collinear reflective markers representing the VICON $x-axis$. The short arm held a single marker representing the $y-axis$. The vertical, $z-axis$ was then found using the vector cross product of the $x-axis$ and $y-axis$. The cameras sampled 100 samples of data with the L-frame alone in the test volume. To

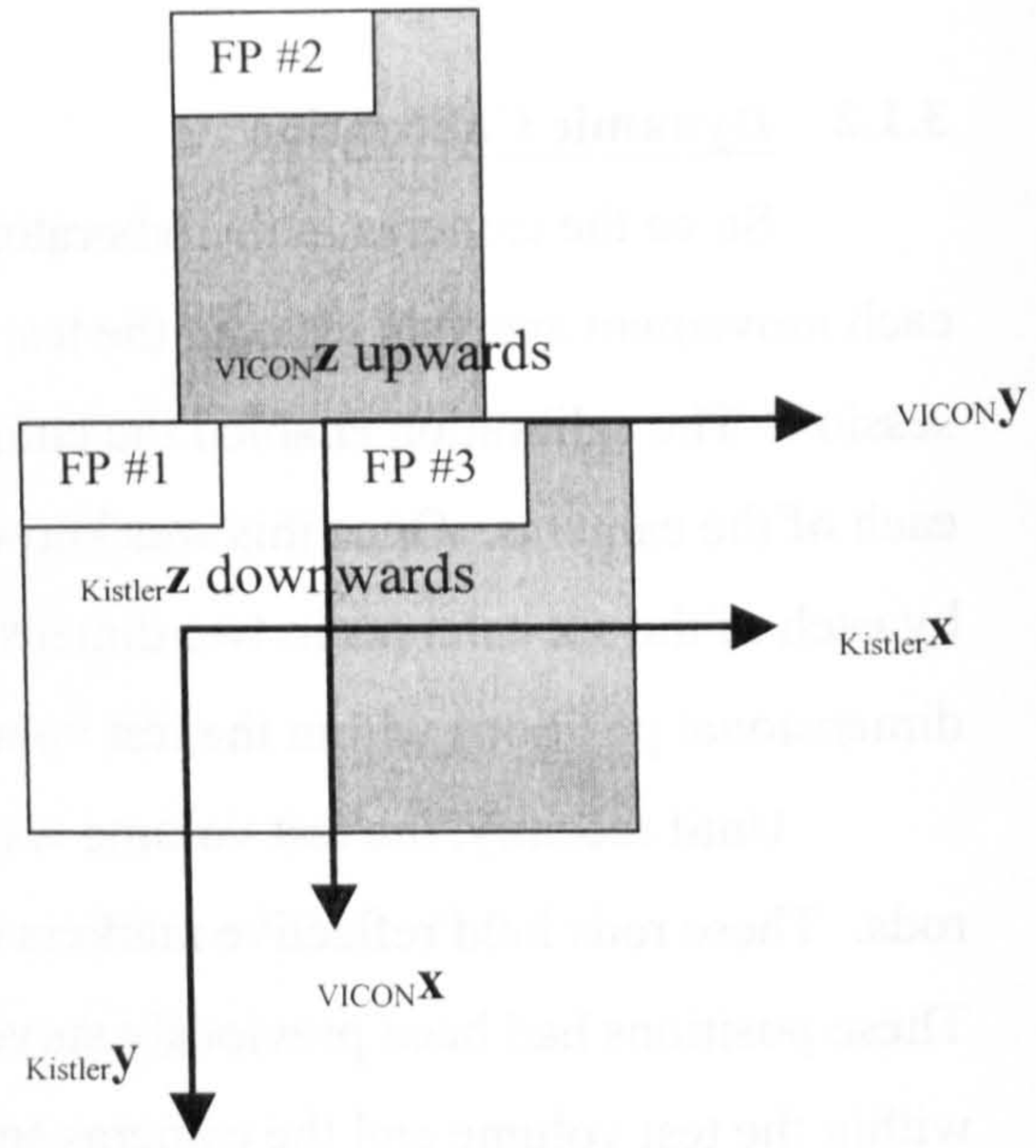

Figure 3.1.2-2 Orientations of the Axes of the VICON (ground) and Kistler frames of Reference.

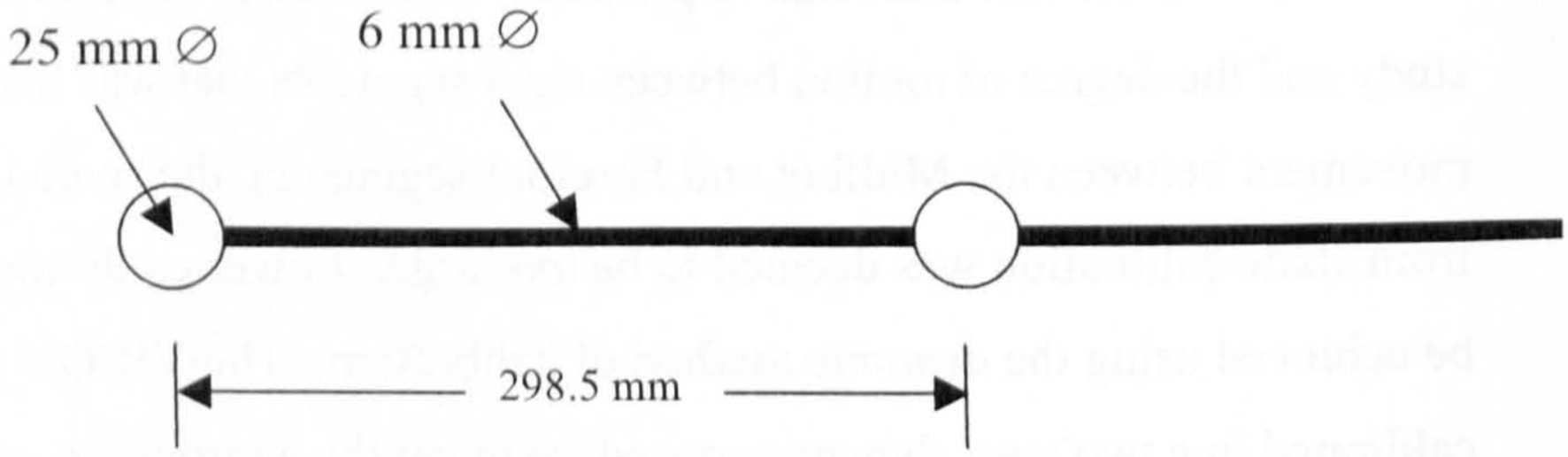

Figure 3.1.2-3 Plan of wand used in Dynamic Calibration procedure.

minimise floor reflection, a sheet of dark fabric was placed over the L-frame. The reflective markers passed through holes in the sheet and were therefore visible above the sheet. This first step defined the VICON $x-$, $y-$, and $z-axes$ and related them to the independent Kistler Force Plate axes. Figure 3.1.2-2 shows the orientation of the VICON axes and the Kistler Force Plate axes attached to Force Plate #1.

The second step used the marker wand in a dynamic way. The wand was a rigid rod with two reflective markers attached at a known separation distance. Figure 3.1.2-3 shows the plan of the wand. For a user-defined number of samples, the wand was waved slowly throughout the test volume. This second step calibrated the test volume with respect to the axes defined in the first step.

Using the dynamic calibration procedure, calibration error residuals of 0.5 to 0.8 mm were repeatably achieved. This corresponded to spatial errors of approximately ± 0.5 to 0.8 mm which was sufficiently small to measure the desired inter-segmental motion.

3.1.3 Force Plates

Ground Reaction Force and Centre of Pressure

The VICON laboratory was equipped with three floor-mounted Kistler Force Plates. Only one of these, Force Plate #1, was used for the movement tasks in the present study. The force plate itself was a rigid plate supported by four pillars, which were each, instrumented with a number of piezoelectric transducers. Analogue data from these transducers was organised into eight channels, which were sampled at 1000 Hz.

The eight Force Plate analogue channels produced the quantities $F_{x_{1+2}}$, $F_{x_{3+4}}$, $F_{y_{4+1}}$, $F_{y_{2+3}}$, F_{z_1}, F_{z_2}, F_{z_3} and F_{z_4}. The subscripted letter represents the force component with respect to the Kistler axes and the sub-subscripted number represents the pillar at which the force was measured. The three components of the Ground Reaction Force (GRF) could be calculated in the Kistler frame of reference as follows,

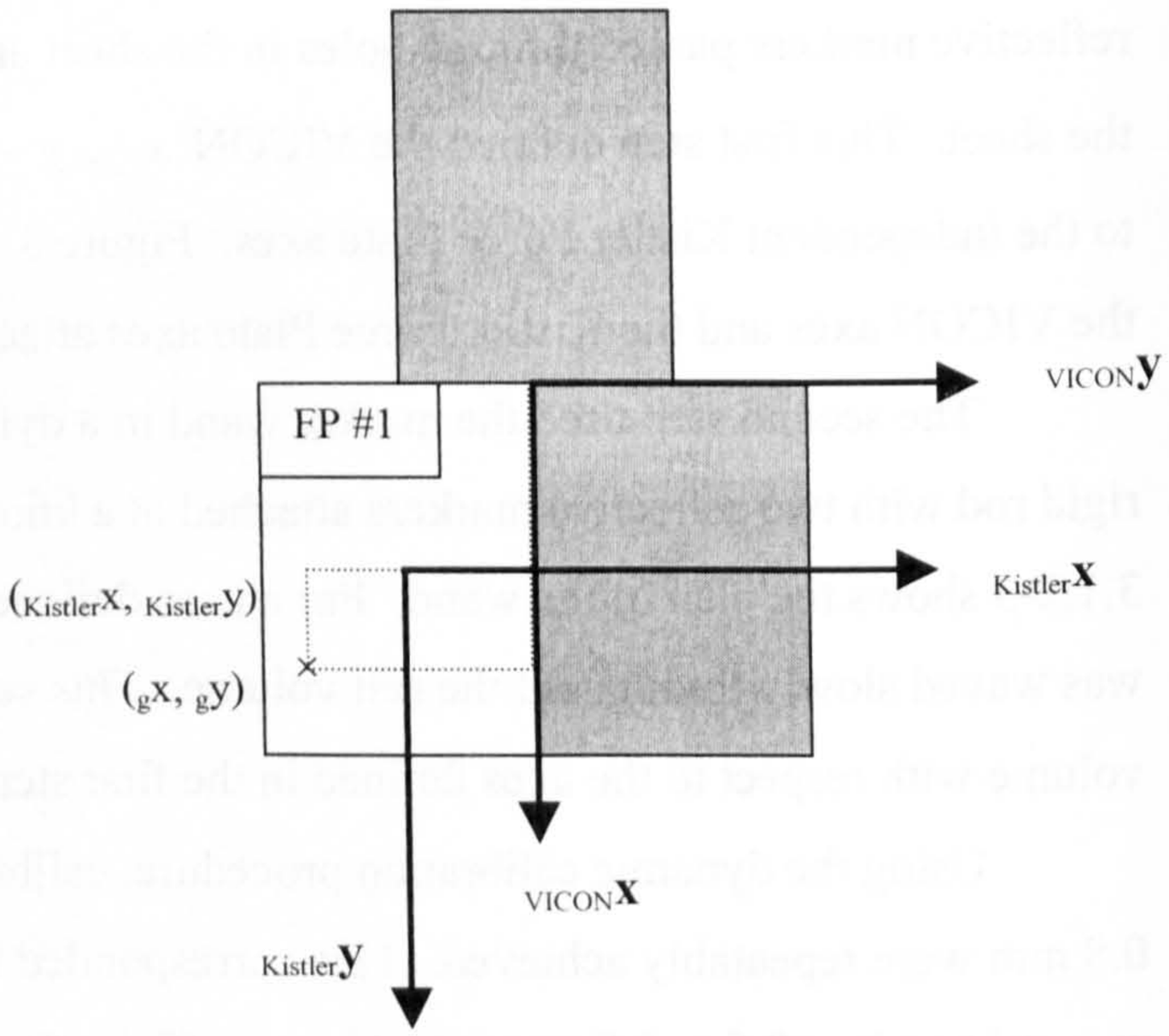

Figure 3.1.3-1 Co-ordinates of the centre of pressure with respect to the VICON (ground) frame and the Kistler frame of reference.

$$
\begin{aligned}
{}_{Kistler}F_x &= F_{x_{1+2}} + F_{x_{3+4}} \\
{}_{Kistler}F_y &= F_{y_{4+1}} + F_{y_{2+3}} \\
{}_{Kistler}F_z &= F_{z_1} + F_{z_2} + F_{z_3} + F_{z_4}
\end{aligned}
\tag{3.1.3-1}
$$

The co-ordinates of the point of application of the GRF on the surface of the Force Plate, also known as the *centre of pressure*, could also be calculated,

$$
{}_{Kistler}\overline{x} = \frac{120\left(F_{z_1} - F_{z_2} - F_{z_3} + F_{z_4}\right) - 52\left(F_{x_{1+2}} + F_{x_{3+4}}\right)}{F_{z_1} + F_{z_2} + F_{z_3} + F_{z_4}}[mm]
$$

$$
{}_{Kistler}\overline{y} = \frac{200\left(F_{z_1} + F_{z_2} - F_{z_3} - F_{z_4}\right) - 52\left(F_{y_{2+3}} + F_{y_{4+1}}\right)}{F_{z_1} + F_{z_2} + F_{z_3} + F_{z_4}}[mm] \tag{3.1.3-2}
$$

The Kistler axes, although parallel with the VICON axes, were not identical to them and did not share a common origin (see Figure 3.1.2-2). The GRF and centre of pressure were transformed from the Kistler frame into the VICON frame of reference. The VICON frame will from here on be referred to as the *ground* frame of reference. The GRF transformation was done as follows,

$$
\begin{aligned}
{}_{g}F_x &= {}_{Kistler}F_y \\
{}_{g}F_y &= {}_{Kistler}F_x \\
{}_{g}F_z &= -{}_{Kistler}F_z
\end{aligned}
\tag{3.1.3-3}
$$

The centre of pressure transformation included a translation from the Kistler origin to the ground frame origin,

$$
\begin{aligned}
{}_{g}\overline{x} &= 300 + {}_{Kistler}\overline{y}[mm] \\
{}_{g}\overline{y} &= -200 + {}_{Kistler}\overline{x}[mm]
\end{aligned}
\tag{3.1.3-4}
$$

The position of the centre of pressure on Force Plate #1 is illustrated Figure 3.1.3-1, in each of the frames of reference.

Free Moment

In addition to applying a three component ground reaction force (GRF) to the Force Plate at the centre of pressure, it is also possible for the subject to apply a *Free Moment*. This is a pure moment acting at the centre of pressure about an axis in the vertical, $z-$direction. The Free Moment arises due to the friction between the sole of the foot or shoe and the surface of the Force Plate. Any rotation of the foot about

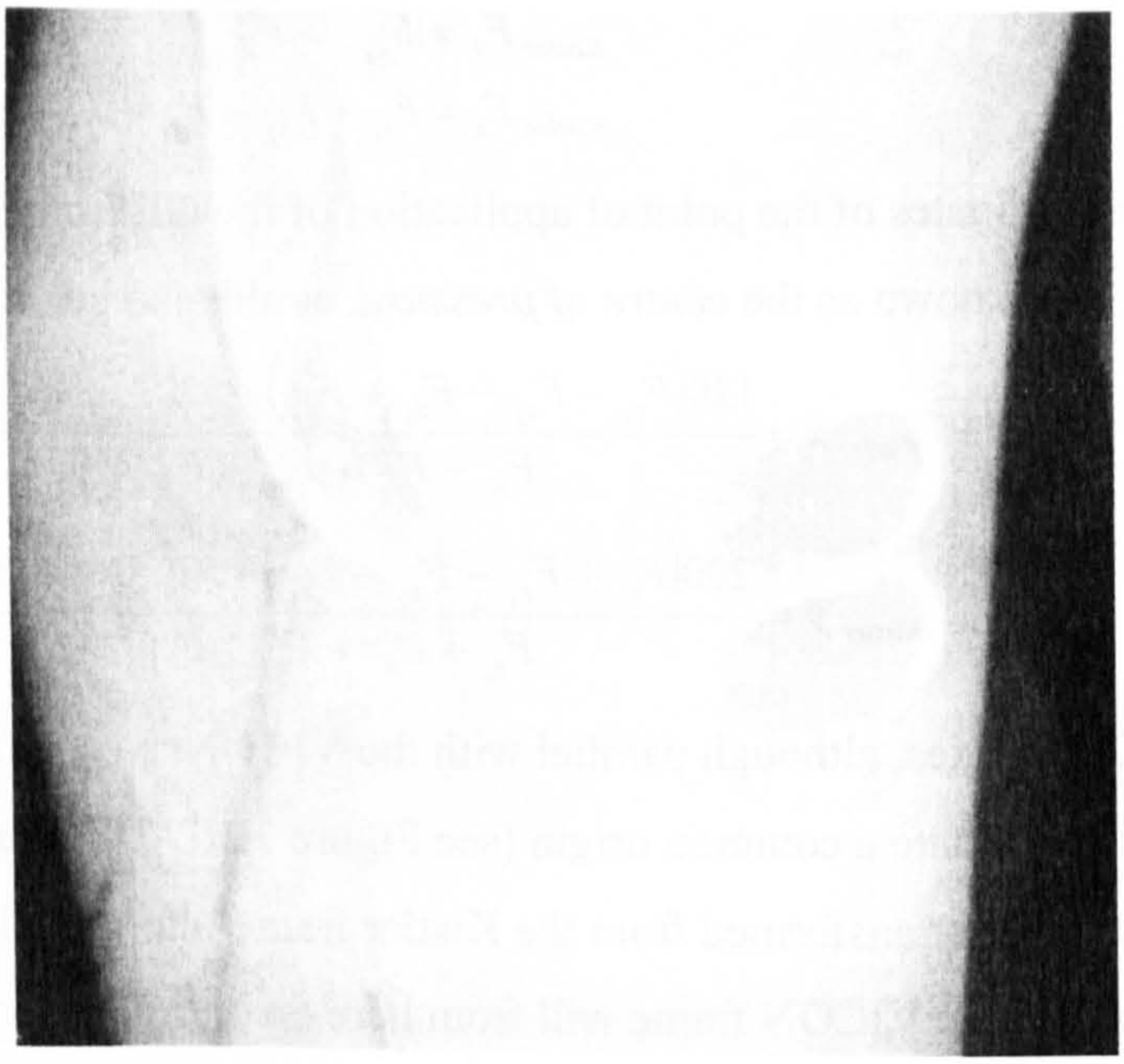

Figure 3.1.4-1 Arrangement of the electrode pair over the Tibialis Anterior muscle.

the surface of the Force Plate during stance phase may be transferred to the Force Plate as a turning moment depending on the friction between the surfaces.

In shoes with a flat, rubber sole, such as sailing trainers, the Free Moment can be quite a large component of the moment experienced by the Ankle Joints. When walking in barefoot over linoleum, as in the current study set-up, the Free Moment is often very small with respect to the overall moments applied to the Ankle Joints or may even be absent.

In order to calculate the Free Moment, the vertical moment is first calculated at the centre of the Force Plate,

$$_{Kistler}M_{z_{centre}} = 200(F_{x_{1+2}} - F_{x_{3+4}}) - 120(F_{y_{2+3}} - F_{y_{4+1)}})[Nmm] \quad (3.1.3\text{-}5)$$

The Free Moment is therefore found using Eq.s 3.1.3-1, -2 and –5,

$$_{Kistler}M_{z_{free}} = \frac{1}{1000}\left[-_{Kistler}F_x \cdot_{Kistler}\bar{y} +_{Kistler}F_y \cdot_{Kistler}\bar{x} + M_{z_{centre}}\right][Nm] \quad (3.1.3\text{-}6)$$

3.1.4 EMG Collection Equipment

Electromyographic data was recorded while the subject performed the movement tasks in the VICON laboratory. EMG was recorded from *five* superficial muscles of the right lower leg. To prepare the skin for EMG electrode placement over each of the muscle sites, the skin was first shaved if necessary. The area was then abraded with dry medical abrading paper to remove dead skin cells which were electrically insulating. Finally the area was cleaned with an alcohol swab. After skin preparation, a pair of Ag-AgCl self-adhering electrodes was stuck to the skin. Before the electrodes were placed, conducting electrode gel was spread over the electrode conducting surface, covering it evenly and completely. The electrode surface was square with an area of 25 mm^2. The electrodes were placed so that the electrode long axis was perpendicular to the muscle fibres in the muscle belly. The electrodes were placed side by side so that their plastic housings were touching. This ensured that the electrode surfaces ran parallel with a separation of 10 mm. Figure 3.1.4-1 shows an electrode pair in position. A single reference electrode was placed over the bony prominence of the patella. The reference electrode was a self-adhesive stimulating

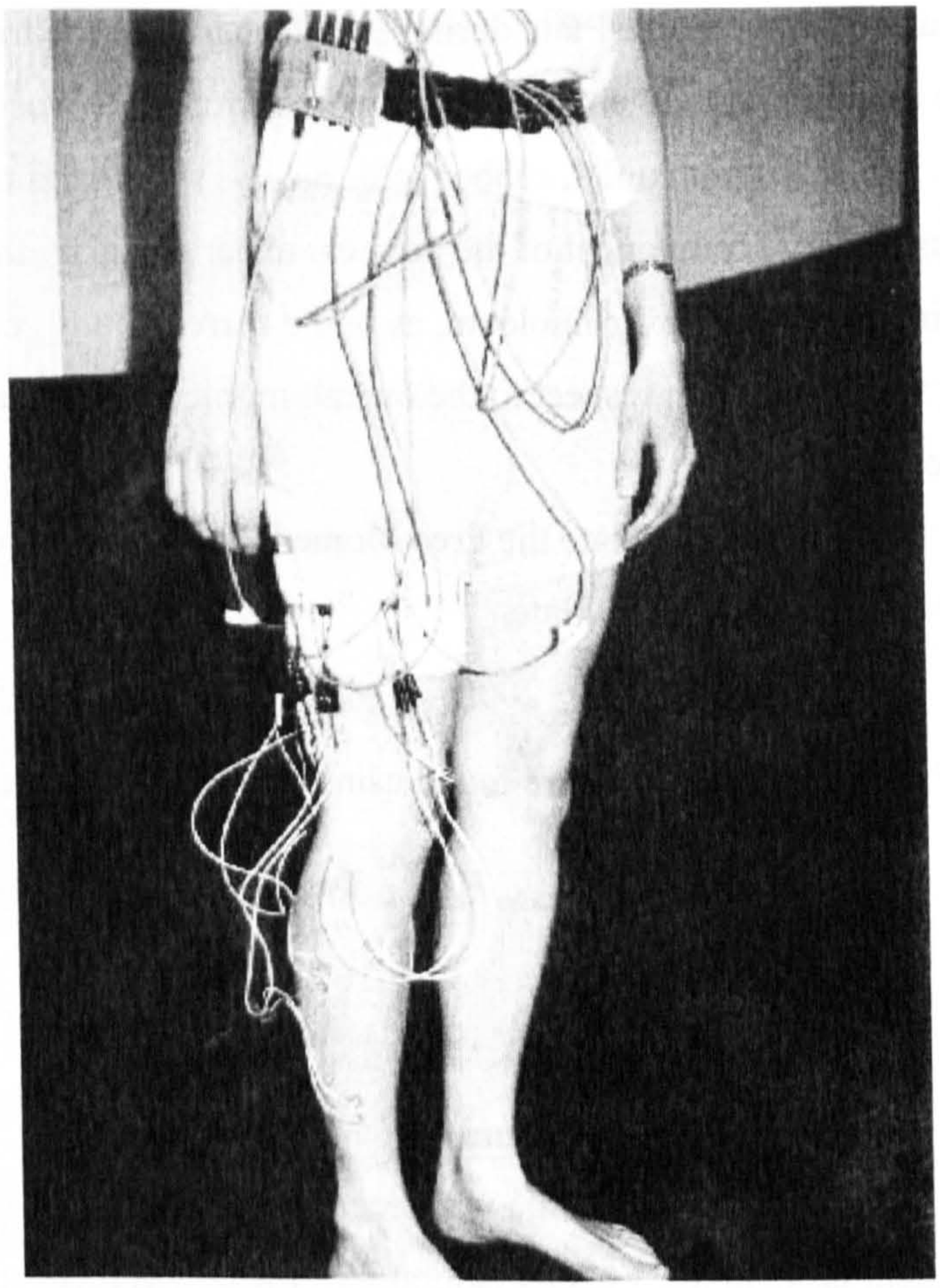

Figure 3.1.4-2 Complete set-up of electrode pairs, pre-amplifiers, thigh bandage and waist belt.

electrode. The electrode surface was circular with a diameter of 40 mm. A stimulating electrode of this configuration was used for its large surface area in order to minimise movement noise artefacts arising from the moving patella.

The lead wires on the electrode pairs were 500 mm long and connected to pre-amplifier units attached at the thigh. The pre-amps were approximately 30x30x10 mm in size and were encased in an insulating, solid gel. The gain of the pre-amplifier was 50. The pre-amps were used to boost the signal immediately after acquisition, before reaching the main amplifier unit, to ensure a large signal-to-noise ratio.

An elastic bandage was strapped around the right mid-thigh of the subject. Its tightness could be adjusted using its Velcro fastener so that a snug, non-slipping fit was achieved. Elasticised pockets on the outside of the thigh bandage allowed the attachment of the pre-amplifiers. The lead wires from the electrodes were taped at intervals to the subject skin using 3M Trans-pore tape to minimise movement of the leads on the way to the pre-amps.

The leads from each of the five pre-amplifiers were then connected to a single, multiplexing box attached at the waist by a belt. The box was approximately 100x50x50 mm in size. A single, multi-wire cable then connected this box to the Analogue-to-Digital Converter of the VICON System. The multiplexing box was attached to the belt by a Velcro fastener to allow it to be quickly detached from the subject if the subject inadvertently moved beyond the length of the multi-wire cable. The complete arrangement of EMG Collecting electrodes and amplifier is shown in Figure 3.1.4-2.

Once all the EMG Collection equipment was in place for each of the muscles, the subject was asked to move their right leg and foot through its full range of motion to ensure that the electrode lead wires and pre-amplifier wires did not interfere with movement. If there was any interference, the lead wires were re-taped to allow free movement.

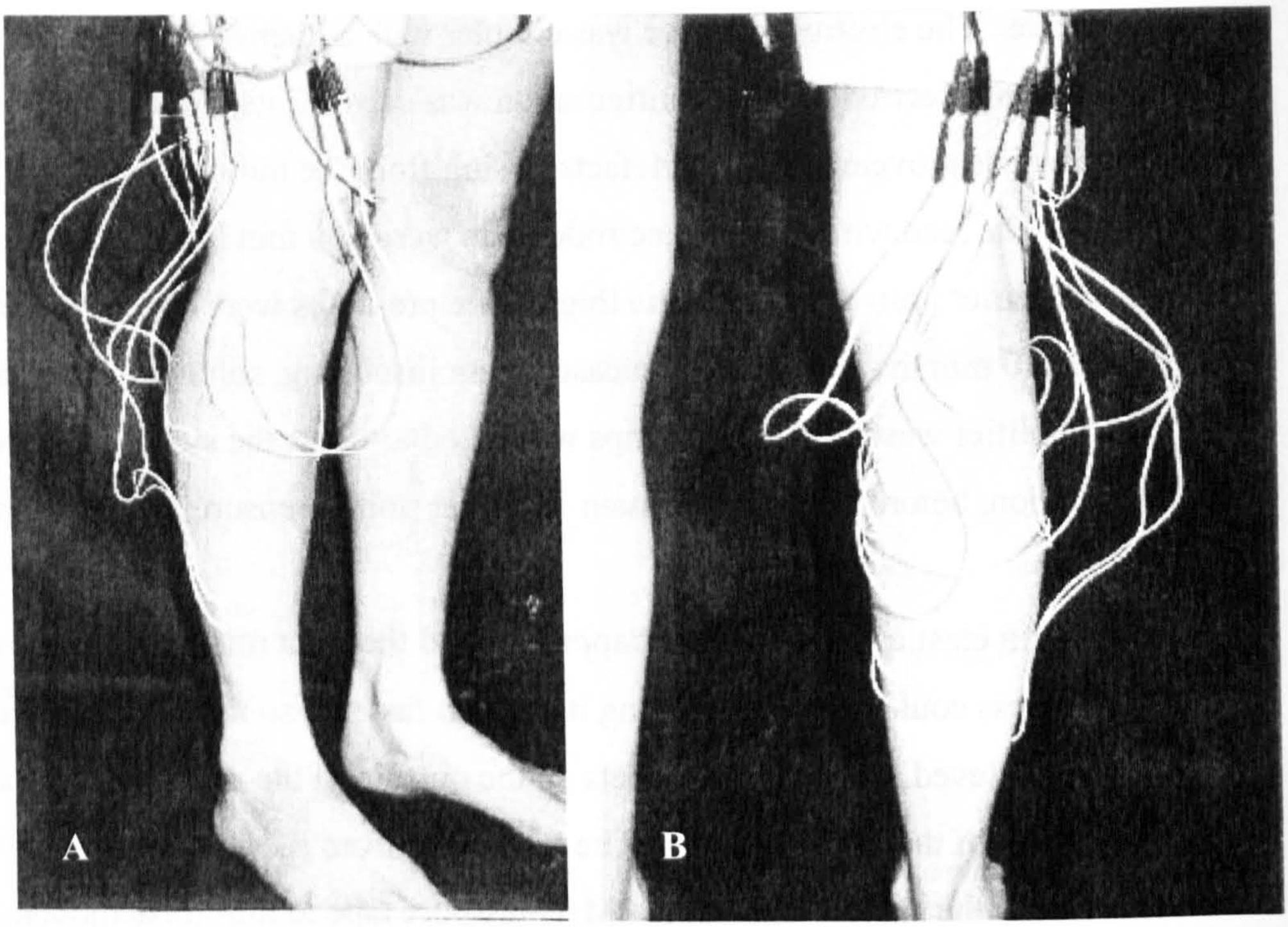

Figure 3.1.5-1 Placement of the eight electrode pairs on the lower leg. Anterior (A) and Posterior (B) views.

3.1.5 Electrode Placement

The muscles of interest were the Medial Head of Gastrocnemius (GaM), Soleus (Sol), Tibialis Anterior (TiA), Peroneus Longus (PeL), and the Extensor Digitorum Longus (EDL) of the right leg. Note that EMG was measured from *five* muscles, and not the total of *eight* that were represented in the Internal Map and the Muscle Model. EMG was not measured from the Lateral Gastrocnemius Head (GaL), Peroneus Brevis (PeB) nor the Extensor Hallucis Longus (EHL). The reason for this will be explained with the Muscle Model in a later section.

Muscle	Placement (on Lower Leg)	Leg Position	Foot Exertion
GaM	-posterior, medial surface -at proximal 1/3 of segment -midway along Medial Gastrocnemius belly	-subject standing on balls of feet -knee straight	-plantar-flexing foot against body weight
Sol	-posterior, medial surface -at 2/3 of segment length -distal to GaM site -distal to Gastrocnemius and medial to Achilles tendon	-subject standing on balls of feet -knees flexed at 80° or greater	-plantar-flexing foot against body weight
TiA	-anterior surface -at proximal 1/3 of segment -20 mm lateral to Anterior Tibial Crest	-subject seated with knee flexed at 90° -ankle 10° dorsi-flexed and inverted slightly	-dorsi-flexing and inverting against resistance downward on First Metatarsal shaft
PeL	-lateral surface -at ½ segment length -10 mm anterior to fascia b/w PeL and Sol	-subject seated with knee flexed at 90° -ankle 10° dorsi-flexed and everted slightly	-everting and dorsi-flexing against resistance downward on Fifth Metatarsal and Upward on First Metatarsal
EDL	-anterior surface -at ¾ of segment length -distal to TiA site -20 mm lateral to Tibial crest	-subject seated with knee flexed at 90° -ankle 10° dorsi-flexed -toes slightly extended	-extending toes and dorsi-flexing against resistance downward on toes

Table 3.1.5-1 Positions of electrode placement, Leg Positions and Directions of Foot Exertion used to selectively contract each muscle.

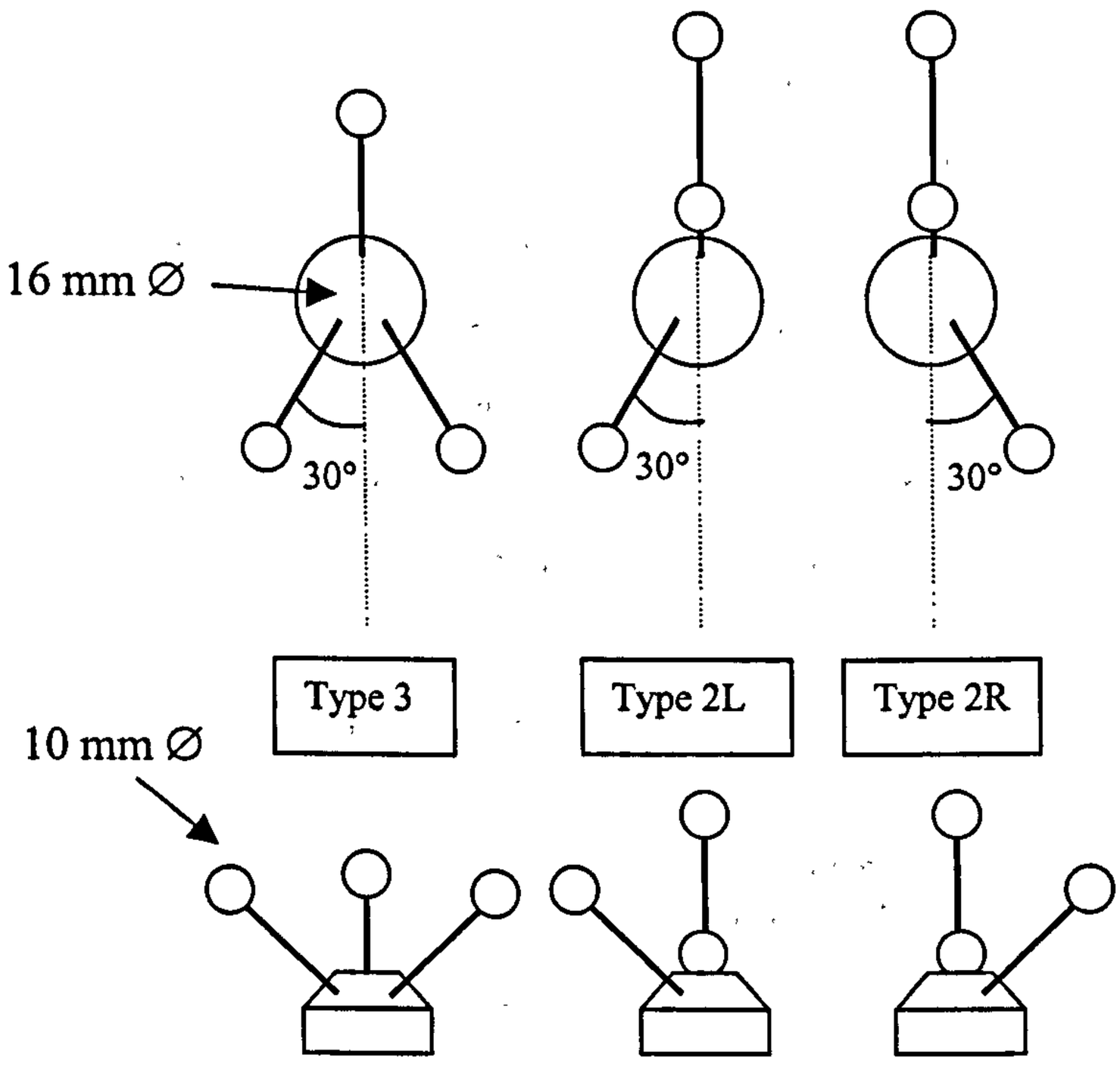

Figure 3.2-1 Plans of the three marker cluster configurations.

To locate the proper electrode placement site over each of the muscles, the muscle belly for each of the muscles was selectively contracted isometrically. The contraction would cause the muscle belly to bulge under the skin, allowing it to be located and the electrode site chosen. To selectively contract a muscle, the right leg and foot were positioned in a specific way. The subject was then asked to attempt to move the foot in a certain direction with the experimenter providing enough resistance in the opposite direction to ensure no foot motion. Table 3.1.5-1 describes the leg and foot positions and subject foot exertions used to identify each of the muscles of interest. Figure 3.1.5-1 shows photographs of the placement sites for the five pairs of electrodes.

3.2 MARKER CLUSTER DESIGN AND PLACEMENT

The model of the Ankle Complex considered the right leg and foot to be composed of seven rigid segments: Thigh, Lower Leg, Talus, Hindfoot, Midfoot and Forefoot (medial) and Forefoot (lateral). The Talus segment was distinct from the other six segments since its movement could not be observed directly during the Motion Analysis trials. Its position was instead inferred from the positions of the neighbouring segments; the Lower Leg and the Hindfoot.

The kinematic data that was collected during the motion analysis experiments therefore tracked the movement of the remaining six rigid segments. To track the movement, reflective markers were attached to the skin at various positions on each of the six segments. The VICON cameras actively strobed infra-red light which reflected off these markers. The reflected light was then received by the cameras. From each of the six, two-dimensional views of reflected light, the VICON computer was able to reconstruct, in three-dimensions, the positions of each of the markers.

The reflective markers used for the Movement Analysis trials were arranged as rigid clusters of three markers. Figure 3.2-1 shows the plans for the three different cluster configurations used. The markers on each cluster were spherical wooden beads of 10 mm diameter. They were covered in 3M Self-adhesive Reflective Tape. The markers were each connected to the cluster base by 3 mm diameter carbon fibre

Figure 3.2-2 Placement of all the marker clusters on the right leg and foot.

rods. The rods were press-fit into both the wooden beads and the polyethylene base. The base was a bevelled cylinder of 16 mm diameter and 8mm height with a 4mm bevel. Each cluster had a mass of approximately 100 grams and the skin was shaved if necessary to provide a smooth surface for adhesion. The cluster was attached to the skin using medical, two-sided tape.

For the VICON System to differentiate between individual markers when reconstructing their positions within the test volume, the markers had to be at least four diameters apart. This required that the distance between markers on the same cluster and between neighbouring clusters be more than 40 mm. This was the primary constriction governing cluster placement and orientation on each of the six rigid segments. Due to the size of the rigid segments of the foot, the foot clusters presented the greatest challenge in placement.

A second constriction on cluster placement was the need to minimise skin movement errors. A significant source of error with the VICON System and all similar motion analysis systems which track skin mounted markers arose from movement of the skin with respect to the underlying bone structures. Markers needed to be placed at sites where the skin was well attached to the underlying structures giving minimal skin movement.

A final concern in marker cluster placement was the visibility of each of the markers during the movements studied. Due to shielding from body segments, insufficient illumination within part of the test volume, or masking from floor reflection, some markers were not always visible to the cameras during some of the movement trials. Three reflective markers was the minimum number needed to fully represent a segment position and orientation in three dimensions. Therefore a single cluster was sufficient per segment for the motion tracking. However on two of the six segments, an extra cluster was attached: Lower Leg and Midfoot segments. This redundancy improved the chances that at least three markers were visible on these segments for all the samples of data in each trial.

Figure 3.2-2 shows the positions and orientations of each of the clusters attached to each of the rigid segments. Table 3.2-1 describes the features to which each cluster was attached.

Segment	Cluster Name	Attachment Site
		Skin characteristics
Thigh	Femur	-distal, lateral Thigh -over isciotibial band, proximal to FLE
		-some anterio-posterior movement -well attached distal-proximally
Lower Leg	T2/3 T1/3	-at 2/3 segment length from ankle, and -at 1/3 segment length -anterior lower limb -on Anterior Tibial Crest surface
		-very well attached
Hindfoot	CA	-posterio-lateral calcaneus -lateral to Achilles T. attachment
		-well attached
Midfoot	N	-dorso-medial foot -over Navicular Tuberosity
		-well attached
	Cii	-mid-dorsal foot -over Inferior Retinacula attachment to 2^{nd} and 3^{rd} cuneiform
		-some elevation during maximal EDL contraction
Forefoot (medial)	Mi	-medial-dorsal foot -over mid-shaft of First Metatarsal
		-some dorsal-plantar movement
Forefoot (lateral)	Mv	-lateral-dorsal foot -over mid-shaft of Fifth Metatarsal
		-some dorsal-plantar movement

Table 3.2-1 Cluster Attachment sites on each of the Six Palpable Segment and likelihood of skin movement.

3.3 MOTION ANALYSIS TRIALS

Each Motion Analysis Session involved a single subject performing forty-four separate trials. The trials were of three different types: Muscle Model Calibration (MMC) trials, Pointer trials and the Movement Task trials. The MMC trials were performed first, followed by the Pointer trials and finally the Movement Task trials.

3.3.1 Subject Selection

The twelve subjects tested in this study were all volunteers selected from the staff and students at the Bioengineering Unit at the University of Strathclyde. Six subjects were male and six were female. The ages ranged from 22 to 40 years. Subjects with any known gait abnormalities of neurological or orthopaedic nature were excluded, as were those with history of surgery or severe trauma to either lower leg or foot.

The duration of a Motion Analysis Session was never longer than ninety minutes and testing was usually performed in the early afternoon. Subjects were clad in shorts and a short-sleeved shirt and all the trials were performed barefoot.

3.3.2 Muscle Model Calibration (MMC) Trials

The first trials of the session were the Muscle Model Calibration trials. During the MMC trials, EMG was recorded along with Force Plate data and positional data from the VICON cameras. The purpose of these trials was to have the subject isometrically contract certain muscles in order to calibrate the Muscle Model. The calibration process itself will be described with the Muscle Model in a later section. Recall that there were five superficial lower leg muscles from which EMG was recorded. During each trial, one or two of these five muscles were preferentially contracted by the subject as they isometrically pressed their foot against a resistive force. The resistance was provided by Force Plate #1. The subject leg positioning determined which muscles were preferentially contracted during the

trial. Therefore the leg positioning was different for each of the five different muscles. Two trials were done for each muscle, totalling ten MMC trials. Table 3.3.2-1 describes the leg positioning and direction of exertion for each of the five muscles.

Muscle	Leg and Foot Position	Foot Exertion
GaM + **Sol**	-knee fully extended -foot slightly plantar-flexed with subject standing on balls of feet	-plantar-flexing the ankle against body weight -resistance at balls of feet
Sol	-knee flexed at 80° -foot slightly plantar-flexed with subject standing on balls of feet	-plantar-flexing the ankle against body weight -resistance at balls of feet
TiA + **EDL**	-using **plate and strap** -knee fully extended -foot dorsi-flexed 10° and slightly inverted -strap runs across dorsum at Midfoot/ Forefoot segment interface	-dorsi-flexing and inverting against strap -resistance downward on dorsum at First Cuneiform/Base of First Metatarsal joint
PeL	-using **plate and strap** -knee fully extended -foot dorsi-flexed 10° and slightly everted -strap runs across dorsum at midshafts of Metatarsals	- everting against strap -resistance downward on dorsum of Base of Fifth Metatarsal and upward on sole at Head of First Metatarsal
EDL	-using **plate and strap** -knee fully extended -foot in neutral -strap runs across dorsum at toes	-extending toes against strap -resistance downward on dorsum of toes

Table 3.3.2-1 Leg and Foot Positioning and Direction of Foot Exertion for the five different MMC trials.

The normal mode of function for the Force Plate was to provide an upward reaction force when stepped on. For the Medial Gastrocnemuis (GaM) and the Soleus (Sol) muscle positions, the resistance force provided by the Force Plate was indeed upward. However, for the other three muscles, the Force Plate was required

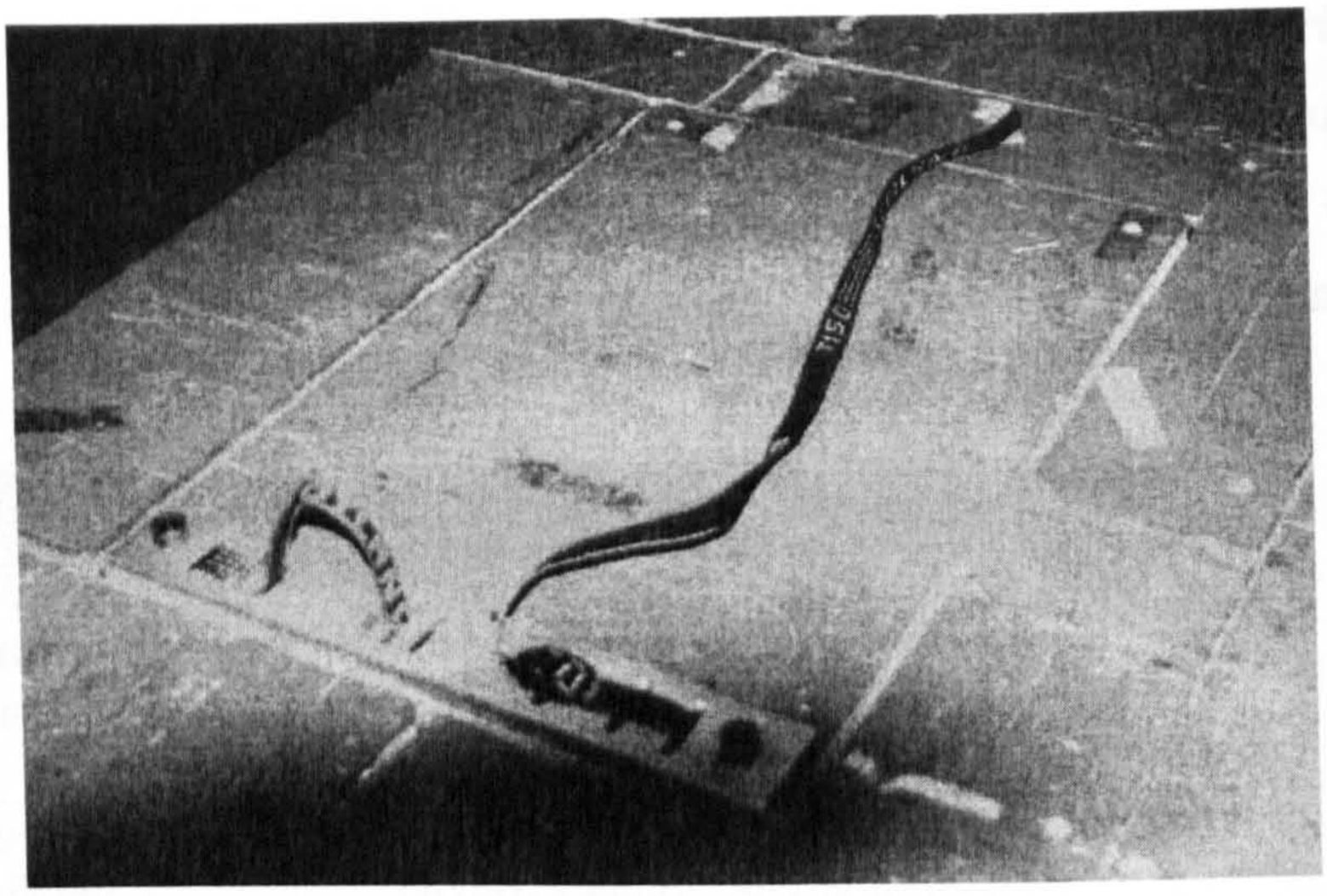

Figure 3.3.2-1 Plate and strap apparatus bolted in place on Force Plate #1.

to produce a *downward* resistive force to an upward foot exertion. In order to accomplish this, a plate and strap device was designed and built in-house. When bolted to Force Plate #1, the subject was able to exert the foot upwards on the strap and the Force Plate could then resist with a downward reaction force. Figure 3.3.2-1 shows the plate and strap device bolted in position on Force Plate #1.

At the beginning of the session, the EMG Collection electrodes and equipment were first attached to the subject and checked to make sure that leg and foot movement was not obstructed. Marker clusters were then placed on four of the six rigid segments. The clusters placed were: Femur (on the Thigh segment), T2/3 and T1/3 (on Lower Leg), CA (on Hindfoot) and N (on Midfoot). Note that the Midfoot segment only has one of its two clusters attached. The other Midfoot cluster and the two Forefoot clusters were not attached for the MMC trials since they would have interfered with the Force Plate plate and strap during the trials for Tibialis Anterior (TiA), Peroneus Longus (PeL) and Extensor Digitorum Longus (EDL).

The author positioned the subject leg and foot in the proper position at the beginning of the trial and instructed the subject on the desired direction of foot exertion. The subject then maintained their exertion for 8 s while EMG, Force Plate and positional data was recorded. Two trials were performed for each muscle. On the first trial, the subject was instructed to exert a moderate force. On the second trial, the exertion was greater, and closer to a maximal voluntary exertion.

3.3.3 Pointer Trials

Once the MMC trials were finished, the remaining three marker clusters were attached to the subject: Cii (on Midfoot segment), Mi and Mv (on medial and lateral Forefoot segments). The next sixteen trials were the Pointer trials during which no EMG nor Force Plate data was recorded.

A pointer with reflective markers was used during these trials which related the positions of the marker clusters on the skin to the underlying bony landmarks defined in the Internal Map. These trials enabled the structures of the Ankle Complex defined in the Internal Map to be related to the Kinematic Data taken

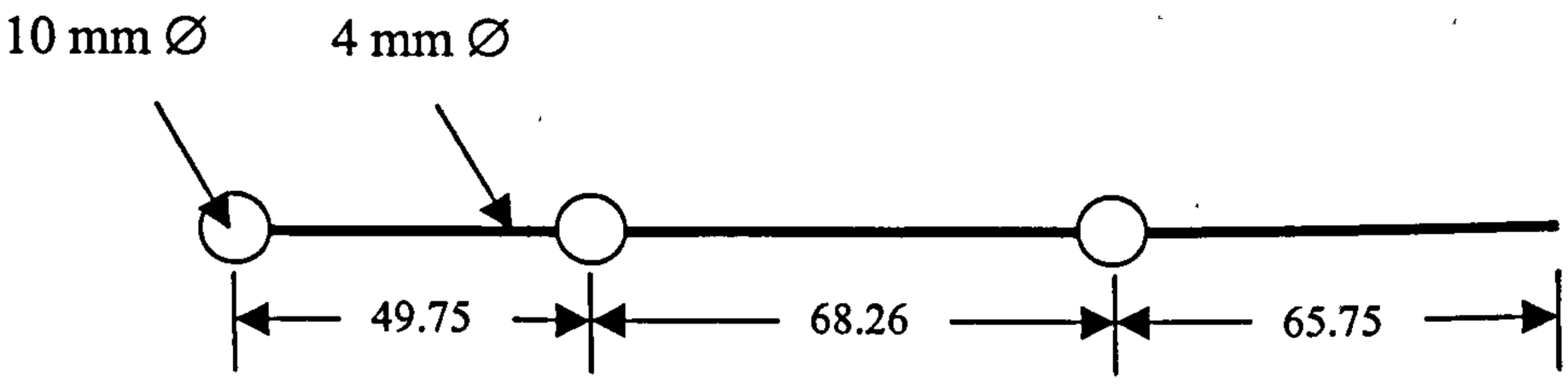

Figure 3.3.3-1 Plans for the pointer used in the Pointer trials.

from the Movement Task trials. Figure 3.3.3-1 shows the plan of the pointer used. Three reflective markers of 10 mm diameter were attached to the pointer. These were of similar construction to those on the marker clusters. The pointer itself was a carbon fibre rod of 4 mm diameter which had one end sharpened. The positions of the pointer markers with respect to the sharpened end and with respect to each other had been previously measured with calipers to an accuracy of ±0.5 mm. During each Pointer trial, a single bony landmark was located and 'pinpointed' using the pointer. Three landmarks per segment were identified on each of the six palpable segments. Table 3.3.3-1 lists the six segments and their associated landmarks. It should be noted that the landmarks identified during the Pointer trials listed in Table 3.3.3-1 were identical to the bony prominences which will be defined in the Internal Map in the Section 4.2.2; listed in Table 4.2.2-1.

Segment	Landmark	Description
Thigh	FLE	Lateral Epicondyle (most lateral point)
	FGT	Greater Trochanter (most lateral point)
	FME	Medial Epicondyle (most medial point)
Lower Leg	FLM	Lateral Malleolus (most lateral point)
	FH	Fibular Head (most lateral point)
	TMM	Medial Malleolus (most medial point)
Hindfoot	CALT	Lateral Tuberosity (lateral to Achilles tendon)
	CAER	Eminentia Retrotrochlearis (greatest elevation)
	CAMT	Medial Tuberosity (medial to Achilles tendon)
Midfoot	NT	Navicular Tuberosity (most medial point)
	Ci	First Cuneiform (distal dorsal crest)
	CU	Cuboid (lateral dorsal edge)
Forefoot	MiH	First Metatarsal Head (most dorsal point)
	MiB	First Metatarsal Base (most dorsal point)
	MvH	Fifth Metatarsal Head (most dorsal point)
	MvB	Fifth Metatarsal Base (most dorsal point)

Table 3.3.3-1 Segment landmarks identified on each of the Six Palpable Segments during the Pointer trials.

During a pointer trial, the subject was stationary while the experimenter palpated the appropriate landmark. Once located, the sharpened end of the pointer was placed on the landmark and held by the experimenter. Positional data was

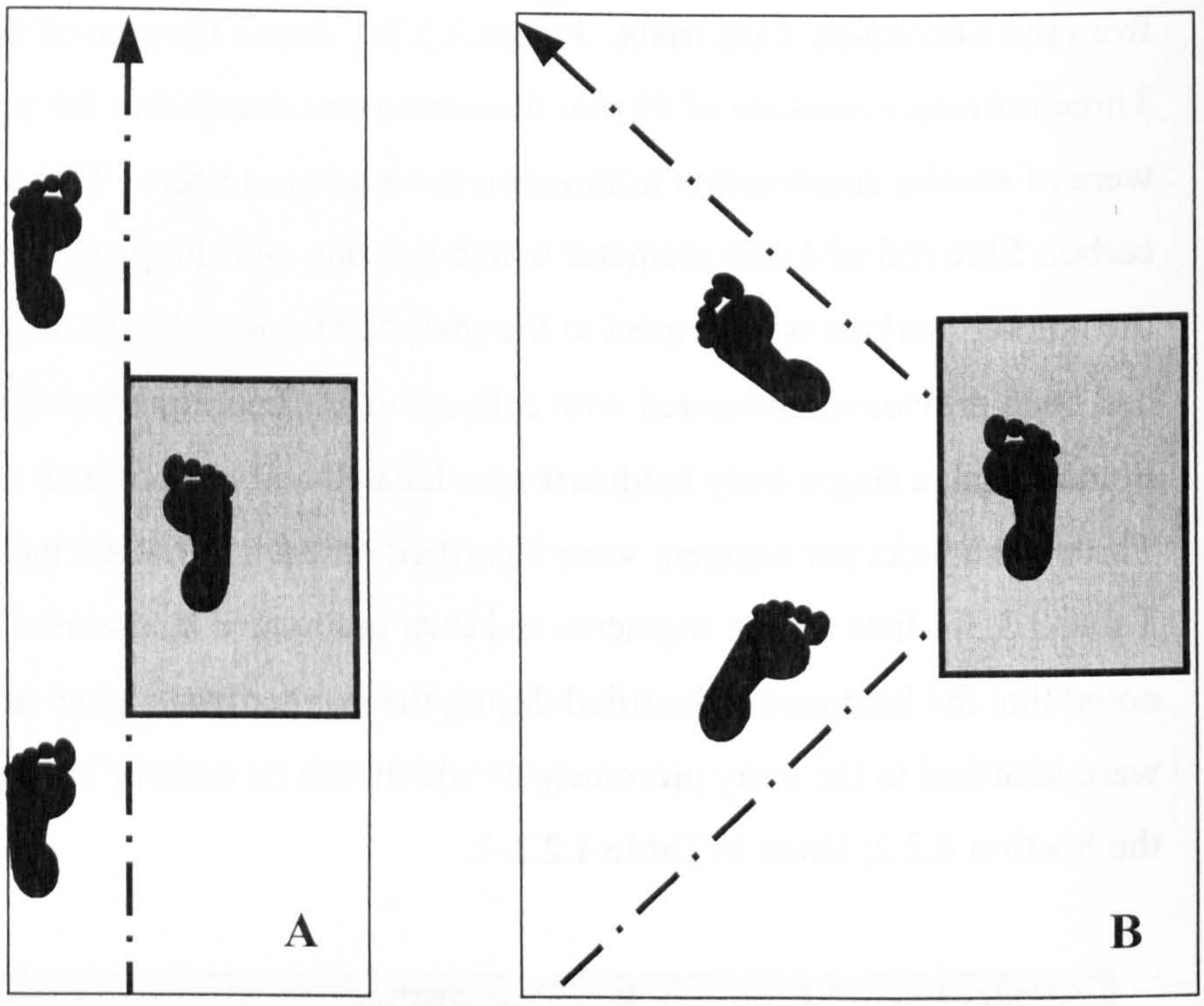

Figure 3.3.4-1 Floor paths and foot falls with respect to Force Plate #1 for the two movement task: Walking and Walking Turn.

sampled by the VICON cameras for 6 s. After each trial, the marker positions were reconstructed in the VICON System. If any of the markers on the pointer or on the clusters were not visible, then the trial was repeated with a slightly different subject position.

3.3.4 Movement Task Trials

The final eighteen trials of the session were the Movement Task trials. In these trials, the subject performed the movements which were to serve as the kinematic input for the Ankle Complex Model. Two different movement tasks were performed, *walking* and a *walking turn*. Both tasks were performed at three speeds: slow, preferred and fast pace. In both tasks, it was the right foot that made contact with Force Plate #1. Figure 3.3.4-1 shows the floor view of the paths of motion for the two tasks.

Walking

The first nine trials of the Movement Task trials were the *walking* trials. The subject was given several practice walks before data was collected to ensure that gait was as representative of the normal subject gait as possible. During a trial, the subject was shown from where to start walking and with which foot to initiate gait. Gait representative of natural walking was the aim of these trials so the subject was instructed to keep their attention on the facing wall of the laboratory as they walked and was told not to anticipate placement of the foot on the Force Plate. As the subject walked, an assistant carried the EMG cable spanning from the subject's waist to the VICON system so that it would not influence gait.

Preferred pace was the first speed to be performed. The subject was asked to walk at a comfortable, average pace. At least four steps were taken before Force Plate contact and about three steps afterward. Data was collected for three separate trials at this pace. The subject was then asked to choose a pace slower than preferred. After initial practice, three trials of data were then taken at slow pace. Finally, the subject was asked to walk faster than preferred with three trials taken at

this pace. The fast pace trials would be redone if the subject gait broke into a trot or run.

Any of these nine trials were repeated if the right foot completely missed or only partially contacted the Force Plate. Before redoing the trial, the starting point for the subject was altered to ensure complete right foot contact. Trials were also redone if the subject altered their normal gait pattern or gait speed in order to contact the Force Plate when they otherwise would have missed or only partially contacted.

Walking Turn

The final nine trials of the Movement Tasks were the *walking turn* trials. As with the walking task, it was the subject right foot which contacted Force Plate #1. For this movement task however, the subject performed a 90° turn to the left when the right foot was in contact with the Force Plate. The subject approached the force plate along a path at 45° to the walking task approach. This is illustrated in Figure 3.3.4-1. Four steps were taken before force plate contact and about four steps afterward. With this task the subject concentrated on the Force Plate and did anticipate foot contact. An assistant held the EMG cable as the subject moved so as to avoid interference with gait pattern.

Practice turns were done before data was collected until the subject was comfortable with each of the three speeds. Preferred pace walking turn was done first. The subject was asked to approach the Force Plate at a speed similar to that of preferred pace walking. The foot was planted on the Force Plate with the long-axis of the foot parallel to the long axis of the Force Plate. The subject then left the Force Plate in a direction 90° to the left of the approach, walking at preferred pace. Three trials of data were taken at preferred pace. Three trials were then done at slower pace. Finally, three trials were performed at fast pace. The subject was instructed to plant the right foot quite heavily on the Force Plate and to change direction as quickly as possible.

The motion trials were all performed in barefoot for a number of reasons which all relate to repeatability of results between different subjects and the inability

to track foot segment motion effectively with stereophotogrammetry motion systems. Had the subjects been instructed to perform the movement tasks in a pair of their own trainers, there would have been a variability in the design, stiffness and wear of the trainers which each subject wore. If the experimenter had decided to supply a standard pair of trainers, many different sizes would have been necessary to ensure standard fit of the shoes on each subject.

The design, stiffness and wear of the shoes affect the gait of the wearer by increasing the dorsiflexing moment about the Ankle Joint at heel strike and by increasing the stiffness of the arches of the foot. The first affect is of relevance to the current study. The heel of the shoe increases the lever arm of the ground reaction force about the Ankle Joint centre primarily and about the Subtalar Joint secondarily. This change in the lever arm has the greatest effect about the Ankle Joint at heel strike. The increased lever arm created by the heel of the shoe combined with the posteriorly directed anterior-posterior component of the ground reaction force causes a larger dorsi-flexing moment about the Ankle Joint than would be experienced barefoot. The higher the heel, the larger the increase in dorsi-flexing moment at heel strike. This effect is particularly pronounced when wearing a pair of women's high heeled shoes.

The ability to observe the relative motion of the segments of the foot is greatly hindered when wearing shoes. Stereophotogrammetry motion analysis systems rely on reflective markers attached to the rigid segments in order to follow motion. With a shoe, markers attached to the foot will not be visible unless they either pass through the shoe from their skin attachments on rods or the shoe has material removed. Interference with marker motion from relative motion of the shoe is also very likely, corrupting the measured marker trajectories.

Since the topics of the current study were to observe the differences in Ankle Complex loading between walk and walking turn and to test the MMAO method for solving the joint indeterminacy, but not to observe the effects of shoed gait versus barefoot gait, all the trials were performed barefoot.

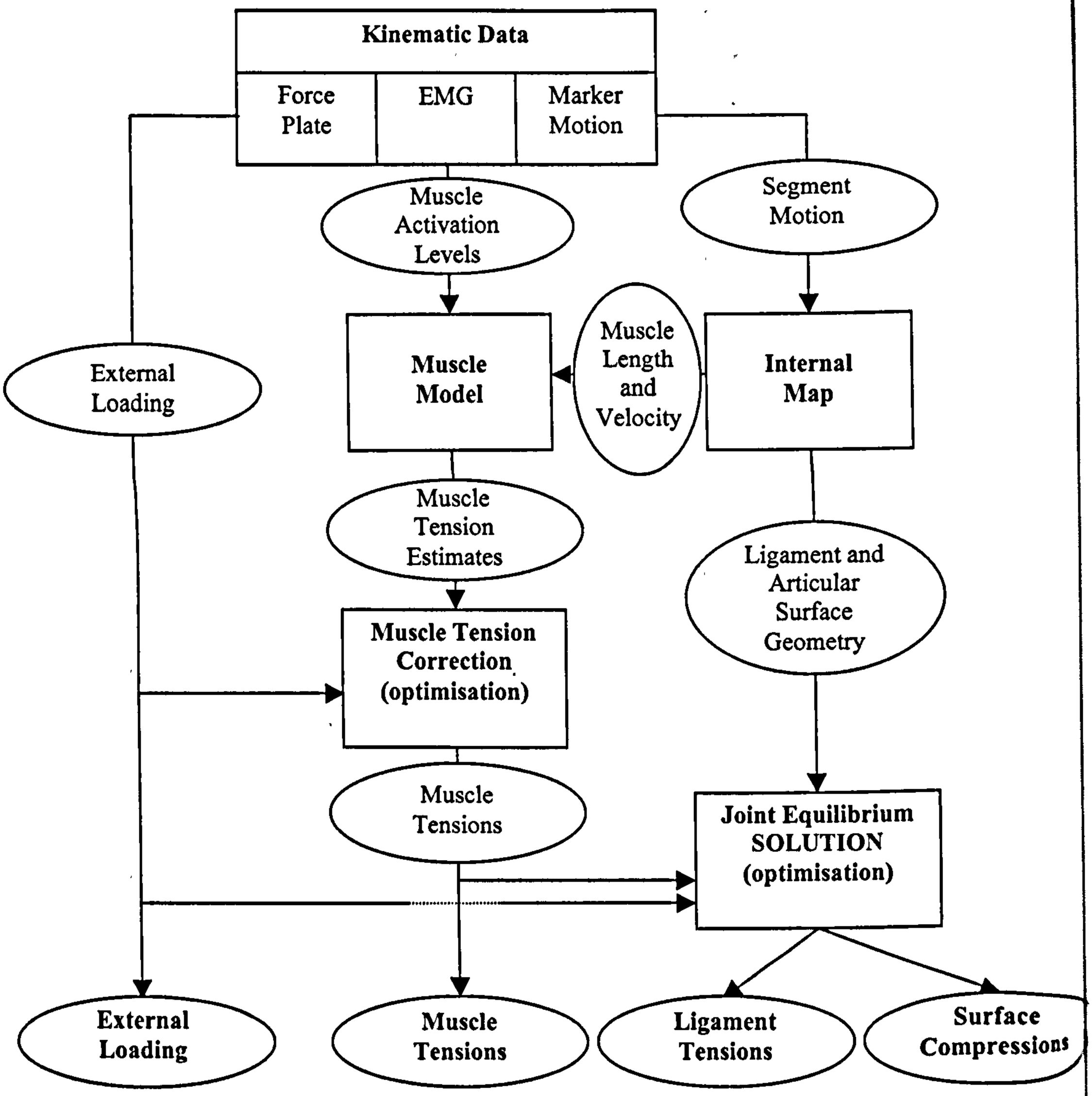

Figure 4.1.1-1 Flow of Calculations in Current MMAO Model.

CHAPTER 4 ANALYSIS OF KINEMATICS

4.1 OUTLINE OF THE CURRENT MODEL

The model of the Ankle Complex developed in this study represented the right leg and foot as seven rigid segments, two segments of the leg: Thigh and Lower Leg, and five segments of the foot: Talus, Hindfoot, Midfoot and Lateral and Medial Forefoot. Two joints were modeled within the Ankle Complex, the Ankle Joint and the Subtalar Joint.

The Ankle and Subtalar Joints were each assumed to possess unique and stationary rotational axes which were fixed with respect to the Lower Leg and the Hindfoot respectively. Modelling the Subtalar Joint with a single rotational axis was supported by the literature as discussed above. With the Ankle Joint though, evidence has shown that the unloaded Ankle Joint, at least in two-dimensions, behaves as a multi-bar linkage mechanism with a moveable rotational axis. However, since no models have yet used this mechanism to model *loaded* ankles and since the difficulties of doing so seemed to outweigh the benefits of this mechanism over a stationary rotational axis, a multi-bar mechanism was not used for the Ankle Joint.

Since the Ankle rotational axis was assumed fixed, despite the fact that it has been shown to migrate with joint motion means errors will appear in the lever arms determined for the internal structures of the Ankle Joint and for the external loading. However, these errors should not significantly affect the overall solutions for Ankle Complex equilibrium since the discrepancy in the lever arm lengths will be small.

4.1.1 Flow of Calculations

Figure 4.1.1-1 illustrates the order of calculations for the current model in the form of a flow chart. The major outputs of the model are listed at the bottom. These include the external loading on the two joints of the Ankle Complex, the tensions in the muscles of the Complex, the tensions in the ligaments and compressions on the

articular surfaces. Other secondary outputs, such as the joints angles, were drawn from the model at various intermediary stages in the flow chart.

4.1.2 Kinematic Data

Kinematic information drawn from the VICON motion laboratory was the input for the Ankle Complex model. Accompanying the kinematic data from the rigid segements were the ground reaction force from the a floor mounted force plate and electromyographic (EMG) data from the muscles of the Ankle Complex. These three types of data, drawn from the motion trials, will be collectively referred to as Kinematic Data.

The Kinematic Data of twelve subjects was collected as they performed the tasks of *walking* and *walking turn*. The data was recorded using an eight camera VICON Motion Analysis System with three floor mounted force plates. The motion of six of the seven rigid segments (Talus excluded) was tracked as the subjects performed the movements. Reflective markers, arranged as rigid clusters of three, were attached to each of the segments. The size, positioning and design of the marker clusters allowed the relative movement of each of the rigid segments to be observed with great accuracy. The very small relative motion of the four segments of the foot was observed. This was remarkable since in the majority of locomotion studies, the foot was considered to be a single rigid segment, and the changing role of the foot from a compliant stabilising structure to a rigid propulsive structure was missed.

4.1.3 Internal Map

The current model employed an extensive mapping of the geometries and relative positions of the internal structures of the Ankle Complex. The Internal Map was constructed from medical images of a single cadaver supplied by the Visible Human Project at the National Institute of Health in the USA. The Map defined the origins, insertions and pulley points for the eight muscles of the Ankle Complex. These positions allowed the instantaneous lengths of the muscles and their tendons,

needed by the Muscle Model, to be determined with the appropriate wrapping of the tendons over their pulley points. The Internal Map also supplied the instantaneous lever arms and lines of action for the eight muscles needed in the Ankle Complex equilibrium solution. The attachments of the twelve ligaments and the positions of the compressive force components on the seven surfaces of the Ankle Complex were also defined in the Internal Map. These allowed the instantaneous lines of action and lever arms of these structures to be determined for Ankle Complex equilibrium.

The geometries of the seven pairs of articular surfaces of the Ankle Complex were defined with the Internal Map. The shapes of the pairs of surfaces at each of the two joints were used to determine the correct position for the joint rotational axes.

4.1.4 Ankle Complex Muscles and Muscle Model

Of the eleven muscles acting about the joints of the Ankle Complex, only seven were included in the current model. The Peroneus Tertius muscle (PeT) was excluded since its influence on the joints was very similar to that of the Extensor Digitorum Longus (EDL). It was also difficult to record an EMG signal exclusively from the PeT without it containing cross-talk from the EDL due to their close relative positions.

None of the three muscles from the Posterior Tibial group were included: Tibialis Posterior (TiP), Flexor Digitorum Longus (FDL) nor Flexor Hallucis Longus (FHL). It was practically very difficult to record individual EMG signals from each of these during locomotion since they were each rather small in volume and therefore produced weak signals and they all lay deep to the Gastrocnemius and Soleus muscles which both produce very large EMG signals. The Posterior Tibial muscles could be ignored since they are assumed to be postural muscles as opposed to propulsive muscles. Therefore these muscle were unlikely to contribute significantly during walking or a walking turn. The Gastrocnemius muscle possesses two distinct heads which were modelled as separate muscles. Therefore the total number of muscles acting about the joints of the Ankle Complex included in the current model was eight.

The equilibrium solution for the loading in the structures of the Ankle Complex was performed using a Muscle Model Assisted Optimisation routine. The muscle tension equilibrium solution was produced in only two dimensions about the rotational axis of both joints. The tensions in the eight muscles of the current Ankle Complex Model were estimated using a Hill-type Muscle Model which employed the surface electromyography (EMG) recorded during the movement tasks and from the instantaneous muscle plus tendon lengths determined using the Internal Map as inputs. The Muscle Model was composed of three components. The Contractile Component and the Parallel Elastic Component were together connected in series to the Series Elastic Component. This arrangement was similar to Winters (1995).

The output of the Muscle Model was then altered minimally using an optimisation routine so that the muscle moments at the two ankle joints would match the external moments determined from the Force Plate data.

4.1.5 Joint Equilibrium Solution and SIMPLEX Optimisation

Once the muscle tensions had been determined, the solution of over-all joint loading equilibrium in all three dimensions for both joints could then be found. The external loading was supplied by the Force Plate part of the Kinematic Data. The lines of action and lever arms of the ligaments and contact surfaces were supplied by the Internal Map and the segments motion parts of the Kinematic Data and the muscle tensions were supplied by the Muscle Model and correction routine.

The Simplex Method of Linear Optimisation was used to solve for the equilibrium loading of the ligaments and surfaces. Linear Optimisation was well suited to the Ankle Complex since linear optimisation has been shown to successfully share loading among the structures of the system when finding equilibrium about multi-joint systems. The equilibrium solution found for the Ankle Complex simultaneously minimised the maximum tension in any of the ligaments and minimised the maximum compression on any of the articular surfaces.

The solution for loading equilibrium about the two joints of the Ankle Complex which balanced the external loading with the internal loading of the structures of the Complex was the ultimate goal of the MMAO model. This

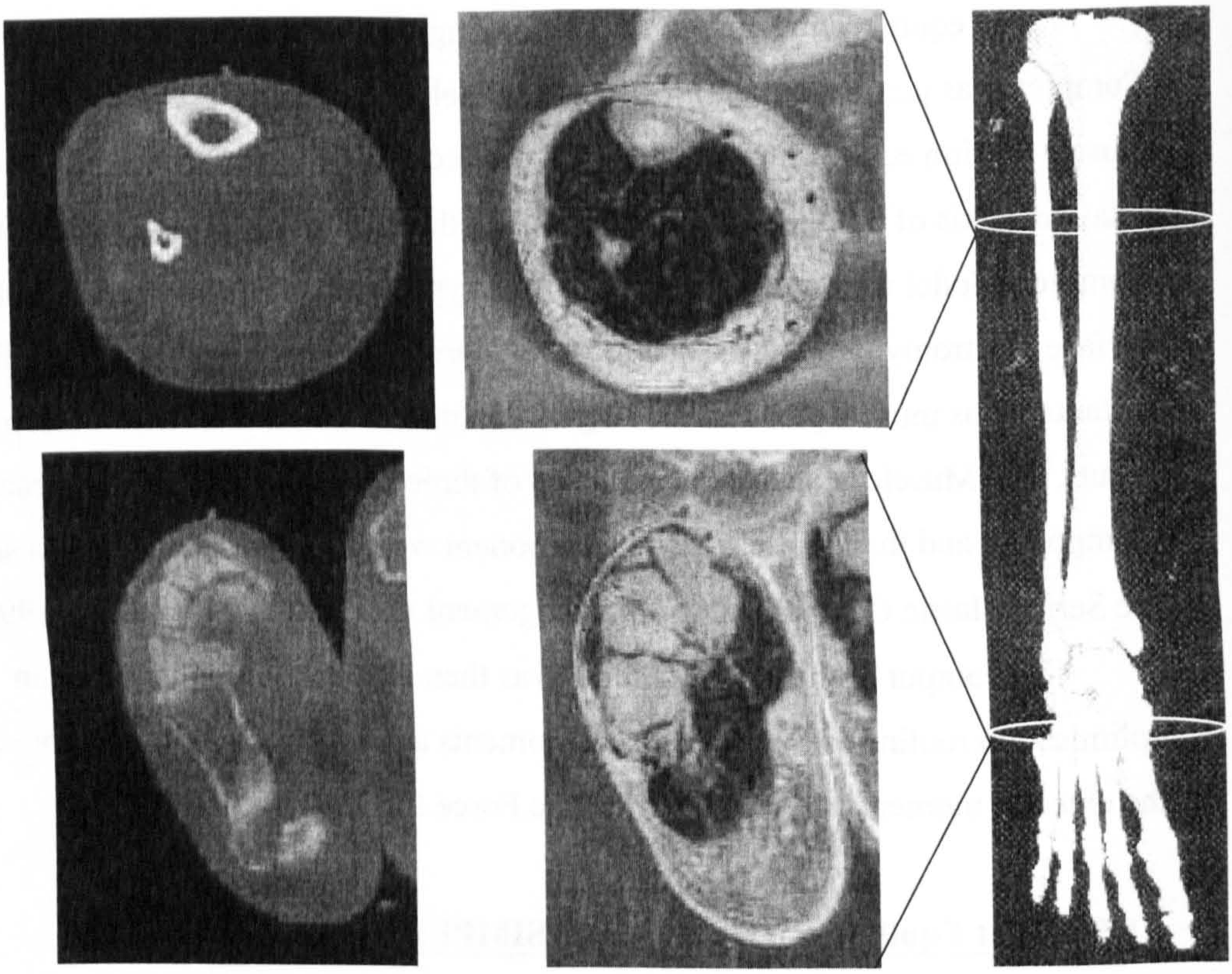

Figure 4.2.1-1 Examples of the Computer Tomography Scans and Anatomical Photographs available from the Visible Human Project.

equilibrium solution was calculated at each sample of Kinematic Data throughout each motion trial for each of the twelve subjects.

4.2 INTERNAL MAP OF SEGMENTS

4.2.1 Digitising the Medical Images

The Internal Map of the right ankle complex and associated structures was constructed from Computer Tomography Images (CTs) and Anatomical Photographs (APs). These medical images were supplied by the Visible Human Project (VHP) which is a programme of the National Library of Medicine at the National Institute of Health in Maryland, USA.

The VHP series of images consisted of CTs, Magnetic Resonance Images (MRIs), and Anatomical Photographs taken from two cadavers; one male and one female. Only the CTs and APs were used to construct the Internal Map and the MRIs were excluded. The resolution of the images taken of the female was greater than those of the male, and therefore the female images were used exclusively to produce the Internal Map. The CTs and MRIs were created by the VHP, before the cadavers were frozen. The cadavers were then frozen and the Anatomical Photographs taken. The process of producing the APs was ultimately destructive to the cadavers. A slice was destructively made across the cadaver in the transverse plane and a digital photograph taken of the cross-section. Another slice was then made slightly further along and another digital photograph taken. This process was continued until the entirety of the cadaver had been sliced and photographed, resulting in the destruction of the cadaver. The result was a series of photographs of the transverse plane progressing through each of the two cadavers.

Computer Tomography Images (CTs)

The CT images supplied by the VHP showed the hard tissue of bone and articular cartilage exclusively. Soft tissue did not appear. This was useful for mapping the shape of the bones and articular surfaces without soft tissue masking the geometry. The CTs were taken with the cadaver lying supine on a plinth. The CT

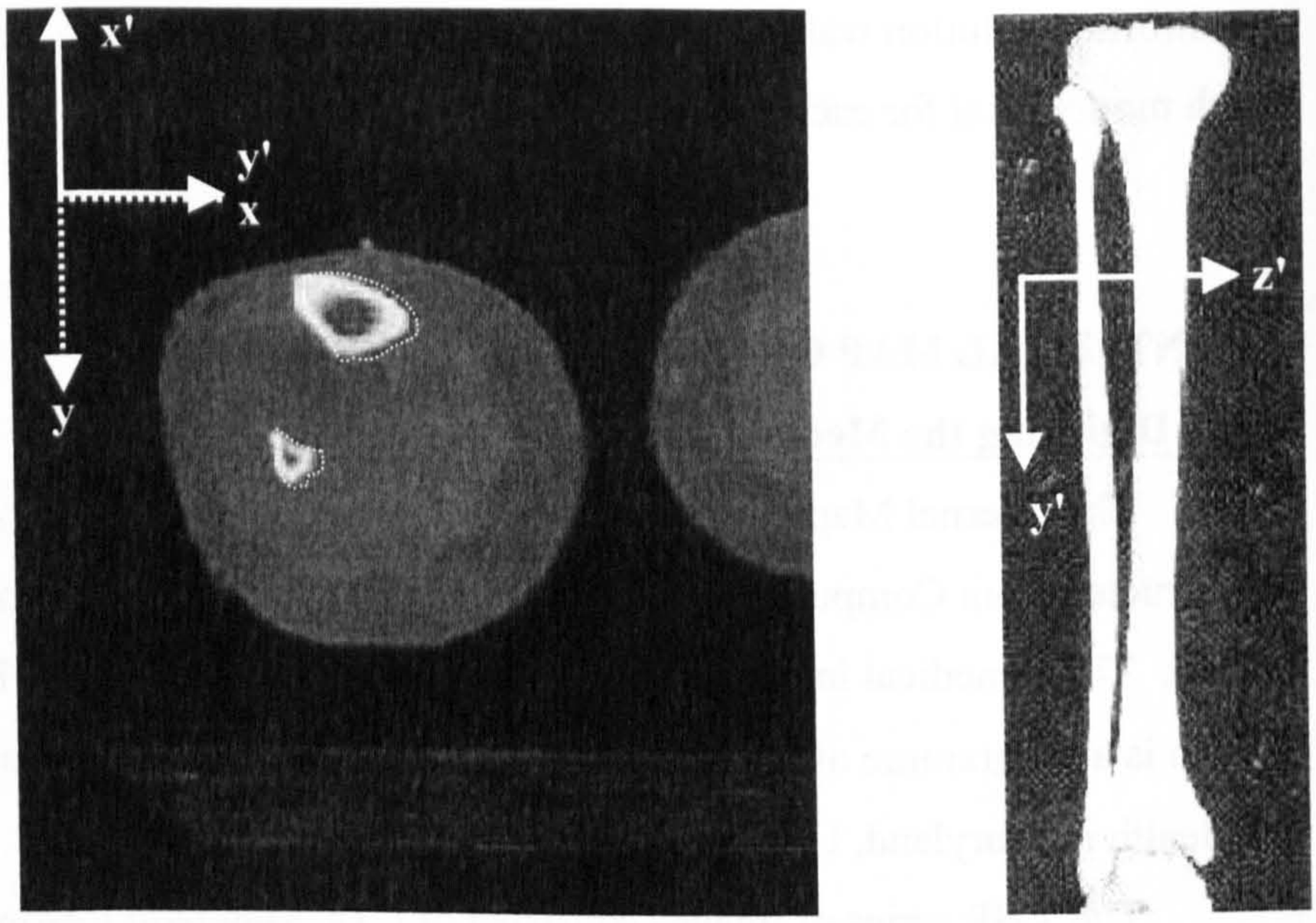

Figure 4.2.1-2 Digitising internal structures from medical images, and transforming co-ordinates into MI-frame of reference (x', y', z').

slices were taken in the vertical plane, perpendicular to the long axis of the body with the cadaver lying supine. For the majority of the slices, the CTs coincided with the transverse plane. The slices were taken at 0.33 mm intervals along the long axis of the body with pixel resolution of 0.33x0.33 mm within each slice. Figure 4.2.1-1 shows two examples of CT slices taken at different positions along the body.

Anatomical Photographs (APs)

The Anatomical Photograph slices were created so that they coincided with the CT slices. The APs showed all the tissues present in the cross-section as different shades of grey. Once the bone and cartilage had been identified from a CT slice, the remaining tissues, the tendons, ligaments, aponeuroses and retinacula, could then be identified using the coincident AP slice. The resolution of the APs was identical and coincident with the CTs with slices at 0.33 mm intervals along the body long axis and the photographs scanned at 0.33x0.33 mm resolution within the slice. Figure 4.2.1-1 also shows two examples of APs, which were coincident with the CTs slices shown.

The images were accessed electronically from an anonymous FTP mirror site at the University of Glasgow. The CTs and APs were downloaded in small groups as needed. Once downloaded, the images were first viewed with the software *3dviewnix*. This program specialised in viewing medical images from various disparate sources. The images were cropped and copied from this programme and inserted into the software *Visilog*. Visilog was the software which enabled the structures within each of the slices to be digitised into individual data points.

Within Visilog, the CT or AP image was displayed. The author digitised the structures of interest within the image (i.e. bone edge in a CT or ligament edge in an AP) by placing data points at approximately 1 mm intervals along the edge of the structure. Figure 4.2.1-2 illustrates a CT scan containing the cross-section of the long shafts of the tibia and fibula, which have been digitised with data points.

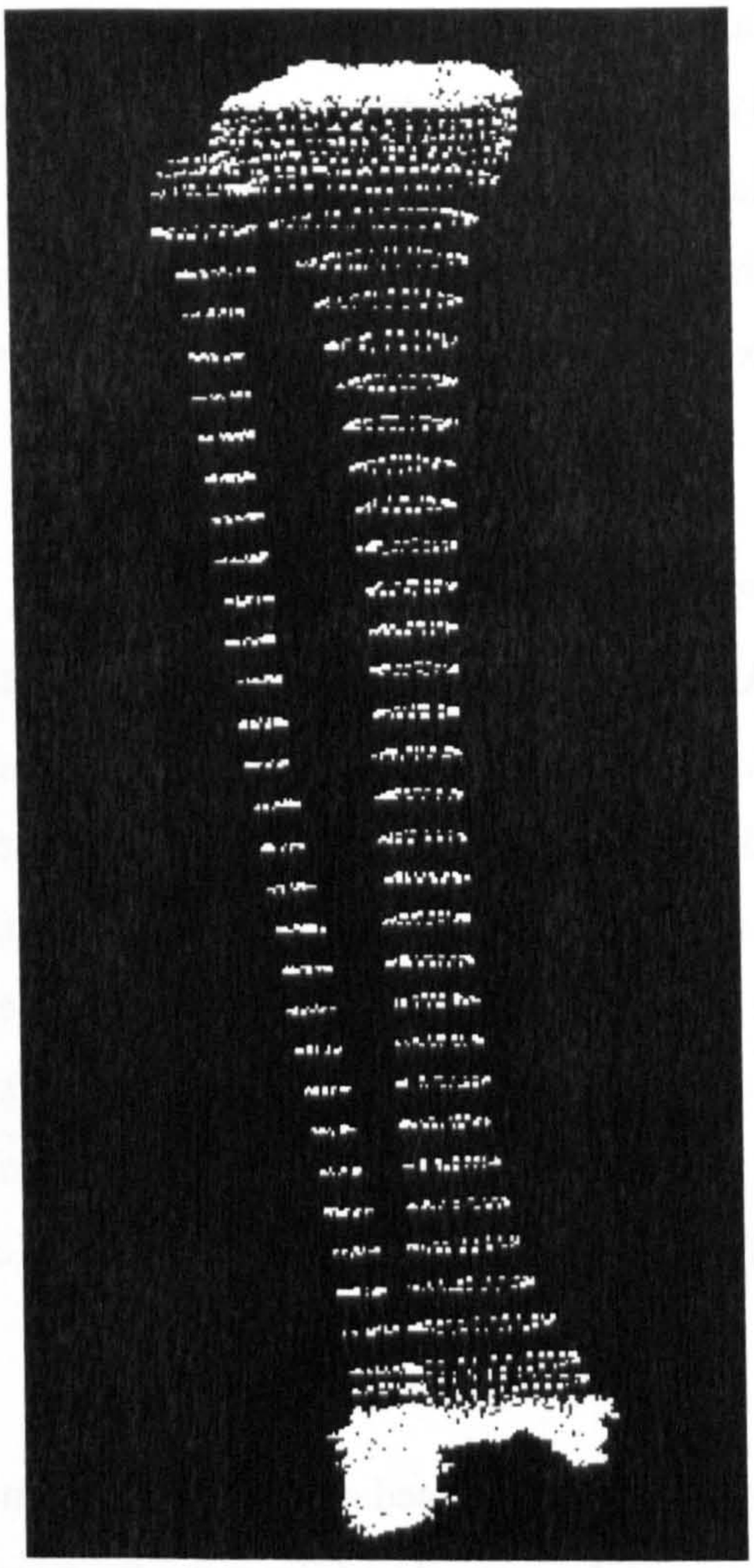

Figure 4.2.1-3 The digitised data-points as displayed in the ANSYS software.

Data points were placed around all the structures of interest within the slice. Once this had been done, the two-dimensional co-ordinates of all the data points within the slice were output into a text file along with a number assigned to the slice. The slices were numbered consecutively from the head down to the toes in increments of 0.33. The origin of the in-slice co-ordinate axes was in the top left corner of the slice. In both the CTs and the APs a reference object was included at the time that the images were created so that the different image types could be aligned. This object served as the in-slice origin. The in-slice $x-axis$ ran horizontally to the right and the $y-axis$ vertically downward in the slice. Figure 4.2.1-2 shows the orientation of the in-slice co-ordinate axes. The Internal Map was composed of digitised CT and AP slices from the hip joint centre down to the final phalanx of the great toe.

The number assigned to each slice was added to the in-slice co-ordinates to produce three co-ordinates in three-dimensional space. However, the in-slice axes, x and y, with the slice number as the third axis did not form a right handed co-ordinate system. Therefore, once a slice had been digitised and the data point co-ordinates had been outputted into the text file, the co-ordinates within the text file were then converted into a right handed system as follows,

$$\begin{aligned} x' &= -y \\ y' &= slice-number \\ z' &= x \end{aligned} \qquad (4.2.1\text{-}1)$$

This new axis system defined the Medical Image (MI) frame of reference. The $y-axis$ ran distally along the long axis of the body. The $x-axis$ was directed anteriorly and the $z-axis$ ran medially for the right leg.

The co-ordinates of all the data points in all the slices, defined in the MI frame, were then input into the finite element programme *ANSYS*. The pre-processor of this software was used to visualise the data points of the Internal Map in three-dimensions. The pre-processor allowed the data points to be manipulated so that they could be viewed from any direction. The software also allowed portions of the data points to be examined in isolation from the rest. Within ANSYS the multitude of data points took on the appearance of the bones, cartilage, tendons, ligaments and

retinacula of the rigid segments of the right leg and foot. Figure 4.2.1-3 shows the appearance of the data points of the digitised tibia and fibula and associated structures.

Within ANSYS the individual bone landmarks, muscle insertions and origins, retinacula and ligaments, and articular surfaces were isolated from the rest of the data points. The sites of interest were located by the user and the co-ordinates of the data points at the sites were recorded. For muscle insertion and origin sites, several data points were isolated since muscle attachment occurred over an extended area. For ligament attachment sites only a single data point was recorded. For articular surfaces, all data points lying on the surface were recorded.

The isolation of the articular surfaces involved a second step. Once all the data points lying on the surface were assigned, they did not form a smooth surface. Although great care was taken by the Visible Human Project while creating the medical images to align the different image slices, some misalignment was still present (±0.66 mm). Also, some error (on the order of ±0.33 mm) was introduced during the digitisation process when data points were placed by the user on the structures of interest. Therefore not all the data points isolated on the articular surface were used to represent the surface geometry and many data points were discarded so that the remaining data points defined a smooth surface.

4.2.2 Defining Segment Bone-fixed Frames

In the Internal Map, the right leg and foot were divided into seven rigid segments: Thigh, Lower Leg, Talus, Hindfoot, Midfoot, and two semi-independent Forefoot segments. On six of the seven segments, three bony prominences were isolated per segment. The prominences on each of these segments were selected since they were easily palpable through the skin. These prominences served as the landmarks used to define a bone-fixed frame of reference attached to each of the six segments.

Segment	Landmark	Description
Thigh	FLE	Lateral Epicondyle (most lateral point)
	FGT	Greater Trochanter (most lateral point)
	FME	Medial Epicondyle (most medial point)
Lower Leg	FLM	Lateral Malleolus (most lateral point)
	FH	Fibular Head (most lateral point)
	TMM	Medial Malleolus (most medial point)
Hindfoot	CALT	Lateral Tuberosity (lateral to Achilles tendon)
	CAER	Eminentia Retrotrochlearis (greatest elevation)
	CAMT	Medial Tuberosity (medial to Achilles tendon)
Midfoot	NT	Navicular Tuberosity (most medial point)
	Ci	First Cuneiform (distal dorsal crest)
	CU	Cuboid (lateral dorsal edge)
Forefoot	MiH	First Metatarsal Head (most dorsal point)
	MiB	First Metatarsal Base (most dorsal point)
	MvH	Fifth Metatarsal Head (most dorsal point)
	MvB	Fifth Metatarsal Base (most dorsal point)

Table 4.2.2-1 Bony prominences on each Segment defining the Bone-fixed Reference Frames.

The Talus segment was treated differently from the other segments since it could not be palpated through the skin throughout most of the range of motion of the Ankle Joint Complex. The bone-fixed frame of reference attached to the Talus was therefore defined differently from the other six segments and will be described in Section 4.2.6. Table 4.2.2-1 shows the landmarks isolated on each of the six bone segments.

Three landmarks per segment was the minimum number of points required to form a bone-fixed frame of reference attached to each segment. The three landmarks on each segment were used to form two vectors,

$$_{MI}\vec{r}_1 \text{ and } _{MI}\vec{r}_2 .$$

The order in which the points were used to form these vectors was specific to each segment. The ordering determined the directions of the three axes of the bone-fixed reference frame and was therefore chosen with care. The axis directions of the bone-fixed frames followed the same general pattern for all the segments. The second,

$2-axis$, ran distally along the long axis of the bone segment. The first, $1-axis$ ran anteriorly and dorsally on the right leg and foot respectively and the third, $3-axis$ ran medially. Table 4.2.2-2 shows each of the bone segments and the ordering of the landmarks for each. Also drawn are the bone-fixed segment axes. The bone-fixed frames were constructed from the vectors ${}_{MI}\vec{r}_1$ and ${}_{MI}\vec{r}_2$ for each of the segments as ordered in Table 4.2.2-2. This was done by first finding the unit vectors from these two vectors,

$$ {}_{MI}\hat{r}_1 = \frac{{}_{MI}\vec{r}_1}{\left|{}_{MI}\vec{r}_1\right|} \text{ and } {}_{MI}\hat{r}_2 = \frac{{}_{MI}\vec{r}_2}{\left|{}_{MI}\vec{r}_2\right|}. \qquad (4.2.2\text{-}1) $$

The vector cross product was then taken of these, producing a new vector, ${}_{MI}\vec{r}_x$. Its unit vector was then found as in Eq. 4.2.2-1,

$$ {}_{MI}\vec{r}_x = {}_{MI}\vec{r}_1 \times {}_{MI}\vec{r}_2 \Rightarrow {}_{MI}\hat{r}_x . \qquad (4.2.2\text{-}2) $$

The axis directions for the bone-fixed frames were then defined as,

$$ \begin{aligned} {}_{MI}\hat{1} &= {}_{MI}\hat{r}_x \\ {}_{MI}\hat{2} &= {}_{MI}\hat{r}_2 \\ {}_{MI}\hat{3} &= {}_{MI}\hat{1} \times {}_{MI}\hat{2} \end{aligned} \qquad (4.2.2\text{-}3) $$

The rotation and translation matrices, which performed the transformation from the MI frame to the bone-fixed frames, were constructed from the unit vectors in Eq. 4.2.2-3, and the origins defined in Table 4.2.2-2,

Bone Segment	Direction of Axes	Defining Vectors
Thigh	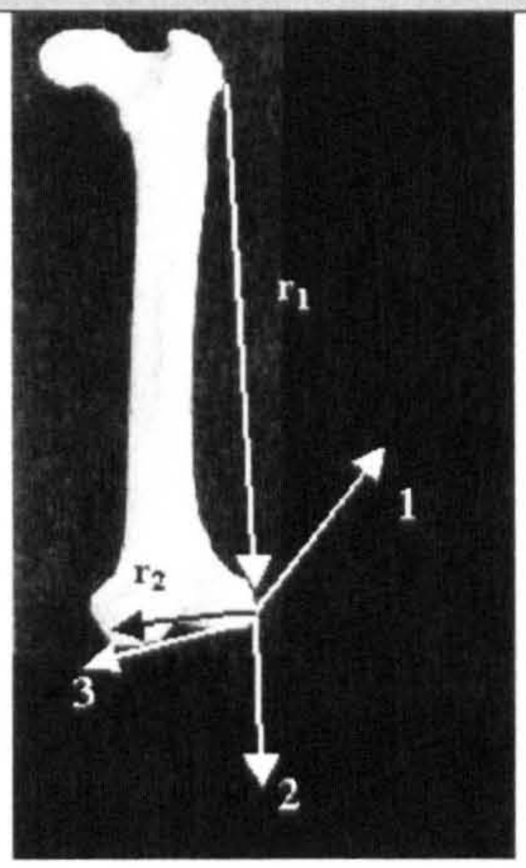	${}_{MI}\vec{r}_1 = {}_{MI}\underline{FLE} - {}_{MI}\underline{FGT}$ ${}_{MI}\vec{r}_2 = {}_{MI}\underline{FME} - {}_{MI}\underline{FLE}$ ${}_{MI}\underline{O} = -{}_{MI}\underline{FLE}$

Lower Leg	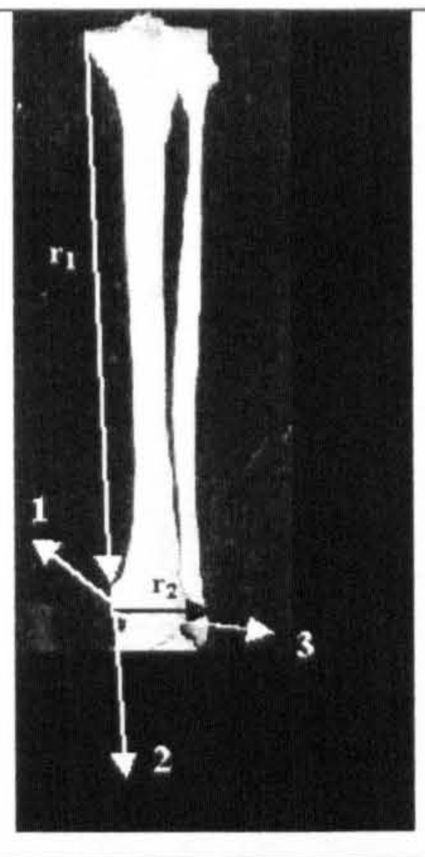	${}_{MI}\vec{r}_1 = {}_{MI}\underline{FLM} - {}_{MI}\underline{FH}$ ${}_{MI}\vec{r}_2 = {}_{MI}\underline{TMM} - {}_{MI}\underline{FLM}$ ${}_{MI}\underline{O} = - {}_{MI}\underline{FLM}$
Hindfoot	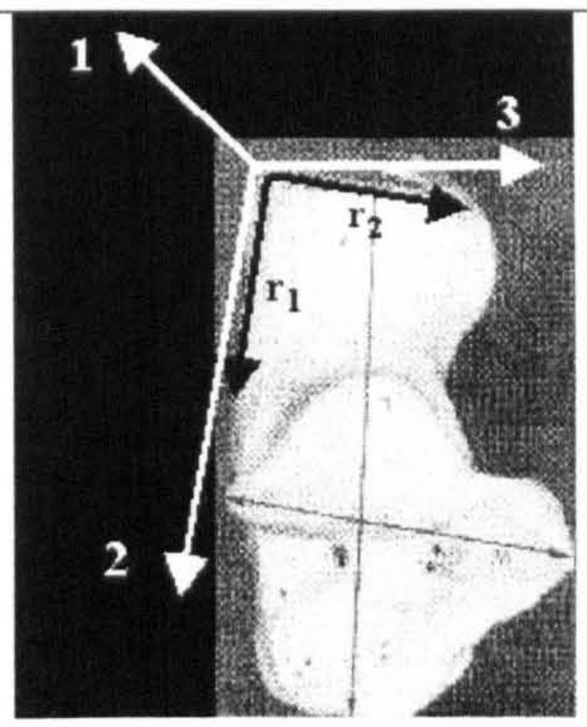	${}_{MI}\vec{r}_1 = {}_{MI}\underline{CAER} - {}_{MI}\underline{CALT}$ ${}_{MI}\vec{r}_2 = {}_{MI}\underline{CAMT} - {}_{MI}\underline{CALT}$ ${}_{MI}\underline{O} = - {}_{MI}\underline{CALT}$
Midfoot	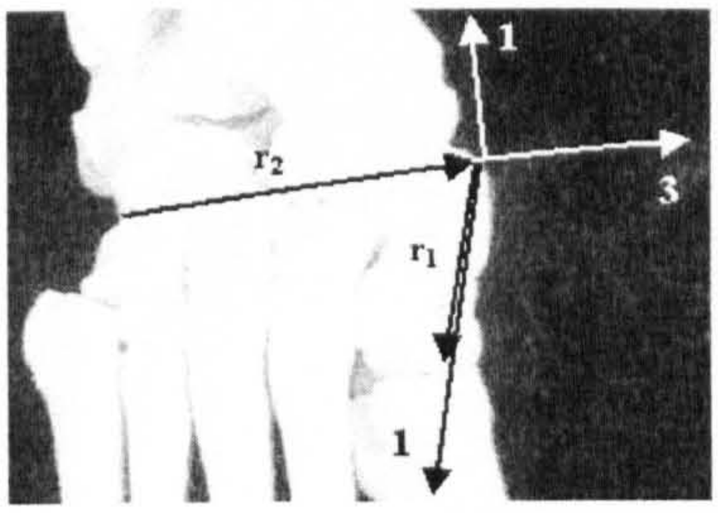	${}_{MI}\vec{r}_1 = {}_{MI}\underline{Ci} - {}_{MI}\underline{NT}$ ${}_{MI}\vec{r}_2 = {}_{MI}\underline{NT} - {}_{MI}\underline{CU}$ ${}_{MI}\underline{O} = - {}_{MI}\underline{NT}$
Forefoot (medial)	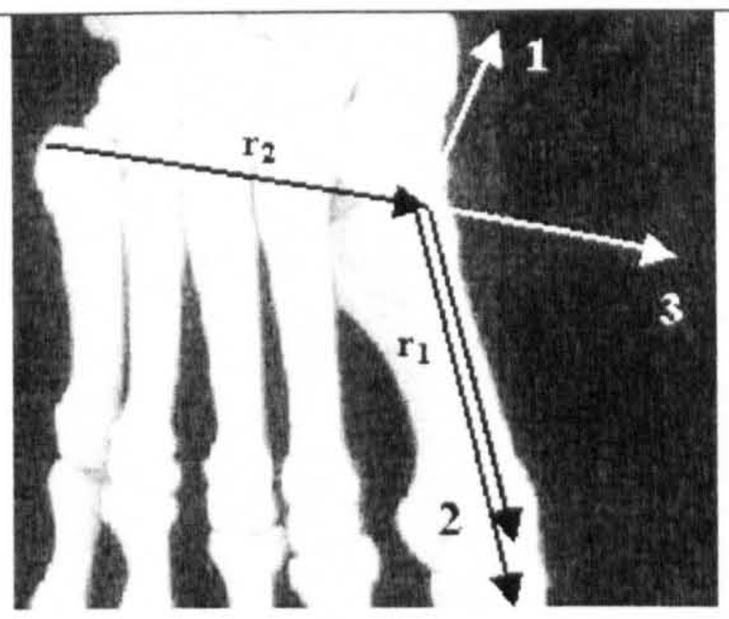	${}_{MI}\vec{r}_1 = {}_{MI}\underline{MiH} - {}_{MI}\underline{MiB}$ ${}_{MI}\vec{r}_2 = {}_{MI}\underline{MiB} - {}_{MI}\underline{MvB}$ ${}_{MI}\underline{O} = - {}_{MI}\underline{MiB}$

Forefoot (lateral)	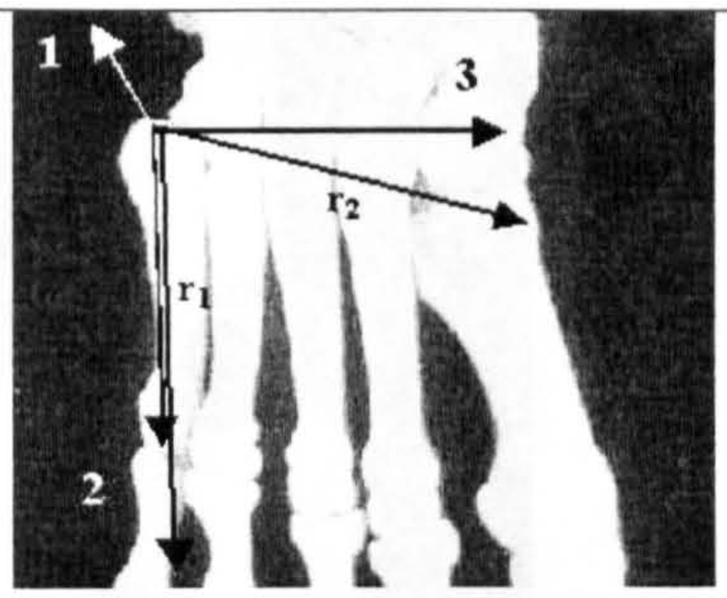	${}_{MI}\vec{r}_1 = {}_{MI}\underline{MvH} - {}_{MI}\underline{MvB}$ ${}_{MI}\vec{r}_2 = {}_{MI}\underline{MiB} - {}_{MI}\underline{MvB}$ ${}_{MI}\underline{O} = -{}_{MI}\underline{MvB}$

Table 4.2.2-2 Direction of Bone-fixed Frame Axes and Landmark ordering for each of the Palpable Segments

$$ {}_{MI}\underline{R}_{MI\to bone} = \begin{bmatrix} {}_{MI}\hat{1}^T \\ {}_{MI}\hat{2}^T \\ {}_{MI}\hat{3}^T \end{bmatrix} \qquad (4.2.2\text{-}4) $$

$$ {}_{MI}\underline{T}_{MI\to bone} = -{}_{MI}\underline{O} $$

Once the bone-fixed reference frames had been defined for each of the six segments, all the structures isolated in the Internal Map were transformed from the Medical Image reference frame into the bone-fixed frame of the segment to which each was attached. For instance the origin of the Soleus was transformed into the Lower Leg frame and the Tibialis Anterior insertion into the Midfoot frame. These transformations were done as follows using the matrices in Eq. 4.2.2-4,

$$ {}_{bone}\underline{p} = {}_{MI}\underline{R}_{MI\to bone}\left({}_{MI}\underline{p} + {}_{MI}\underline{T}_{MI\to bone}\right). \qquad (4.2.2\text{-}5) $$

4.2.3 Structures Defined in the Internal Map

The Internal Map defined three types of structure: muscle attachments, ligament attachments and articular surfaces. The muscle attachments included the origins, insertions and pulley points of the eight muscles of the Muscle Model shown in Table 4.2.3-1. The pulley points of the muscles were the points where the tendon of the

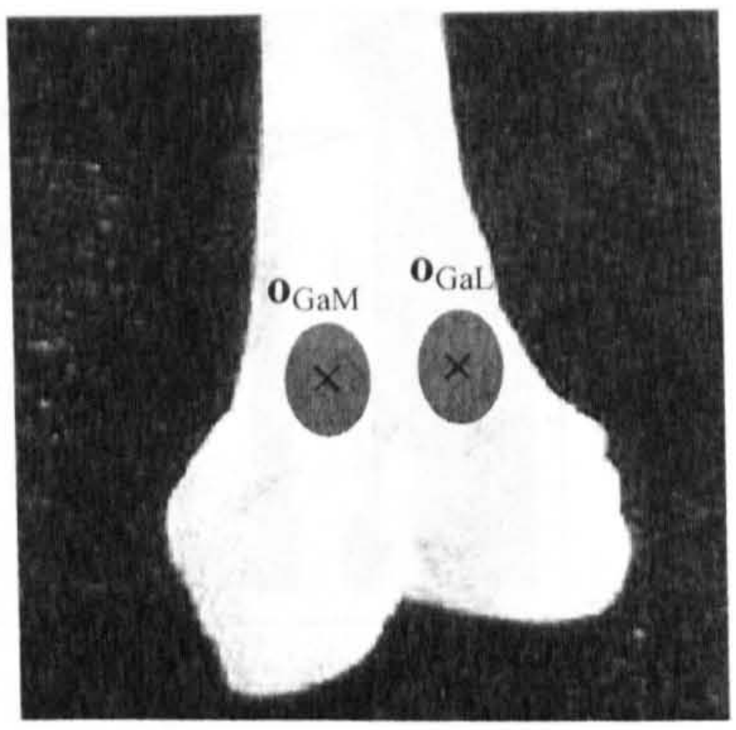

Figure 4.2.3-1A Attachment sites on the Thigh Segment. Posterior view of Femur (Gosling, et al, 1993).

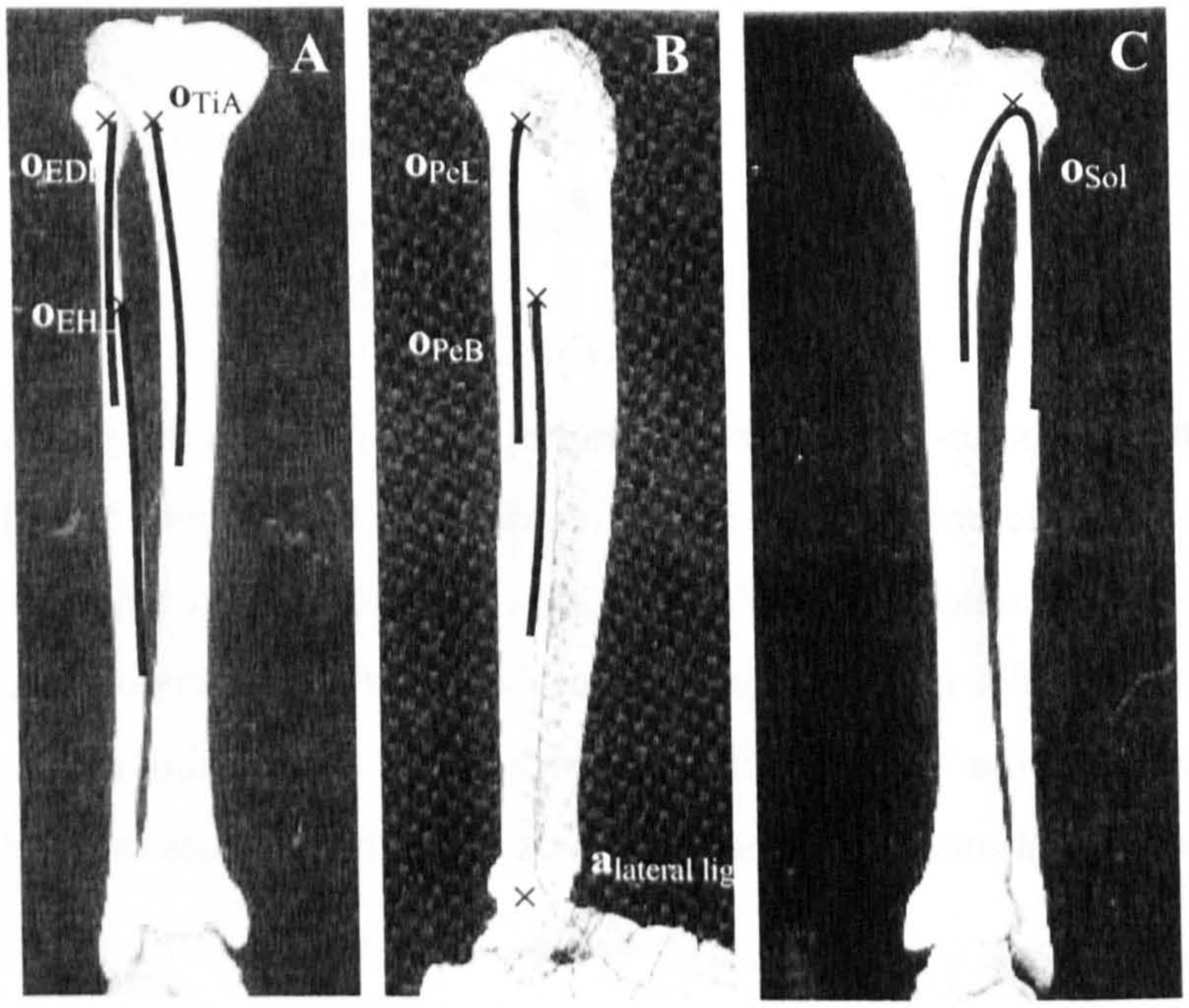

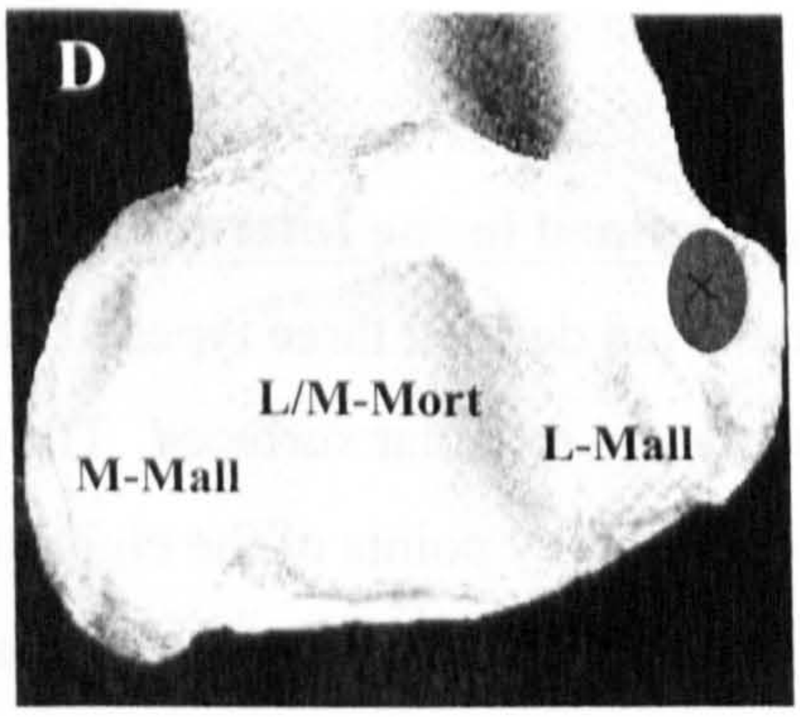

Figure 4.2.3-1B Attachment and Pulley sites on Lower Leg Segment. Anterior view (A), lateral view (B), posterior view (C) and inferior view (D) of Tibia and Fibula (Gosling, et al, 1993).

Structure	Group	Structure Name	Label
Muscles	Calf	Lateral Head of Gastrocnemius	GaL
		Medial Head of Gastrocnemius	GaM
		Soleus	Sol
	Anterior	Tibialis Anterior	TiA
		Extensor Hallucis Longus	EHL
		Extensor Digitorum	EDL
	Peroneal	Peroneus Longus	PeL
		Peroneus Brevis	PeB
Ligaments	Lateral	Anterior Talofibular	L-Ant
		Calcaneofibular	L-Mid
		Posterior Talofibular	L-Post
	Medial (Deltoid)	Anterior Talotibial	M-Ant
		Calcaneotibial	M-Mid
		Posterior Talotibial	M-Lat
		Tibionavicular	M-Nav
	Subtalar	Cervical	Cerv
		Medial Interosseus	M-IO
		Lateral Interosseus	L-IO
		Medial Talocalcaneal	M-Tc
		Posterior Talocalcaneal	P-Tc
Surfaces	Tibiofibular Mortice	Lateral Malleolar	L-MalM
		Lateral Mortice	L-Mort
		Medial Mortice	M-Mort
		Medial Malleolar	M-MalM
	Talar Trochlea	Lateral Malleolar	L-MalT
		Lateral Trochlear	L-Troch
		Medial Trochlear	M-Troch
		Medial Malleolar	M-MalT
	Inferior Talus	Posterior Talocalcaneal	Post
		Middle Talocalcaneal	Mid
		Talar Head	Head
	Superior Calcaneus	Posterior Talocalcaneal	Post
		Middle Talocalcaneal	Mid
		Navicular Socket	Socket

Table 4.2.3-1 The Muscle, Ligament and Surface structures defined within the Internal Map.

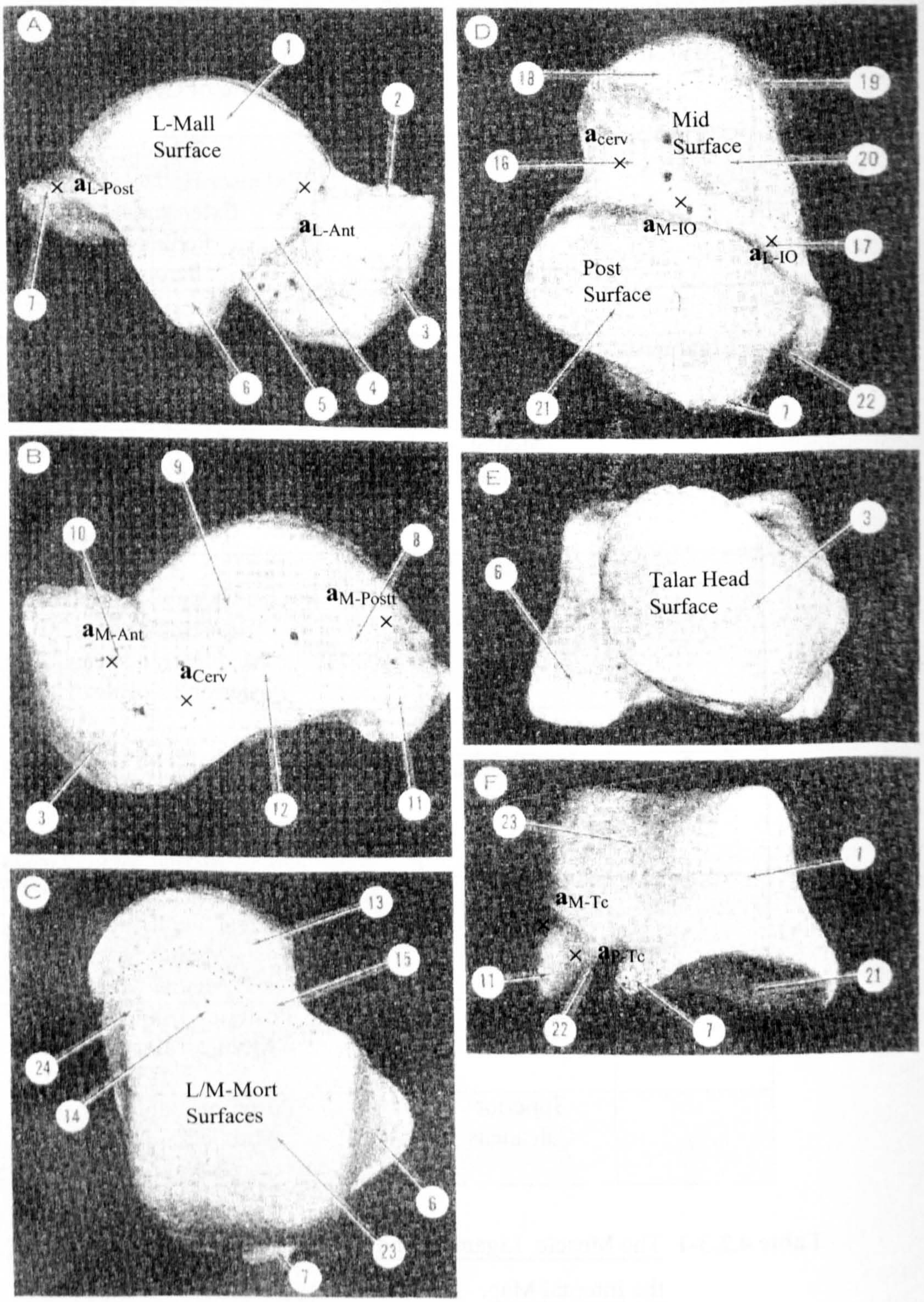

Figure 4.2.3-1C Attachments sites on the Talus Segement. Lateral (A), Medial (B), Superior (C), Inferior (D), Anterior (E) and Posterior (F) views (Sarrafian, 1983).

Segment	Structure	Attachment Type	Description	
Thigh	Muscles	origin	GaL	Lateral Gastrocnemius Head
			GaM	Medial Gastrocnemuis Head
Lower Leg	Muscles	origin	Sol	Soleus
			TiA	Tibialis Anterior
			EHL	Extensor Hallucis Longus
			EDL	Extensor Digitorum Longus
			PeL	Peroneus Longus
			PeB	Peroneus Brevis
		pulley	TiA	Superior Extensor Retinacula
			EHL	Superior Extensor Retinacula
			EDL	Superior Extensor Retinacula
			PeL	Posterior Lateral Malleolus
			PeB	Posterior Lateral Malleolus
	Ligaments	lateral	L-Ant	Anterior Talofibular
			L-Mid	Calcaneofibular
			L-Post	Posterior Talofibular
		medial (deltoid)	M-Ant	Anterior Talotibial
			M-Mid	Calcaneotibial
			M-Post	Posterior Talotibial
			M-Nav	Tibionavicular
	Surfaces	ankle	L-MalM	Lateral Malleolar
			L-Mort	Lateral Mortice
			M-Mort	Medial Mortice
			M-MalM	Medial Malleolar
Talus	Ligaments	lateral	L-Ant	Anterior Talofibular
			L-Post	Posterior Talofibular
		medial (deltoid)	M-Ant	Anterior Talotibial
			M-Post	Posterior Talotibial
		subtalar	Cerv	Cervical
			M/L-IO	Interosseus
			M-Tc	Medial Talocalcaneal
			P-Tc	Posterior Talocalcaneal
	Surfaces	ankle	L-MalT	Lateral Malleolus
			L-Troch	Lateral Trochlea
			M-Troch	Medial Trochlea
			M-MalT	Medial Malleolus
		subtalar	Post	Posterior Talocalcaneal
			Mid	Middle Talocalcaneal
			Head	Talar Head
	Axes	ankle	**lat**	Lateral Axis Point
			med	Medial Axis Point

Hindfoot	Muscles	insertion	GaL GaM Sol	Lateral Gastrocnemius Head Medial Gastrocnemius Head Soleus
	Ligaments	lateral	L-Mid	Calcaneofibular
		medial (deltoid)	M-Mid	Calcaneotibial
		subtalar	Cerv M/L-IO M-Tc P-Tc	Cervical Interosseus Medial Talocalcaneal Posterior Talocalcaneal
	Surfaces	subtalar	Post Mid	Posterior Talocalcaneal Middle Talocalcaneal
	Axes	subtalar	**post** **ant**	Posterior Axis Point Anterior Axis Point
Midfoot	Muscles	pulley	PeL EHL EDL	Cuboidal Tuberosity Inferior Extensor Retinacula Inferior Extensor Retinacula
		insertion	TiA PeL	Tibialis Anterior Peroneus Longus
	Ligaments	medial (deltoid)	M-Nav	Tibionavicular
	Surface	subtalar	Socket	Navicular Socket
Forefoot (medial)	Muscles	insertion	EHL	Extensor Hallucis Longus
Forefoot (lateral)	Muscles	insertion	EDL	Extensor Digitorum Longus

Table 4.2.3-2 Attachments of Structures on each of the Bone Segments.

muscle changed direction as it passed under a retinacular sling or over a bony groove. The ligament attachments defined the points where ligaments exerted forces on the bones of the Ankle Complex. The articular surfaces were defined as a number of data points that represented the shape of the bone where it bore load imposed by a neighbouring bone in the joint. The ligaments and surfaces defined in the Internal Map are also listed in Table 4.2.3-1. The structural attachments which were defined on each of the seven bone segments of the Internal Map are listed in Table 4.2.3-2.

The attachment and pulley sites for the muscles and the attachments for the ligaments were defined as single points. However, the attachments of these structures actually occurred over an area of bone, as can be seen in Figure 4.2.3-1, as

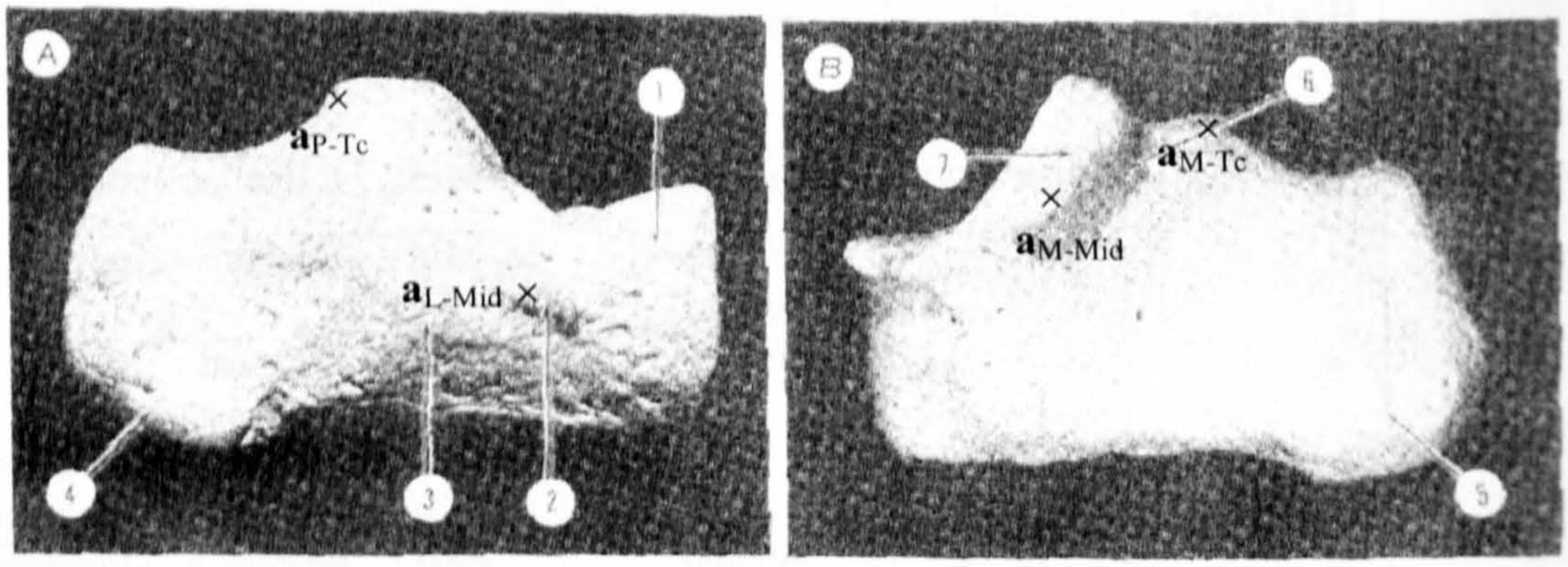

Figure 4.2.3-1D Attachment sites on the Hindfoot segment. Lateral (A), Medial (B) and Superior (C) views (Sarrafian, 1983).

opposed to a single point. The points which were chosen to define these attachment areas in the Internal Map are indicated in the diagrams of Figure 4.2.3-1. In the majority of cases, the point chosen was the centroid of the attachment area. For the origins of six of the eight muscles in the Internal Map, however, the point chosen was the most proximal extent of the attachment area.

Anatomically the originating tendons for the two heads of the Gastrocnemius pulley over the posterior surfaces of the femoral condyles as they run distally from their origins. These pulley points were not defined in the Internal Map since the change in direction of the GaL and GaM muscle lines of action and the lengths of these muscles were minimally altered by their inclusion. For simplicity, the lines of action for the two heads of the Gastrocnemius were therefore defined as running from the origin attachments on the Femur to the insertion attachement on the Calcaneus.

4.2.4 Defining the Two Joint Axes

The Internal Map also defined the position and orientation of the two joint rotation axes of the Ankle Joint Complex: the *Ankle Joint* and the *Subtalar Joint*. As described earlier, these two joints were defined as each rotating about their own single rotational axis.

The Ankle Joint axis was defined as fixed with respect to the Lower Leg bone segment. The rotational axis was represented by two points which both lay on the axis at the lateral end, lat, and at the medial end, med. The Subtalar Joint axis was defined as fixed with respect the Hindfoot segment. The two points defining this axis lay at the anterior, dorsal end, ant, and the posterior, plantar end, post.

In addition to the two points which lay on the axis of joint rotation, a third point was defined which lay some distance from the joint axis, for each of the joints. The Ankle Joint included the position of the fibular head, FH, which was one of the three landmarks forming the Lower Leg bone-fixed frame. The Subtalar Joint included the head of the first metatarsal, MiH. The three points which defined each of the joint axes were used to create joint-fixed frames of reference for the Ankle and

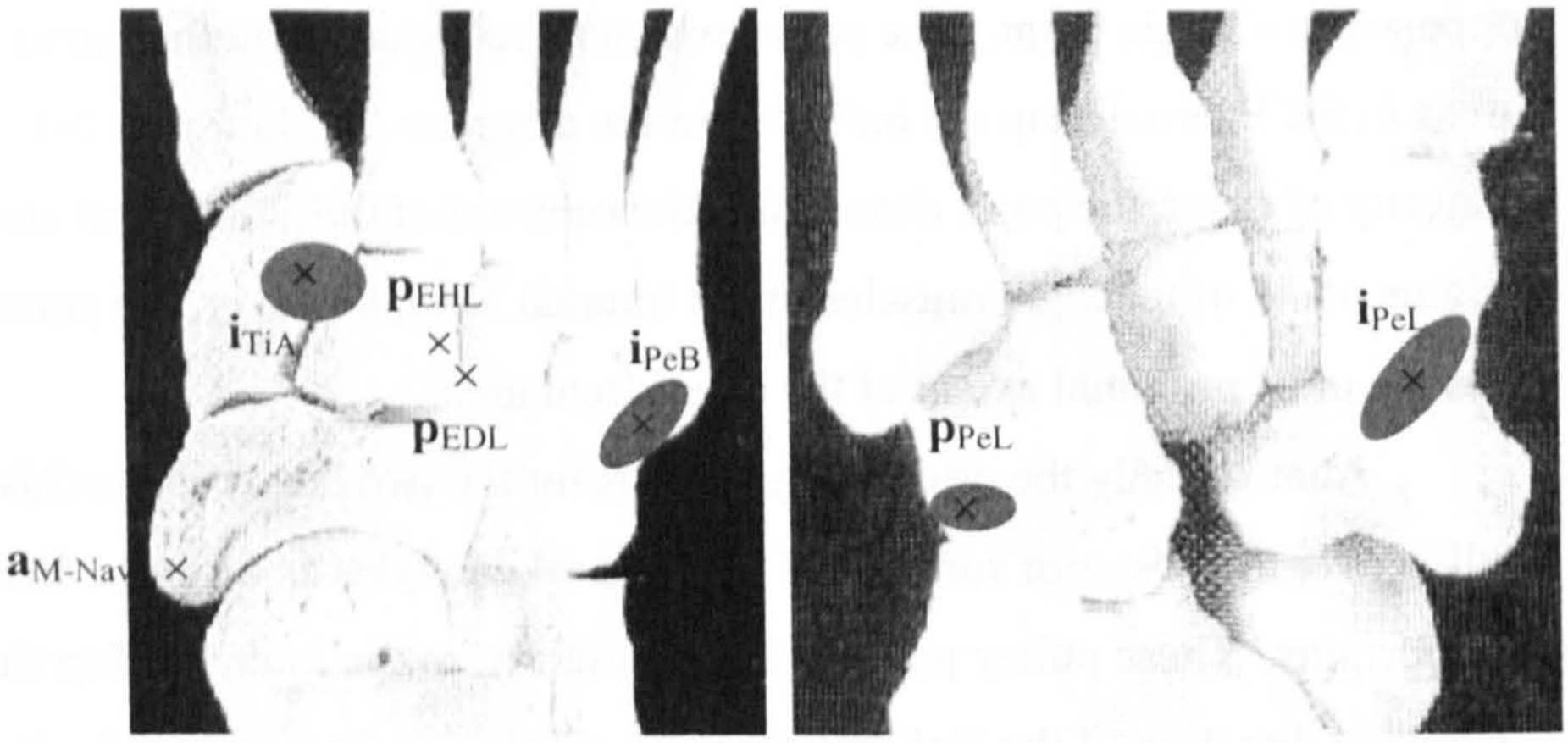

Figure 4.2.3-1E Attachments and Pulley sites on Midfoot Segment. Superior view (A) and Inferior view (B) (Gosling, et al, 1993).

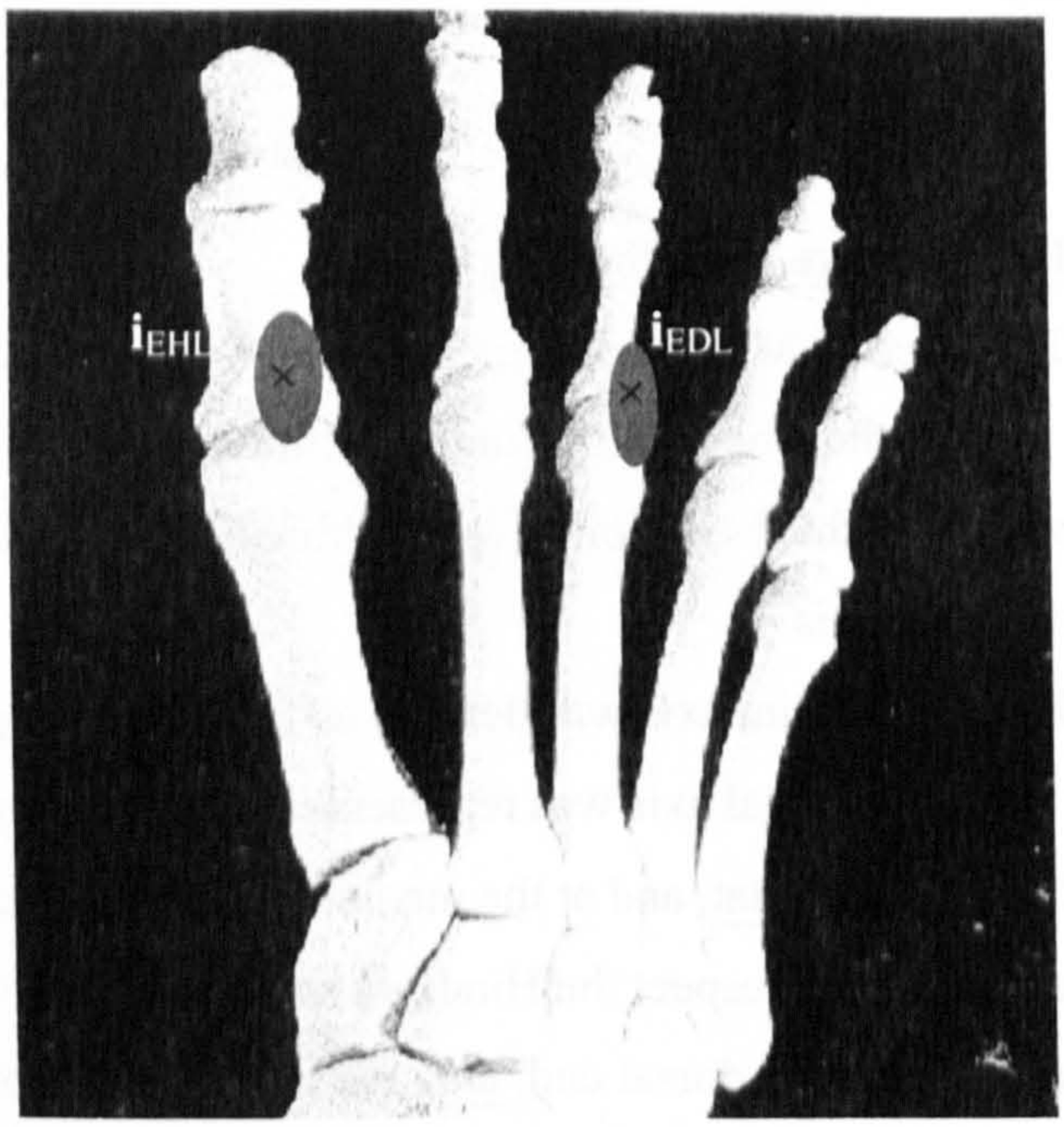

Figure 4.2.3-1F Attachment sites on Forefoot Segment. Superior view (Gosling, et al, 1993).

Subtalar Joints. The defining points were ordered so that the second, $2-axis$, was aligned with the axis of rotation for the joint. Figure 4.2.4-1 shows the axes of the joint-fixed reference frames for the Ankle and Subtalar Joints.

The frames were created as follows. The three defining points produced two vectors and their associated unit vectors,

$$\begin{aligned} {}_{MI}\vec{r}_1 &= {}_{MI}\underline{lat} - {}_{MI}\underline{med} \Rightarrow {}_{MI}\hat{r}_1 \\ {}_{MI}\vec{r}_2 &= {}_{MI}\underline{lat} - {}_{MI}\underline{FH} \Rightarrow {}_{MI}\hat{r}_2 \end{aligned} \qquad \text{Ankle Joint}$$

$$\begin{aligned} {}_{MI}\vec{r}_1 &= {}_{MI}\underline{ant} - {}_{MI}\underline{post} \Rightarrow {}_{MI}\hat{r}_1 \\ {}_{MI}\vec{r}_2 &= {}_{MI}\underline{MiH} - {}_{MI}\underline{post} \Rightarrow {}_{MI}\hat{r}_2 \end{aligned} \qquad \text{Subtalar Joint} \qquad (4.2.4\text{-}1)$$

These were crossed to produce a third vector and its unit vector,

$${}_{MI}\vec{r}_x = {}_{MI}\hat{r}_1 \times {}_{MI}\hat{r}_2 \Rightarrow {}_{MI}\hat{r}_x \ . \qquad (4.2.4\text{-}2)$$

The joint-fixed reference frame axes were then defined as,

$$\begin{aligned} {}_{MI}\hat{1} &= {}_{MI}\hat{r}_x \\ {}_{MI}\hat{2} &= {}_{MI}\hat{r}_1 \\ {}_{MI}\hat{3} &= {}_{MI}\hat{1} \times {}_{MI}\hat{2} \end{aligned} \qquad (4.2.4\text{-}3)$$

The matrices which transformed from the Medical Image frame into the joint-fixed reference frame were therefore,

$${}_{MI}\underline{R}_{MI\to joint} = \begin{bmatrix} {}_{MI}\hat{1}^T \\ {}_{MI}\hat{2}^T \\ {}_{MI}\hat{3}^T \end{bmatrix} \qquad (4.2.4\text{-}4)$$

$${}_{MI}\underline{T}_{MI\to joint} = -{}_{MI}\underline{O}$$

where ${}_{MI}\underline{O} = {}_{MI}\underline{lat}$ for the Ankle Joint and ${}_{MI}\underline{O} = {}_{MI}\underline{post}$ for the Subtalar Joint.

Points defined in the MI frame could then be transformed into either of the joint-fixed frames using,

$${}_{joint}\underline{p} = {}_{MI}\underline{R}_{MI\to joint}\left({}_{MI}\underline{p} + {}_{MI}\underline{T}_{MI\to joint}\right) \qquad (4.2.4\text{-}5)$$

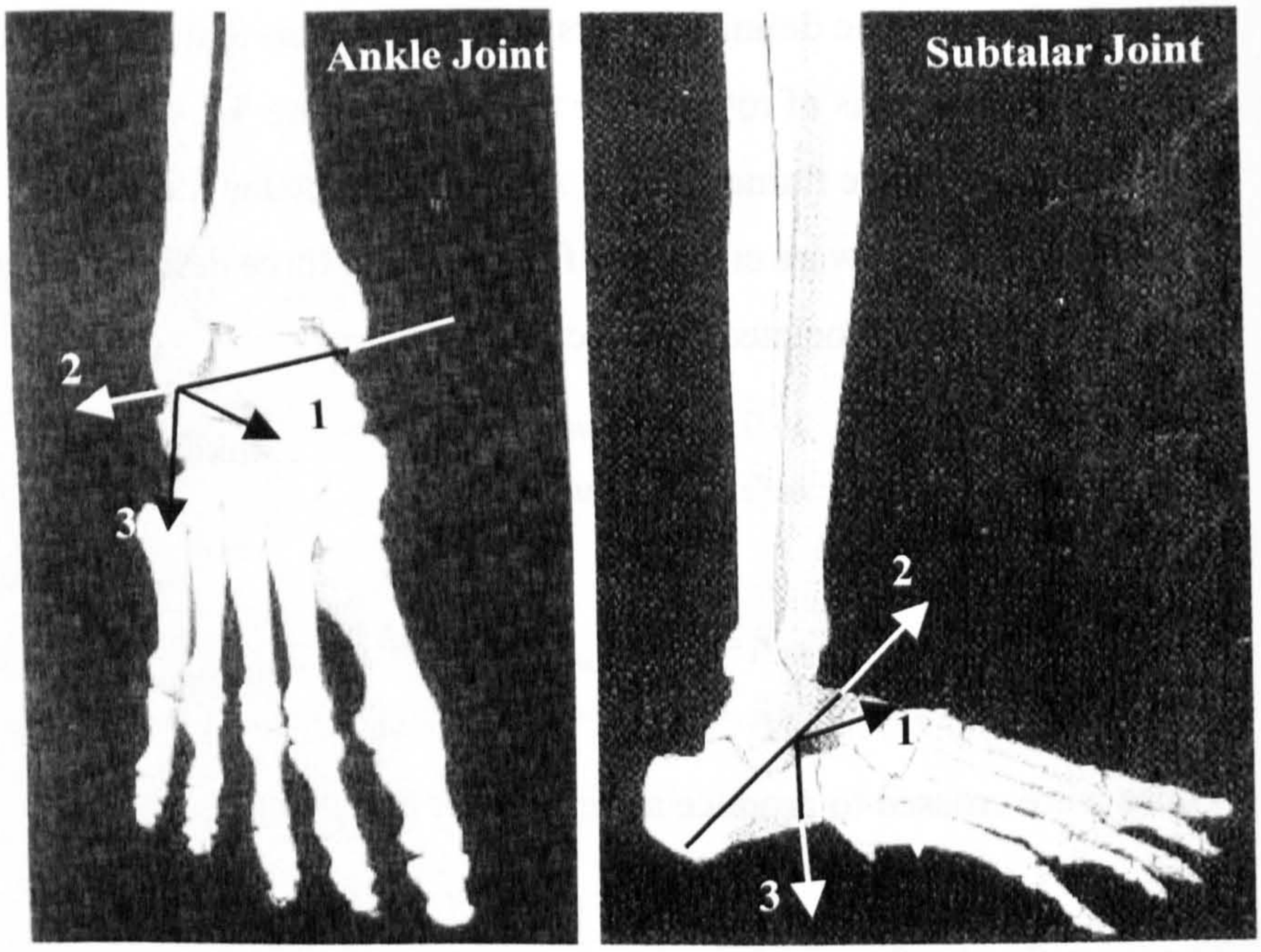

Figure 4.2.4-1 Joint-fixed Frames of Reference for the Ankle and Subtalar Joints (Gosling, et al, 1993).

4.2.5 Determining Joint Rotational Axes Positions

The orientations of the two joint axes were defined by the points lat and med for the Ankle Joint and post and ant for the Subtalar Joint. Determining the positions of these points correctly was therefore critical for characterising the behaviour of the Ankle Complex properly.

Deciding on the proper positions for these points was an iterative process. Initial estimates were made based on the available anatomical literature. According to Sarrafian (1983) lat and med lay several millimetres below the most distal points of the lateral and medial malleoli respectively; med lay anterior and proximal to lat. The position post was reported as attached to the distal, medial border of the Posterior Talocalcaneal Surface on the calcaneus and ant lay on the middle of the dorsal, medial surface of the talar neck. Each of these points was defined within the MI frame of reference.

Using these estimated positions, along with the third defining point, FH for the Ankle and MiH for the Subtalar Joint, the joint-fixed frames were formed. Each of the surface pairs involved in the articulation of the joint were then transformed into the joint-fixed frames using Eq. 4.2.4-5. Since the surfaces were transformed directly from the MI reference frame, the joints were in the positions held by the Ankle Complex of the cadaver at the time the medical images were produced. The Ankle Joint was maximally plantar-flexed and the Subtalar Joint slightly inverted.

In order to evaluate the correctness of the chosen orientation of each joint axis, the surfaces on one side of joint were moved with respect to the surfaces on the other side of the joint by rotating about the chosen axis. Since the joint rotational axis ran parallel to the $2-axis$ of the joint-fixed frame, the rotation matrix which accomplished the joint rotation was,

$$ {}_{joint}\underline{R}_{\theta} = \begin{bmatrix} \cos\theta & 0 & \sin\theta \\ 0 & 1 & 0 \\ -\sin\theta & 0 & \cos\theta \end{bmatrix} \qquad (4.2.5\text{-}1) $$

where θ was the angle through which the joint surfaces were rotated.

In the Ankle Joint, the surfaces of the Tibia-fibular Mortice were moved, therefore the joint was plantar-flexing with a rotation of positive angle. The surfaces

of the Calcaneus and Navicular were rotated in the Subtalar Joint. Therefore the joint was inverting with positive angle. The points which defined the moving surfaces were rotated using the matrix in Eq. 4.2.5-1 as follows,

$$_{joint}\underline{p}(\theta) = {}_{joint}\underline{R}_{\theta}\ {}_{joint}\underline{p} \qquad (4.2.5\text{-}2)$$

The surfaces were rotated in increments through the whole range of motion for the joint: from full plantar-flexion to full dorsi-flexion in the Ankle Joint and full inversion to full eversion in the Subtalar Joint. At each incremental position, the surfaces were all plotted together within the ANSYS pre-processor. If the joint rotational axis was in the correct orientation, then the pairs of surfaces on either side of the joint should remain at a constant amount of separation from each other as they rotated. The surface pairs should not move apart nor move together nor intersect one another. If this occurred at any of the increments of rotation within the joint range of motion, then the orientation of the joint axis was incorrect. A new axis orientation was then tried. A new rotational axis was chosen by altering the positions of the defining points: lat, med or ant, post. With the new joint axis orientation, the surfaces were again moved through the joint range of motion. When the joint surfaces could be rotated through the entire joint range of motion and maintain their relative separation, then the axis orientation was considered correct.

4.2.6 Defining the Talus Segment Bone-fixed Frame

Since the Talus could not be palpated from the skin surface for most of the range of motion of the Ankle Complex, the Talus bone-fixed frame of reference had to be defined differently from the other six palpable bone segments. Instead of using three landmarks isolated on the bone surface, the Talus was defined using three of the four points which defined the Ankle and Subtalar Joint axes: lat, med and ant. Since the these points were defined in the Lower Leg and Hindfoot segment reference frames, the Talus therefore only possessed a single rotational degree of freedom with respect to each of these segments. Figure 4.2.6-1 illustrates the directions of the bone-fixed axes for the Talus segment.

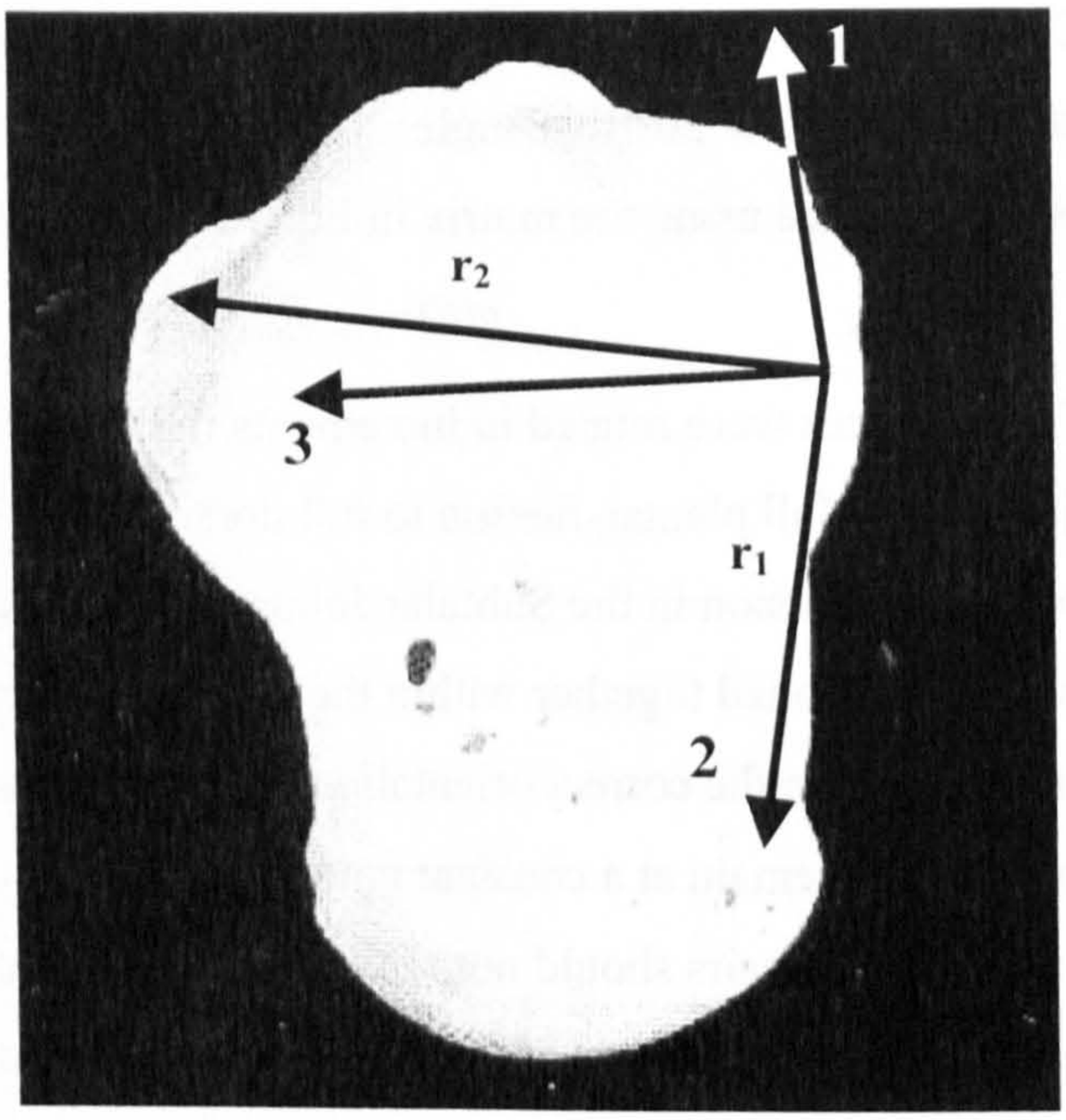

Figure 4.2.6-1 Axes directions for the Talus Segment bone-fixed Reference Frame (Gosling, et al, 1993).

The Talus segment was created as follows. Two vectors and their unit vectors were constructed from these three points,

$$
\begin{aligned}
{}_{MI}\vec{r}_1 &= {}_{MI}\underline{ant} - {}_{MI}\underline{med} \Rightarrow {}_{MI}\hat{r}_1 \\
{}_{MI}\vec{r}_2 &= {}_{MI}\underline{lat} - {}_{MI}\underline{med} \Rightarrow {}_{MI}\hat{r}_2
\end{aligned}
\tag{4.2.6-1}
$$

These were then crossed and the unit vector was found,

$$
{}_{MI}\vec{r}_x = {}_{MI}\hat{r}_1 \times {}_{MI}\hat{r}_2 \Rightarrow {}_{MI}\hat{r}_x \tag{4.2.6-2}
$$

The Talus bone-fixed axes were then defined as,

$$
{}_{MI}\hat{1} = {}_{MI}\hat{r}_x \tag{4.2.6-3}
$$

$$
{}_{MI}\hat{2} = {}_{MI}\hat{r}_1
$$

$$
{}_{MI}\hat{3} = {}_{MI}\hat{1} \times {}_{MI}\hat{2}
$$

and the transformation matrices moving from the MI frame to the Talus frame were therefore,

$$
{}_{MI}\underline{R}_{MI\rightarrow joint} = \begin{bmatrix} {}_{MI}\hat{1}^T \\ {}_{MI}\hat{2}^T \\ {}_{MI}\hat{3}^T \end{bmatrix} \tag{4.2.6-4}
$$

$$
{}_{MI}\underline{T}_{MI\rightarrow joint} = -{}_{MI}\underline{med}
$$

The attachments on the Talus of the structures in the Internal Map could then be transformed from the MI frame into the Talus bone-fixed frame using,

$$
{}_{joint}\underline{p} = {}_{MI}\underline{R}_{MI\rightarrow joint}\left({}_{MI}\underline{p} + {}_{MI}\underline{T}_{MI\rightarrow joint}\right) \tag{4.2.6-5}
$$

4.3 SEGMENT KINEMATICS

4.3.1 Linking Bone-fixed Frames to Cluster Frames

The positions of the landmarks on each segment found during the Pointer trials enabled the structures on each segment defined in the Internal Map to be defined in terms of the marker clusters attached to the segment. The three markers on each cluster defined a frame of reference, which was attached to that cluster. Each of the seven rigid bone segments defined in the Internal Map possessed a bone-fixed frame of reference. All the structures and attachments on that segment were defined within this frame. The next step was to determine the transformation required to move from the bone-fixed frame to the cluster frame. The structures on

each bone segment could then be defined within the frame of reference of the marker cluster(s) attached to that segment. Since the Talus bone segment did not have clusters attached to it during the Motion Analysis trials, it had to be dealt with in a separate manner. This is described in Section 4.2.6.

Locating the Segment Landmarks

During a pointer trial, the end of the pointer located a bony landmark, ${}_g\underline{l}(h)$, for a number of samples, h. The positions of the three pointer markers were measured for these samples in the ground (VICON) frame of reference: ${}_g\underline{Top}(h)$, ${}_g\underline{Mid}(h)$, ${}_g\underline{Bot}(h)$. Figure 3.3.3-1 shows the dimensions of the pointer. The three pointer markers could be paired to form three different vectors as follows,

$$\begin{aligned} {}_g\vec{v}_1(h) &= {}_g\underline{Mid}(h) - {}_g\underline{Top}(h) \\ {}_g\vec{v}_2(h) &= {}_g\underline{Bot}(h) - {}_g\underline{Top}(h) \\ {}_g\vec{v}_3(h) &= {}_g\underline{Bot}(h) - {}_g\underline{Mid}(h) \end{aligned} \qquad (4.3.1\text{-}1)$$

The unit vector for each of these vectors was then found,

$$\hat{v}_i(h) = \frac{\vec{v}_i(h)}{|\vec{v}_i(h)|} \quad \text{for i= 1, 2, 3.} \qquad (4.3.1\text{-}2)$$

Each of these vectors could then be used to estimate the pointer end position,

$$\begin{aligned} {}_g\underline{l}_1(h) &= {}_g\underline{Top}(h) + (49.75 + 68.26 + 65.75)\,{}_g\hat{v}_1(h) \\ {}_g\underline{l}_2(h) &= {}_g\underline{Top}(h) + (49.75 + 68.26 + 65.75)\,{}_g\hat{v}_2(h) \\ {}_g\underline{l}_3(h) &= {}_g\underline{Mid}(h) + (68.26 + 65.75)\,{}_g\hat{v}_3(h) \end{aligned} \qquad (4.3.1\text{-}3)$$

The pointer end position coincided with the bony landmark position. For each sample h, the pointer end position was taken as the average of the three estimates, ${}_g\underline{l}_1(h)$, ${}_g\underline{l}_2(h)$ and ${}_g\underline{l}_3(h)$. Still defined in the ground frame, the averaged position were therefore,

$${}_g\underline{l}(h) = \frac{1}{3}\left({}_g\underline{l}_1(h) + {}_g\underline{l}_2(h) + {}_g\underline{l}_3(h)\right) \qquad (4.3.1\text{-}4)$$

Note that the landmark position ${}_g\underline{l}(h)$ would change for each of the samples, h, as the subject moved about slightly during the trial. The next step was to transform ${}_g\underline{l}(h)$ into the reference frame of the cluster attached to the segment. Defined in this frame,

the landmark position, ${}_g\underline{l}(h)$, should not change between samples with subject motion since the cluster and landmark were both attached to the same rigid segment.

The positions of the three markers on the segment cluster were known for each of the h samples: ${}_g\underline{b}_1(h), {}_g\underline{b}_2(h), {}_g\underline{b}_3(h)$. The cluster frame was constructed as follows. The three markers were used to make two vectors, whose unit vectors were then determined using Eq. 4.3.1-2, for each sample h,

$$\begin{aligned} {}_g\vec{r}_1(h) &= {}_g\underline{b}_1(h) - {}_g\underline{b}_2(h) \Rightarrow {}_g\hat{r}_1(h) \\ {}_g\vec{r}_2(h) &= {}_g\underline{b}_1(h) - {}_g\underline{b}_3(h) \Rightarrow {}_g\hat{r}_2(h) \end{aligned} \tag{4.3.1-5}$$

A third vector and unit vector were then created by taking the vector cross product of these,

$${}_g\vec{r}_x(h) = {}_g\hat{r}_1(h) \times {}_g\hat{r}_2(h) \Rightarrow {}_g\hat{r}_x(h) \tag{4.3.1-6}$$

The unit vectors ${}_g\hat{r}_1(h)$ and ${}_g\hat{r}_x(h)$ then defined the first and second axis directions for the cluster reference frame,

$$\begin{aligned} {}_g\hat{1}(h) &= {}_g\hat{r}_x(h) \\ {}_g\hat{2}(h) &= {}_g\hat{r}_1(h) \end{aligned} \tag{4.3.1-7}$$

The cross product of these created the third axis of the frame,

$${}_g3(h) = {}_g1(h) \times {}_g2(h) \tag{4.3.1-8}$$

These three unit vectors ${}_g\hat{1}(h), {}_g\hat{2}(h)$ and ${}_g\hat{3}(h)$ represented the three axes of the cluster frame of reference for each sample, h. A rotation and a translation were necessary to move from the ground frame of reference into the new cluster frame. The transformation matrices were constructed from the cluster frame axes and by defining marker #1 as the frame origin,

$$\begin{aligned} {}_g\underline{R}_{g\rightarrow cluster}(h) &= \begin{bmatrix} {}_g\hat{1}^T(h) \\ {}_g\hat{2}^T(h) \\ {}_g\hat{3}^T(h) \end{bmatrix} \\ {}_g\underline{T}_{g\rightarrow cluster}(h) &= -{}_g\underline{b}_1(h) \end{aligned} \tag{4.3.1-9}$$

Using the rotation matrix ${}_g\underline{R}_{g\rightarrow cluster}(h)$ and translation matrix ${}_g\underline{T}_{g\rightarrow cluster}(h)$ for each of the h samples, the landmark position could then be transformed into the cluster reference frame,

$$_{cluster}\underline{l}(h) = {}_{g}\underline{R}_{g\rightarrow cluster}(h)\left({}_{g}\underline{l}(h) + {}_{g}\underline{T}_{g\rightarrow cluster}(h)\right) \qquad (4.3.1\text{-}10)$$

Since the cluster and the landmark were both attached to the same rigid segment, the landmark position defined in the cluster frame should not change between samples. Therefore, the final landmark position was taken as the average of this position over the H samples,

$$_{cluster}\bar{\underline{l}}(h) = \frac{1}{H}\sum^{H} {}_{cluster}\underline{l}(h) \qquad (4.3.1\text{-}11)$$

The rotation and translation matrices found in Eq. 4.3.1-9 transformed from the bone-fixed frame of each rigid segment to a cluster frame that was either attached to the skin surface of that segment or of a neighbouring segment. The actual transformations done for the Kinematic Data from the Movement Task trials and Pointer trials are listed in Table 4.3.1-1. In each case, the segment bone-fixed frame was transformed into the frame of one of the clusters attached to that segment.

However, the MMC trials presented a problem in this regard since the two Forefoot bone segments did not have clusters attached. Table 4.3.1-1 also shows the transformations done for the MMC trials. The two Forefoot bone-fixed frames had to be transformed into the cluster frame formed by the Midfoot cluster, N, since neither Mi

Bone Segment	**Movement Task and Pointer trials** Cluster Markers	**Muscle Model Calibration trials** Cluster Markers
Thigh	Femur 1,2,3	Femur 1,2,3
Lower Leg	T2/3 1,2,3	T2/3 1,2,3
Hindfoot	CA 1,2,3	CA 1,2,3
Midfoot	N 2,3 + Cii 2	N 1,2,3
Forefoot (medial)	Mi 1,2,3	N 1,2,3
Forefoot (lateral)	Mv 1,2,3	N 1,2,3

Table 4.3.1-1 Transformations from Bone-fixed frames to Cluster frames for each segment during the MMC, Pointer, and Movement Task trials.

nor Mv were attached. By defining the structures of the Forefoot within the reference frame of a Midfoot cluster introduced a small error since the Forefoot segments were not rigid fixed with respect to the Midfoot segment. However, since the subject was stationary during the activities of the MMC trials and the positioning of the Forefoot segments were therefore likely to remain reasonably constant with respect to the Midfoot segment during the MMC trials, the error was considered acceptable.

Transformation into Bone Frame

Once the three landmarks from a segment had been located and defined within the cluster frame of reference, it was possible to then create the segment bone-fixed frame of reference. The procedure was identical to the procedure used to create the bone-fixed frames of reference for each of the segments in the Internal Map. When creating the frames, the landmarks were ordered so that the second, $2-axis$, ran distally along the bone segment long axis. The $1-axis$ pointed generally anteriorly for the leg segments or dorsally for the foot segments and the $3-axis$ pointed medially. Table 4.3.1-2 shows the ordering of landmarks for each bone segment.

As in the Internal Map, the bone segment reference frames were constructed as follows. First the unit vectors ${}_{cluster}\hat{r}_1$ and ${}_{cluster}\hat{r}_2$ were formed as shown in Table 4.3.1-2. They were then crossed,

$$ {}_{cluster}\vec{r}_x = {}_{cluster}\hat{r}_1 \times {}_{cluster}\hat{r}_2 \Rightarrow {}_{cluster}\hat{r}_x \tag{4.3.1-11} $$

The bone-fixed frame axes were then defined as,

$$ \begin{aligned} {}_{cluster}\hat{1} &= {}_{cluster}\hat{r}_x \\ {}_{cluster}\hat{2} &= {}_{cluster}\hat{r}_1 \\ {}_{cluster}\hat{3} &= {}_{cluster}\hat{1} \times {}_{cluster}\hat{2} \end{aligned} \tag{4.3.1-12} $$

The matrices for transforming from the cluster to the bone segment were therefore,

$$
{}_{cluster}\underline{R}_{cluster\rightarrow bone} = \begin{bmatrix} {}_{cluster}\hat{1}^T \\ {}_{cluster}\hat{2}^T \\ {}_{cluster}\hat{3}^T \end{bmatrix}
$$

$$
{}_{cluster}\underline{T}_{cluster\rightarrow bone} = -{}_{cluster}\underline{A} \qquad (4.3.1\text{-}13)
$$

Axes Directions	Defining Vectors	Rigid Segments	Landmarks
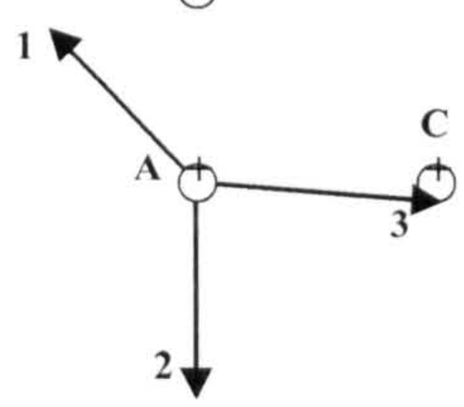	${}_{cluster}\vec{r}_1 = {}_{cluster}\underline{A} - {}_{cluster}\underline{B}$ ${}_{cluster}\vec{r}_2 = {}_{cluster}\underline{C} - {}_{cluster}\underline{A}$ ${}_{cluster}\underline{O} = -{}_{cluster}\underline{A}$	**Thigh** **Lower Leg**	A- FLE B- FGT C- FME A- FLM B- FH C- TMM
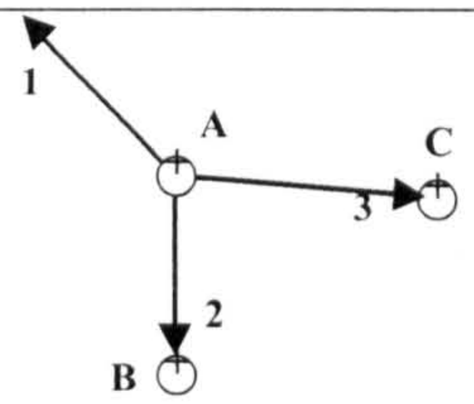	${}_{cluster}\vec{r}_1 = {}_{cluster}\underline{B} - {}_{cluster}\underline{A}$ ${}_{cluster}\vec{r}_2 = {}_{cluster}\underline{C} - {}_{cluster}\underline{A}$ ${}_{cluster}\underline{O} = -{}_{cluster}\underline{A}$	**Hindfoot** **Forefoot (lateral)**	A- CALT B- CAER C- CAMT A- MvB B- MvH C- MiB
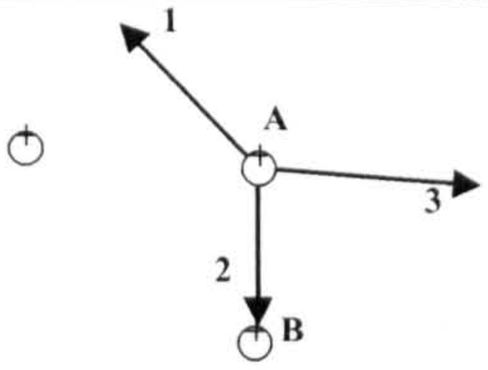	${}_{cluster}\vec{r}_1 = {}_{cluster}\underline{B} - {}_{cluster}\underline{A}$ ${}_{cluster}\vec{r}_2 = {}_{cluster}\underline{A} - {}_{cluster}\underline{C}$ ${}_{cluster}\underline{O} = -{}_{cluster}\underline{A}$	**Midfoot** **Forefoot (medial)**	A- NT B- Ci C- CU A- MiB B- MiH C- MvB

Table 4.3.1-2 Ordering of the segments landmarks and subsequent direction of Bone-fixed Reference Frame axes for each of the Six Palpable Segments.

4.3.2 Scaling Internal Map to each Subject

The Internal Map was constructed from medical images of a single cadaver. The structures defined in the Internal Map had to therefore be resized to fit the dimensions of each individual subject. This resizing was done independently in two

directions, along the bone segment long axis ($2-axis$ of bone-fixed frame) and perpendicularly to the long axis ($1-axis$ and $3-axis$). In each of the two directions a multiplicative Scaling Factor was found which expanded or contracted the Internal Map along that axis direction.

On each segment, there were three landmarks which defined the bone-fixed reference frame. These landmarks were defined first within the Internal Map. Then, during the Pointer trials for each subject, these same landmarks were identified. The scaling factors were chosen so that the dimensions defining the three landmarks on each segment defined within the Internal Map would be resized to match the relative positions of the same three landmarks measured during the Pointer trials.

The three landmarks for a segment defined in the bone-fixed frame within the Internal Map were known: ${}_{bone}\underline{A}$, ${}_{bone}\underline{B}$ and ${}_{bone}\underline{C}$. From the Pointer trials, the positions of the same landmarks on the subject were also known: ${}_{cluster}\underline{l}_A$, ${}_{cluster}\underline{l}_B$ and ${}_{cluster}\underline{l}_C$. Since the Pointer trial landmarks were defined in the cluster reference frame, they could not yet be compared with those from the Internal Map. First, they had to be transformed into the bone-fixed frame using the matrices defined Eq. 4.3.1-13, as follows,

$$ {}_{bone}\underline{l}_A = {}_{cluster}\underline{R}_{cluster\rightarrow bone}\left[{}_{cluster}\underline{l}_A + {}_{cluster}\underline{T}_{cluster\rightarrow bone}\right] \qquad (4.3.2\text{-}1) $$

and similarly for ${}_{bone}\underline{l}_B$ and ${}_{bone}\underline{l}_C$. Within the bone frames for each of the segments, landmark ${}_{bone}\underline{l}_A$ was defined as the origin, or

$$ {}_{bone}\underline{l}_A = \begin{bmatrix} 0 \\ 0 \\ 0 \end{bmatrix} $$

The unit vector ${}_{bone}\hat{r}_1$, within the bone-fixed frames of each of the segments defined the $\hat{2}-axis$ direction. Therefore, for each bone-fixed frame,

$$ {}_{bone}\hat{r}_1 = \begin{bmatrix} 0 \\ 1 \\ 0 \end{bmatrix} $$

Since this vector was constructed from ${}_{bone}\underline{l}_A$ and ${}_{bone}\underline{l}_B$, then within the bone frame ${}_{bone}\underline{l}_B$ would only have a component in the $\hat{2}-axis$ direction. Therefore the

landmark represented by ${}_{bone}\underline{l}_B$ from the Pointer trial and ${}_{bone}\underline{B}$ in the Internal Map was used to determine the scale factor in the $\hat{2}-axis$ direction.

Due to the way the three landmarks on each segment were chosen, the second unit vector, ${}_{bone}\hat{r}_2$ ran nearly parallel to the $\hat{3}-axis$ direction. Since this unit vector was constructed from ${}_{bone}\underline{l}_A$ and ${}_{bone}\underline{l}_C$, the landmark ${}_{bone}\underline{l}_C$ (defined in the bone frame) would have a large component in the $\hat{3}-axis$ direction with relatively much smaller $\hat{2}-axis$ component. Therefore, landmark represented by ${}_{bone}\underline{l}_C$ and ${}_{bone}\underline{C}$ was used to determine the scale factor perpendicular to the $\hat{2}-axis$.

The scale factors were found as follows,

$$ {}^{\hat{2}}S = \frac{\left|{}_{bone}^{\hat{2}}\underline{l}_B\right|}{\left|{}_{bone}^{\hat{2}}\underline{B}\right|} \quad \text{along the bone long axis}$$

$$ {}^{\hat{1},\hat{3}}S = \frac{\left|{}_{bone}^{\hat{3}}\underline{l}_C\right|}{\left|{}_{bone}^{\hat{3}}\underline{C}\right|} \quad \text{perpendicular to bone long axis} \qquad (4.3.2\text{-}2)$$

where ${}_{bone}^{\hat{2}}B$ represents the $\hat{2}-axis$ component of ${}_{bone}\underline{B}$.

4.3.3 Linking Bone-fixed Frames to Ground Frame

The Pointer trials enabled the structures defined in the Internal Map for each segment to be transformed into the reference frames of the segment marker clusters. During the MMC and Movement Task trials the positions of the marker clusters attached to each of the rigid segments were tracked as the subject moved. Using this positional data, the transformation from each cluster frame into the laboratory ground frame could then be calculated for each sample of positional data, h. The Internal Map could then be transformed from the bone-fixed frames into the cluster frames and ultimately into the ground frame of reference for each sample, h.

At sample h during the trial, the positions of the three markers on a cluster were known,

$$ {}_g\underline{b}_1(h), {}_g\underline{b}_2(h), {}_g\underline{b}_3(h) $$

Using Eqs.4.3.1-5 to 4.3.1-8, the three axis direction vectors for the cluster frame were found for that sample,

$$ {}_g\hat{1}(h), {}_g\hat{2}(h), {}_g\hat{3}(h) $$

The matrices for a transformation from the ground frame to the cluster frame had the following relationship to the inverse transformation (from the cluster frame to the ground frame),

$$ \begin{aligned} {}_g\underline{\underline{R}}_{g\rightarrow cluster}(h) &= {}_g\underline{\underline{R}}^{T}_{cluster\rightarrow g}(h) \\ {}_g\underline{T}_{g\rightarrow cluster}(h) &= -{}_g\underline{T}_{cluster\rightarrow g}(h) \end{aligned} \qquad (4.3.3\text{-}1) $$

The inverse transformation to the one in Eq. 4.3.1-9, which moved from the cluster frame to the ground frame, was therefore performed with the following matrices,

$$ \begin{aligned} {}_g\underline{\underline{R}}_{cluster\rightarrow g}(h) &= \left[{}_g\hat{1}(h) \quad {}_g\hat{2}(h) \quad {}_g\hat{3}(h) \right] \\ {}_g\underline{T}_{cluster\rightarrow g}(h) &= {}_g\underline{b}_1(h) \end{aligned} \qquad (4.3.3\text{-}2) $$

The matrices transforming from the bone-fixed frame to cluster frame were found by inverting the transformation in Eq. 4.3.1-13,

$$ \begin{aligned} {}_{cluster}\underline{\underline{R}}_{bone\rightarrow cluster} &= {}_{cluster}\underline{\underline{R}}^{T}_{cluster\rightarrow bone} \\ {}_{cluster}\underline{T}_{bone\rightarrow cluster} &= -{}_{cluster}\underline{T}_{cluster\rightarrow bone} \end{aligned} \qquad (4.3.3\text{-}3) $$

Consider an attachment point defined in the Internal Map, ${}_{bone}\underline{p}$. The point was transformed into the ground frame of reference at a particular sample h in three steps. Figure 4.3.3-1 illustrates the three step process. The point was first scaled to the dimensions of the subject using the Scaling Factors in Eq 4.3.2-2,

$$ \begin{aligned} {}_{bone}\underline{\hat{1}p}' &= {}_{bone}\underline{\hat{1}p} \times {}^{\hat{1},\hat{3}}S \\ {}_{bone}\underline{{}^{2}p}' &= {}_{bone}{}^{2}p \times {}^{\hat{2}}S \\ {}_{bone}\underline{{}^{3}p}' &= {}_{bone}\underline{{}^{3}p} \times {}^{\hat{1},\hat{3}}S \end{aligned} \qquad (4.3.3\text{-}4) $$

The point was then transformed into the appropriate cluster frame,

$$ {}_{cluster}\underline{p} = {}_{cluster}\underline{\underline{R}}_{bone\rightarrow cluster}\left({}_{bone}\underline{p} \right) + {}_{cluster}\underline{T}_{bone\rightarrow cluster} \qquad (4.3.3\text{-}5) $$

and then into the ground frame at sample h,

$$ {}_g\underline{p}(h) = {}_g\underline{\underline{R}}_{cluster\rightarrow g}(h)\left({}_{cluster}\underline{p} \right) + {}_g\underline{T}_{cluster\rightarrow g}(h) \qquad (4.3.3\text{-}6) $$

This three step transformation and scaling process was done for each of the structures defined by the Internal Map for each sample h throughout each trial. In this way, the

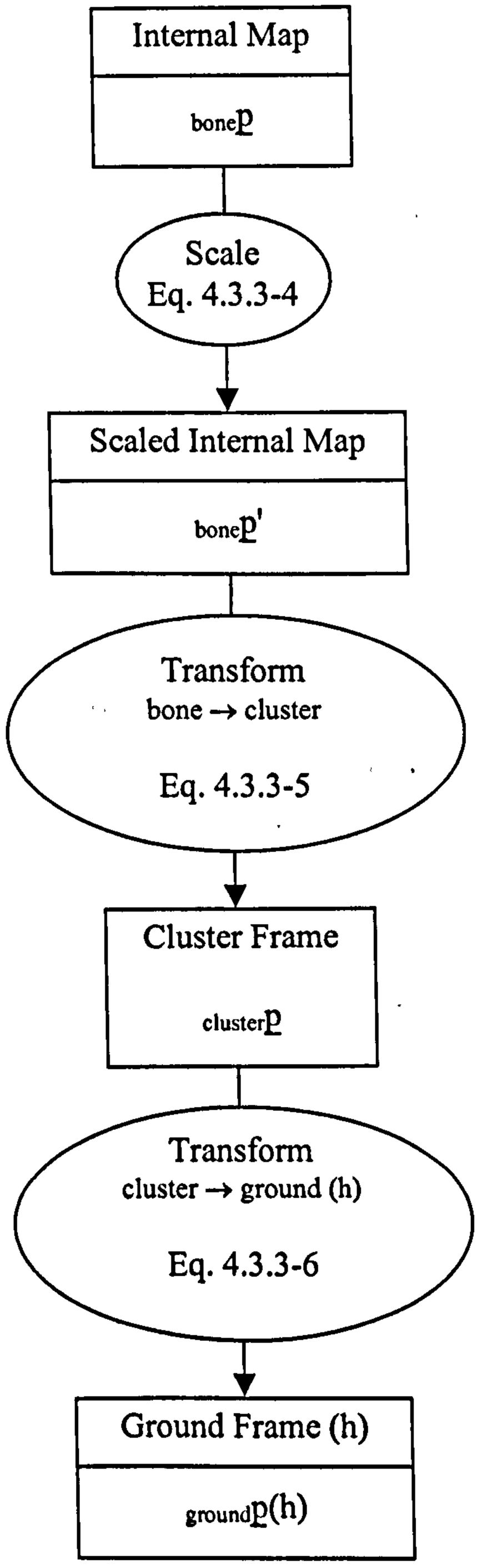

Figure 4.3.3-1 Scaling and Transforming the Internal Map to the Cluster frame and then to the Ground Frame at sample h.

structures of the Internal Map were moved along with the motion of the subject as the subject performed the various MMC and Movement Task trials.

4.3.4 Visibility and Filling Gaps

As mentioned in Section 3.1.1, the reflective markers were not always visible to enough of the VICON cameras to have their positions reconstructed in the test volume. The loss of visibility resulted from a number of causes: shielding by body segments, insufficient illumination from the cameras or masking within the glare of floor reflections. Loss of visibility resulted in gaps in the reconstructed trajectory of that marker during the trial. These gaps ranged in length from a few samples long to the complete absence of the marker from the trial reconstruction.

A number of measures were used to improve visibility during the trials. Redundancy in markers was introduced on the two segments susceptible to shielding from other segments: the Lower Leg and Midfoot segments. This improved the chance that the minimum number of three markers per segment was visible for every sample throughout the trials. The cameras were also arranged so as to be as close to the subject as possible to enhance visibility. The cameras were pointed downwards as little as possible to minimise any reflection off the floor obscuring marker reflections. To further reduce floor reflection, a dark sheet of fabric was laid on the ground on either side of the subject path.

The parameters used by the VICON reconstruction procedure could also be adjusted by the user to influence the effectiveness of the marker reconstruction. These parameters governed how the computer interpreted the reflected light from the markers and how these were reconstructed to form the markers. The parameters were adjusted individually for each trial to optimise the completeness of marker trajectories. Although the reconstruction procedure was optimised for each trial and experimental precautions were incorporated to improve visibility, it was still impossible to ensure that all marker trajectories were free of gaps throughout each of the trials. For this reason, several mathematical techniques were used after data

collection and reconstruction in order to fill the gaps by estimating the missing marker trajectories.

Three separate techniques were available. The appropriate technique was chosen for a particular gap based on the number of samples missing from the gap and the availability of redundant or related marker trajectories. When a marker trajectory was missing in a gap, the trajectory possessed three degrees of freedom; translation in each of the three spatial dimensions. Each of these degrees of freedom therefore needed to be estimated in order to fill the gap. The three techniques were the *Splice Interpolation Fill*, the *Two-Marker Fill* and the *Three-Marker Fill*. The Spline Interpolation Fill technique estimated the trajectory for each of the three degrees of freedom independently. The Two-Marker Fill used the trajectories of the two other markers attached to the cluster, which were visible, to reduce the three degrees of freedom down to a single degree of freedom. The Three-Marker Fill used the trajectories of three other related, visible markers to reduce the degrees of freedom down to zero. The missing trajectory was therefore not estimated with the Three-Marker Fill technique, but was reconstructed.

Spline Interpolation Fill

When the gap was less than ten data samples long, the trajectory could be reasonably estimated without using positional information from other trajectories. Since no extra positional information was used in the form of redundant markers, the missing marker had three degrees of freedom. Therefore, the gap was filled by fitting three cubic splines across the gap, one for each of the three spatial dimensions: x, y and z. The splines fit were cubic splines of minimum curvature. The slope of the splines at each end of the gap equalled the slopes of the discontinuous ends of the trajectory. This way the overall marker trajectory remained smoothly differentiable throughout the trial. The method for computing the minimum curvature cubic spline was taken from Golub and Ortega (1992). This reference supplies the complete proof and derivation for the following method.

Consider a gap in a marker trajectory with a length of h samples, beginning at h_s and ending at h_f. To fit the spline to the gap for one of the three degrees of

freedom, the position and the sample number were first taken for the two samples before the gap and the two after,

h	h_s-2	h_s-1	h_f+1	h_f+2
x	x(h_s-2)	x(h_s-1)	x(h_f+1)	x(h_f+2)

The three intervals between each of these four sample numbers were found,

$$\begin{aligned}\Delta h_1 &= (h_s - 1) - (h_s - 2)\\ \Delta h_2 &= (h_f + 1) - (h_s - 1)\\ \Delta h_3 &= (h_f + 2) - (h_f + 1)\end{aligned} \qquad (4.3.4\text{-}1)$$

and a matrix $\underline{H}$ was constructed with these,

$$\underline{H} = \begin{bmatrix} 2(\Delta h_1 + \Delta h_2) & \Delta h_2 \\ \Delta h_2 & 2(\Delta h_2 + \Delta h_3) \end{bmatrix} = \begin{bmatrix} H\{1,1\} & H\{1,2\} \\ H\{2,1\} & H\{2,2\} \end{bmatrix} \qquad (4.3.4\text{-}2)$$

Two other quantities were then found,

$$\begin{aligned}\gamma_2 &= 6 \times \left[\frac{x(h_f + 1) - x(h_s - 1)}{\Delta h_2} - \frac{x(h_s - 1) - x(h_s - 2)}{\Delta h_1} \right]\\ \gamma_3 &= 6 \times \left[\frac{x(h_f + 2) - x(h_f + 1)}{\Delta h_3} - \frac{x(h_f + 1) - x(h_s - 1)}{\Delta h_2} \right]\end{aligned} \qquad (4.3.4\text{-}3)$$

The accelerations at the sample before and the sample after the gap could then be found using,

$$\underline{H} \begin{bmatrix} x''(h_s - 1) \\ x''(h_f + 1) \end{bmatrix} = \begin{bmatrix} \gamma_2 \\ \gamma_3 \end{bmatrix} \qquad (4.3.4\text{-}4)$$

Solving for x"(h_s–1) and x"(h_f+1) yielded,

$$\begin{aligned} x''(h_s - 1) &= \frac{H\{2,2\} \cdot \gamma_2 - H\{1,2\} \cdot \gamma_3}{\det|\underline{H}|}\\ x''(h_f + 1) &= \frac{H\{1,1\} \cdot \gamma_3 - H\{2,1\} \cdot \gamma_2}{\det|\underline{H}|} \end{aligned} \qquad (4.3.4\text{-}5)$$

where $\det|\underline{H}|$ was the determinant of the matrix $\underline{H}$,

$$\det|\underline{H}| = H\{1,1\} \cdot H\{2,2\} - H\{1,2\} \cdot H\{2,1\} \qquad (4.3.4\text{-}6)$$

The velocity of the samples before and after the gap could then be found,

$$x'(h_s-1)=\frac{x(h_f+1)-x(h_s-1)}{\Delta h_2}-x''(h_f+1)\cdot\frac{\Delta h_2}{6}-x''(h_s-1)\cdot\frac{\Delta h_2}{3}$$
$$x'(h_f+1)=\frac{x(h_f+2)-x(h_f+1)}{\Delta h_3}-x''(h_f+2)\cdot\frac{\Delta h_3}{6}-x''(h_f+1)\cdot\frac{\Delta h_3}{3} \quad (4.3.4\text{-}7)$$

The cubic spline could then be fit across the gap for the samples $h_s \le h \le h_f$, to interpolate the trajectory of the missing degree of freedom, $x(h)$,

$$\begin{aligned} x(h)=&\left[x(h_s-1)-x'(h_s-1)\cdot(h_s-1)+\frac{1}{2}x''(h_s-1)\cdot(h_s-1)^2-\frac{1}{6(h_s-1)}\Delta x''(h_s-1)^3\right] \\ &+h\times\left[x'(h_s-1)-x''(h_s-1)\cdot(h_s-1)+\frac{1}{2(h_s-1)}\Delta x''(h_s-1)^2\right] \\ &+h^2\times\left[\frac{1}{2}x''(h_s-1)-\frac{1}{2(h_s-1)}\Delta x''(h_s-1)\right] \\ &+h^3\times\left[\frac{1}{6(h_s-1)}\Delta x''\right] \end{aligned} \quad (4.3.4\text{-}8)$$

where $\Delta x''=\left[x''(h_f+1)-x''(h_s-1)\right]$.

The Spline Interpolation technique supplied an estimated trajectory, $x(h)$, for the samples $h_s \le h \le h_f$. This would be done for each of the three missing degrees of freedom in order to fill the gap without using any other marker trajectories.

Three-Marker Fill

When the gap was longer than ten samples, one of the two other fill techniques was used; either the Two-Marker Fill or the Three-Marker Fill technique. Deciding which technique was appropriate depended on the number of redundant marker trajectories that were available on the segment or on neighbouring segments. The Three-Marker method was used if at least three redundant markers were available throughout the gap.

When the redundant markers were all attached to the same segment as the missing marker, then there was enough information to reconstruct the actual trajectory of the missing marker. This occurred often with the markers of the Lower Leg and Midfoot segments.

Sometimes three redundant marker trajectories were not available on the same segment as the missing marker. In this case, markers of neighbouring segments were used only if the neighbouring segment was not likely to move a great deal with respect to the first segment. This process was consequently less accurate but was acceptable for certain special cases. For instance, if one marker from the Hindfoot segment cluster, CA, was missing, then the other two CA markers plus one of the Midfoot markers would be used. Also, if a Forefoot marker was missing (from the Mi or Mv cluster), a marker from the other semi-independent Forefoot cluster could be used.

The Three-Marker technique, when used in any of the preceding situations, relied on an appropriate example where all the markers of interest were visible. The example would give the missing marker position relative to the positions of the redundant markers. Five separate examples were used by the method. These examples were taken from individual samples within the same trial, or from other trials in the session where all the markers in question were visible and where the rigid segments were in the same positions relative to one another as during the gap.

Example	Clusters involved
1	**Lower Leg** clusters T2/3 and T1/3
2	**Midfoot** plus **Hindfoot** clusters: Cii, N and CA
3	**Forefoot** clusters: Mi and Mv **(early stance)**
4	**Forefoot** clusters: Mi and Mv **(mid stance)**
5	**Forefoot** clusters: Mi and Mv **(late stance)**

Table 4.3.4-1 The five examples of marker position used in Three-Marker Fill technique.

The five examples are listed in Table 4.3.4-1. Each example was composed of a single sample from the chosen trial.

The Three-Marker Fill technique was performed as follows. From the example, the positions of the three redundant markers were known during the example sample e,

$$ {}_g\underline{b}_1(e), {}_g\underline{b}_2(e), {}_g\underline{b}_3(e) $$

as well as the position of the missing marker,

$$ {}_g\underline{b}_f(e) $$

A frame of reference was created from the redundant markers similarly to Eqs. 4.3.1-5 to 4.3.1-8,

$$ \begin{aligned} {}_g\vec{r}_1(e) &= {}_g\underline{b}_1(e) - {}_g\underline{b}_2(e) \Rightarrow {}_g\hat{r}_1(e) \\ {}_g\vec{r}_2(e) &= {}_g\underline{b}_1(e) - {}_g\underline{b}_3(e) \Rightarrow {}_g\hat{r}_1(e) \end{aligned} \qquad (4.3.4\text{-}9) $$

and

$$ {}_g\vec{r}_x(e) = {}_g\hat{r}_1(e) \times {}_g\hat{r}_2(e) \Rightarrow {}_g\hat{r}_x(e) \qquad (4.3.4\text{-}10) $$

which defined the axes directions,

$$ \begin{aligned} {}_g\hat{1}(e) &= {}_g\hat{r}_x(e) \\ {}_g\hat{2}(e) &= {}_g\hat{r}_1(e) \\ {}_g\hat{3}(e) &= {}_g\hat{1}(e) \times {}_g\hat{2}(e) \end{aligned} \qquad (4.3.4\text{-}11) $$

Using Eq. 4.3.1-9, the transformation matrices moving from the ground frame to the example frame were,

$$ {}_g\underline{R}_{g\rightarrow example} = \begin{bmatrix} {}_g\hat{1}^T(e) \\ {}_g\hat{2}^T(e) \\ {}_g\hat{3}^T(e) \end{bmatrix} \qquad (4.3.4\text{-}12) $$

$$ {}_g\underline{T}_{g\rightarrow example} = -{}_g\underline{b}_1(e) $$

The missing marker was then transformed into the example frame as in Eq. 4.3.1-10,

$$ {}_{example}\underline{b}_f = {}_gR_{g\rightarrow example}\left({}_g\underline{b}_f(e) + {}_g\underline{T}_{g\rightarrow example} \right) \qquad (4.3.4\text{-}13) $$

Since the missing marker and the redundant markers were rigidly fixed with respect to each other, this position, ${}_{example}\underline{b}_f$, should not change during subject movement. This position was therefore used to reconstruct the missing trajectory within the gap.

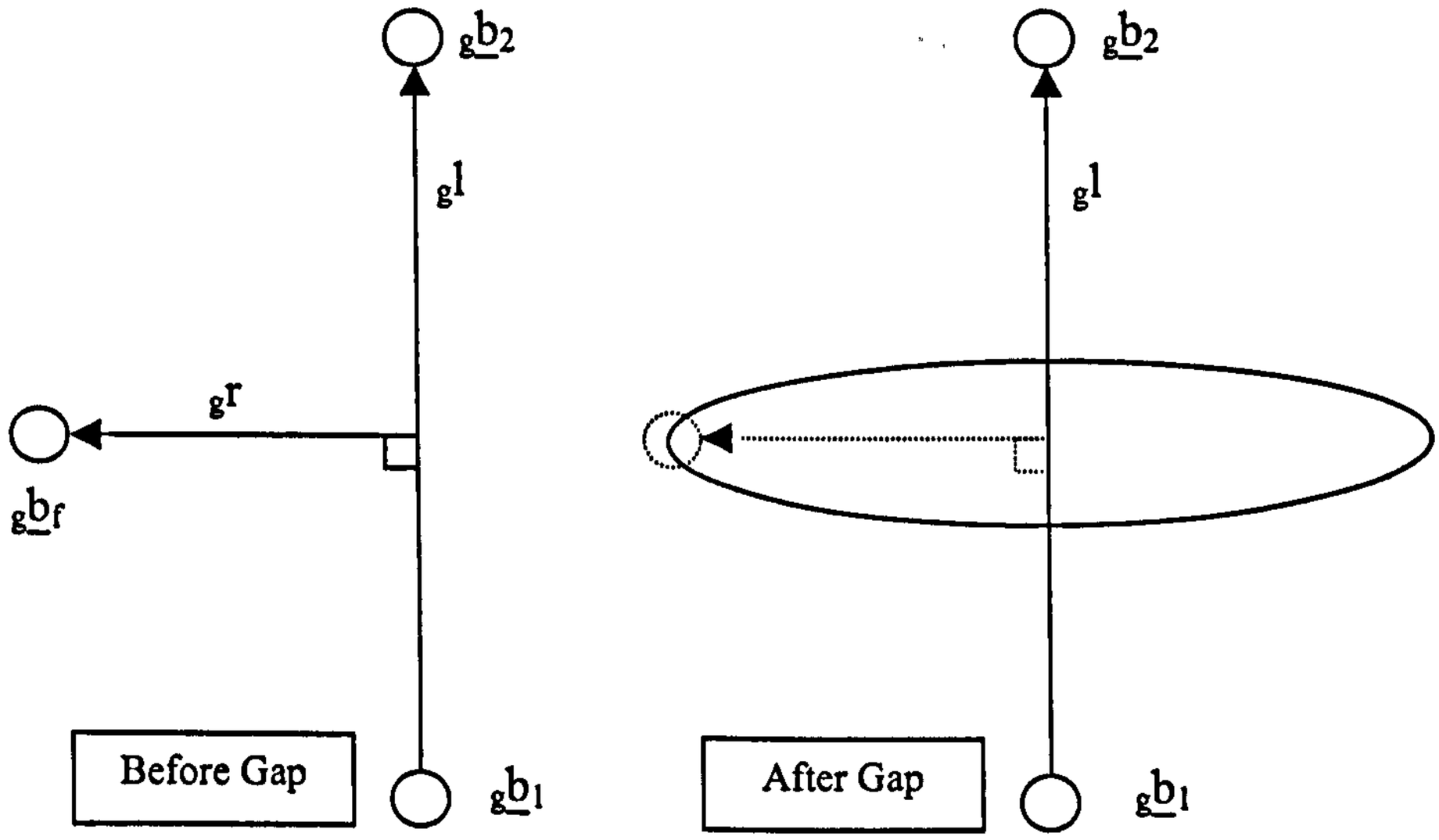

Figure 4.3.4-1 The vectors $_g$l and $_g$r formed before the gaps and the single degree of freedom disc formed by rotating $_g$r about $_g$l. The missing marker must lie on this disc.

At each sample, h, within the gap the positions of the redundant markers were known,

$$ {}_g\underline{b}_1(h), {}_g\underline{b}_2(h), {}_g\underline{b}_3(h) $$

As in Eqs. 4.3.4-9 to 4.3.4-12, a frame of reference was constructed from these for each sample h within the gap. The inverse transformation matrices were then found using Eqs. 4.3.4-13 and 4.3.3-1,

$$ \begin{aligned} {}_g\underline{R}_{example\to g}(h) &= {}_g\underline{R}^T_{g\to example}(h) \\ {}_g\underline{T}_{example\to g}(h) &= -{}_g\underline{T}_{g\to example}(h) \end{aligned} \qquad (4.3.4\text{-}14) $$

So, for each sample h within the gap, the missing marker trajectory was reconstructed using the position ${}_{example}\underline{b}_f$ and the inverse transformation matrices in Eq. 4.3.4-14, as follows

$$ {}_g\underline{b}_f(h) = {}_gR_{example\to g}(h)\cdot\left({}_{example}\underline{b}_f\right) + {}_g\underline{T}_{example\to g}(h) \qquad (4.3.4\text{-}15) $$

Two-Marker Fill

The Two-Marker Fill was employed when only two reliable redundant marker trajectories were available, discounting the Three-Marker Fill, and the gap was longer than ten samples discounting a Spline Interpolation. This was sometimes the case for the Femur cluster. Since this method drew on less information than the Three-Marker method when estimating the missing trajectory it was consequently less accurate. The missing trajectory had three degrees of freedom. By using the trajectories of the two related markers, the degrees of freedom were reduced to one.

Given the two redundant marker positions, ${}_g\underline{b}_1$ and ${}_g\underline{b}_2$, and the missing marker position, ${}_g\underline{b}_f$, a vector, ${}_g\vec{l}$ could be drawn from ${}_g\underline{b}_1$ to ${}_g\underline{b}_2$. A perpendicular ${}_g\vec{r}$ could then be drawn from ${}_g\vec{l}$ to the missing marker ${}_g\underline{b}_f$ as shown in Figure 4.3.4-1. Since the markers were rigidly fixed to the same base, the lengths of vectors ${}_g\vec{l}$ and ${}_g\vec{r}$ were fixed. When marker ${}_g\underline{b}_f$ was missing then, it had to lie within the disc formed by rotating ${}_g\vec{r}$ about the line ${}_g\vec{l}$. The only degree of freedom in the trajectory of the missing marker ${}_g\underline{b}_f$ was therefore the position of ${}_g\vec{r}$ within this disc.

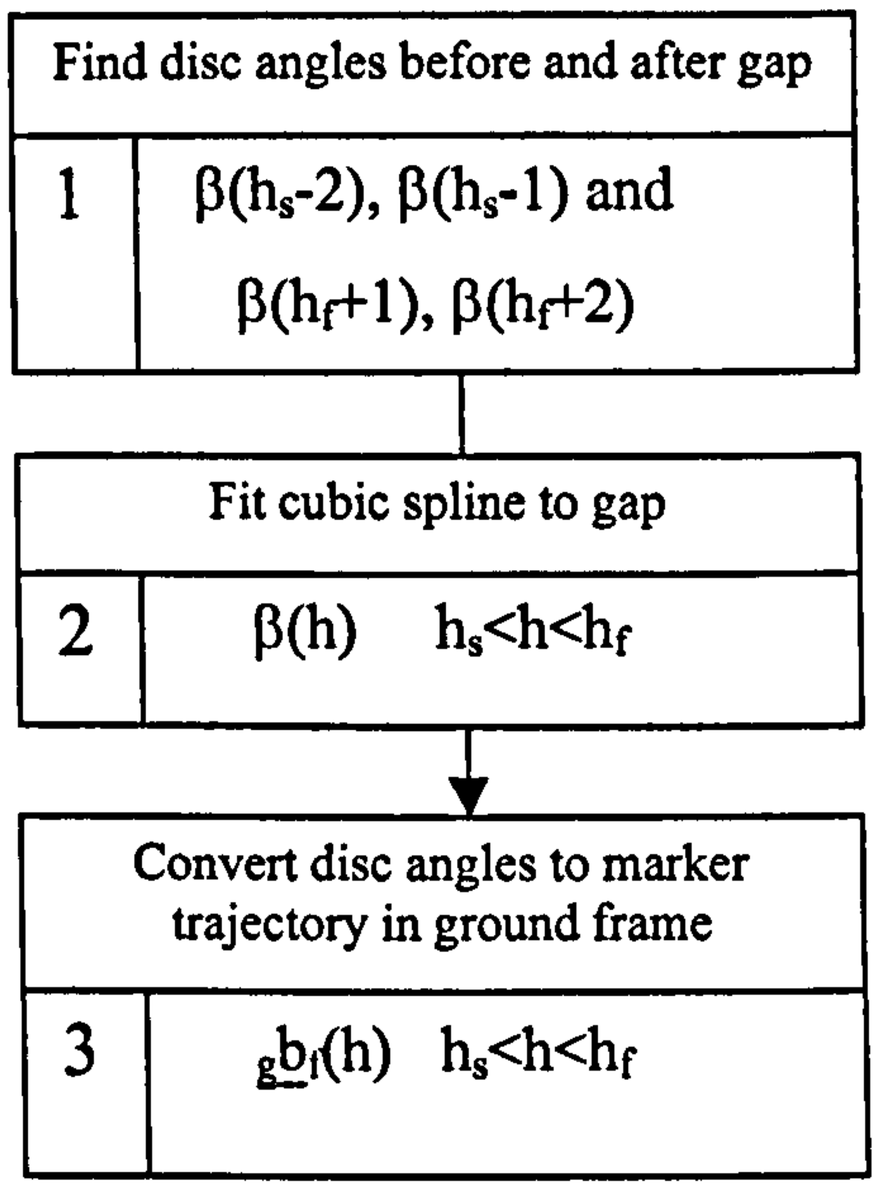

Figure 4.3.4-2 Three steps of Two-Marker Fill method.

The Two-Marker Fill method operated in three steps. First, the two samples before the start of the gap and the two after the end were taken. The gap ran from $h_s \le h \le h_f$, so as in the Spline Interpolation technique, two samples before the gap and two after were taken at samples $h = h_s - 2, h_s - 1, h_f + 1, h_f + 2$. For each of these, the vector ${}_g\vec{l}$ and the perpendicular ${}_g\vec{r}$ were formed. Within the disc formed by the rotation of ${}_g\vec{r}$ about ${}_g\vec{l}$, an angle β was found. The position of ${}_g\vec{r}(h_s - 2)$ defined the zero position for the angle, $\beta(h_s - 2) = 0$. The angle β was found for the three other samples which yielded $\beta(h_s - 2) = 0$ and $\beta(h_s - 1)$ before the gap and $\beta(h_f + 1)$ and $\beta(h_f + 2)$ after the gap. The second step was fitting a minimum curvature cubic spline to the trajectory of the disc angle, $\beta(h)$, within the gap and using $\beta(h_s - 2)$, $\beta(h_s - 1)$, $\beta(h_f + 1)$, $\beta(h_f + 2)$ as the endpoints. Third, the estimated angles $\beta(h)$ within the gap were converted back into a marker trajectory in the three dimensions of the ground reference frame. Figure 4.3.4-2 illustrates the three steps in the Two-Marker Fill technique.

To begin, the two redundant markers were identified, ${}_g\underline{b}_1(e)$ and ${}_g\underline{b}_2(e)$, along with the missing marker, ${}_g\underline{b}_f(e)$. The two samples of the positions of these three markers were taken before the gap and two after. For each of these four samples at $e = h_s - 2, h_s - 1, h_f + 1, h_f + 2$, the following was calculated,

$$\begin{aligned}
{}_g\vec{l}(e) &= {}_g\underline{b}_2(e) - {}_g\underline{b}_1(e) \Rightarrow {}_g\hat{l}(e) \\
{}_g\vec{n}(e) &= {}_g\underline{b}_f(e) - {}_g\underline{b}_1(e) \Rightarrow {}_g\hat{n}(e) \\
D &= {}_g\hat{l}(e) \cdot {}_g\vec{n}(e) \\
{}_g\underline{x}(e) &= {}_g\underline{b}_1(e) + D \cdot {}_g\hat{l}(e)
\end{aligned} \tag{4.3.4-16}$$

therefore

$${}_g\vec{r}(e) = {}_g\underline{b}_f(e) - {}_g\underline{x}(e) \tag{4.3.4-17}$$

This vector ${}_g\vec{r}(e)$ was the perpendicular which lay within the disc. Figure 4.3.4-3 illustrates this vector.

The perpendicular formed from the marker positions of the first sample, ${}_g\vec{r}(h_s - 2)$ defined the position of zero disc angle, $\beta(h_s - 2) = 0$. Before the

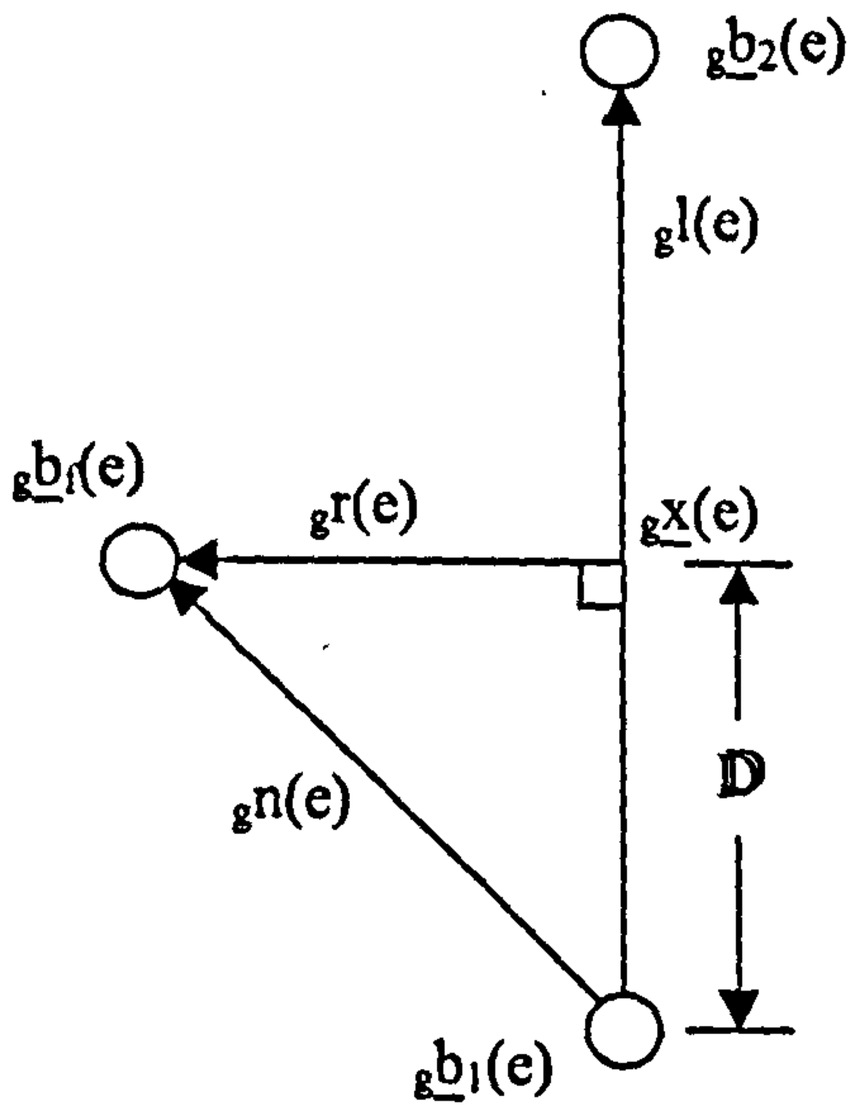

Figure 4.3.4-3 Construction of the perpendicular $_{g}r$ during an example sample e.

perpendiculars from the other three samples, ${}_g\vec{r}(e)$, could be compared with ${}_g\vec{r}(h_s-2)$ in order to calculate their disc angles, the discs from each sample had to first be aligned so that they were all co-planar. The disc from sample $e=h_s-2$ was taken as the reference plane. The marker positions at sample e were first translated so that position ${}_g\underline{x}(e)$ coincided with ${}_g\underline{x}(h_s-2)$. This was done by adding,

$${}_gT_{e\to h_s-2}(e)={}_g\underline{x}(h_s-2)-{}_g\underline{x}(e) \tag{4.3.4-17}$$

to the marker positions ${}_g\underline{b}_1(e)$, ${}_g\underline{b}_2(e)$ and ${}_g\underline{b}_f(e)$. This is the first step in Figure 4.3.4-2. The vectors ${}_g\vec{l}(h_s-2)$ and ${}_g\vec{l}(e)$ were then crossed,

$${}_g\vec{l}_x(e)={}_g\vec{l}(h_s-2)\times{}_g\vec{l}(e)\Rightarrow{}_g\hat{l}_x(e) \tag{4.3.4-18}$$

A frame of reference was then formed using this vector, ${}_g\vec{l}_x(e)$, and the vector ${}_g\vec{l}(h_s-2)$. This frame was attached to the marker positions in sample $e=h_s-2$. The axes directions were defined as,

$$\begin{aligned}
{}_g\hat{1}(e)&={}_g\hat{l}_x(e)\\
{}_g\hat{2}(e)&={}_g\hat{l}(h_s-2)\\
{}_g\hat{3}(e)&={}_g\hat{1}(e)\times{}_g\hat{2}(e)
\end{aligned} \tag{4.3.4-19}$$

The rotation matrix for rotating from the ground frame to the $e=h_s-2$ sample frame was therefore,

$${}_g\underline{R}_{g\to h_s-2}(e)=\begin{bmatrix} {}_g\hat{1}(e)\\ {}_g\hat{2}(e)\\ {}_g\hat{3}(e)\end{bmatrix} \tag{4.3.4-20}$$

The vectors ${}_g\hat{l}(h_s-2)$, ${}_g\hat{l}(e)$ and ${}_g\vec{r}(e)$ were then rotated into the sample frame,

$${}_{h_s-2}\hat{l}(h_s-2)={}_g\underline{R}_{g\to h_s-2}(e)\cdot{}_g\hat{l}(h_s-2) \tag{4.3.4-21}$$

and similarly for ${}_g\hat{l}(e)$ and ${}_g\vec{r}(e)$. The angle between the vectors ${}_{h_s-2}\hat{l}(h_s-2)$ and ${}_{h_s-2}\hat{l}(e)$ was found using,

$$\theta(e)=\arccos\left({}_{h_s-2}\hat{l}(h_s-2)\cdot{}_{h_s-2}\hat{l}(e)\right) \tag{4.3.4-22}$$

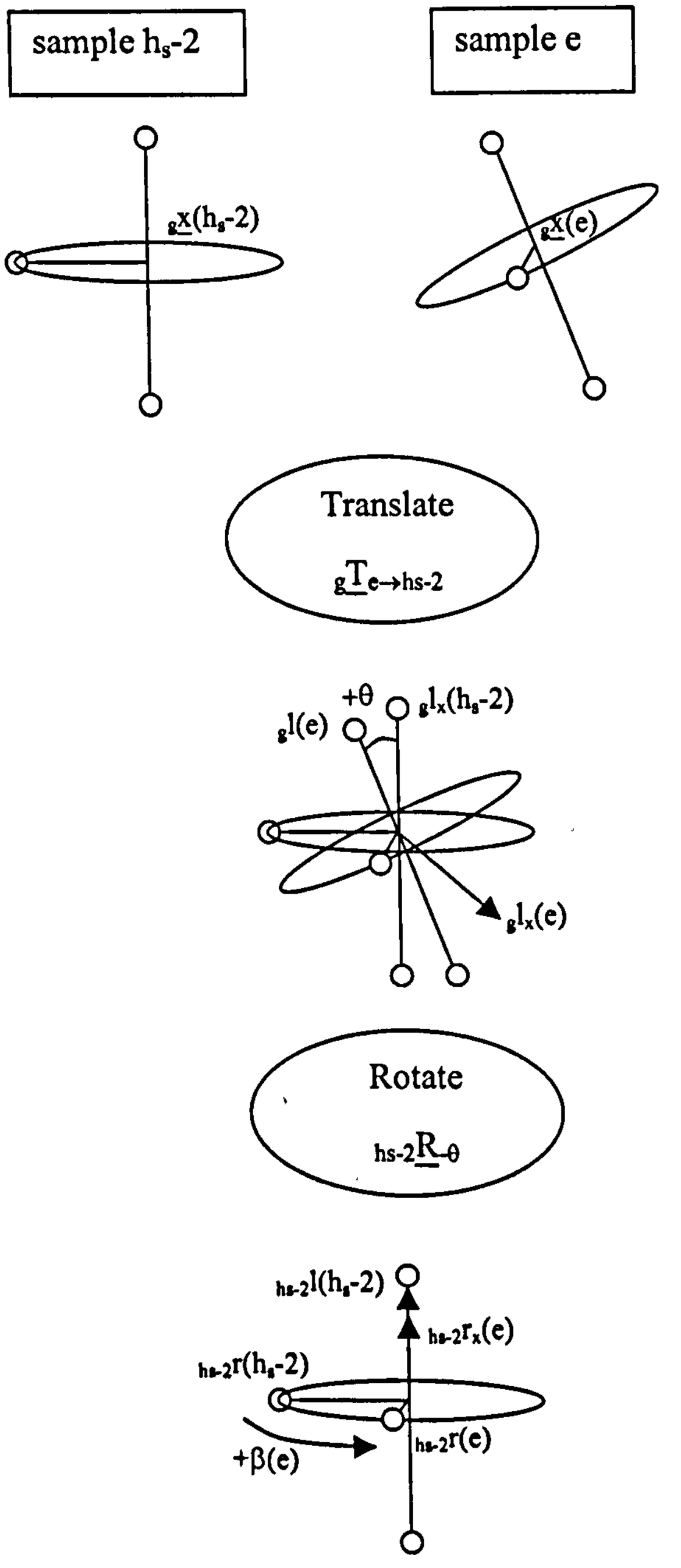

Figure 4.3.4-4 The translation and rotation required to make the discs at sample h_s-2 and e co-planar.

and therefore the rotation matrix which rotated ${}_{h_s-2}\hat{l}(e)$ parallel to ${}_{h_s-2}\hat{l}(h_s-2)$ about the axis formed by ${}_{h_s-2}\vec{l}_x(e)$ was constructed as,

$$ {}_{h_s-2}\underline{R}_{-\theta}(e)=\begin{bmatrix}1 & 0 & 0\\ 0 & \cos(-\theta(e)) & -\sin(-\theta(e))\\ 0 & \sin(-\theta(e)) & \cos(-\theta(e))\end{bmatrix} \qquad (4.3.4\text{-}23)$$

The perpendiculars for each sample, e, ${}_{h_s-2}\vec{r}(e)$, were then rotated,

$$ {}_{h_s-2}\vec{r}'(e)={}_{h_s-2}R_{-\theta}(e)\cdot{}_{h_s-2}\vec{r}(e) \qquad (4.3.4\text{-}24)$$

This is the second step in Figure 4.3.4-4. Once this procedure has been done for each of the samples, $e=h_s-1, h_f+1, h_f+2$, the perpendiculars then all lay in the same disc and could therefore be compared directly to ${}_{h_s-2}\vec{r}(h_s-2)$ to produce the disc angles.

The magnitude of the angle between the perpendicular, ${}_{h_s-2}\vec{r}'(e)$, and the reference perpendicular, ${}_{h_s-2}\vec{r}(h_s-2)$, could be found using,

$$ \beta(e)=\arccos\left({}_{h_s-2}\vec{r}(h_s-2)\cdot{}_{h_s-2}\vec{r}(e)\right) \qquad (4.3.4\text{-}25)$$

This however gave no information about the sign of the angle. This had to be determined by first finding the vector cross product of ${}_{h_s-2}\vec{r}(h_s-2)$ and ${}_{h_s-2}\vec{r}'(e)$,

$$ {}_{h_s-2}\hat{r}_x(e)={}_{h_s-2}\vec{r}(h_s-2)\times{}_{h_s-2}\vec{r}'(e) \qquad (4.3.4\text{-}26)$$

and comparing it to the vector ${}_{h_s-2}\hat{l}(h_s-2)$ as follows,

$$ sign(\beta(e))=sign\left({}_{h_s-2}\vec{r}_x(e)\cdot{}_{h_s-2}\hat{l}(h_s-2)\right) \qquad (4.3.4\text{-}27)$$

This yielded the disc angle, $\beta(e)$, for the sample before the gap and the two after the gap:

$$ \beta(h_s-2)=0,\ \beta(h_s-1),\ \beta(h_f+1),\ \beta(h_f+2)$$

The next step was to use these four values of β at either side of the gap as the endpoints with which to fit a minimum curvature cubic spline within the gap, using the method in Eqs. 4.3.4-1 to 4.3.4-8. This yielded the gap trajectory in the form of the disc angles $\beta(h)$ for the samples $h_s \le h \le h_f$ within the gap.

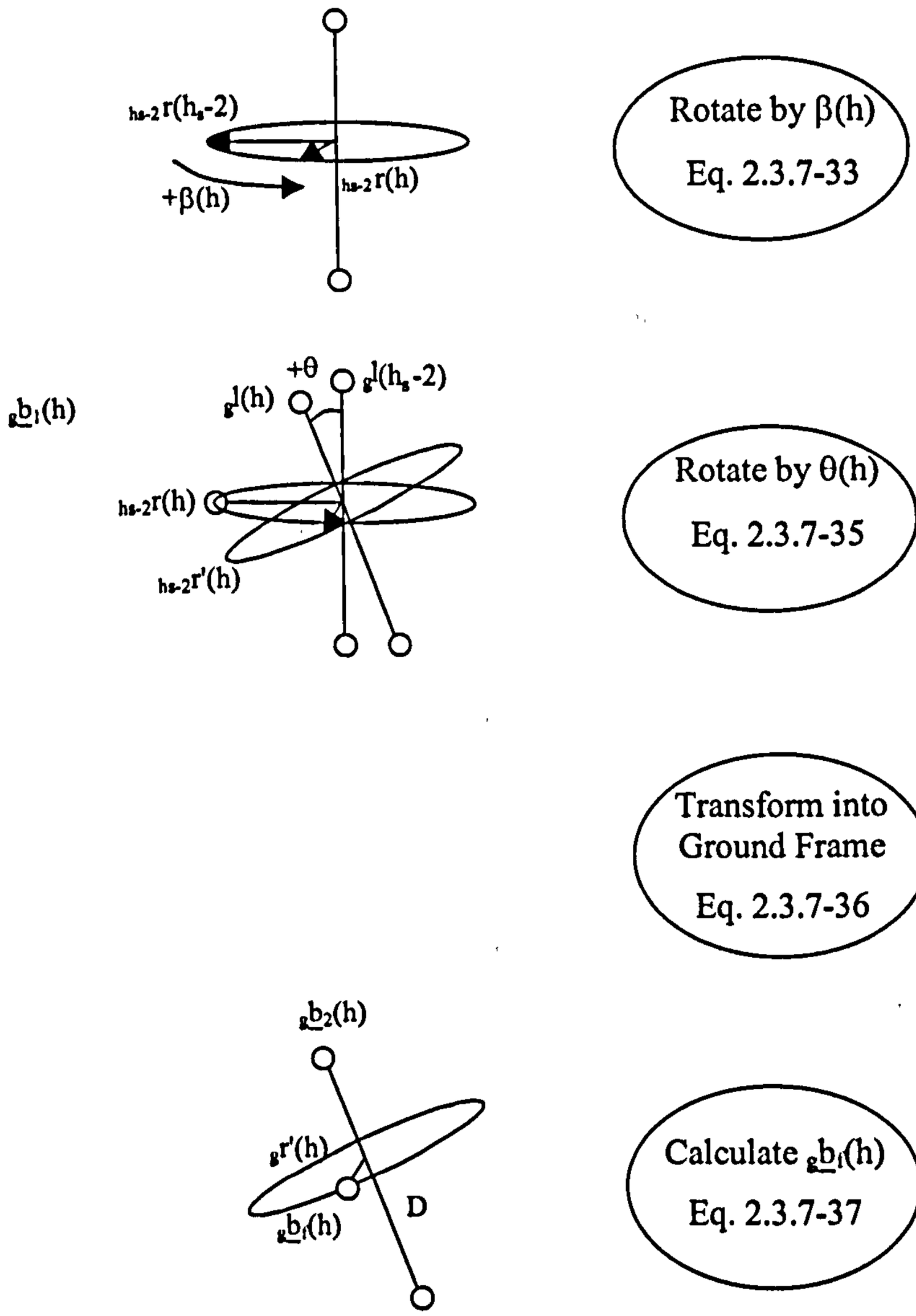

Figure 4.3.4-5 Two rotations and a transformation takes the h_s-2 sample perpendicular into the position of the interpolated perpendicular at sample h. Then the missing position can be found.

The final step in the Two-Marker Fill technique was to convert the disc angle trajectory $\beta(h)$ into a trajectory defined in the three axis directions of the ground frame of reference. Figure 4.3.4-5 illustrates the final step. For a sample, h, within the gap, the positions of the two redundant markers were known,

$$ {}_g\underline{b}_1(h) \text{ and } {}_g\underline{b}_2(h). $$

The vector, ${}_g\hat{l}(h)$ and the position, ${}_g\underline{x}(h)$ were found as before in Eqs. 4.3.4-16. The vector ${}_g\hat{l}(h)$ was then crossed with ${}_g\hat{l}(h_s-2)$ similarly to Eq. 4.3.4-18, to form,

$$ {}_g\vec{l}_x(h)={}_g\vec{l}(h_s-2)\times{}_g\vec{l}(h)\Rightarrow{}_g\hat{l}_x(h) \tag{4.3.4-28} $$

As in Eq. 4.3.4-19, a reference frame was created with respect to the marker positions in the sample $e=h_s-2$,s

$$ \begin{aligned} {}_g\hat{1}(h)&={}_g\hat{l}_x(h)\\ {}_g\hat{2}(h)&={}_g\hat{l}(h_s-2)\\ {}_g\hat{3}(h)&={}_g\hat{1}(h)\times{}_g\hat{2}(h) \end{aligned} \tag{4.3.4-29} $$

with the rotation and translation matrices,

$$ {}_g\underline{R}_{g\to h_s-2}(h)=\begin{bmatrix} {}_g\hat{1}(h)\\ {}_g\hat{2}(h)\\ {}_g\hat{3}(h) \end{bmatrix} \tag{4.3.4-30} $$

$$ {}_g\underline{T}_{g\to h_s-2}(h)={}_g\underline{x}(h_s-2)-{}_g\underline{x}(h) $$

The process then took the perpendicular ${}_g\vec{r}_2(h_s-2)$ and rotated it into the sample frame,

$$ {}_{h_s-2}\vec{r}(h_s-2)={}_g\underline{R}_{g\to h_s-2}(h)\cdot{}_g\vec{r}(h_s-2) \tag{4.3.4-31} $$

The perpendicular was then rotated within the disc by the angle $\beta(h)$ to its interpolated position at sample h, using the following rotation matrix,

$$ {}_{h_s-2}\underline{R}_{\beta}(h)=\begin{bmatrix} \cos(\beta(h)) & 0 & -\sin(\beta(h))\\ 0 & 1 & 0\\ \sin(\beta(h)) & 0 & \cos(\beta(h)) \end{bmatrix} \tag{4.3.4-32} $$

to form the perpendicular,

$$ {}_{h_s-2}\vec{r}(h)={}_{h_s-2}\underline{R}_{\beta}(h)\cdot{}_{h_s-2}\vec{r}(h_s-2) \tag{4.3.4-33} $$

The angle between ${}_g\hat{l}(h_s-2)$ and ${}_g\hat{l}(h)$ was found as in Eq. 4.3.4-22 and the following rotation matrix was formed,

$$ {}_{h_s-2}\underline{R}_{+\theta}(h)=\begin{bmatrix}1 & 0 & 0\\ 0 & \cos(\theta(h)) & -\sin(\theta(h))\\ 0 & \sin(\theta(h)) & \cos(\theta(h))\end{bmatrix} \qquad (4.3.4\text{-}34) $$

The perpendicular ${}_{h_s-2}\vec{r}_2(h)$ was rotated as follows,

$$ {}_{h_s-2}\vec{r}'(h)={}_{h_s-2}\underline{R}_{+\theta}(h)\cdot{}_{h_s-2}\vec{r}(h) \qquad (4.3.4\text{-}35) $$

Finally this perpendicular was transformed into the ground frame of reference by inverting rotation matrix from Eq. 4.3.4-30,

$$ {}_g\vec{r}'(h)={}_g\underline{R}^T_{g\to h_s-2}(h)\cdot{}_{h_s-2}\vec{r}'(h) \qquad (4.3.4\text{-}36) $$

This perpendicular could then be used to estimate the position of the missing marker ${}_g\underline{b}_f(h)$, in the ground frame of reference,

$$ {}_g\underline{b}_f(h)={}_g\underline{b}_1(h)+D\cdot{}_g\hat{l}(h)+{}_g\vec{r}'(h) \qquad (4.3.4\text{-}37) $$

This final procedure was done for each of the samples, h, within the gap. In this way, the trajectory of the missing marker was estimated within the ground frame of reference while interpolating in only a single degree of freedom.

4.3.5 Filtering Marker Trajectory Noise

Once all the gaps in the marker trajectories had been filled, the trajectories of the markers on each of the clusters were continuous throughout the Movement Analysis trials. These marker trajectories, however, contained noise from a number of sources.

The smallest of the errors came from the VICON System itself. Small errors arose from the digitisation of the two-dimensional marker reflection image seen by each camera. This error depended on the resolution of the opto-electronic cameras. Errors in the synchronisation between the individual cameras and between each camera and the VICON computer were also possible. The parallax effects present in the marker reflection images seen by each of the cameras were assumed to be linear when they were corrected by the VICON System. Non-linearities in the image

would therefore introduce error. The three preceding errors were estimated to introduce noise to the marker trajectories of magnitude no larger than ±0.3 mm. The magnitude of these errors was less than the ±0.8 mm uncertainty in marker position which remained after the reconstruction of the trajectories (recall the *calibration error residuals* of Section 2.3.1). Therefore the errors due to the opto-electronic cameras and VICON System electronics could be considered negligible compared to the reconstruction errors.

Noise of a larger magnitude was introduced to the marker trajectories by movement of the skin to which the marker clusters were attached with respect to the underlying bone structures. Movement of the skin was introduced as a concern when deciding on the cluster placement in Section 3.2. The marker cluster moving with the skin while the underlying bone trajectory, which the marker cluster was meant to be following, was either stationary or moving in another direction created an error in the marker trajectory. Fortunately, the noise introduced by skin movement occurred at frequencies that were higher and distinct from the frequencies of locomotion and they could therefore by effectively removed from the marker trajectories by filtering.

According to Winter (1990) and Woltring (1986), the frequencies contained within the trajectories of the segments of the lower limb and foot during locomotion ranged from 0 to 6 Hz. The highest and lowest frequencies would both occur at the segments most distal from the hip. The highest frequencies occurred during the swing phase and the lowest during the stance phase of gait. This frequency range was observed in the present study in the marker trajectories from the walking and the walking turn trials. The noise due to skin movement occurred predominately at frequencies significantly higher than 6 Hz, in the range of 15-25 Hz. For this reason, the skin movement noise could be removed from the marker trajectories by passing them through a *low-pass* filter with a pass-band of 0-6 Hz.

When constructing a filter, two choices presented themselves: the Infinite Impulse Response (IIR) filter and the Finite Impulse Response (FIR) filter (Orfanidis, 1996). IIR filters are recursive and therefore are less complex computationally and operate on less data points when filtering the trajectory. This gives the IIR filters greater economy in terms of computation time and memory

requirements. Examples of IIR filters are the Butterworth and Chebyshev filters. However, IIR filters have the draw back that the phase delay introduced to the output trajectory is not linear, but changes non-linearly for each frequency. The IIR filter therefore introduces some distortion to the output signal, even within the pass-band, where the input and output signals should be identical.

FIR filters, while requiring much more computational complexity, have a linear phase delay and can often be designed with a phase delay that is constant for all frequencies. FIR filters have two other advantages. The transient response for an FIR filter is faster than that of an IIR filter with an identical band-pass range. Therefore, the FIR filter responds to rises and drops in the input signal faster than the IIR. Secondly, the noise attenuation of an FIR filter for the frequency components in the stop-band of the filter response is greater than that of an IIR filter with identical band-pass range.

Since as great an importance was attached to the *temporal* accuracy of the marker trajectories as to the *spatial* accuracy, an FIR filter was used to filter out skin movement noise so as not the distort the trajectory with respect to time. The filter frequency response was designed using the software MATLAB with a least squares routine which produced a filter of constant phase delay across all frequencies. The pass-band for the filter was 0 to 6 Hz where the input signal was passed unattenuated. A transition-band from 6 to 7 Hz separated the pass-band from the stop-band. The stop-band for the filter ranged from 7 to 500 Hz.

The actual filtering of the trajectories was performed within the MATLAB software. The filtering was done twice. The trajectory was passed through the filter first in the forward time direction and then was passed back through the filter in the reverse time direction. The first pass introduced the constant phase delay to the output signal. The second pass, since it was done in the reverse time direction, removed the phase delay. Once the noise had been removed from the marker trajectories, they could then be used to relate the Internal Map to the ground frame as described in the preceding sections.

CHAPTER 5 EXTERNAL LOADING RESULTS AND DISCUSSION

5.1 INTRODUCTION

The Kinematic Data from the twelve subjects formed the input for the Ankle Complex Biomechanical Model. Three categories of results were output from the Model: the external loading on the Ankle Complex, the tensions in the muscles, and the loading on the passive structures of the Ankle Complex; the ligaments and surfaces. These last two categories of results: muscle tensions and passive structural loading, will be presented and discussed in Chapter 8. The external loading results are presented and discussed in this chapter.

The external loading results were composed of the Ground Reaction Forces (GRFs) acting on the right foot, the moments due to the GRF acting about the two joint rotational axes and the joint angles.

Since there was so much data output for each individual subject, it was decided that presenting the complete results for each of the twelve subjects would be impracticably large. Therefore, two subjects were chosen from the twelve who represented the two extremes in the range of body masses and body heights. Subject A was a female of height 1.63 m and body mass 53.5 kg and 23 years old. Subject B was a male of height 1.88 m and body mass 76 kg and 25 years old. The complete range of output from the Model for these two subjects is presented and discussed in the following sections. The results from the remaining ten subjects are summarised in the Appendix A.2.

All the forces that are reported are normalised with respect to subject *body weight (BW)*, where BW was equal to the body mass multiplied by the acceleration due to gravity, 9.81 ms^{-2}. The moments reported in this section are also normalised with respect to body weight. It has been the practice in other papers to normalise moments with respect to both BW and the body height. However, the relationship between the subject height and the length of the lever arms within the Ankle Complex was considered less reliable than the relationship between forces acting on

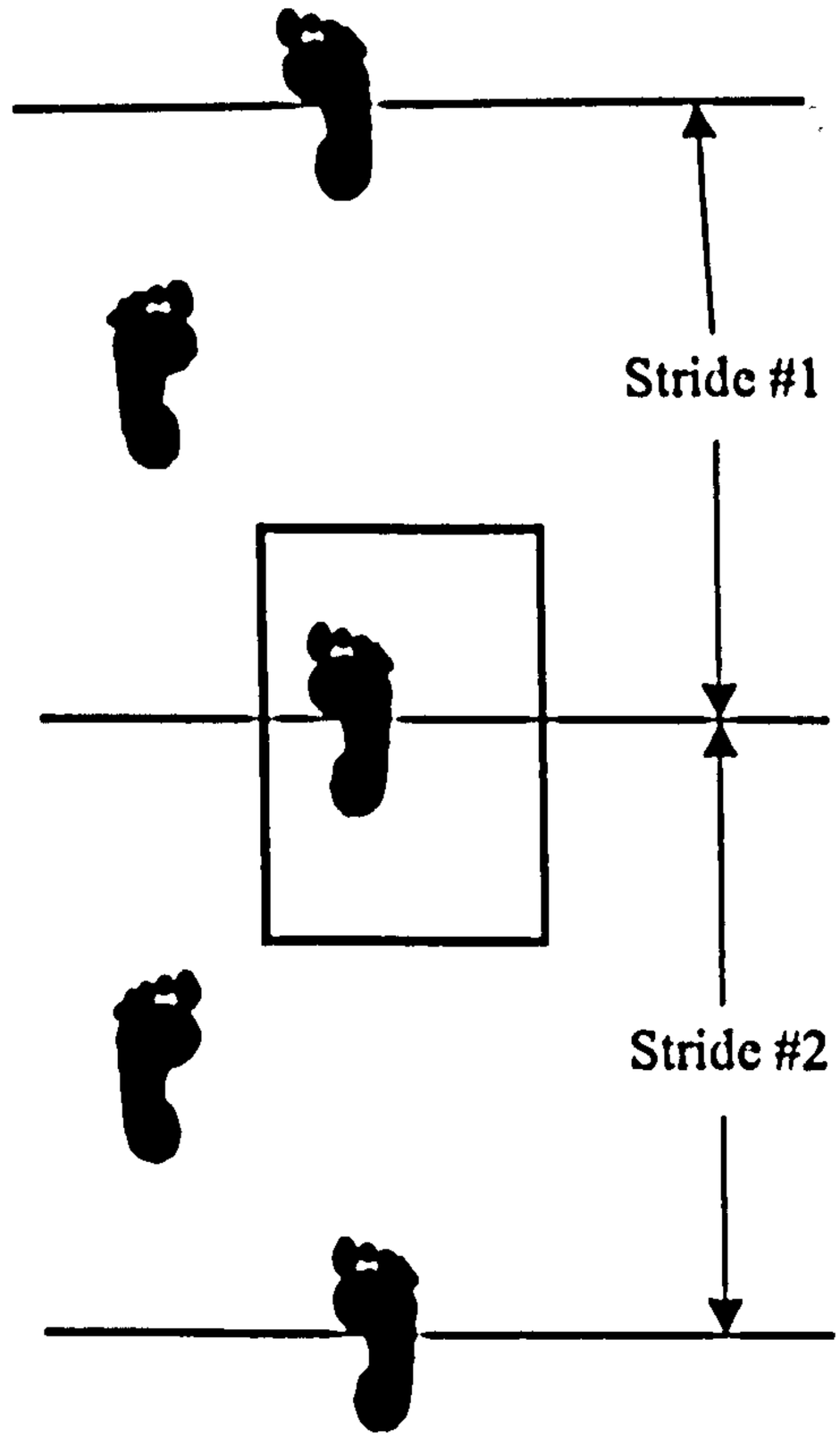

Walking

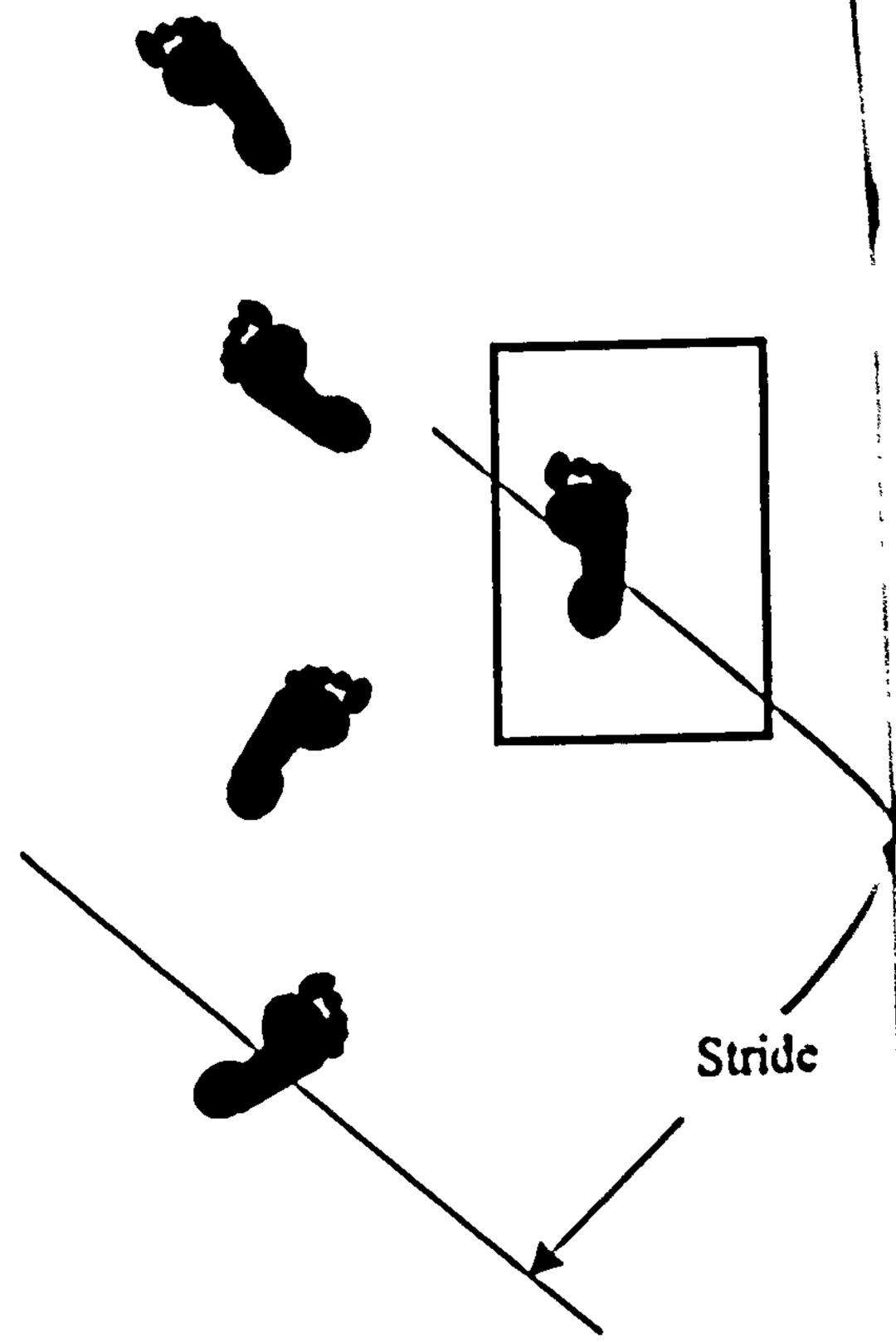

Walking Turn

Figure 5.1-1 Calculation of gait speed for the Walking and Walking Turn tasks.

the body and the body weight. Therefore including height in the normalisation of the moments may be misleading.

Each of the twelve subjects performed the two movement tasks at three different speeds: walking at slow, preferred and fast speed, and turning at slow, preferred and fast speed. For each of these six sorts of trial, the subject repeated the task three times. The average speeds of gait from each of the six sorts of trial are summarised in Table 5.1-1. The speeds quoted are the average of the speeds from the three repetitions. The speed of walking gait was taken as the average over two strides (or four steps). The speed of the turn was taken as the average over a single stride during the approach to the Force Plate. Recall that at least four steps were taken before foot contact with the Force Plate. The stride was defined as ending with foot contact on the Force Plate and beginning two steps prior to this. This is illustrated in Figure 5.1-1.

Units: [m/s]		**Subject A**	**Subject B**
Walk	**Slow**	1.1±0.4	1.3±0.5
	Preferred	2.2±0.3	2.4±0.4
	Fast	3.4±0.3	3.9±0.2
Turn	**Slow**	0.9±0.3	1.1±0.3
	Preferred	2.0±0.5	2.2±0.4
	Fast	2.8±0.3	3.6±0.5

Table 5.1-1 Average gait speeds for the six different types of trials for Subjects A and B.

All the results presented were normalised in time with respect to the duration of *stance phase*. Stance phase was defined as the portion of gait starting with Heel Strike (HS) and ending with Toe Off (TO) of the right foot. The normalised time scale therefore ranged from 0.0 at HS to 1.0 at TO. This was a useful exercise since the length of the stance phase in time changed as the speed of gait increased and decreased. Comparison of results from trials of different speeds, and indeed, from

trials of the same speed, where the stance phase was not of the same time period would not have been as demonstrative had the lengths of stance phase remained at different lengths. A number of events occurred during stance phase. Soon after HS, the sole of the foot landed on the ground defining the stage Foot Flat (FF), usually at 0.25 of stance phase. Mid-stance (MS) was defined as 0.5 and soon after that, around 0.6, the heel of the foot rose off the ground at Heel Raise (HR).

5.2 GROUND REACTION FORCES

The Ground Reaction Forces (GRFs) in this section are defined in the ground (or VICON) frame of reference. Recall from Section 3.1 that the $x-axis$ of the ground frame was anterior-posterior (A-P), the $y-axis$ was medio-lateral (M-L) and the $z-axis$ was vertical. Given the directions of subject gait during the walking and walking turn tasks, the $-x-axis$ pointed anteriorly, the $-y-axis$ pointed medially for the right leg and foot and the $+z-axis$ was directed upward. The forces quoted are those *exerted on the foot* by the Force Plate.

Figures 5.2-1 to 5.2-3 plot the A-P, M-L and vertical GRFs for the all of the walking trials for Subjects A and B. The trials are organised with respect to the speed of gait. There was very little variability in the GRFs both between the trials of the same subject and between subjects. At each of the three speeds, the GRFs followed the same pattern. The vertical GRF possessed two peaks, one in early stance (0.2) and the other in late stance (0.8). The magnitudes of the peaks were larger than BW (1.25×BW for preferred speed) and the peaks were separated by a dip below BW (0.75×BW for preferred speed). The vertical GRF did possess a difference between the two subjects for preferred and fast speeds. The force rose more slowly to the first peak for Subject B compared to Subject A. The first peak also occurred later for Subject B than for Subject A (0.25 of stance phase as opposed to 0.2). The vertical GRF for Subject A showed a small, sharp peak immediately after HS during one of the preferred speed trials and during each of the slow speed trials. This peak was an consequence of the impact of the heel onto the Force Plate.

The A-P GRF was initially pointing posteriorly with a peak of 0.24×BW at 0.15 stance phase during preferred speed. At around mid-stance (0.5), the A-P GRF

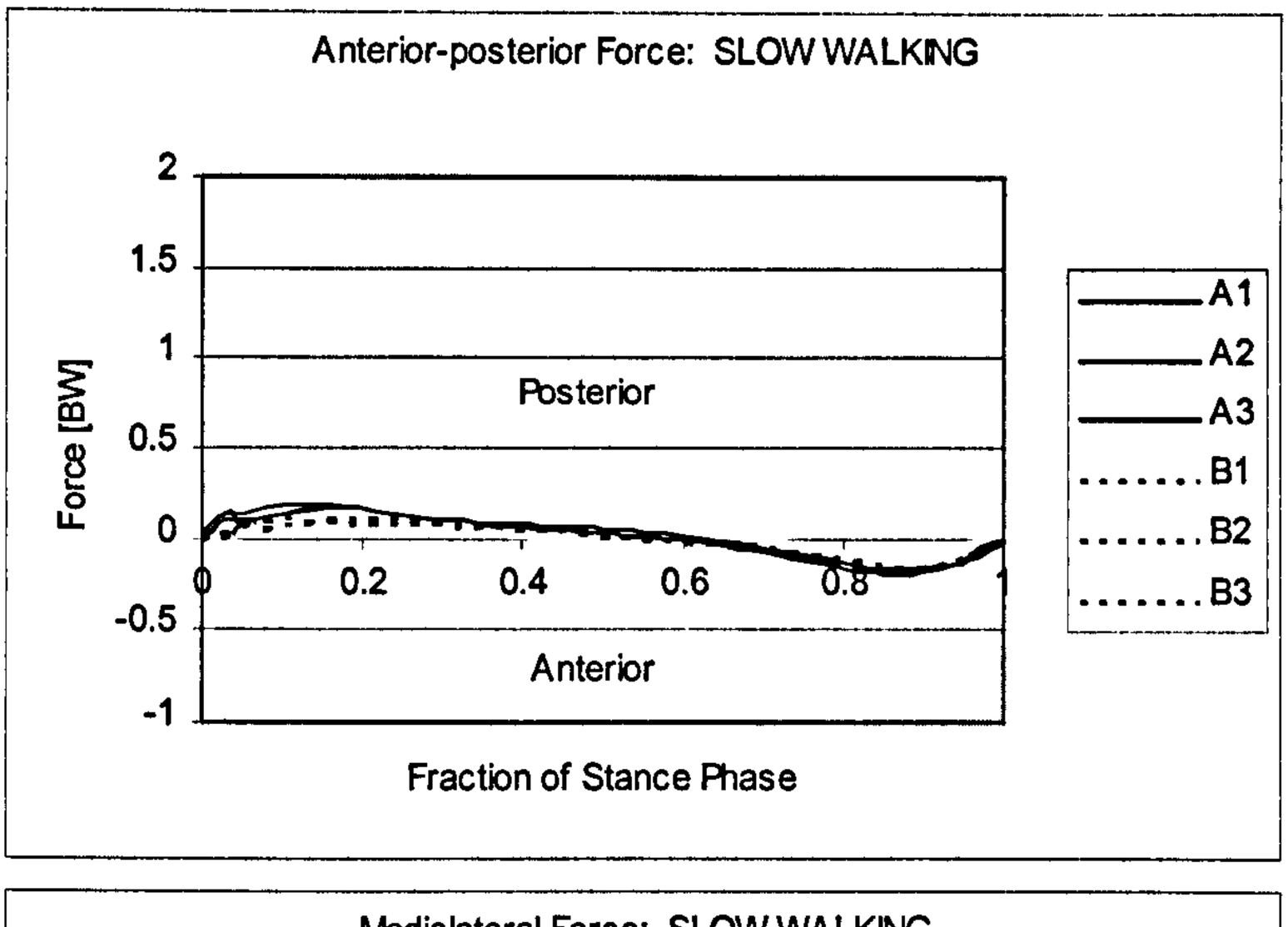

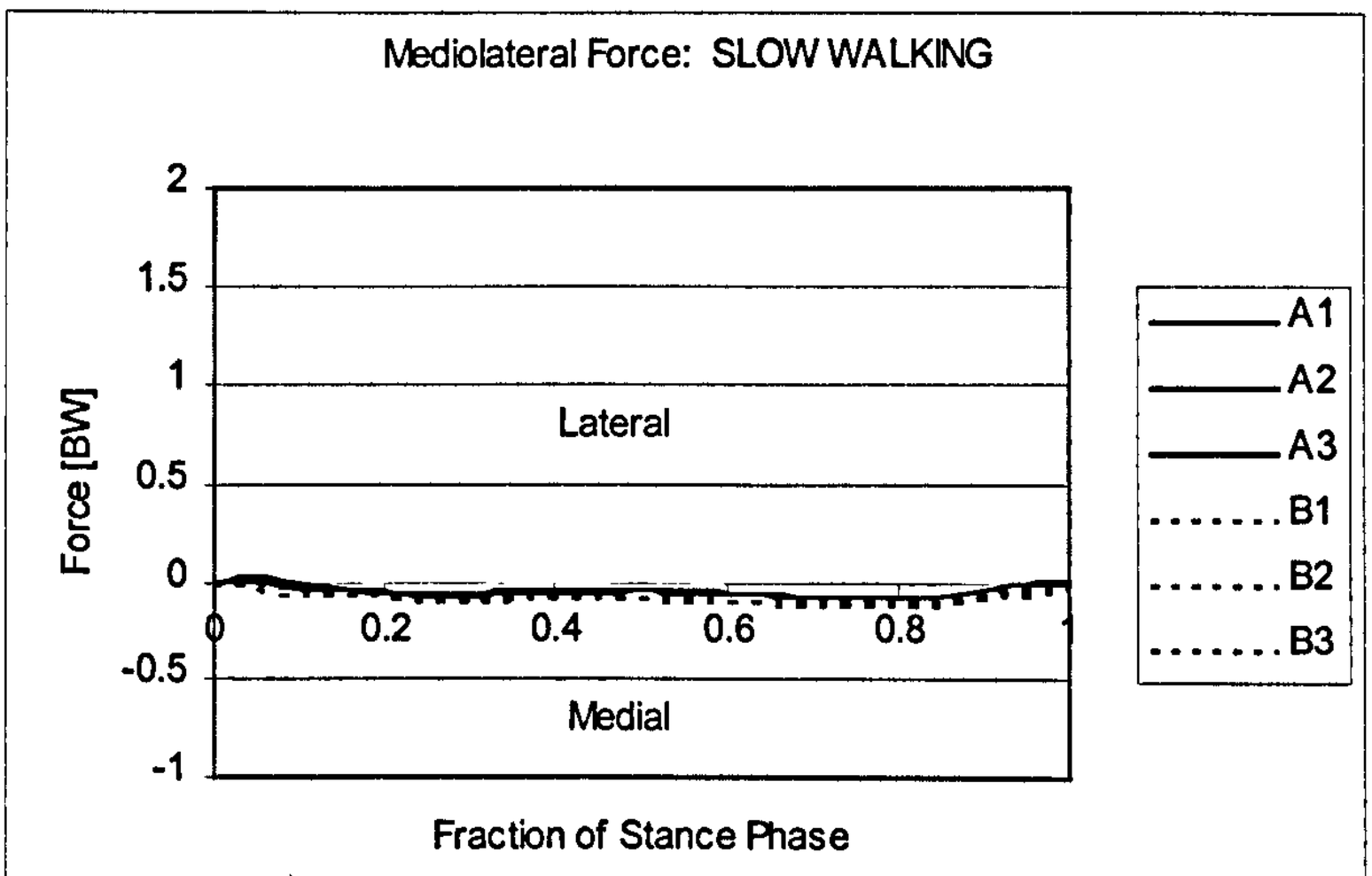

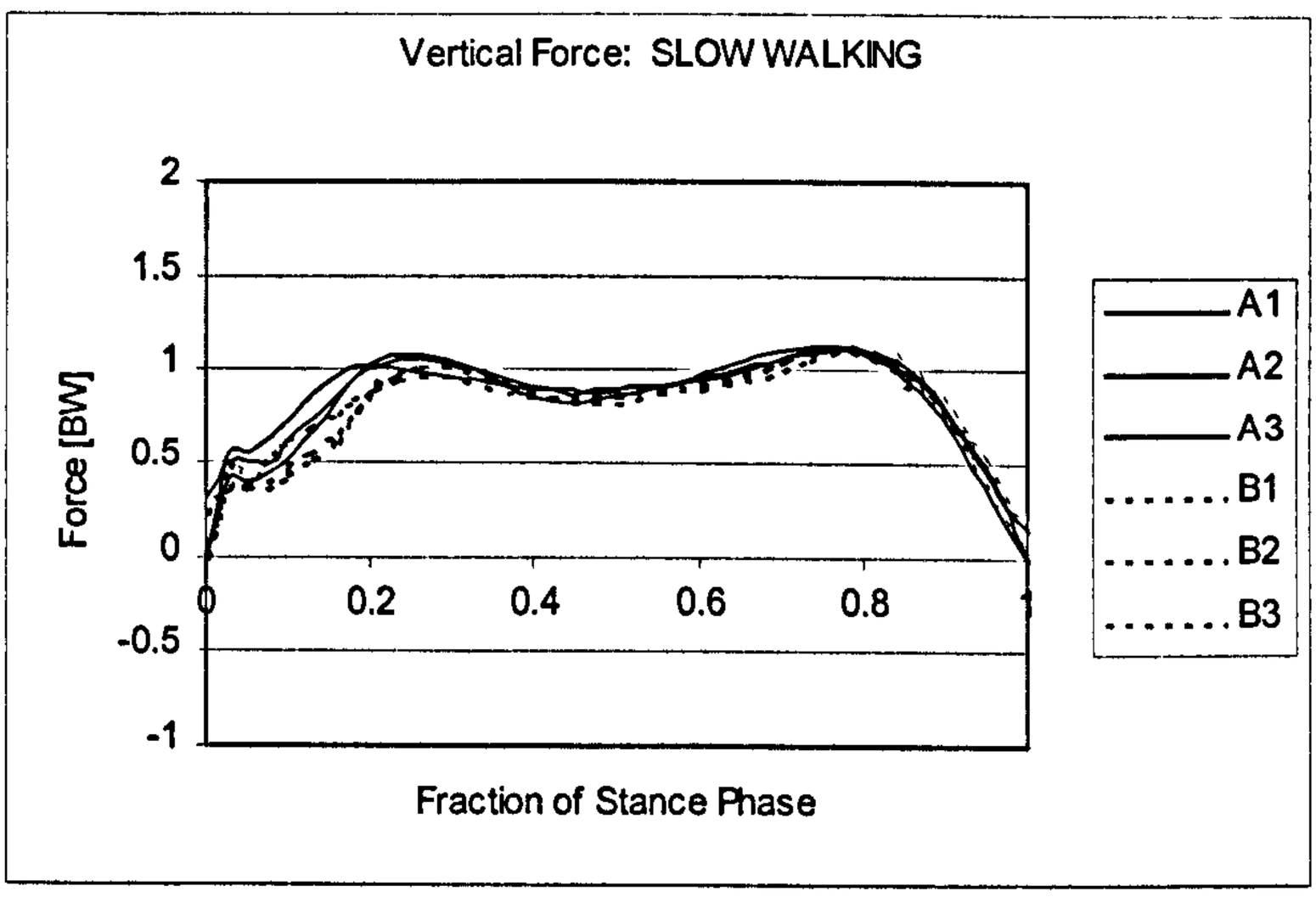

Figure 5.2-1 Ground Reaction Forces for Slow Speed Walking for Subjects A and B.

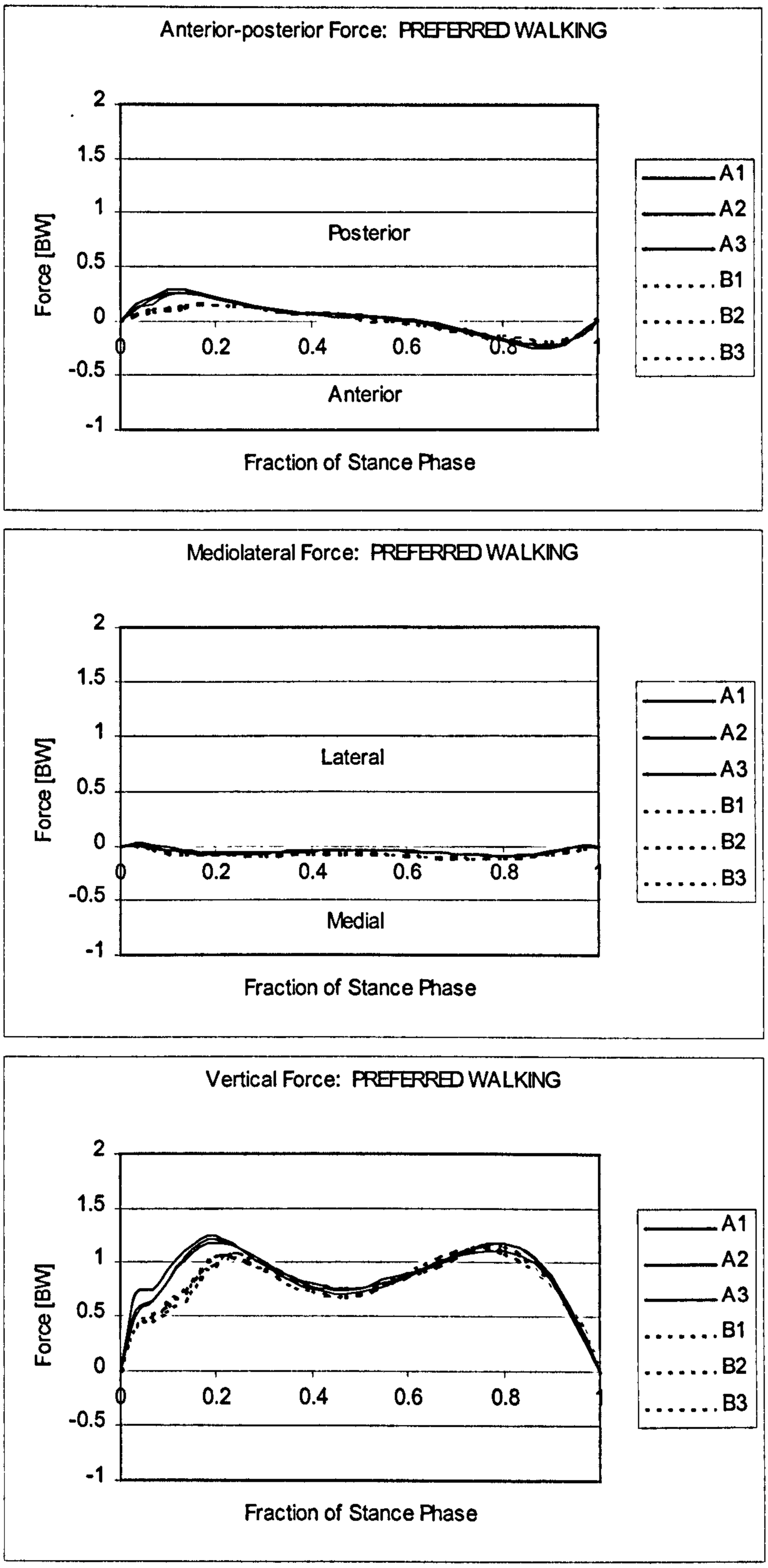

Figure 5.2-2 Ground Reaction Forces for Preferred Speed Walking for Subjects A and B.

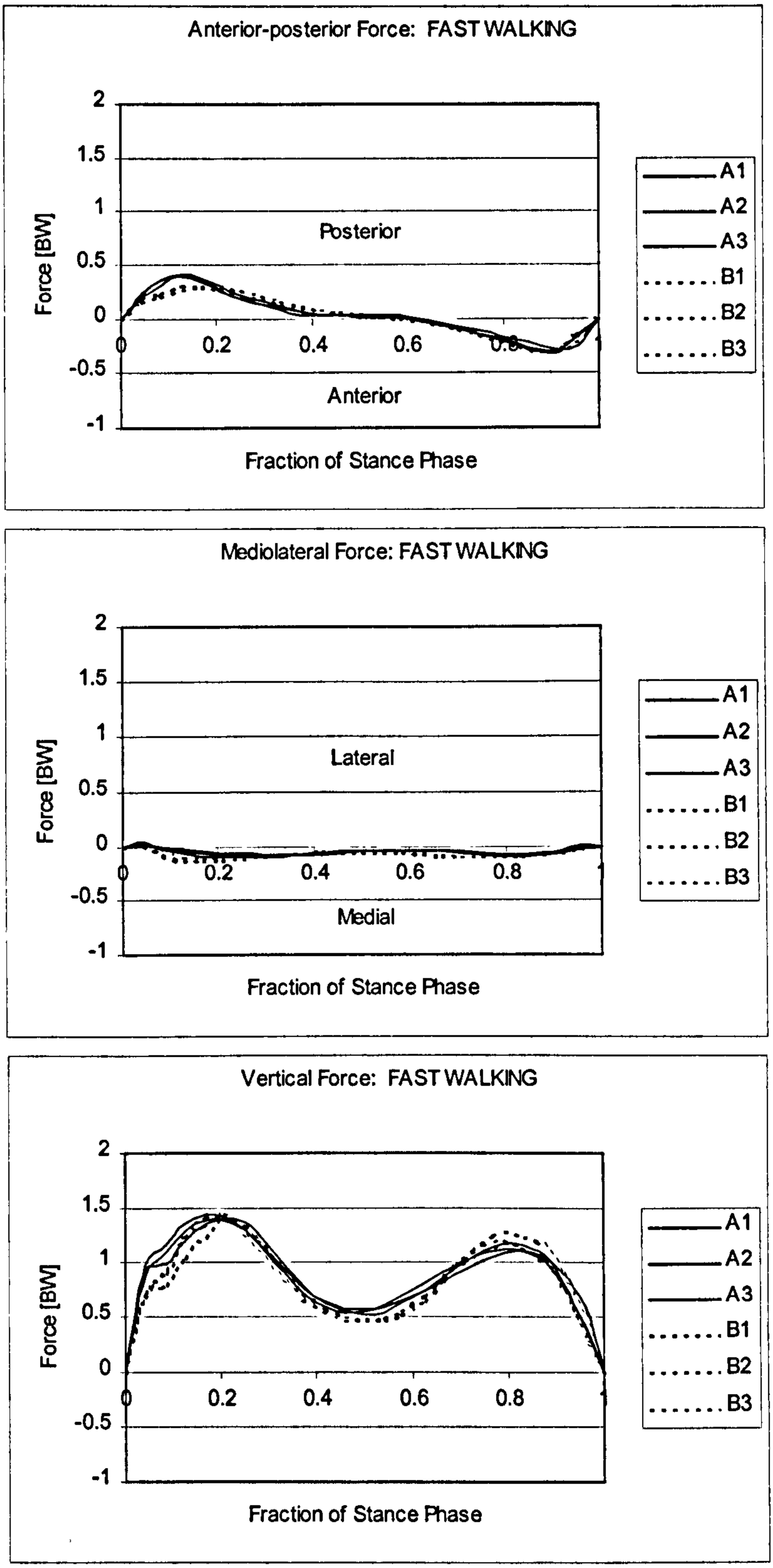

Figure 5.2-3 Ground Reaction Forces for Fast Speed Walking for Subjects A and B.

became directed anteriorly and developed a peak at 0.9 of stance phase of 0.24×BW. The A-P GRF was initially pointed posteriorly which served to decelerate the subject from the instant of HS until the middle of stance. It then became anteriorly directed and served to propel the subject forward up till TO and on into the swing phase. The stance phase could therefore be divided during walking into two sections: the decelerating and the accelerating phases. These were roughly divided by mid-stance at 0.5. For both the subjects, the M-L GRF was rather small compared to the other two components and was directed medially throughout the stance phase for all the speeds.

Figure 5.2-4 to 5.2-6 show all the turning trials for each of the three speeds for the two subjects. The variability between the trials of the same subject and between subjects was very small (around 0.1×BW). The vertical and the A-P GRFs possessed the same patterns for turning as they did for walking. The vertical GRF had two peaks, at 0.2 and 0.8 of stance phase, both with magnitudes of 1.25×BW for preferred speed. The peak magnitudes were both larger than body weight and were separated by a dip below BW at 0.75×BW for preferred speed. An impact spike was present in the vertical GRF in two of the slow speed trials and for all of the fast speed trials for Subject B. The A-P GRF was initially pointed posteriorly, peaking at 0.25×BW at 0.1 of stance phase, until mid-stance and was then pointed anteriorly in the propulsive phase of stance. The magnitudes of the deceleration peaks were smaller for Subject B than they were for Subject A.

The mediolateral GRF for the turning task was quite different than that observed during walking. Throughout all the trials, the M-L GRF was pointed medially on the right foot. Its magnitude was relatively constant for both the slow and preferred speeds. For the fast speed, the M-L force showed two peaks, one early (0.2) and one late (0.8) which coincided in time with the peaks in the vertical GRF. The early peak was larger than the late peak. The early peak in Subject B was slightly earlier than for Subject A with it occuring just before 0.2.

Figures 5.2-7 to 5.2-9 compare the differences between the walking and turning Ground Reaction Forces for each of the three speeds. The A-P GRF was unchanged between tasks for any of the speeds. There was a small reduction in the

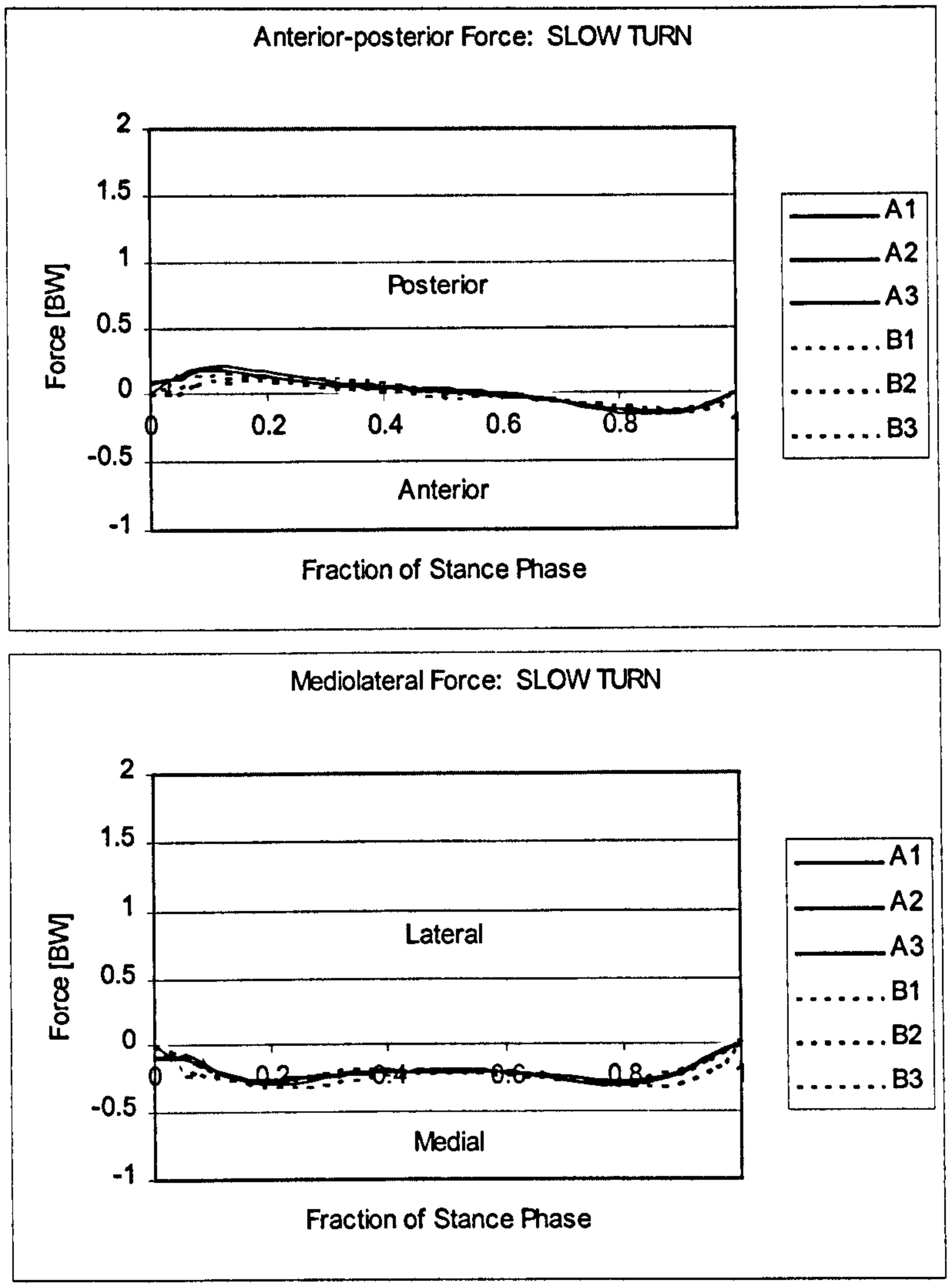

Figure 5.2-4 Ground Reaction Forces for Slow Speed Turning for Subjects A and B.

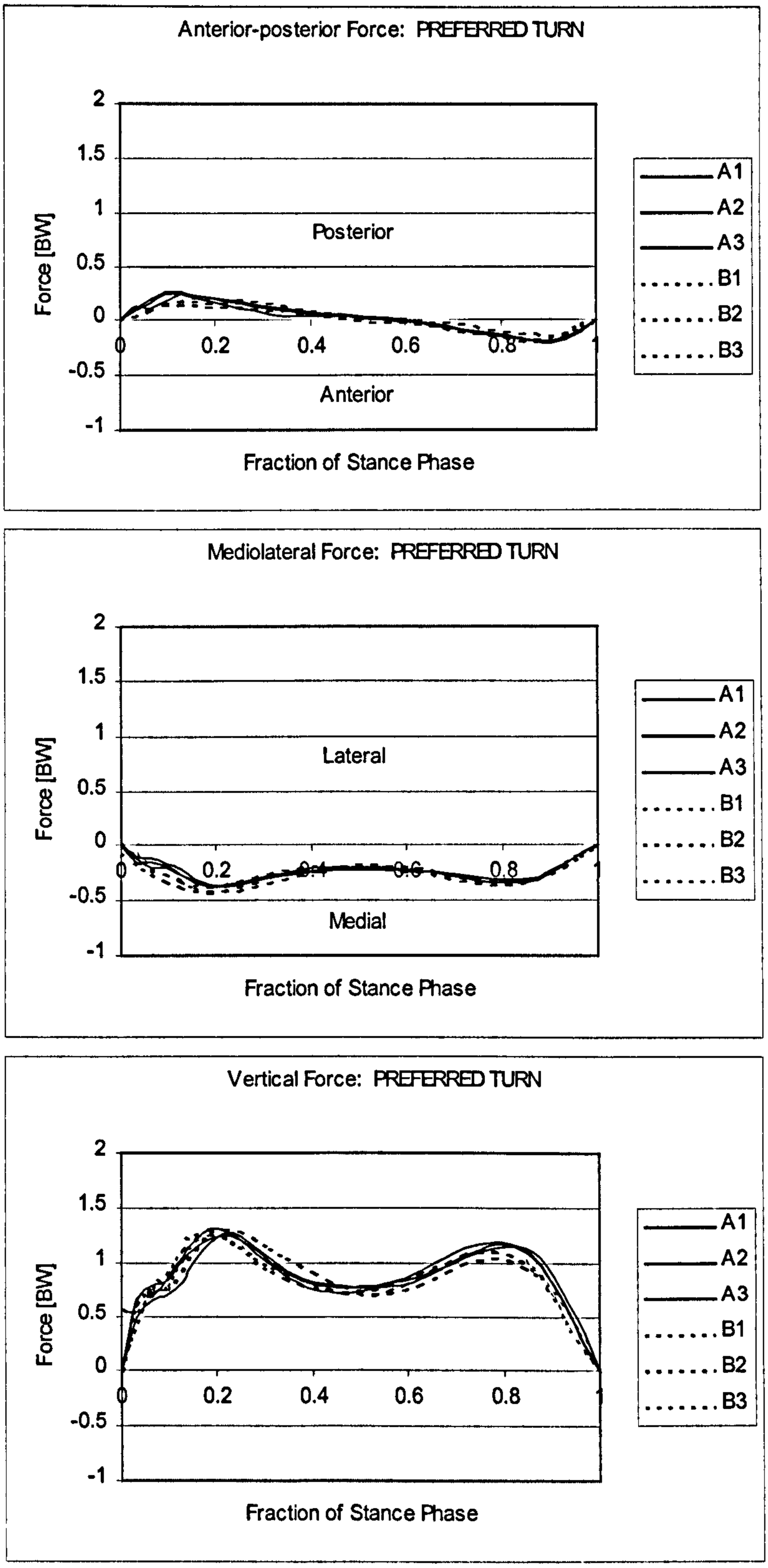

Figure 5.2-5 Ground Reaction Forces for Preferred Speed Turning for Subjects A and B.

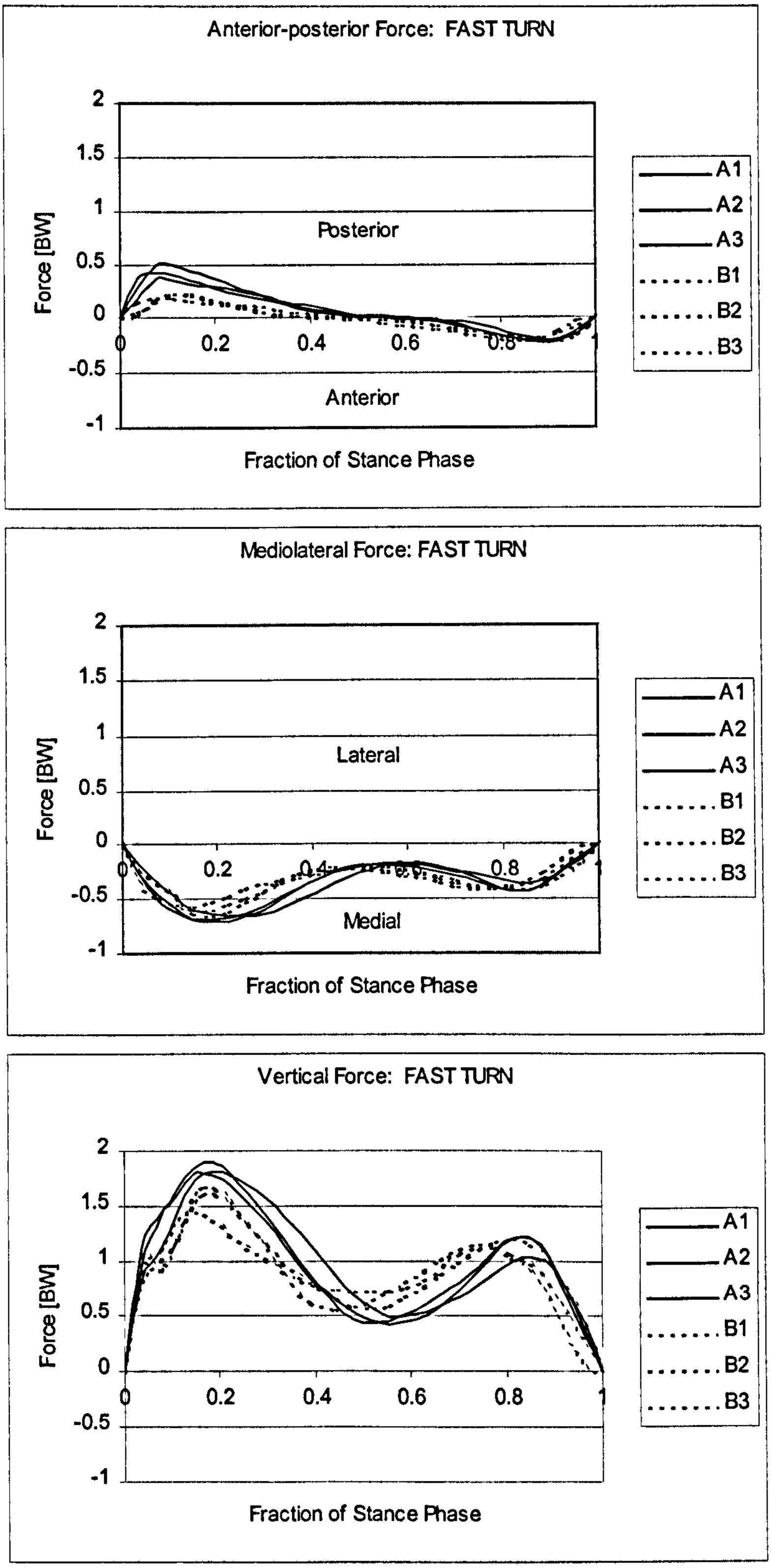

Figure 5.2-6 Ground Reaction Forces for Fast Speed Turning for Subjects A and B.

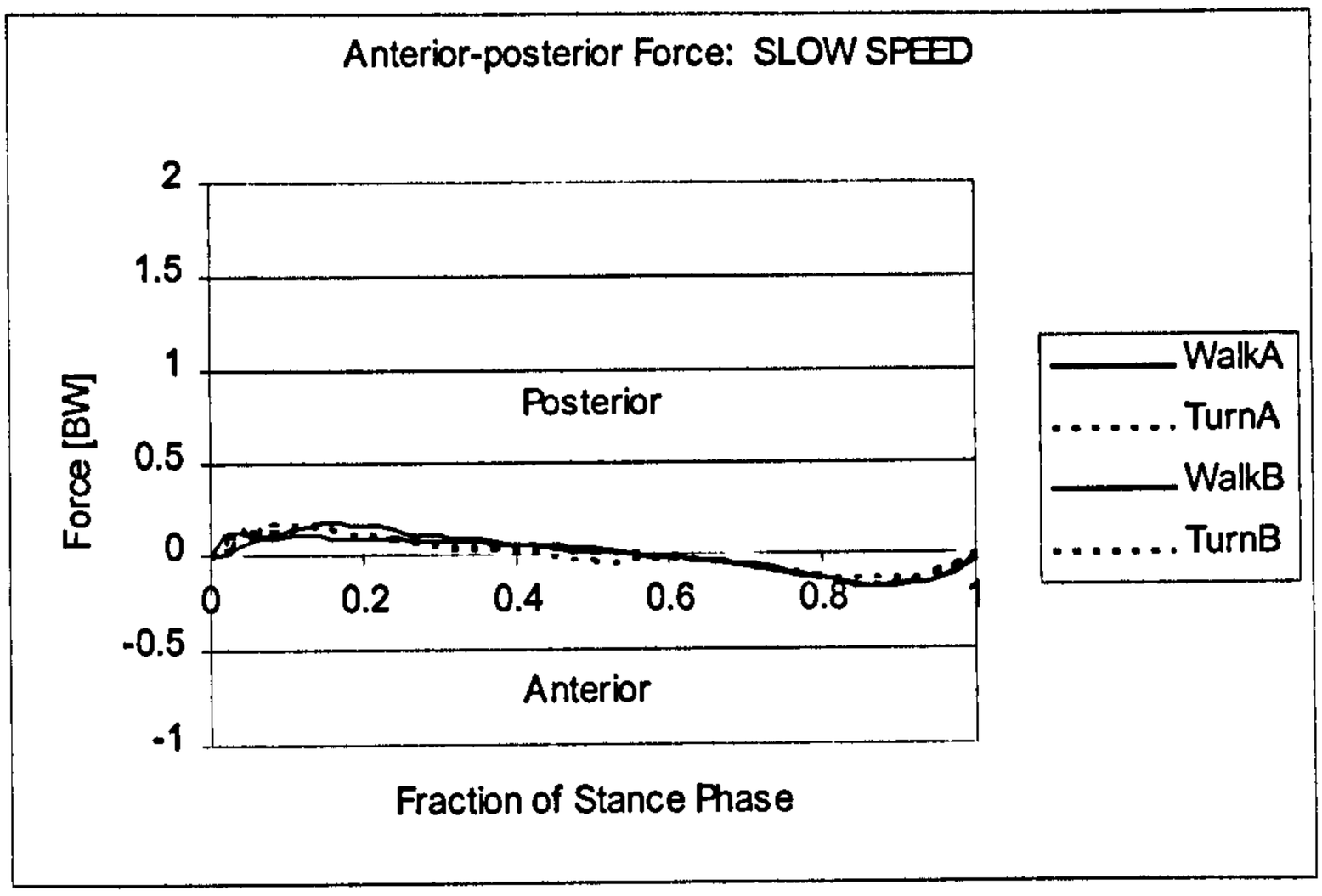

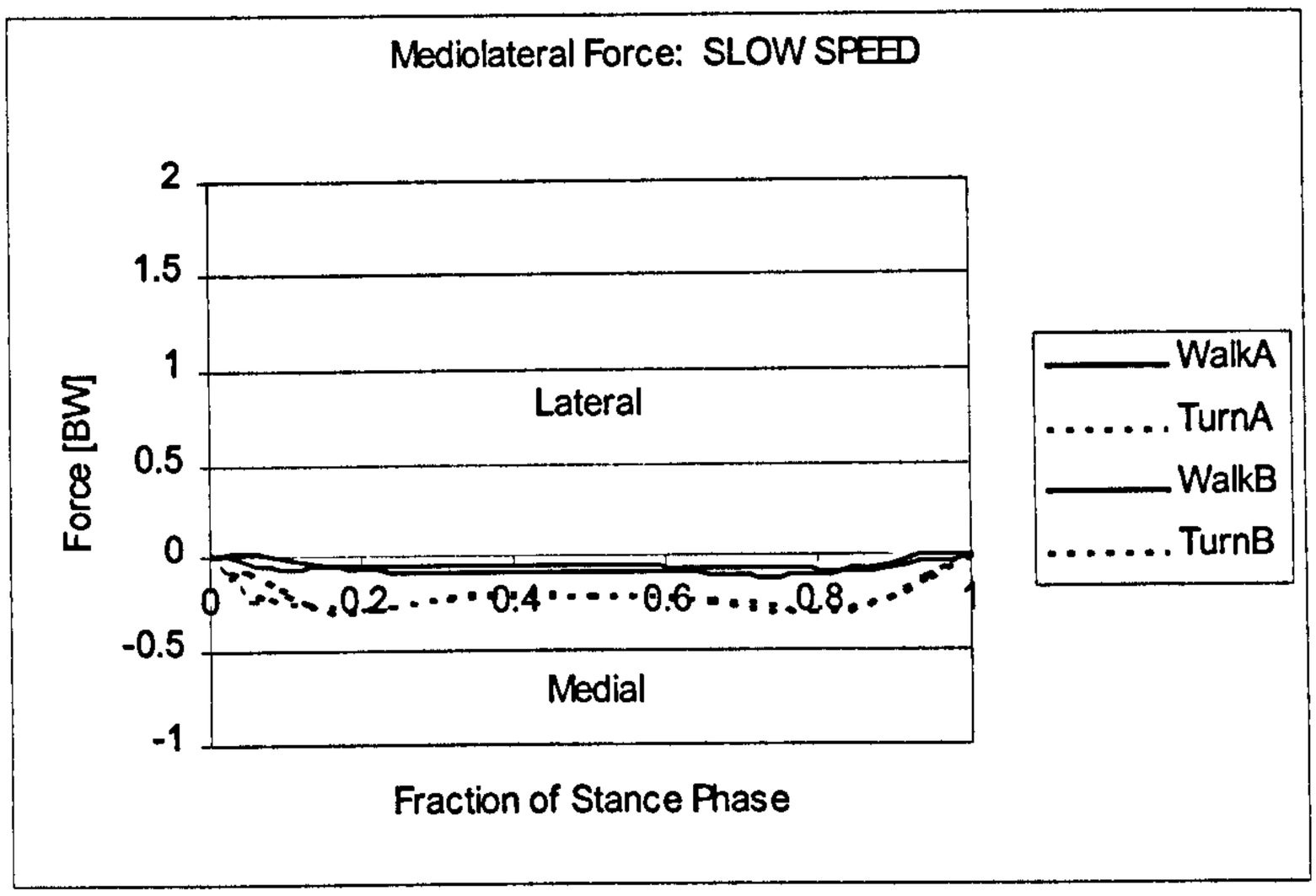

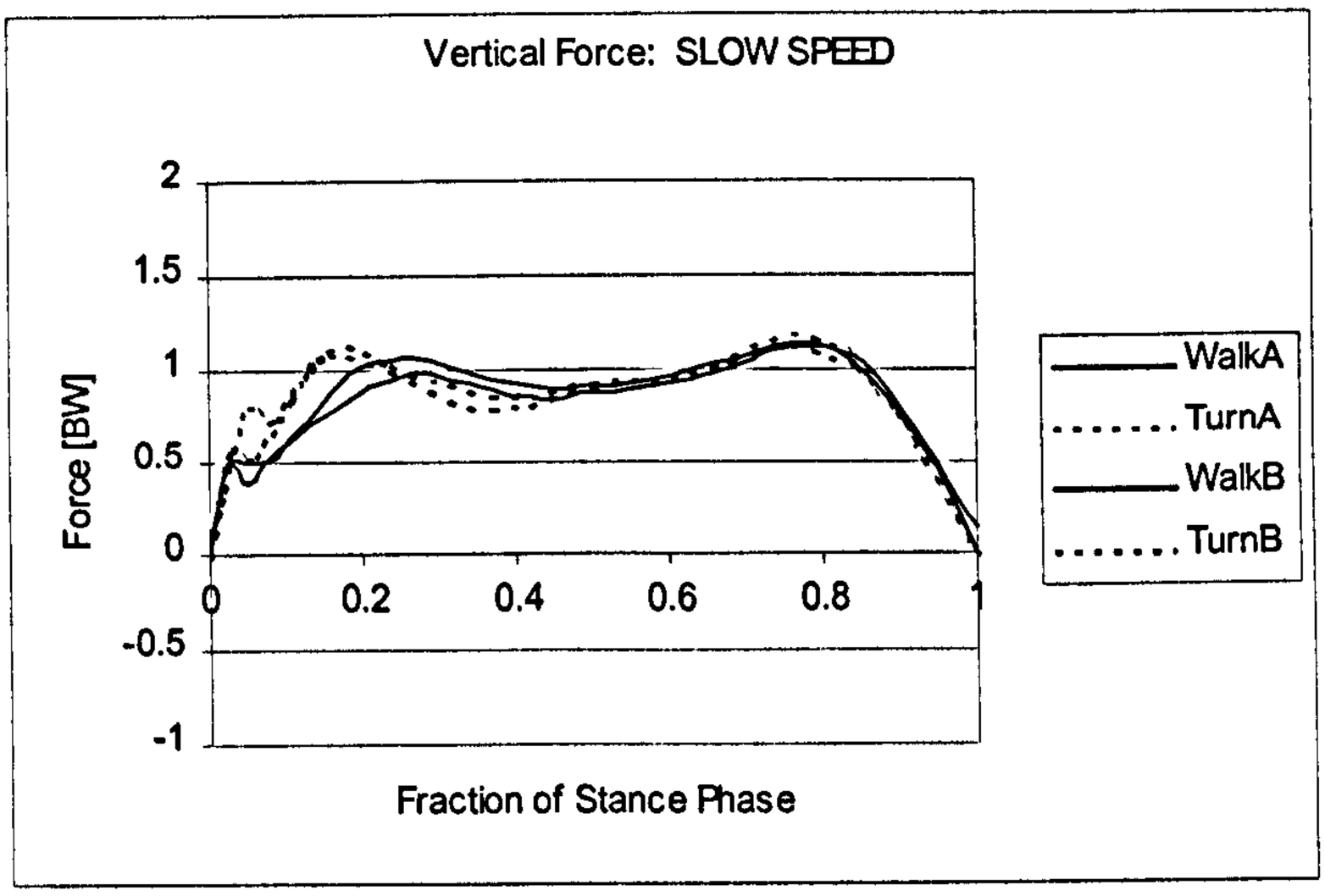

Figure 5.2-7 Comparing Task differences in Ground Reaction Forces for Slow Speed Walking and Turning for Subjects A and B.

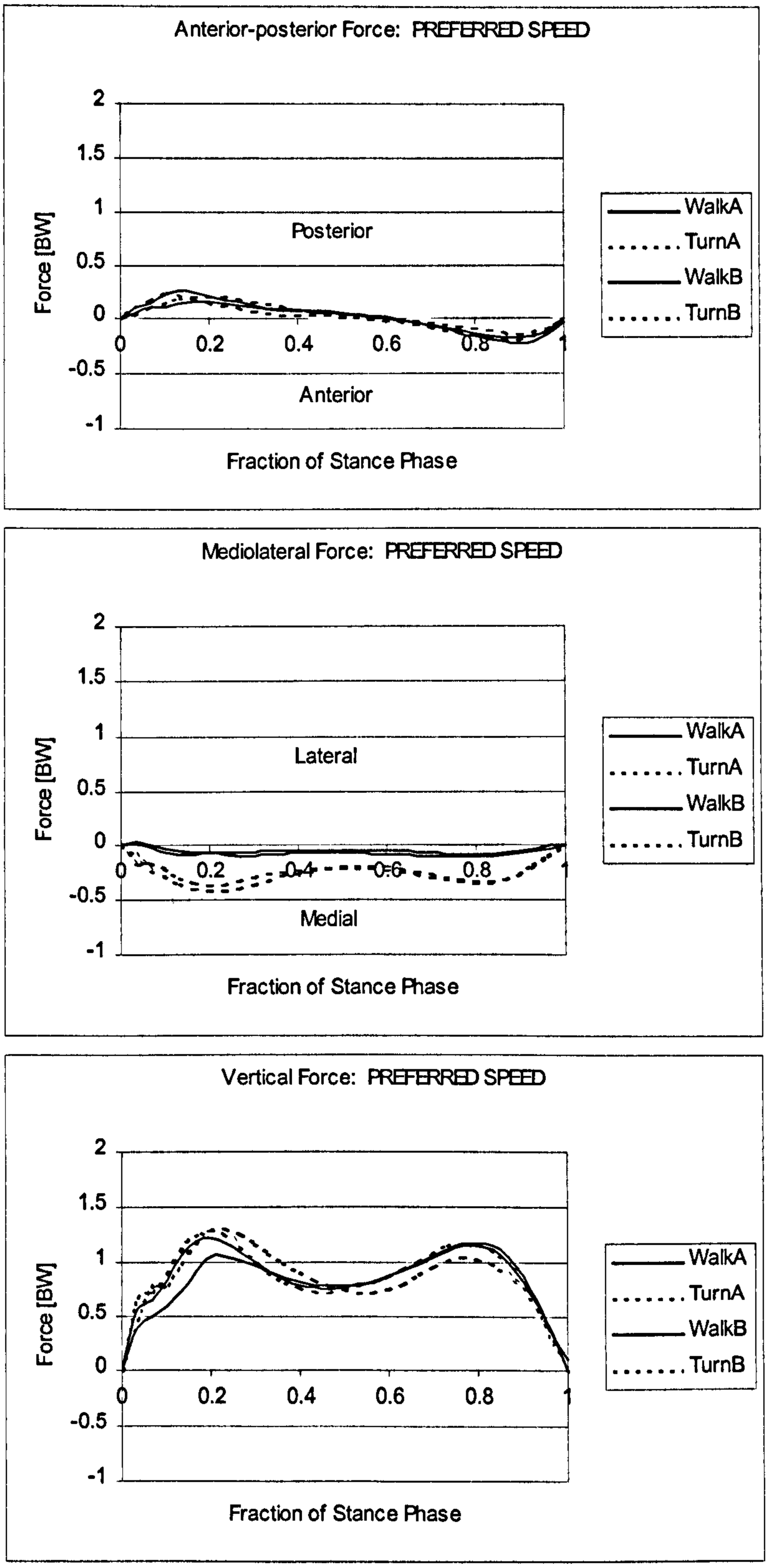

Figure 5.2-8 Comparing Task differences in Ground Reaction Forces for Preferred Speed Walking and Turning for Subjects A and B.

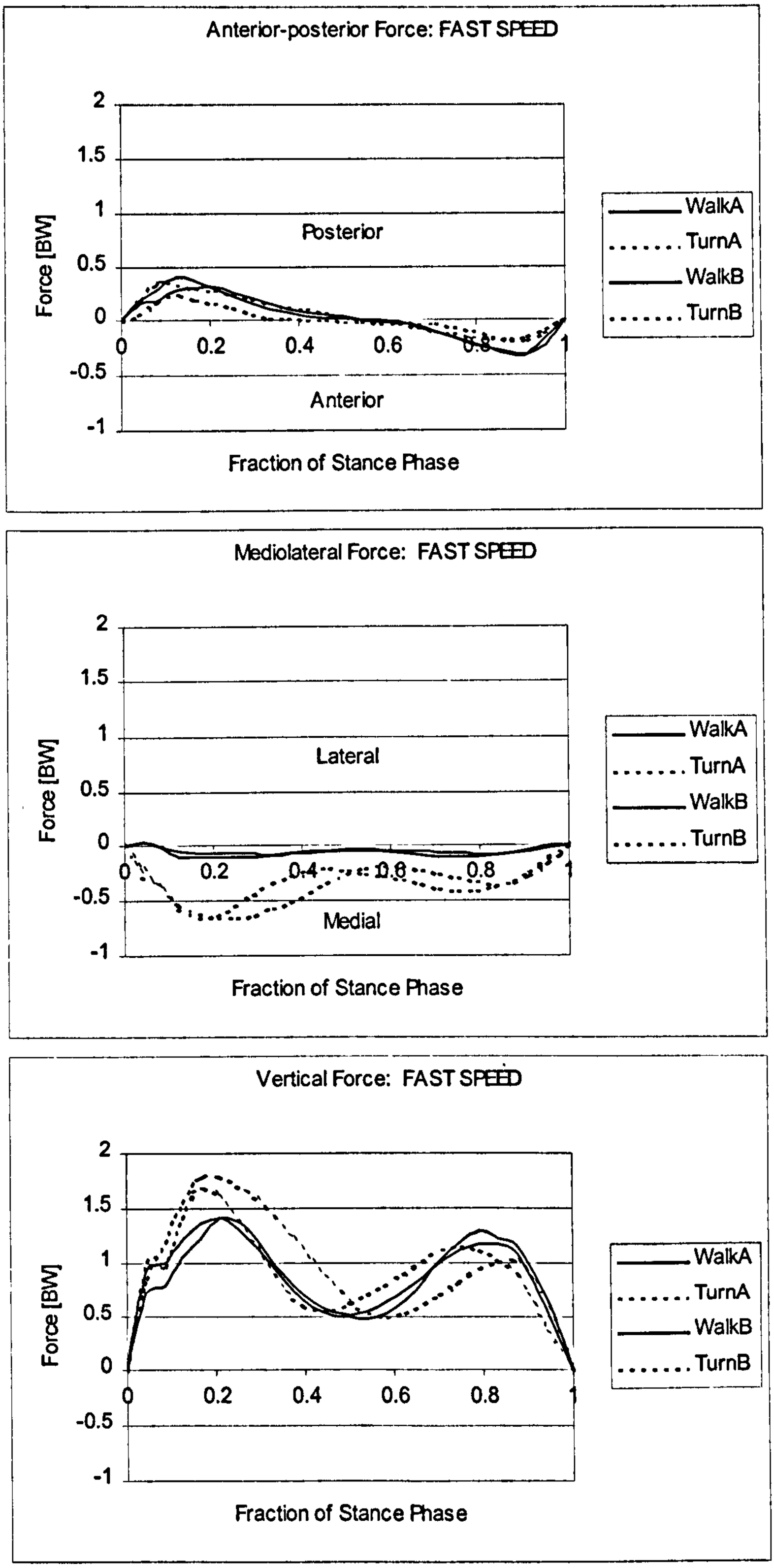

Figure 5.2-9 Comparing Task differences in Ground Reaction Forces for Fast Speed Walking and Turning for Subjects A and B.

acceleration peak between a fast turn and a fast walk with the peak at 0.26×BW during walking and 0.20×BW during turning. The vertical GRF was identical for walking and turning for the slow and preferred speeds for both subjects. During the fast speed trials though, the early, decelerating peak was larger for turning (at 1.75×BW) than for walking (1.42×BW) although they both occurred at the same time during stance phase (0.2).

The obvious difference in GRF pattern between walking and turning was seen in the M-L force. During walking, this force component remained constantly medially directed at below 0.10×BW for the three speeds. During turning, the M-L force was also constant and medially directed for the slow and preferred speeds, but had increased in magnitude to 0.24×BW and 0.30×BW respectively. The M-L GRF during fast turning showed two peaks, which coincided with the peaks in the vertical force. The early peak was larger than the late peak at 0.70×BW and 0.40×BW respectively.

The differences in the Ground Reaction Forces due to speed are compared in Figures 5.2-10 and 5.2-11 for walking and turning. The deceleration and acceleration peaks in the A-P GRF during walking and turning were increased to 0.40×BW and 0.30×BW respectively for fast speed, but were unchanged between slow and preferred speed. The M-L force during walking was unaffected by speed of gait. For turning however, the M-L force changed from being constant at 0.40×BW for slow and preferred speed to having two peaks during fast speed at 0.70×BW and 0.40×BW.

The vertical GRFs were affected by speed during both walking and turning. As speed increased during walking, the two peaks increased from 1.20×BW at preferred speed to 1.40×BW at fast speed. The dip between the two peaks became deeper with fast speed, dropping from 0.80×BW during slow and preferred speed to 0.50×BW during fast speed. For turning, the second, acceleration peak in the vertical GRF was unaffected by changes in speed. The first, deceleration peak however, was increased from 1.25×BW at slow and preferred speeds to 1.75×BW at fast speed.

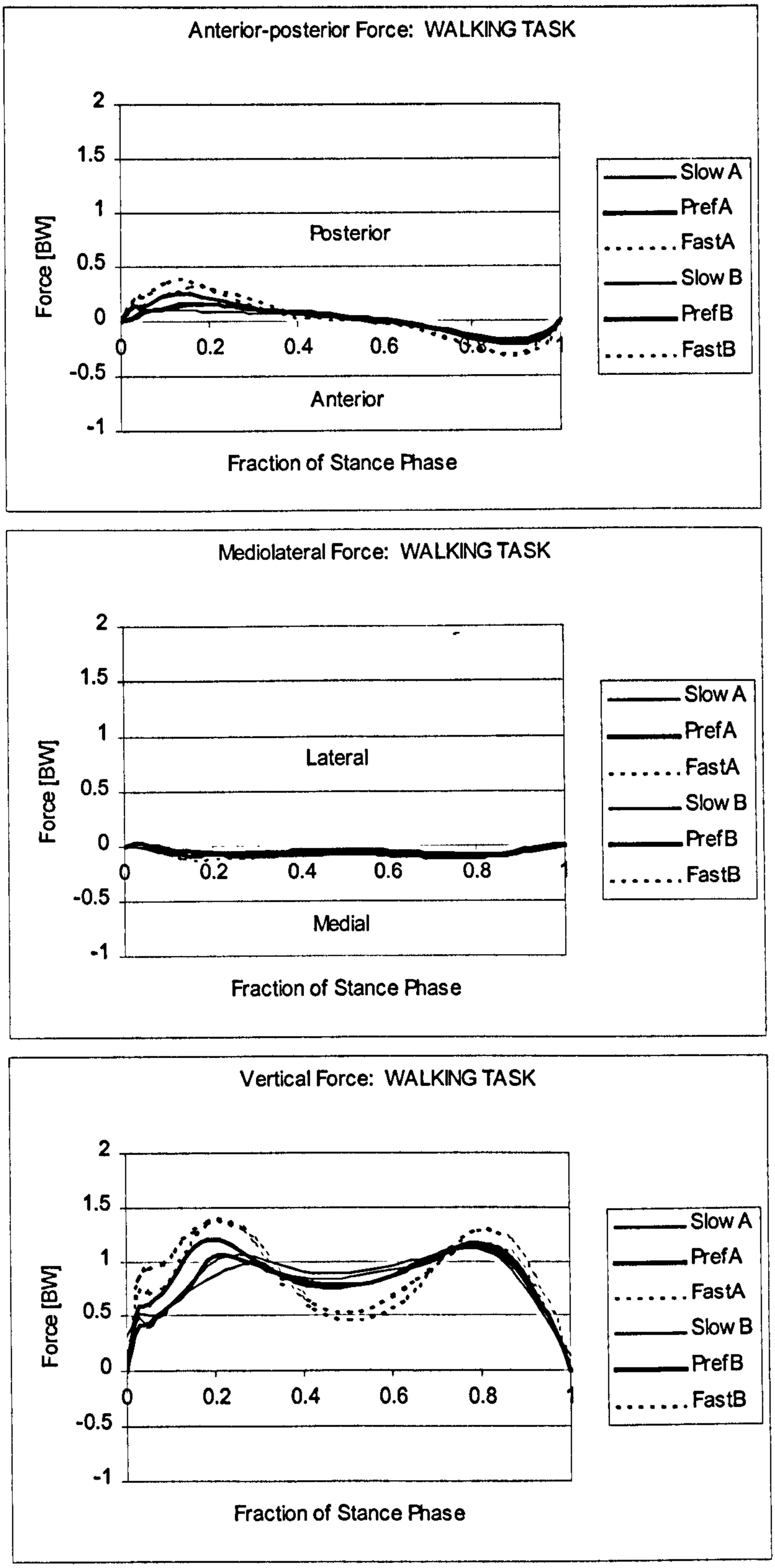

Figure 5.2-10 Comparing Speed differences in Ground Reaction Forces for the Walking Task for Subjects A and B.

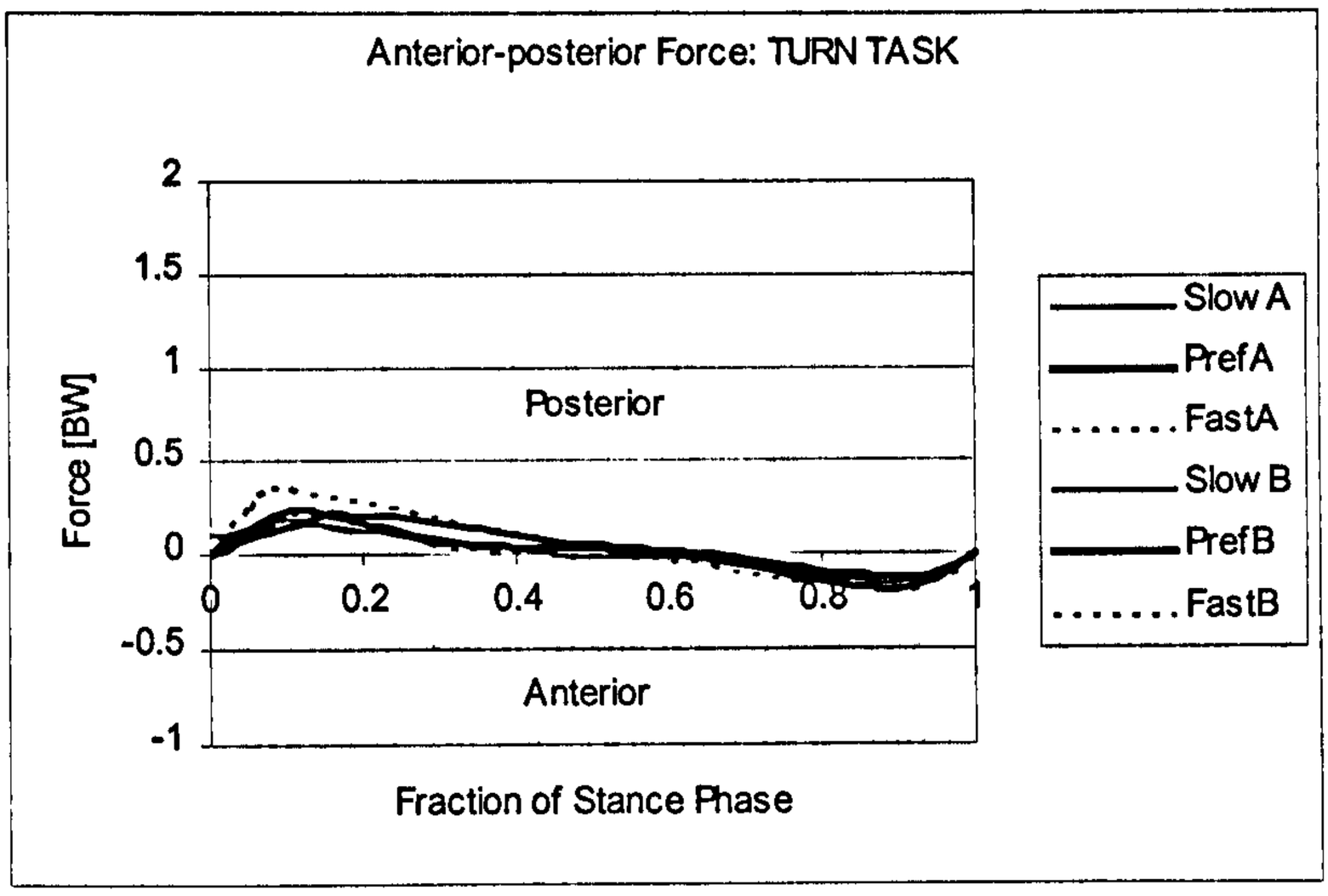

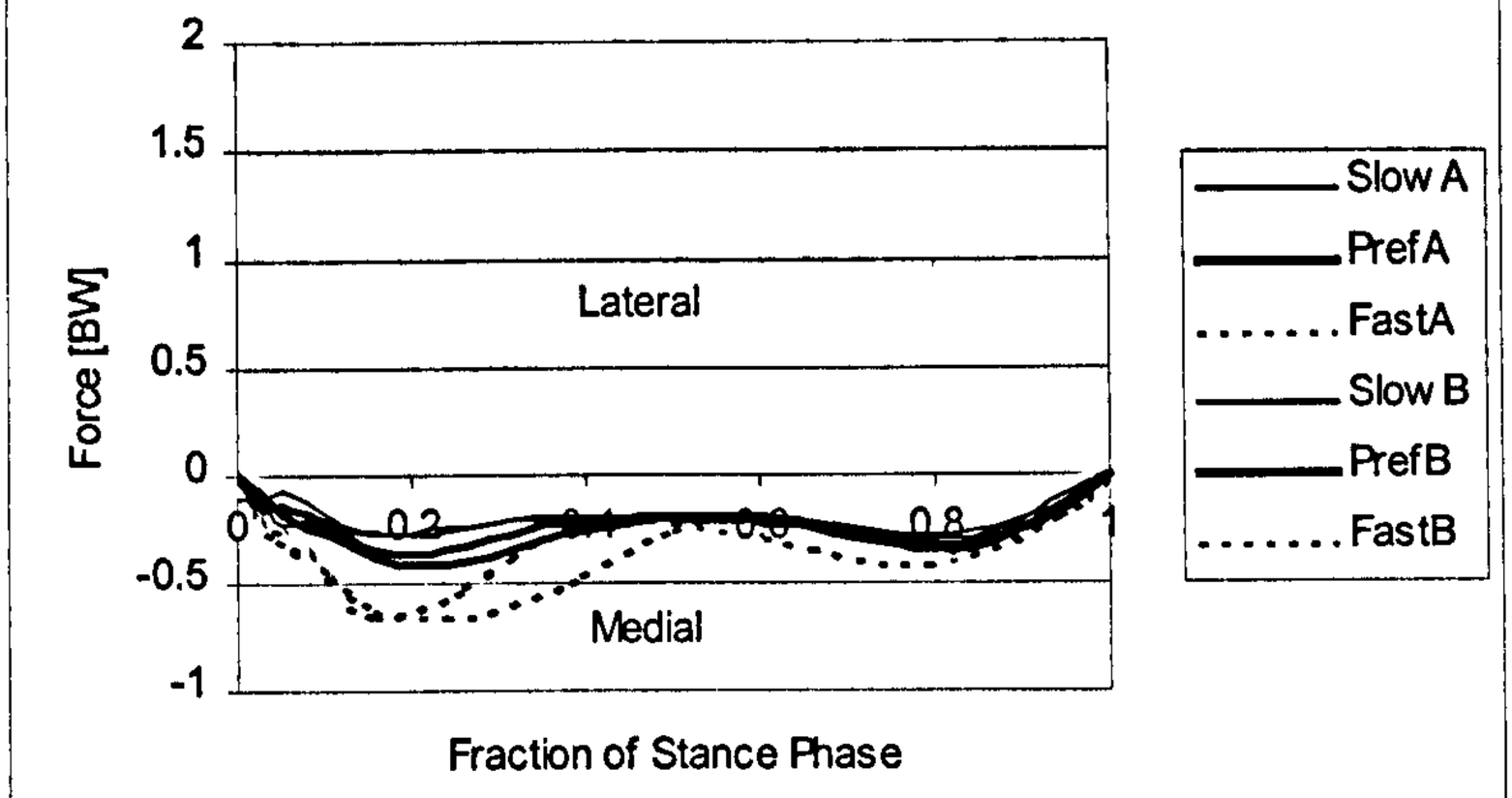

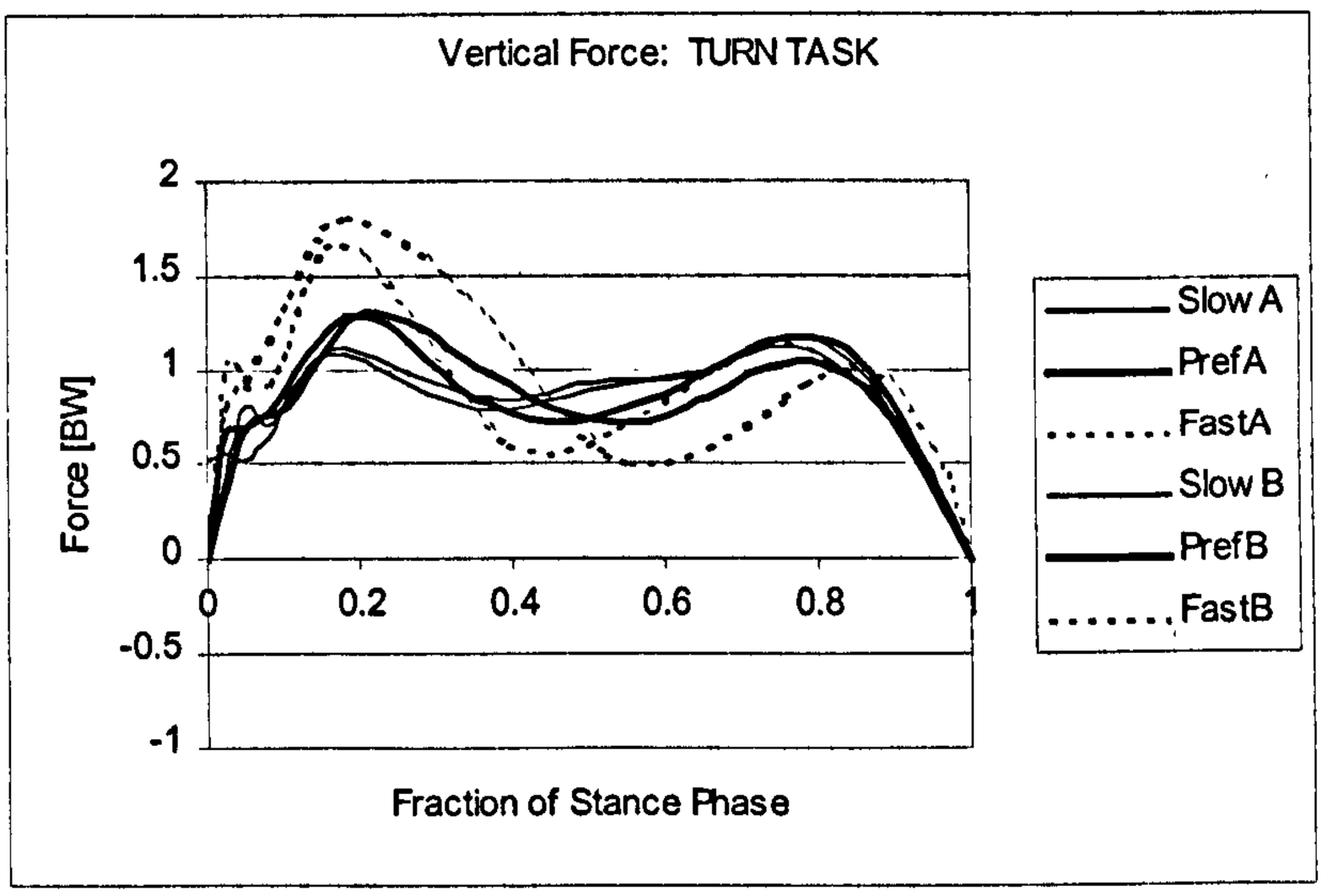

Figure 5.2-11 Comparing Speed differences in Ground Reaction Forces for the Turning Task for Subjects A and B.

The most interesting aspect of the Ground Reaction Forces was how little variability there was, both within trials of the same subject and between subjects. When each subject repeated a task at a certain speed, the forces exerted on the foot were little changed between trials of the same trial type (i.e. slow walking) despite the fact that the subject speed and timing of stepping were not externally cued.

Once the forces had been normalised with respect to body weight, the similarity in the GRFs between the two example subjects was also interesting. Despite the large difference in body types characterised by the subject body weight and height, the forces imposed on the foot by the ground were very similar for the two subjects. There was a subtle difference in the force patterns between the two subjects, though, and this was evident in the timing of the first peak in the vertical GRF during walking. The early peak in the vertical force during preferred speed walking in Figure 5.2-2 occurred earlier for Subject A than for Subject B (at 0.2 and 0.25 respectively) although the speeds of the two subjects was similar (2.2 and 2.4 ms^{-1}). This represents a subtle difference in the style of gait, where Subject B took longer to reach foot flat after heel strike.

5.3 JOINT ANGLES

Recall from Section 1.3 that the two joints of the Ankle Complex, the Ankle and Subtalar Joints, each possessed a single, stationary joint rotational axis. The rotational axis of the Ankle Joint was oriented generally medial to lateral, with the axis moving posteriorly and distally as it travelled laterally. Positive rotations about the axis would dorsi-flex the foot and negative rotations would plantar-flex. The axis of the Subtalar Joint ran generally posterior to anterior, with the axis moving medially and dorsally as it travelled anteriorly. Positive rotations would invert the foot and negative rotations would evert.

Angles about the two rotational axes were defined with respect to the foot in neutral position. In neutral, if the sole of the foot was flat on a level surface, then the lower leg was oriented vertically over the foot. When the foot was in neutral, the two joint angles were both 0°.

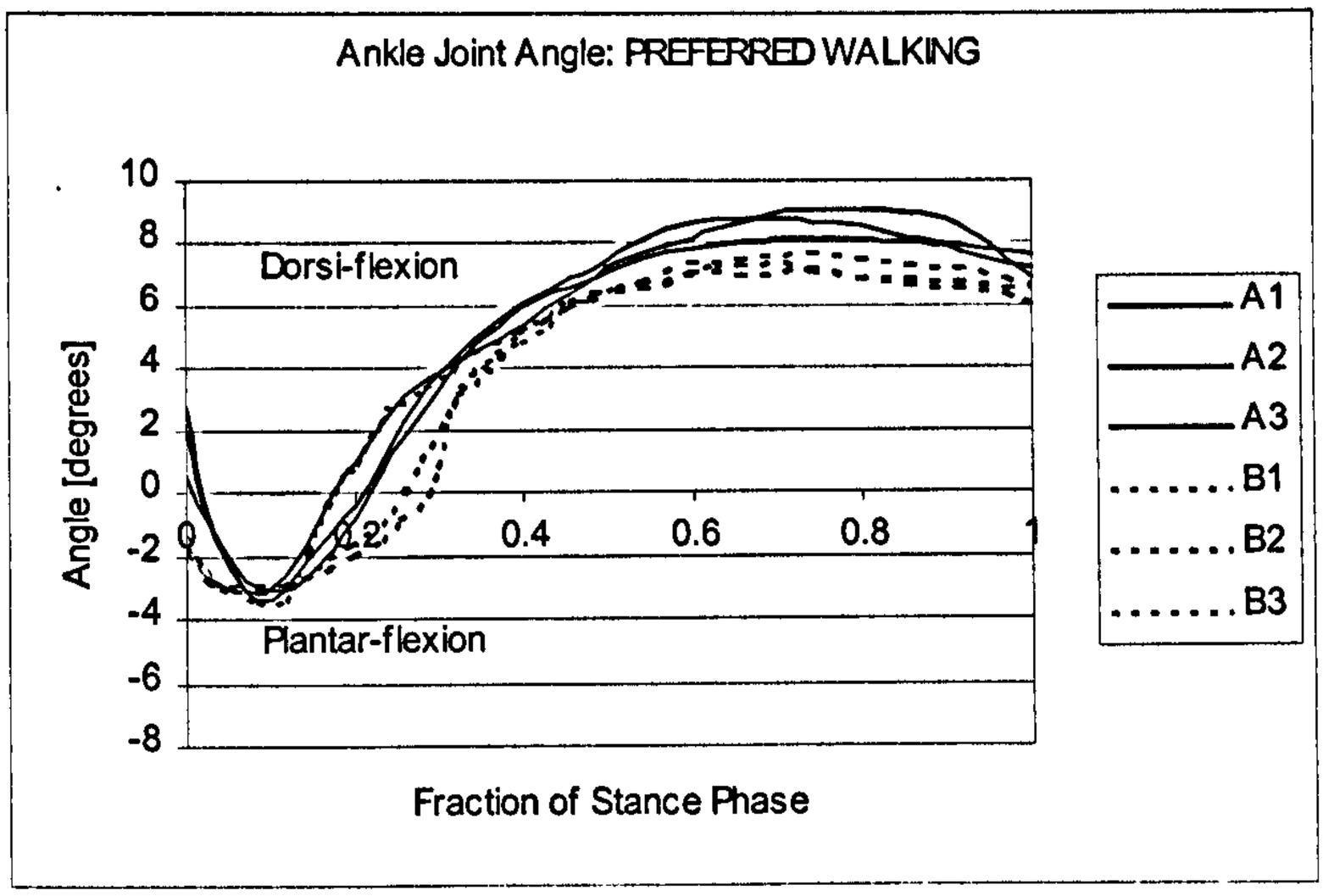

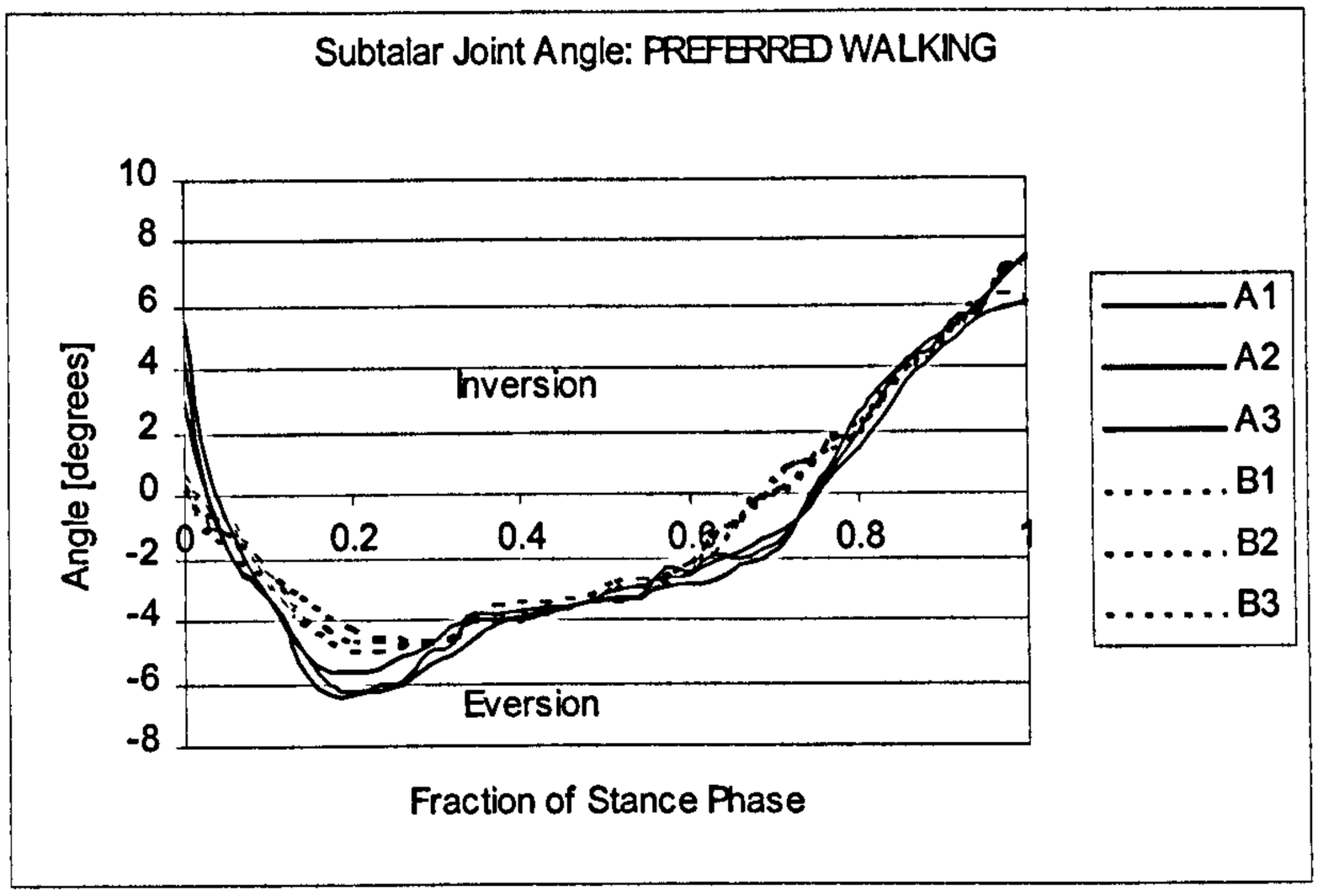

Figure 5.3-1 Joint Angles for Preferred Speed Walking for Subjects A and B.

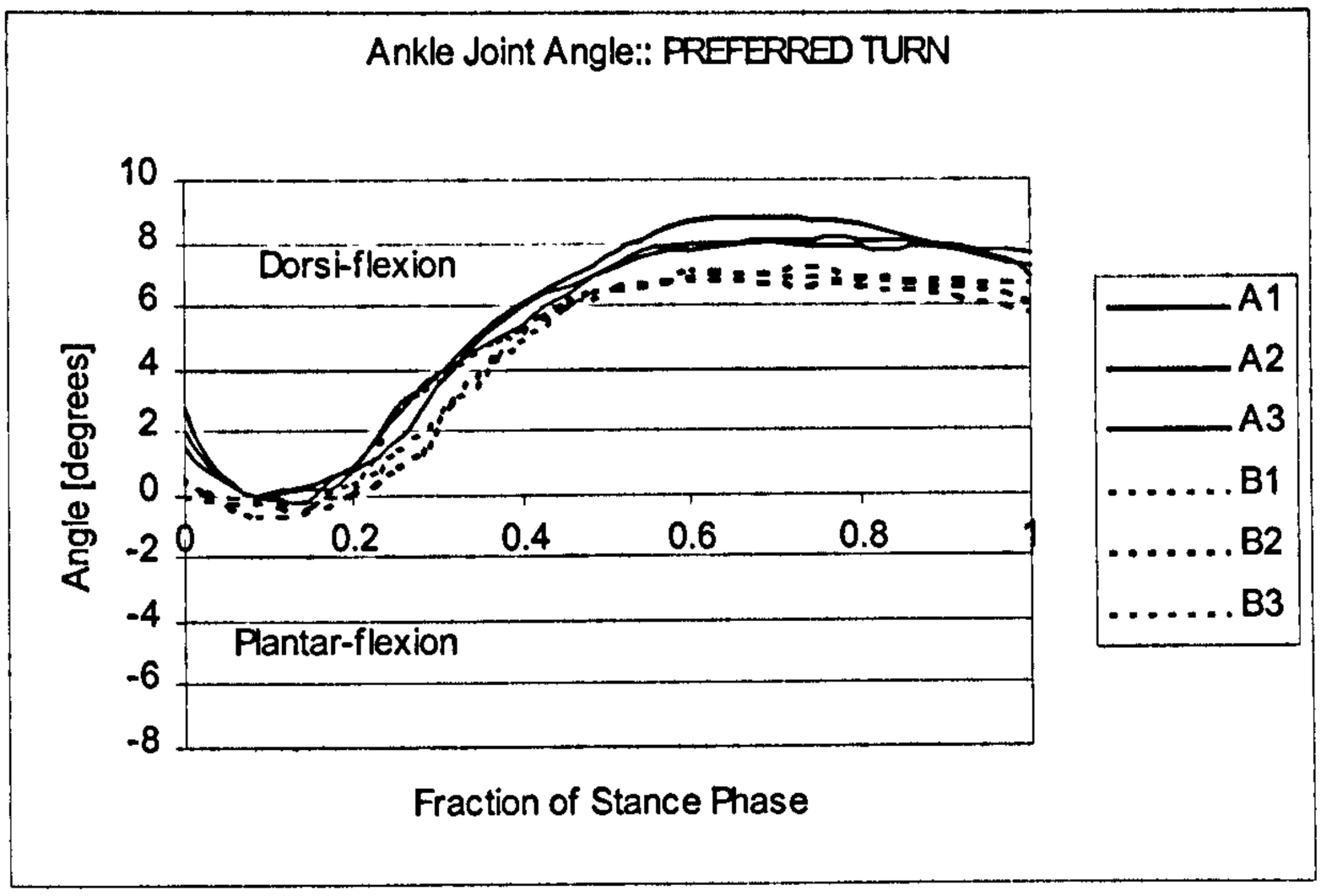

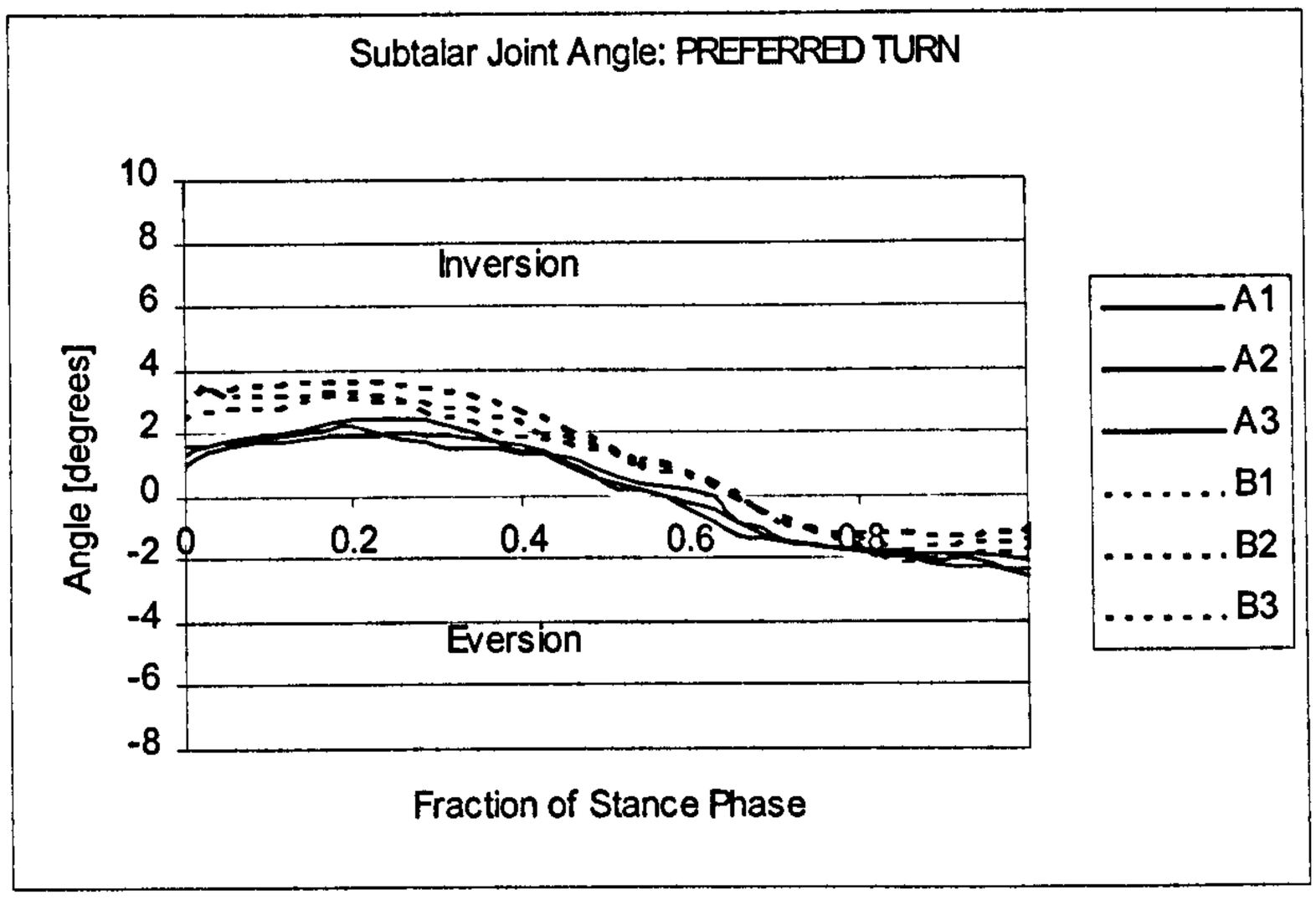

Figure 5.3-2 Joint Angles for Preferred Speed Turning for Subjects A and B.

Figure 5.3-1 plots the joint angles for the Ankle and Subtalar Joints during preferred speed walking. The pattern of joint angles showed very little variability for all the walking and turning trials at each of the three speeds. During walking, the heel struck the ground, beginning stance phase, with the foot dorsi-flexed by about 3°. The foot quickly plantar-flexed after HS to a peak plantar-flexed angle of 3° before returning to nearly neutral at foot flat. After FF, the foot dorsi-flexed again, with the Ankle Joint angle increasing to a peak of around 8° at 0.8 of stance phase. The dorsi-flexion of the foot remained near this angle until TO. At HS, the foot was slightly inverted at about 5°. The foot slowly everted to a peak eversion of 6° for Subject A and 5° for Subject B at about 0.2 of stance phase. The foot then inverted again, reaching neutral at 0.6 of stance phase, and then on to a maximum inversion at TO of 7°. The joint angle patterns for the two subject differed slightly in the amount of eversion during walking and in the timing of dorsi-flexion after the plantar-flexion peak in walking. Apart from these subtle differences, the patterns of joint angles for walking showed little variability between to two subjects.

Figure 5.3-2 plots the joint angle for each of the preferred speed turning trials for Subjects A and B. The pattern of the Ankle Joint angle during the turning task was similar to that during walking. At HS the foot was dorsi-flexed by about 3°. After HS, the foot plantar-flexed to neutral (as opposed to 3° plantar-flexion in walking) and then began dorsi-flexing again from around 0.2 of stance phase. The foot continued to dorsi-flex until TO, reaching a peak at 0.8 of stance phase of 7° dorsi-flexion for Subject B and 9° for Subject A.

The Subtalar Joint angle behaviour was very different for the turning task than for the walking task. Similar to walking, the foot was inverted to around 3° at heel strike. Unlike walking, the foot remained at the same amount of inversion until 0.4 of stance phase, when the foot began to slowly evert, reaching neutral at 0.6 of stance phase. The foot continued to evert to a maximum of 2° for both subjects at TO. Figures 5.3-3 to 5.3-5 compare the joint angles between the walking and turning tasks at each of the three speeds.

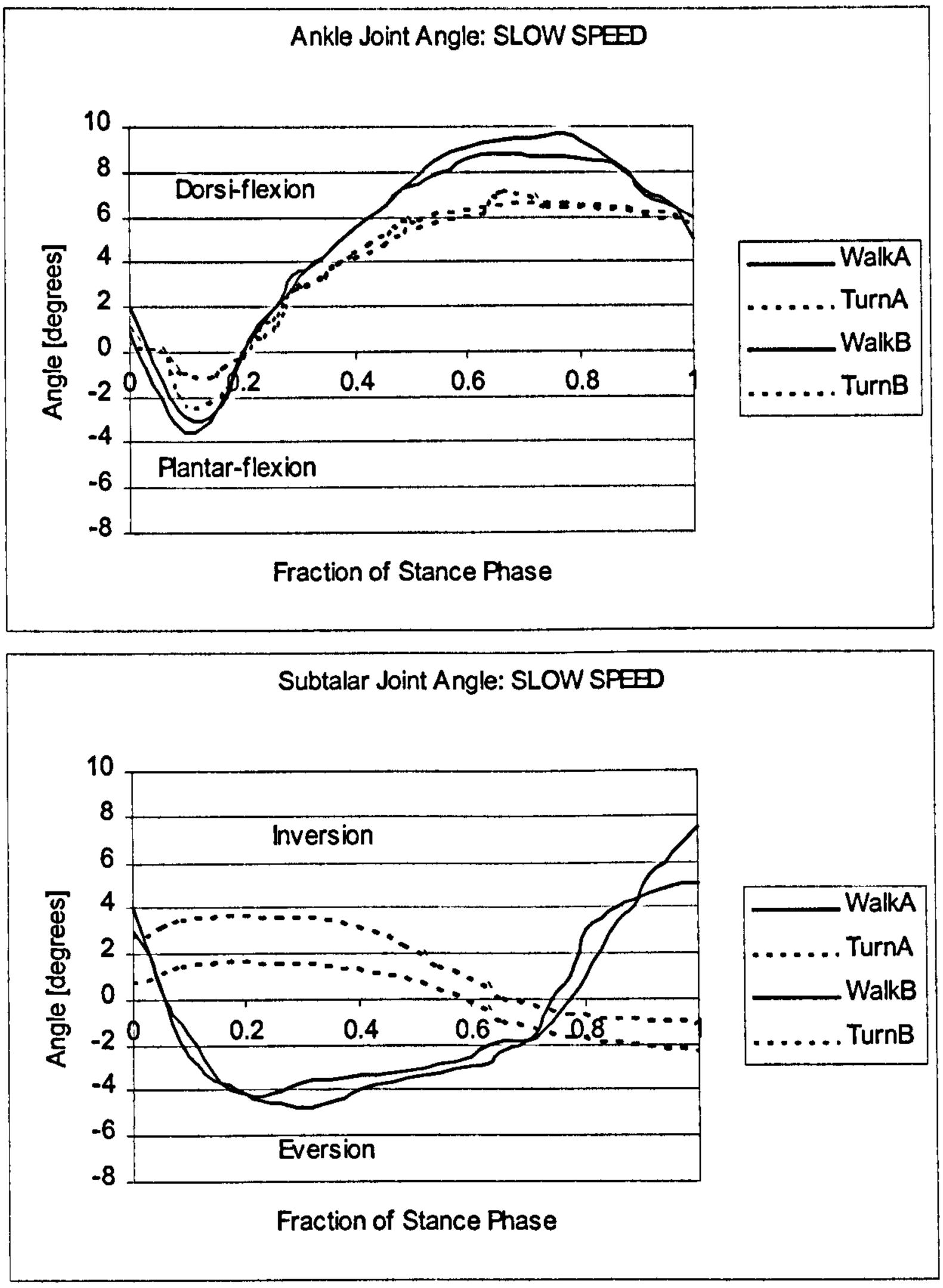

Figure 5.3-3 Comparing Task differences in Joint Angles for Slow Speed Walking and Turning for Subjects A and B.

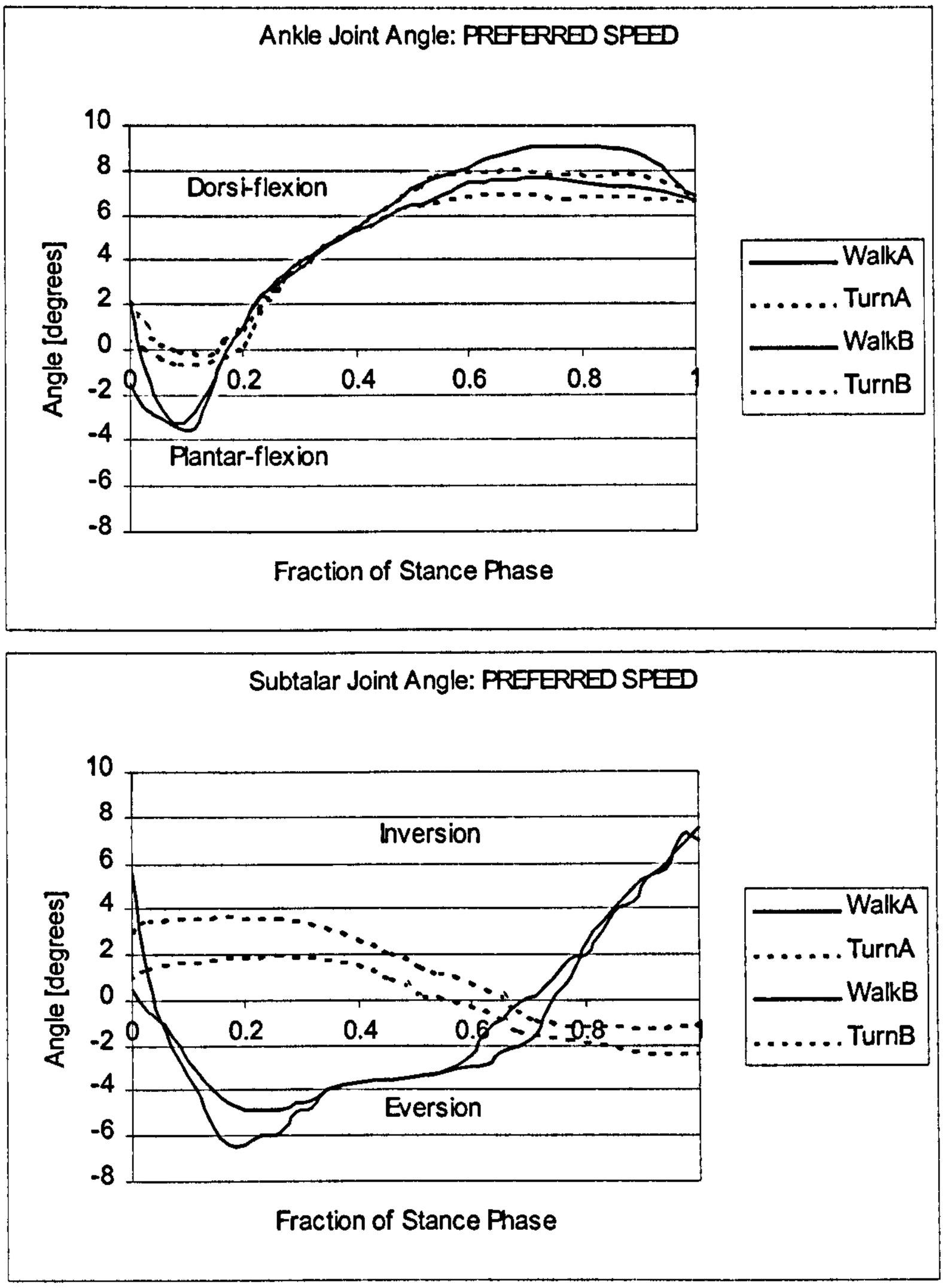

Figure 5.3-4 Comparing Task differences in Joint Angles for Preferred Speed Walking and Turning for Subjects A and B.

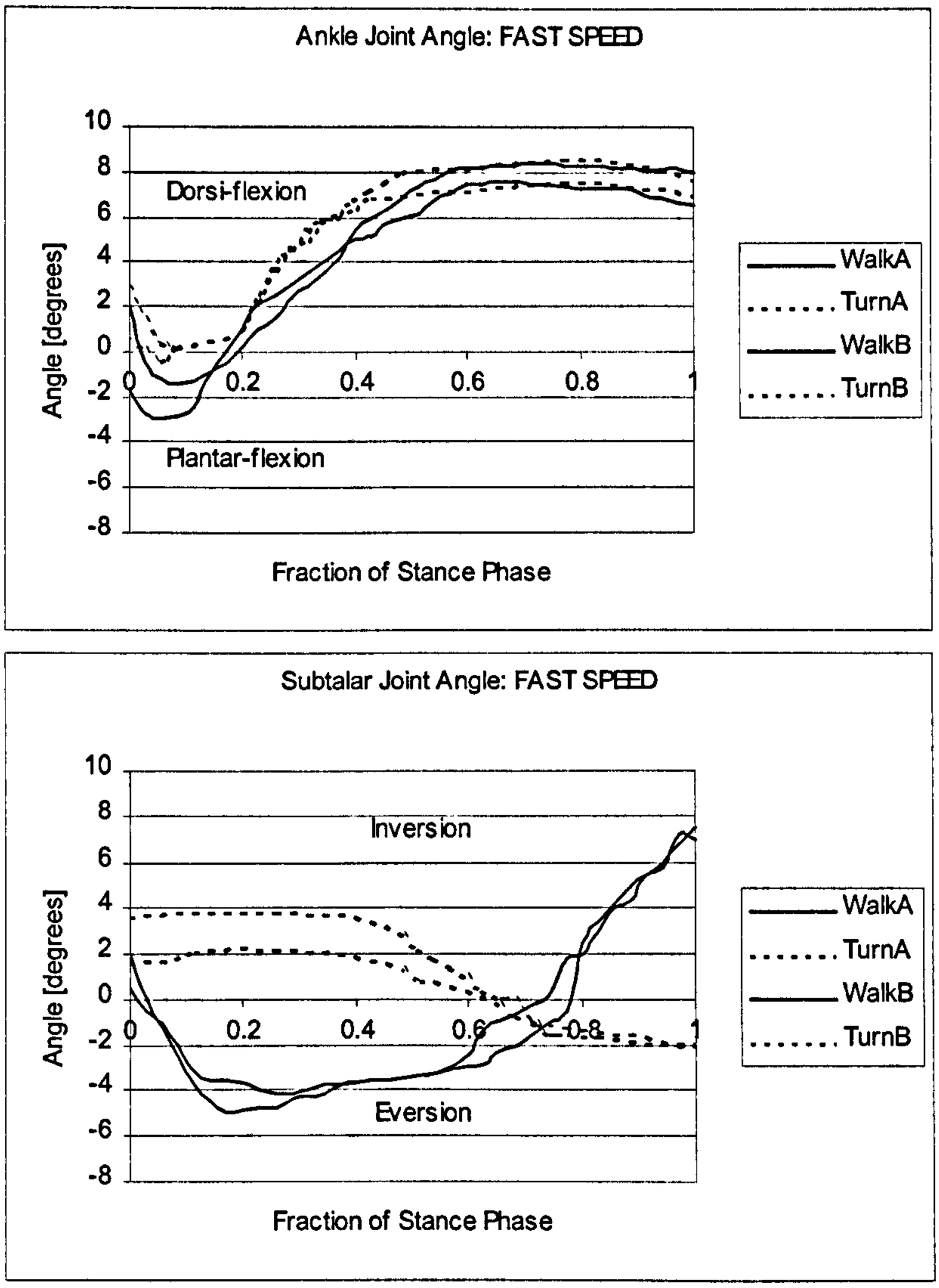

Figure 5.3-5 Comparing Task differences in Joint Angles for Fast Speed Walking and Turning for Subjects A and B.

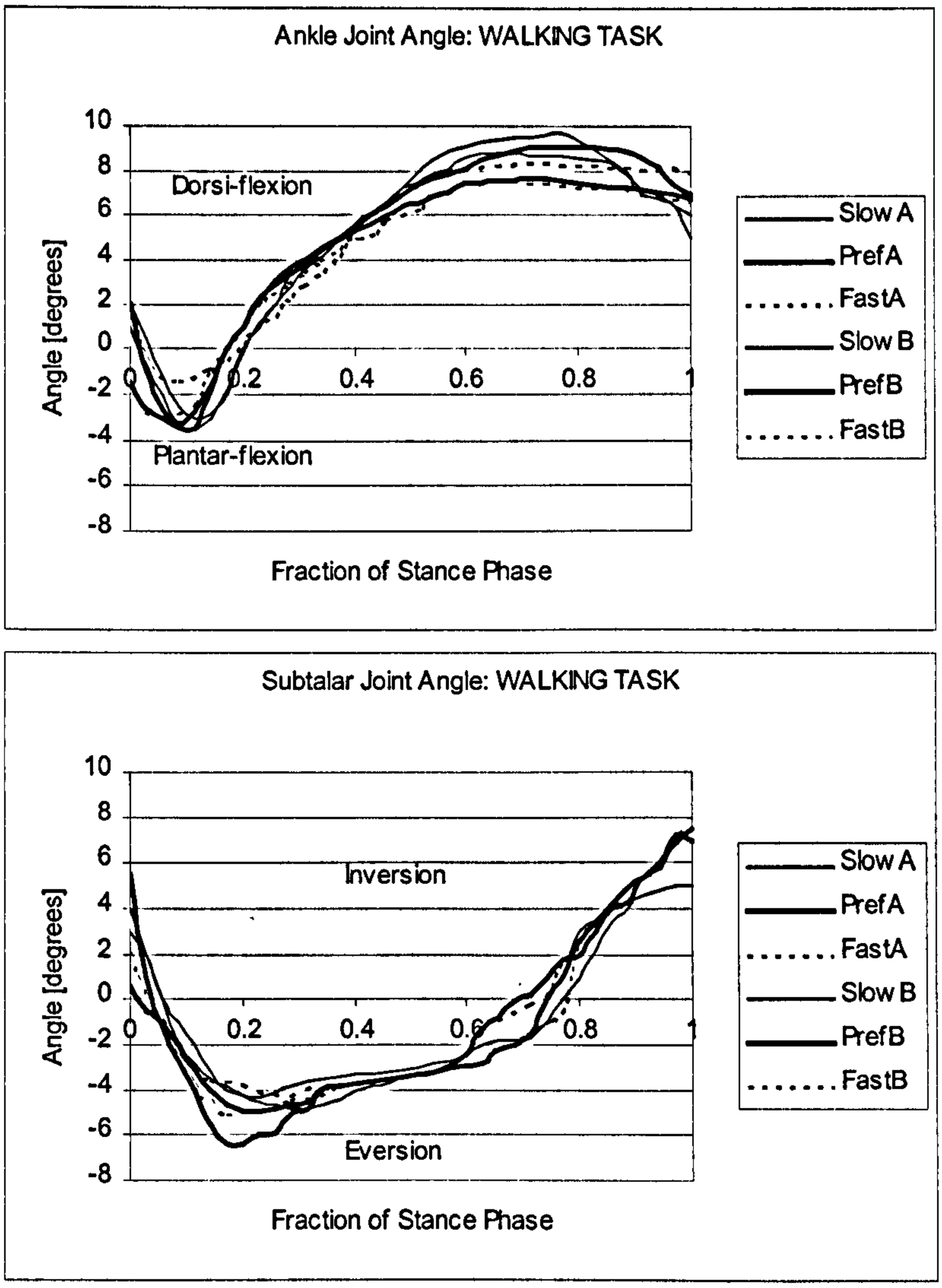

Figure 5.3-6 Comparing Speed differences in Joint Angles for the Walking Task for Subjects A and B.

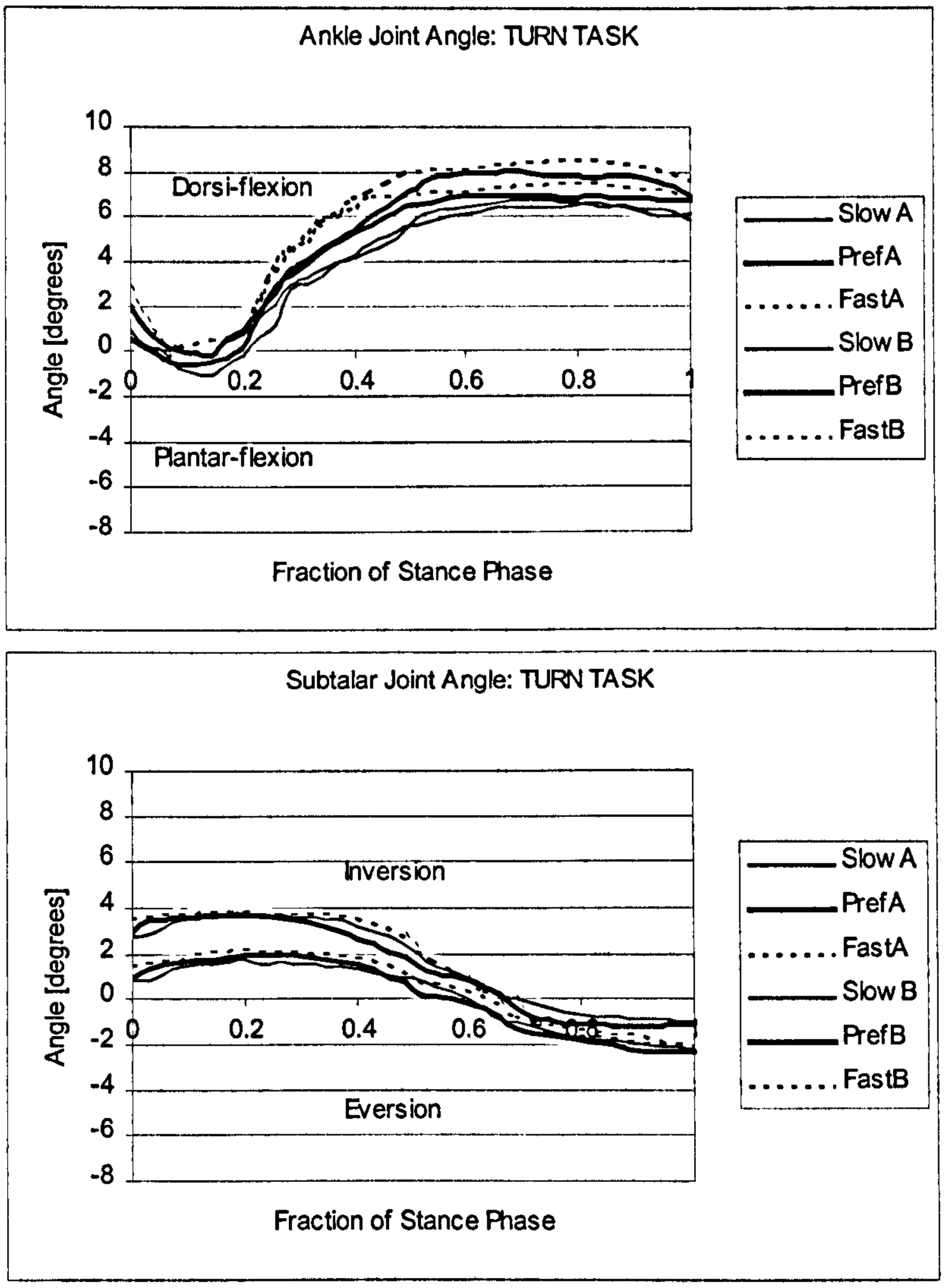

Figure 5.3-7 Comparing Speed differences in Joint Angles for the Turning Task for Subjects A and B.

The joint angle patterns are compared between the three gait speeds for the walking and turning tasks in Figures 5.3-6 and 5.3-7. These plots show that there was little difference in joint angles due to gait speed.

Similar to the patterns of the Ground Reaction Forces acting on the foot, the angles of the two joints of the Ankle Complex showed very little variability between trials of the same subject and between the subjects. This may indicate that the structures of the Ankle Complex and the orientations of the two joints are designed to produce a set of motions for positioning the foot during walking and turning that is very specific. The foot possesses structures such as the heel pad, lateral border of the sole and ball of the foot, which are specifically designed to contact the ground in a certain way and in a certain sequence. This sequence of contact: heel pad then lateral border then ball of foot, may change in timing with changing tasks, but does not change in order. If this ordering remains the same for walking and turn at all the speeds tested, then the joints of the Ankle Complex can be expected to move in a similarly invariant order. For example, during the stance phase of walking: dorsi-flexion and inversion then plantar-flexion and eversion then dorsi-flexion and inversion. The timing of this sequence of joint motion may change with changing task, but the ordering of the sequence is invariable.

The invariable nature of the motions of the two joints when performing a certain task at various speeds, may indicate that the two joints are not operating independently. The system of control which positions the foot during walking and turning seems to link the motion of the Ankle and Subtalar Joints into a compound motion with few degrees of freedom. The lack of variability between subjects also seems to indicate that the number of compound motions available to the Ankle Complex in order to perform various tasks is limited. Despite the apparent freedom of movement of the Ankle Complex, the joint complex is very much a locomotive joint like the knee or hip, and unlike the wrist, possessing few degrees of freedom.

5.4 MOMENTS ABOUT THE JOINT ROTATIONAL AXES

Recall from Section 2.5.3 that the muscles that cross the joints of the Ankle Complex were assumed to balance the moments about the joint rotational axes imposed by the Ground Reaction Force. The passive structures of the Complex were assumed to constrain the joints from moments about the other axes. Therefore, the moments created by the GRF about the joint rotational axes are presented in this section to illustrate the moments that must be balanced by the muscles for Ankle Complex equilibrium.

Figure 5.4-1 shows the moments about the two joint rotational axes during preferred speed walking. The patterns of Subtalar Joint moments showed little variability between trials of the same subject and between subjects. At HS, there was very little moment about the Subtalar Joint. As stance phase progressed, an inverting moment developed, peaking at around 0.015 Nm/N at 0.9 of stance phase for the two subjects. The moment then dropped back to 0.0 at TO.

The moments about the Ankle Joint showed little variability between trials of the same subject, but the moments were variable between Subjects A and B. For subjects, the Ankle Joint moment followed the same pattern. At HS there was no moment, this rose to a maximum dorsi-flexing moment of 0.14 Nm/N for Subject A and 0.10 Nm/N for Subject B, both at 0.8 of stance phase. The moments then dropped back to 0.0 at TO. The moments for Subject B were lower than those of Subject A throughout the trials.

The joint moments for slow walking were very similar to preferred walking and are not shown. Figure 5.4-2 shows the joint moments for fast walking. The Subtalar Joint moments were similar to those at preferred speed. The moments for the two subjects showed the same general pattern, but the moments were greater for Subject B about this joint. About the Ankle Joint, the moments for Subject B showed a different pattern than for Subject A, however. The moments on Subject A increased into dorsi-flexion after HS toward a peak at 0.8 of stance phase. This was similar to the pattern at preferred speed. The moments for Subject B, instead, were plantar-flexing after HS until foot flat. The plantar-flexing moments than developed into dorsi-flexing moments at 0.25 of stance phase and followed the pattern of

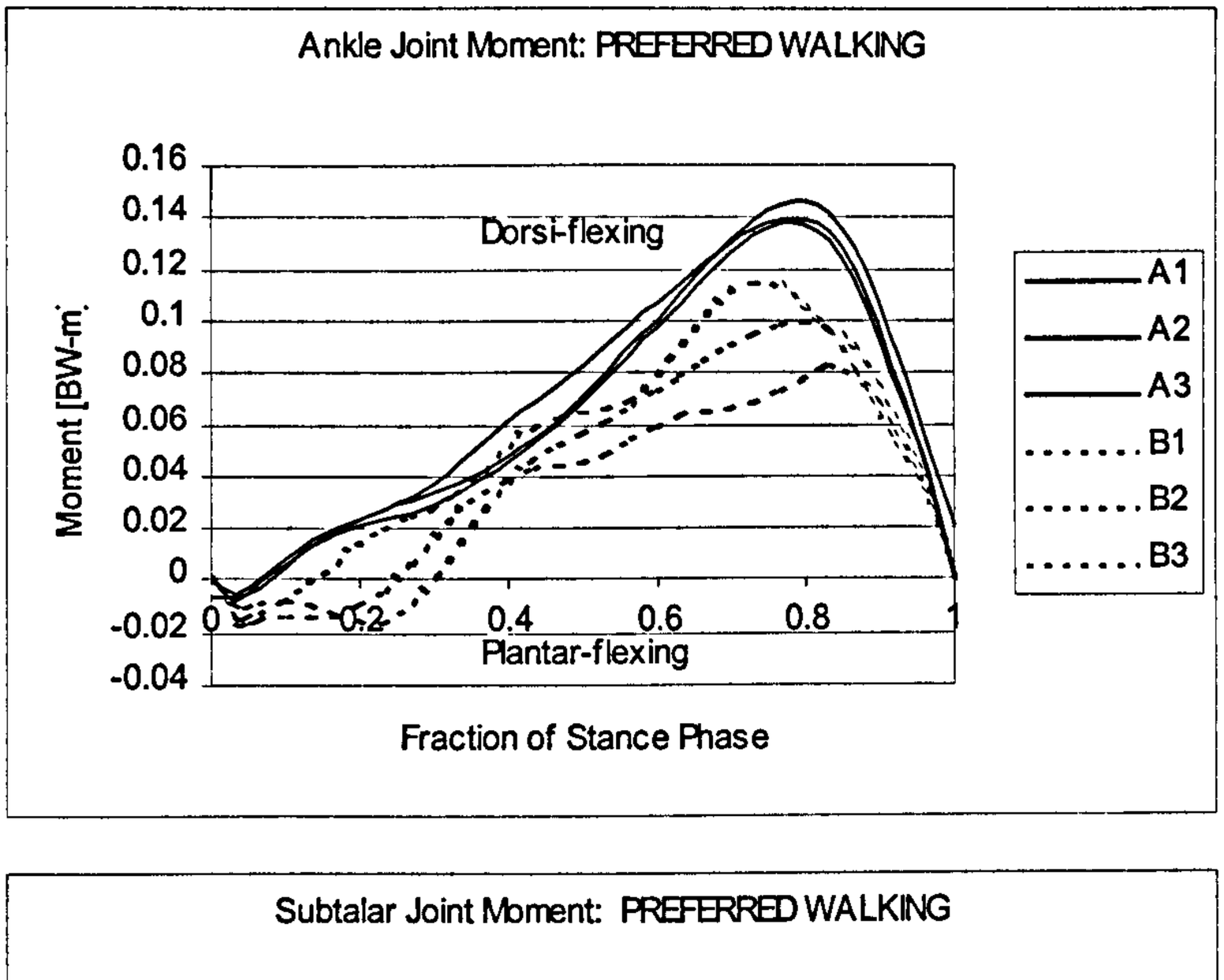

Figure 5.4-1 Joint Axis Moments for Preferred Speed Walking for Subjects A and B.

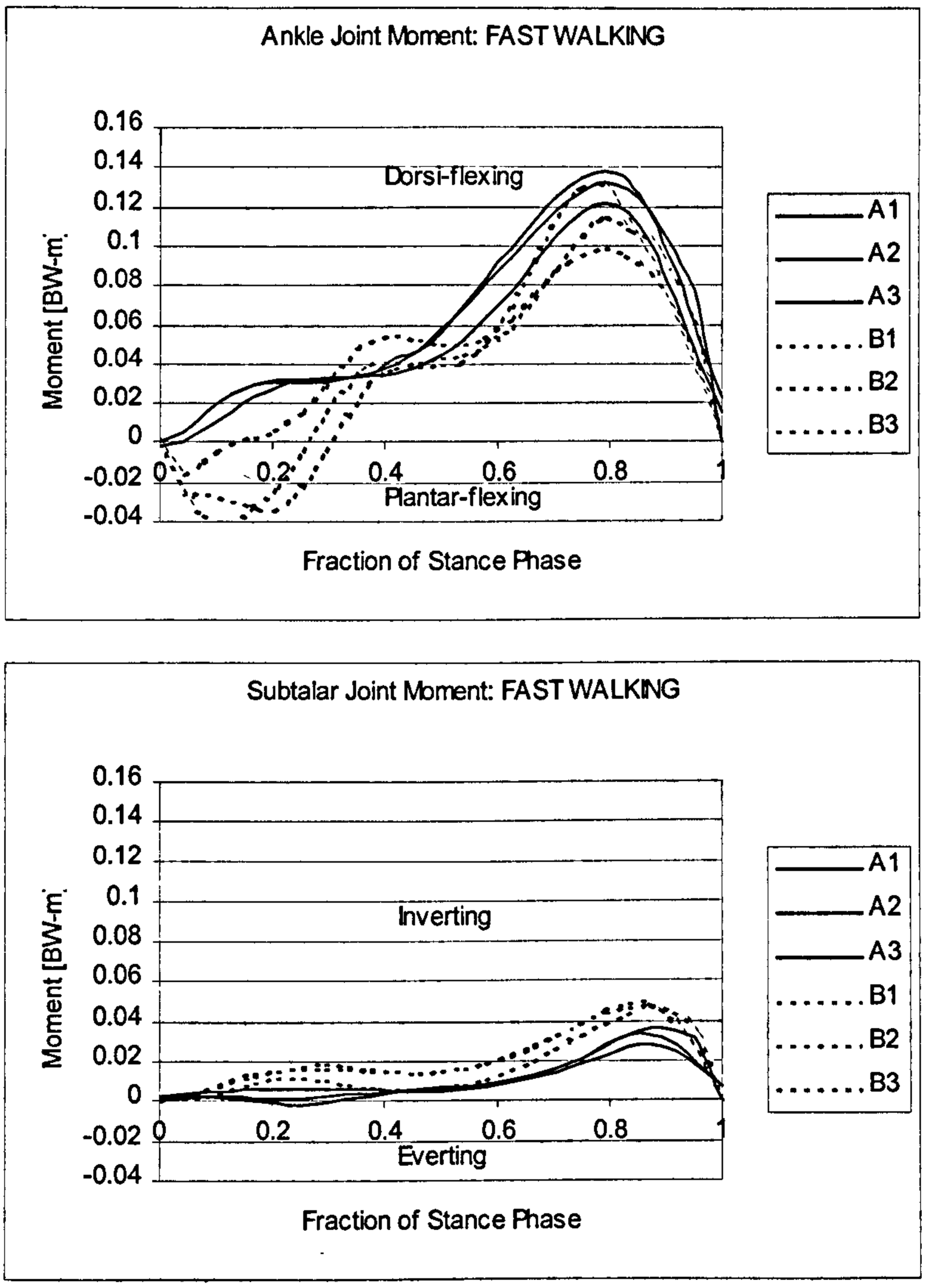

Figure 5.4-2 Joint Axis Moments for Fast Speed Walking for Subjects A and B.

Subject A until TO. The dorsi-flexing peak at 0.8 of stance phase was the same for both subjects at 0.12 Nm/N.

Figure 5.4-3 shows the joint moments for the preferred speed turning task. The moments about the Subtalar Joint axis during turning were similar to those during walking. After HS, inverting moments developed at the joint which reached a peak at 0.8 of stance phase and then dropped back to 0.0 at TO. Subject B showed a moment pattern with two peaks in addition to the single peak of Subject A. The early peak occurred at 0.25 of stance phase with a moment of 0.04 Nm/N. The late peak for Subject B was larger than that of Subject A, with the two being 0.05 and 0.04 Nm/N respectively. The moments about the Ankle Joint showed a great deal of variability, between trials and between subjects. The same general pattern of moments as during walking was shown with a late peak of 0.14 Nm/N and 0.12 Nm/N for Subjects A and B respectively. The peak in the Ankle Joint moment for Subject B occurred earlier than that of Subject A at 0.7 and 0.8 of stance phase, respectively.

Figures 5.4-4 to 5.4-6 compare the moments from the walking and turning tasks for each of the three speeds. The moments were very similar between the tasks at slow speed. The differences in the moment patterns became greater as the speed increased. The Subtalar Joint moments changed from having a single late peak at about 0.9 of stance phase during preferred and fast speed walking to having two peaks at 0.2 and 0.8 of stance phase during turning. The peaks increased with increasing speed.

The Ankle Joint moments for slow speed walking and turning both had a single late dorsi-flexion moment peak at around 0.8 of stance phase. Walking at preferred and fast speeds maintained the same, single peak pattern. The turning task at preferred and fast speed developed a second, earlier dorsi-flexion peak at around 0.4 of stance phase. The late peak for the turning task was the same as that for the walking task. In Figure 5.4-6, the different fast walking Ankle Joint moment patterns for Subjects A and B can be seen in the early, deceleration portion of stance phase. The moment at the Subtalar Joint was initially plantar-flexing for Subject B and dorsi-flexing for Subject A.

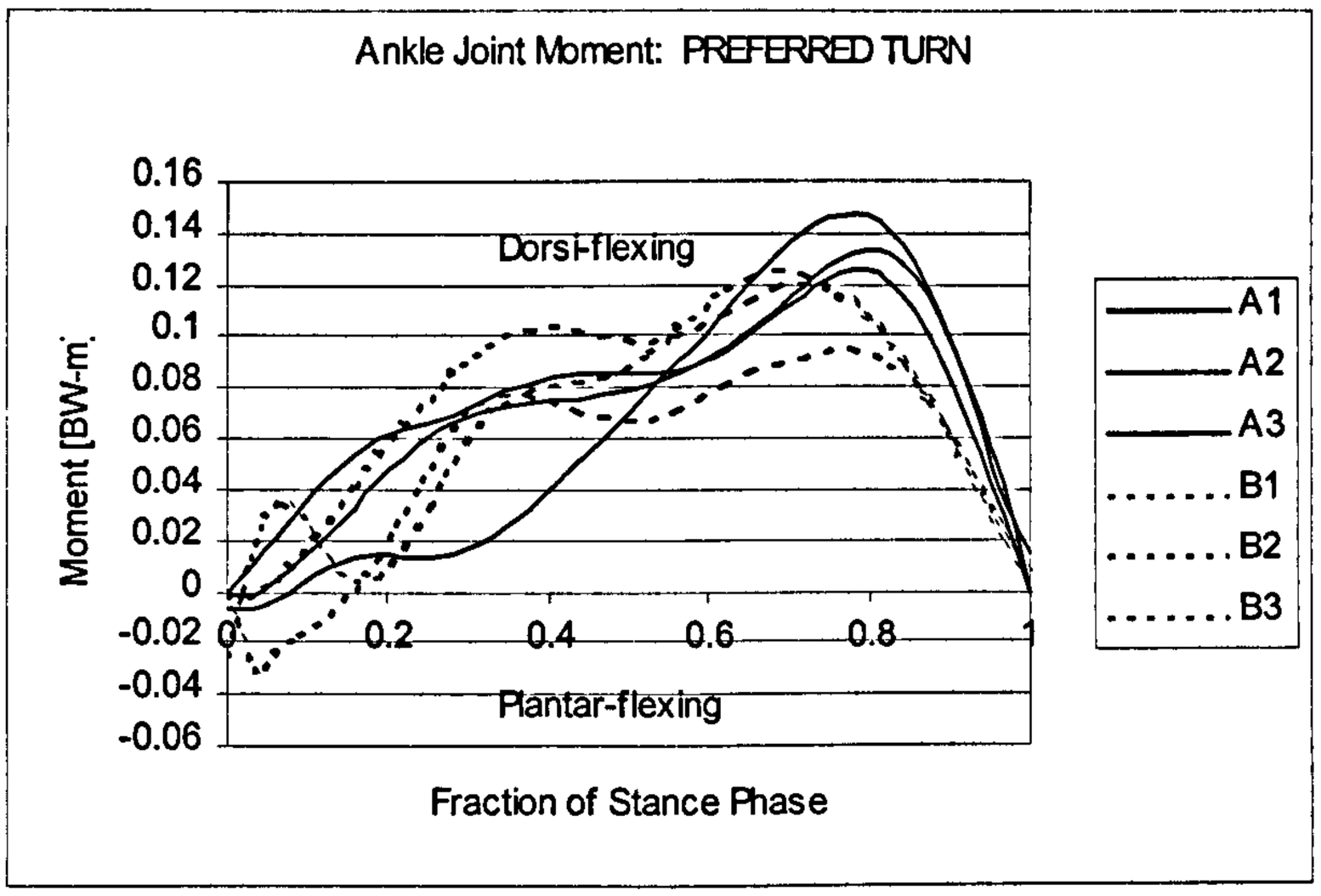

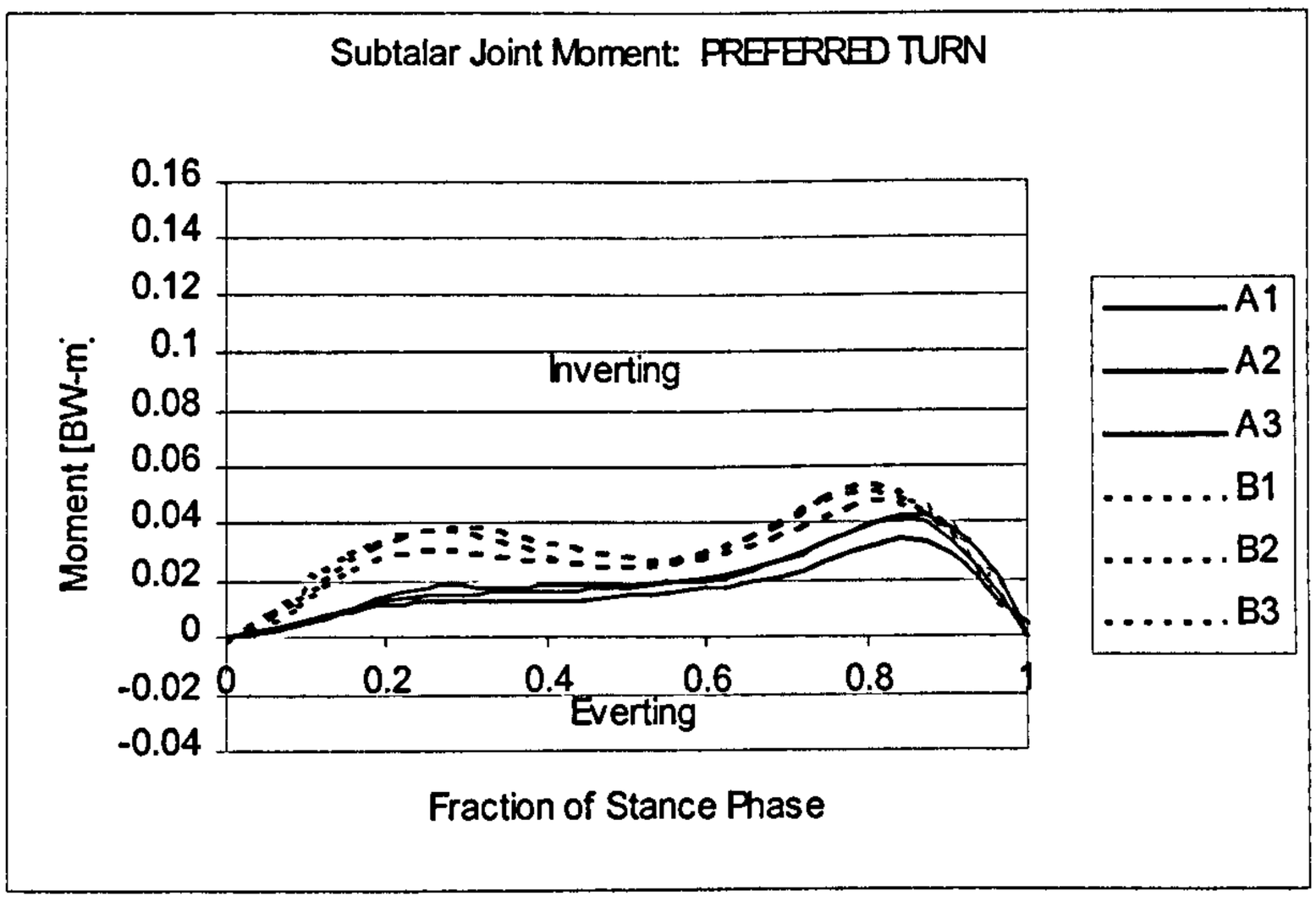

Figure 5.4-3 Joint Axis Moments for Preferred Speed Turning for Subjects A and B.

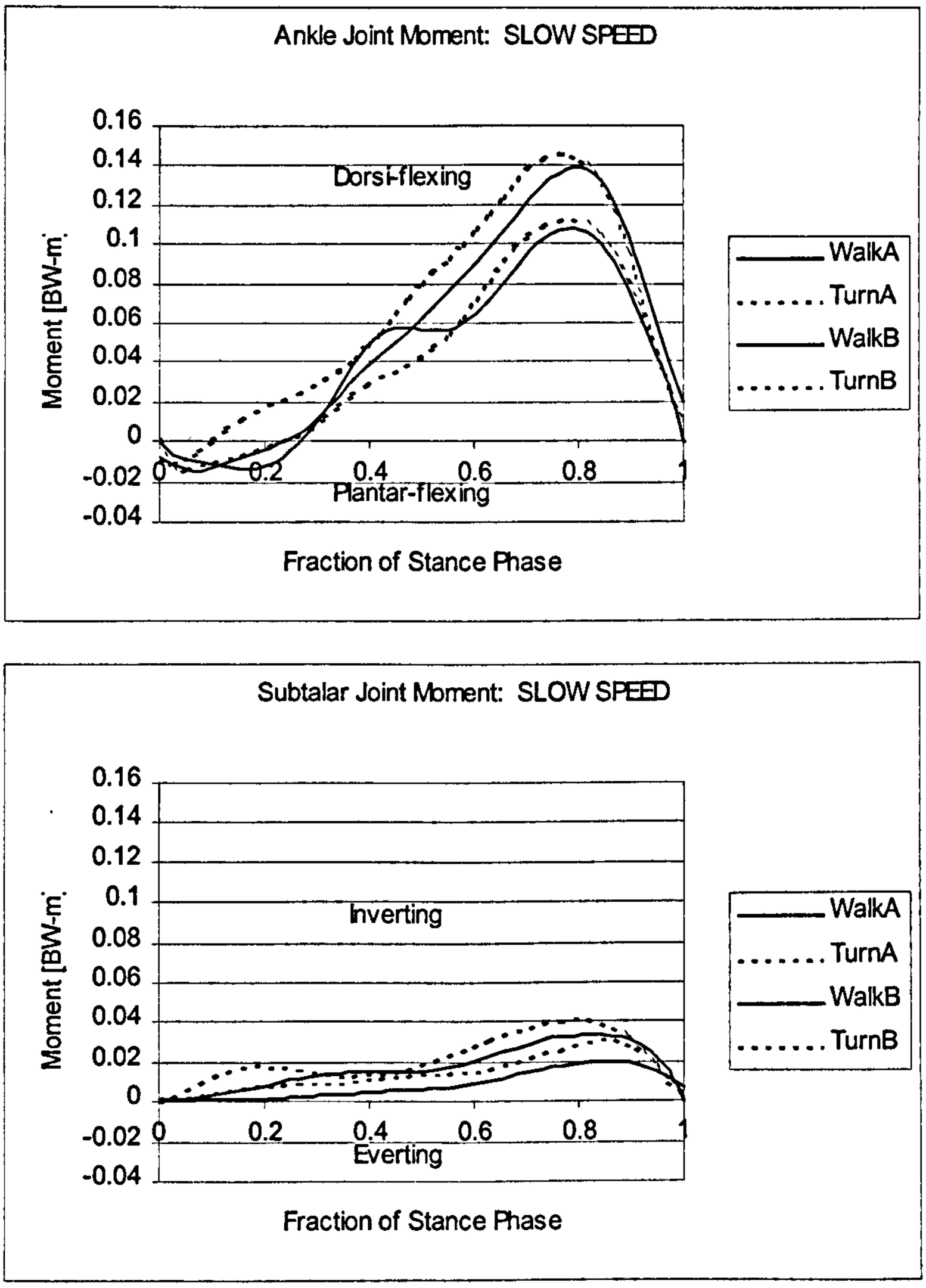

Figure 5.4-4 Comparing Task differences in Joint Axis Moments for Slow Speed Walking and Turning for Subjects A and B.

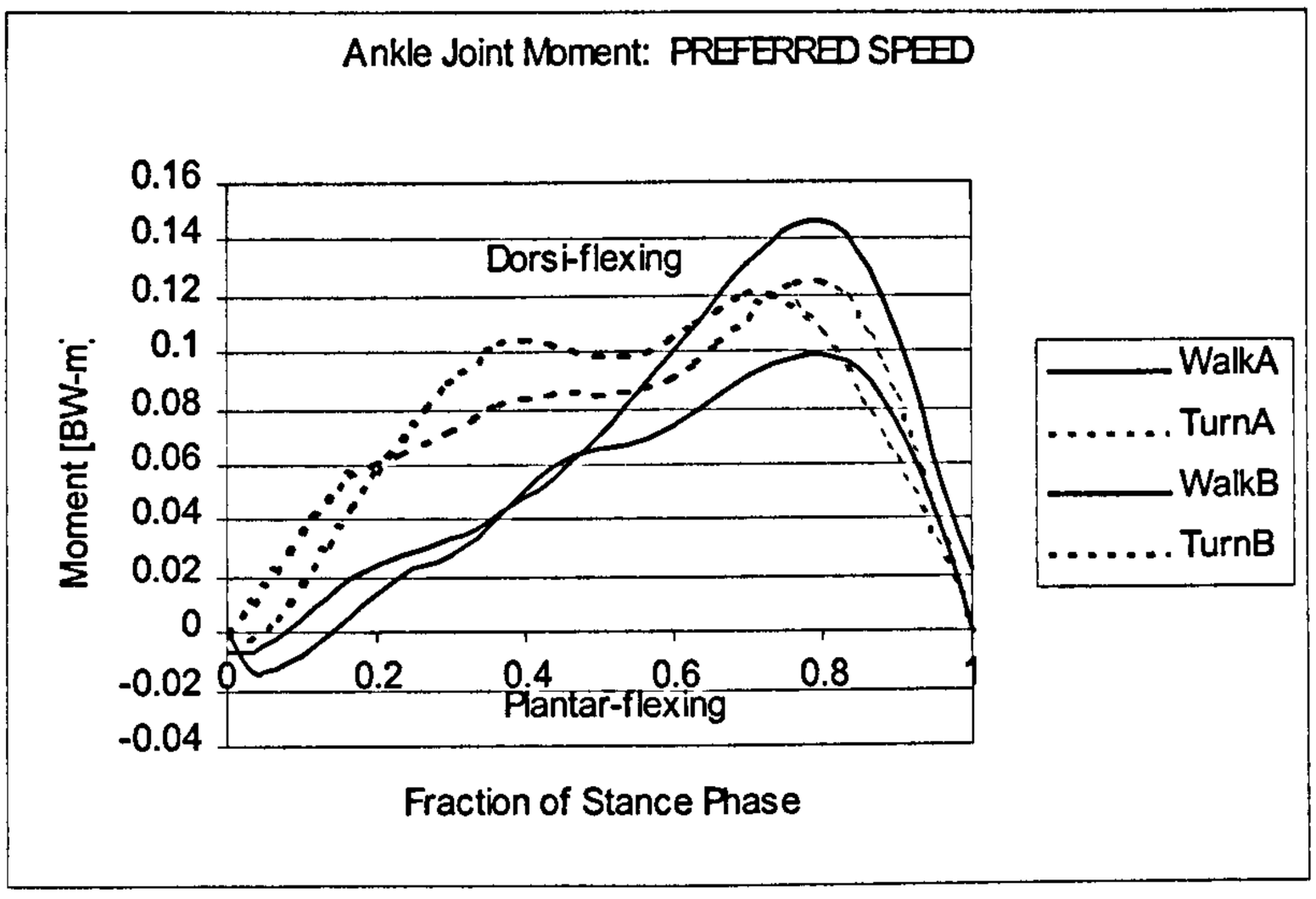

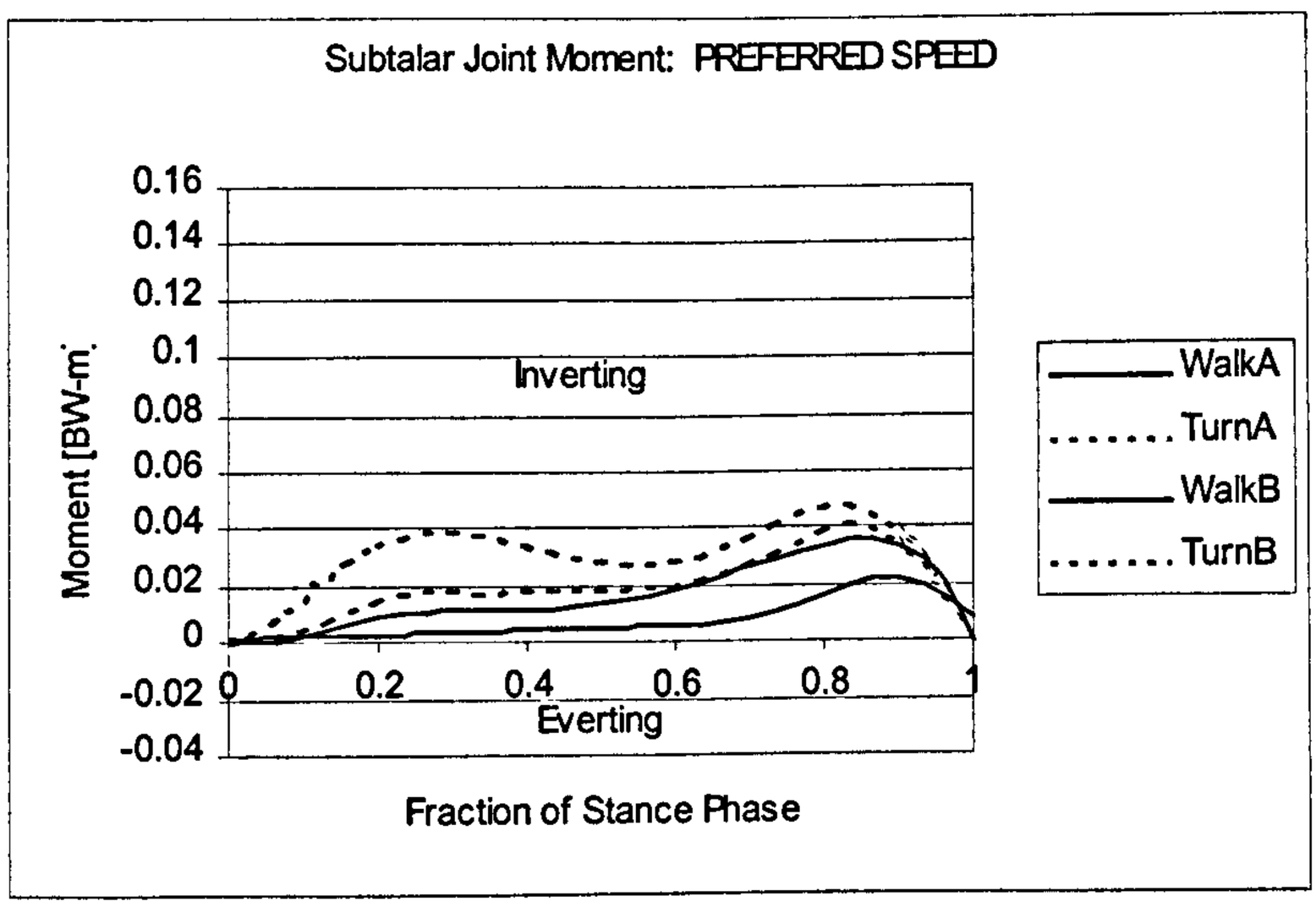

Figure 5.4-5 Comparing Task differences in Joint Axis Moments for Preferred Speed Walking and Turning for Subjects A and B.

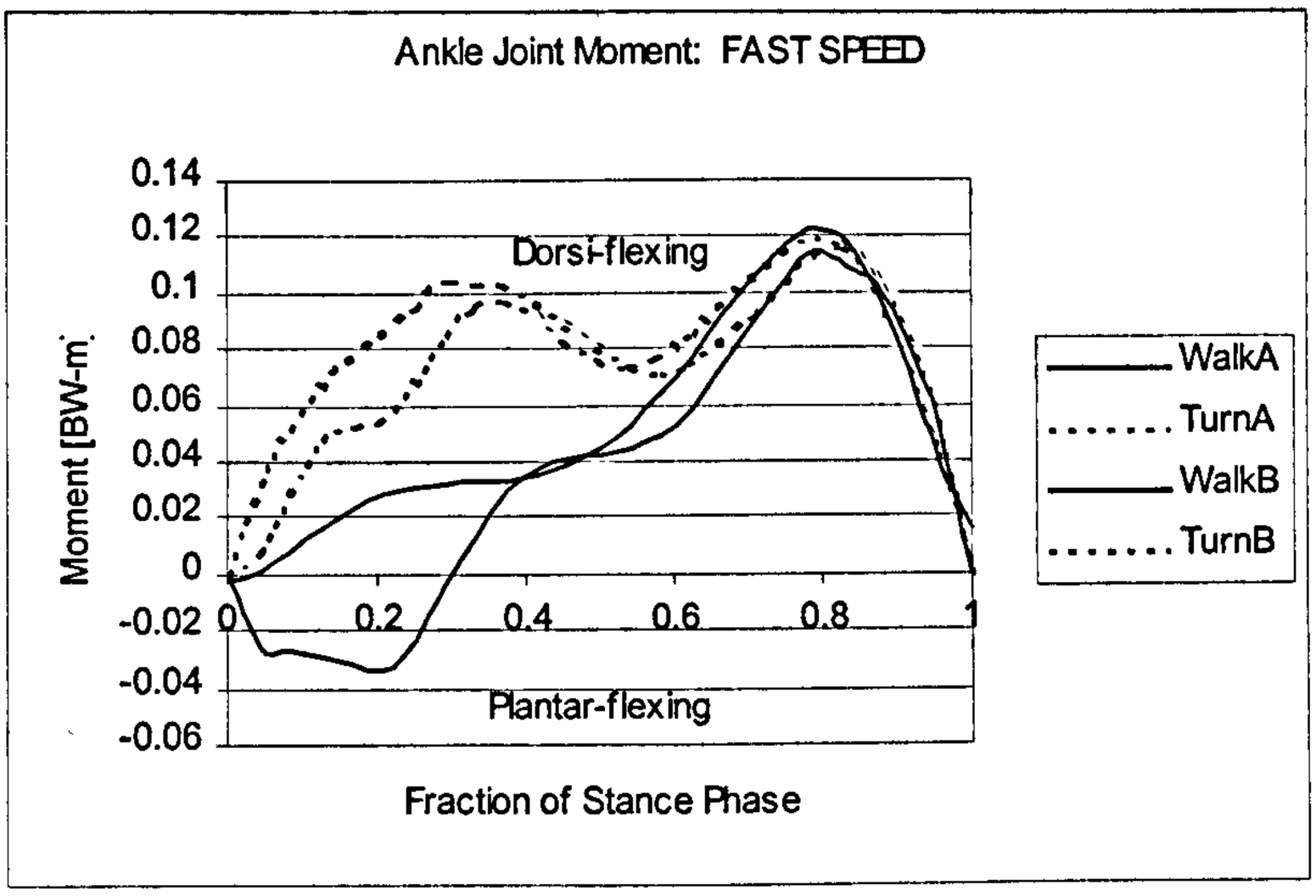

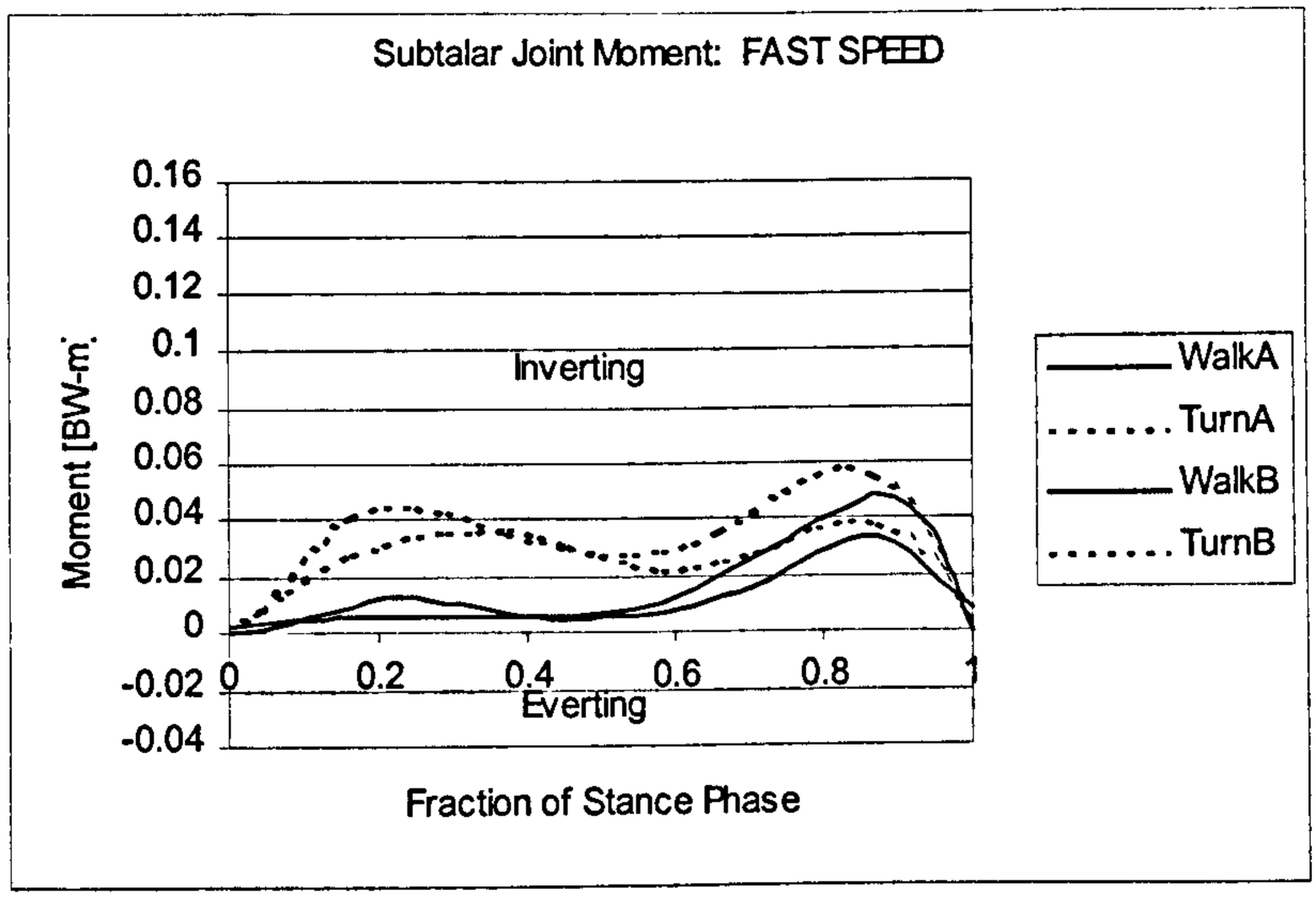

Figure 5.4-6 Comparing Task differences in Joint Axis Moments for Fast Speed Walking and Turning for Subjects A and B.

Figures 5.4-7 and 5.4-8 compare the joint axis moments for the different speeds during the walking and turning tasks. The moments were similar for all speeds of walking. The moments about the Ankle Joint in turning can be seen to develop a second, earlier peak for preferred and fast speed at around 0.4 of stance phase. This second peak was also seen to develop in the Subtalar Joint moments for preferred and fast speed turning.

For the turning task trials at each of the three speeds and the walking trials at slow and preferred speeds there was little variability between the subjects. It was only in the fast walking trials that a difference was seen in the pattern of moments about the Ankle Joint between the two example subjects. During the deceleration phase of stance, Subject B developed a plantar-flexing moment about the Ankle Joint axis. Subject A had a dorsi-flexing moment. At foot flat, both of these moments changed into dorsi-flexing moments and the patterns were from then on similar between the subjects for the rest of stance phase. This early difference in Ankle Joint moment was likely due to a difference in the style of walking in early stance. However, since no such inter-subject difference was seen in either the Ground Reaction Force or joint angles during fast walking, this difference in style must arise from the behaviour of the other two joints of the leg. Unfortunately, these joints were not monitored in the current study and therefore the nature of this difference in style can only be speculation.

Apart from this single inter-subject difference, the external loading and kinematics of the two example subjects, and of the other ten subjects, has been remarkably similar despite differences in body type and in gait speeds. The interesting question now to consider is whether or not the loading of the internal structures of the Ankle Complex, the muscles, ligaments and surfaces, will also be similar for each of the subjects given that the external loading was so similar.

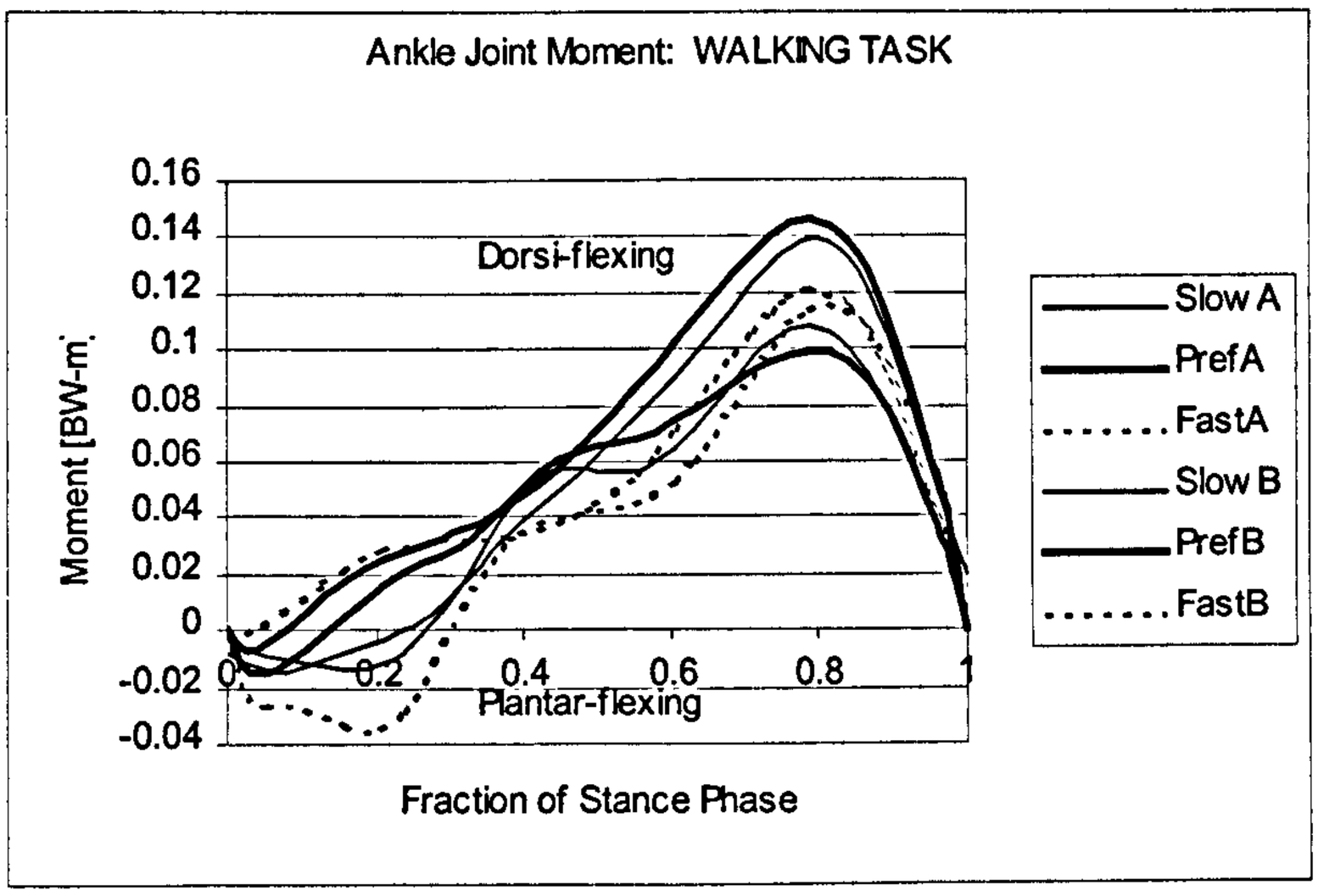

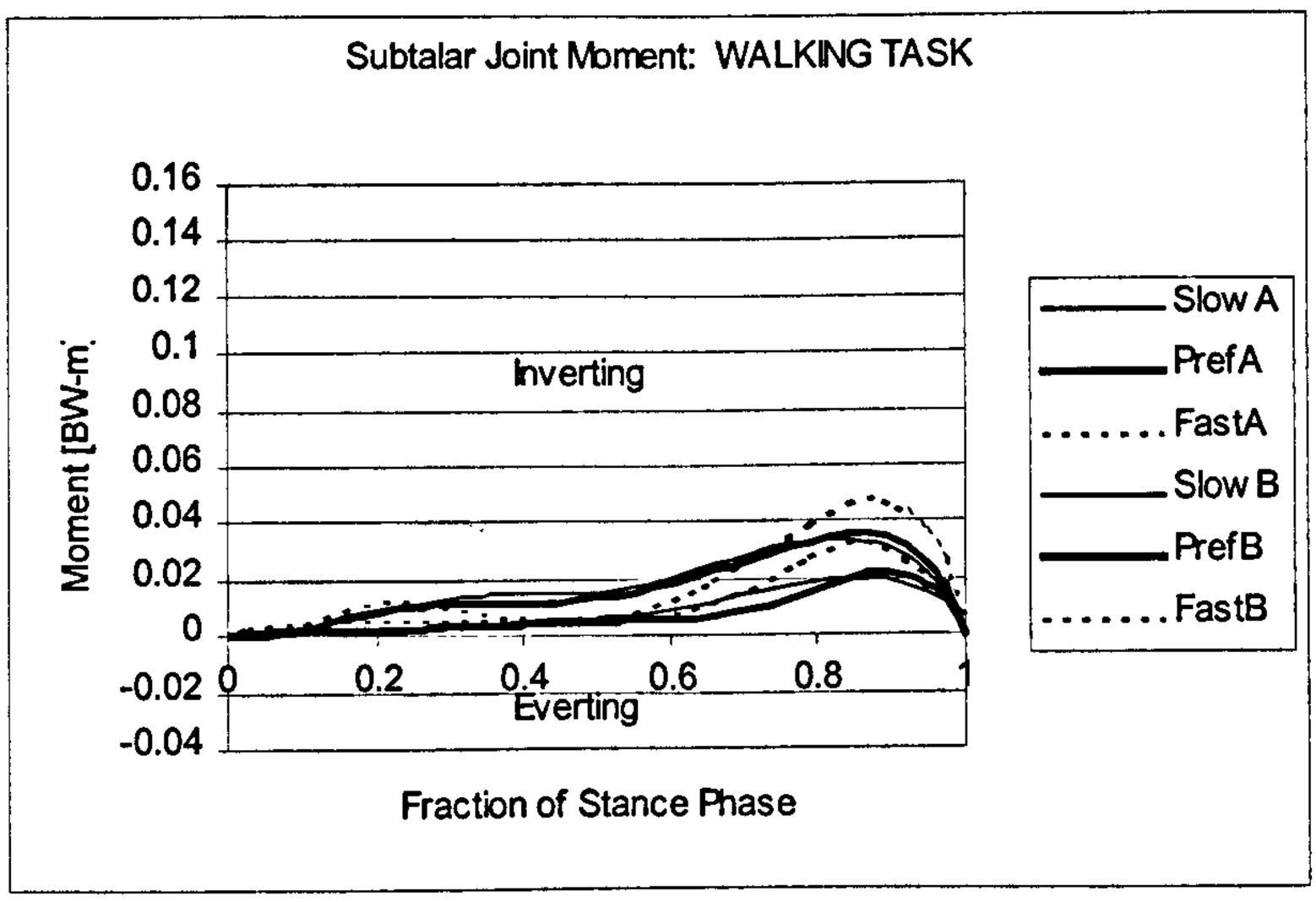

Figure 5.4-7 Comparing Speed differences in Joint Axis Moments for the Walking Task for Subjects A and B.

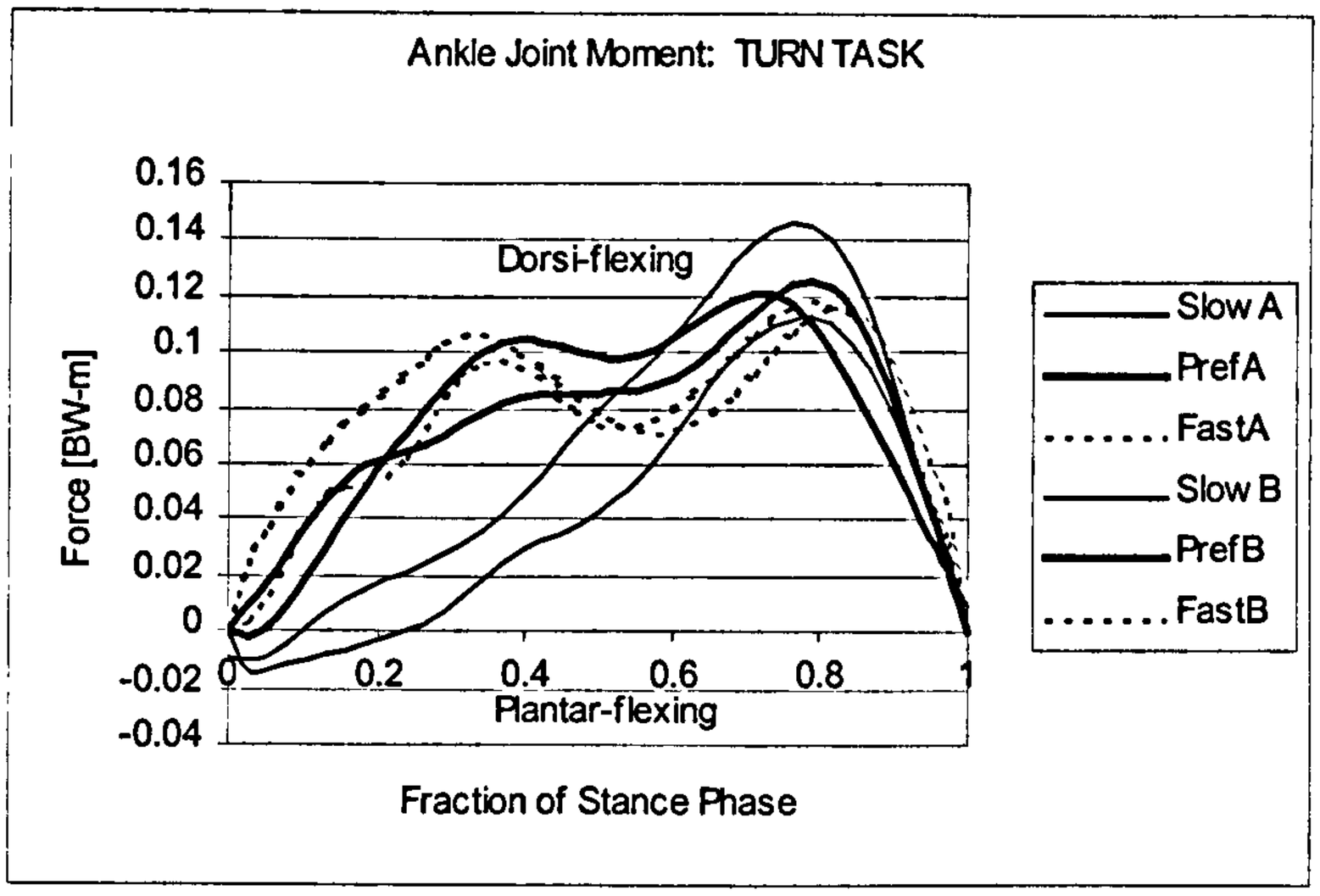

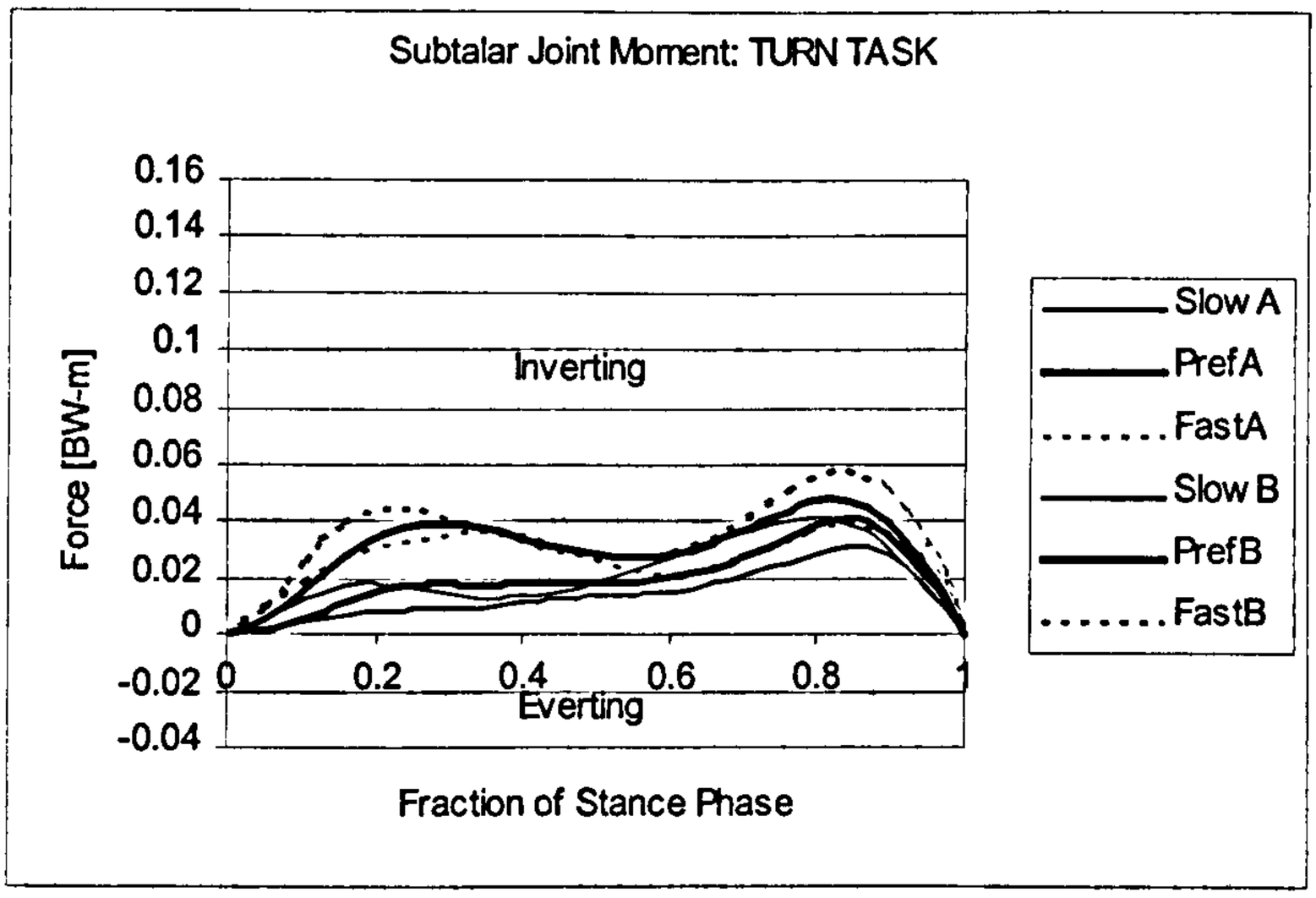

Figure 5.4-8 Comparing Speed differences in Joint Axis Moments for the Turning Task for Subjects A and B.

5.5 FREE MOMENT RESULTS

Recall from Section 3.1.3 how the Force Plate could apply a Free Moment about a vertical axis to the foot during stance phase. This Free Moment was dependent on both the amount of friction between the sole of the foot or shoe and the surface of the Force Plate and on the amount of twisting of the lower limb that the subject performs about the long axis of the shank. In the current experiment, the friction could have been low since the subject performed the movement tasks with cold, bare feet over a linoleum surface. Figure 5.4-9 shows the Free Moment for Subjects A and B during preferred speed walking for a single trial. Figure 5.4-10 shows the Free Moments for both subjects during preferred speed turning. Note from these figures that Subject A experienced a greater free moment than B with the larger magnitude of -0.0140 Nm/N occurring at 0.25 of stance phase during preferred walking. The maximum magnitude was -0.006 Nm/N for Subject B at 0.15 of stance phase during walking. During preferred speed turning, Subject A experienced a maximum Free Moment of0.0114 Nm/N at 0.8 of stance phase and Subject B had -0.008 Nm/N at 0.20 of stance phase.

In the worst case, the Free Moment occurring during preferred walking in Subject A at 0.25 of stance phase was nearly 20% of the magnitude of the moment about the Ankle Joint axis at that time (see Figure 5.4-1). For the rest of the stance phase of these trials, and for all the other task trials of Subject A, the Free Moment was approximately 5 to 10% of the total external moment acting at the Ankle Complex.

For Subject B, the worst case occurred at 0.8 of stance phase during preferred walking, where the Free Moment of 0.0114 was 11% of the total external Ankle Joint moment component. Since for the majority of trials, the Free Moment never comprised more than 11% of the total external moment (apart from the exception described above for Subject A), the Free Moment component of the external moment was ignored from the equilibrium solution. It was assumed that this would negligibly affect the solution of Ankle Complex loading.

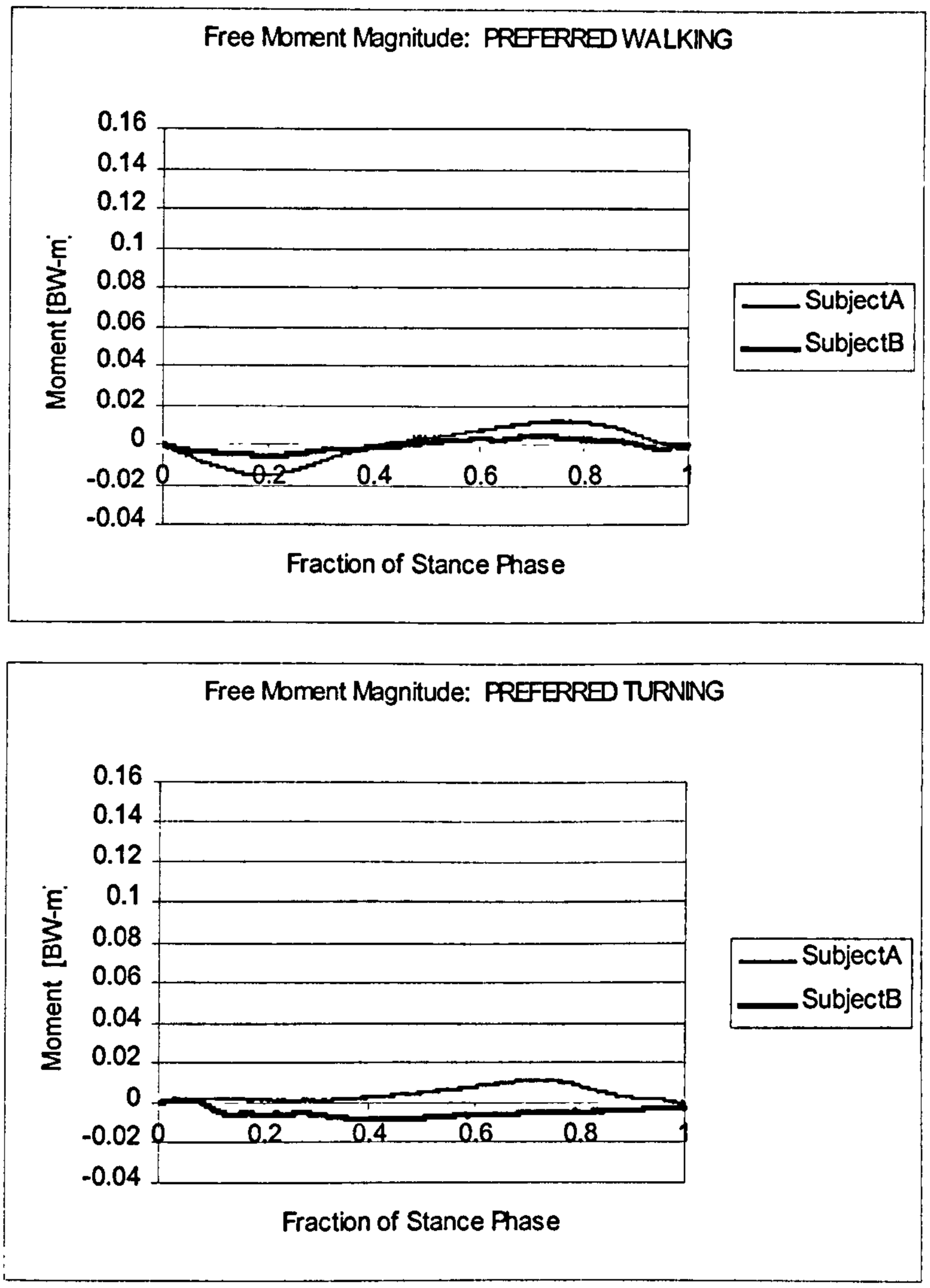

Figure 5.4-9 Worst case magnitudes of Free Moments for Subjects A and B during Preferred Speed Walking and Turning.

What should be noted from the free moment results, which showed that the subjects of the current study imparted little moment to the ground about the vertical axis, is that the anterior-posterior (A-P) and mediolateral (M-L) ground reaction forces presented in Figure 5.2-1 to 5.2-11 were normal for walking. As mentioned above, the free moment is dependent on the amount of twist applied to the lower leg and to the friction between the floor and the foot. However, the A-P and M-L GRFs are also dependent on foot-floor friction. Therefore, since these latter quantities were normal, the lack of free moment must be due more to the lack of twist in the lower leg and less to low floor friction.

The lack of normal twist in the lower leg brings into question whether the subjects in the current study were indeed walking in their preferred gait patterns. This possible divergence from preferred or *normal* walking is discussed in greater detail in Section 8.2.3 where the EMG data indicate that the subjects were perhaps walking with a more "guarded" gait (i.e. holding the ankle complex joints more stiffly than normal with antagonistic muscle activity). This guarded gait pattern could tend to reduce the amount of twist of the lower limb about the vertical axis. Therefore a more guarded gait would exhibit a reduced free moment from that during normal walking.

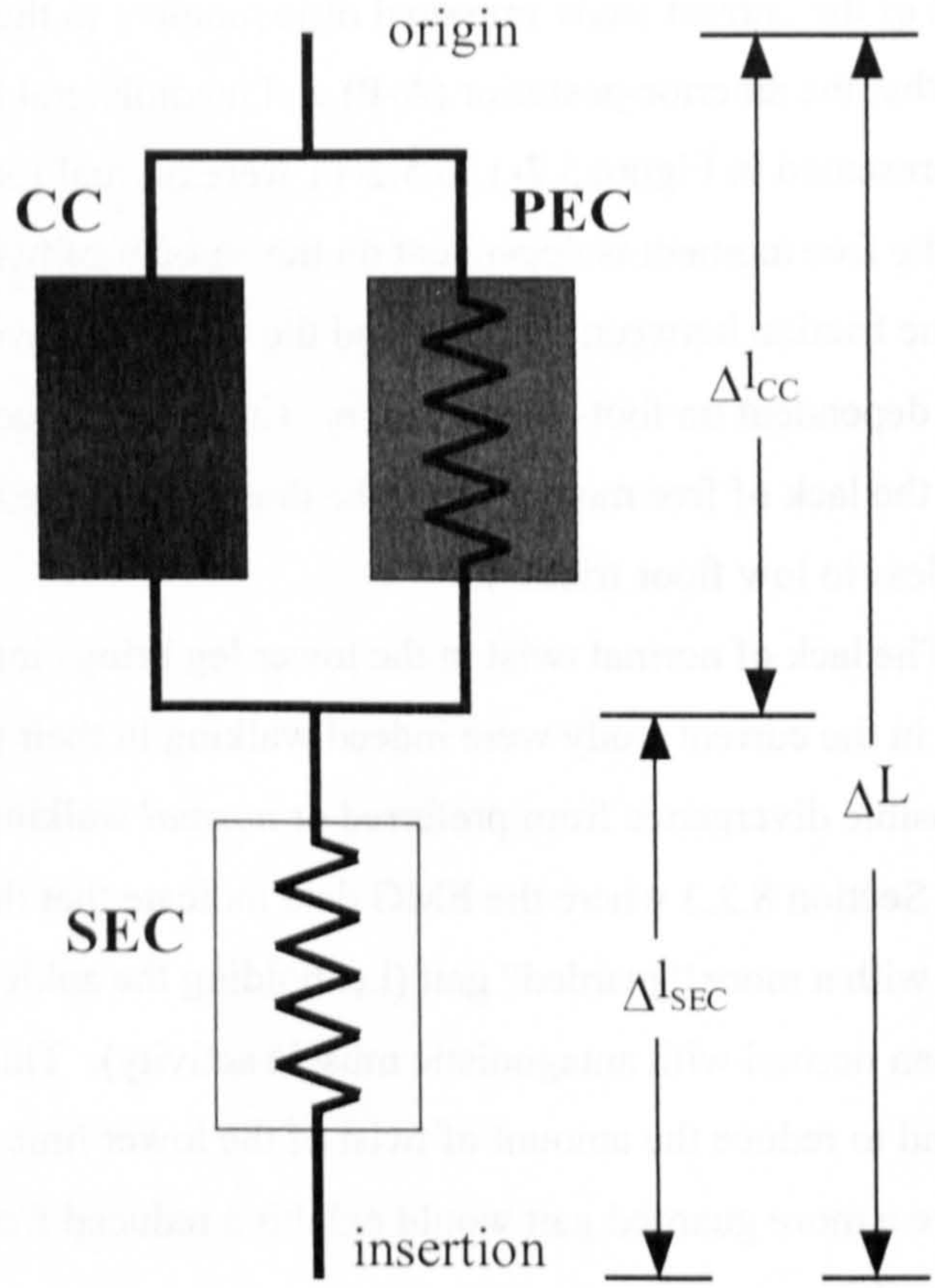

Figure 6.1-1 Arrangement of the three components in the Muscle Model.

CHAPTER 6 MUSCLE-TENDON TENSION EQUILIBRIUM

6.1 THREE COMPONENT MUSCLE-TENDON MODEL

The Muscle Model portion of the Ankle Complex Model considered each muscle plus its associated tendon, each *muscle-tendon*, as a single functional system. The behaviour of this system was modelled by three separate components: the *Contractile Component (CC)*, the *Parallel Elastic Component (PEC)*, and the *Series Elastic Conponent (SEC)*. Figure 6.1-1 shows the arrangement of the three components within a muscle-tendon system. This arrangment is identical to Winters (1995). The Contractile Component was the component which *actively* produced tension in the muscle-tendon when it was activated by the Nervous System. In the physical muscle and tendon, the CC corresponded to the muscle fibres in the belly of the muscle. The Parallel Elastic Component corresponded to the elastic tissue of the muscle belly; the fascicles which held the muscle fibres in position and the aponeurosis that attached the tendon to the muscle. The PEC developed tension passively when it was stretched. The third component, the Series Elastic Component, could be considered as the tendon, which passively produced tension when stretched.

The Muscle Model predicted the behaviour of the eight muscle-tendons defined in the Internal Map. These muscle-tendons were the Lateral and Medial Heads of the Gastrocnemius (GaL and GaM), the Soleus (Sol), the Tibialis Anterior (TiA), the Peroneus Longus and Brevis (PeL and PeB), the Extensor Digitorum Longus (EDL) and the Extensor Hallucis Longus (EHL). The specific behaviour of the three components within each of the eight muscle-tendons was determined by the varying architecture of the different muscle-tendons. The architecture of the eight muscle-tendons was determined from the available literature.

6.1.1 Contractile Component

The tension produced by the Contractile Component when it was activated by the Nervous System was dependent on three inputs: the level of neurological

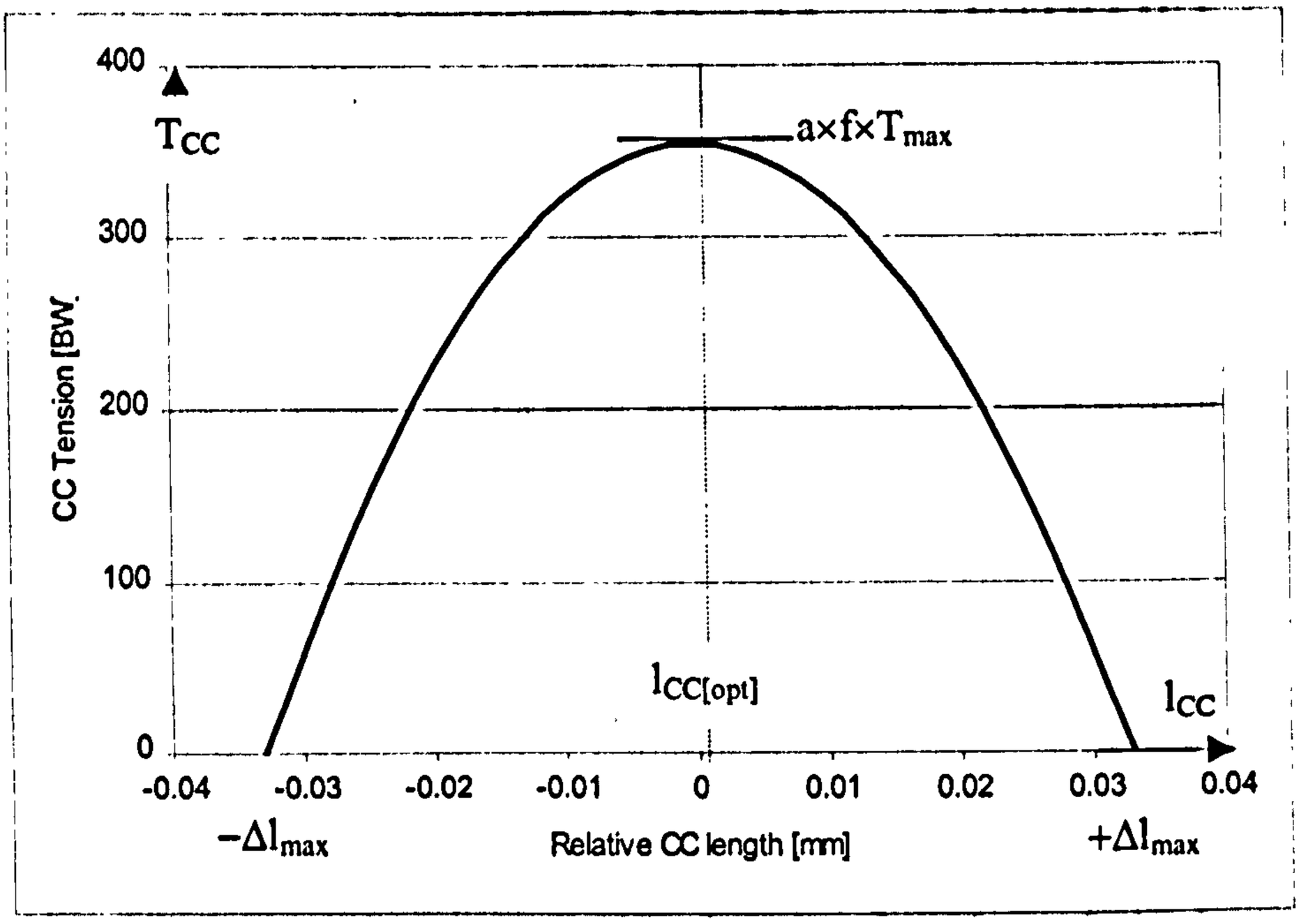

Figure 6.1.1-1 Length-tension Relationship of the Contractile Component (CC).

activation, the instantaneous CC length and instantaneous CC velocity. The terms *contractile* and *contraction* were somewhat misleading. The CC was able to produce tension while it was either being shortened (concentric contraction) or lengthened (eccentric contraction) by its attachments. The term contraction was therefore used to describe the state of the CC when it was actively producing tension.

CC Length-Tension Relationship

Figure 6.1.1-1 shows the *length-tension* relationship for the Contractile Component. The CC produced maximum tension when it was at its optimal length. When the CC was longer or shorter than this optimal length at the time of contraction, the tension produced during a contraction was reduced. The CC could produce tension only within a discrete range of component length, outside of which the CC was unable to produce any tension at all. The length-tension relationship was defined as an inverted parabola, which was symmetrical about the optimal length.

Instead of considering the absolute length of the CC, it was more useful to consider the CC length relative to its optimal length,

$$\Delta l_{CC} = l_{CC} - l_{CC[opt]} \qquad (6.1.1\text{-}1)$$

The length-tension relationship could then be defined as an inverted parabola symmetric about $\Delta l_{CC} = 0$. This revised length measure is also plotted in Figure 6.1.1-1. The length-tension relationship was defined as a function of the CC relative length, Δl_{CC}, as follows

$$T_{CC} = afT_{\max}\left(1 - \frac{\Delta l_{CC}{}^2}{\Delta l_{\max}{}^2}\right) \qquad (6.1.1\text{-}2)$$

where $\Delta l_{\max}$ was the maximum amount of shortening or lengthening from the optimal length for which the CC could still produce tension. The active length range for the CC was $2 \times \Delta l_{\max}$. The factor f was a function of CC velocity and represented the effect of the *velocity-tension* relationship of the CC tension. The factor a was the neurological activation level. This factor was non-zero when the CC was actively contracting. The production of these two factors, f and a, is discussed in the next sections.

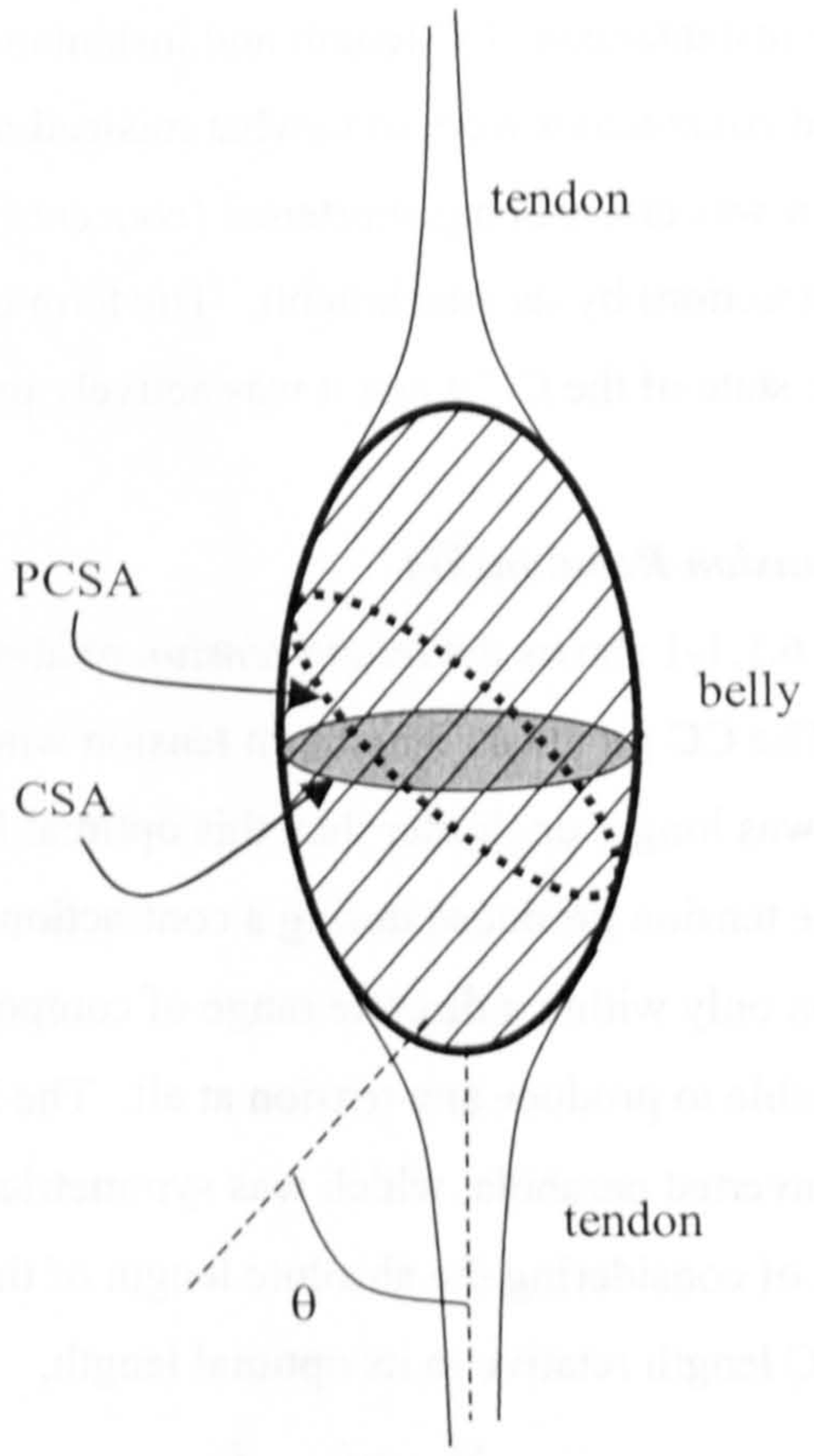

Figure 6.1.1-2 Physiological Cross-sectional Area (PCSA) and the Pennation Angle, θ.

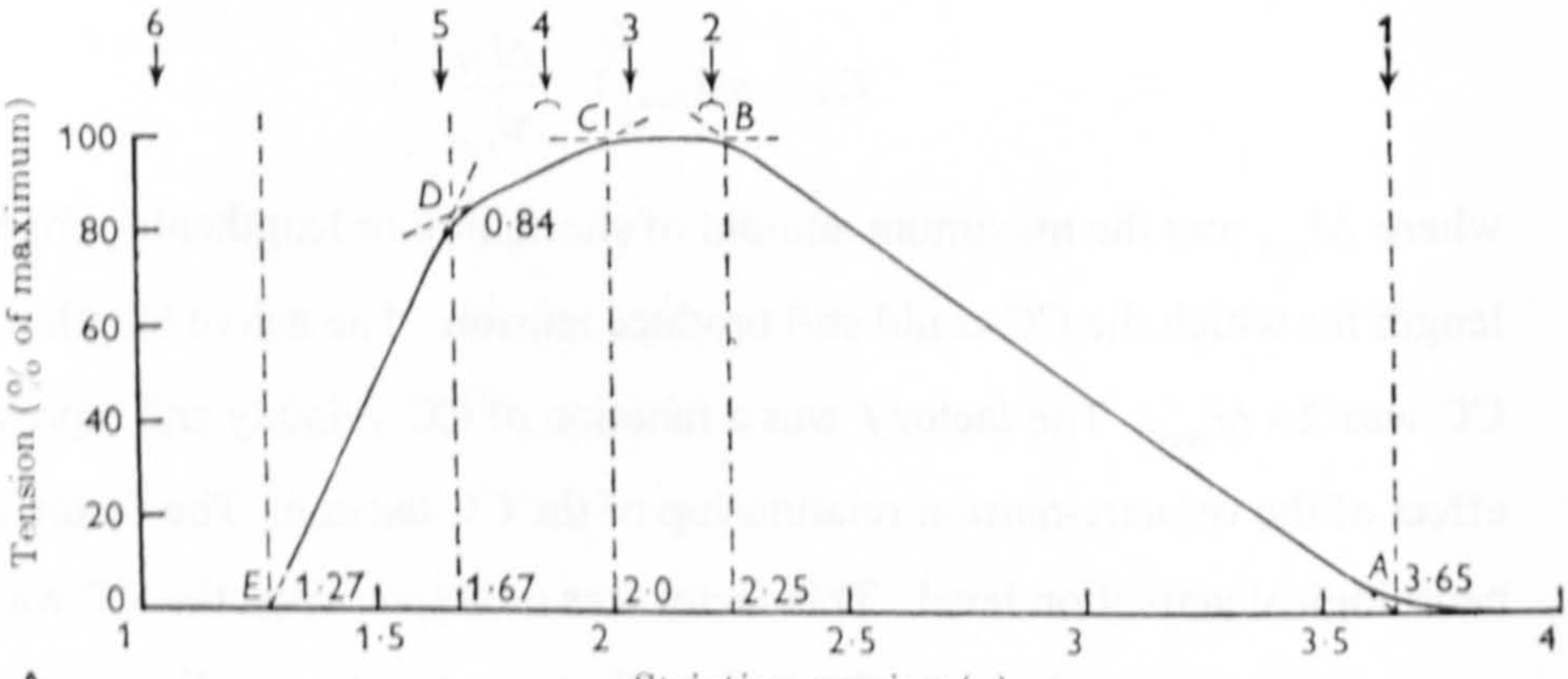

Figure 6.1.1-3 Length-tension Relationship for an individual Sarcomere.

The constant T_{max} in Eq. 6.1.1-2 was the tension produced by the CC when it was at optimal length and the factors f and a were both equal to 1. The constant was found using,

$$T_{max} = s \times PCSA \times SF \qquad (6.1.1\text{-}3)$$

where $PCSA$ was the *Physiological Cross-sectional Area* of the muscle. The $PCSA$ was the average cross-sectional area of the muscle belly when the area was measured in a plane perpendicular to the path of the muscle fibres. This is plotted in Figure 6.1.1-2. The PCSA is related to the cross-sectional area, CSA, of the muscle belly as follows:

$$PCSA = CSA \cdot \cos\theta \qquad (6.1.1\text{-}4)$$

The CSA is also plotted in Figure 6.1.1-3.

SF was the *Specific Tension* (per physiological cross-sectional area) for muscle tissue. This value has been found to be constant for all mammalian muscle tissue; $SF = 0.225\ \text{Nmm}^{-2}$ (Edgerton et al., 1986).

The constant s in Eq. 6.1.1-3 was a calibration constant which was required due to the dependence of the EMG signal, and therefore the dependence of the activation level, on the placement of the EMG electrodes during the Motion Analysis Experiments. This constant accounted for the variability in electrode pair placements and the variability of the electrical properties of the underlying tissues for the different subjects tested. Unlike the other factors in Eqs. 6.1.1-2 to 6.1.1-4, which were determined by the architecture of the muscle-tendons, this calibration constant had to be determined individually for each subject. The process is described in a later section.

The value of Δl_{max} was determined using,

$$\Delta l_{max} = 0.659 \times N_{sarc} \times l_{sarc[opt]} \times \cos\theta \qquad (6.1.1\text{-}5)$$

The active length range of the Contractile Component was determined by the active length range and architecture of the muscle fibres in the muscle belly. The active range for the fibres were themselves determined by the behaviour of the individual sarcomeres that were arranged in series within each fibre. N_{sarc} was the number of sarcomeres arranged in series in each muscle fibre. This number has been shown in

the literature to be constant for all the fibres within the same muscle, but to differ between muscles (Wickiewicz et al., 1983). The constant $l_{sarc[opt]}$ was the optimal length of an individual sarcomere. Sarcomeres have been shown to behave identically in all human muscles. The length-tension relationship for an individual sarcomere is plotted in Figure 6.1.1-3. The optimal length for each sarcomere was taken to be 2.2 μm. The product $N_{sarc} \times l_{sarc[opt]}$ therefore equalled the optimal length of an individual muscle fibre. Note that the active length range for the saromere was not symmetrical about its optimal length. The minimum length at which the sarcomere could produce tension was 1.27 μm and the maximum length was 3.65 μm. The relative amount of shortening was therefore 42% of $l_{sarc[opt]}$ and for lengthening 65.9% (Gordon, Huxley and Julian, 1966).

It has been shown experimentally that when the sarcomeres were joined in series to form muscle fibres, the active length range of contraction extended at the shortening end making the active range more symmetrical about the optimal fibre length (Goldspink, 1977, White, 1977). The maximum amount of shortening or lengthening that could be applied to a muscle fibre at which the fibre could still produce tension was therefore defined as 65.9% of the length $N_{sarc} \times l_{sarc[opt]}$.

Muscle	T_{max} [N]	Δl_{max} [mm]
GaL	272.6×s	33.0
GaM	456.4×s	21.3
Sol	1305×s	18.4
TiA	222.8×s	42.3
PeL	276.8×s	20.4
PeB	128.3×s	18.8
EHL	40.5×s	44.7
EDL	126.0×s	38.8

Table 6.1.1-1 Values of T_{max} and Δl_{max} for each of the eight Muscle-tendons.

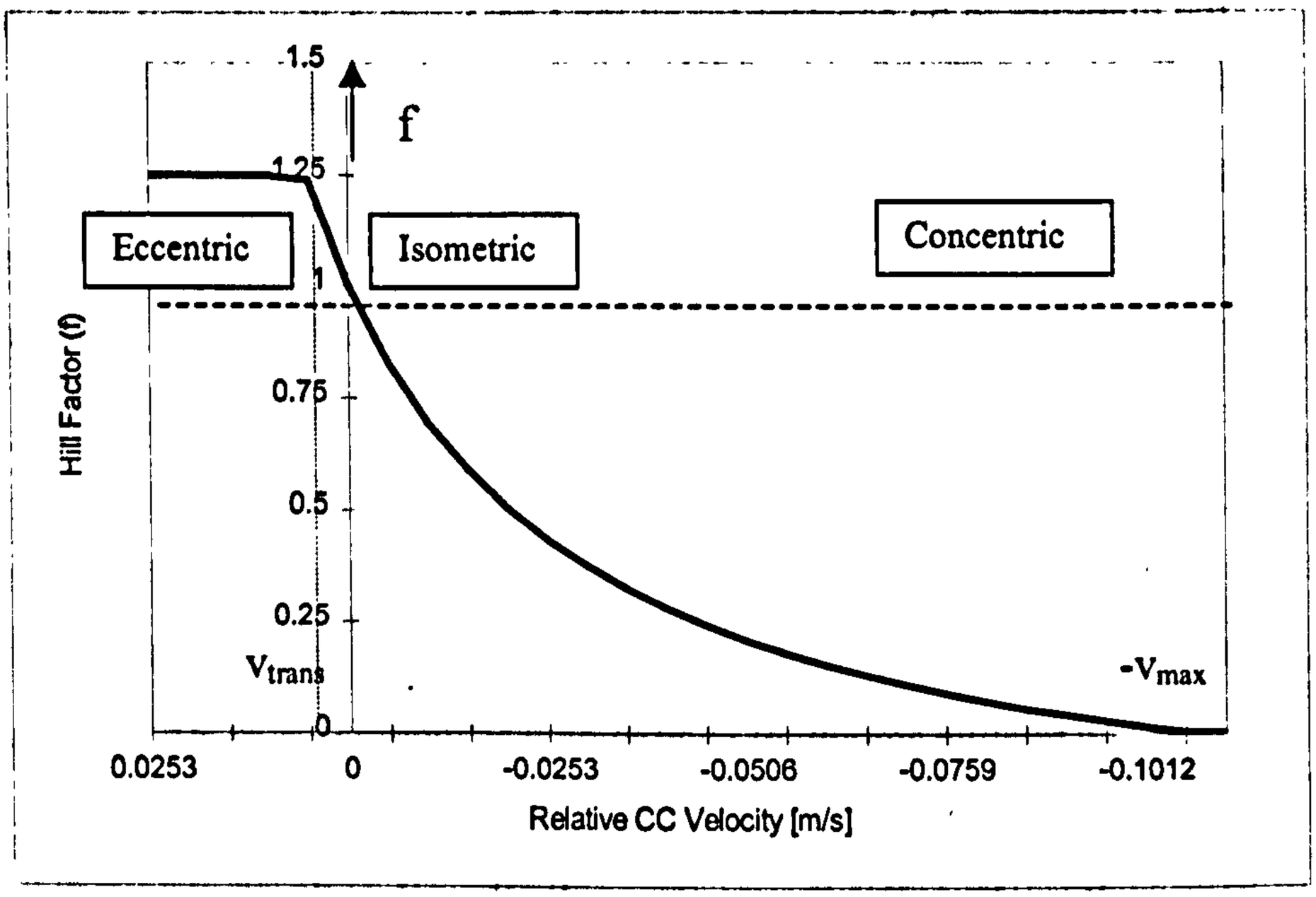

Figure 6.1.1-4 Velocity-tension (Hill) Relationship of the Contractile Component.

When determining the CC active length range from the fibre length range behaviour, the *pennation angle* of the fibres, θ, had to be taken into account. The pennation angle was the angle between the path of the muscle fibres within the muscle belly and the line of action of the tendon leaving the muscle belly. This is shown in Figure 6.1.1-2.

The collective behaviour of each of the sarcomeres in the muscle fibres and all the muscle fibres in the muscle belly resulted in the active length range value, Δl_{max}, defined in Eq. 6.1.1-5. The values for T_{max} and Δl_{max} for each of the eight muscle-tendons are listed in Table 6.1.1-1. The complete list of parameters describing muscle-tendon architecture which were used in the calculation of their values is included in the Appendix (Table A.1).

Velocity-Tension Relationship

Figure 6.1.1-4 plots the *velocity-tension* relationship for the Contractile Component. This was modelled as a hyperbolic function, which is also known as the *Hill Relation*. The velocity-tension relationship produced a factor f, which appeared in the equation governing CC tension, Eq. 6.1.1-2. The factor f introduced the velocity dependence of the CC tension. The factor was defined as $f = 1.0$ for an *isometric* (zero velocity) contraction. For concentric contraction, as the velocity of CC shortening increased, moving away from the isometric condition, the factor f dropped toward 0.0. At the maximum shortening velocity, $-v_{max}$, the contracting Contractile Component could produce no tension ($f = 0.0$). The muscle was incapable of shortening any faster than this velocity. For eccentric contractions, the factor f increased hyperbolically above the isometric value of 1.0 with greater lengthening velocity until a transitional velocity was met, v_{trans}. At lengthening velocities faster than the transition velocity, the tension factor was constant at $f = 1.25$. The physical mechanisms responsible for this behaviour are not yet clear. It seems as though this results from the behaviour of the individual sarcomeres during eccentric contraction conditions.

The velocity-tension relationship was defined by the function,

$$\begin{aligned} f &= 1.25 && \text{for} \quad v_{trans} \le v \\ f &= \frac{B + Av}{B - v} && \text{for} \quad -v_{\max} \le v \le v_{trans} \\ f &= 0.0 && \text{for} \quad v \le -v_{\max} \end{aligned} \tag{6.1.1-6}$$

The maximum shortening velocity, $-v_{\max}$, and the transition velocity, v_{trans} were therefore found using Eq. 6.1.1-6 to be,

$$\begin{aligned} -v_{\max} &= -\frac{B}{A} \\ v_{trans} &= \frac{0.25B}{A + 1.25} \end{aligned} \tag{6.1.1-7}$$

The shape of the hyperbolic portion of the velocity-tension relationship was based on the curves determined by Wickiewicz, et al. (1983, 1984) during isokinetic muscle studies of the ankle plantar-flexors and dorsi-flexors. These curves were each normalised in the vertical axis by dividing by the isometric muscle tension. The isometric tension was therefore defined in each of the curves as $f = 1.0$. The horizontal axis was normalised by dividing by the optimal muscle fibre length, $l_{f[opt]}$. The velocities were therefore measured as optimal fibre lengths per second. Thus normalised, all the muscles about the ankle which were studied in Wickiewicz, et al. (1984) showed the same velocity-tension curve shape. Maximum velocity of shortening, $-v_{\max}$, was equal to -2.69 ± 0.42 s^{-1}. The two shape defining constants, A and B, which characterised the hyperbolic portion of the normalised curve where then determined to be,

$$\begin{aligned} A &= 0.304 \\ B &= 0.650 \end{aligned}$$

This normalised curve served as the template for the individual velocity-tension relationships for each of the eight muscle-tendons. The curves for each of the muscles remained normalised vertically so that an isometric contraction produced a factor $f = 1.0$. The template was adjusted horizontally to fit the architecture of each muscle.

Muscle	v_{max} [mm/s]	v_{trans} [mm/s]	A	B
GaL	136.1	6.66	0.304	0.04137
GaM	90.7	4.44	0.304	0.02757
Sol	82.9	4.05	0.304	0.02520
TiA	173.5	8.48	0.304	0.05274
PeL	84.7	4.14	0.304	0.02575
PeB	76.9	3.76	0.304	0.02338
EHL	183.5	8.97	0.304	0.05578
EDL	159.8	7.82	0.304	0.04858

Table 6.1.1-2 Parameters defining the Velocity-tension Relationship for each of the eight Muscle-tendons.

The maximum shortening velocity, $-v_{\max}$, was a function of the muscle fibre optimal length,

$$-v_{\max} = -2.69 \times l_{f[opt]} \tag{6.1.1-8}$$

where the optimal fibre length was,

$$l_{f[opt]} = N_{sarc} \times l_{sarc[opt]} \tag{6.1.1-9}$$

where N_{sarc} was the number of sarcomeres in series per muscle fibre and $l_{sarc[opt]} = 2.2$ μm was the optimal length of a single sarcomere.

The shape constant A defined the shape of the curve vertically. Since the velocity curves for each of the eight muscles were normalised vertically, this constant was the same for all the muscles, $A = 0.304$. Using this value for the constant A and Eq. 6.1.1-7, the horizontal shape constant B was found for each of the muscles,

$$B = Av_{\max} \tag{6.1.1-10}$$

Table 6.1.1-2 lists the maximum shortening velocities, transition velocities and shape constants for each of the eight muscle-tendons of the Muscle Model.

Activation Level-Tension Relationship

Perhaps the most influential factor governing the tension in the Contractile Component was the *activation level.* As can be seen in Eq. 6.1.1-2, the activation level was represented in the CC tension function by the factor a. The activation level was the amount of neurological drive from the Central Nervous System (CNS) which controlled whether or not the CC was in an active contracting state. It also determined to a large extent the strength of the contraction. When the CNS had not activated the CC in a particular muscle-tendon, then the activation level was $a = 0.0$ and the CC would produce no tension, regardless of its instantaneous length or velocity.

As will be described in a later section, the time-varying activation level was determined by processing the EMG recorded from each muscle during the Motion Analysis Sessions. While the Muscle Model and Internal Map both defined *eight* muscle-tendons of the lower leg, EMG was recorded from only *five* muscles. EMG was not recorded from all the eight of the muscles modelled since the skin surface area available on the lower leg would not easily allow the placement of eight pairs of electrodes. If all eight pairs were placed on the limited skin surface area they would likely physically interfere with subject gait and electrically interfere with each other; both situations being unacceptable.

Additionally, when electrode pairs were placed too closely together, the EMG from a certain muscle may not be recorded exclusively by the electrode pair immediately superficial to the muscle, but also by neighbouring electrode pairs. A neighbouring electrode pair would therefore be recording two or more EMG signals simultaneously. This is known as *cross talk.* When the signal recorded by an electrode pair was corrupted by cross talk, the activation level processed from that signal would be misleading since it would represent the neurological activation of two or more muscles superimposed in unknown proportions.

Fortunately, EMG did not need to be recorded from all eight muscle-tendons individually since the literature has shown that the neurological activation of certain pairs of muscles were linked (University of California, 1953, Houtz and Walsh,

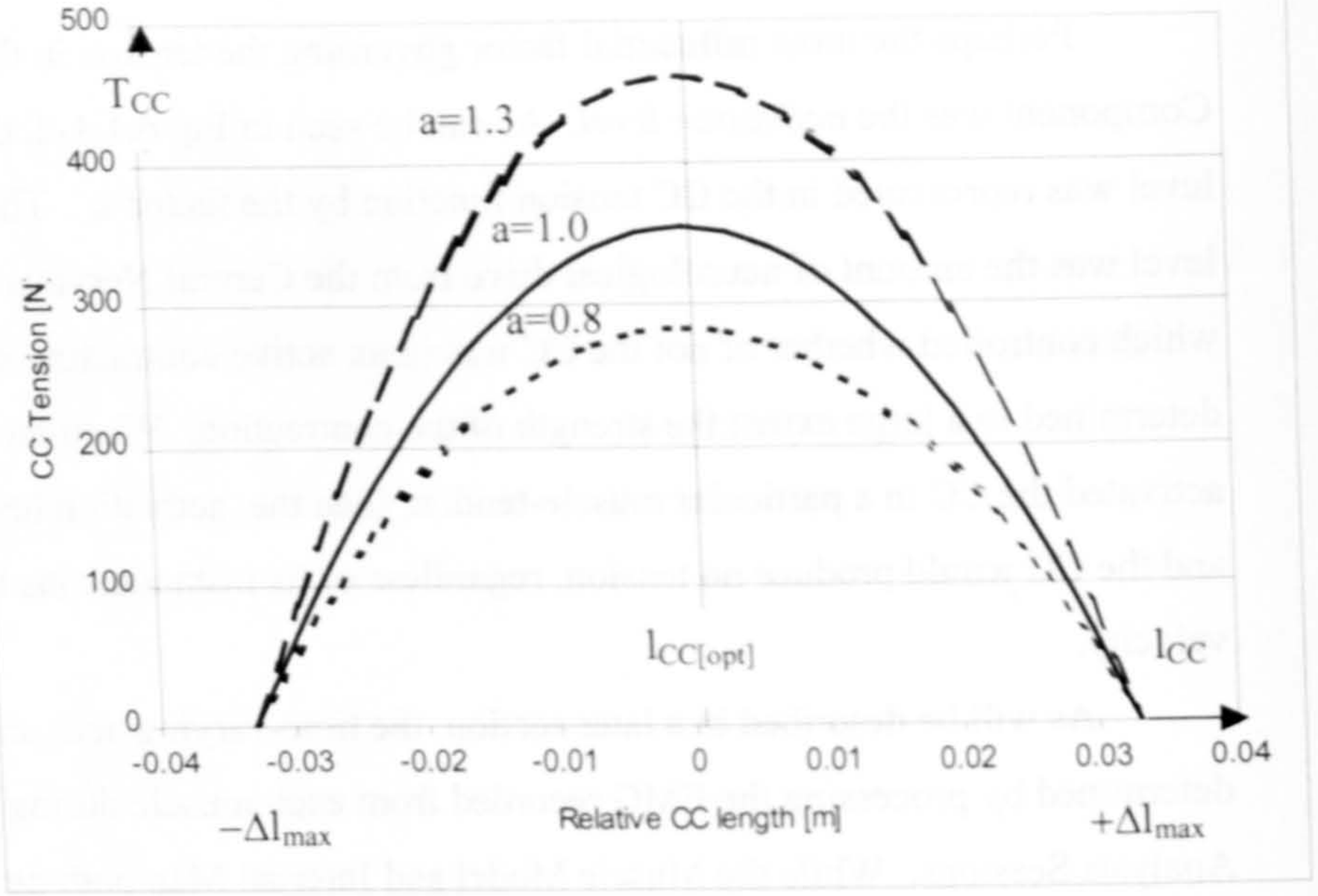

Figure 6.1.1-5 Activation level-tension Relationship of Contractile Component.

1959). Table 6.1.1-3 shows the linking of the EMG from three of the recorded muscles to the three non-recorded muscles.

The pairs of muscle-tendons which had their EMG signals linked were each similar in the functions they performed about the joints of the Ankle Complex. The Lateral and Medial Heads of the Gastrocnemius were both contained within the same muscle belly and shared an aponeurosis and tendon. The Peroneal muscles shared similar positioning and identical lever arms about the Ankle Joint. The Extensor Digitorum Longus and Extensor Hallucis Longus, although functionally distinct when manipulating the digits and hallux, were functionally identical when actuating the Ankle Joint as dorsi-flexors.

Recorded	Non-recorded
GaM	GaL
Sol	-
TiA	-
PeL	PeB
EDL	EHL

Table 6.1.1-3 Linking of EMG between Recorded and Non-recorded Muscle-tendons.

The activation level factor, a, scaled the tension of the Contractile Component linearly along the vertical axis. The active length range, defined by Δl_{max} from Eq. 6.1.1-2, was unaffected by changing the activation level. The scaling behaviour of the tension with activation level is plotted in Figure 6.1.1-5.

During the Muscle Model Calibration (MMC) trials of the Motion Analysis Sessions, the subjects performed voluntary contractions in different positions. These positions individually targeted each of the five muscles from which EMG was recorded so that one muscle-tendon was predominately contracted isometrically in each trial. For each muscle, two trials were performed where the subject contracted the target muscle at two different contraction strengths. These trials provided two

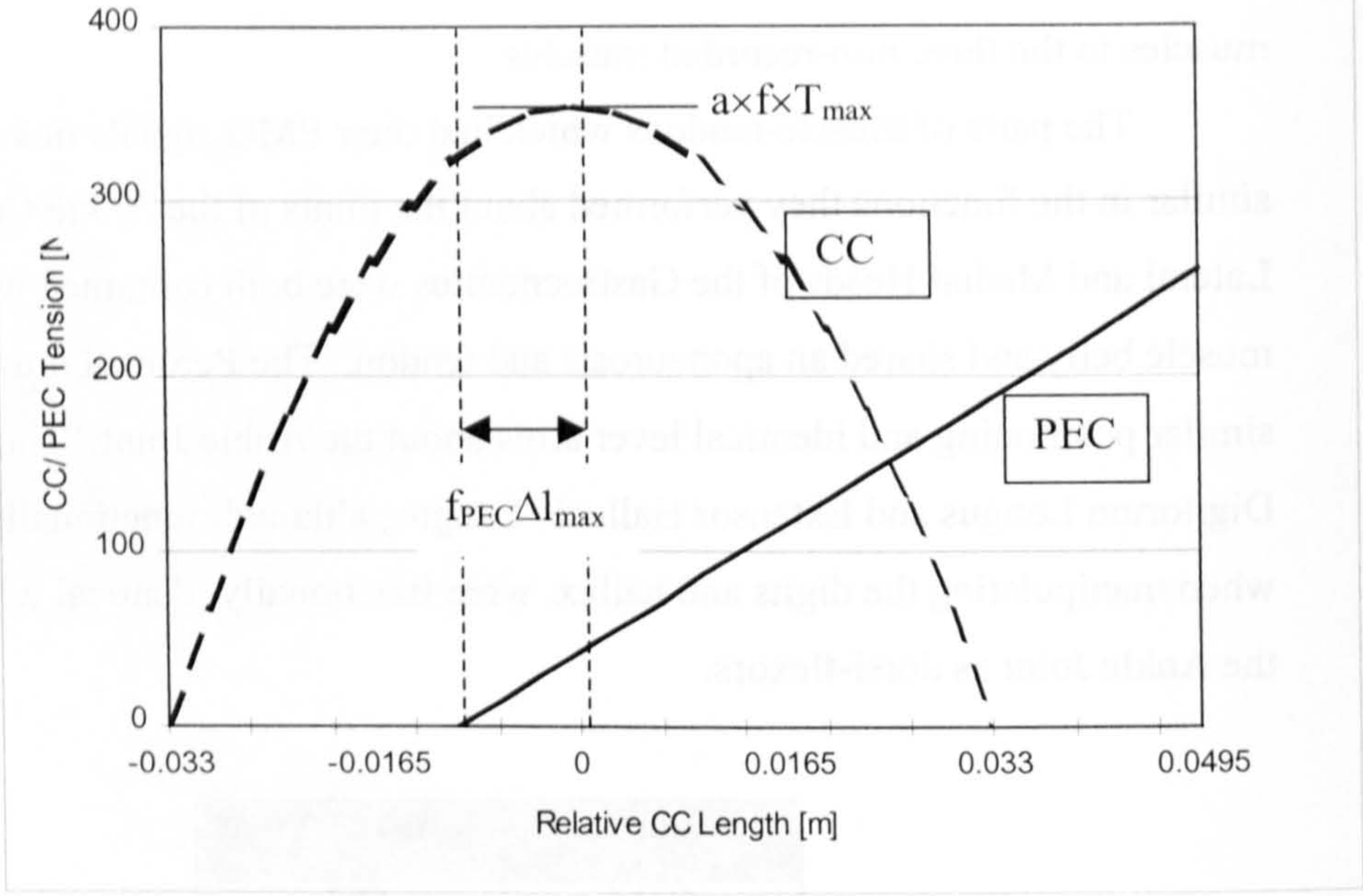

Figure 6.1.2-1 Length-tension Relationship of Parallel Elastic Component (PEC) plotted with CC Length-tension Relationship.

Reference Voluntary Isometric Contractions (RVICs) for each muscle. The EMG from each trial was processed to produce the activation level of the target muscle throughout the MMC trial. Due to the isometric nature of the RVIC, the activation level was reasonably constant throughout the trial. For each of five muscles, the activation level from one of the two RVICs was chosen as the *reference* activation level for that muscle. The RVIC chosen for each of the muscles was the one which was more constant through the trial. The reference activation *value* defined for each muscle was the average of the reference activation level over a user-defined stable range.

Thereafter, the activation levels for each of the muscles from all the other trials of the session were normalised with respect to these reference activation values. When the activation level during a Movement Task trial was the same as the reference activation value, then the activation level was normalised to $a = 1.0$. When the activation level was lower than that during the RVIC, a would drop below 1.0. When the CC was not activated at all by the Nervous System, the activation level was $a = 0.0$. Note that it was possible for the normalised activation level to be greater than 1.0 since normalisation was done with respect to a RVIC and not a Maximal Voluntary Isometric Contraction (MVIC). Reference Voluntary Isometric Contractions were used for normalising the activation levels since the neurological activation of muscle tissue lost its linear relationship with isometric tension as the maximal strength of contraction was approached (Huijing, 1995). Also, maximal contractions were unlikely to occur during the gait tasks studied. Therefore the RVICs normalised the activation levels within their linear scaling range at values experienced during locomotion.

6.1.2 Parallel Elastic Component

The muscle belly was composed of elastic tissue which held the muscle fibres together in position and which attached the muscle fibres to the tendon. Since this tissue lay parallel to the actively contracting muscle fibres, it was represented by the Parallel Elastic Component (PEC). The elastic tissue in the muscle belly produced tension passively when the muscle belly was lengthened from its rest length. The

tension developed linearly as a function of the change in length from the rest length (the relative PEC length),

$$\Delta l_{PEC} = l_{PEC} - l_{PEC[rest]} \tag{6.1.2-1}$$

The PEC tension was defined as,

$$T_{PEC} = \frac{N_{PEC}}{\sqrt{1 - N_{PEC}}} \cdot \frac{T_{\max}}{\Delta l_{\max}} \times \Delta l_{PEC} \tag{6.1.2-2}$$

Figure 6.1.2-1 shows the length-tension behaviour of the PEC. This is plotted with the CC length-tension behaviour from Figure 6.1.1-1. Note that the rest length of the PEC, $l_{PEC[rest]}$, was not necessarily equal to the optimal length of the CC, $l_{CC[opt]}$. The offset between the rest length of the PEC, $l_{PEC[rest]}$, and the optimal CC length,

Muscle	f_{PEC}
GaL	-0.3
GaM	-0.3
Sol	0.0
TiA	-0.3
PeL	0.1
PeB	0.1
EHL	0.2
EDL	0.2

Table 6.1.2-1 PEC Rest Length Offset factors for each of the eight Muscle-tendons.

$l_{CC[opt]}$, was defined by f_{PEC} which was a fraction of $\Delta l_{\max}$. The relative PEC length could therefore be related to the relative CC length as follows,

$$\Delta l_{PEC} = \Delta l_{CC} - f_{PEC} \times \Delta l_{\max} \tag{6.1.2-3}$$

Table 6.1.2-1 lists the PEC length offset factors, f_{PEC}, for the eight muscles of the Muscle Model.

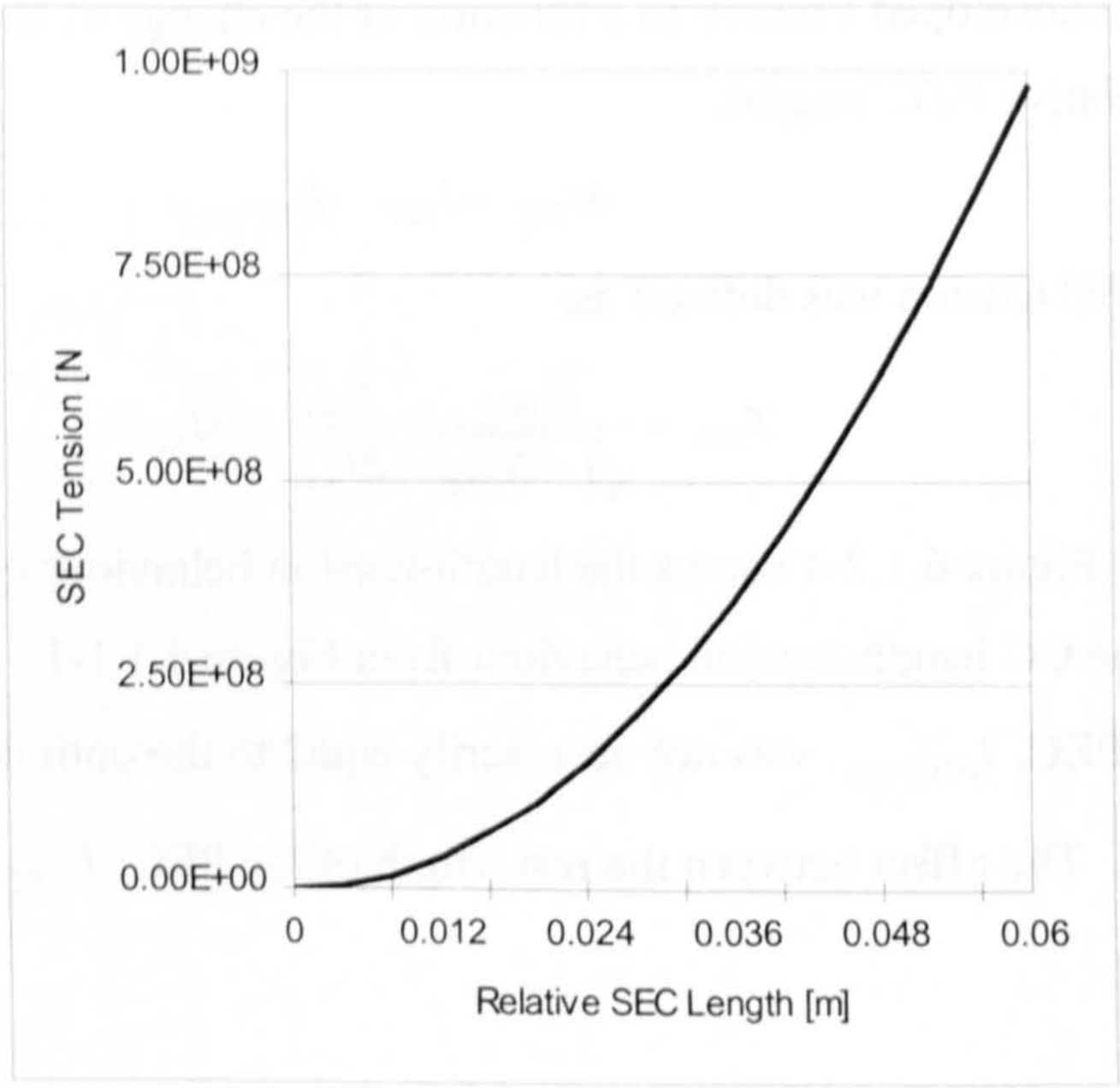

Figure 6.1.3-1 Length-tension Relationship of Series Elastic Component (SEC).

The slope of the PEC length-tension relationship was defined by the fraction N_{PEC}, and the constants $T_{\max}$ and $\Delta l_{\max}$ from the CC length-tension relationship defined in Eqs. 6.1.2-3 and 6.1.2-4. When the PEC was stretched to the point where Δl_{PEC} was equal to $\Delta l_{\max}$, then the tension in the PEC, T_{PEC}, was equal to $N_{PEC} \times T_{\max}$. This could also be written as

$$T_{PEC}(\Delta l_{PEC} = \Delta l_{\max}) = N_{PEC} \times T_{\max} \qquad (6.1.2\text{-}3)$$

For all the eight muscle-tendons of the Muscle Model, the fraction N_{PEC} was set at 1/3. Since the slope of the PEC length-tension relationship was defined by the same fraction of $T_{\max}$ for each muscle, an examination of Eq. 6.1.2-2 shows that the slope of T_{PEC} for each muscle was therefore proportional to the *PCSA* of the muscle belly.

6.1.3 Series Elastic Component

The tendon portion of the muscle-tendon system was also composed of elastic tissue. Since this tissue lay in series with the PEC and the muscle fibres of the CC, it was represented by the Series Elastic Component (SEC). The tendon tissue modelled by the SEC produced tension passively when it was stretched. Unlike the PEC, however, the SEC was *stress stiffening*. This meant that the tension did not increase linearly with elongation, but as the square of elongation. It was useful to define elongation of the SEC as the change in length with respect to its resting, zero tension length as follows,

$$\Delta l_{SEC} = l_{SEC} - l_{SEC[rest]} \qquad (6.1.3\text{-}1)$$

The SEC length-tension relationship was defined as a function of the square of Δl_{SEC} as follows,

$$T_{SEC} = \frac{k \times CSA}{l_{SEC[rest]}^2} \cdot \Delta l_{SEC}^2 \qquad (6.1.3\text{-}2)$$

where *CSA* was the average cross-sectional area of the tendon and k was the material stiffness coefficient for tendon tissue,

$$k = 3.5 \times 10^9 \text{ Pa}$$

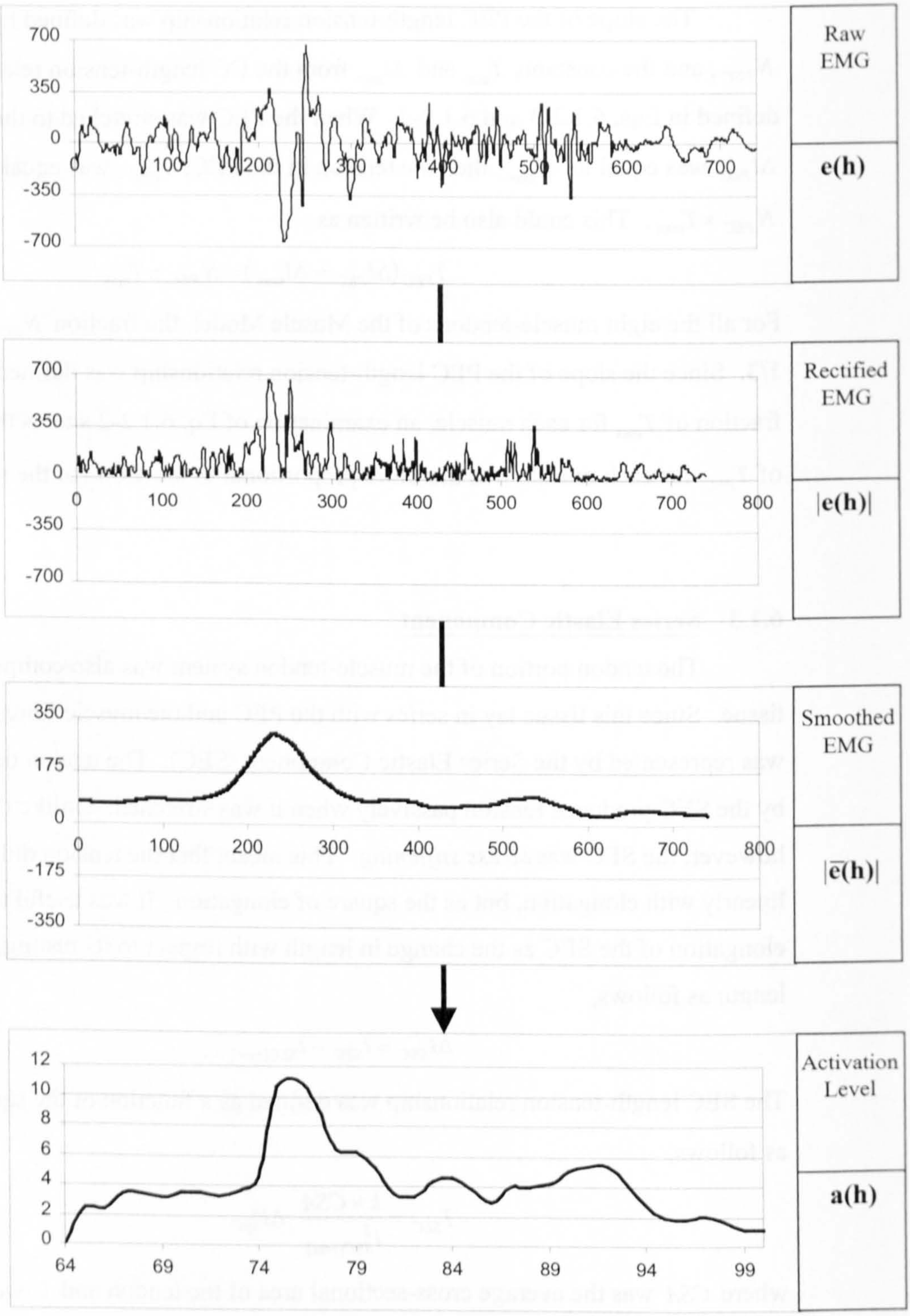

Figure 6.2-1 Stages of processing raw EMG to Muscle Activation Level.

The coefficient k was taken from the stress-strain behaviour of tendon tissue found in the literature (Van Brocklin and Ellis, 1965). The length-tension relationship for the SEC is plotted in Figure 6.1.3-1.

6.2 EMG TO ACTIVATION LEVEL PROCESSING

As mentioned in the previous section, EMG was recorded from only five of the eight muscle-tendons modelled in the Muscle Model. The first step in processing the EMG into the muscle activation levels for each of the muscle-tendons was to duplicate the EMG signals from three recorded muscles, GaM, PeL and EDL and assigning these to the linked, non-recorded muscles, GaL, PeB and EHL respectively. The linking of the recorded and non-recorded was listed in Table 6.1.2-1. The EMG signals were then passed through a bandpass filter, which attenuated frequencies below 20 Hz and above 450 Hz. Movement of the electrodes and electrode lead wires caused by the movement of the subject during gait could introduce low frequency components to the EMG (De Luca, 1997). High frequency noise could be introduced by the pre-amplifier units and by insufficient shielding on the multi-wire cable. The bandpass filter reduced the presence of these noise artefacts. The eight EMG signals were then full wave rectified.

The process for converting the rectified EMG into the muscle activation level then took place in two steps. First the signals were smoothed with a Finite Impulse Response (FIR) Averaging Filter of width of τ_1 samples. The second step applied a more complex filter. In the second step, the smoothed input signal was left unchanged when it was rising, but a falling input signal was replaced by a plateau followed by an exponential decay. Figure 6.2-1 plots the various stages of the EMG to Activation Level processing. This method of processing the raw EMG into the Activation Level was similar to that used by Hof and van Den Berg (1981a).

The rectified EMG was first smoothed using an FIR Averaging Filter. The filter had an averaging window of τ_1 samples. The window width, τ_1, in an FIR filter was effectively the same as the time constant for a Infinite Impulse (IIR) Smoothing

Filter with an identical transient response. This time constant, τ_1 governed how quickly the smoothed signal responded to rises or drops in the input signal.

The second filter, which acted on the smoothed signal, was called the *Twitch* Filter. Twitching of the input signal introduced two characteristics to the output which were governed by the time constants τ_2 and τ_3, respectively. The behaviour of the Twitching Filter had three distinct states: rising, plateau and decay. The state of the Twitching Filter depended on whether the input signal was rising or dropping. While the input was rising, the output signal was identical to the input. This was the rising state. If the input reached a maximum and then dropped below the maximum, the Twitch Filter maintained the output at the maximum, forming a plateau. The plateau was maintained for τ_2 samples unless the input signal rose above the plateau, in which case the filter would switch from the plateau state back into the rising state. After τ_2 samples, if the plateau had not been interrupted by a new rising state, the Twitch Filter entered the decay state and imposed an exponential decay on the output. The decay was characterised by the time constant, τ_3. The Twitch Filter remained in the decay state until the input rose above the decaying output signal and the filter re-entered the rising state.

The Twitch Filter response was defined as,

$$a(h) = \max\begin{cases} \left|\bar{e}(h)\right| & \textit{Rise} \\ \left|\bar{e}(h-\tau)\right| & 0 \le \tau \le \tau_2 \quad \textit{Plateau} \\ \left|\bar{e}(h-\tau_2)\right| \cdot \exp\left\{-\dfrac{\tau-\tau_2}{\tau_3}\right\} & \tau_2 \le \tau \quad \textit{Decay} \end{cases} \qquad (6.2\text{-}1)$$

The outputs from the Twitch Filter were the unnormalised muscle activation levels for each of the eight muscle-tendons.

By applying the smoothing, plateau and decays to the rectified EMG signal, the output activation level signal mimicked the electrical behaviour of the *twitch* in a group of activated muscle fibres. The Twitch Filter was used in addition to an Averaging Filter since this provided three independent time constants, τ_1, τ_2 and τ_3, with which to determine the timing of the output activation level. Due to the

different muscle architecture and histology of the eight muscle-tendons modelled, the twitch timing of the muscle fibres was individually assigned to each muscle-tendon. These three time constants allowed three degrees of freedom when fitting the twitch timing to each.

6.2.1 Determining Twitch Time Constants

The muscle fibres that make up the muscles of the human body are not all the same. Both physiologically and histologically they can vary quite remarkably in a number of ways such as their speed of contraction, susceptibility to fatigue and oxygen usage during metabolism. Biomechanically, muscle fibres could be divided into two types based on their speed of contraction: slow twitch and fast twitch fibres (Lieber, 1992 *Skeletal Muscle Structure and Function*). The speed of the twitch for these two fibres types was quite different, with the fast fibres contracting faster in response to a neurological stimulus than the slow fibres. Each of the eight muscles modelled was composed of varying proportions of these two types of fibres. The twitch timing of the whole muscle was the summation of the twitch timing of the fibres making up the muscle. Therefore the twitch timing of each muscle was a function of the proportion of fast and slow twitch fibres in the muscle.

The twitch timing for the slow and fast twitch fibres had to be estimated from the twitch timing of whole muscles since the behaviour of isolated muscle fibres found in the literature could not be reliably applied to in-vivo muscles. The twitch timing was therefore estimated from the twitch behaviour of the *Orbicularis Oculi* and *Soleus* muscles which were mostly composed of fast and slow twitch fibres, respectively.

The total twitch contraction time, τ_{total} , for a single slow twitch fibre was defined as 180 ms and for a fast twitch fibre as 55 ms (Faulkner et al., 1986, Sica and McComas, 1971, Garnett et al., 1979). The total twitch time for each fibre type was equal to the sum of the three twitch time constants,

$$\tau_{total} = \tau_1 + \tau_2 + \tau_3 \qquad (6.2.1\text{-}1)$$

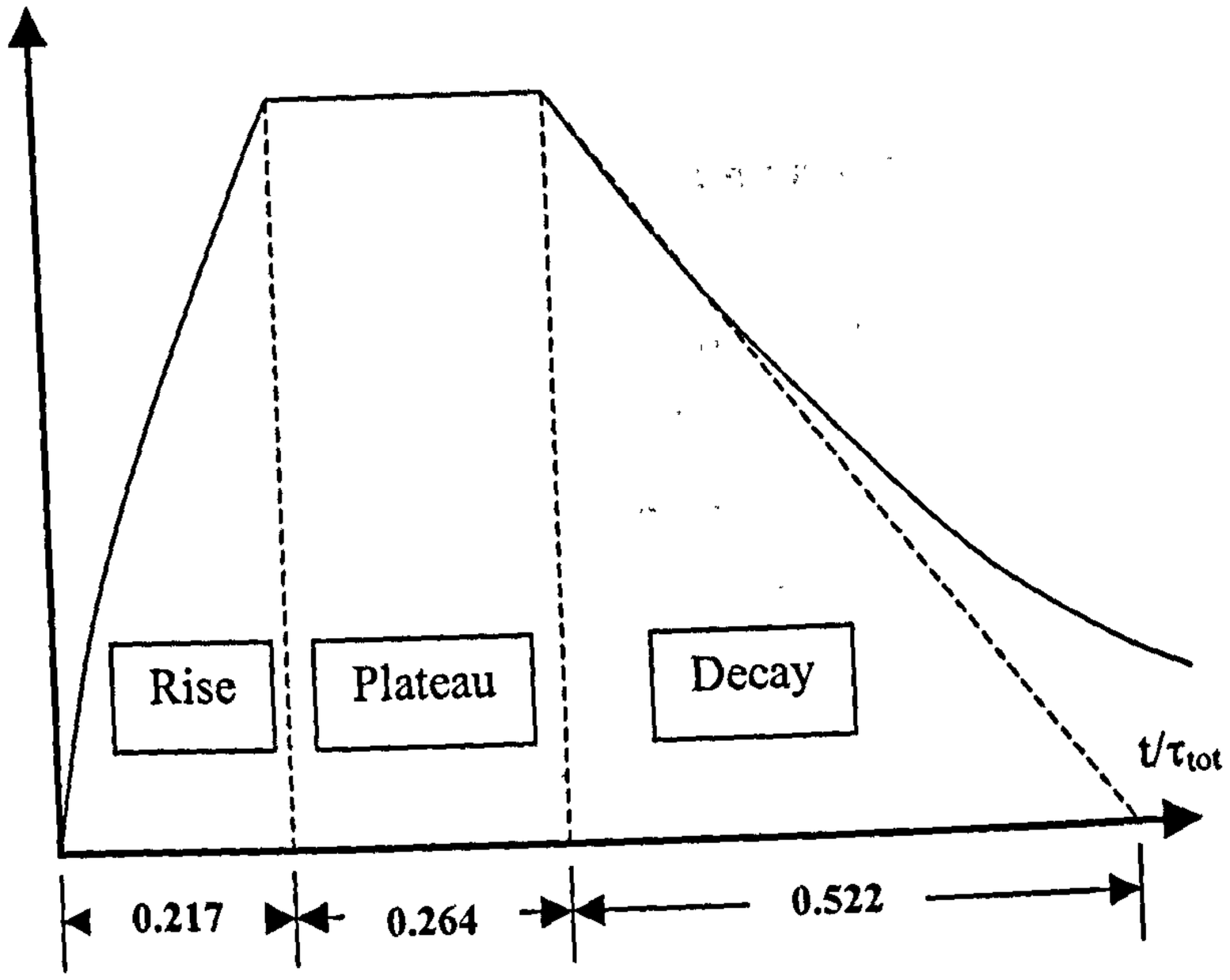

Figure 6.2.1-1 Timing template for twitch filter.

The assumption was made that the fraction of the total contraction time made up by each of the time constants was the same for both fibre types. For a total twitch time of 1.0, the *specific* time constants were,

$$\begin{aligned} \hat{\tau}_1 &= 0.217 \\ \hat{\tau}_2 &= 0.261 \\ \hat{\tau}_3 &= 0.522 \end{aligned} \qquad (6.2.1\text{-}2)$$

Figure 6.2.1-1 shows the template of twitch timing applied to both the slow and fast twitch fibres (Hof and Van den Berg, 1981a).

Muscle	proportion fast	proportion slow	τ_1 [ms]	τ_2 [ms]	τ_3 [ms]	τ_{total} [ms]
GaL	0.51	0.49	25.2	30.4	60.7	116.3
GaM	0.45	0.55	26.9	32.3	64.2	123.8
Sol	0.20	0.80	33.6	40.5	80.9	155.0
PeL	0.60	0.40	22.8	27.4	54.8	105.0
PeB	0.60	0.40	22.8	27.4	54.8	105.0
TiA	0.48	0.52	26.0	31.3	62.6	120.0
EDL	0.70	0.30	20.1	24.1	48.3	92.5
EHL	0.70	0.30	20.1	24.1	48.3	92.5

Table 6.2.1-1 Fibre composition of the eight Muscle-tendons and the consequent Twitch Time Constants.

Table 6.2.1-1 lists the proportions of fast to slow twitch fibres in each of the eight muscles modelled. These proportions were drawn from the literature (Green et al., 1981, Gollnick et al., 1974). Since the values quoted in the literature were contradictory for some muscles and absent for others, estimates of the proportions had to be used for the muscles: GaM, PeB and EDL. The total twitch contraction time for a particular muscle, $\tau_{total}(muscle)$, was found first using these proportions and the total twitch times for the two fibre types as follows,

$$\tau_{total}(muscle) = 55 \times proportion\{fast\} + 180 \times proportion\{slow\}\,[\text{ms}] \qquad (6.2.1\text{-}3)$$

The individual time constants for each of the muscles were then found using $\tau_{total}(muscle)$ and the specific time constants in Eq. 6.2.1-2,

$$\begin{aligned} \tau_1(muscle) &= 0.217 \times \tau_{total}(muscle) \\ \tau_2(muscle) &= 0.261 \times \tau_{total}(muscle) \\ \tau_3(muscle) &= 0.522 \times \tau_{total}(muscle) \end{aligned} \qquad \text{[ms]}$$

Table 6.2.1-1 also lists the time constants found for each of the eight muscles.

6.3 DETERMINING INSTANTANEOUS LENGTH

Using the kinematic data from the subject trials and employing the Internal Map as in described earlier sections, the positions of the muscle origins, pulleys and insertions for each of the eight muscles were determined within the ground frame of reference for each data sample throughout each trial. So, for each muscle at sample h within a trial, the positions of the origin, the insertion and the pulley point(s) were known,

$${}_g\underline{origin}(h)$$
$${}_g\underline{insertion}(h)$$
$${}_g\underline{pulley}(h)$$

From these positions, the instantaneous length of the muscle-tendon system could be found. For example, the instantaneous length of a muscle-tendon with a single pulley point was found as follows,

$$\begin{aligned} {}_g\vec{v}_1(h) &= {}_g\underline{origin}(h) - {}_g\underline{pulley}(h) \\ {}_g\vec{v}_2(h) &= {}_g\underline{pulley}(h) - {}_g\underline{insertion}(h) \\ l_{muscle-tendon}(h) &= \left|{}_g\vec{v}_1(h)\right| + \left|{}_g\vec{v}_2(h)\right| \end{aligned} \qquad (6.3\text{-}1)$$

It was useful to use the muscle-tendon length relative to its optimal length, as opposed to the absolute muscle-tendon length determined in Eq. 6.3-1. The relative muscle-tendon length, $\Delta l_{muscle-tendon}(h)$, was found as follows,

$$\Delta l_{muscle-tendon}(h) = l_{muscle-tendon} - l_{muscle-tendon[opt]} \qquad (6.3\text{-}2)$$

In order to find the instantaneous relative length for each muscle-tendon, the optimal length for each had to first be determined. Two pieces of information for each muscle-tendon were taken from the literature. The first was the joint position which put each muscle-tendon at its optimal length. The second was the optimal length of the muscle belly. The muscle belly optimal lengths, $l_{muscle-tendon[opt]}$, were taken from cadaver studies (Wickiewicz et al., 1983). Isometric and isokinetic studies of the moment to joint angle relationship of the ankle joint complex for stimulated and voluntarily contracted muscles determined the joint position giving optimal muscle-tendon length. In general the dorsi-flexors were at optimal length when the Ankle Joint was moderately dorsi-flexed. Plantar-flexor optimal length occurred when the Ankle Joint was moderately plantar-flexed. The exception was the Soleus muscle-tendon which was at optimal length when the Ankle Complex was in a neutral position (Wickiewicz et al., 1983).

Knowing the proper joint positions for each of the eight muscle-tendon optimal lengths, the Internal Map was numerically manipulated to place the rigid segments of the Ankle Complex into these positions. The manipulation was done by rotating the segments about the Ankle and Subtalar joint rotational axes as described in Section 4.2.5. The lengths of the appropriate muscle-tendons could then be determined from the Internal Map while it was in this proper position, yielding the optimal muscle-tendon length for each of the muscle-tendons in turn.

Using the optimal muscle-tendon length, $l_{muscle-tendon[opt]}$, and the optimal length of the muscle belly from the literature, $l_{muscle[opt]}$, the rest length for each of the tendons could then be calculated as follows,

$$l_{tendon[rest]} = l_{muscle-tendon[opt]} - l_{muscle[opt]} \qquad (6.3\text{-}3)$$

Since these muscle-tendon lengths were formed using the Internal Map, they had to be scaled to the dimensions of each of the subjects. Since each muscle-tendon ran along the long axis of the Lower Leg segment, the scaling was done using the Scale Factor for the $2-direction$ of the Lower Leg segment (recall Section 4.3.2). The scaling was done

Muscle	$l_{muscle\text{-}tendon[opt]}$ [mm]	$l_{muscle[opt]}$ [mm]	$l_{tendon[rest]}$ [mm]
GaL	491.2	217	274.2
GaM	486.3	248	238.3
Sol	421.3	310	111.3
PeL	550.2	286	264.2
PeB	359.7	230	129.7
TiA	437.6	298	139.6
EDL	506.8	355	151.8
EHL	374.7	273	101.7

Table 6.3-1 Optimal lengths of the eight Muscles and Muscle-tendons and the Rest lengths of the eight Tendons.

as follows,

$$l'_{muscle-tendon[opt]} = l_{muscle-tendon[opt]} \times^{\hat{2}} S_{LowerLeg} \qquad (6.3\text{-}4)$$

and similarly for $l'_{muscle[opt]}$ and $l'_{tendon[rest]}$.

Table 6.3-1 lists the optimal lengths of the eight muscles and muscle-tendons and the rest lengths found for each of the eight tendons.

6.4 ITERATIVE SOLUTION PROCESS

The Contractile and Parallel Elastic Components were arranged in parallel and were attached in series to the Series Elastic Component. This was illustrated in Figure 6.1-1. Given this arrangement, the lengths and tensions of each of the components were subject to the following consequent constraints,

$$T_{CC} + T_{PEC} = T_{SEC} = T_{muscle-tendon}$$
$$\Delta l_{CC} + \Delta l_{SEC} = \Delta l_{muscle-tendon} \qquad (6.4\text{-}1)$$
$$\Delta l_{CC} = \Delta l_{PEC}$$

For each of the samples in the Movement Task trials, the EMG had been processed into the muscle activation level for each of the eight muscle-tendons. The

Internal Map and Kinematic Data provided the instantaneous relative muscle-tendon lengths. The final step in the Muscle Model, given the preceding inputs, was to determine the tension in each muscle-tendon by solving simultaneously the tension equations for the three components of the muscle-tendon subject to the constraints in Eq. 6.4-1.

The first problem encountered in finding a solution was that the inputs drawn from the Kinematic Data and the Internal Map were the instantaneous relative lengths of the whole muscle-tendon, from origin to insertion, $\Delta l_{muscle-tendon}(h)$, whereas the input required by the length-tension relationship for each of the components was the length of that particular component *only*. The CC required $\Delta l_{CC}(h)$, the SEC required $\Delta l_{SEC}(h)$ and the PEC required $\Delta l_{PEC}(h)$ for Eqs. 6.1.1-2-2, 6.1.2-2 and 6.1.3-2 respectively. The constraints on the system in Eq. 6.4-1 defined four equations in terms of four unknowns. Although an analytical solution may therefore exist for this system, its form was not immediately apparent, and would likely not be of a form useful to the current purpose. For this reason, an iterative, numerical process was used to solve for $\Delta l_{CC}(h)$, $\Delta l_{SEC}(h)$, $\Delta l_{PEC}(h)$ with their associated component tensions and ultimately to solve for the instantaneous tensions in the muscle-tendon system: $T_{muscle-tendon}(h)$.

The solution to the system in Eq. 6.4-1 was approached iteratively by initially estimating the relative lengths of the CC, PEC and SEC and then calculating the consequent tensions in each of the components. The initial estimates of component length were evaluated to determine if they represented the solution to the system by comparing the tension in the SEC with the sum of the tensions in the CC and PEC. According to Eq. 6.4-1 these should be equal. If the magnitude of the difference between the two was below a threshold value, then the process was considered to have converged on the solution. If the magnitude of the difference was larger than the threshold, the estimates of the component relative length were altered and a new solution estimated. This iterative process was continued until it converged on the solution to the system.

At a sample, h, during a Movement Task trial, the relative length of a particular muscle-tendon system was known, $\Delta l_{muscle-tendon}(h)$. As an initial estimate, the relative length of the CC was set equal to this,

$$\Delta l^*_{CC} = \Delta l_{muscle-tendon}(h) \tag{6.4-2}$$

The asterisk on the relative CC length indicated the value was only an estimate. With the CC relative length estimate, the PEC and SEC relative lengths could then be estimated using Eqs. 6.1.2-3 and 6.4-1,

$$\begin{aligned} \Delta l^*_{PEC} &= \Delta l^*_{CC} - f_{PEC} \times \Delta l_{\max} \\ \Delta l^*_{SEC} &= \Delta l_{muscle-tendon}(h) - \Delta l^*_{CC} \end{aligned} \tag{6.4-3}$$

The estimated velocity of the CC could be calculated using the solution for the CC relative length from the previous sample, $\Delta l_{CC}(h-1)$, and the current estimate,

$$v^* = \Delta l^*_{CC} - \Delta l_{CC}(h-1) \tag{6.4-4}$$

Using the CC velocity-tension relationship defined in Eq. 6.1.1-6, the estimated velocity factor, f^*, for the Contractile Component was found,

$$\begin{aligned} f^* &= 1.25 && v > v_{trans} \\ f^* &= \frac{B + Av^*}{B - v^*} && v_{trams} \geq v \geq -v_{\max} \\ f^* &= 0.0 && -v_{\max} \geq v \end{aligned} \tag{6.4-5}$$

The estimated tensions in each of the three components were then found using Eqs. 6.1.1-2, 6.1.2-2 and 6.1.3-2. This yielded $T^*_{CC}\left(a(h), \Delta l^*_{CC}, f^*\right)$, $T^*_{PEC}\left(\Delta l^*_{PEC}\right)$ and $T^*_{SEC}\left(\Delta l^*_{SEC}\right)$. The difference between the tension in the SEC and the sum of the tensions in the CC and PEC was calculated,

$$diff = T^*_{SEC} - \left(T^*_{CC} + T^*_{PEC}\right) \tag{6.4-6}$$

This value was used to evaluate the current estimated tension and to determine if the iterations had converged on the solution. The value *diff* would be zero for the analytical solution. However this was unlikely to be reached by the iterative procedure. Therefore a threshold value was set, below which the magnitude of *diff* had to fall before the solution was considered converged. The threshold was set at 0.001. If the magnitude of *diff* was indeed less than this threshold for the

current iteration, then the estimates of the relative lengths for each component were output as the actual component lengths for that sample h: $\Delta l_{CC}(h)$, $\Delta l_{SEC}(h)$, $\Delta l_{PEC}(h)$. Most importantly, using Eq. 6.4-1, the muscle-tendon tension for the sample was output,

$$T_{muscle-tendon}(h) = T^{*}_{SEC} \tag{6.4-7}$$

If the magnitude of *diff* was not below the threshold, then the process had not yet converged and another iteration was required. Two things were considered when assigning a new value to the estimate of CC relative length, Δl^{*}_{CC}. First, the sign of *diff* indicated whether the estimate of Δl^{*}_{CC} was too large or too small. If *diff* was positive in sign, then the estimate was too small and Δl^{*}_{CC} was *increased* by the amount *step*. If *diff* was negative, then Δl^{*}_{CC} was *decreased* by *step*. Second, it was important to see if the sign of *diff* in its current iteration was the same as its sign in the previous iteration. If the sign of *diff* was currently the same as it was previously, then the two iterations were approaching the solution from the same direction. If the sign had changed from the previous iteration, then the solution had been overshot, and the iterative procedure had reversed itself in direction. This had an influence on the size of *step* when reassigning Δl^{*}_{CC} for the next iteration. If the signs of *diff* in the current iteration and the previous iteration were the same and the iterations were approaching from the same direction, then *step* could be kept the same. If, however, the iterations had overshot the solution, then *step* had to be changed for the next iteration. Otherwise, an infinite loop would occur in the iteration process. If the signs were different and the solution had indeed been overshot, then *step* was reduced as follows,

$$step = 0.55 \times step \tag{6.4-8}$$

The fraction 0.55 was chosen since this produced a more stable and more quickly converging iterative procedure than the fraction 0.5.

This iterative procedure was applied to each of the eight muscles of the Muscle Model for each of the data samples, h, throughout the Movement Task trials. The output from this numerical procedure was primarily the muscle-tendon tension,

$T_{muscle-tendon}(h)$, and secondarily the instantaneous relative lengths and tensions of each of the three constituent components.

6.5 CALIBRATING THE MUSCLE MODEL

Recall in Section 6.1.1, a calibration factor, s, was defined in Eq. 6.1.1-3 for each of the muscle-tendons of the Muscle Model. This factor was required for calibrating the Muscle Model for two reasons. First, there was a significant variability in the placement of the electrodes between subjects. Second, there was a significant anatomical variability between subjects in the positions of the muscles of the lower leg and in the composition of the tissues present within the muscle belly and between the muscle belly and the recording electrode surfaces.

The magnitude of the surface EMG signal recorded from each muscle was greatly influenced by the distance between the muscle fibres and the recording electrode surfaces. The signal was also influenced by the electrical properties of the tissues between the electrodes and the muscle. Since neither of these factors could be controlled nor quantified using anatomical data, the relationship between the magnitude of the activation level determined from the EMG signal and the muscle-tendon tension would be unknown without calibration. The factor s within the Contractile Component tension governing equation accounted for this EMG to tension relationship. Since this relationship was different for each subject, these factors had to be determined individually for each subject. The Muscle Model Calibration (MMC) trials were used to determine the values for these factors.

During an MMC trial, the subject contracted the muscles of the lower leg isometrically. Due to the subject positioning, one or two of the five recorded muscles was contracted with significantly greater tension than the others. During the trial, the EMG signals for the five muscles were recorded. The positions of the segments of the Ankle Complex were tracked and the force exerted on Force Plate #1 was recorded. The EMG signals from the recorded muscle-tendons were linked to the non-recorded muscle-tendons as described in Section 6.1.1, yielding eight EMG signals. The EMG signal for each muscle-tendon, m, was processed into the

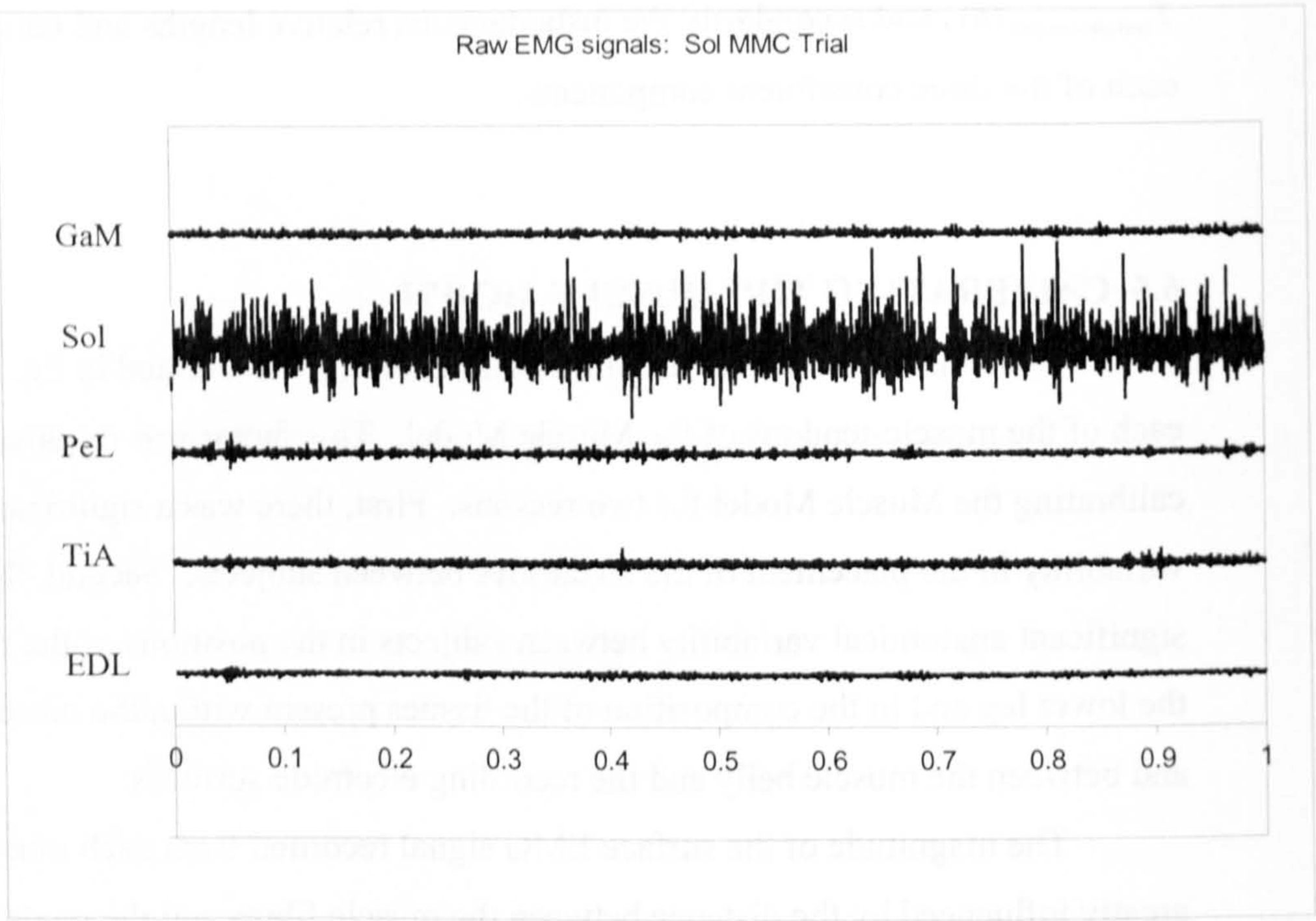

Figure 6.5.-1 Raw EMG signals recorded from the five recorded muscles: Sol, GaM, PeL, TiA and EDL during the Soleus Muscle Model Calibration trial. This is characteristic of a single-muscle calibration trial.

activation level, $a\{m\}(h)$, for each sample of the trial, using the method in Section 6.2. The Force Plate data was processed to produce the Ground Reaction Force, $\underline{F}(h)$, and the centre of pressure, $\underline{x}_{cp}(h)$, with which the Force Plate resisted subject exertion (Section 3.1.3).

Recall from Table 3.3.2-1 in Section 3.3.2 that of the five different MMC trials, three of the trials preferentially contracted a single muscle (i.e. Sol, PeL and EDL) while two of the trials contracted multiple muscles (i.e. GaM+GaL+Sol and TiA+EDL). The calibration procedure was carried out on the three single-muscle trials first: Sol, PeL and EDL. This yielded the calibration factors, s_i, for these three individual muscles. Once these muscles had been calibrated, the tensions in these muscles could be calculated using the Muscle Model as described in the previous section during the remaining two, multi-muscle MMC trials. The order in which the eight muscles were calibrated from a complete set of MMC trials is listed in Table 6.5-1.

	Muscle(s) Calibrated	**MMC Trial used**	**Other muscles involved**
1st	Sol	**Sol**	-
2nd	PeL+PeB	**PeL**	-
3rd	EDL+EHL	**EDL**	-
4th	GaM+GaL	**GaM**	Sol
5th	TiA	**TiA**	EDL+EHL

Table 6.5-1 The order in which the eight muscles were calibrated from a complete set of MMC trials.

The soleus muscle was calibrated first. An example of the EMG signals recorded during an Soleus MMC trial from each of the five recorded muscles is shown in Figure 6.5-1. Since the Sol muscle alone was contracting, its calibration factor alone was determined. The PeL and EDL muscles were then similarly calibrated. In these two latter cases, however, the EMG from these muscles was

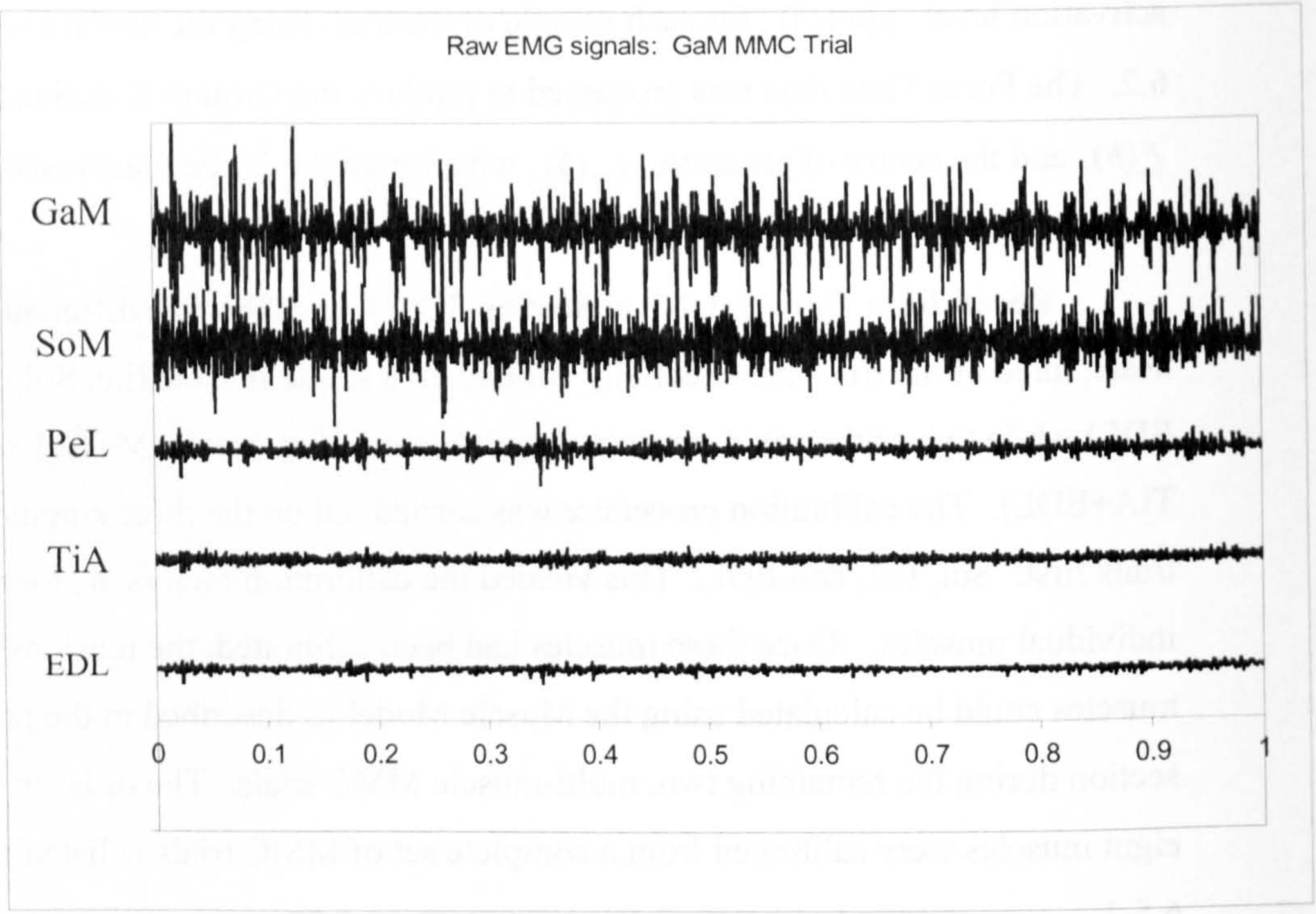

Figure 6.5.-2 Raw EMG signals recorded from the five recorded muscles: Sol, GaM, PeL, TiA and EDL during the GaM Muscle Model Calibration trial. This is characteristic of a multi-muscle calibration trial.

linked to two non-recorded muscles: PeB and EHL, respectively. Therefore, these two additional muscles were also calibrated as will be described later in this section.

The remaining two MMC trials that had yet to be used: GaM and TiA, involved the preferential contraction of more than one muscle. These were the GaM, GaL and Sol during the GaM trial and TiA, EDL and EHL in the TiA trial. The raw EMG from each of the five muscles recorded during a GaM MMC trial is plotted in Figure 6.5-2. However, since the Sol, EDL and EHL had been already calibrated in the previous trials, the tension in these muscles could be calculated during the GaM and TiA trials using the Muscle Model.

The joint rotational axes for the Ankle Joint and the Subtalar Joint were attached to the Lower Leg and Hindfoot segments respectively. The Talus segment lay in between these two segments and therefore marked the division between *leg* segments and the *foot* segments. Each of the muscle-tendons acted to move the foot segments with respect to the leg segments by rotating them about the two joint rotational axes of the Ankle Complex. The muscle attachments, the origins, pulleys and insertions, were therefore divided into those on leg segments and those on foot segments. The attachments for each of the muscle-tendons and their assignments to either leg or foot segments are listed in Table 6.5-2.

The positions of the origins, pulley points and insertions for each of the muscle-tendons were determined in the ground frame for each sample throughout the trial using the Kinematic Data and the Internal Map. These positions yielded a number of quantities. As in Section 6.3, the instantaneous lengths of the *eight* muscle-tendons of the Muscle Model were found, $l\{m\}_{muscle-tendon}(h)$, which were converted into the instantaneous relative lengths, $\Delta l\{m\}_{muscle-tendon}(h)$. Two important vectors were determined in addition to these for each muscle-tendon; the instantaneous *lever arms*, $\vec{d}\{m\}(h)$, and the instantaneous *lines of action*, $\vec{l}\{m\}(h)$. These two vectors were each found slightly differently for each of the muscle-tendons due to the differing number of pulley points each possessed.

Two lever arms were found for each of the muscle-tendons, one acting about the Ankle Joint and one about the Subtalar Joint. The lever arm, $\vec{d}\{m\}(h)$, in each case was defined as the vector which pointed from the joint rotational axis to the most proximal muscle-tendon attachment on a foot segment. The line of action for each muscle-tendon, $\vec{l}\{m\}(h)$, was defined as the vector pointing from the most

Muscle	Leg Segment attachments	Foot Segment attachments	Lever Arms $\vec{d}\{m\}$	Line of Action $\vec{l}\{m\}$
GaL	$\underline{o}_{GaL}$	$\underline{i}_{GaL}$	$\underline{i}_{GaL} - \underline{lat}$	$\underline{o}_{GaL} - \underline{i}_{GaL}$
			$\underline{i}_{GaL} - \underline{post}$	
GaM	$\underline{o}_{GaM}$	$\underline{i}_{GaM}$	$\underline{i}_{GaM} - \underline{lat}$	$\underline{o}_{GaM} - \underline{i}_{GaM}$
			$\underline{i}_{GaM} - \underline{post}$	
Sol	$\underline{o}_{Sol}$	$\underline{i}_{Sol}$	$\underline{i}_{Sol} - \underline{lat}$	$\underline{o}_{Sol} - \underline{i}_{Sol}$
			$\underline{i}_{Sol} - \underline{post}$	
TiA	$\underline{o}_{TiA}$, $\underline{p1}_{TiA}$	$\underline{i}_{TiA}$	$\underline{i}_{TiA} - \underline{lat}$	$\underline{p1}_{TiA} - \underline{i}_{TiA}$
			$\underline{i}_{TiA} - \underline{post}$	
PeL	$\underline{o}_{PeL}$, $\underline{p1}_{PeL}$	$\underline{p2}_{PeL}$, $\underline{i}_{PeL}$	$\underline{p2}_{PeL} - \underline{lat}$	$\underline{p1}_{PeL} - \underline{p2}_{PeL}$
			$\underline{p2}_{PeL} - \underline{post}$	
PeB	$\underline{o}_{PeB}$, $\underline{p1}_{PeB}$	$\underline{i}_{PeB}$	$\underline{i}_{PeB} - \underline{lat}$	$\underline{p1}_{PeB} - \underline{i}_{PeB}$
			$\underline{i}_{PeB} - \underline{post}$	
EHL	$\underline{o}_{EHL}$, $\underline{p1}_{EHL}$	$\underline{p2}_{EHL}$, $\underline{i}_{EHL}$	$\underline{p2}_{EHL} - \underline{lat}$	$\underline{p1}_{EHL} - \underline{p2}_{EHL}$
			$\underline{p2}_{EHL} - \underline{post}$	
EDL	$\underline{o}_{EDL}$, $\underline{p1}_{EDL}$	$\underline{p2}_{EDL}$, $\underline{i}_{EDL}$	$\underline{p2}_{EDL} - \underline{lat}$	$\underline{p1}_{EDL} - \underline{p2}_{EDL}$
			$\underline{p2}_{EDL} - \underline{post}$	

Table 6.5-2 Attachments, Lever Arms and Lines of Action for the eight Muscle-tendons.

proximal foot segment attachment to the most distal leg segment attachment. The two vectors defining the lever arms and the lines of action vectors for each of the muscle-tendons are listed in Table 6.5-2.

The Kinematic Data and Internal Map also gave the positions of the points which defined the two joint-fixed reference frames: $\underline{lat}(h)$, $\underline{med}(h)$, $\underline{FH}(h)$, and $\underline{ant}(h)$, $\underline{post}(h)$, $\underline{MiH}(h)$. Using the method in Section 4.2.2, the joint-fixed reference frames for the Ankle and Subtalar Joints were created. The vectors representing the Ground Reaction Force, $\underline{F}(h)$, the lever arms, $\vec{d}\{m\}(h)$, and lines of action, $\vec{l}\{m\}(h)$, were rotated into two joint-fixed frames. The centre of pressure position, $\underline{x}_{cp}(h)$, was also transformed into each of the two joint frames. The centre of pressure was used to determine the lever arms of the GRF about each of the two joint rotational axes as follows,

$$\begin{aligned} {}_{Ankle}\vec{d}\{GRF\}(h) &= {}_{Ankle}\underline{x}_{CP}(h) - {}_{Ankle}\underline{lat}(h) \\ {}_{Subtalar}\vec{d}\{GRF\}(h) &= {}_{Subtalar}\underline{x}_{CP}(h) - {}_{Subtalar}\underline{post}(h) \end{aligned} \qquad (6.5\text{-}1)$$

The factors, s, for each of the muscles in the Muscle Model were determined by balancing the moments about the two joint rotational axes caused by the externally applied GRF and the internally applied muscle-tendon tensions. As will be described in Section 7.3, the muscle-tendons alone were considered responsible for balancing the externally applied moments about the two joint rotational axes. The ligaments were assumed to exert moments only about the other axes in each of the two joint-fixed frames.

A stable range was chosen within each MMC trial where the GRF, centre of pressure and activation level were constant. Over this range the average values for $\underline{F}$, $\vec{d}\{GRF\}$, $a\{m\}$, $\Delta l\{m\}_{muscle-tendon}$, $\vec{d}\{m\}$ and $\vec{l}\{m\}$ were calculated within both the Ankle-fixed and Subtalar-fixed reference frames. These average values were then used for the calibration procedure.

The moments due to the GRF were found as follows,

$$\begin{aligned} {}_{Ankle}\underline{M}\{GRF\} &= {}_{Ankle}\vec{d}\{GRF\} \times {}_{Ankle}\underline{F} \\ {}_{Subtalar}\underline{M}\{GRF\} &= {}_{Subtalar}\vec{d}\{GRF\} \times {}_{Subtalar}\underline{F} \end{aligned} \qquad (6.5\text{-}2)$$

The equations in Eq. 6.5-2 calculated the moments about all three axes in the joint-fixed frames. Only the moments about the joint rotational axes were needed. Therefore only the $2-axis$ component of $\underline{M}\{GRF\}$ was needed,

$$
\begin{aligned}
&{}^{\hat{2}}_{Ankle}M\{GRF\} \\
&{}^{\hat{2}}_{Subtalar}M\{GRF\}
\end{aligned}
$$

where the superscripted $\hat{2}$ represents the $2-axis$ component.

In order to calculate the moments generated by the muscle-tendon tensions, the *moment potentials* for each muscle-tendon were found. The moment potential for the muscle-tendon m was,

$$
\begin{aligned}
{}_{Ankle}\vec{dl}\{m\}_x &= {}_{Ankle}\vec{d}\{m\}\times {}_{Ankle}\vec{l}\{m\} \\
{}_{Subtalar}\vec{dl}\{m\}_x &= {}_{Subtalar}\vec{d}\{m\}\times {}_{Subtalar}\vec{l}\{m\}
\end{aligned}
\qquad (6.5\text{-}3)
$$

If the tension in the muscle-tendon, m, was $T\{m\}_{muscle-tendon}$, then the moments caused by that muscle-tendon were,

$$
\begin{aligned}
{}_{Ankle}\underline{M}\{m\} &= {}_{Ankle}\vec{dl}\{m\}_x \cdot T\{m\}_{muscle-tendon} \\
{}_{Subtalar}\underline{M}\{m\} &= {}_{Subtalar}\vec{dl}\{m\}_x \cdot T\{m\}_{muscle-tendon}
\end{aligned}
\qquad (6.5\text{-}4)
$$

The moments about the joint rotational axes due to muscle-tendon m were therefore the $2-axis$ components from Eq. 6.5-4,

$$
\begin{aligned}
{}^{\hat{2}}_{Ankle}M\{m\} &= {}^{\hat{2}}_{Ankle}\vec{dl}\{m\}_x \cdot T\{m\}_{muscle-tendon} \\
{}^{\hat{2}}_{Subtalar}M\{m\} &= {}^{\hat{2}}_{Subtalar}\vec{dl}\{m\}_x \cdot T\{m\}_{muscle-tendon}
\end{aligned}
\qquad (6.5\text{-}5)
$$

The moment balance between the external GRF moments and the internal muscle-tendon moments was therefore constructed as,

$$
\begin{aligned}
0 &= {}^{\hat{2}}_{Ankle}M\{GRF\} + \sum_{m=1}^{8} {}^{\hat{2}}_{Ankle}M\{m\} \\
0 &= {}^{\hat{2}}_{Subtalar}M\{GRF\} + \sum_{m=1}^{8} {}^{\hat{2}}_{Subtalar}M\{m\}
\end{aligned}
\qquad (6.5\text{-}6)
$$

Since there were eight muscle-tendons causing moments about the two joints, the system in Eq. 6.5-6 represented an indeterminate system of eight unknowns and only two equations. This indeterminacy presented a problem in how to partition the moment contributions of each muscle-tendon, which would assign the tensions to each muscle-tendon. The Three Component Muscle Model could be used to

determine the tension in the muscle-tendons that had been thus far calibrated. However, for each of the five MMC trials, the system was still indeterminate about the $2-axis$. A major assumption therefore had to be made in order to overcome the indeterminacy of the system. The assumption made was that the tension in each of the uncalibrated muscle-tendons was assumed to be proportional to its activation level, $a\{m\}$, the Physiological Cross-sectional Area, $PCSA\{m\}$ and to the instantaneous muscle-tendon length, $\Delta l\{m\}_{muscle-tendon}$ as follows,

$$T\{m\}_{muscle-tendon} = a\{m\} \times PCSA\{m\} \times SF \times \left(1 - \frac{\Delta l\{m\}^2_{muscle-tendon}}{\Delta l\{m\}^2_{\max}}\right) \times q \quad (6.5\text{-}7)$$

where q was the proportionality factor. This assumption considered each muscle-tendon to behave as a single component system, with only a contractile component. The proportionality factor was included to account for the absence of any elastic components. The factor q was assumed to be constant and equal for all eight muscle-tendons. With this assumption, the Eqs. 6.5-7 and 6.5-5 could then be inserted into the two equations in Eq. 6.5-6 and solved for the factor q.

The tensions in each of the muscle-tendons calibrated thus far were calculated using the Muscle Model as described in the previous section. The moment contributions of these muscles about the $2-axis$ were then found using Eqns. 6.5-5. This yielded known moment contributions from j muscle-tendons about the Ankle and Subtalar Joints: ${}_{Ankle}M\{m\}_{calibrated}$ and ${}_{Subtalar}M\{m\}_{calibrated}$. The j known muscle-tendon moments were summed with the known moment due to the GRF. The remaining 8-j muscle-tendons were summed in the denominator of Eqn. 6.5-8. Two values of q were found this way, one from the balance about the Ankle Joint and the other about the Subtalar Joint,

$$
{}_{Ankle}q = \frac{-{}_{Ankle}^{\hat{2}}M\{GRF\} - \sum_{m=1}^{j} {}_{Ankle}^{\hat{2}}M\{m\}_{calibrated}}{\sum_{m=1}^{8-j}\left[{}_{Ankle}^{\hat{2}}\vec{dl}\{m\}_x \cdot a\{m\} \times PCSA\{m\} \times SF \times \left(1 - \frac{\Delta l\{m\}^2_{muscle-tendon}}{\Delta l\{m\}^2_{\max}}\right)\right]}
$$

$$
{}_{Subtalar}q = \frac{-{}_{Subtalar}^{\hat{2}}M\{GRF\} - \sum_{m=1}^{j} {}_{Subtalar}^{\hat{2}}M\{m\}_{calibrated}}{\sum_{m=1}^{8-j}\left[{}_{Subtalar}^{\hat{2}}\vec{dl}\{m\}_x \cdot a\{m\} \times PCSA\{m\} \times SF \times \left(1 - \frac{\Delta l\{m\}^2_{muscle-tendon}}{\Delta l\{m\}^2_{\max}}\right)\right]}
$$

(6.5-8)

It should be noted that the moment contributions from all the uncalibrated muscle-tendons were included in the denominator in Eqns. 6.5-8 for all the MMC trials. Even for the single-muscle trials when a single muscle was contracting and all the remaining muscles were near quiescence, the activation levels for all the uncalibrated muscle-tendons were calculated and included in Eqns. 6.5-8. In the case of multi-muscle MMC trials, the moment contributions from two or three muscles were significant while the remaining muscles were near quiescence. However, with the assumption of a constant proportionality constant, q, the moments are partitioned among all the uncalibrated muscles. Therefore in a multi-muscle MMC trial, the contribution of none of the significantly contracting muscles is ignored.

If the assumption that the proportionality factor q in all the uncalibrated muscle-tendon tensions was constant, then the values of q determined from the balancing of moments about the two separate joint rotational axes should be equal (i.e. ${}_{Ankle}q = {}_{Subtalar}q$). This was not the case, however the two values were usually within 10% of each other. This indicated that, while the assumption used to partition the muscle-tendon moments was not entirely correct, it was nonetheless reasonable.

As will be described in a later section, the weakness of the constant proportionality factor assumption was mitigated by correcting the muscle-tendon tensions later, during the Movement Task trials, so that they produced moment equilibrium about the joint rotational axes for each sample of the trial.

To account for the slight discrepancy in the values of ${}_{Ankle}q$ and ${}_{Subtalar}q$, the average value of the two was used for the remainder of the calibration process,

$$\bar{q} = \frac{1}{2}\left({}_{Ankle}q + {}_{Subtalar}q\right) \tag{6.5-9}$$

Using this value for the proportionality factor, the tensions of each of the eight muscle-tendons to be calculated were found using Eq. 6.5-7,

$$T\{m\}_{muscle-tendon} = a\{m\} \times PCSA\{m\} \times SF \times \left(1 - \frac{\Delta l\{m\}^2_{muscle-tendon}}{\Delta l\{m\}^2_{\max}}\right) \times \bar{q} \tag{6.5-10}$$

Once this had been completed, the moment contributions of each of the uncalibrated muscle-tendons had been partitioned. The next step in the calibration process was to apply these tensions to the Three Component Muscle Model System. The muscle-tendon system was solved in the reverse order compared to the process described in Section 6.4. Rather than using the instantaneous relative length of the muscle-tendon as the input and solving for the tensions in each of the three components and then the tension of the muscle-tendon system, it was the tension of the system which served as the input.

Consider the muscle-tendon, m. The tension in this muscle-tendon system was known from the partitioning of the moments, $T\{m\}_{muscle-tendon}$. Using one of the constraints on the three component system stated in Eq. 6.4-1, the SEC tension was found,

$$T\{m\}_{muscle-tendon} = T\{m\}_{SEC} \tag{6.5-11}$$

This was then used in a rearranged Eq. 6.1.3-12 to solve for the SEC relative length,

$$\Delta l\{m\}_{SEC} = \sqrt{\frac{T\{m\}_{SEC} \cdot l\{m\}^2_{SEC[rest]}}{k \cdot CSA\{m\}}} \tag{6.5-12}$$

Using another constraint from Eq. 6.4-1 and Eq. 6.1.2-3, the relative lengths of the CC and the PEC were found,

$$\begin{aligned} \Delta l\{m\}_{CC} &= \Delta l\{m\}_{muscle-tendon} - \Delta l\{m\}_{SEC} \\ \Delta l\{m\}_{PEC} &= \Delta l\{m\}_{CC} - f\{m\}_{PEC} \cdot \Delta l\{m\}_{\max} \end{aligned} \tag{6.5-13}$$

The PEC tension was then found using Eq. 6.1.2-2,

$$T\{m\}_{PEC} = \frac{N_{PEC}}{\sqrt{1 - N_{PEC}}} \cdot \frac{T\{m\}_{\max}}{\Delta l\{m\}_{\max}} \cdot \Delta l\{m\}_{PEC} \tag{6.5-14}$$

Once the tensions in the PEC and the SEC were known, a third constraint from Eq. 6.4-1 was used to find the CC tension,

$$T\{m\}_{CC} = T\{m\}_{SEC} - T\{m\}_{REC} \tag{6.5-15}$$

The equation governing isometric CC tension, which included the calibration factor for the muscle-tendon m, $s\{m\}$, could then be recalled from Eq. 6.1.1-2 and 6.1.1-3,

$$T\{m\}_{CC} = a\{m\} \cdot T\{m\}_{\max} \cdot \left(1 - \frac{\Delta l\{m\}_{CC}^2}{\Delta l\{m\}_{\max}^2}\right) \tag{6.5-16}$$

where $T\{m\}_{\max} = s\{m\} \cdot PCSA\{m\} \cdot SF$. Finally, the two relationships involving the CC tension in Eqs. 6.5-15 and 6.5-16 were equated and rearranged to solve for the calibration factor as follows,

$$s\{m\} = \frac{T\{m\}_{SEC} - T\{m\}_{PEC}}{a\{m\} \cdot T\{m\}_{\max} \cdot \left(1 - \frac{\Delta l\{m\}_{CC}^2}{\Delta l\{m\}_{\max}^2}\right)} \tag{6.5-17}$$

After the muscle-tendon moments had been partitioned, this procedure was performed on the muscle-tendons which were to be calibrated from the particular MMC trial (i.e. TiA from the TiA MMC trial or GaM and GaL from the GaM MMC trial). Once this had been done, the Muscle Model was calibrated to a specific subject.3

CHAPTER 7 JOINT AND LIGAMENT LOADING EQUILIBRIUM

7.1 JOINT INDETERMINACY

The aim of the Ankle Complex Model developed in the present study was to determine the loading experienced by the internal structures of the Ankle Complex during the stance phase of walking and walking turn. The Internal Map defined the positions and geometries of the internal structures of the Ankle Complex. The Kinematic Data collected during the Motion Analysis experiments provided the externally observed motion of the seven rigid segments of the Ankle Complex during these two movements tasks as well as the externally applied loading on the foot segments from the Ground Reaction Force. With the Internal Map, the Kinematic Data and the external loading, the Ankle Complex Model sought the solution for equilibrium between internal and external loading.

Each of the two joints that made up the Ankle Complex, the Ankle Joint and the Subtalar Joint, possessed six degrees of freedom which were constrained by the structures of the Ankle Complex. Each of the joints could bear *forces* in the three separate spatial dimensions and could bear *moments* about the three spatial dimensions. Equilibrium of the Ankle Complex was achieved when the internal and external loading was balanced about each of the degrees of freedom simultaneously. The *six* degrees of freedom about each joint therefore supplied *twelve* independent equilibrium equations in total, which needed to be solved simultaneously. A system of twelve simultaneous equations for the twelve degrees of freedom could determine the values of twelve independent unknowns within the system. The unknowns of the system were the loads in each of the internal structures of the Ankle Complex.

There were three types of internal structure in the Ankle Complex: muscle-tendons, ligaments and surfaces. All of these structures were likely to be loaded during the Movement Tasks and therefore each of these structures represented unknowns in the Ankle Complex system of equilibrium equations. Table 7.1-1 lists all the internal structures involved in the equilibrium of the Ankle Complex. Within the Internal Map, eight separate muscle-tendons, twelve separate ligaments and

seven pairs of surfaces were defined. Each of the muscle-tendons and ligaments carried an unknown tension during joint equilibrium and each of the seven surface

Structure Type	Group	Structure Name	Label
Muscles	Calf	Lateral Head of Gastrocnemius	GaL
		Medial Head of Gastrocnemius	GaM
		Soleus	Sol
	Anterior	Tibialis Anterior	TiA
		Extensor Hallicus Longus	EHL
		Extensor Digitorum	EDL
	Peroneal	Peroneus Longus	PeL
		Peroneus Brevis	PeB
Ligaments	Lateral	Anterior Talofibular	L-Ant
		Calcaneofibular	L-Mid
		Posterior Talofibular	L-Post
	Medial (Deltoid)	Anterior Talotibial	M-Ant
		Calcaneotibial	M-Mid
		Posterior Talotibial	M-Lat
		Tibionavicular	M-Nav
	Subtalar	Cervical	Cerv
		Medial Interosseus	M-IO
		Lateral Interosseus	L-IO
		Medial Talocalcaneal	M-Tc
		Posterior Talocalcaneal	P-Tc
Surfaces	Tibiofibular Mortice	Lateral Malleolar	L-MalM
		Lateral Mortice	L-Mort
		Medial Mortice	M-Mort
		Medial Malleolar	M-MalM
	Talar Trochlea	Lateral Malleolar	L-MalT
		Lateral Trochlear	L-Troch
		Medial Trochlear	M-Troch
		Medial Malleolar	M-MalT
	Inferior Talus	Posterior Talocalcaneal	Post
		Middle Talocalcaneal	Mid
		Talar Head	Head
	Superior Calcaneus	Posterior Talocalcaneal	Post
		Middle Talocalcaneal	Mid
		Navicular Socket	Socket

Table 7.1-1 The Internal Structures of the Ankle Complex defined in the Internal Map.

pairs experienced an unknown compression. If all of these structures were considered to be loaded during equilibrium, then they introduced twenty-seven unknowns to the system of equations. The Ankle Complex system of twelve simultaneous equations was only able to solve for twelve unknowns, therefore the Ankle Complex was *mathematically indeterminate.*

The Muscle Model determined the tensions in the eight muscle-tendons using the Kinematic Data and EMG signals as inputs. This removed the eight muscle-tendon tension unknowns from the Ankle Complex system. However, although this reduced the number of unknowns in the system to nineteen, the system was still indeterminate.

Two methods have been used in past biomechanical models to overcome the problem of indeterminacy and solve for equilibium: Functional Grouping and Optimisation. With Functional Grouping, the number of unknowns in the system would be reduced to twelve to render the system determinate. This could be done by (a) assuming that only twelve of the structures of the Ankle Complex were loaded during equilibrium and that the remainder were unloaded, or (b) by assuming that certain structures were functionally related. The loading in these structures would then be grouped together as a single unknown, reducing the overall number of unknowns. The drawback in reducing the number of unknowns is that the internal structure of the Ankle Complex must be greatly simplified. The simplification, while yielding an equilibrium solution, may compromise the validity of the model and produce non-physiological solutions.

The Optimisation method did not require a reduction in the number of unknowns in the system. Instead, a unique equilibrium solution was determined for the indeterminate system by optimising some aspect of the Ankle Complex. The drawback with optimisation is that the solution found for the indeterminate system was dependent on the choice of system parameter to be optimised. The objective of the optimisation therefore had to be chosen with great care. Since the *optimisation* method did not require the Ankle Complex structure to be simplified in order to solve for equilibrium, this was the method used to overcome the system indeterminacy.

7.2 SIMPLEX METHOD OF LINEAR OPTIMISATION

A system of simultaneous equations was considered fully determined, or *determinate*, if the number of unknowns in the equations of the system equalled the number of equations. For a determinate system there was either a unique solution which simultaneously satisfied all the equations or there was no solution at all. If the number of equations exceeded the number of unknowns then the system was considered *over-determined*. A unique solution only existed for the system if the extra equations were linear combinations of other system equations and the system was actually an improperly defined determinate system. Otherwise no solution existed for an over-determined system. When the number of unknowns in the system exceeded the number of equations, then the system was considered *under-determined* or *indeterminate*. An indeterminate system may possess no solution or an infinite number of solutions.

Insight into the behaviour of these classes of system could be gained by considering the *solution space* of the system of equations. Given a system of M equations and N unknowns, the solution to the system resided in an N-dimensional solution space. Each of the M equations of the system existed as N-dimensional surfaces within the solution space. When the equations of the system were all linear, then each surface would be an N-dimensional hyper-plane. The solutions to the system existed at the common intersection of these surfaces. For the fully determinate and the over-determined systems, when all the surfaces intersected at the same unique point within the solution space, the N-dimensional co-ordinates of the intersection point represented the values of each of the unknowns in a unique solution. If the surfaces failed to all intersect at the same point then the system had no solution.

As with determinate and over-determined systems, the solutions of an indeterminate system resided at the common intersection of all the surfaces defined by the system equations. However, since there were less surfaces than there were dimensions in the solution space, the common intersection of the surfaces was a surface with between one and N-M dimensions. Since the intersection surface was

unbounded within the solution space, then there were an infinite number of solutions to the indeterminate system of equations.

The method of optimisation added an extra equation to the indeterminate system. This added equation was known as the *objective function*. Once the common intersection surface containing the solutions for the indeterminate system had been determined within the solution space, the objective function was evaluated with each of the possible solutions which resided on the solution surface. The solution which optimised the objective function, either maximising it or minimising it, was chosen as the unique solution for the indeterminate system.

A method of *linear* optimisation, the *Simplex Method*, was employed in the present study. Linear optimisation was readily applied to the Ankle Complex system since each of the twelve joint system equations were linear equations.

The Simplex Method of Linear Optimisation allowed system *constraints* of three types. The first type were the familiar equations discussed above, which were of the form,

$$a_{i1}x_1 + a_{i2}x_2 + \cdots + a_{iN}x_N = b_i \geq 0 \qquad (7.2\text{-}1)$$

The other two types of constraints were inequalities. The *lesser* inequalities were of the form,

$$a_{j1}x_1 + a_{j2}x_2 + \cdots + a_{jN}x_N \leq b_j \geq 0 \qquad (7.2\text{-}2)$$

and the *greater* inequalities,

$$a_{k1}x_1 + a_{k2}x_2 + \cdots + a_{kN}x_N \geq b_j \geq 0 \qquad (7.2\text{-}3)$$

The values of the unknowns in the solution were limited to non-negative numbers,

$$x_i \geq 0 \qquad (7.2.\text{-}4)$$

Consider a system of N unknowns, constrained by m_3 equations, m_1 lesser inequalities and m_2 greater inequalities with $M = m_1 + m_2 + m_3$ constraints in total. If the system was indeterminate, then $M > N$, and the solutions to the system would reside on an $N - m_3$ dimensional hyper-plane. The inequality constraints did not act to define the dimensionality of the solution hyper-plane as the equalities did. Instead the inequalities divided each dimension of the solution hyper-plane into two regions; one region where the solutions resided and the other where the solutions did not.

The solution hyper-plane was therefore chipped away by the inequalities to form a multi-dimensional convex polyhedron, or *simplex*. The solution simplex possessed the same number of dimensions as the solution hyper-plane, but the solutions within it were *bounded* by the inequality constraints. This reduced the number of solutions from an infinite number to a finite number.

The set of possible system solutions, which resided within the solution simplex, were called the *feasible vectors*. The feasible vector which maximised the objective function was called the *optimal feasible vector* and this was the solution that was sought. Since the objective function was a linear function, it possessed a maximum value at one of the boundaries of the solution simplex. Therefore, the optimal feasibility vector was sought systematically along the boundary of the solution simplex. Once the optimal feasibility vector had been found, the indeterminate system was considered solved. The process for this systematic solution process was taken from Press, et al., (1989).

7.3 CORRECTING THE MUSCLE-TENDON TENSIONS

Given the organisation of the ligaments, muscle-tendons and joint surfaces that composed the Ankle Complex, it was assumed that the muscle-tendons that crossed the two joints were solely responsible for creating moments about the axes of rotation of the two joints. The ligaments and joint surfaces of the Ankle and Subtalar Joints were therefore assumed to constrain the bone segments from rotating about the other two joint-fixed frame axes or translating in any of the three spatial directions. This assumption was supported by cadaver studies which demonstrated non-restricted passive rotation about the joint rotational axes of the Ankle and Subtalar Joints in cadavers with the muscle-tendons removed. Translating motion and rotational motion about the other axes remained constrained (Leardini et al, 1999b).

This assumption meant that the muscle-tendons alone were responsible for moment equilibrium about the joint rotational axes and the remaining structures of the Ankle Complex, the ligaments and joint surfaces, were responsible for equilibrium in all the other degrees of freedom. The muscle-tendon tensions were

therefore responsible for balancing the moments about the joint rotational axes created by the externally applied Ground Reaction Force (GRF).

The tensions in the muscle-tendons, however, were determined in the Muscle Model without any consideration of their effects on the equilibrium of the Ankle Complex joints. The tensions were determined entirely from the Kinematic Data and the EMG Data recorded during the Motion Analysis experiments and from a consideration of the architecture and histological composition of the muscles. Ideally, the moments about the two joints caused by the muscle-tendon tensions determined by the Muscle Model would balance the GRF moments about the joint rotational axes at every sample within each trial. This, however, was not always the case.

Throughout most of the Movement Task trials for each of the subjects, there was a discrepancy between the moments caused by the GRF and the moments caused by the muscle-tendon tensions. The reason for the discrepancy was likely to be due to a weakness in the Muscle Model Calibration method described in Section 6.5. The weakness probably lay in the assumption of a constant proportionality factor, q, needed during the assignment of values to the calibration constants, $s\{m\}$.

The moment discrepancy about the two joint axes was corrected independently for each sample throughout each of the trials by slightly altering the muscle-tendon tensions. These alterations balanced the moments about the joint rotational axes and removed the discrepancy in externally and internally generated moments. The alterations imposed on the muscle-tendon tensions were chosen so as to minimally alter the overall pattern of tensions.

At a sample h during a Movement Task trial, the Ground Reaction Force and its centre of pressure were measured by the Force Plate, $\underline{F}(h)$ and $\underline{x}_{cp}(h)$. The Muscle Model determined the tensions in the eight muscle-tendons, $T\{m\}_{muscle-tendon}(h)$. The Kinematic Data and Internal Map gave the positions of the muscle-tendon attachments in the ground frame. As in Section 6.3, these were used to calculate the instantaneous relative muscle-tendon lengths, $\Delta l\{m\}_{muscle-tendon}(h)$. As in the Muscle Model Calibration procedure in Section 6.5, the vectors representing

Ankle Joint

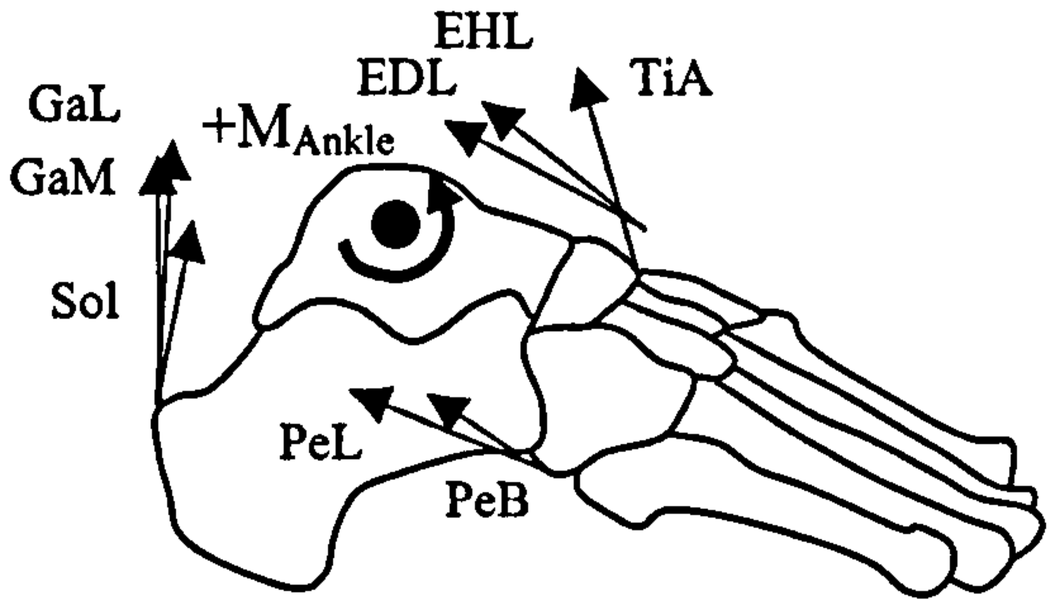

Lateral View

Subtalar Joint

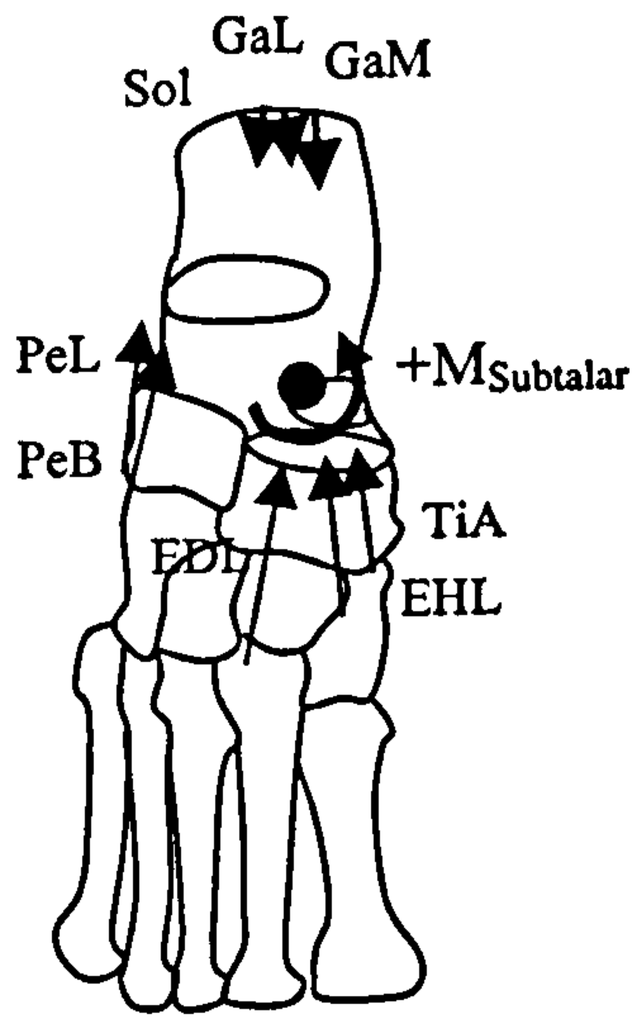

Superior View

Figure 7.3-1 Diagram showing the muscle-tendon tensions acting about the Ankle and Subtalar Joints and the orientations of positive joint moments.

the muscle-tendon lines of action and lever arms about the two joints were calculated. The muscle-tendon attachments used to create these vectors were slightly different for each muscle-tendon and depended on the number of pulley points that each muscle-tendon possessed. The lever arm and line of action vectors used for each muscle-tendon are listed in Table 7.3-1.

The Kinematic Data and Internal Map also provided the positions of the points defining the joint-fixed reference frames for Ankle Joint and Subtalar Joint; $\underline{lat}(h)$, $\underline{med}(h)$, $\underline{FH}(h)$ and $\underline{ant}(h)$, $\underline{post}(h)$, $\underline{MiH}(h)$ respectively. As in Section 4.2.2, the two joint-fixed frames were constructed. Each of the preceding vectors and attachment points was then transformed into both of these joint-fixed frames. The diagrams showing of the GRF and muscle-tendon tensions acting about the Ankle and the Subtalar Joints are shown in Figure 7.3-1.

The lever arms of the GRF about the Ankle Joint and Subtalar Joint were found as in Eq. 6.5-1,

$$\begin{aligned} {}_{Ankle}\vec{d}\{GRF\}(h) &= {}_{Ankle}\underline{x}_{CP}(h) - {}_{Ankle}\underline{lat}(h) \\ {}_{Subtalar}\vec{d}\{GRF\}(h) &= {}_{Subtalar}\underline{x}_{CP}(h) - {}_{Subtalar}\underline{post}(h) \end{aligned} \tag{7.3-1}$$

The moments about the two joints caused by the GRF could then be calculated,

$$\begin{aligned} {}_{Ankle}\underline{M}\{GRF\}(h) &= {}_{Ankle}\vec{d}\{GRF\}(h) \times {}_{Ankle}\underline{F}(h) \\ {}_{Subtalar}\underline{M}\{GRF\}(h) &= {}_{Subtalar}\vec{d}\{GRF\}(h) \times {}_{Subtalar}\underline{F}(h) \end{aligned} \tag{7.3-2}$$

Only the moments about the joint rotational axes, the $2-axis$ of the joint-fixed frames, were needed for the moment balance. Therefore, just the $2-axis$ components from Eq. 7.3-2 were considered,

$$\begin{aligned} {}_{Ankle}^{\hat{2}}M\{GRF\}(h) \\ {}_{Subtalar}^{\hat{2}}M\{GRF\}(h) \end{aligned}$$

where the superscripted $\hat{2}$ represented the $2-axis$ component of $\underline{M}$.

The lever arms and lines of action from Table 7.3-1 for each of the muscle-tendons were crossed to determine their *moment potentials*, $\vec{dl}\{m\}_x(h)$, for each about the two joints. These were found about the Ankle Joint and the Subtalar Joint as in Eq. 6.5-3,

$$
\begin{aligned}
{}_{Ankle}\vec{dl}\{m\}_x(h) &= {}_{Ankle}\vec{d}\{m\}(h) \times {}_{Ankle}\vec{l}\{m\}(h) \\
{}_{Subtalar}\vec{dl}\{m\}_x(h) &= {}_{Subtalar}\vec{d}\{m\}(h) \times {}_{Subtalar}\vec{l}\{m\}(h)
\end{aligned}
\qquad (7.3\text{-}3)
$$

The moment potentials were then used to find the moments caused by each of the

#	Muscle	Leg Segment attachments	Foot Segment attachments	Lever Arms $\vec{d}\{m\}$	Line of Action $\vec{l}\{m\}$
1	**GaL**	$\underline{o}_{GaL}$	$\underline{i}_{GaL}$	$\underline{i}_{GaL} - \underline{lat}$	$\underline{o}_{GaL} - \underline{i}_{GaL}$
				$\underline{i}_{GaL} - \underline{post}$	
2	**GaM**	$\underline{o}_{GaM}$	$\underline{i}_{GaM}$	$\underline{i}_{GaM} - \underline{lat}$	$\underline{o}_{GaM} - \underline{i}_{GaM}$
				$\underline{i}_{GaM} - \underline{post}$	
3	**Sol**	$\underline{o}_{Sol}$	$\underline{i}_{Sol}$	$\underline{i}_{Sol} - \underline{lat}$	$\underline{o}_{Sol} - \underline{i}_{Sol}$
				$\underline{i}_{Sol} - \underline{post}$	
4	**TiA**	$\underline{o}_{TiA}$, $\underline{p1}_{TiA}$	$\underline{i}_{TiA}$	$\underline{i}_{TiA} - \underline{lat}$	$\underline{p1}_{TiA} - \underline{i}_{TiA}$
				$\underline{i}_{TiA} - \underline{post}$	
5	**PeL**	$\underline{o}_{PeL}$, $\underline{p1}_{PeL}$	$\underline{p2}_{PeL}$, $\underline{i}_{PeL}$	$\underline{p2}_{PeL} - \underline{lat}$	$\underline{p1}_{PeL} - \underline{p2}_{PeL}$
				$\underline{p2}_{PeL} - \underline{post}$	
6	**PeB**	$\underline{o}_{PeB}$, $\underline{p1}_{PeB}$	$\underline{i}_{PeB}$	$\underline{i}_{PeB} - \underline{lat}$	$\underline{p1}_{PeB} - \underline{i}_{PeB}$
				$\underline{i}_{PeB} - \underline{post}$	
7	**EHL**	$\underline{o}_{EHL}$, $\underline{p1}_{EHL}$	$\underline{p2}_{EHL}$, $\underline{i}_{EHL}$	$\underline{p2}_{EHL} - \underline{lat}$	$\underline{p1}_{EHL} - \underline{p2}_{EHL}$
				$\underline{p2}_{EHL} - \underline{post}$	
8	**EDL**	$\underline{o}_{EDL}$, $\underline{p1}_{EDL}$	$\underline{p2}_{EDL}$, $\underline{i}_{EDL}$	$\underline{p2}_{EDL} - \underline{lat}$	$\underline{p1}_{EDL} - \underline{p2}_{EDL}$
				$\underline{p2}_{EDL} - \underline{post}$	

Table 7.3-1 Attachments, Lever Arms and Lines of Action for the eight Muscle-tendons.

muscle-tendon tensions about the two joint rotational axes,

$$\begin{aligned} {}_{Ankle}\underline{M}\{m\}(h) &= {}_{Ankle}\vec{dl}\{m\}_x(h)\cdot T\{m\}_{muscle-tendon}(h) \\ {}_{Subtalar}\underline{M}\{m\}(h) &= {}_{Subtalar}\vec{dl}\{m\}_x(h)\cdot T\{m\}_{muscle-tendon}(h) \end{aligned} \quad \text{for } m=1,8 \qquad (7.3\text{-}4)$$

The $2-axis$ components of the moments in Eq. 7.3-4 were the muscle-tendon moments acting about the joint rotational axes,

$$\begin{aligned} {}_{Ankle}\hat{2}M\{m\}(h) &= {}_{Ankle}\hat{2}\vec{dl}\{m\}_x(h)\cdot T\{m\}_{muscle-tendon}(h) \\ {}_{Subtalar}\hat{2}M\{m\}(h) &= {}_{Subtalar}\hat{2}\vec{dl}\{m\}_x(h)\cdot T\{m\}_{muscle-tendon}(h) \end{aligned} \qquad (7.3\text{-}5)$$

If the externally applied GRF moments balanced the internally applied muscle-tendon moments, then ignoring the inertia of the foot, the equilibrium balance of moments about the two joint rotational axes would be,

$$\begin{aligned} 0 &= {}_{Ankle}\hat{2}M\{GRF\} + \sum_{m=1}^{8}\left[{}_{Ankle}\hat{2}\vec{dl}\{m\}_x(h)\cdot T\{m\}_{muscle-tendon}(h)\right] \\ 0 &= {}_{Subtalar}\hat{2}M\{GRF\} + \sum_{m=1}^{8}\left[{}_{Subtalar}\hat{2}\vec{dl}\{m\}_x(h)\cdot T\{m\}_{muscle-tendon}(h)\right] \end{aligned} \qquad (7.3\text{-}6)$$

However, the right side of these two equations was not zero for all the samples within the Movement Task trials.

In order to correct for the imbalance between external and internal moments, at each sample, each muscle-tendon tension was multiplied by a correction factor, $c\{m\}(h)$. The moment balance in Eq. 7.3-6 then became,

$$\begin{aligned} 0 &= {}_{Ankle}\hat{2}M\{GRF\} + \sum_{m=1}^{8}\left[{}_{Ankle}\hat{2}\vec{dl}\{m\}_x(h)\cdot T\{m\}_{muscle-tendon}(h)\cdot c\{m\}(h)\right] \\ 0 &= {}_{Subtalar}\hat{2}M\{GRF\} + \sum_{m=1}^{8}\left[{}_{Subtalar}\hat{2}\vec{dl}\{m\}_x(h)\cdot T\{m\}_{muscle-tendon}(h)\cdot c\{m\}(h)\right] \end{aligned} \qquad (7.3\text{-}7)$$

The system in Eq. 7.3-7 contained two equations, about the Ankle and Subtalar Joints, in terms of eight unknowns, the correction factors, $c\{m\}(h)$, and was therefore indeterminate. To overcome the indeterminacy of the system, the Simplex optimisation method was used to solve the system. The objective of the optimisation was to *minimally* alter the muscle-tendon tension pattern output from the Muscle Model. When all the corrective factors were equal to 1.0, then the muscle-tendon tensions were all unchanged. The objective function therefore minimised the maximum difference between any of the corrective factors, $c\{m\}(h)$ and 1.0.

The two moment balance equations stated in Eq. 7.3-6 were the equalities of the system solved by the Simplex Optimisation routine. In order to constrain the values assigned to the unknowns, $c\{m\}(h)$, a number of inequalities were added to the system. The minimum and maximum values which could be assigned to $c\{m\}(h)$ were 0.8 and 1.25 respectively. These constraints took the form of eight greater inequalities and eight lesser inequalities,

$$\begin{aligned} c\{m\} - 0.8 \geq 0 \\ c\{m\} - 1.25 \leq 0 \end{aligned} \qquad \text{for } m = 1,8 \qquad (7.3\text{-}8)$$

The objective function introduced two more unknowns to the system, $c\{\max\}(h)$ and $c\{\min\}(h)$. The first, $c\{\max\}(h)$, was equal to the maximum value taken on by any of the eight correction factors, $c\{m\}(h)$. The second, $c\{\min\}(h)$, was the minimum value assigned to any of the $c\{m\}(h)$. In order for these two unknowns to be assigned the overall maximum and minimum values, another eight greater and eight lesser inequalities were added to the system,

$$\begin{aligned} c\{\max\} - c\{m\} \geq 0 \\ c\{\min\} - c\{m\} \leq 0 \end{aligned} \qquad \text{for } m = 1,8 \qquad (7.3\text{-}9)$$

The objective function was maximised when the sum of these two unknowns was minimised. Therefore the objective function was the equality,

$$z = -c\{\max\} - c\{\min\} \qquad (7.3\text{-}10)$$

where z was the variable to be maximised.

The system solved by the Simplex Method was composed of the objective function in Eq. 7.3-10, the inequalities in Eqs. 7.3-8 and 7.3-9 and the moment balance equalities in Eq. 7.3-7. This system was solved for each sample h within each of the Movement Task trials. The solution process output the values of each of the eight muscle-tendon correction factors, $c\{m\}(h)$, and the two optimised unknowns, $c\{\max\}(h)$ and $c\{\min\}(h)$. When there was no imbalance between the externally applied GRF moments and the internally applied muscle-tendon moments, then the values assigned to the eight $c\{m\}(h)$ were all 1.0. Otherwise, values were assigned to the corrective factors, $c\{m\}(h)$, which corrected the moment imbalance

Ankle Joint

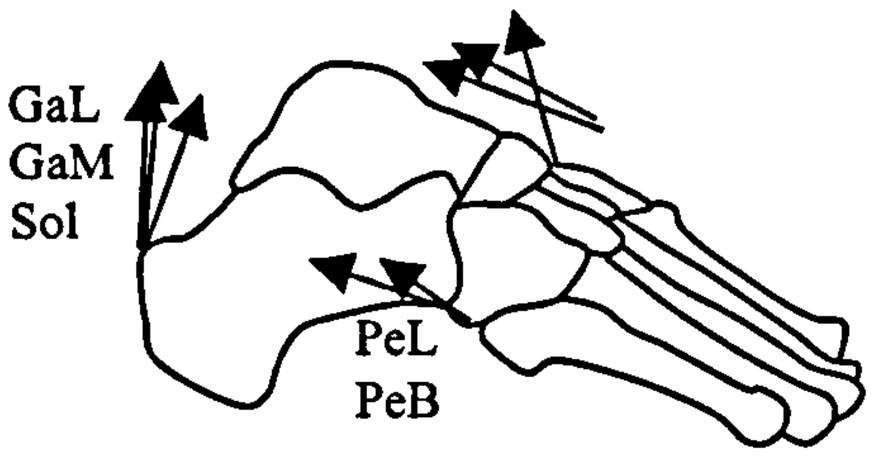

lateral view

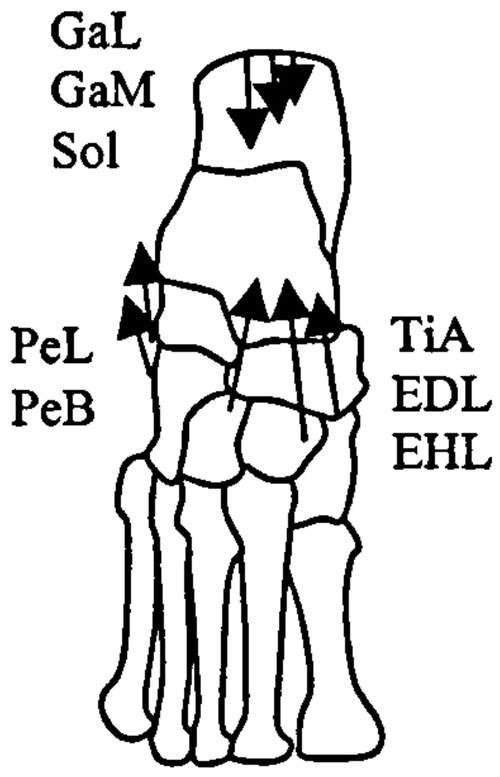

superior view

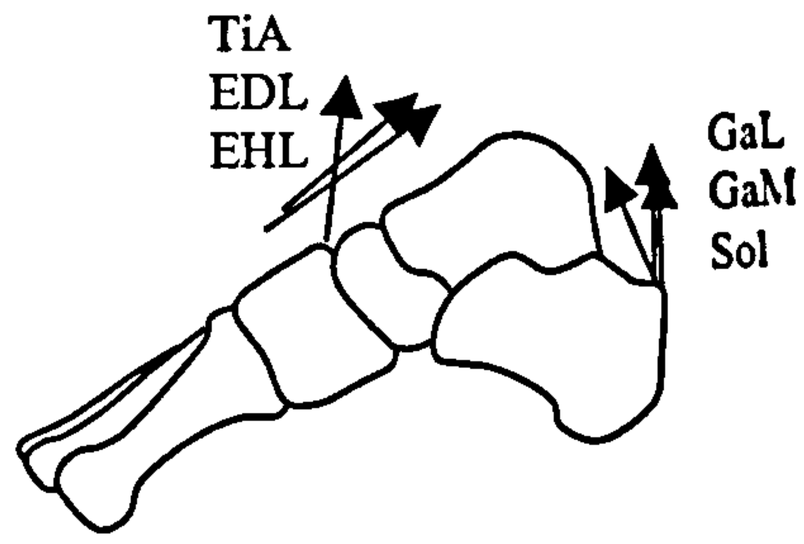

medial view

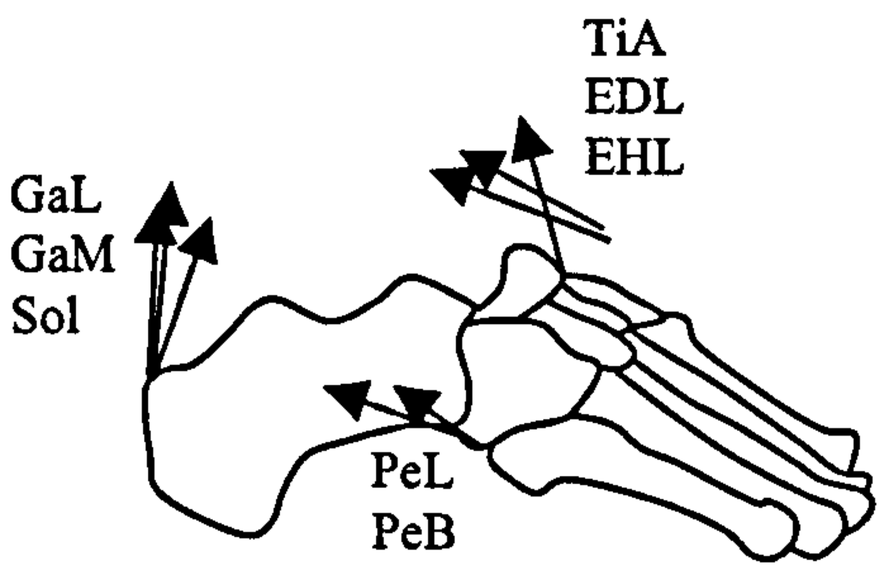

lateral view

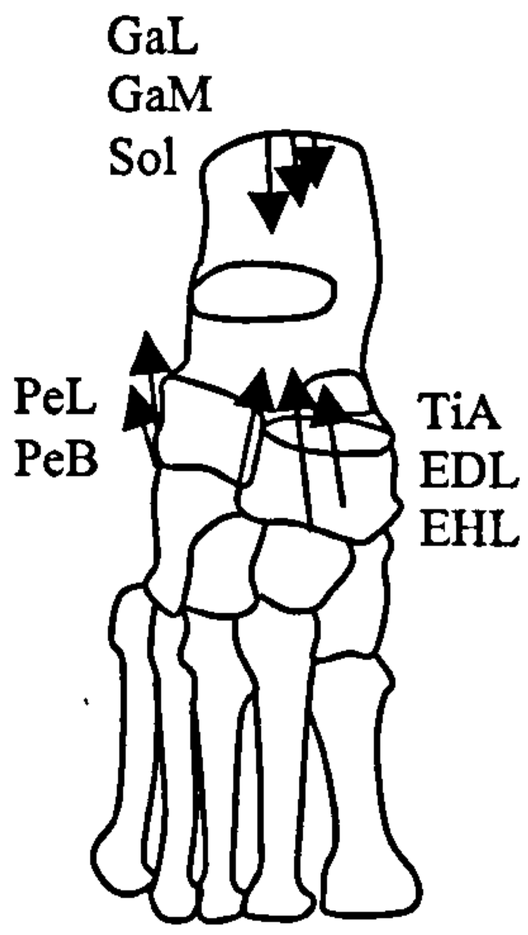

superior view

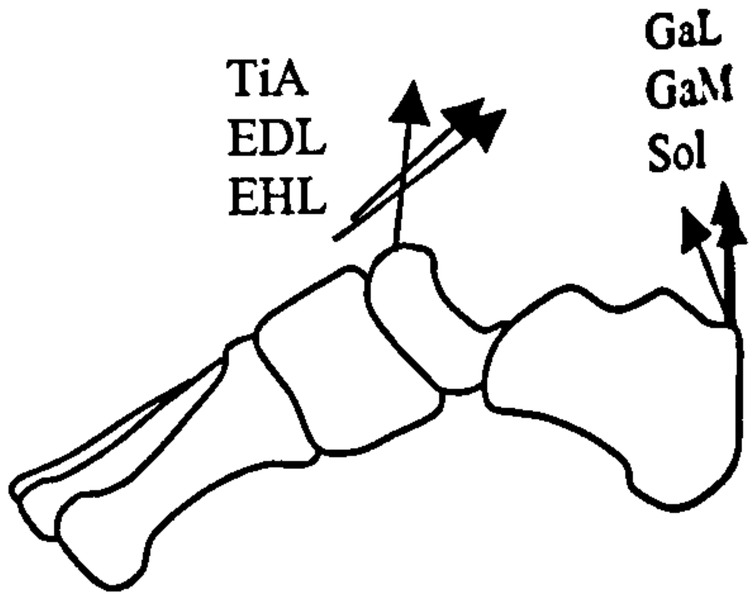

medial view

Subtalar Joint

Figure 7.4-1 Free body diagrams for Ankle Joint and Subtalar Joint equilibrium showing only the **Muscle-tendon tensions**. Three views: lateral, superior and medial.

about the two joint rotational axes simultaneously, while minimally altering the overall muscle-tendon tension pattern.

7.4 ANKLE COMPLEX EQUILIBRIUM SOLUTION

Once the tensions in the eight muscle-tendons had been corrected, the equilibrium solution for all twelve degrees of freedom of the Ankle Complex could then be found. The equilibrium solution for the Ankle Complex determined the tensions in the ligaments and the compression on the joint surfaces of the Ankle and Subtalar Joints. As mentioned in Section 6.5, the seven rigid segments of the Ankle Complex were subdivided into two types; Leg Segments and Foot Segments. The Leg Segments were the Thigh and Lower Leg segments and the Foot Segment were the Hindfoot, Midfoot and Forefoot segments. The Talus segment was classified as belonging to either group and formed the boundary between the Leg and Foot.

When considering the equilibrium of the two joints of the Ankle Complex, two separate free bodies were used. For the Ankle Joint, the Foot Segments plus the Talus were the body which moved with respect to the Leg Segments. The Subtalar Joint considered the Foot Segments to move with respect to the Leg Segments plus Talus.

When defining the directions of the forces and moments caused by each of these structures, the actions of the ligament tensions and surface compressions were defined as having an effect on the Foot segments. The muscle-tendon tensions are plotted in Figure 7.4-1 as they are applied to the Ankle Joint and Subtalar Joint free bodies.

7.4.1 Ankle Complex Ligaments

Twelve ligaments were included in the equilibrium of the Ankle Complex. The ligaments are listed in Table 7.4-1. For each of the twelve ligaments there were two attachment sites; one on a Foot segment and the other on a Leg segment. The segments to which the ligaments attached is also listed in Table 7.4-1. The lines of

Ankle Joint

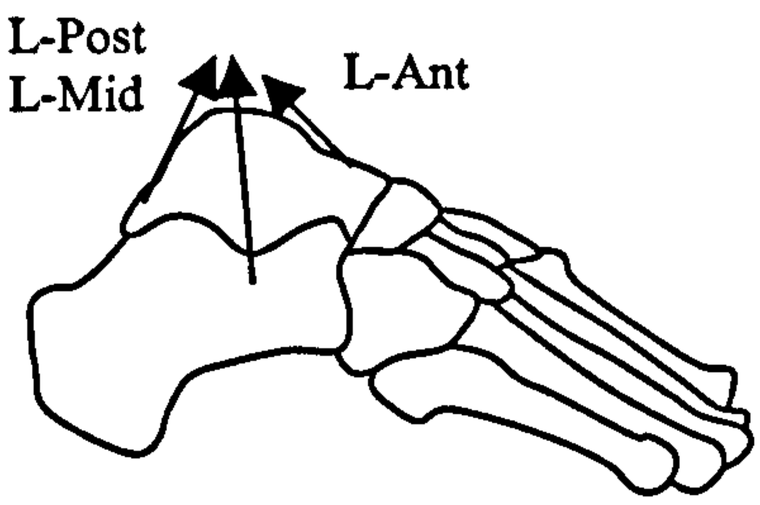

lateral view

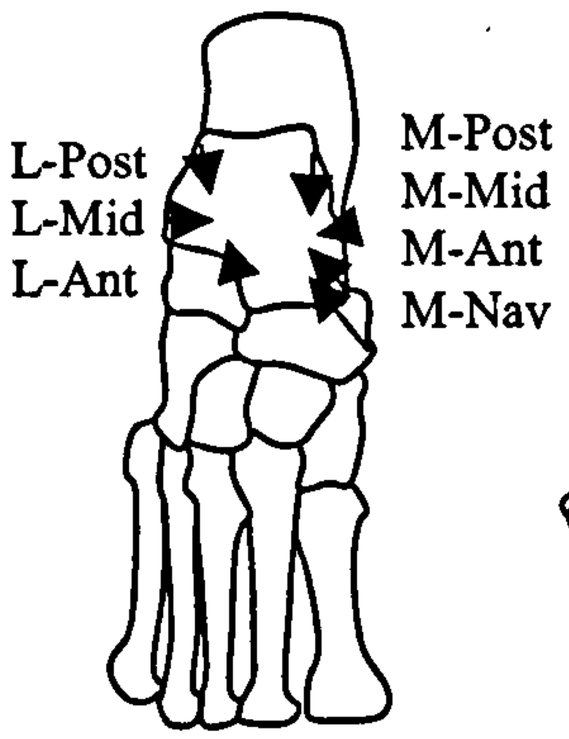

superior view

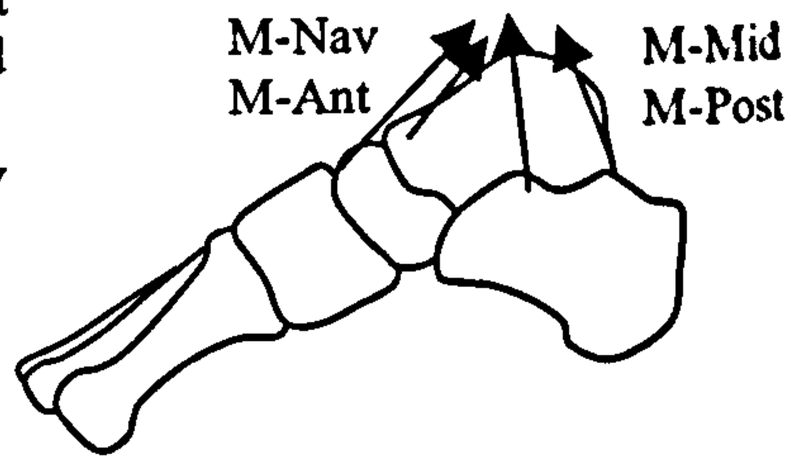

medial view

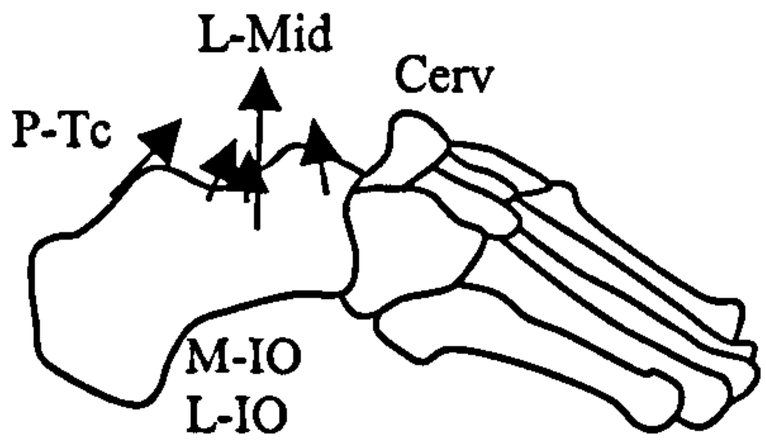

lateral view

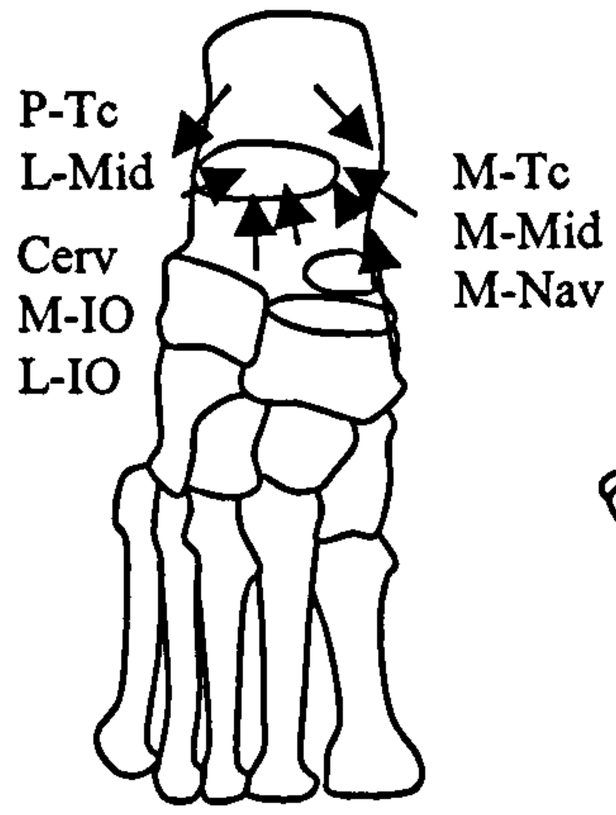

superior view

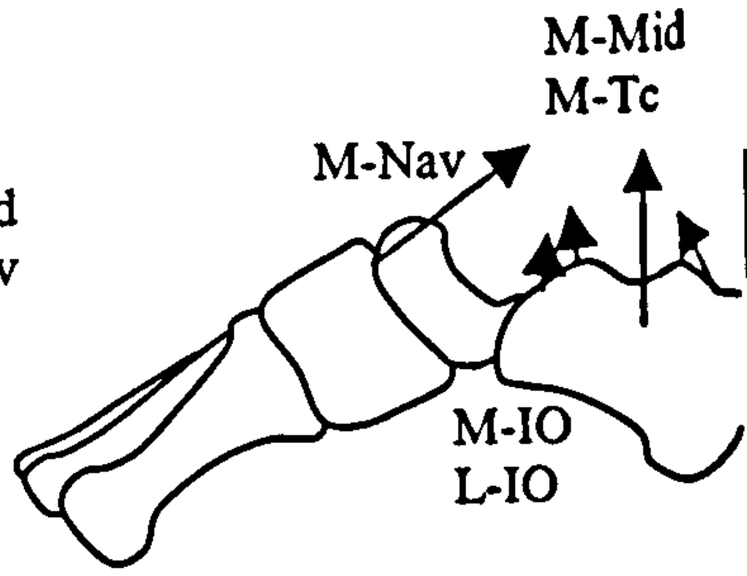

medial view

Subtalar Joint

Figure 7.4-2 Free body diagrams for Ankle Joint and Subtalar Joint equilibrium showing only the **Ligament tensions.** Three views: lateral, superior and medial.

action for the ligaments were defined as the vector pointing from the Foot segment attachment to the Leg segment attachment. The lever arms for each were defined as the vector pointing from a point on the joint rotational axis to the Foot segment attachment. Some of the ligaments acted about only one of the joints, while others acted about both joints. Therefore either one or two lever arms were found for each ligament. the free body diagrams with the ligament tensions are plotted in Figure 7.4-2.

#	Ligament		Joint	Leg Segment	Foot Segment
1	**Anterior Talofibular**	L-Ant	Ankle	Lower Leg	Talus
2	**Calcaneofibular**	L-Mid	Ankle + Subtalar	Lower Leg	Hindfoot
3	**Posterior Talofibular**	L-Post	Ankle	Lower Leg	Talus
4	**Anterior Talotibial**	M-Ant	Ankle	Lower Leg	Talus
5	**Calcaneotibial**	M-Mid	Ankle + Subtalar	Lower Leg	Hindfoot
6	**Posterior Talotibial**	M-Post	Ankle	Lower Leg	Talus
7	**Tibionavicular**	M-Nav	Ankle + Subtalar	Lower Leg	Midfoot
8	**Cervical**	Cerv	Subtalar	Talus	Hindfoot
9	**Medial Interosseus**	M/L-IO	Subtalar	Talus	Hindfoot
10	**Lateral Interosseus**	M/L-IO	Subtalar	Talus	Hindfoot
11	**Medial Talocalcaneal**	M-Tc	Subtalar	Talus	Hindfoot
12	**Posterior Talocalcaneal**	P-Tc	Subtalar	Talus	Hindfoot

Table 7.4-1 The twelve Ligaments of the Ankle Complex and the segments to which they attach.

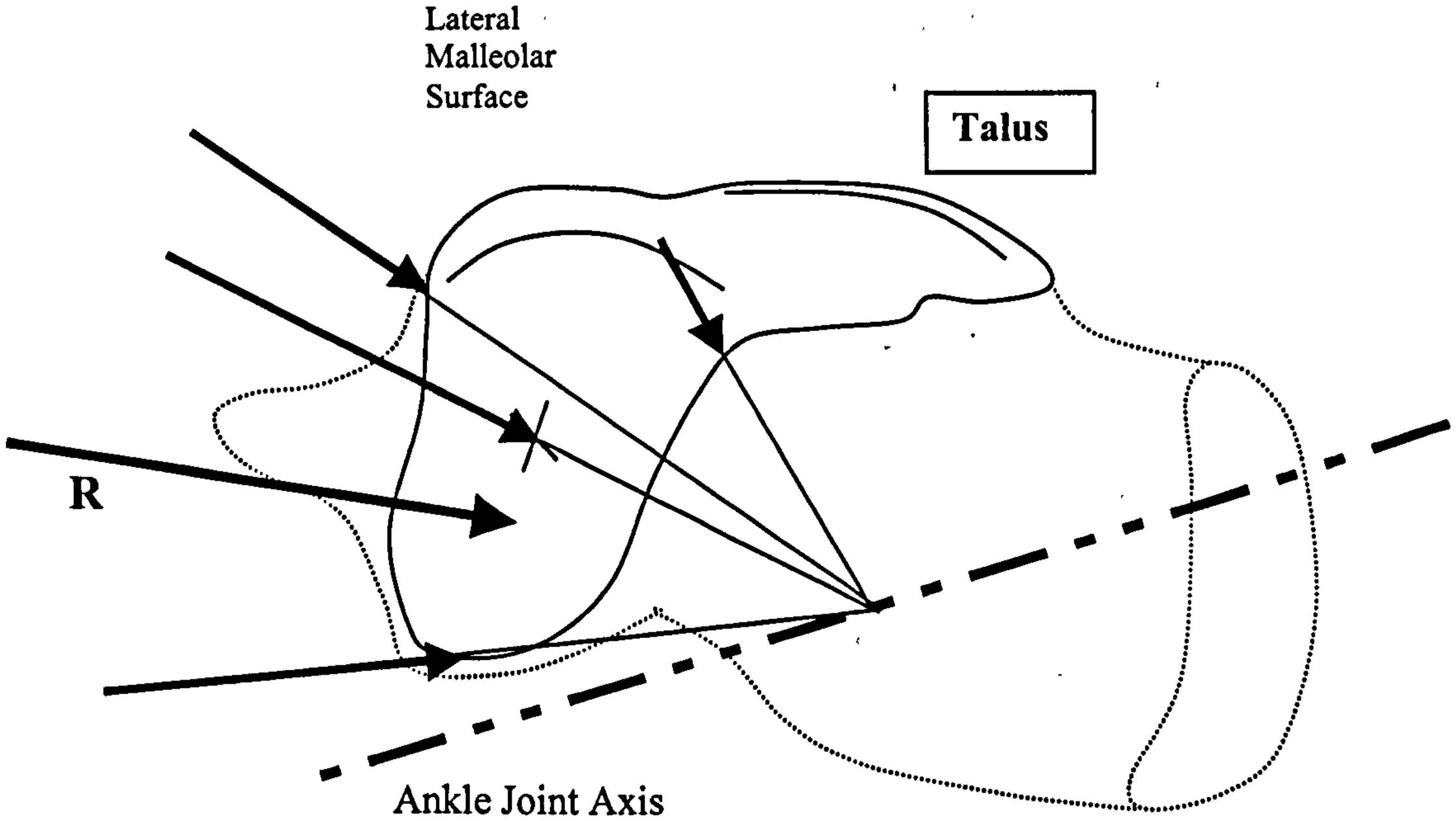

Figure 7.4.-3 Non-orthogonal and Resultant (R).surface force components acting on Lateral Malleolar Surface.

7.4.2 Ankle Complex Surfaces

Seven separate pairs of surfaces were considered in the solution of Ankle Complex equilibrium. The surfaces are listed in Table 7.4-2. In the Ankle Joint, the surfaces on the Lower Leg segment were considered to bear compressive loads produced by the corresponding surfaces on the Talus segment. In the Subtalar Joint, the surfaces of the Hindfoot and Midfoot segments were considered to bear the compressive loads imposed by the corresponding surfaces of the Talus segment.

#	Joint	Surface		# of force components
1, 4	Ankle	Lateral Malleolus	L-MalM	4
5, 9		Lateral Mortice	L-Mort	5
10, 14		Medial Mortice	M-Mort	5
15, 18		Medial Malleolus	M-MalM	4
19, 23	Subtalar	Posterior Talocalcaneal	Post	5
24		Middle Talocalcaneal	Mid	1
25, 29		Navicular Socket	Socket	5

Table 7.4-2 The seven Joint Surfaces of the Ankle Complex with the number of force components defined on each surface.

Each of these seven bearing surfaces bore a single resultant compressive load. On each surface the resultant could be assigned anywhere on the entire surface and was always normal to the surface. The resultant for each surface was constructed from either four or five *non-orthogonal* force components which were defined on each of the bearing surfaces. The non-orthogonal force components and the resultant surface force for the Lateral Malleolar surface are plotted in Figure 7.4-3.

When calculating surface load resultants, the common practice in most models has been to define three orthogonal force components for each surface which

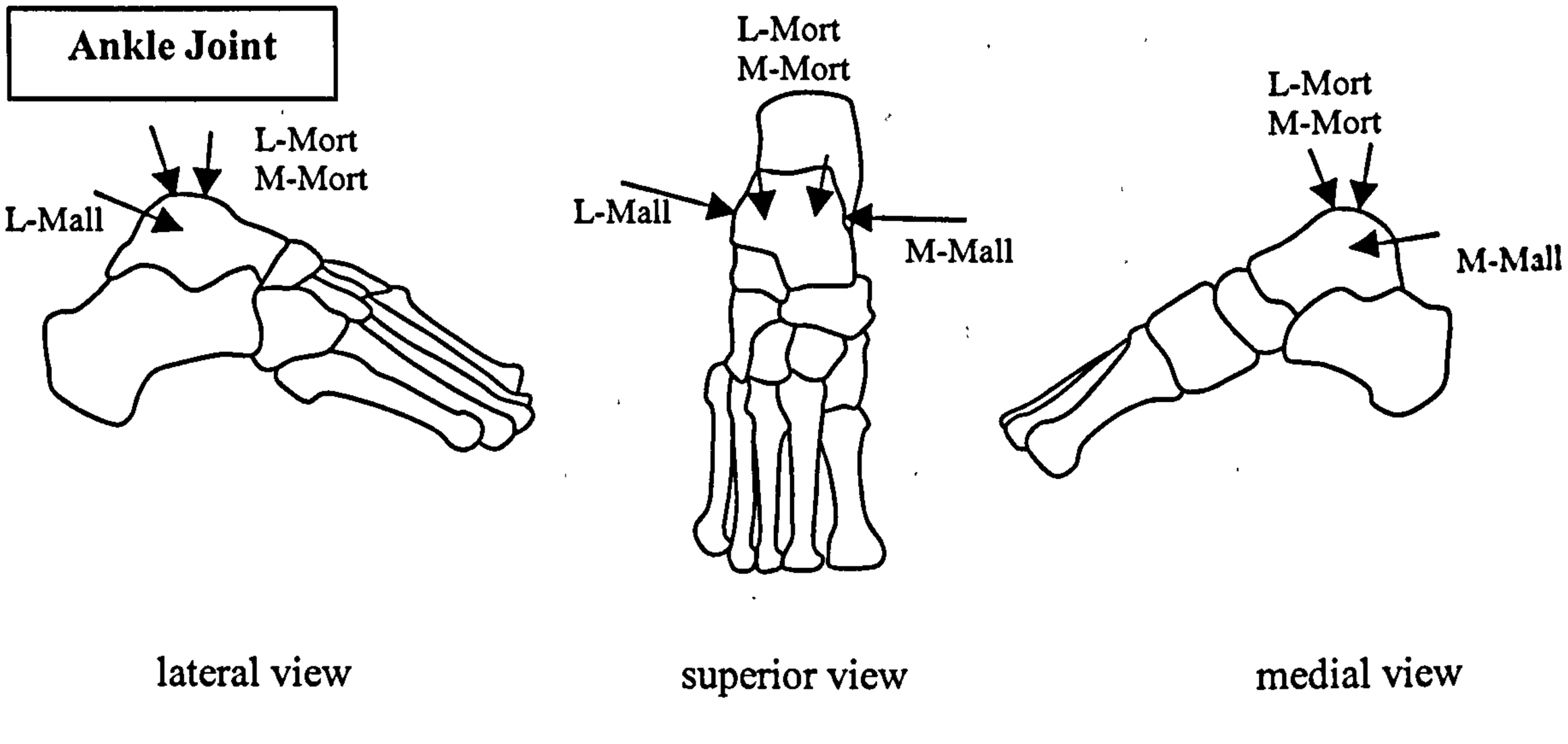

Figure 7.4-4 Free body diagrams for Ankle Joint and Subtalar Joint equilibrium showing only the central **Surface Compression** force components. Three views: lateral, superior and medial.

were parallel to the three axes of the joint-fixed frame of reference (Fowler, 1996, Chadwick, 1999). However, additional constraints then had to be added to these force components to ensure that the resultant force produced from the force components was constrained to the surface area. Given the complex geometry of the seven surfaces which comprised the two joints of the Ankle Complex, the required additional constraints needed to ensure that each of the resultants was contained within the appropriate surfaces were considered to be cumbersome. For this reason, an original method using non-orthogonal force components was used to find the resultant compressive load on each surface during equilibrium.

On each surface, a force component was defined which ran from a point on the joint rotational axis to the centre of the surface. Around this central force component, three or four boundary force components were defined. These boundary components each began at the same point on the joint rotational axis and ended at points on the edge of the surface. The rest of the surfaces had a similar arrangement of force components. The exception to this set-up was the Middle Talocalcaneal surface which had only a central force component assigned to it. In total there were twenty-nine force components defined over the seven surfaces. The force components of the Ankle Joint surfaces were defined in the Lower Leg segment frame of reference and those of the Subtalar Joint surfaces were defined in the Hindfoot and Midfoot segment-fixed frames.

The equilibrium solution found for the Ankle Complex assigned magnitudes to each of the force components. Since the Simplex Optimisation Method was used, the magnitudes assigned to each component had to be non-negative, as stated in Eq. 7.2-4. Since all the force component magnitudes were non-negative, then the resultant surface force constructed from the force components had to lie within the volume formed by the force component vectors. The resultant was therefore always confined to the surface. This was the benefit of using non-orthogonal force components; no additional constraints on the resultant vector were necessary. Table 7.4-2 lists each of the bearing surfaces within the Ankle Complex and the number of force components assigned to each surface.

The lever arms for each of the surface force components were defined as the vector running from a point on the appropriate joint rotational axis to the point on the surface where the force component was applied. Each surface force component only acted about one of the Ankle Complex joints, therefore only a single lever was found for each component. The free body diagrams for the Ankle and Subtalar Joints with the central surface force components applied to each surface are plotted in Figure 7.4-4.

7.4.3 Solving Ankle Complex System for Equilibrium

From the Internal Map and the Kinematic Data, the positions of the points which defined the two joint-fixed reference frames were known at sample h, $\underline{lat}(h)$, $\underline{med}(h)$, $\underline{FH}(h)$, and $\underline{ant}(h)$, $\underline{post}(h)$, $\underline{MiH}(h)$. Using these, the reference frames for the two joints were created. The lever arms and lines of action for each of the ligaments and surface force components were transformed into these two frames, as in Section 4.2.2. The lever arms and lines of action of the GRF and the corrected muscle-tendon tensions were also transformed into the joint-fixed reference frames.

The forces and moments acting in each of the twelve degrees of freedom of the Ankle Complex due to the Ground Reaction Force and the corrected muscle-tendon tensions were calculated. Since they contained no system unknowns, they were lumped together to form,

$$
\begin{aligned}
{}_{Ankle}\underline{F}_{GRF+mus}(h) &= {}_{Ankle}\underline{F}(h) + \sum_{m=1}^{8}\left[T\{m\}_{muscle-tendon}(h)\cdot c\{m\}(h)\right] \\
{}_{Subtalar}\underline{F}_{GRF+mus}(h) &= {}_{Subtalar}\underline{F}(h) + \sum_{m=1}^{8}\left[T\{m\}_{muscle-tendon}(h)\cdot c\{m\}(h)\right] \\
{}_{Ankle}\underline{M}_{GRF+mus}(h) &= {}_{Ankle}\underline{M}\{GRF\}(h) + \sum_{m=1}^{8}\left[{}_{Ankle}\underline{M}\{m\}(h)\right] \\
{}_{Subtalar}\underline{M}_{GRF+mus}(h) &= {}_{Subtalar}\underline{M}\{GRF\}(h) + \sum_{m=1}^{8}\left[{}_{Subtalar}\underline{M}\{m\}(h)\right]
\end{aligned}
\qquad (7.4\text{-}1)
$$

where ${}_{joint}\underline{M}\{GRF\}(h) = {}_{joint}\vec{dl}\{GRF\}(h) \times {}_{joint}\underline{F}\{GRF\}(h)$ and

$${}_{joint}\underline{M}\{m\}(h) = {}_{joint}\vec{dl}\{m\}(h) \times \left(\underline{T}\{m\}_{muscle-tendon}(h)\cdot c\{m\}(h)\right)$$

for $joint = Ankle, Subtalar$.

The lever arms and lines of actions for the ligaments were used to find the moment potentials for each ligament about the appropriate joint(s) (as Table 7.4-1),

$$_{Ankle}\vec{dl}\{l\}_x(h)=_{Ankle}\vec{d}\{l\}(h)\times_{Ankle}\vec{l}\{l\}(h) \qquad \text{for } l=1,7 \qquad (7.4\text{-}2)$$

$$_{Subtalar}\vec{dl}\{l\}_x(h)=_{Subtalar}\vec{d}\{l\}(h)\times_{Subtalar}\vec{l}\{l\}(h) \qquad \text{for } l=2 \text{ and } 5 \text{ and } 7,12$$

Note that seven of the ligaments acted about the Ankle Joint and eight acted about the Subtalar Joint. The force and moment contributions of each of the twelve ligaments were then found to be,

$$\begin{aligned}
_{Ankle}\underline{F}_{lig}(h) &= \sum_{l=1}^{7}\left[L\{l\}(h)\right] \\
_{Subtalar}\underline{F}_{lig}(h) &= \sum_{l=2+5+7}^{29}\left[L\{l\}(h)\right] \\
_{Ankle}\underline{M}_{lig}(h) &= \sum_{l=1}^{7}\left[_{Ankle}dl\{l\}_x(h)\times L\{l\}(h)\right] \\
_{Subtalar}\underline{M}_{lig}(h) &= \sum_{l=2+5+7}^{29}\left[_{Subtalar}dl\{l\}_x(h)\times L\{l\}(h)\right]
\end{aligned} \qquad (7.4\text{-}3)$$

where $L_{lig}(h)$ were the twelve unknown ligament tensions.

The moment potentials for each of the surface force components were found similarly to Eq. 7.4-2,

$$_{Ankle}\vec{dl}\{s\}_x(h)=_{Ankle}\vec{d}\{s\}(h)\times_{Ankle}\vec{l}\{s\}(h) \qquad \text{for } s=1,18$$

$$_{Subtalar}\vec{dl}\{s\}_x(h)=_{Subtalar}\vec{d}\{s\}(h)\times_{Subtalar}\vec{l}\{s\}(h) \qquad \text{for } s=19,29 \qquad (7.4\text{-}4)$$

Therefore the force and moment contributions of each of the surface force components were,

$$\begin{aligned}
_{Ankle}\underline{F}_{surf}(h) &= \sum_{s=1}^{18}\left[C\{s\}(h)\right] \\
_{Subtalar}\underline{F}_{surf}(h) &= \sum_{s=19}^{29}\left[C\{s\}(h)\right] \\
_{Ankle}\underline{M}_{surf}(h) &= \sum_{s=1}^{18}\left[_{Ankle}\vec{dl}\{s\}(h)\times C\{s\}(h)\right] \\
_{Subtalar}\underline{M}_{surf}(h) &= \sum_{s=19}^{29}\left[_{Subtalar}\vec{dl}\{s\}(h)\times C\{s\}(h)\right]
\end{aligned} \qquad (7.4\text{-}5)$$

The system of twelve equations which governed the loading in the twelve degrees of freedom of the two joints of the Ankle Complex could then be

constructed. The equilibrium system ignored the inertia of the foot, assuming it to be negligible. For the Ankle Joint and for the Subtalar Joint, there were vector equations for force and for moment equilibrium. This yielded four vector equations in all. Each vector equation contained three scalar equations. Therefore, the twelve scalar equations governing the force and moment equilibrium in the Ankle Complex, written as four vector equations were,

$$\begin{aligned}
0 &= {}_{Ankle}\underline{F}_{GRF+mus}(h) + {}_{Ankle}\underline{F}_{lig}(h) + {}_{Ankle}\underline{F}_{surf}(h) \\
0 &= {}_{Subtalar}\underline{F}_{GRF+mus}(h) + {}_{Subtalar}\underline{F}_{lig}(h) + {}_{Subtalar}\underline{F}_{surf}(h) \\
0 &= {}_{Ankle}\underline{M}_{GRF+mus}(h) + {}_{Ankle}\underline{M}_{lig}(h) + {}_{Ankle}\underline{M}_{surf}(h) \\
0 &= {}_{Subtalar}\underline{M}_{GRF+mus}(h) + {}_{Subtalar}\underline{M}_{lig}(h) + {}_{Subtalar}\underline{M}_{surf}(h)
\end{aligned} \qquad (7.4\text{-}6)$$

The indeterminate system was solved by simultaneously minimising the maximum tension in the ligaments and the maximum compression in the surface force components. The objective function therefore introduced two additional unknowns, $L\{\max\}(h)$ and $C\{\max\}(h)$. The maximum ligament and surface force component loads were assigned to these optimising unknowns by adding the following inequalities to the system,

$$\begin{aligned}
L\{\max\} - L\{l\} &\geq 0 \qquad \text{for } l = 1,12 \\
C\{\max\} - C\{s\} &\geq 0 \qquad \text{for } s = 1,29
\end{aligned} \qquad (7.4\text{-}7)$$

The objective function was maximised when the sum of these two unknowns was minimised. Therefore the objective function was the equality,

$$z = -L\{\max\} - C\{\max\} \qquad (7.4\text{-}8)$$

where z was the variable to be maximised.

The twelve degree of freedom Ankle Complex system solved for equilibrium by the Simplex Optimisation procedure was composed of the objective function in Eq. 7.4-8, the inequalities in Eqs. 7.4-7 and the force and moment equalities in Eq. 7.4-6. The Ankle Complex system was solved for each sample h within each of the Movement Task trials. This yielded the tensions in the twelve ligaments and the compression on the twenty-nine separate surface load components at that sample. The resultants for each surface were then found by summing the load components for each surface. This gave the resultant magnitudes and lines of action on each of the seven surface pairs.

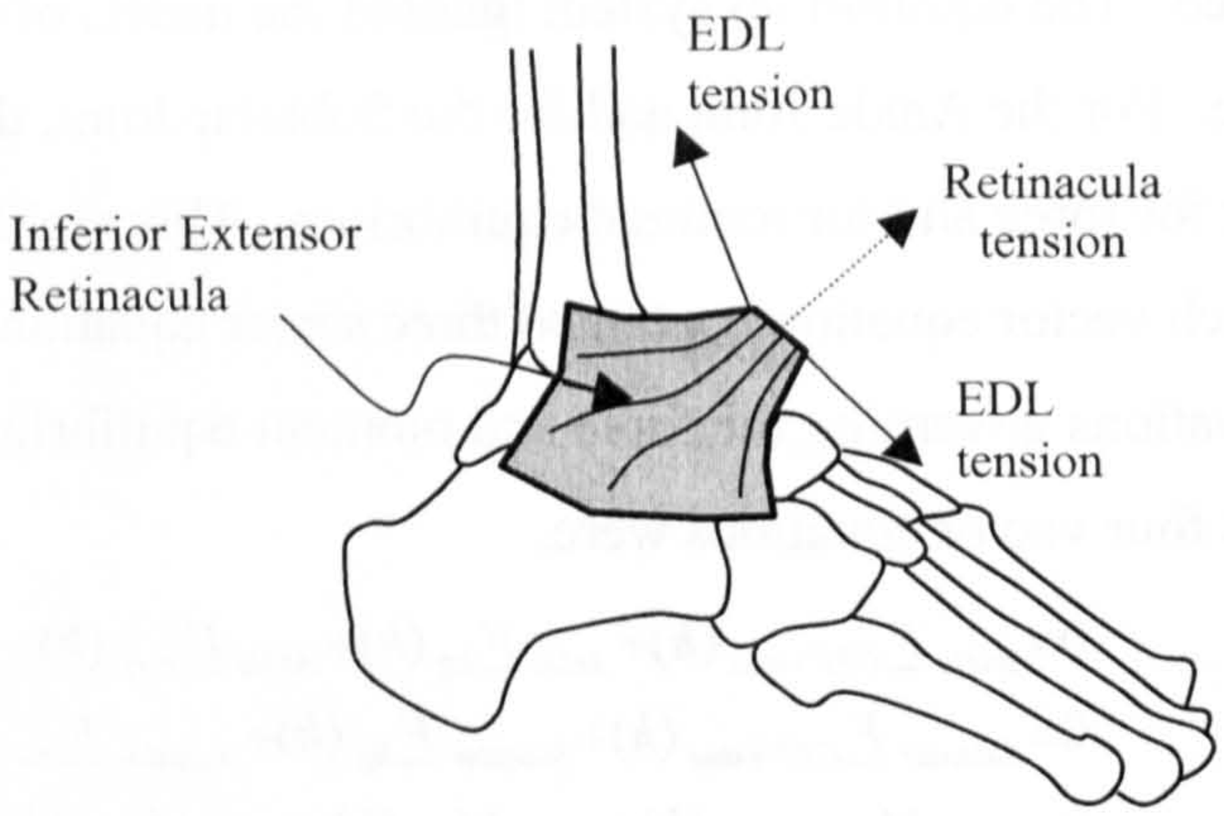

Figure 7.4-5 The forces imposed on the foot and leg segments by the Inferior Extensor Retinacula due to the change in direction of the EDL muscle-tendon tension.

7.4.4 Inertial Loading and Retinacular Effects

The preceding description of the solution of equilibrium about the joints of the Ankle Complex was *quasi-static*. The Ground Reaction Force experienced by the foot was a result of the accelerations of the masses of the various segments of the body. However, the inertial effects of the masses of the five segments of the foot were not included in the equilibrium solution. The masses of the foot segments were considered sufficiently small with respect to the mass of the rest of the body that the inertia of the foot would negligibly affect the equilibrium. The inclusion of the inertial effects would have increased the complexity of the solution with little affect on the solution. Therefore, for the sake of simplicity, the foot segments were considered to be massless and their inertial effects omitted from equilibrium.

Also omitted from the mechanics of the ankle joints was any retinacular loading on the segments of the leg or foot. This loading arises due to the change in direction of the muscle-tendon forces caused by the various retinacula. An example of retinacular loading is plotted in Figure 7.4-5. For instance, the Inferior Extensor Retinacula (IER) causes the tension in the EDL muscle-tendon to change direction from being mostly posteriorly directed in its distal section to mostly superiorly in its proximal section. The change in direction creates tension in the Inferior Extensor Retinacula itself, which pulls anteriorly on its attachments to the Navicular bone, the Medial Malleolus of the Tibia and the Calcaneus. The tendons of the EDL and EHL will therefore introduce some loading across the Ankle and Subtalar Joints via the IER. The TiA muscle-tendon also passes under the IER before its insertion. However, Sarrafian, 1983 shows that this portion of the IER is slack and does not change the direction of the TiA tendon. The TiA tension is entirely redirected by the Superior Externsor Retinacula which is attached to the shank rigid segment. Therefore negligible loading will be transferred to the IER attachments from the TiA.

The difficulty in including these retinacular effects within the equilibrium solution arise from the ill-defined attachments of the retinacula to bones and soft tissues of the Ankle Complex, on *both* sides of each of the joints. Since the retinacula attach so widely to so many structures, it is exceedingly difficult to

partition the retincular tensions among them. There is a danger that the assignment of the tension components using such vague anatomical clues will lead to misleading or incorrect equilibrium loading solutions. Therefore, the retinacula tensions were omitted from the solution of equilibrium.

The omission of IER loading may introduce an error to the internal loading solution produced in the current model. In order to quantify this error, the loading in the branch of the IER which attaches to the anterior portion of the medial malleolus arising from tension in the EDL and EHL during walking and walking turn is estimated in Section 8.2.4.

CHAPTER 8 INTERNAL LOADING RESULTS AND DISCUSSION

8.1 INTRODUCTION

Recall from Section 5.1 that due to the large amount of data and results generated by the model for all twelve subjects, just two representative subjects will be presented to demonstrate the two extremes of the range of results. Subject A was a female of height 1.63m and was 53.5kg and 23 years old. Subject B was a male of height 1.88m, body mass of 76kg and 25 years old. The complete range of model internal loading for all twelve subjects is presented in Appendix.

All the tensions and compressions were normalised by dividing by subject body weight (BW) where BW=body mass × 9.81 ms^{-2}. The average gait speeds for each of the tasks were summarised in Table 5.1-1 in Chapter 5.

8.2 MUSCLE-TENDON TENSIONS

8.2.1 Muscle-tendon Tension Results

Eight muscles were included in the Ankle Complex Model. These could be subdivided into three different groups: the Triceps Surae, the Peroneals and the Dorsi-flexors. The Triceps Surae group contained the lateral and medial heads of the Gastrocnemius (GaL and GaM) and the Soleus (Sol). There were two Peroneal muscles, the Peroneus Longus (PeL) and Peroneus Brevis (PeB). The Dorsi-flexors were the Tibialis Anterior (TiA) and the toe extensors, Extensor Digitorum Longus (EDL) and Extensor Hallucis Longus (EHL).

The tensions in the eight muscles were first determined by the Muscle Model. Recall from Section 7.3 that the muscle tensions were then corrected so that the moment about the joint rotational axes created by the muscle tensions would balance the externally imposed joint moments which were presented in the previous section.

Figures 8.2-1 to 8.2-3 show the tensions in the eight muscles for each of the trials at preferred speed walking for Subjects A and B. The muscle tensions showed little variability between trials of the same subject, but great variability between

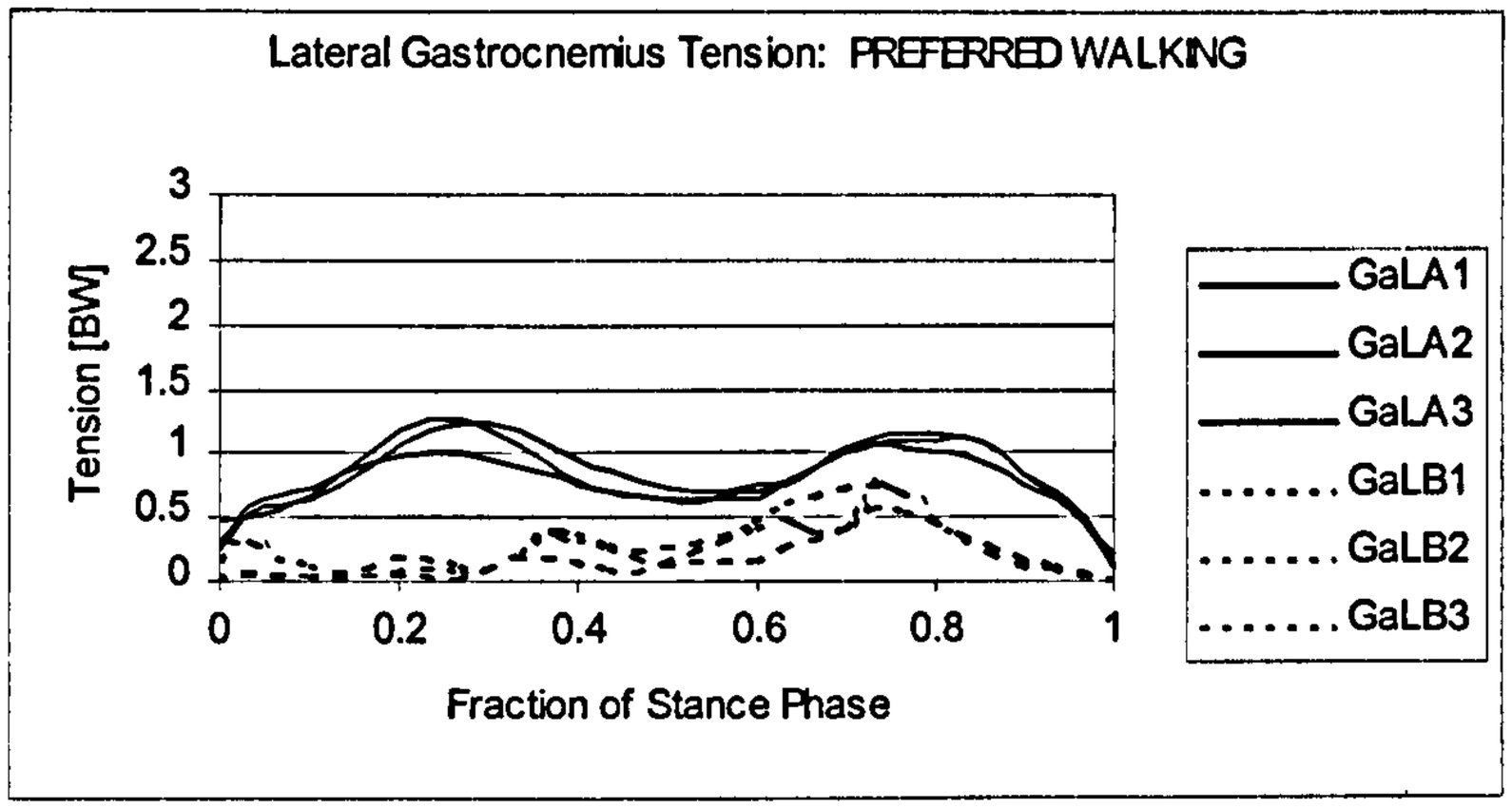

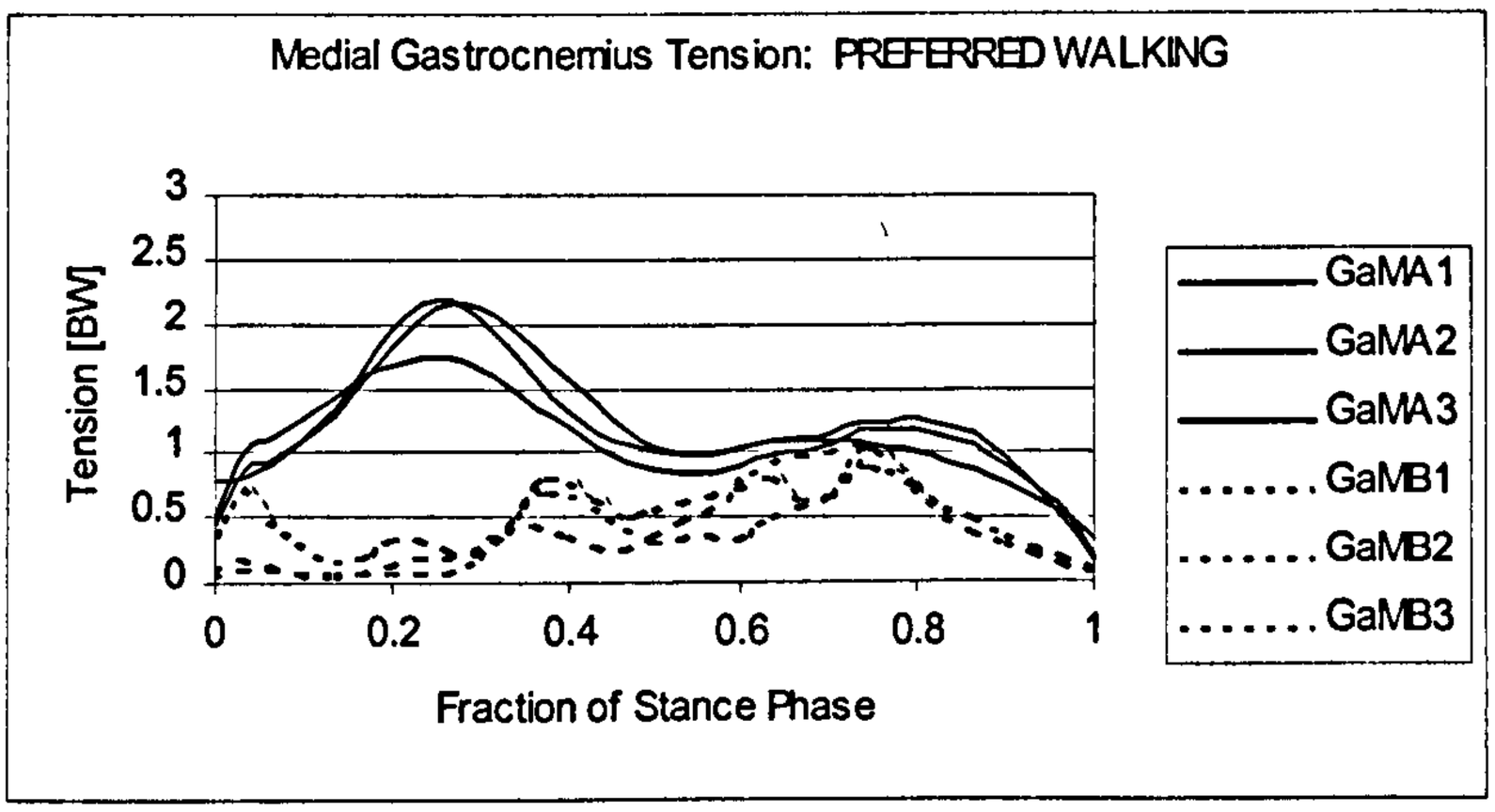

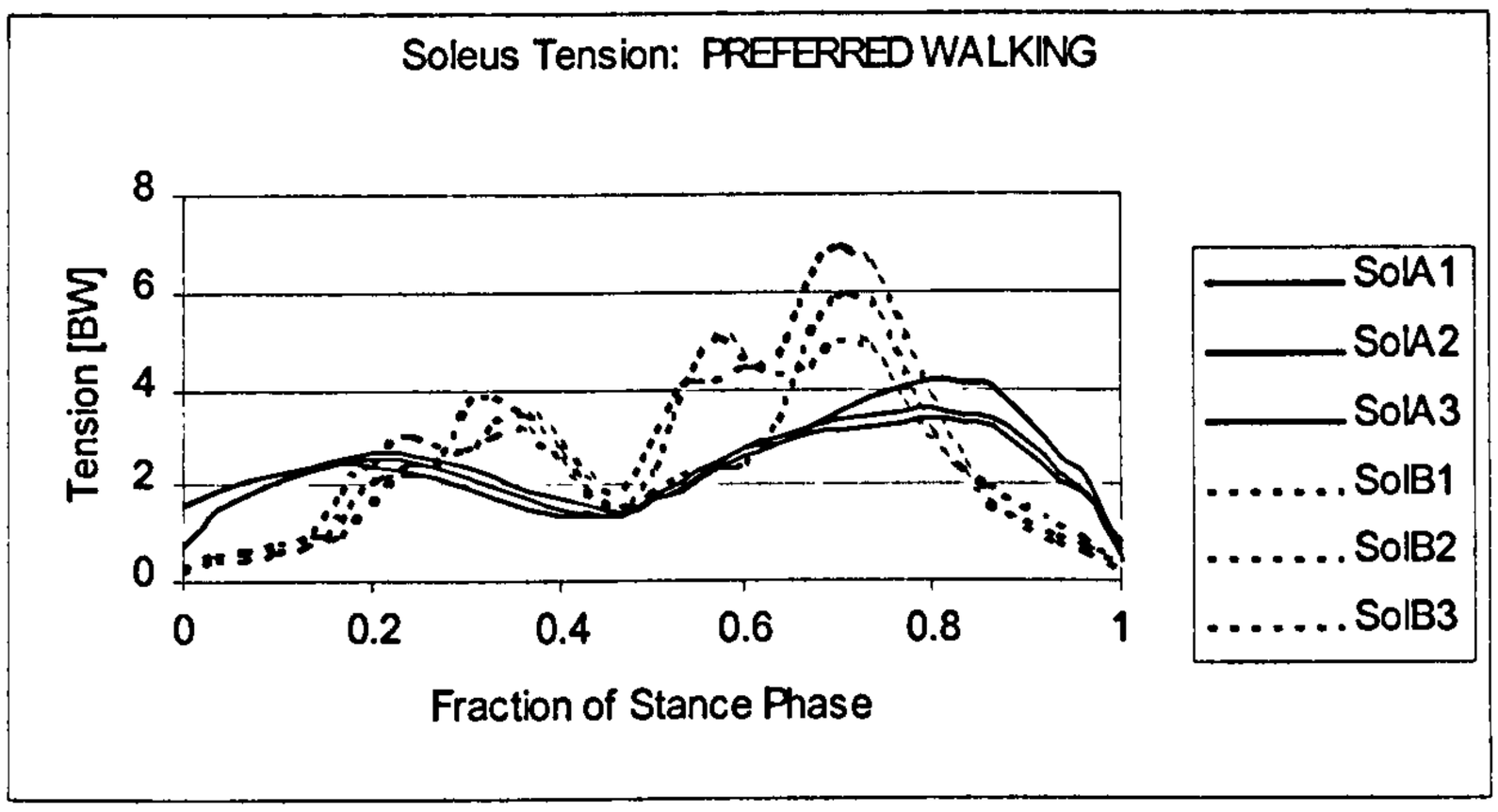

Figure 8.2-1 Triceps Surae Muscle Tensions for Preferred Speed Walking for Subjects A and B.

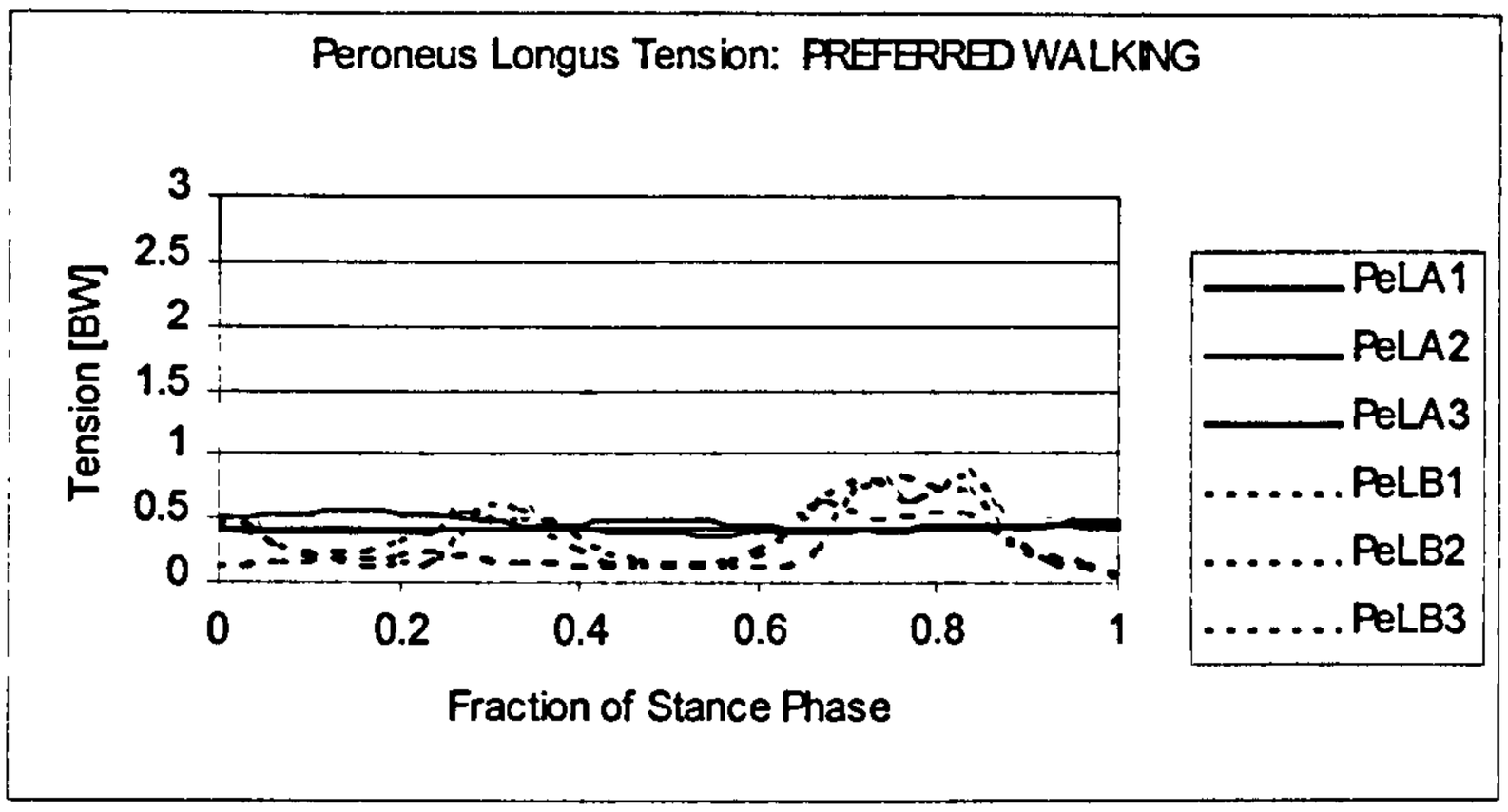

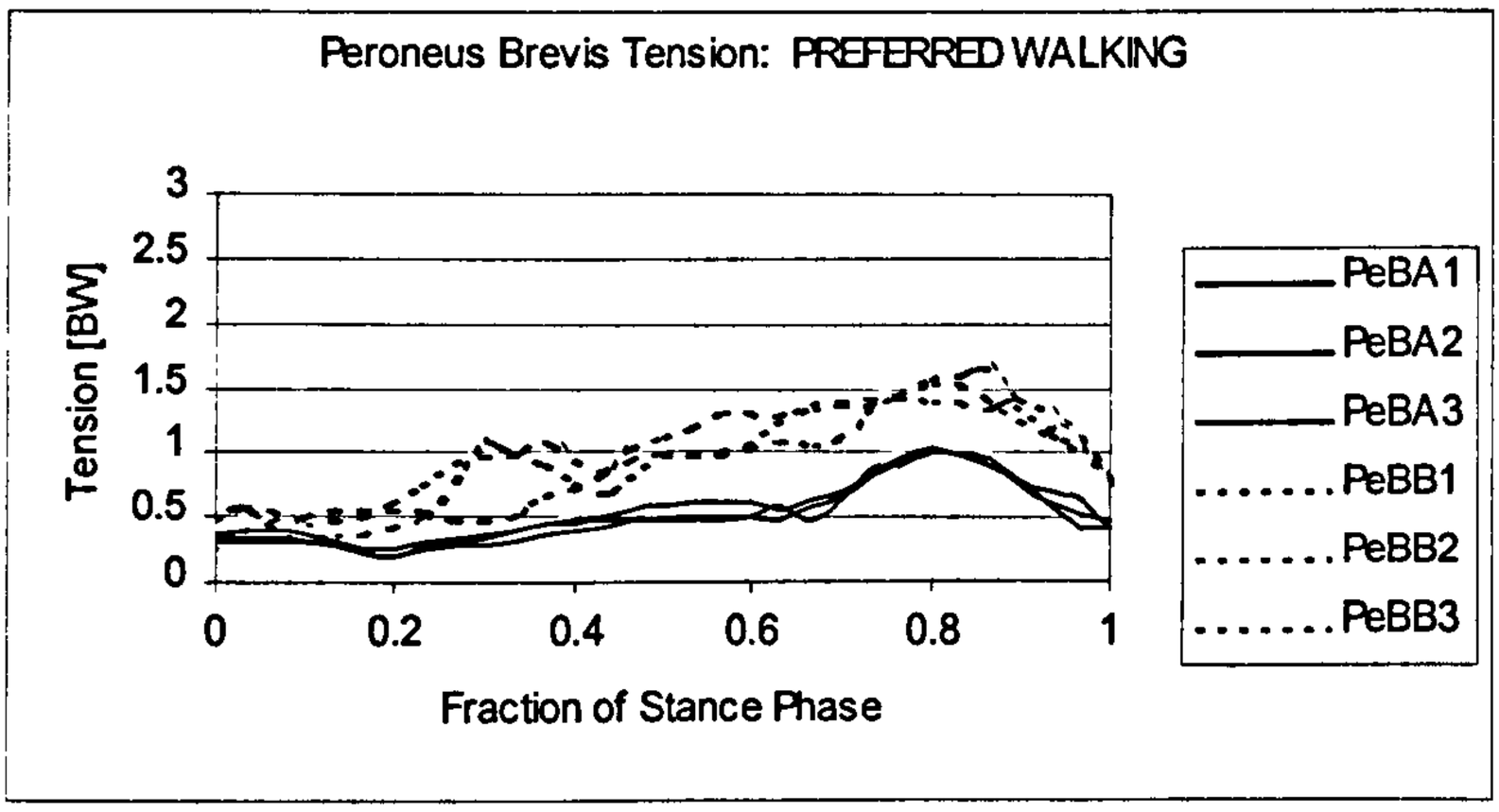

Figure 8.2-2 Peroneal Muscle Tensions for Preferred Speed Walking for Subjects A and B.

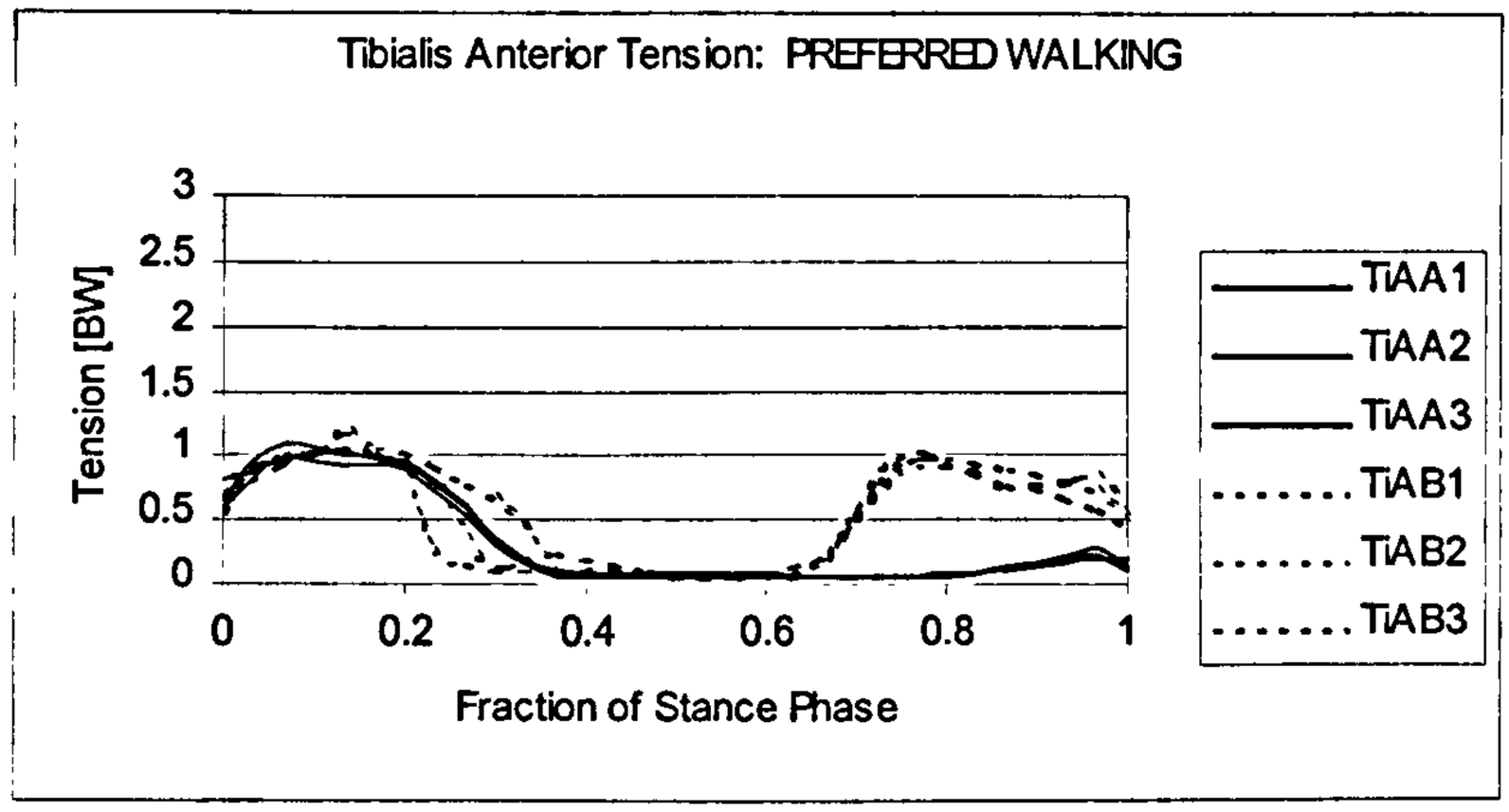

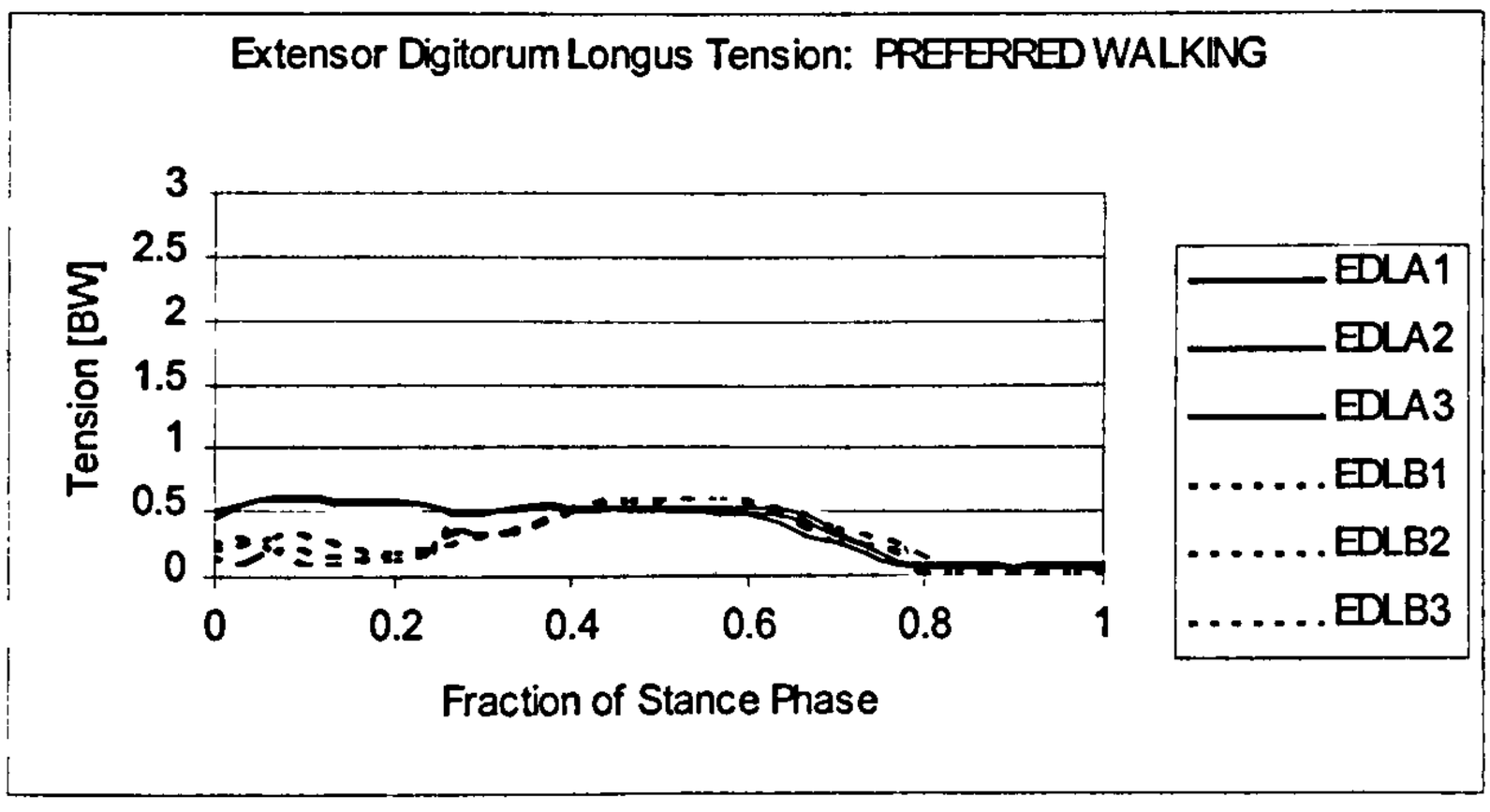

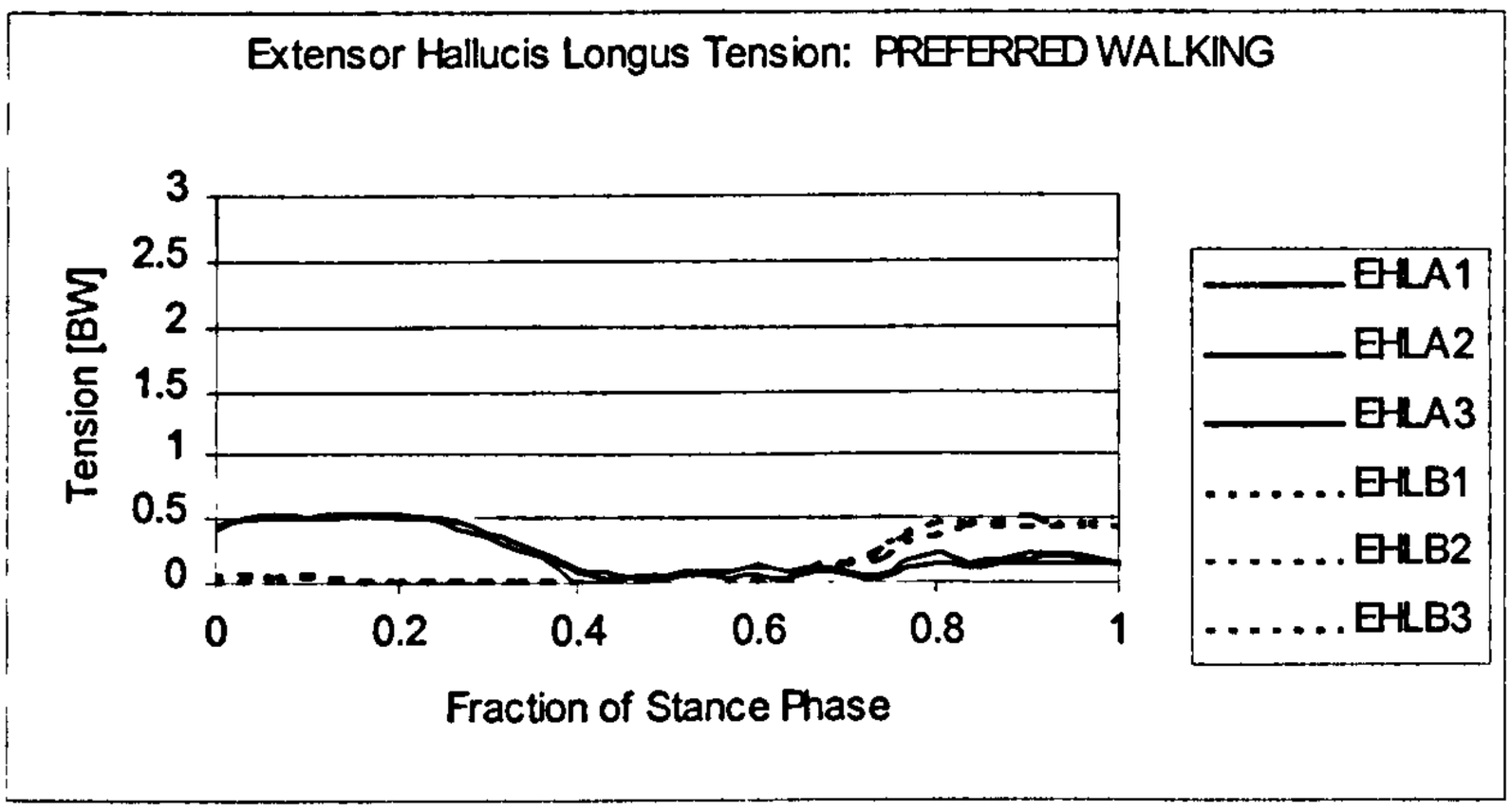

Figure 8.2-3 Dorsi-flexor Muscle Tensions for Preferred Speed Walking for Subjects A and B.

subjects. The muscle tensions of Subjects A and B were the rather different patterns and well represented the range of muscle-tendon tension patterns for all twelve subjects. The Subjects A and B were originally chosen since they represented the two extremes in body mass and body height. The two seemed to be employing different muscle tension strategies for balancing similar external loading.

The Triceps Surae group of muscles were exerting the largest tensions of all the muscles for both subjects. Note that the vertical scale on the plot of Soleus tension in Figure 8.5-1 is larger than the scale on the plots of all the other muscles. Therefore the magnitudes of Sol will appear smaller than the other muscles. The Gastrocnemius and Soleus of Subject A all show a similar, two peak pattern. The two peaks in the tensions of each of the Triceps Surae muscles coincided in time, with the early peak at 0.25 of stance phase in each case being larger than the late peak at 0.85 of stance phase. Sol produced the greatest tension of the three for Subject A, and the medial head of Gastrocnemius produced more tension than the lateral head. In Subject B, the Soleus produced nearly all the tension of the Triceps Surae group. The Sol curve possessed two general peaks, one early at 0.35 of stance phase and one late at 0.7. The curve for Sol was less smooth for Subject B than for Subject A. The two Gastrocnemius heads of Subject B seemed to possess a single late peak in tension occurring at the same time as the late peak in Subject A, at 0.7 of stance phase. The tension in the Achilles tendon was the sum of the tensions in the muscles of the Triceps Surae group. During preferred speed walking, the peak tension in the Achilles tendon was therefore 6.35×BW occurring at 0.85 of stance phase for Subject A and 7.90×BW occurring at 0.7 of stance phase for Subject B.

The tensions in the Peroneal group shown in Figure 8.2-2 were also different between the two subjects. In Subject A, the PeL muscle maintained a constant level of tension at 0.50×BW throughout the walking task. This may indicate that the Longus muscle of the Peroneal group has a postural role in the Ankle Complex as opposed to a propulsive role. The tension in PeL for Subject B, rather than being constant, showed two peaks at 0.35 and 0.75 of stance phase. Therefore the postural role of PeL seemed specific to Subject A.

The PeB tension for Subject A possessed a single late peak at 0.8 of stance phase. This late peak had a magnitude of 1.0×BW. In Subject B, the PeB tension also showed a single peak which coincided with the peak in PeB for Subject A. However, the tension in PeB for Subject B was larger at 1.5×BW.

The tensions in the Doris-flexor group shown in Figure 8.2-3 were different between Subjects A and B. TiA for the two subjects showed a single early peak at around 0.15 of stance phase and this peak was similar for the two subjects. The early peaks in TiA represent the muscle opposing the early external plantar-flexing moment acting on the foot between HS and FF. Recall from the Section 5.4, which described the joint moments, that there was a subtle difference between the two subjects. At fast walking, the moment about the Ankle Joint axis in early stance was plantar-flexing for Subject B, as opposed to dorsi-flexing in Subject A. This inter-subject difference in early stance was also present in preferred speed of walking but was more subtle and appeared as a delay in the timing of the dorsi-flexing moment in Subject B. This may indicate that Subject B took relatively longer to move from HS to FF than Subject A, and the increased tension in the Tibialis Anterior in early stance was enabling this.

Subject B displayed a late peak in TiA at 0.75 of stance phase with a magnitude of 1.0×BW. This late activity was completely absent in Subject A and represents a differing amount of antagonism for the two subjects. The tension in EDL for Subject A was 0.5×BW from FS to around 0.65 of stance phase. For the remainder of stance there was minimal tension. For Subject B, however, the EDL rose from 0.25×BW at FS to 0.5×BW at 0.4 of stance phase. This then dropped at 0.65 of stance and was minimally tensed until TO similar to EDL in Subject A.

The EHL tensions were different for the two subjects. Subject A began at FS with 0.5×BW which dropped to a variable tension of around 0.1×BW at 0.25. Subject B instead began with minimal EHL tension from FS to 0.8 of stance phase. The tension then rose to 0.5×BW. It would seem as though the Dorsi-flexor group was providing a significant antagonism to the Triceps Surae group, although the pattern of this antagonism varies with subject during Walking task.

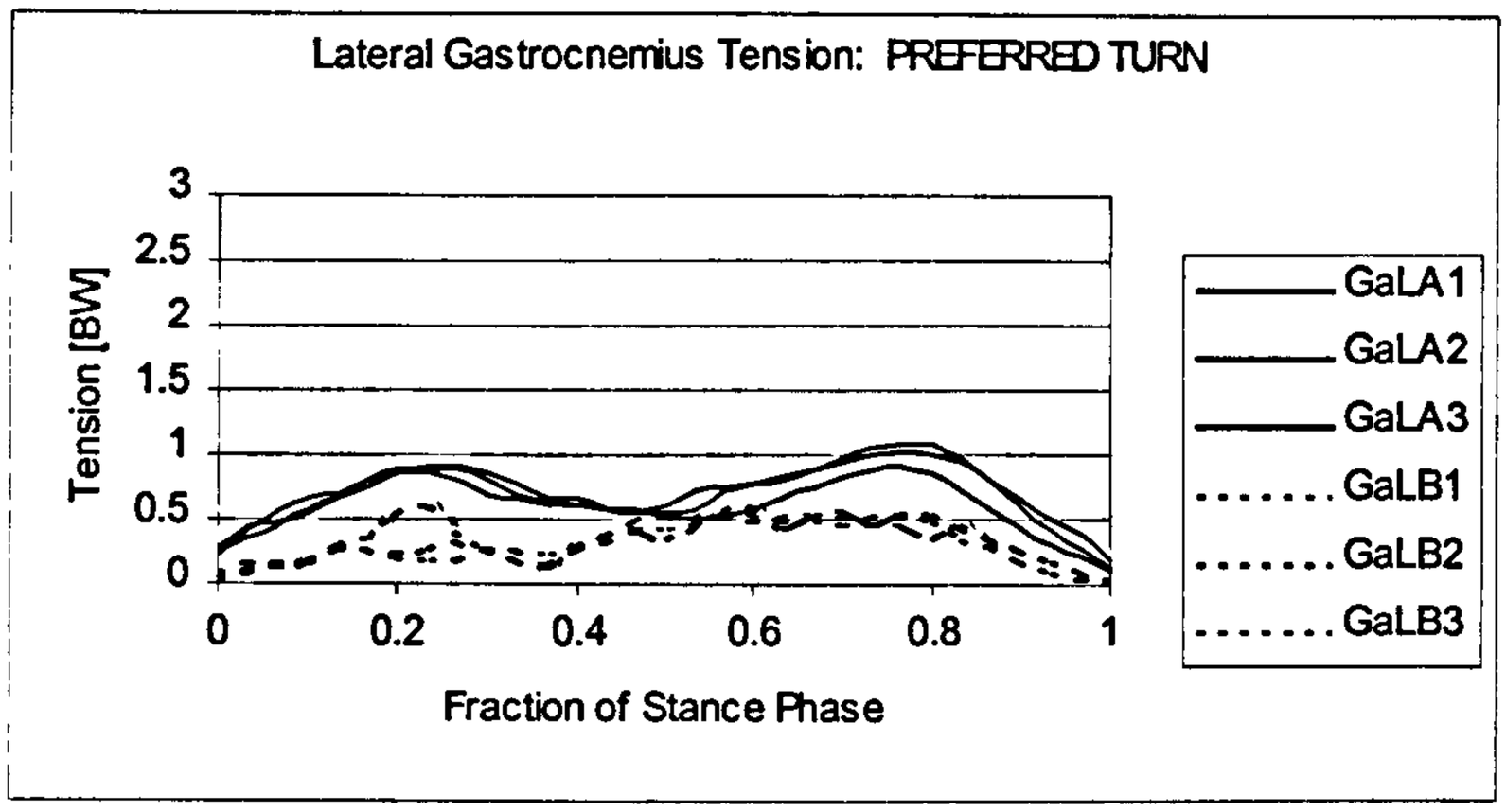

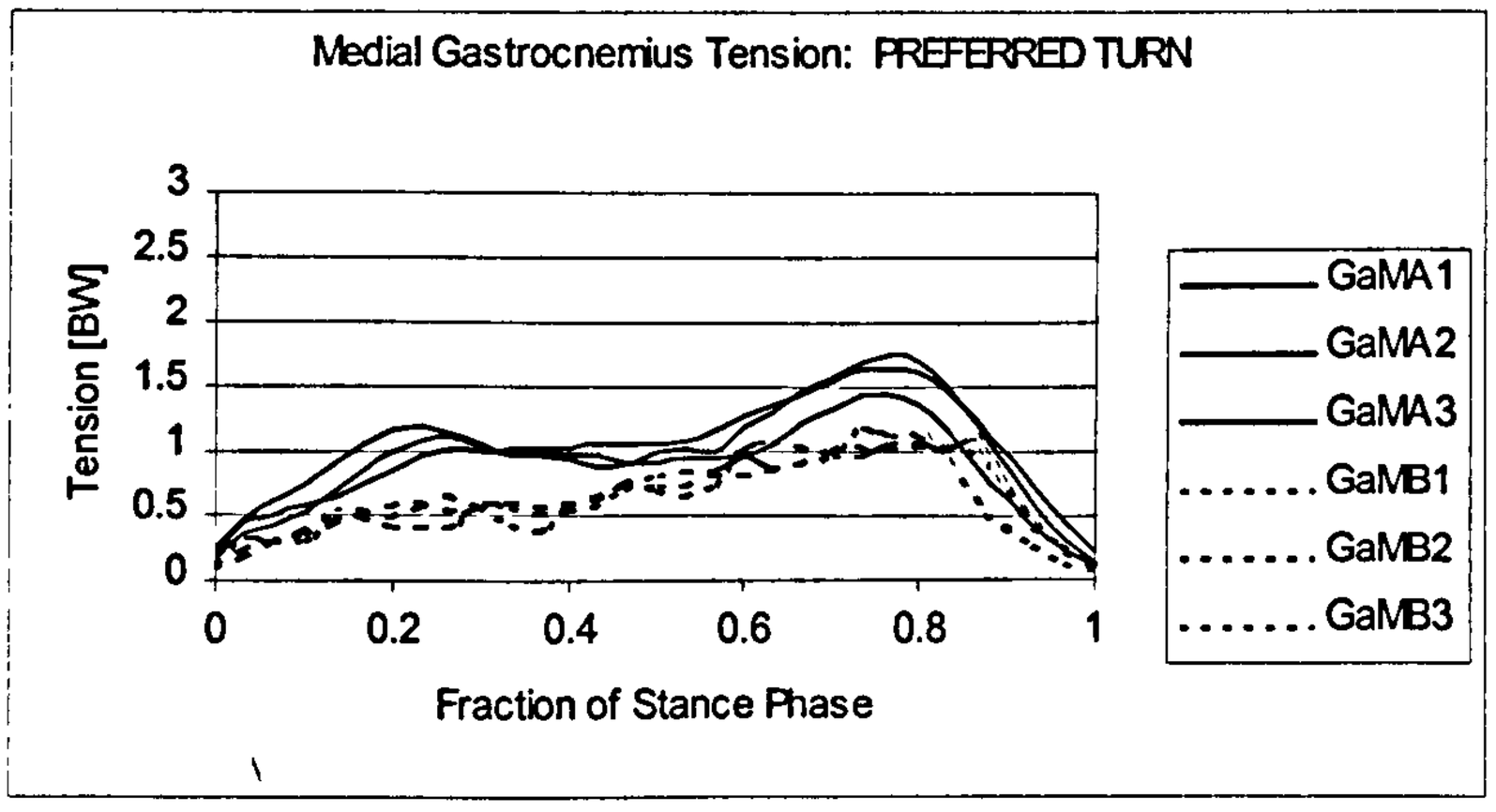

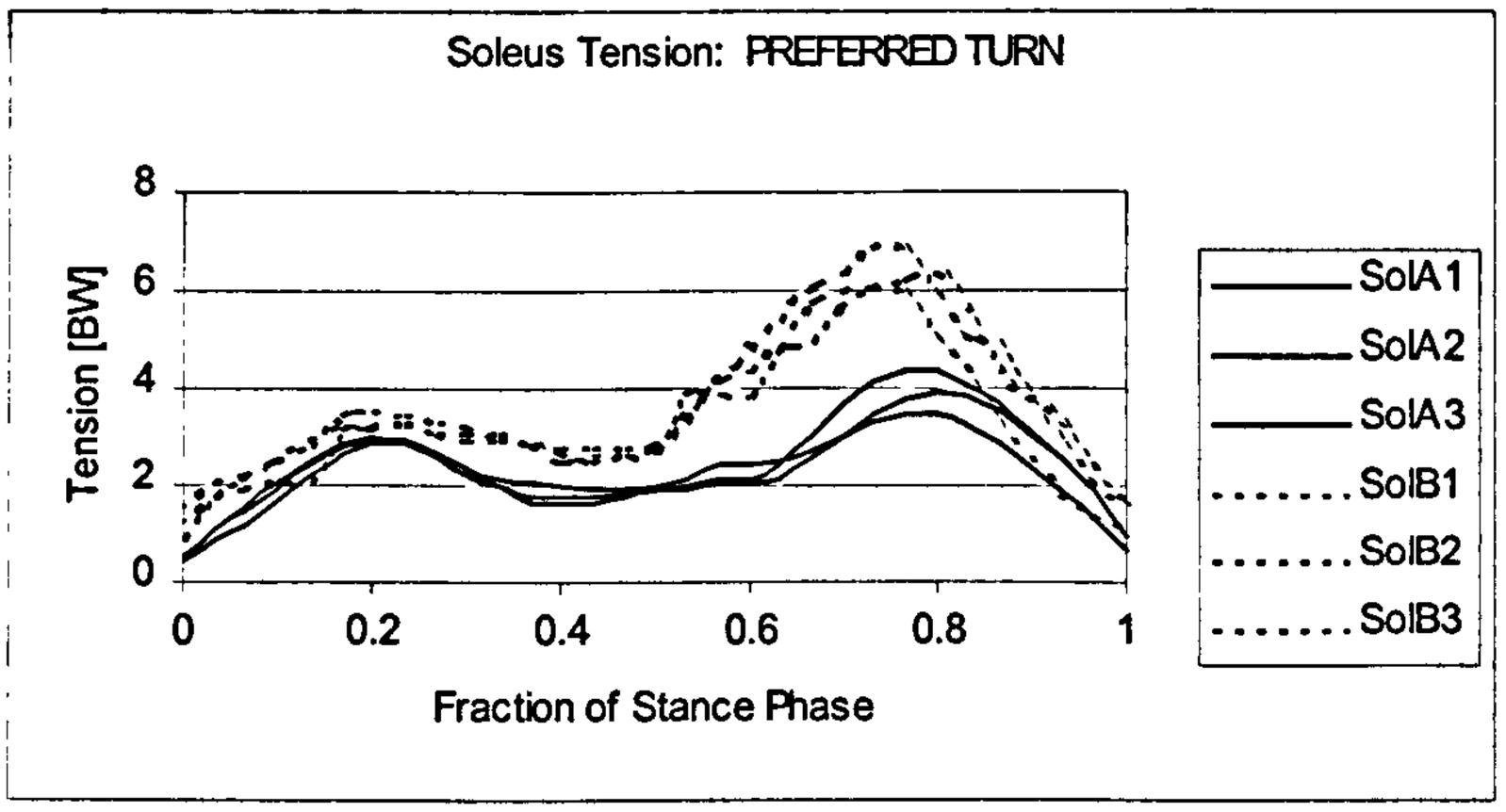

Figure 8.2-4 Triceps Surae Muscle Tensions for Preferred Speed Turning for Subjects A and B.

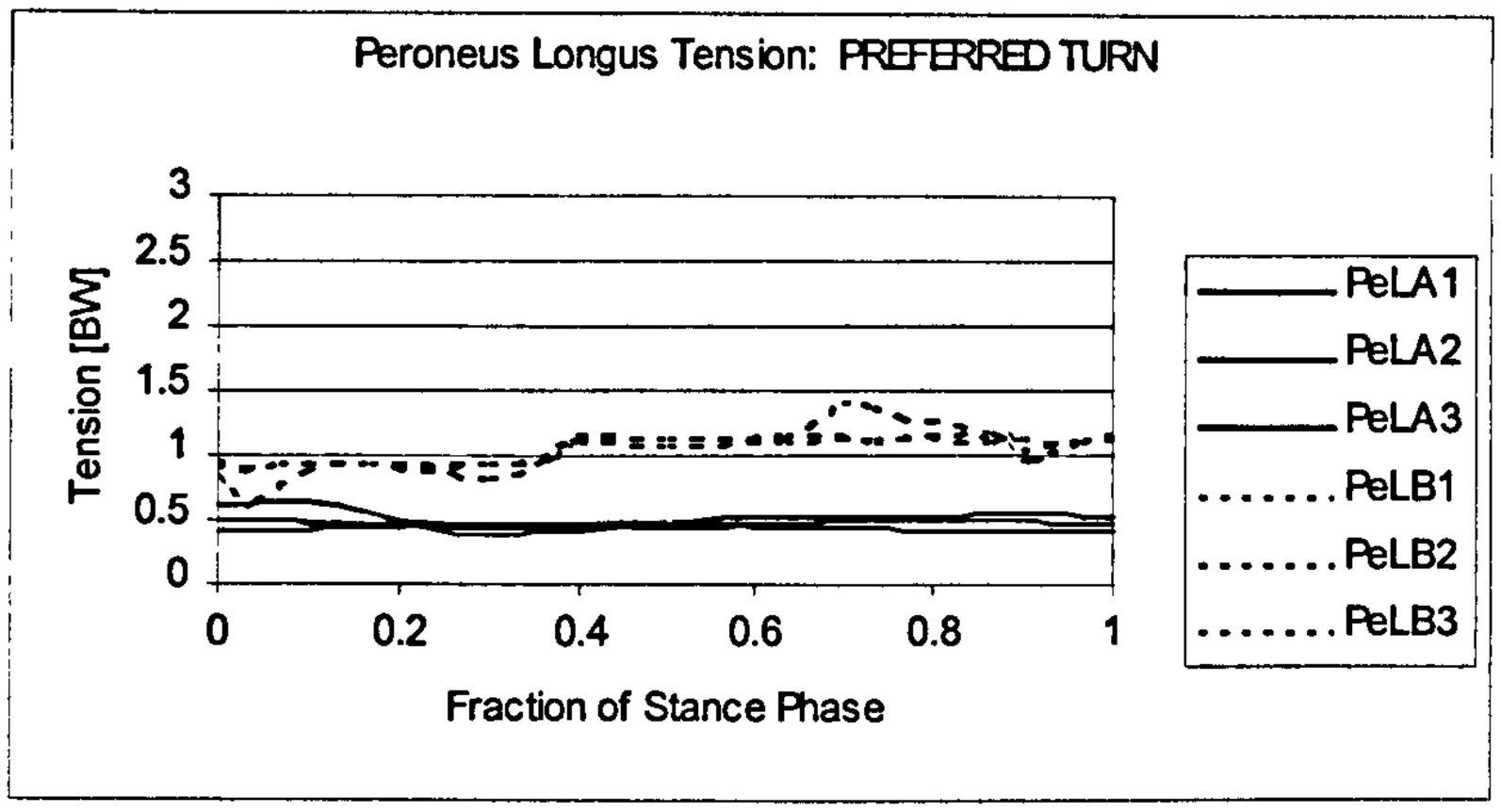

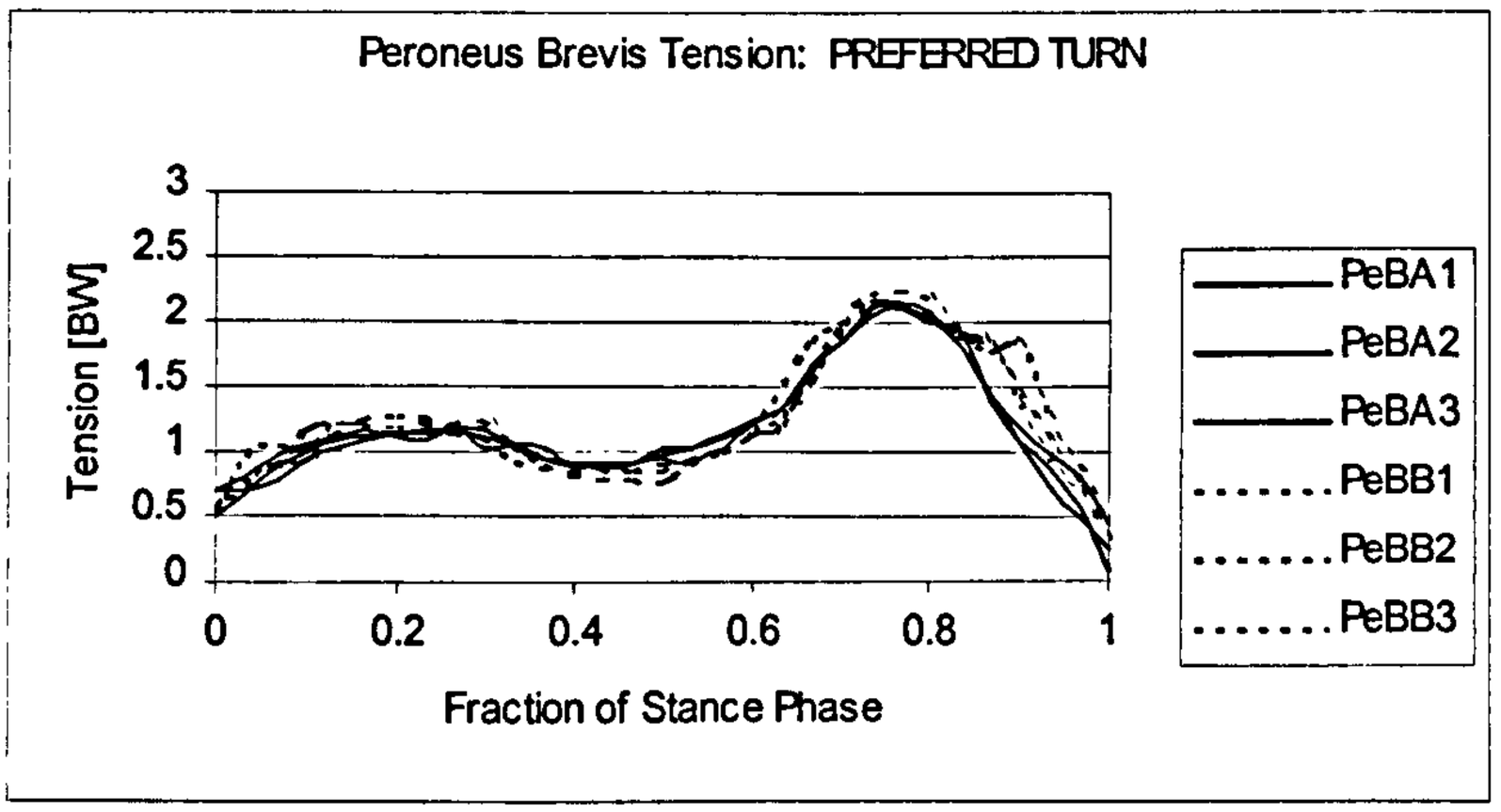

Figure 8.2-5 Peroneal Muscle Tensions for Preferred Speed Turning for Subjects A and B.

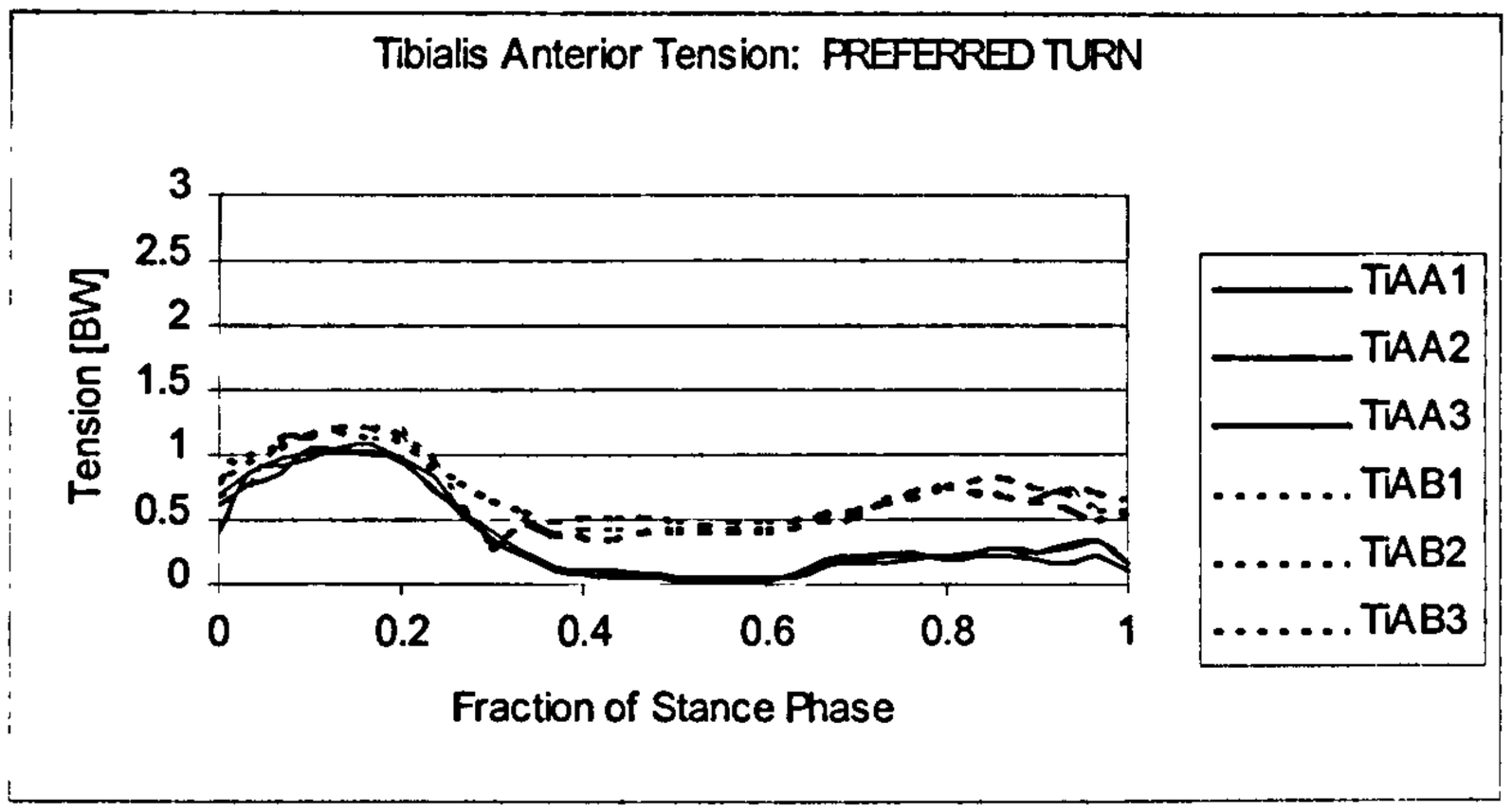

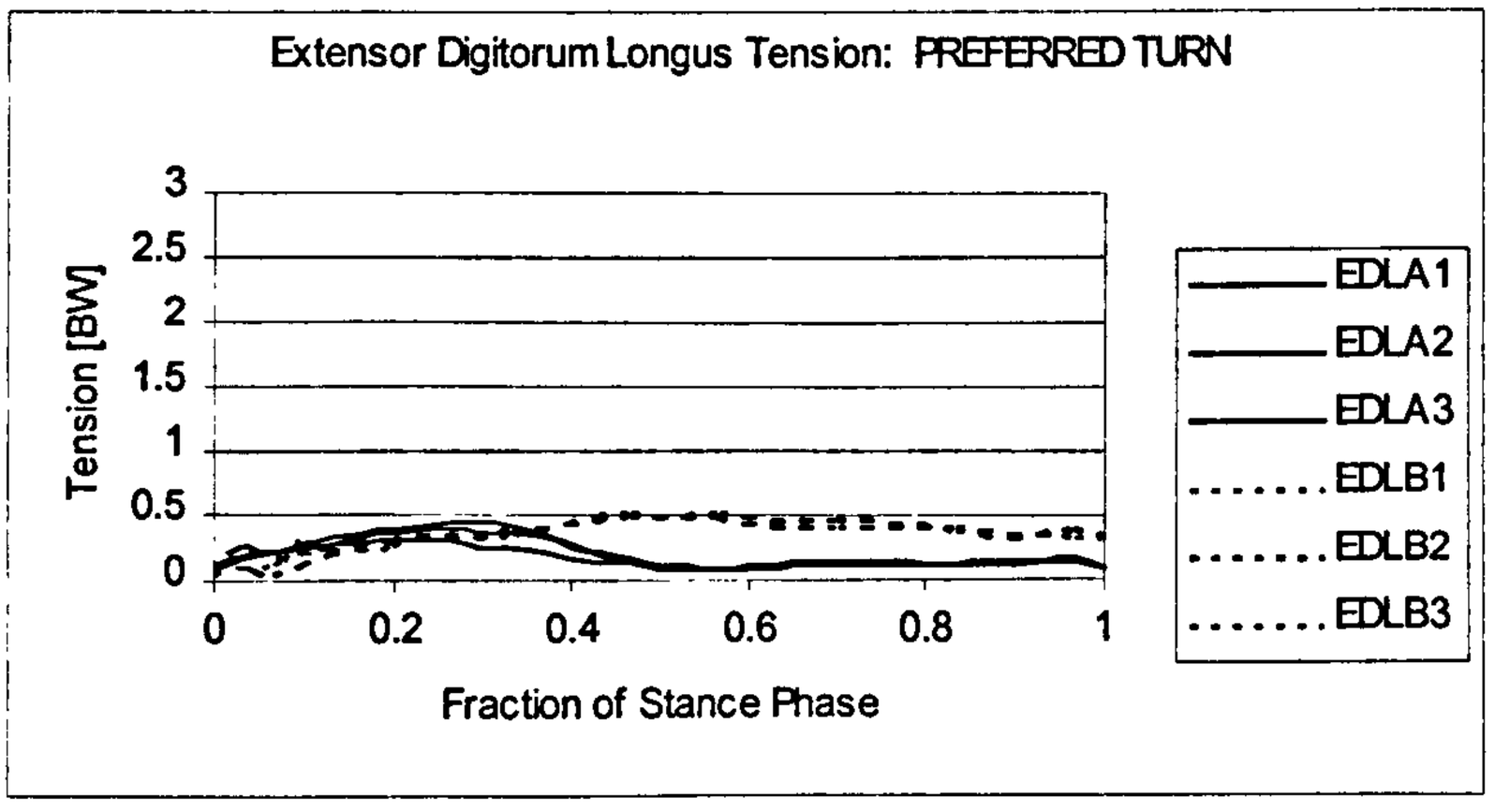

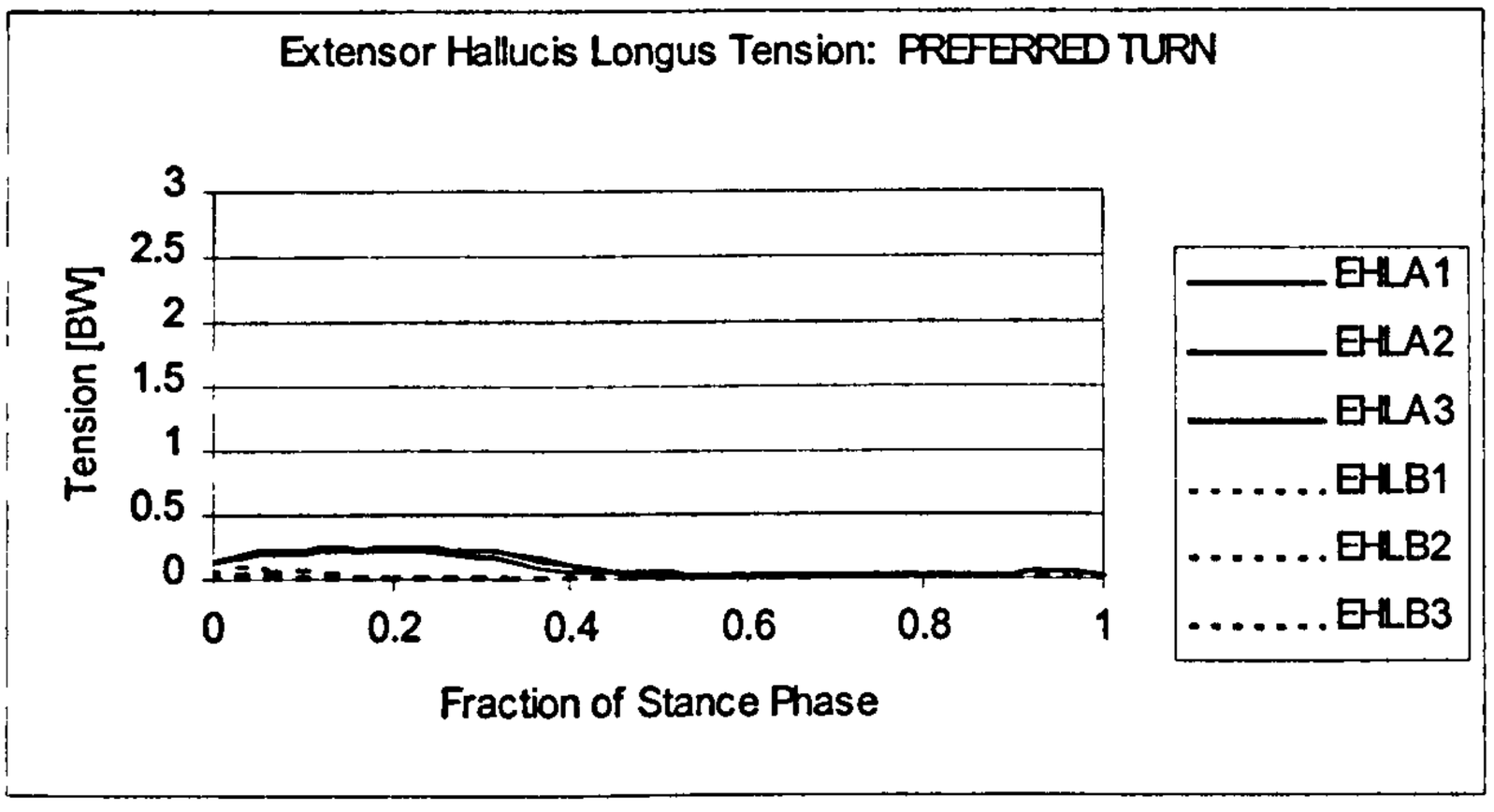

Figure 8.2-6 Dorsi-flexor Muscle Tensions for Preferred Speed Turning for Subjects A and B.

Figures 8.2-4 to 8.2-6 plot the tensions in the eight muscles for each of the turning trials at preferred speed for Subjects A and B. As with the trials for the walking task, there was good repeatability between the trials of the same subject, but variability between subjects. The Triceps Surae group exerted the greatest tensions about the joints. As in the walking task for Subject A, the two heads of Gastrocnemius and the Soleus muscle showed two peaks, one early at 0.25 and one late at 0.8 of stance phase. These peaks coincided in each of the three muscles. The first peak in each case was smaller than the second. The tensions in the two heads of Gastrocnemius for Subject B showed a single, broad peak late in stance phase, at 0.6 to 0.7. This peak was larger in GaM than in GaL. The tension in the Soleus for Subject B was more variable, but seemed to show a diffuse peak around 0.25 and a large distinct peak at 0.8 of stance phase. The magnitude of the late peak in the Gastrocnemius tension for Subject B was similar to that of Subject A, although the timing of the peaks was different. The peak tension in the Soleus however, was larger in Subject B, at around 6.5×BW, than in Subject A, which peaked at 4.0×BW. The peak tension in the Achilles tendon during preferred speed turning was 6.7×BW occurring at 0.2 of stance phase for Subject A and 8.0×BW occurring at 0.7 of stance phase for Subject B.

The Peroneal muscle tensions were also different for the two subjects. This is plotted in Figure 8.2-5. The tension in PeL for Subject A was constant at 0.50×BW, similar to the walking task, indicating that it may be fulfilling a postural role in turning. The PeL tension for Subject B was also reasonably constant for much of the turning task, but at a larger magnitude of just below 1.0×BW at FS rising to just above 1.0×BW at TO. The Peroneus Brevis muscle pattern of tension was nearly identical for Subjects A and B. The tension showed two peaks. The early peak was smaller at 0.2 of stance and the later, larger peak around 0.8 of stance phase. The magnitude for the first peak was around 1.2×BW and was around 2.1×BW for the second peak.

The tensions in the Dorsi-flexors was different for the two subjects. The TiA for both showed an early peak from FS to 0.2 of stance phase with a magnitude of around 1.1×BW. The TiA tension for Subject A then dropped to minimal until 0.65

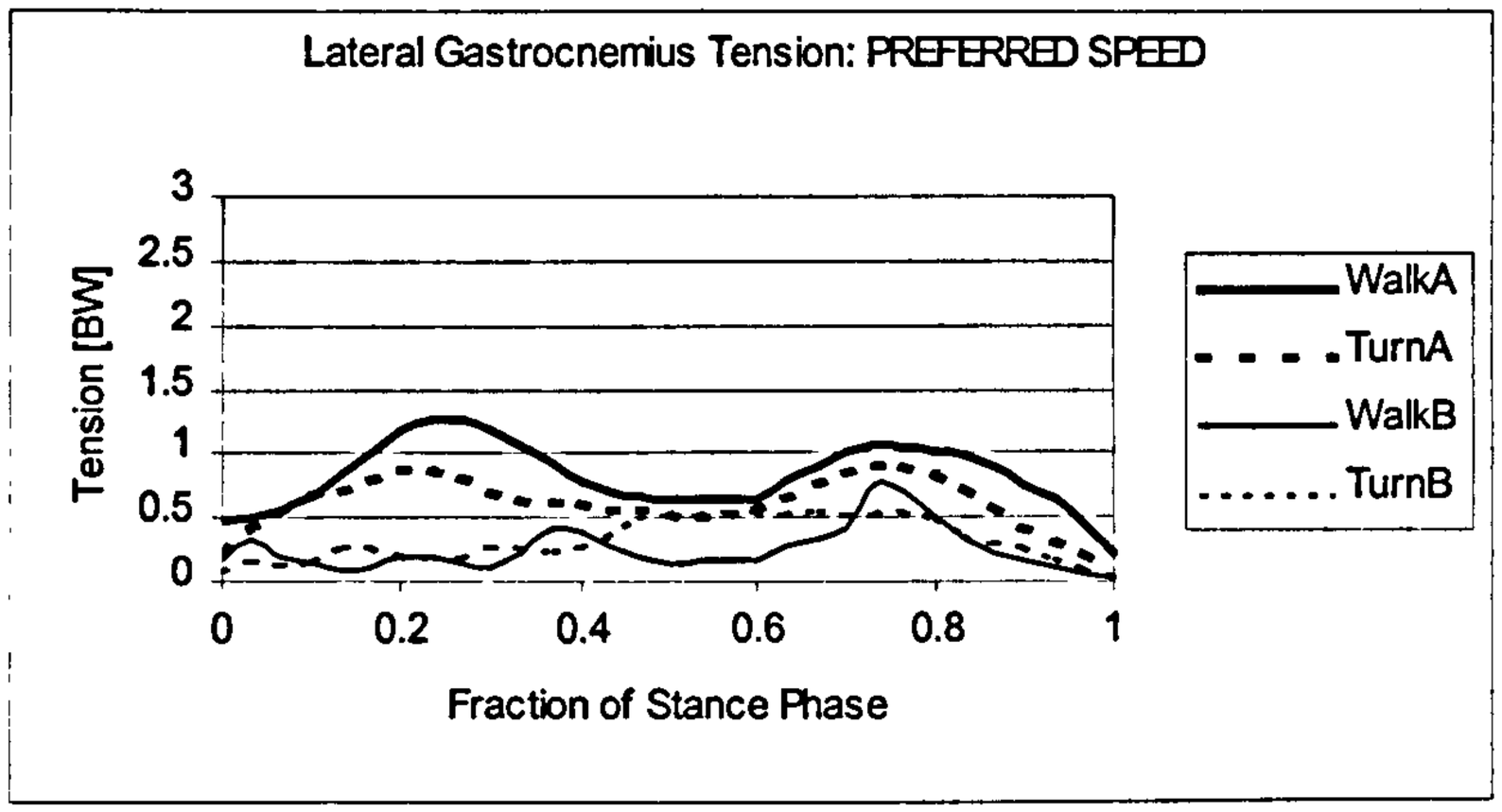

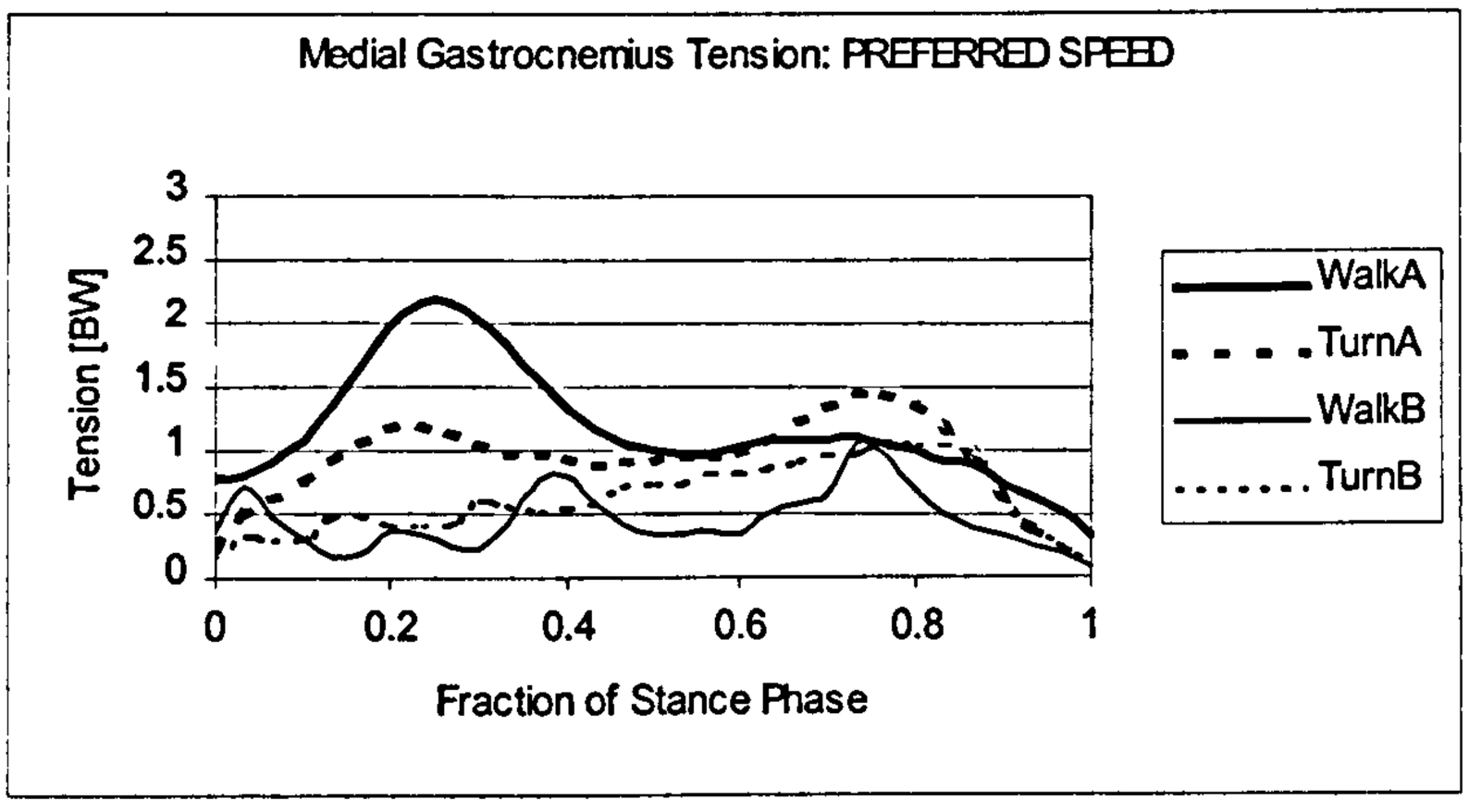

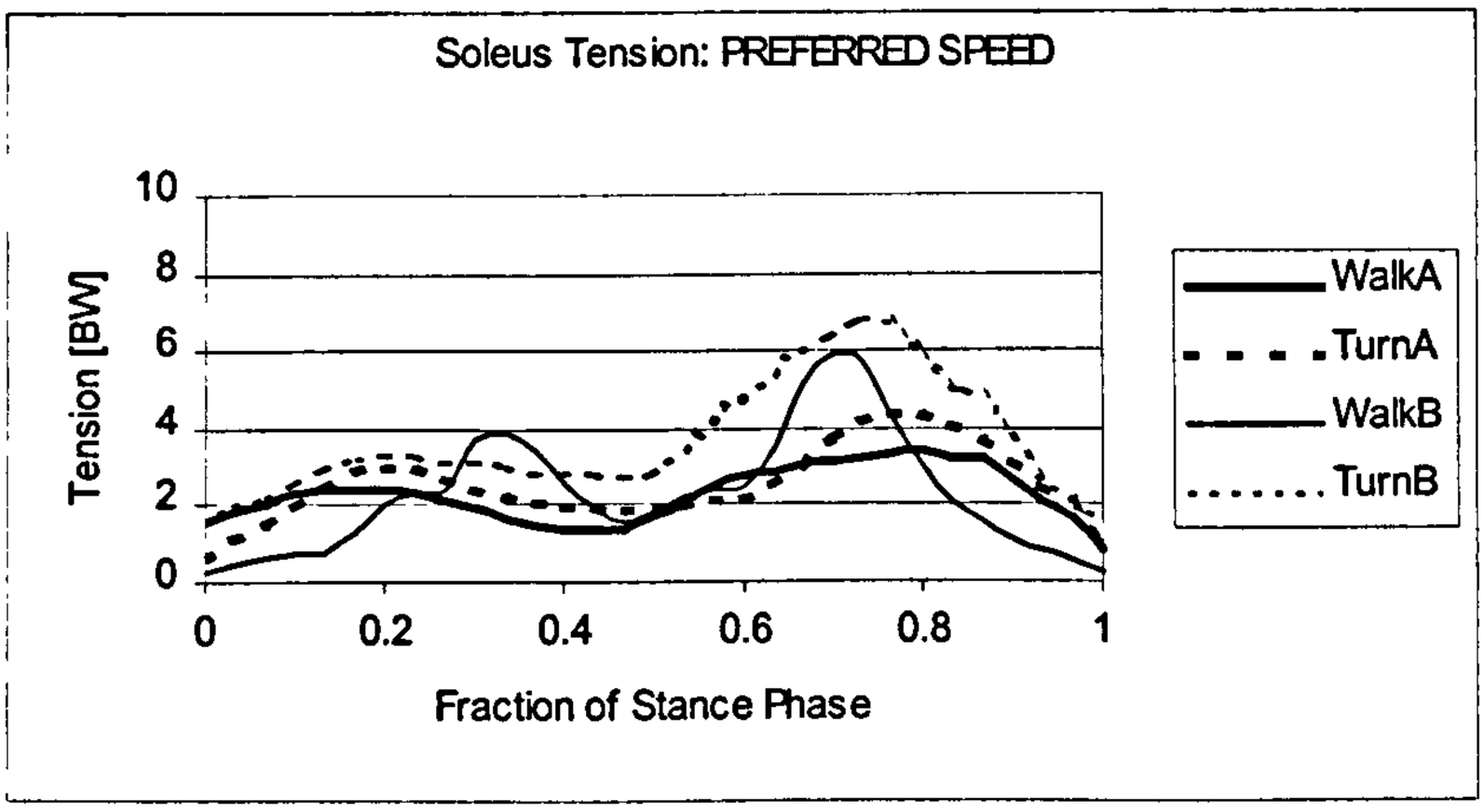

Figure 8.2-7 Comparing Task differences in Triceps Surae Muscle Tensions for Preferred Speed Walking and Turning for Subjects A and B.

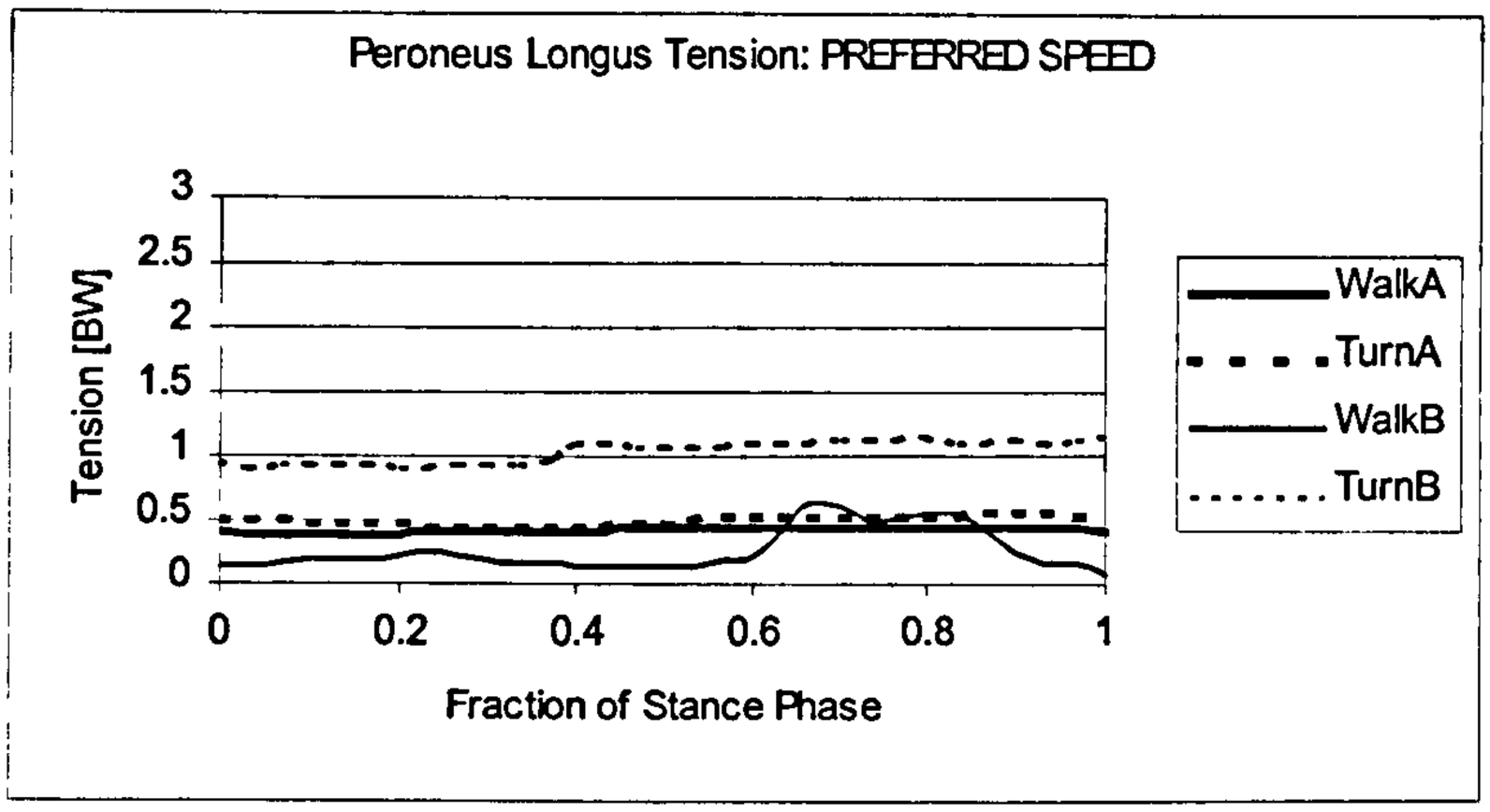

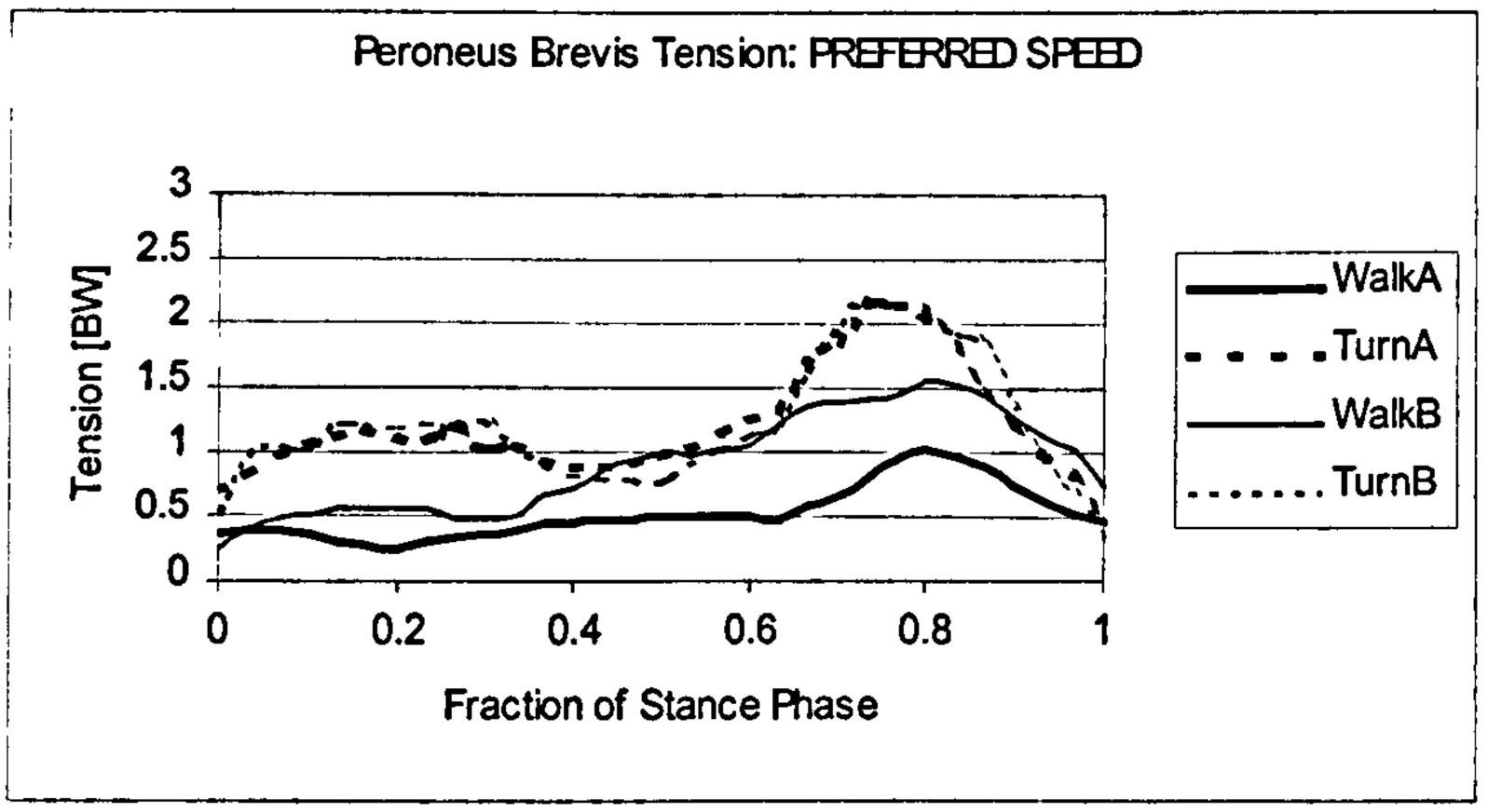

Figure 8.2-8 Comparing Task differences in Peroneal Muscle Tensions for Preferred Speed Walking and Turning for Subjects A and B.

of stance and then rose to 0.25×BW. For Subject B, after the first peak the tension dropped to 0.5×BW and then rose again at 0.8 of stance to a peak of 0.75×BW. The EDL tension in Subject A had a single early peak of 0.4×BW at 0.15 of stance phase and then a constant tension of 0.2×BW to TO. In Subject B, EDL was active at around 0.4×BW to 0.5×BW throughout stance. EHL was quiet throughout stance for Subject B but showed an early peak in Subject A at 0.2 of stance of 0.25×BW.

Since the Dorsi-flexion group of muscles showed relatively less involvement about the joints of the Ankle Complex during walking and turning compared to the tensions of the Peroneals and the Triceps Surae, this group is not included in the remaining figures of this section. Figure 8.2-7 and 8.2-8 compare the muscle tensions in the Triceps Surae and Peroneal groups between tasks for preferred speed for the two subjects. The PeL tension for Subject A was little changed between tasks. Subject B however showed a magnitude and pattern change, moving from a constant tension during turning to a late peaked tension in walking. The PeB tensions became similar for the two subjects during turning which which was interesting. The tension patterns were distinct between subjects during the walking tasks. The main feature to be observed in the task comparison is the presence of a large late peak in PeB tension during the turning tasks. The peak for both Subjects A and B occurred at 0.8 of stance phase and had a magnitude of over 2.0×BW. This peak was probably opposing the large late inverting moment applied to the Ankle Complex during turning produced by the increased, medially directed mediolateral Ground Reaction Force.

The muscles of the Triceps Surae group were affected by changing from walking to turning. Although the shapes of the curves of the muscle tensions differed between subjects, changing from a walking task to a turning task altered the tension curves for the two subjects similarly. The peak tensions were increased during the turning task compared to the walking tasks for GaL, GaM and Sol.

Figures 8.2-9 and 8.2-10 compare the differences in the muscle tensions between speeds of walking for Subject A. The tensions in the heads of the Gastrocnemius were similar for preferred and fast speed of walking, with peaks of around 1.35×BW and 2.25×BW for GaL and GaM respectively. At slow walking,

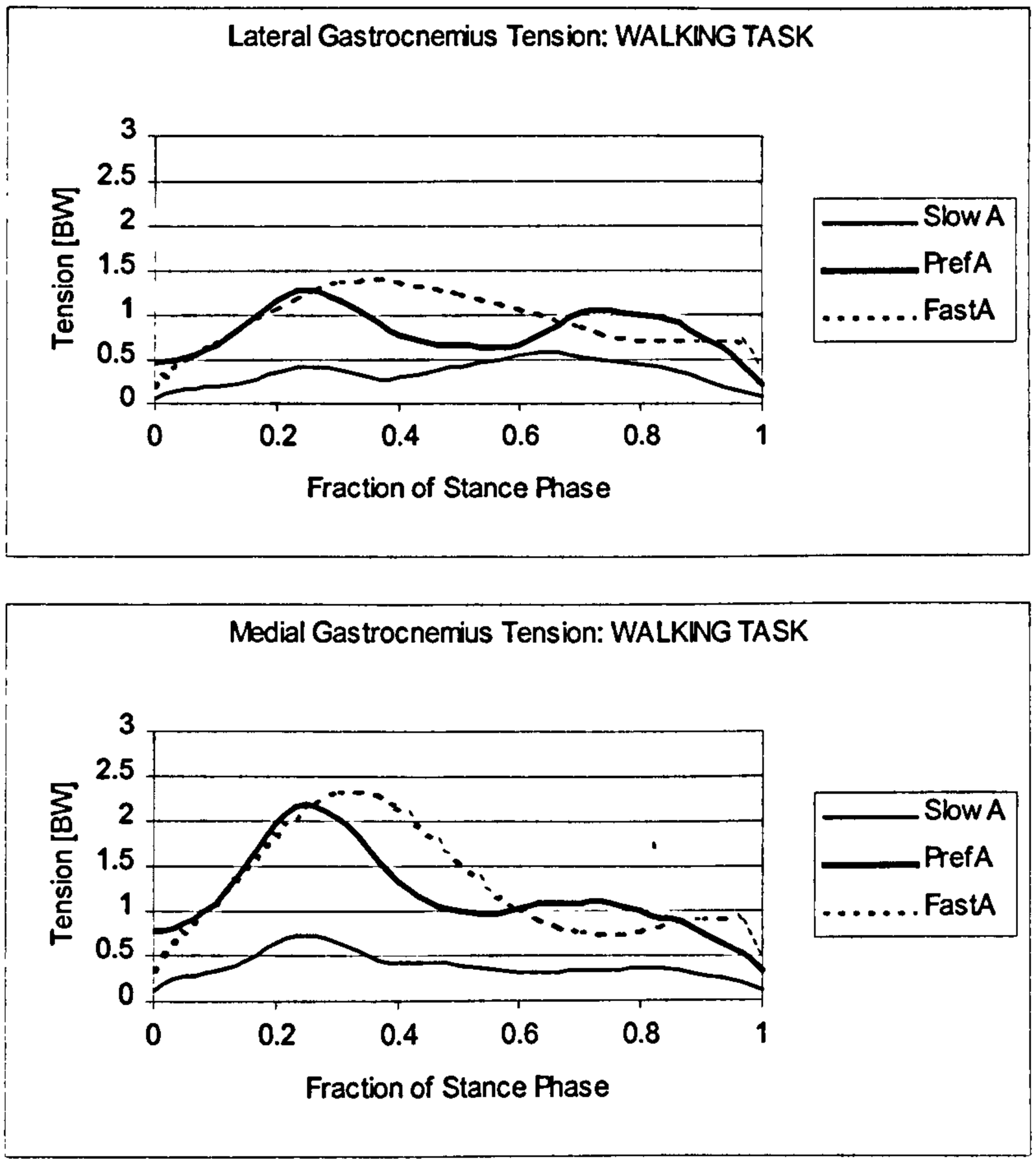

Figure 8.2-9 Comparing Speed differences in Triceps Surae Muscle Tensions for the Walking Task for Subjects A and B.

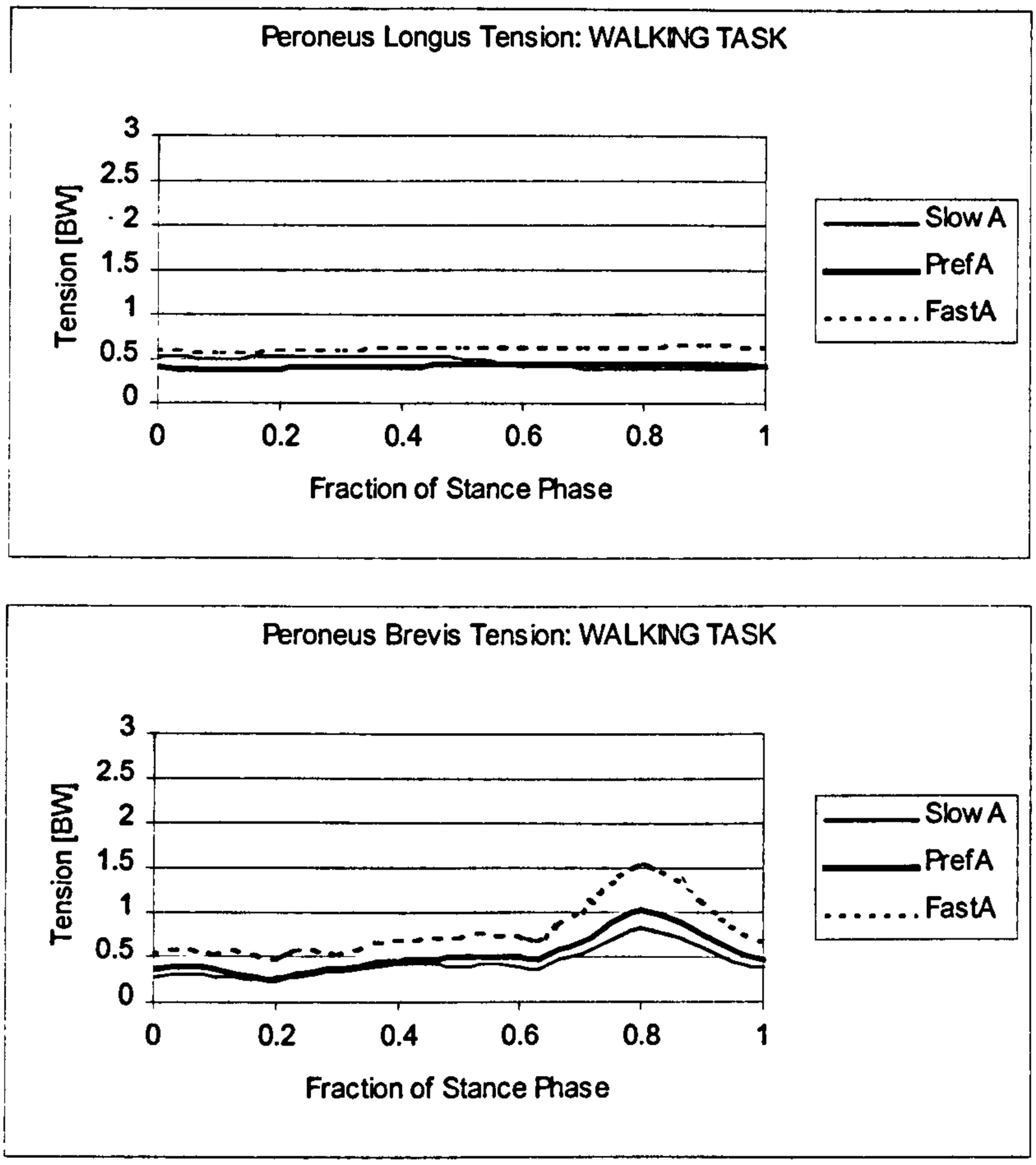

Figure 8.2-10 Comparing Speed differences in Peroneal Muscle Tensions for the Walking Task for Subjects A and B.

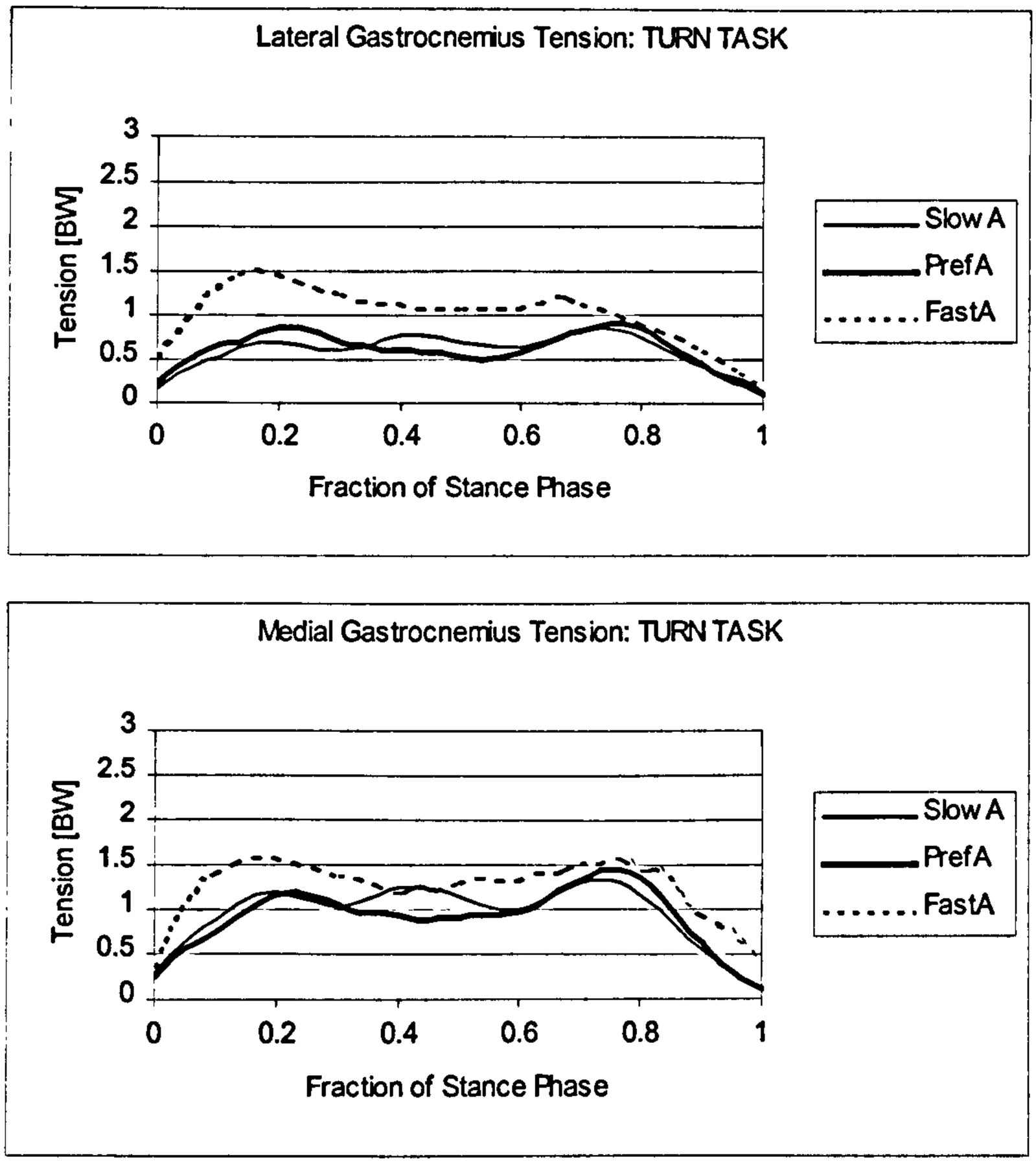

Figure 8.2-11 Comparing Speed differences in Triceps Surae Muscle Tensions for the Turning Task for Subjects A and B.

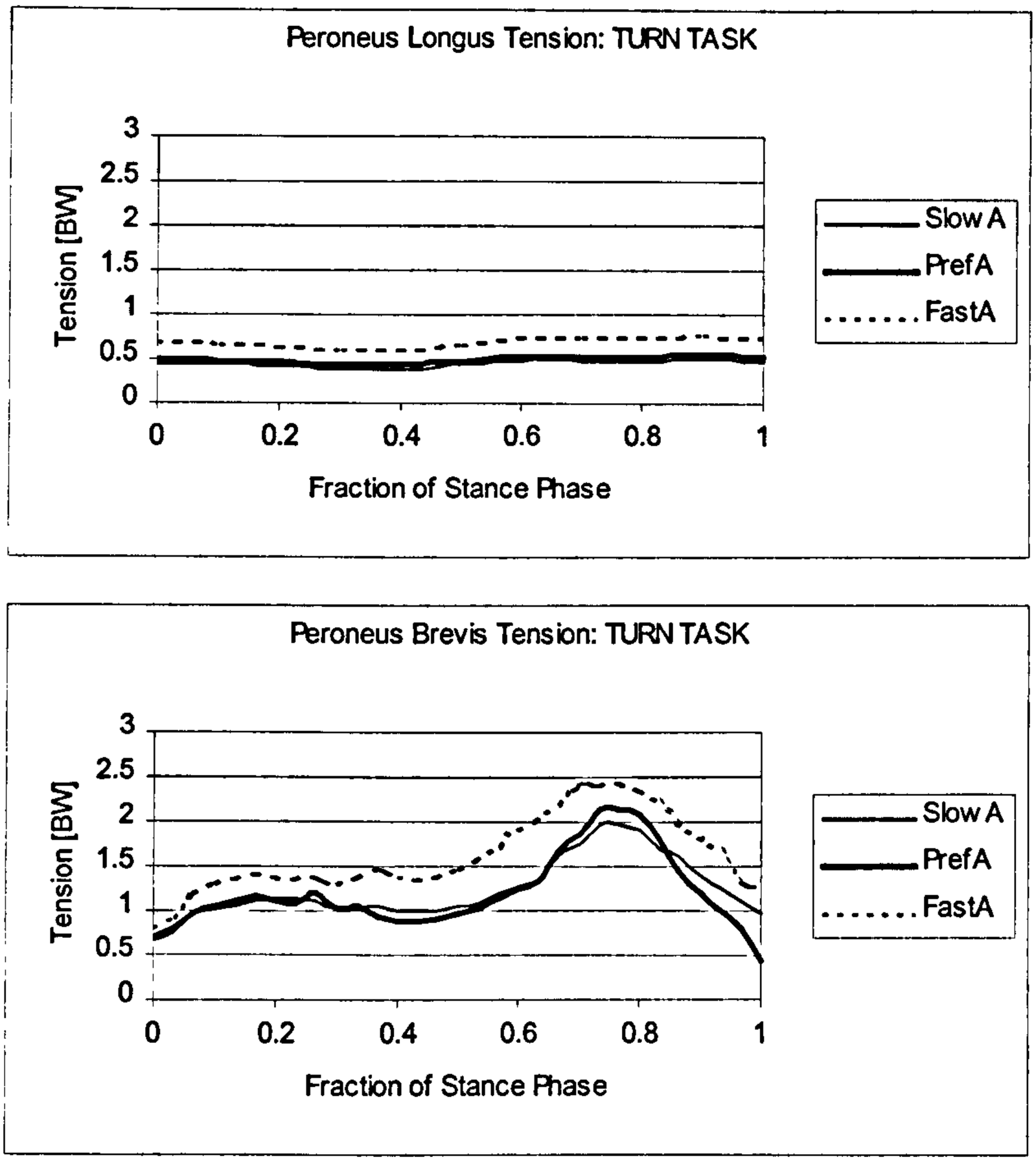

Figure 8.2-12 Comparing Speed differences in Peroneal Muscle Tensions for the Turning Task for Subjects A and B.

both of these tensions were lower at around 0.55×BW and 0.75×BW. Soleus tension changed between slow and preferred speeds and between preferred and fast walking. At slow walking there were no distinct peaks. At preferred speed there were two distinct peaks that developed, which then changed into a single early peak during fast walking. The Peroneus Brevis pattern of tensions was generally similar for each of the three speeds with the magnitude increasing with increasing speed.

The comparison of different speeds of turning are plotted in Figures 8.2-11 and 8.2-12. In the heads of the Gastrocnemius, the patterns of tensions changed less between slow and preferred speed of turning then between preferred speed fast speed. The tension in the Soleus was different for each of the three speeds. At slow speed, the tension possessed two peaks, one early and one late. The early peak decreased and the late peak increased as speed increased. During fast speed turning, the Soleus tension pattern lost the early peak and possessed only a large late peak of 5.0×BW occurring at 0.8 of stance phase.

The tension in the Peroneus Longus muscle was unaffected by speed changes during the turning task. The magnitude of tension rose slightly from 0.5×BW at slow and preferred speed up to 0.65×BW during fast speed. The pattern for PeB tensions were also variable between speeds. However, for PeB, the tension magnitude changed more significantly with the late peak rising from 2.0×BW for slow speed to 2.45×BW for fast speed.

8.2.2 Muscle-tendon Discussion

The peak tension passing through the Achilles tendon during preferred speed walking and turning was 6.35×BW and 6.70×BW respectively for Subject A and 7.90×BW and 8.0×BW for Subject B. In absolute terms, these values are 3332 N and 4995 N respectively for Subject A and 4146 N and 5964 N for Subject B. While these tensions many seen enormous for a biological tissue, particularly in the case of Subject B, there is a point of comparison in the literature. Komi (1990) fitted buckle transducers to the Achilles tendon of a number of subjects which enabled the *in vivo* tension in the Achilles tendon to be measured during a number of movement tasks such as running, hopping and jumping. The maximum in vivo tensions recorded by

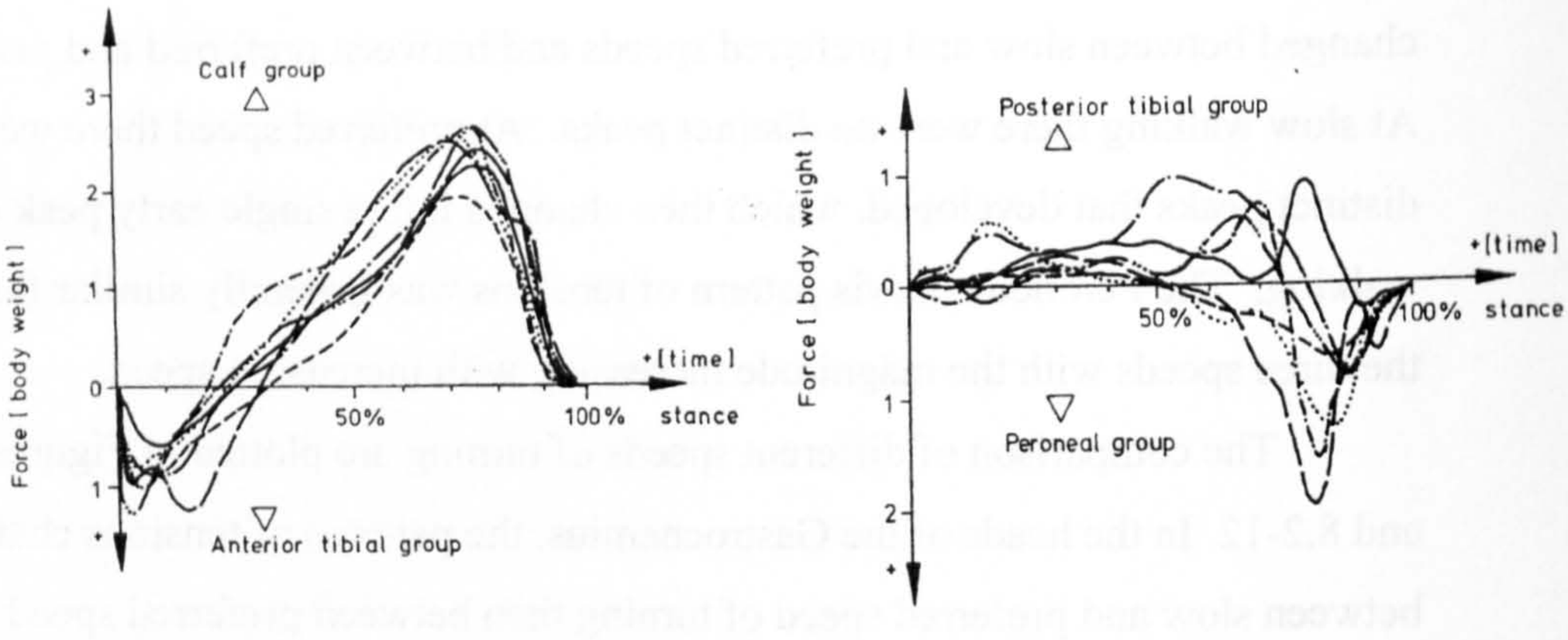

Figure 8.2-13 Muscle loads in the four functional muscle groups: Calf, Anterior Tibial, Posterior Tibial and Peroneal, as predictedby Procter, 1980.

Komi were on the order of 9000 N which was normalised to 12.5×BW for running at 4.0 m/s. Therefore the tensions predicted by the present model are within the physiological range of tensions that can be withstood by the Achilles tendon.

The muscle loading reported by Procter, 1980 (recall Section 2.3 and Figure 2.3-4) bears similarities and differences to the results presented in this section. Figure 8.2-13 (repeated from Figure 2.3-4) shows the muscle loads for each of the four functional muscle groups calculated by Procter, 1980. Note that no antagonism was allowed between the calf and anterior tibial groups or between the posterior tibial and peroneal groups. This restriction in the Procter model produces the main difference between that model and the present model. Figure 8.2-4 shows the triceps surae muscles to be active for Subjects A and B throughout stance phase with a small peak in load at 0.25 of stance phase, during the decceleration portion. Procter implies that the calf is relaxed during this portion of stance. Conversely, Figure 8.2-6 shows two dorsi-flexors (TiA and EDL) to be minorly active for Subject B during late stance phase. Procter model results infer that the dorsi-flexors are inactive during this portion of stance.

The load patterns are similar for the two models in that the major peak in calf loading occurs in late stance for both Procter (at 0.75 stance) and the present model (at 0.8 stance). As well, the major peak in dorsi-flexor loading (anterior tibial group) occurs early in stance: Procter at 0.1 stance and the present model at 0.2.

The magnitude of muscle loading in the present model was larger than for Procter. The peak load summed from all three calf muscles in the present study was 5.75×BW for Subject A and 7.5×BW for Subject B. Procter reported 3.0×BW for calf muscles plus 1.75×BW for the posterior tibial muscle group. The sum of loading passing posterior to the ankle is therefore 4.75×BW. This may be a more appropriate comparison since the present model does not explicitly calculate posterior tibial muscle group tensions and includes this loading with the triceps surae muscles.

The peroneal muscles in the current model are more active than in the Procter model, with significant tension in PeB during early stance. However, a peak in tension late in stance is predicted by both models with similar magnitudes: 2.5×BW

for Subject A and 3.2×BW for Subject B in the present model and 2.0×BW from Procter.

A number of overall observations can be drawn from this large collection of muscle tension data. The most important point to be made is that despite the external loading acting on the right feet of Subjects A and B being remarkably similar which created moments about the joint rotational axes that were also similar, the two subjects employed different muscle patterns to achieve equilibrium about the Ankle Complex. Since the external loading was so similar, it would seem that the different muscle tension patterns employed by the two subjects arose not from differing loading conditions imposed on the joint complex, but from the neurological system controlling the Ankle Complex. This may indicate that there exist several control strategies for performing the same tasks with the Ankle Complex and that each individual employs one of these strategies exclusively for a specific task such as walking or turning.

Had the Ankle Complex been modelled solely using a more conventional Optimisation routine these different muscle tension patterns would not have been produced. Given such similar input, the optimisation procedure would have produced similar output for the patterns of muscle tensions and this subject specific behaviour would have been missed. As was mentioned earlier, Subjects A and B were selected as the extremes in the range of body masses and heights of the twelve subjects. These two subjects also displayed the extremes in the muscle tension strategies employed by the subjects.

A final observation from the muscle tension patterns is that the Peroneus Brevis plays the greater role in actuating the Subtalar Joint than the Peroneus Longus. This was unexpected since the Longus muscle possesses a larger lever arm about the Subtalar Joint. The Peroneus Longus muscle maintained a constant tension throughout stance and played a postural role in stabilising the Subtalar Joint during the walking and turning tasks. The Peroneus Brevis muscle produced the power about that joint. This was most obvious in the comparison of PeB tension between the speeds of turning plotted in Figure 8.2-12. During fast speed turning, the tension in the PeB had quite a large, late peak with respect to its tension during preferred and

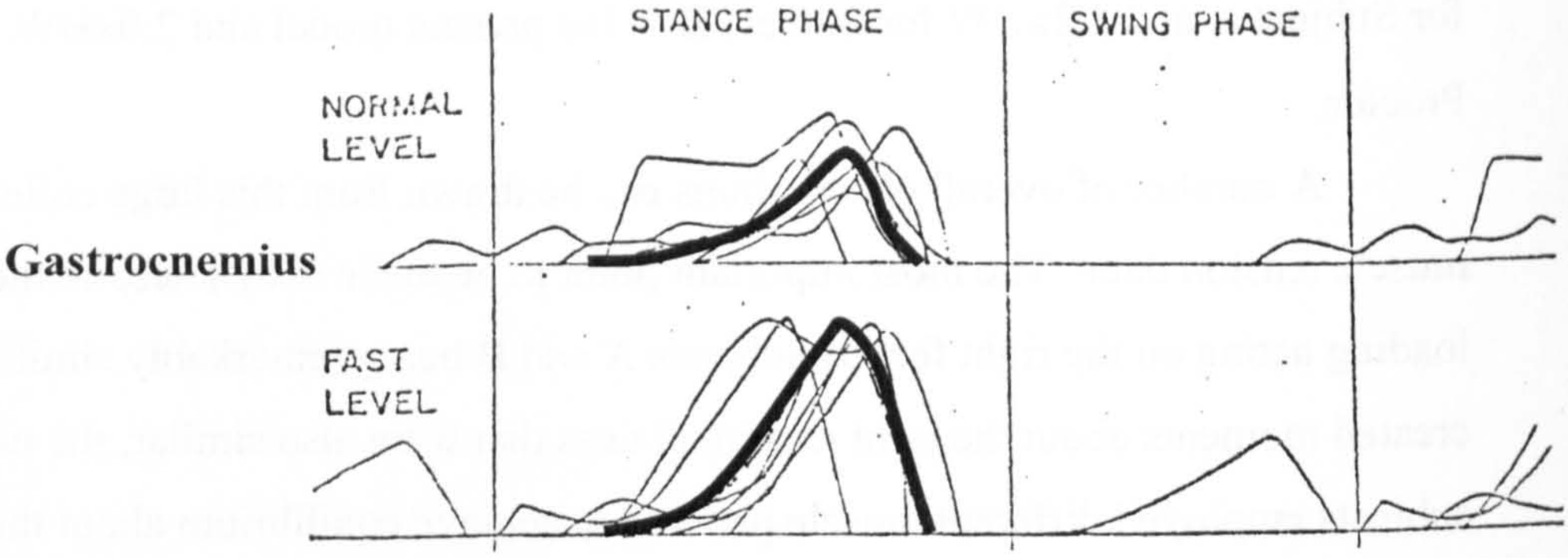

Figure 8.2-14A Results for the triceps surae muscles during normal and fast level walking taken from University of California, 1953.

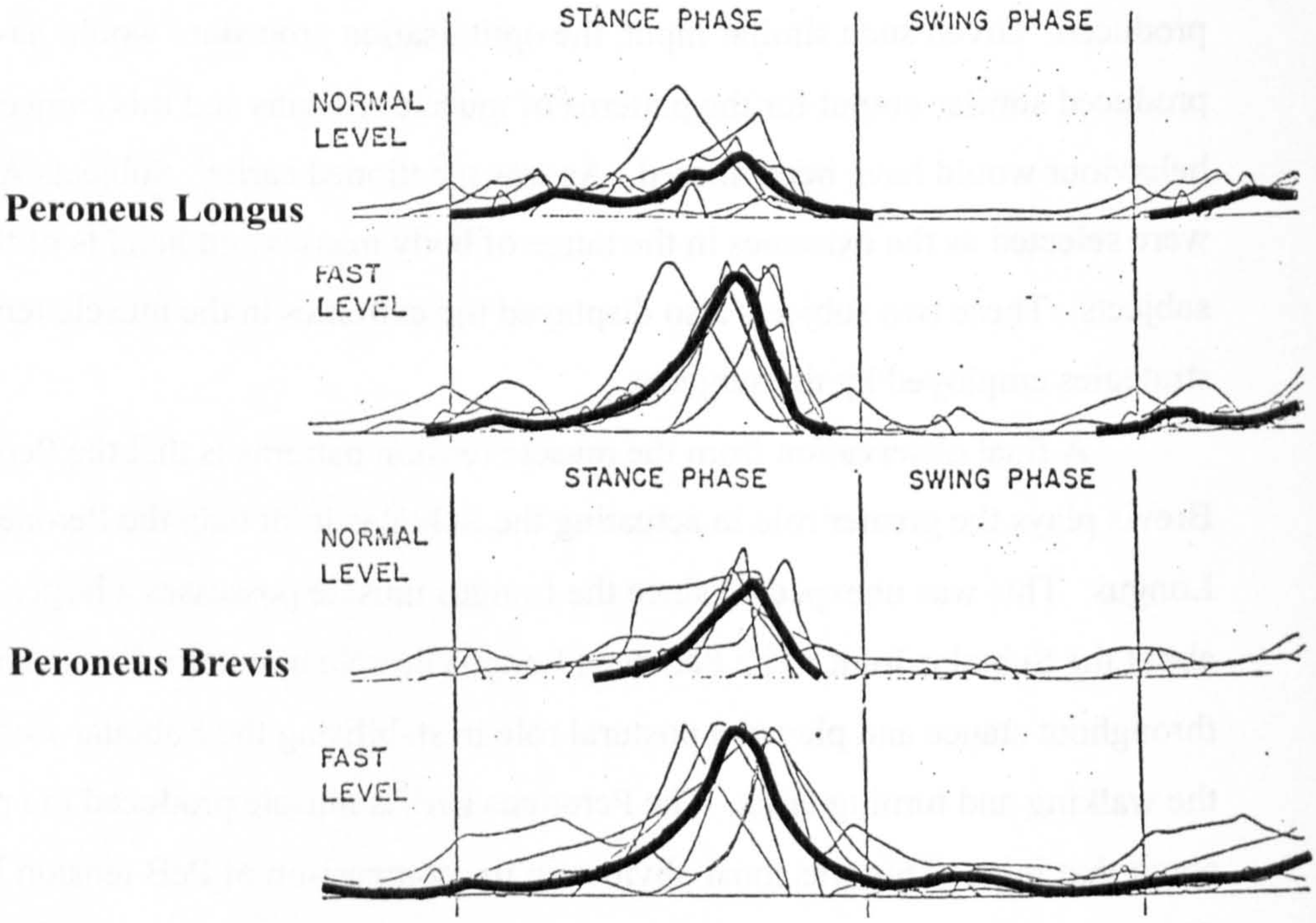

Figure 8.2-14B Results for the peroneal muscles during normal and fast level walking taken from University of California, 1953.

slow speed turning. This muscle therefore seems the most active in changing from the task of walking, which creates very little mediolateral GRFs, to the task of turning, which introduces large medially directed GRFs.

8.2.3 Electromyographic Results and Discussion

As described in Chapter 6, the muscle loading calculated in the current model is driven primarily by the EMG signals recorded from five muscles of the lower leg and is modified by the instantaneous muscle length and velocity. Since there is a discrepancy between the muscle tension results of this model and the Procter, 1980 model, it would be useful to examine the EMG signals that were collected from the subjects of this study. These data can then be compared to what is considered *normal* EMG activity for lower leg muscles during walking. This way it can be seen whether the large amount of antagonism arises from the EMG of the subjects themselves.

The EMG results from the University of California, 1953 study for normal level walking and fast level walking through both stance and swing phase are plotted in Figures 8.2-14A, B and C and will be considered normal. The muscles of the triceps surae (gastrocnemius and soleus) are plotted first (Figure 8.2-14A). The peroneal muscles are next: peroneus longus and brevis (Figure 8.2-14B) and the dorsi-flexors are plotted last: extensor digitorum and hallucis longus and tibialis anterior (Figure 8.2-14C). Note the large amount of variability present for each of the muscles in the integrated signals recorded for the same task in different subjects. The results from all the subjects are resolved into an average activity for each muscle and plotted in the heavy solid line.

The gastrocnemius shows the most activity late in stance with a peak around 0.8 of stance phase. Very little activity is seen early in stance phase on average. The soleus shows similar timing to the gastrocnemius, however more activity is seen on average early in stance and some subjects exhibited significant activity early on during faster walking. The greatest variability is seen in soleus during fast level walking where the timing of peaks is noticeably different for a few subjects. The two peroneal muscles showed peaks in later stance ranging from 0.7 to 0.8 of stance

Extensor Digitorum Longus

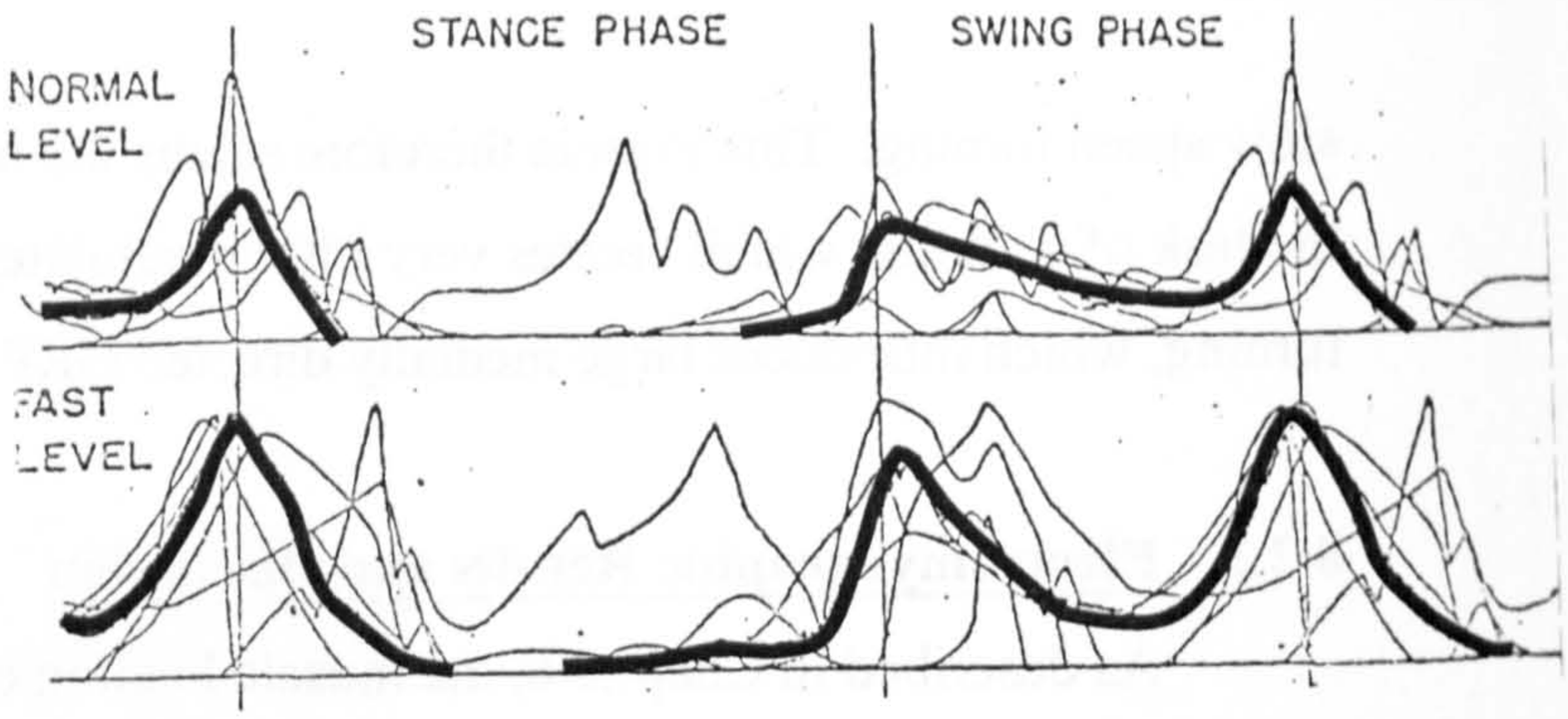

Extensor Hallucis Longus

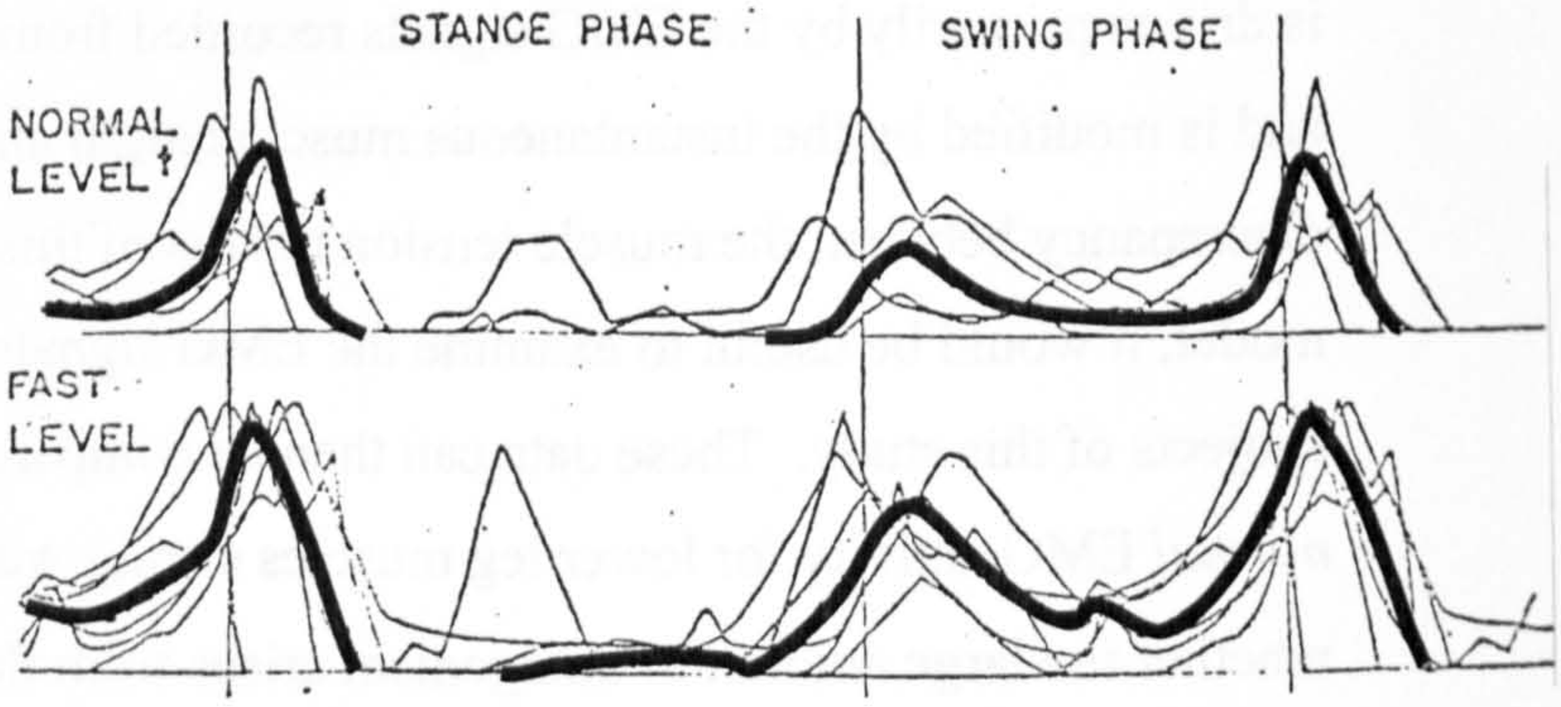

Tibialis Anterior

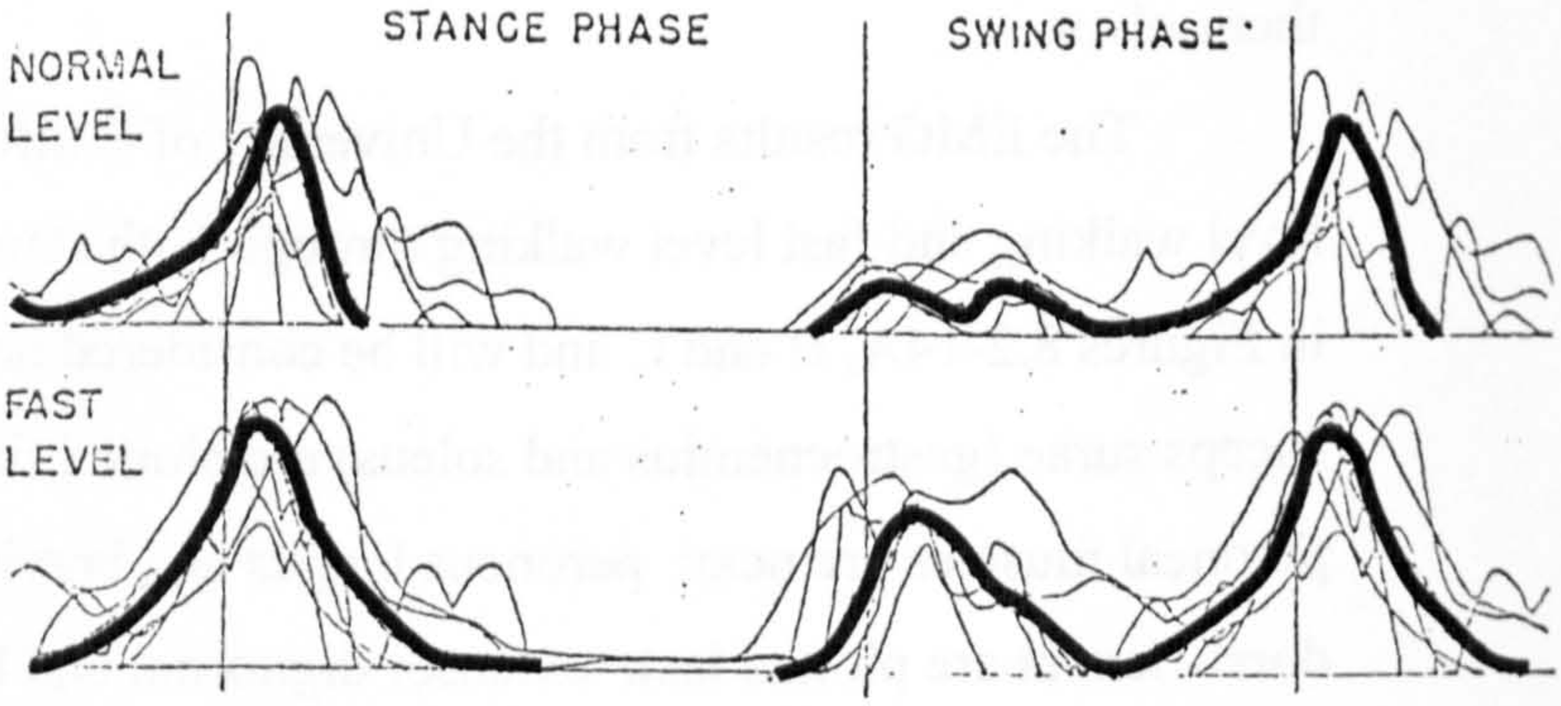

Figure 8.2-14C Results for the dorsi-flexor muscles during normal and fast level walking taken from University of California, 1953.

phase. Many of the subjects showed significant peroneal activity in both longus and brevis throughout stance despite the fact that the average peroneus brevis integrated signal showed no early stance activity. The peaks in the peroneal activity seem to be coincident with the triceps surae muscle activity peaks; although a tremendous amount of variability is seen in the timing, sharpness and magnitude of these peaks between subjects.

The dorsi-flexor EMG results show similar timing for both the toe extensors and the tibialis anterior. All three show a large peak on average at the very beginning of stance or early in stance. Little activity on average is seen through stance until the end of stance when a second peak was seen as the foot and leg entered swing phase. The greatest variability was seen in the toe extensors where some subjects seemed to be using these muscles throughout stance although this does not appear in the average activity. The initial peak in activities for the extensors also shows variability between subjects in terms of timing and magnitude. Tibialis anterior is the least variable muscle of the three dorsi-flexors. Very little activity was seen through midstance. The initial peak showed variability in timing between subjects as did the late peak.

The raw EMG traces for Subjects A and B during preferred speed walking are shown in Figure 8.2-15. These plots contains the recordings from the five muscles recorded in the lower leg: GaM, Sol, PeL, TiA and EDL. These signals are smoothed as described in Chapter 6 (but not "twitched") and plotted in Figure 8.2-16A and B. The first plots show the integrated EMG (IEMG) from the triceps surae muscles: GaM and Sol. The second plot shows the peroneal muscle (PeL) and the dorsi-flexors (TiA and EDL).

Some differences are immediately apparent between the normal walking EMG from Figure 8.2-14A, B and C and the EMG collected in the current study. The IEMG from GaM for Subject B agrees well with the normal; little activity in early stance and a large peak in later stance. Subject A however shows a great deal of activity in early stance with a peak around 0.25 of stance, in addition to the late peak around 0.7. The second peak is much broader than normal and stretches from 0.55 to 0.85 of stance phase. An early peak exists for both subjects in the IEMG of

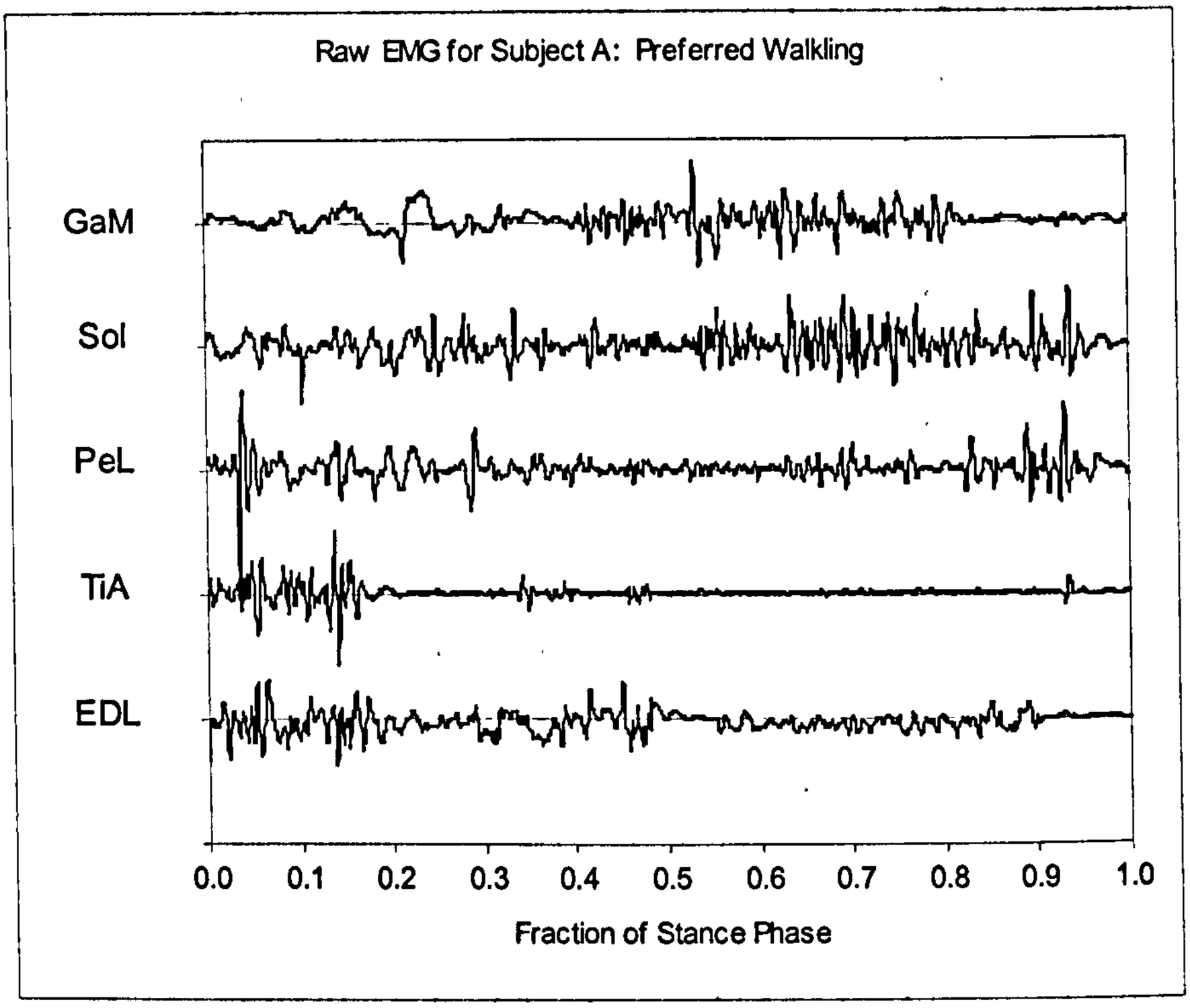

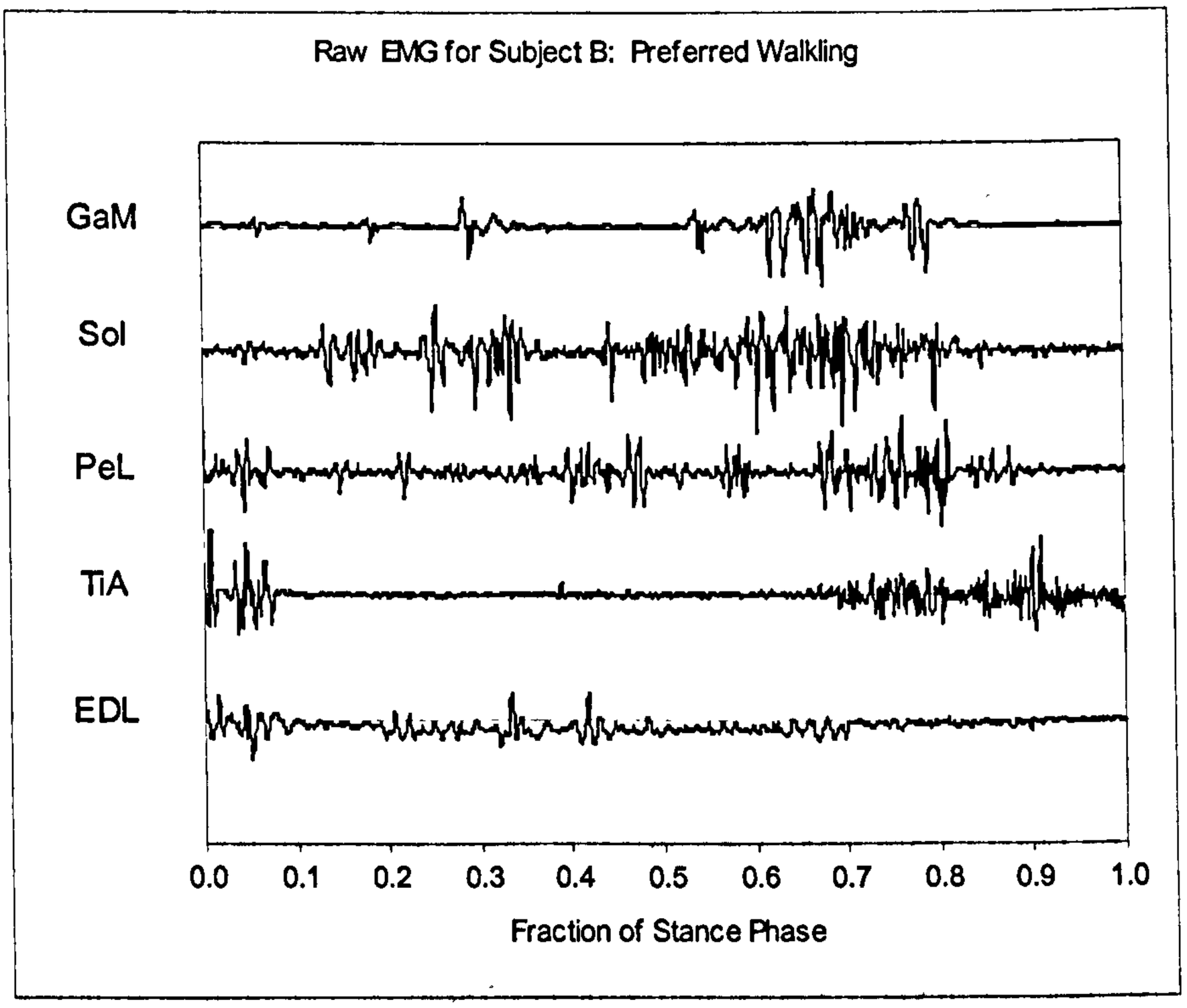

Figure 8.2-15 Raw EMG signals from the five recorded muscles of the lower leg during preferred walking for Subject A (top) and Subject B (top).

soleus with the two subjects showing very similar activity. For both, there is an early, smaller peak at around 0.3 of stance and a dip in activity at mid-stance. The second, normal late peak occurs around 0.75. Recall that there was a great deal of variability in the soleus activity in the University of California normal data, especially in early stance activity. However none of the normal data exhibited the early stance peak recorded from Subjects A and B. The later, diffuse peaks appear normal for both these subjects.

The IEMG for the PeL for Subject B appears normal. There is a small initial peak in the University of California study. The later second peak around 0.8 of stance was demonstrated on the average normal result. Subject A however shows a real divergence from normal. The early peak is much larger and more diffuse than for Subject B and not present in the average normal data. The late peak occurs later than normal at the transition between stance and swing phases.

Subject A demonstrates normal IEMG for TiA. Here, there is a large early peak in activity with little activity for the remainder of stance. In this case, Subject B is not showing normal activity for TiA during walking. The early peak agrees well with the normal activity, but there is a large second peak occurring late in stance at the transition between stance and swing. The IEMG for EDL for both subjects does not agree with the average normal activity, but the both fall well within the variability of activity for the toe extensors. Both show that the toe extensors were active throughout stance.

The trends in the IEMG recorded for Subjects A and B in the current study in Figures 8.2-16A and B can be compared to the consequent muscle tensions produced by the three component muscle model in Figures 8.2-1, 8.2-2 and 8.2-3. Since these tensions were driven primarily by the EMG input, it is expected that the tensions would behave similarly to the IEMG. This indeed turns out to be the case. The gastrocnemius for Subject B shows the normal, single late peak in tension similar to the IEMG. Subject A however, shows a second earlier peak around 0.3 of stance. This is the same pattern seen in the IEMG. The trend for tension in soleus for Subject B differs somewhat from that of Subject A. Both showed very similar IEMG

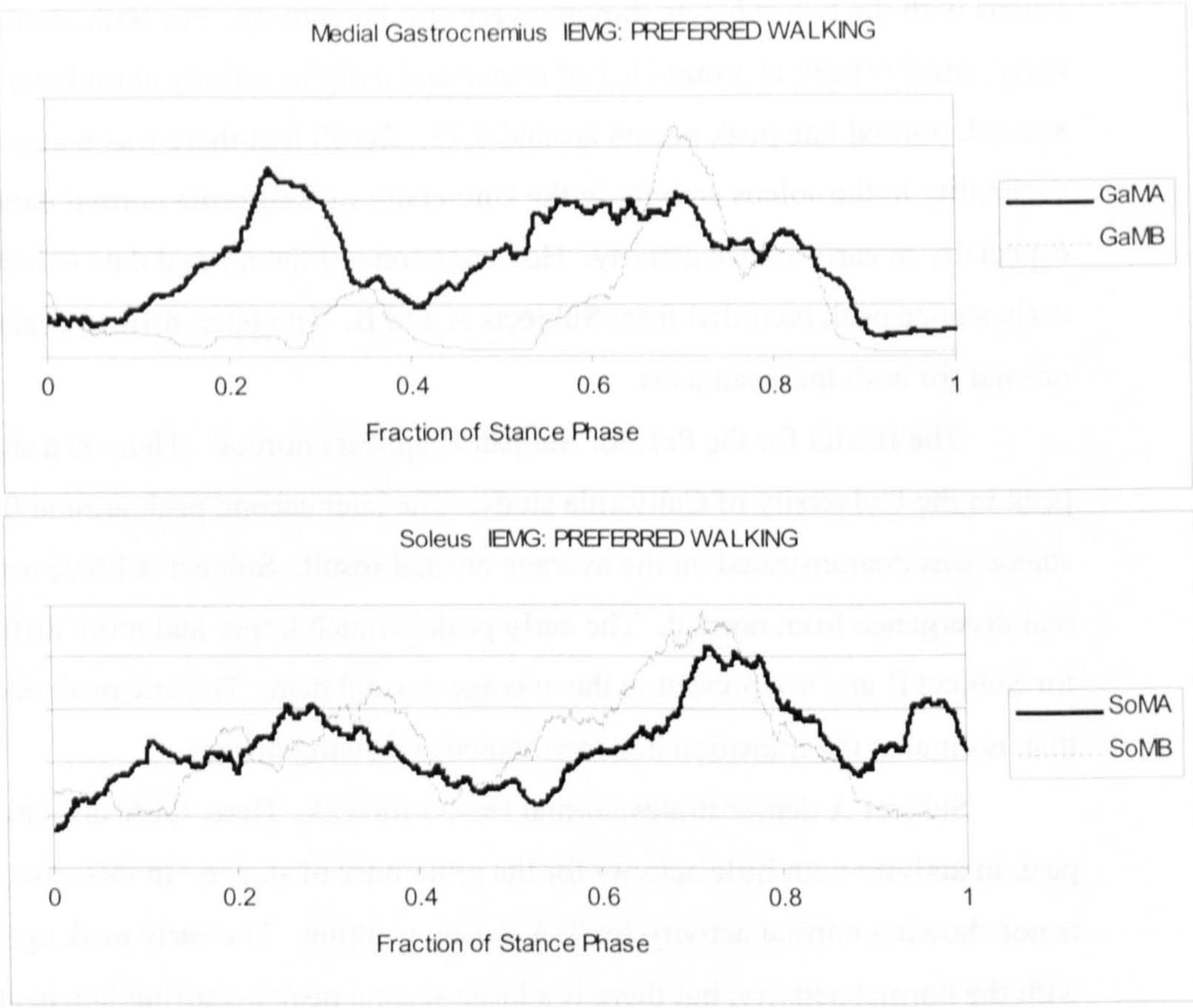

Figure 8.2-16A Integrated EMG (IEMG) of the triceps surae muscles: GaM and Sol during preferred walking for Subjects A and B.

activity for soleus during preferred walking. However the muscle tensions that were produced showed differing timing on the early and late peaks. Subject A had wider and broader peaks while Subject B possessed two sharp peaks.

The IEMG for PeL showed similar trends to the resulting tensions for both Subjects A and B. Subject B's IEMG possessed two broad peaks, one early in stance and one quite late. This produced a few peaks in tensions with different timings. The IEMG for Subject A produced a constant tension in PeL. The IEMG and tension patterns for the two dorsi-flexors (TiA and EDL) were also quite similar. The patterns for TiA were almost identical with the peaks in IEMG producing peaks in tension of similar timing. The EDL patterns also showed similar timing of peaks for both subjects.

There exists a discrepancy between the muscle loading predicted by the Procter, 1980 model and the current model. While some of this can be assigned to technical differences in the models (i.e. lack of ligaments in Procter, assumption of limitations on antagonism), there remain other possible factors. First, the muscle model used in the current model may be producing muscle tension from EMG input where the muscle is nearly quiescent. A study by Bogey, Perry, et al, 2000 showed that surface EMG recordings can show a significant amount of activity in the soleus muscles when the muscle is in fact quiescent. The muscle model in this case would amplify this errant muscle activity into muscle tendon when in fact the muscle is relaxed. This may be the case in a limited number of instances such as during early stance phase for the GaM of Subject B. From 0.0 to just before 0.3 of stance phase the IEMG signal (muscle activity in Figure 8.2-16A) is very near quiescent. However the tension produced by the muscle model shows a small peak near 0.05 of stance and significant tension throughout stance.

The muscle model may also be sensitive to large muscle velocities. Recall from Chapter 6 that muscle instantaneous length and velocity are also inputs to the muscle model, in addition to EMG. Muscle velocity may be the reason why very similar EMG traces for Subjects A and B soleus muscles lead to dissimilar muscle tensions. The peaks for Subject A are wider and lower than the sharp peaks in soleus

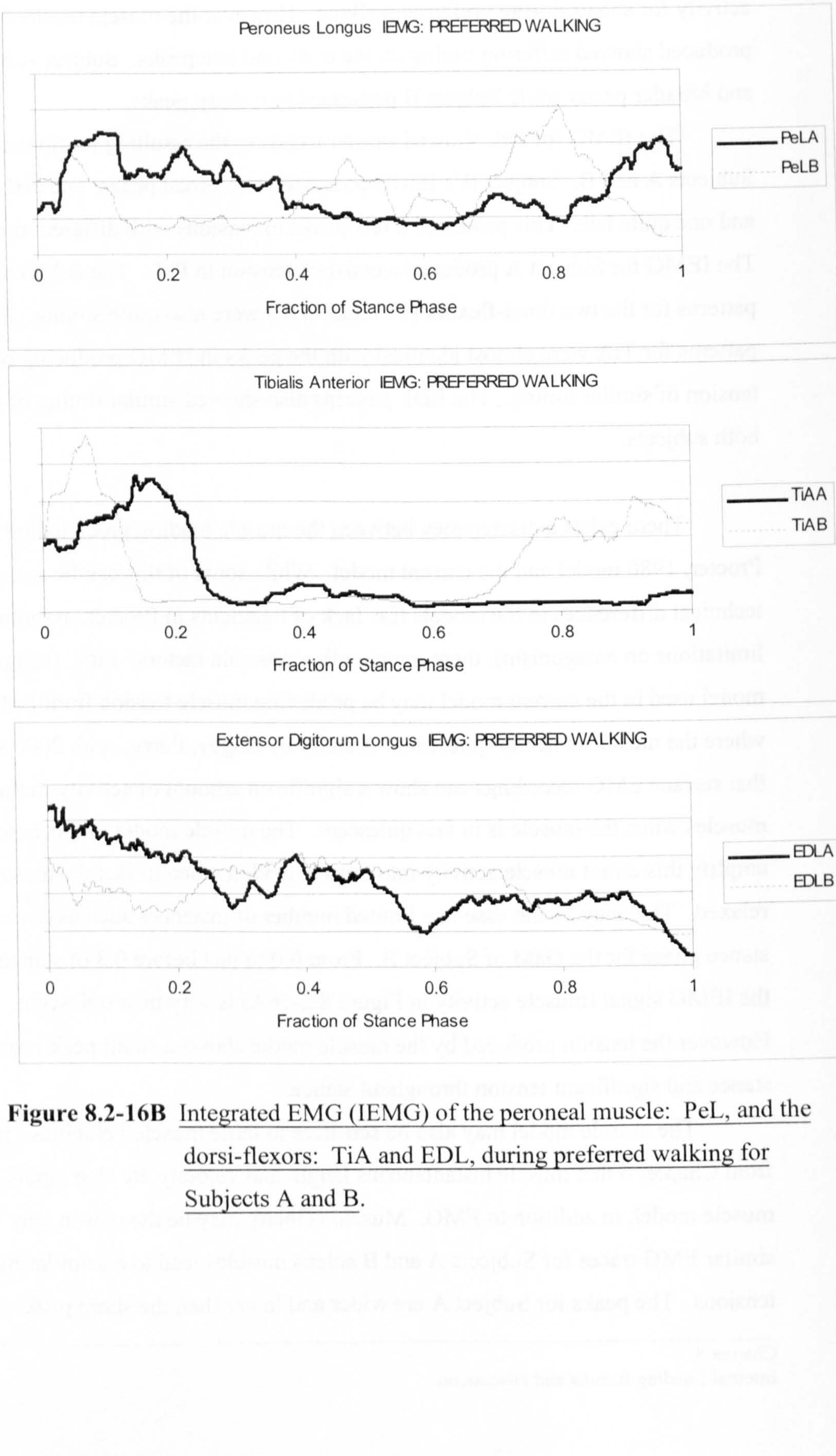

Figure 8.2-16B Integrated EMG (IEMG) of the peroneal muscle: PeL, and the dorsi-flexors: TiA and EDL, during preferred walking for Subjects A and B.

tension for Subject B. Since Subject B is a good deal taller than A (1.88 m as versus 1.63 m respectively), Subject B's soleus would be longer and changing length more rapidly given the same joint kinematics. If the muscle model were sensitive to muscle velocity, then similar EMG inputs would produce larger tension results for the taller subject.

However, neither of these possible muscle model sensitivities explain the fact that the EMG signals from Subjects A and B do no agree with the EMG collected in the University of California, 1953 study of normal and fast level walking. Despite the presence of variability in the data collected in the 1953 study, the current EMG data still cannot be considered normal walking activity. The conclusion that can be drawn is that the subjects of the current study were not walking entirely normally or in a way representative of their preferred pattern of walking.

Given the large amount of antagonism between the plantar- and dorsi-flexors that is evident in the EMG recorded, it seems as though the subjects are walking with a more "guarded" or tentative gait than usual. That is, it seems as though during walking, the ankle is being held more stiffly. This behaviour may be adopted somewhat differently in each subject, which would give rise to the differing muscle tension patterns between subjects seen in Section 8.2 results. A guarded, stiff ankle reduces ankle range of motion somewhat, but also seems to reduce the initial impact at heel strike and minimises the anterior-posterior and mediolateral loading on the foot.

This guarded gait pattern may be a protective strategy in reaction to the testing environment. The floor of the gait laboratory was a hard and cold linoleum surface and the subjects performed the walking and turning movement tasks in bare feet. The floor had been recently buffed and polished and the air temperature in the sub-ground level gait laboratory was colder than usual room temperature. The floor hardness and temperature made the movement tasks uncomfortable in bare feet, particularly the heel strike initiating stance. Some subjects did comment that during the fast speed walking and some preferred speed walking trials, they experienced some heel pain at heel strike. The newly polished floor may have been slightly slippery for bare feet as well. Particularly since the air temperature was colder than

usual, the feet of the subjects would have been rather dry, and therefore had a lower coefficient of friction on the sole of the foot than a warm foot with a normal amount of friction-enhancing moistness.

The presence of antagonism in the muscle tensions and the resulting discrepancy between these results and Procter, 1980 could therefore in large part be due to this guarded, tentative walking strategy which deviates from the 'normal' walking strategies studied in other work. Despite this alteration in gait from normal walking, the current model results for the internal muscle tensions, ligament tensions and surface compressions are still useful in elucidating the biomechanics of ankle and foot function during walking and especially during the more demanding task of turning. But this alteration in gait pattern should be borne in mind when reviewing the preceding muscle results and proceeding ligament and surface results.

8.2.4 Estimating Joint-crossing Load in the Inferior Extensor Retinacula

As has been described in Sections 1.1.4 and 7.4.4, the tendons of the EDL and EHL (and in a portion of the population, the TiA) pass under the Inferior Extensor Retinacula (IER) on the dorsum of the foot. The EDL and EHL tendons change direction as they pass under the IER and therefore impart a tension to the structure. The TiA tendon was shown in Sarrafian, 1983 to not change direction as it passed under a slack portion of the IER and it therefore imparts negligible load to this retaining structure.

The IER attaches to the superior surface of the navicular and the anterior surface of the medial malleolus on the medial side, and the sulcus of the calcaneus on the lateral side. Therefore the IER on the medial side crosses both joints of the ankle complex and may possibly apply loading to these joints. In Section 7.4.4 it was explained that this possible loading had been omitted from the current model since it made the solution of the internal loading intractable. This omission may introduce an error to the solution. In this section, an estimate is made of the loading in the IER branch which attaches to the medial malleolus and the subsequent loading due to the EDL and EHL is calculated.

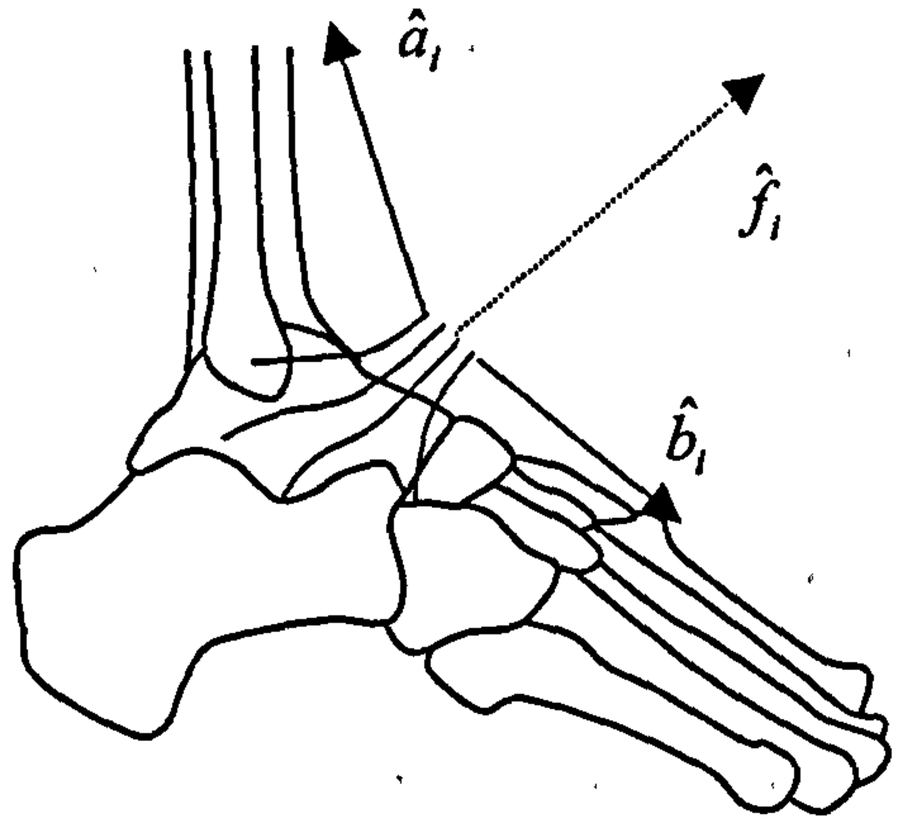

Figure 8.2-17 Direction of the Inferior Extensor Retinacula resultant force due to the tension in muscle tendon i.

From the Internal Map described in Chapter 4, the insertions and origins of the EDL and EHL are identified and defined on their respective segments. The pulley points on the IER where the tendons change directions are also known, along with the IER attachments at the medial malleolus, superior navicular and calcaneus sulcus. Using the kinematic data from the walking and turning trials, these points can all be transformed into the ground frame of reference for each frame of data. At time t during a trial, these points are:

$$\text{insertions and origins:} \quad \underline{i}_{EDL}, \underline{o}_{EDL}$$
$$\underline{i}_{EHL}, \underline{o}_{EHL}$$

$$\text{pulley points:} \quad \underline{p}_{EDL}, \underline{p}_{EHL}$$

$$\text{IER attachments:} \quad \underline{p}_{MedM}, \underline{p}_{Nav}, \underline{p}_{Calc}$$

The vectors pointing from the pulley point to the origin and insertion of the muscle can each be formed from these for the two muscles,

$$\begin{aligned} \vec{a}_{EDL} &= \underline{o}_{EDL} - \underline{p}_{EDL}, \vec{b}_{EDL} = \underline{i}_{EDL} - \underline{p}_{EDL} \\ \vec{a}_{EHL} &= \underline{o}_{EHL} - \underline{p}_{EHL}, \vec{b}_{EHL} = \underline{i}_{EHL} - \underline{p}_{EHL} \end{aligned} \tag{8.2-1}$$

and the unit vectors then found,

$$\hat{a}_{EDL}, \hat{b}_{EDL}$$
$$\hat{a}_{EHL}, \hat{b}_{EHL}$$

The resulting tension in the IER due to a muscle tendon change of direction at the pulley point will lie within the plane formed by $\hat{a}_i, \hat{b}_i$ along the bisector of the angle between these vectors. This is plotted in Figure 8.2-17 and can be written as follows,

$$\vec{f}_i = \hat{a}_i + \hat{b}_i \Rightarrow \hat{f}_i = \frac{\vec{f}_i}{|\vec{f}_i|} \tag{8.2-2}$$

The magnitude of the resultant will be the projection of the tendon tension vectors onto the unit vector in Eq. 8.2-2,

$$F_i = (T_i \hat{a}_i) \cdot \hat{f}_i + (T_i \hat{b}_i) \cdot \hat{f}_i \tag{8.2-3}$$

where T_i is the magnitude of the tension in the tendon.

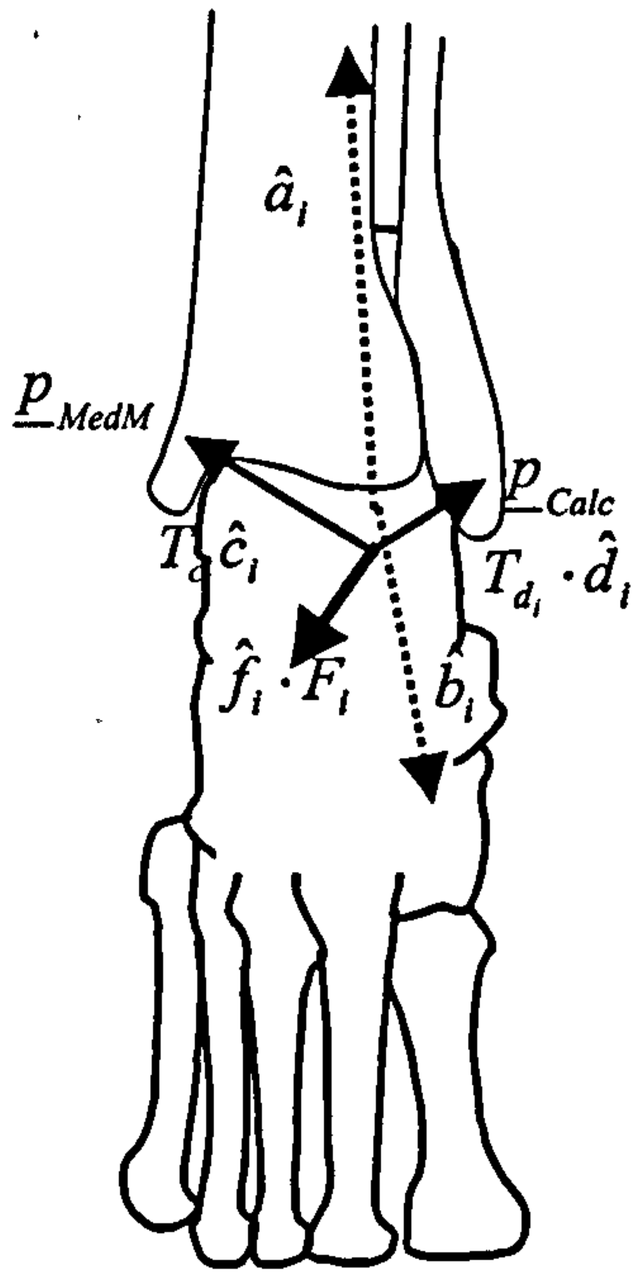

Figure 8.2-18 Equilibrium between the resultant force of muscle tendon i changing direction and two branches of the inferior extensor retinacula.

We now have the resultant force acting on the IER due to the tendons of the EDL and EHL changing direction,

$$F_{EDL} \cdot \hat{f}_{EDL} \text{ and } F_{EHL} \cdot \hat{f}_{EHL} \tag{8.2-4}$$

The next step is to calculate the loading on each of the three attachments of the IER due to these resultants. Since two of the three IER attachments are on the foot segments, below the Subtalar Joint, they are not of interest since they will reside on the same rigid body as the tendon forces acting about both joints. The attachment of interest is the medial malleolus since this point lies off the rigid body on which the tendon, ligament, surface and ground reaction force (GRF) loads act. The tension in the IER between this attachment and the muscle pulley points could therefore apply loading across the Ankle and Subtalar Joints.

The assumption is now made that the resultant force due to the tendon direction change is borne by the attachments at the calcaneal sulcus laterally and the medial malleolus medially. This load sharing solution will over-estimate the loading on the medial malleolus since, in reality, some load will be taken at the superior navicular attachment. However the load sharing solution for all three attachments at equilibrium with the tendon force resultant was found to be intractable.

The vectors from the pulley point to the two attachments were found for the two muscles,

$$\begin{aligned} \vec{c}_{EDL} &= \underline{p}_{MedM} - \underline{p}_{EDL}, \vec{d}_{EDL} = \underline{p}_{Calc} - \underline{p}_{EDL} \\ \vec{c}_{EHL} &= \underline{p}_{MedM} - \underline{p}_{EHL}, \vec{d}_{EHL} = \underline{p}_{Calc} - \underline{p}_{EHL} \end{aligned} \tag{8.2-5}$$

The unit vectors were then found,

$$\hat{c}_{EDL}, \hat{d}_{EDL}$$
$$\hat{c}_{EHL}, \hat{d}_{EHL}$$

The load sharing problem is defined for each muscle as equilibrium between the force resultant and the tension in the vectors $\hat{c}_i$ and $\hat{d}_i$,

$$-F_i \cdot \hat{f}_i = T_{C_i} \cdot \hat{c}_i + T_{d_i} \cdot \hat{d}_i \tag{8.2-6}$$

where T_{c_i} and T_{d_i} were the tensions in vectors $\hat{c}_i$ and $\hat{d}_i$. This is shown in Figure 8.2-18.

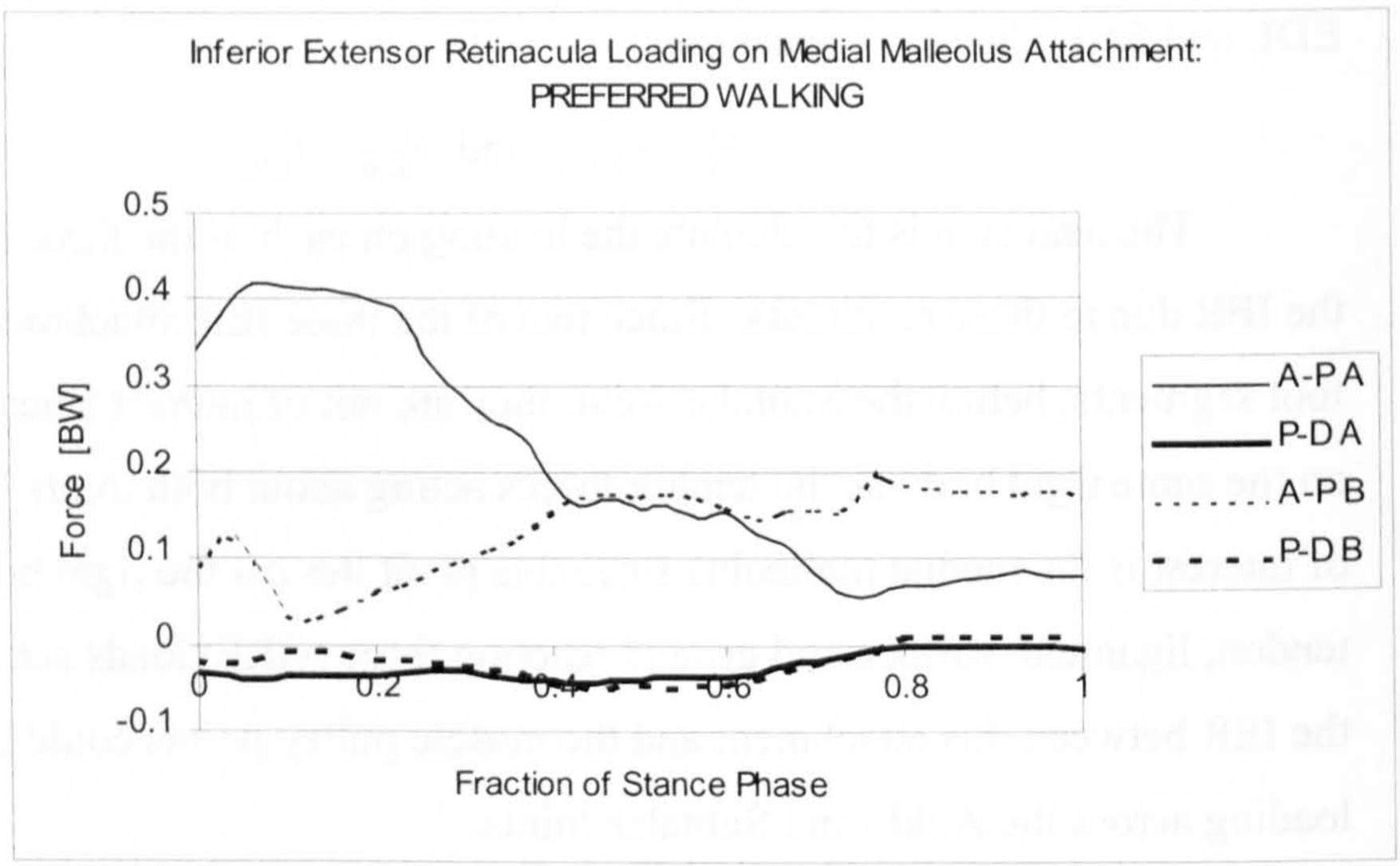

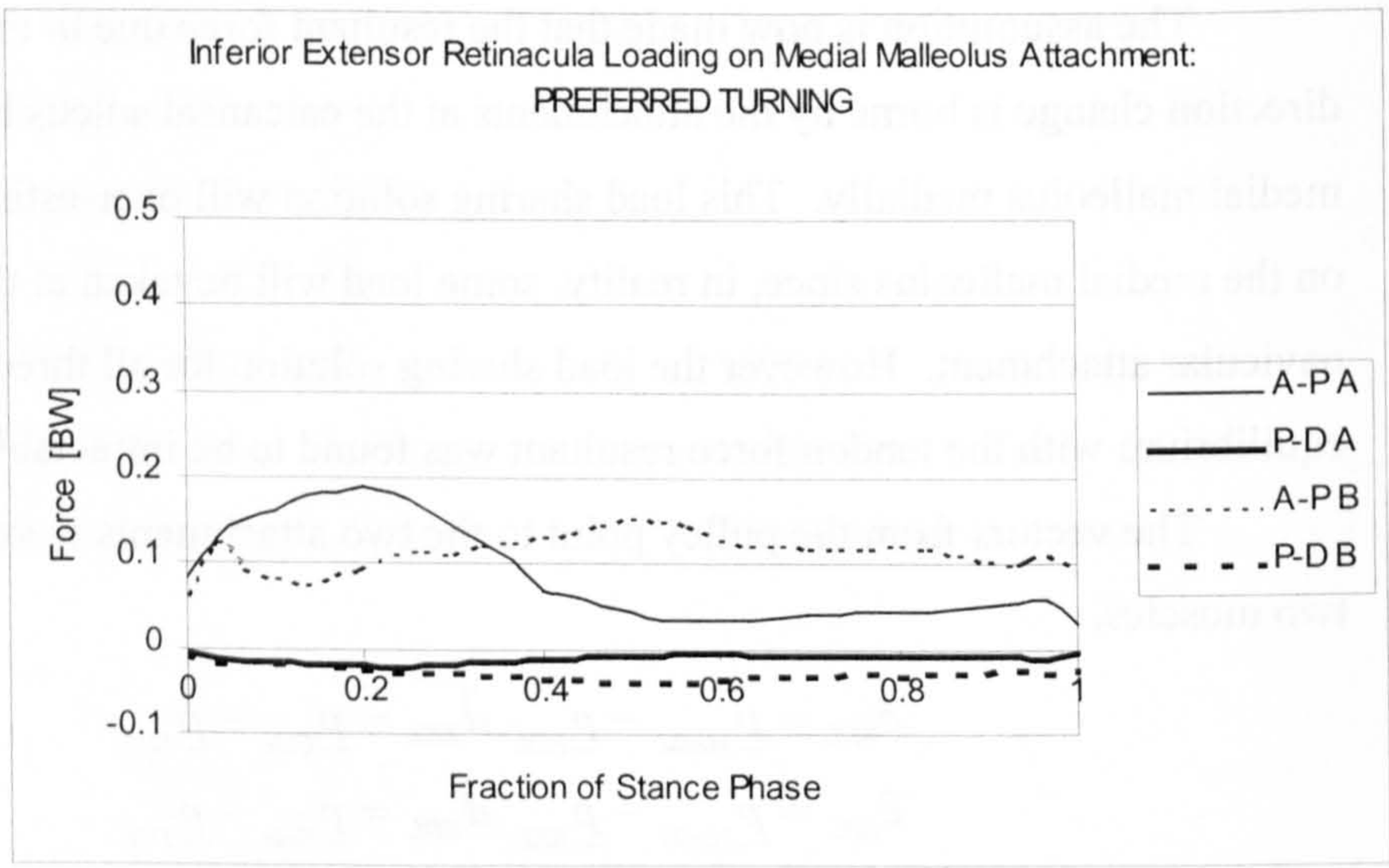

Figure 8.2-19 Loading on the medial malleolar attachment of the IER during preferred speed walking and turning for Subjects A and B. These loads have been resolved into the anterior-posterior (A-P) direction and proximal-distal (P-D) directions.

Since the tension in only two vectors is sought, we can only solve for equilibrium in two directions. It was decided to solve for equilibrium in the anterior-posterior (A-P) and the proximal-distal (P-D: along the tibial long axis) directions since the tendon tension vectors $\hat{a}_i$ and $\hat{b}_i$ lie primarily in the sagittal plane formed by the A-P and P-D axes. Eq. 8.2-6 can be rewritten for equilibrium about the A-P and P-D axes ($\hat{1}$ and $\hat{2}$ axes) as follows for each muscle,

$$-F_i \cdot \begin{bmatrix} {}^{\hat{1}}f_i \\ {}^{\hat{2}}f_i \end{bmatrix} = \begin{bmatrix} {}^{\hat{1}}c_i & {}^{\hat{1}}d_i \\ {}^{\hat{2}}c_i & {}^{\hat{2}}d_i \end{bmatrix} \begin{bmatrix} T_{C_i} \\ T_{d_i} \end{bmatrix} \tag{8.2-7}$$

which is solved as,

$$\begin{bmatrix} T_{C_i} \\ T_{d_i} \end{bmatrix} = \begin{bmatrix} {}^{\hat{1}}c_i & {}^{\hat{1}}d_i \\ {}^{\hat{2}}c_i & {}^{\hat{2}}d_i \end{bmatrix} (-F_i) \cdot \begin{bmatrix} {}^{\hat{1}}f_i \\ {}^{\hat{2}}f_i \end{bmatrix} \tag{8.2-8}$$

Thus we have the tension in the IER branch attaching to the medial malleolus due to the two muscle tensions. Acting *on the medial malleolus*,

$$-T_{c_{EDL}} \text{ and } -T_{c_{EHL}}$$

These magnitudes can be resolved into the A-P and P-D direction as follows,

$$-T_{c_{EDL}} \cdot \hat{c}_{EDL} \text{ and } -T_{c_{EHL}} \cdot \hat{c}_{EHL} \tag{8.2-9}$$

The loads on the medial malleolar attachment in the A-P and P-D directions are therefore,

$$\text{A-P direction: } -T_{c_{EDL}} \cdot {}^{\hat{1}}c_{EDL} - T_{c_{EHL}} \cdot {}^{\hat{1}}c_{EHL}$$

$$\text{P-D direction: } -T_{c_{EDL}} \cdot {}^{\hat{2}}c_{EDL} - T_{c_{EHL}} \cdot {}^{\hat{2}}c_{EHL} \tag{8.2-10}$$

A sample calculation of the loading on the medial malleolus is included in the Appendix.

The loading on the medial malleolar attachment of the IER during preferred speed walking and turning was calculated for Subjects A and B. This is plotted in Figure 8.2-19. It is interesting that in both tasks, the A-P component of loading is much larger than the P-D component, indicating that the EDL and EHL tendons predominantly cause the IER to be pulled anteriorly from the medial malleolar attachment due to their changes in direction.

The A-P loading for walking and turning were of similar magnitude and showed similar trends for Subject B with maximum magnitudes of around 0.15×BW from midstance to toe off. The trends in A-P loading were similar for Subject A for walking and turning, but the magnitude of the walking A-P loading was larger than during turning, peaking at 0.4×BW and 0.2×BW respectively. Recall the EHL and EDL muscle tensions plotted in Figures 8.2-3 and 8.2-6. Subject A showed early peaks in tension around 0.2 of stance phase while Subject B did not. This is reflected in the IER loading in Figure 8.2-19. The initial peak in EDL and EHL tensions during these tasks causes an early peak in the IER A-P loading. The proximally directed force component remains constant throughout stance for both walking and turning around 0.03×BW.

Recall the anterior-posterior ground reaction loading on the foot reported in Chapter 5 for preferred walking and turning; plotted in Figures 5.2-2 and 5.2-5 respectively. The A-P GRF for both tasks peaks around 0.15 of stance phase acting in the posterior direction at a value of 0.3×BW. The IER loading will be posteriorly directed on the foot segment since it is anteriorly directed on the shank segment at the medial malleolar attachment. The magnitude in early stance is therefore around the same order of magnitude as the A-P GRF and will increase the posterior translation force acting on the ankle complex. Since the IER force was not included, the current model underestimates this translational loading early in stance. In late stance, the A-P GRF is anteriorly directed with a peak of around 0.3×BW which counteracts the posteriorly directed IER loading with magnitude of around 0.2×BW. The current model therefore overestimates the translational force acting on the ankle complex in the A-P direction in late stance. The greatest error arising from the omission of the IER loading will occur in early stance between 0.0 and 0.3 of stance phase. Since the IER loading acting on the medial malleolar attachment is greatest at this time.

8.3 LIGAMENT TENSIONS

8.3.1 Ligament Tension Results

There were twelve separate ligaments defined within the Ankle Complex. Seven of these acted about the Ankle Joint and eight about the Subtalar, therefore three of the ligaments acted about both joints. The ligaments could be subdivided into four groups: the lateral group, the medial group, and the inner and outer subtalar groups. The lateral group of ligaments contained the Anterior Talofibular (L-Ant), the Calcaneofibular (L-Mid) and the Posterior Talofibular (L-Post). The medial group was formed by the Anterior Talotibial (M-Ant), the Tibionavicular (M-Nav), the Calcaneotibial (M-Mid) and the Posterior Talotibial (M-Post). The inner subtalar ligaments were those within the sinus tarsi and canalis tarsi between the Talus and the Calcaneus. These were the Cervical (Cerv) and the Medial and Lateral Interosseus ligaments (M/L-IO). The outer subtalar ligaments were the Medial and Posterior Talocalcaneal ligaments (M-Tc and P-Tc).

Figures 8.3-1 to 8.3-4 plot the tensions in the twelve ligaments during a single trial of preferred speed walking for Subjects A and B. Due to the variability between the trials of the same subjects as well as the variability between subjects, these two trials were chosen to demonstrate the general trends in the ligament tensions. The lateral group of ligaments showed the same general pattern of tension for the two subjects. L-Ant seemed to be tensed primarily during the deceleration phase of stance. L-Ant was only tensed from 0.0 to 0.45 of stance phase for Subject B. The tension in L-Ant had a broad peak during this time for Subject A as well, although the ligament maintained some tension in the later, acceleration phase of stance as well. The peak tension in L-Ant for both subjects was around 1.5×BW to 1.75×BW. The L-Mid ligament was also tensed during the deceleration phase of stance, similarly to L-Ant for both subjects. The tension peaked at 1.45×BW for Subject A and 1.55×BW for Subject B. The tension in L-Mid for Subject B however, was intermittent between 0.0 and 0.45 of stance phase. It possessed two peaks during this time, one early at 0.08 of stance phase and the second at 0.35. The L-Post ligament of the lateral group was mostly tensed during the later, acceleration phase of stance. From MS to TO, the tension in L-Post for both subjects seemed to plateau somewhat around 0.9×BW

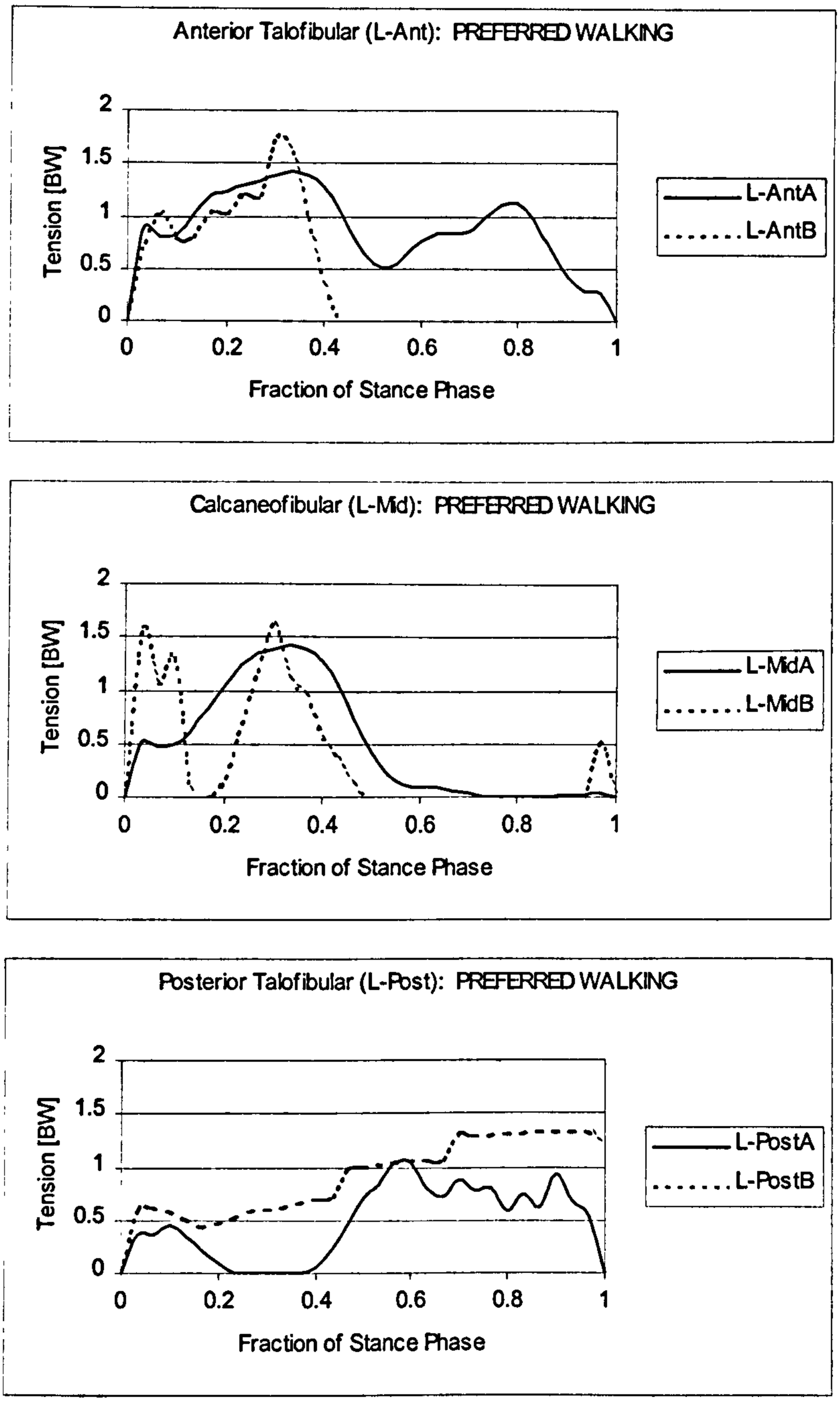

Figure 8.3-1 Lateral group Ligament Tensions for Preferred Speed Walking for Subjects A and B.

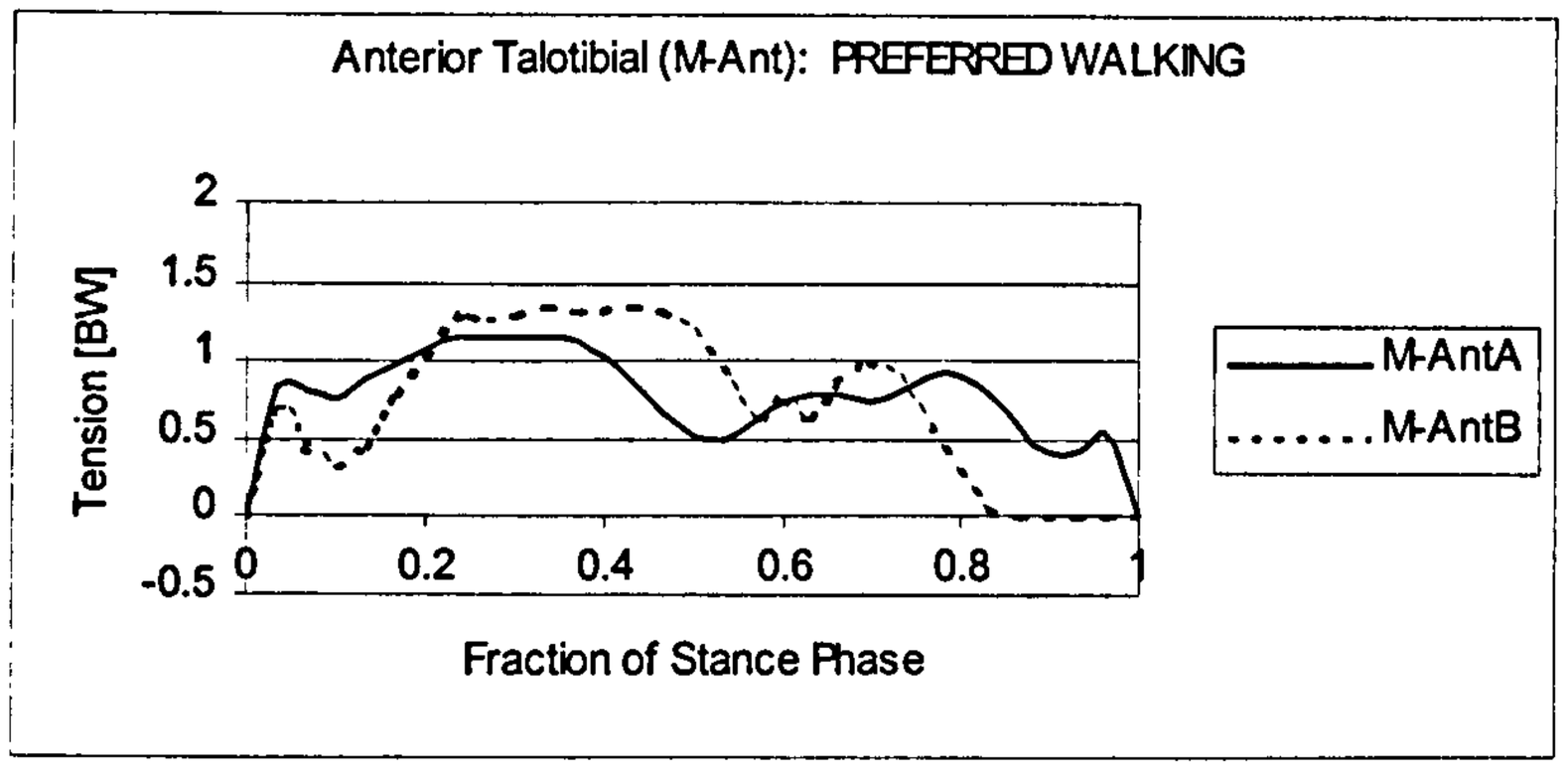

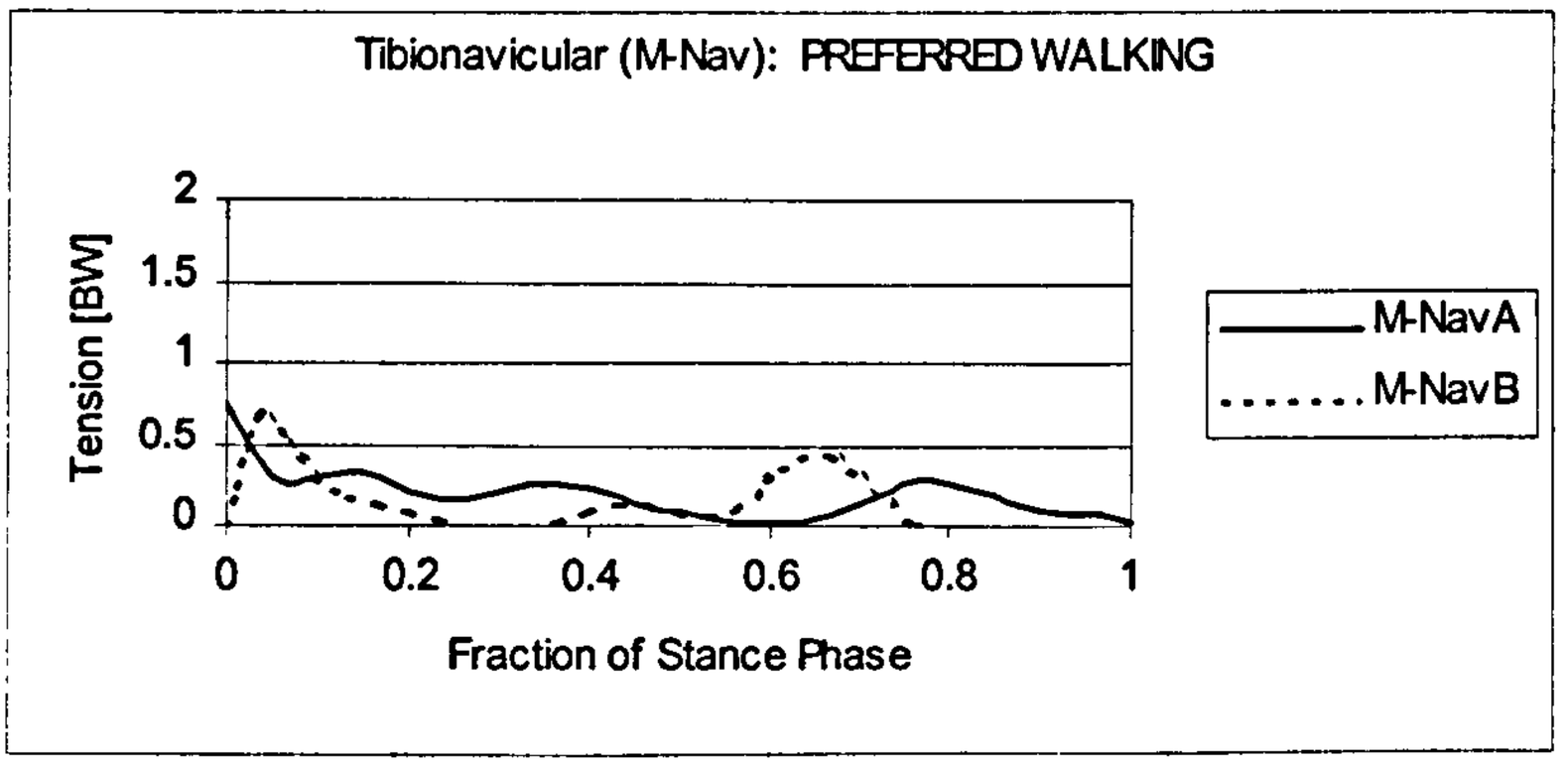

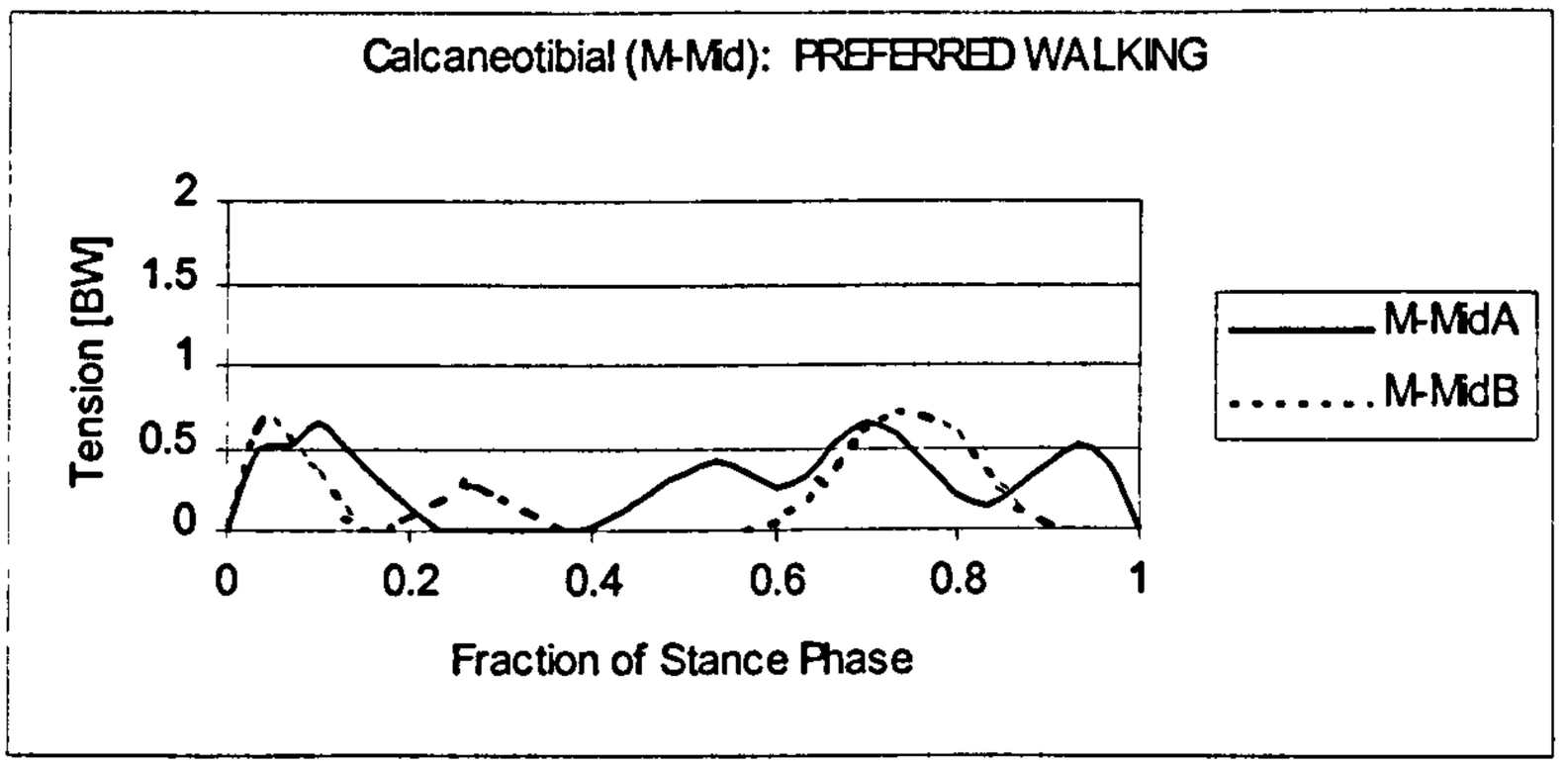

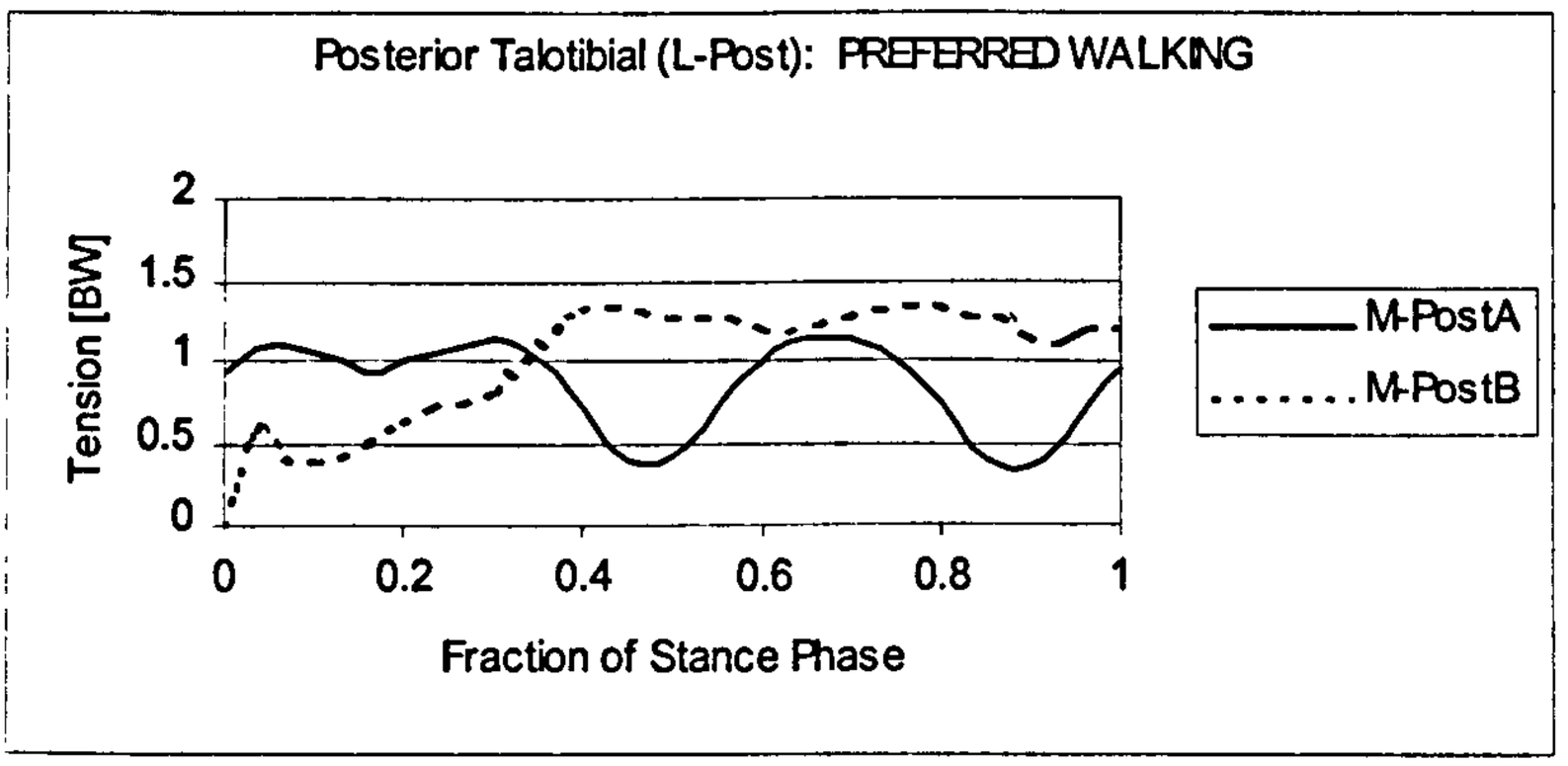

Figure 8.3-2 Medial group Ligament Tensions for Preferred Speed Walking for Subjects A and B.

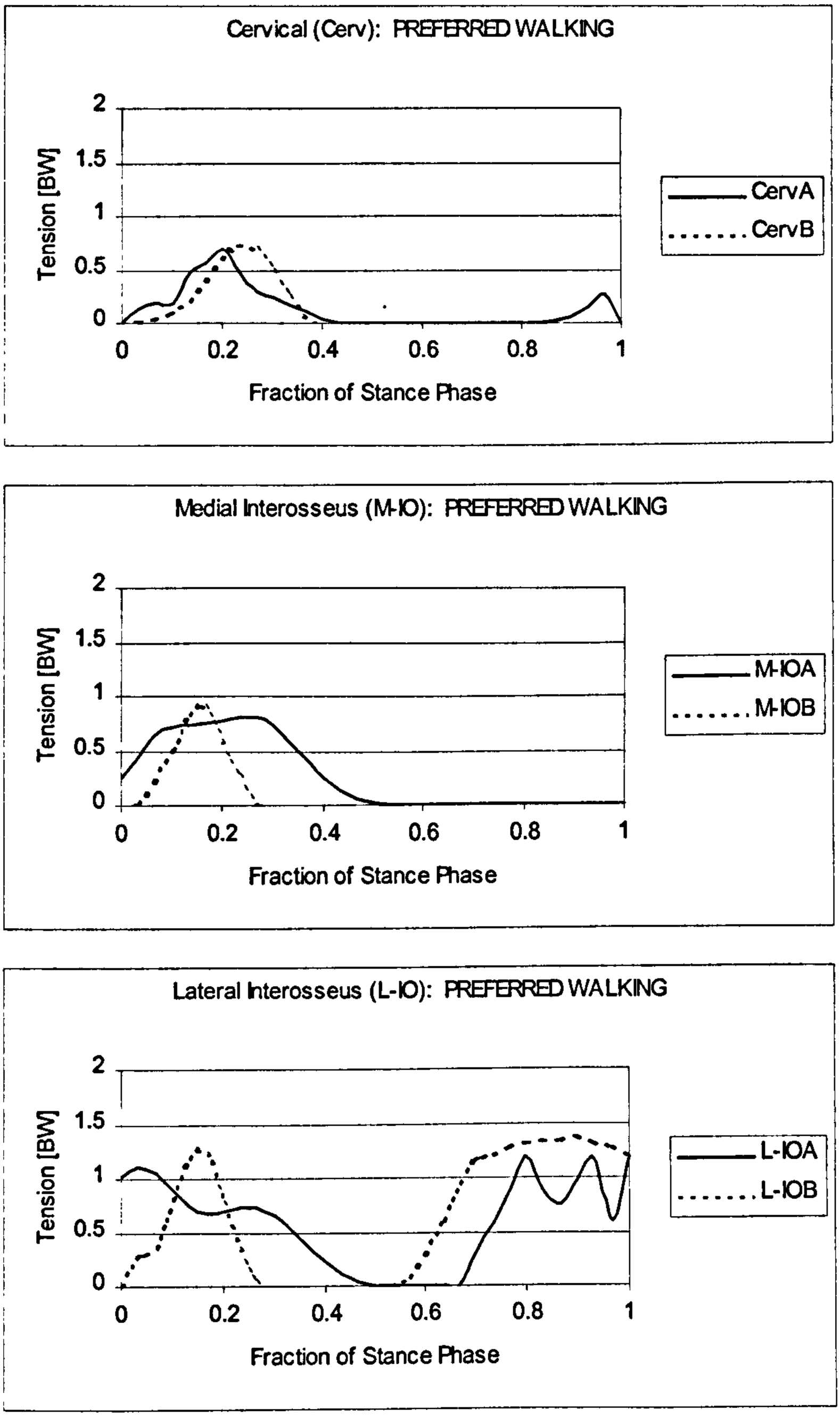

Figure 8.3-3 Inner Subtalar group Ligament Tensions for Preferred Speed Walking for Subjects A and B.

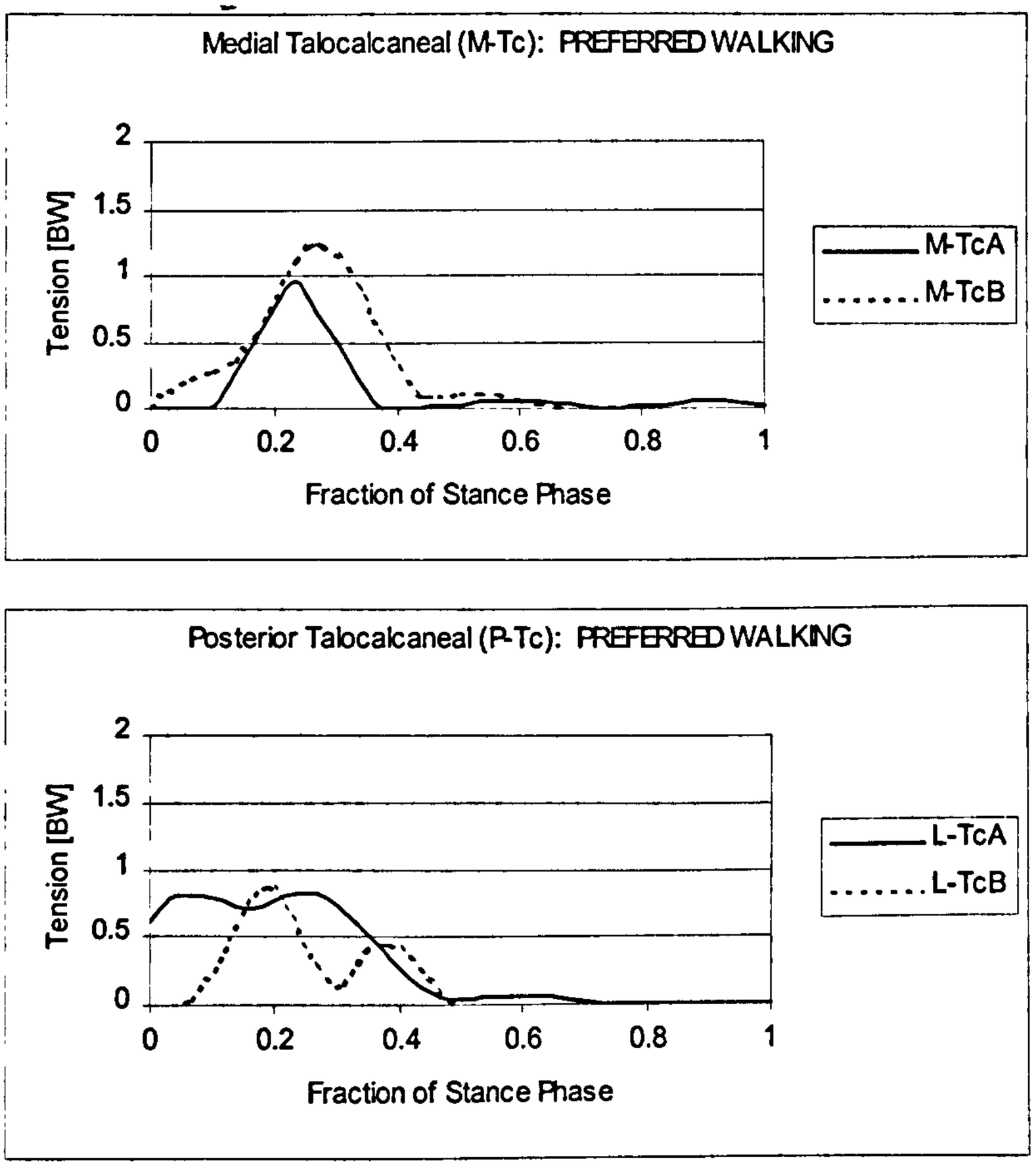

Figure 8.3-4 Outer Subtalar group Ligament Tensions for Preferred Speed Walking for Subjects A and B.

for Subject A and 1.35×BW for Subject B. There was also some tension in this ligament early in stance.

The tensions in the medial group are plotted in Figure 8.3-2. The M-Ant ligament tension followed a similar pattern to that of L-Ant. It was primarily tensed in the deceleration phase of stance and less tensed during the acceleration phase. The magnitudes of the peaks in the M-Ant tension for Subject A was 1.1×BW and 1.35×BW for Subject B. The M-Nav ligament curiously bore relatively little tension although it follows nearly an identical line of action to M-Ant, attaching on the medial Navicular instead of the medial Talus. The tension in the M-Nav ligament was quite variable between trials and between subjects, but the tension never rose above 0.60×BW. The tension the M-Mid ligament was similar to that in the M-Nav ligament and was just as variable. The M-Mid tension never rose above 0.60×BW for any of the trials. The M-Post ligament tensions seemed to be tensed both during the deceleration and the acceleration phases of stance for Subject A, but was tensed just during the acceleration phase for Subject B. The peak tension for M-Post was around 1.15×BW for both subjects.

The tensions in the inner subtalar group of ligaments were less variable than the ligaments of the Ankle Joint. These are plotted in Figure 8.3-3. Recall from Section 2.2.3 that the Interosseus ligament was a single ligament that was considered in the present model as two separate components: the lateral L-IO and the medial M-IO. The medial component of the IO ligament, M-IO, was located close to the Cervical ligament and the two possessed similar lines of action. Due to this, they seemed to bear tension similarly. Both Cerv and M-IO were tensed in the middle of the deceleration phase of stance at around 0.2. The peak in Cerv tension was 0.70×BW and in M-IO was around 0.80×BW for both subjects. The lateral component of IO seemed to perform a different role than the medial component. L-IO was tensed both early in deceleration phase (around 0.2 of stance phase) and throughout acceleration phase of stance. The peak tension in L-IO at both of these times was about 1.25×BW for the two subjects.

The tensions in the outer subtalar group of ligaments are plotted in Figure 8.3-4. The M-Tc and P-Tc ligaments were both tensed only within the deceleration

phase of stance. Similar in shape to the tension pattern in Cerv, the tension in the M-Tc ligament peaked at around 0.25 of stance phase with a magnitude of 1.0×BW for Subject A and 1.25×BW for Subject B. The P-Tc ligament was tensed more variably in deceleration phase of stance with a peak of 0.75×BW for both subjects.

Figure 8.3-5 compares the ligament tensions between the different gait speeds for the lateral group of ligaments during the walking task for Subject A. The tensions in the ligaments were relatively unaffected by changing the speed of walking or turning. The timing of the tensions and the magnitudes of the peaks were very similar for each of the gait speeds, although much variability was present between trials and between subjects. Figure 8.3-5 uses the lateral ligament group to demonstrate the lack of change in tensions due to changing speed. The variability in the tensions for L-Ant, L-Mid and L-Post is clearly shown. For each of these curves though, the ligament was still tensed at the same time during stance phase and possessed the same peak magnitudes, regardless of the speed of the task.

The tensions in the lateral group of ligaments are compared between the walking and turning tasks for both subjects in Figure 8.3-6. The tension patterns for the medial, and inner and outer subtalar groups of ligaments showed little change with changing task. The lateral group of ligaments however, showed a number of changes during the turning task compared to the walking task. The L-Ant tension during turning possessed an early peak in the deceleration phase of stance similar to walking. However in the acceleration phase of stance during turning, L-Ant was tensed again with a larger peak at about 0.8 of stance phase. The peak tension was 2.0×BW for Subject B and 1.65×BW for Subject A. A second peak in the acceleration phase of stance was also seen in the L-Mid ligament during turning. The peaks in L-Mid were 1.1×BW and 1.5×BW for Subject A and B respectively. In the tension pattern of L-Post, a second peak appeared during turning around 0.4 of stance phase for both subjects. This peak had a magnitude of around 1.5×BW for both subjects.

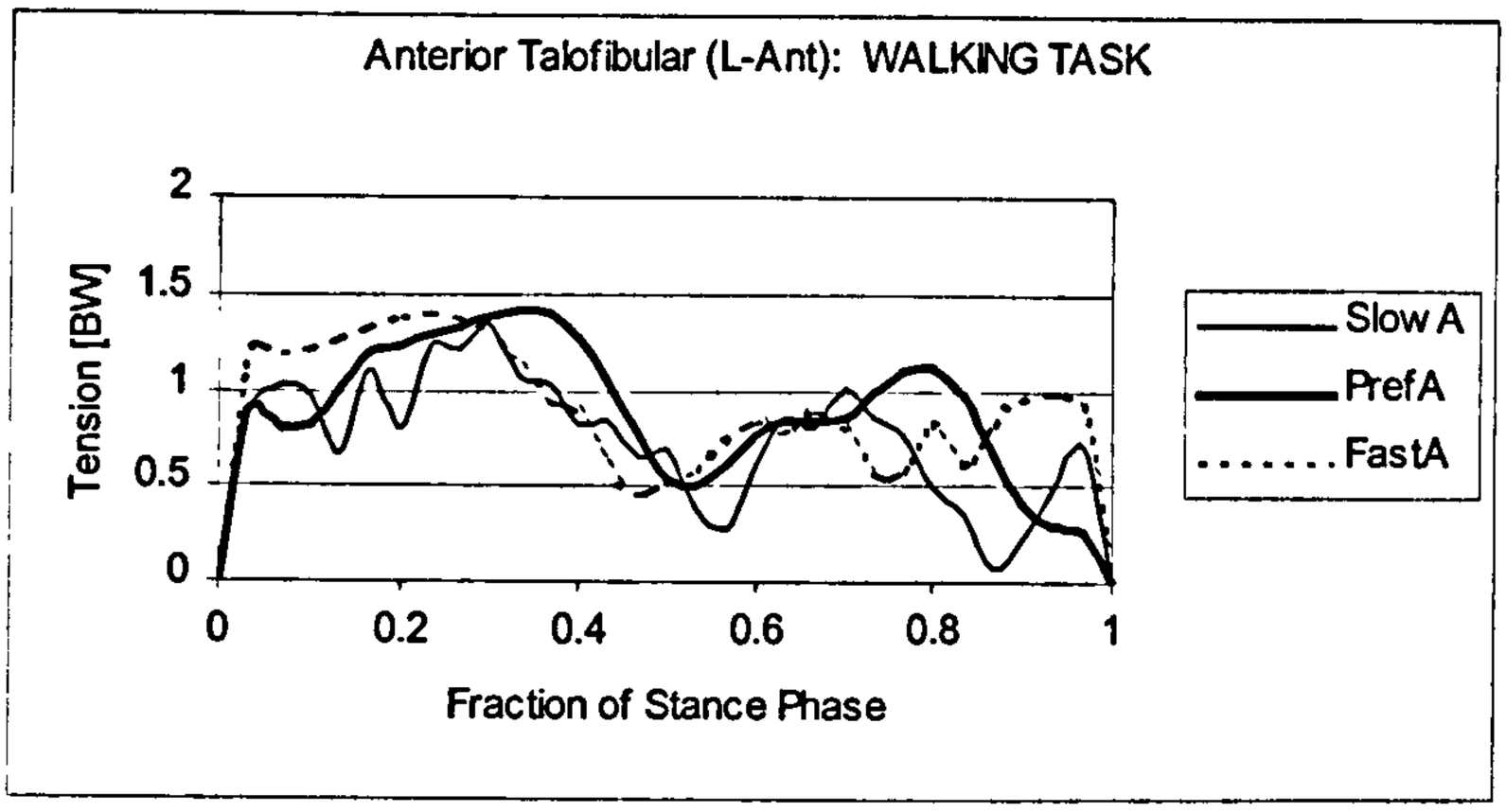

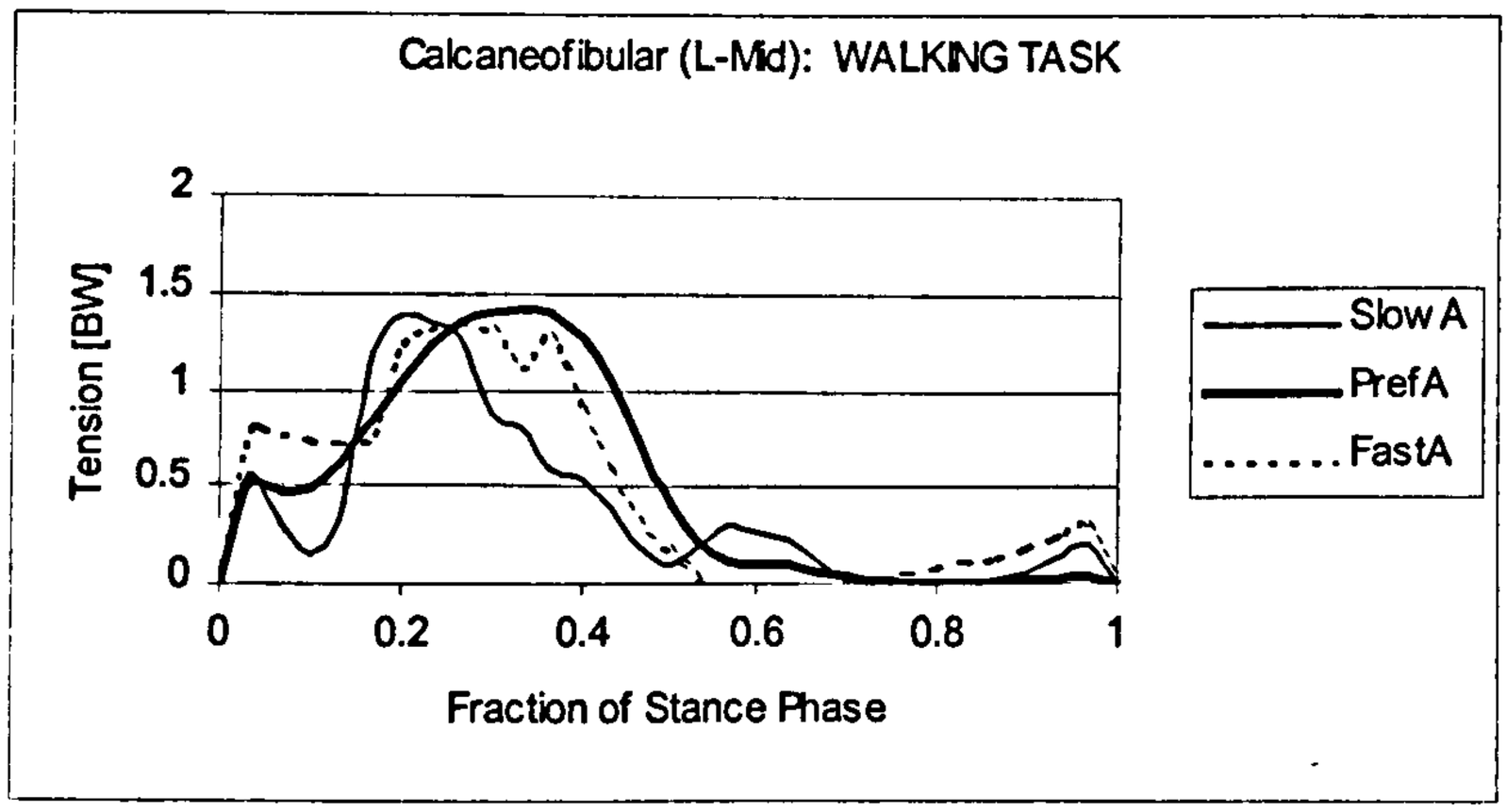

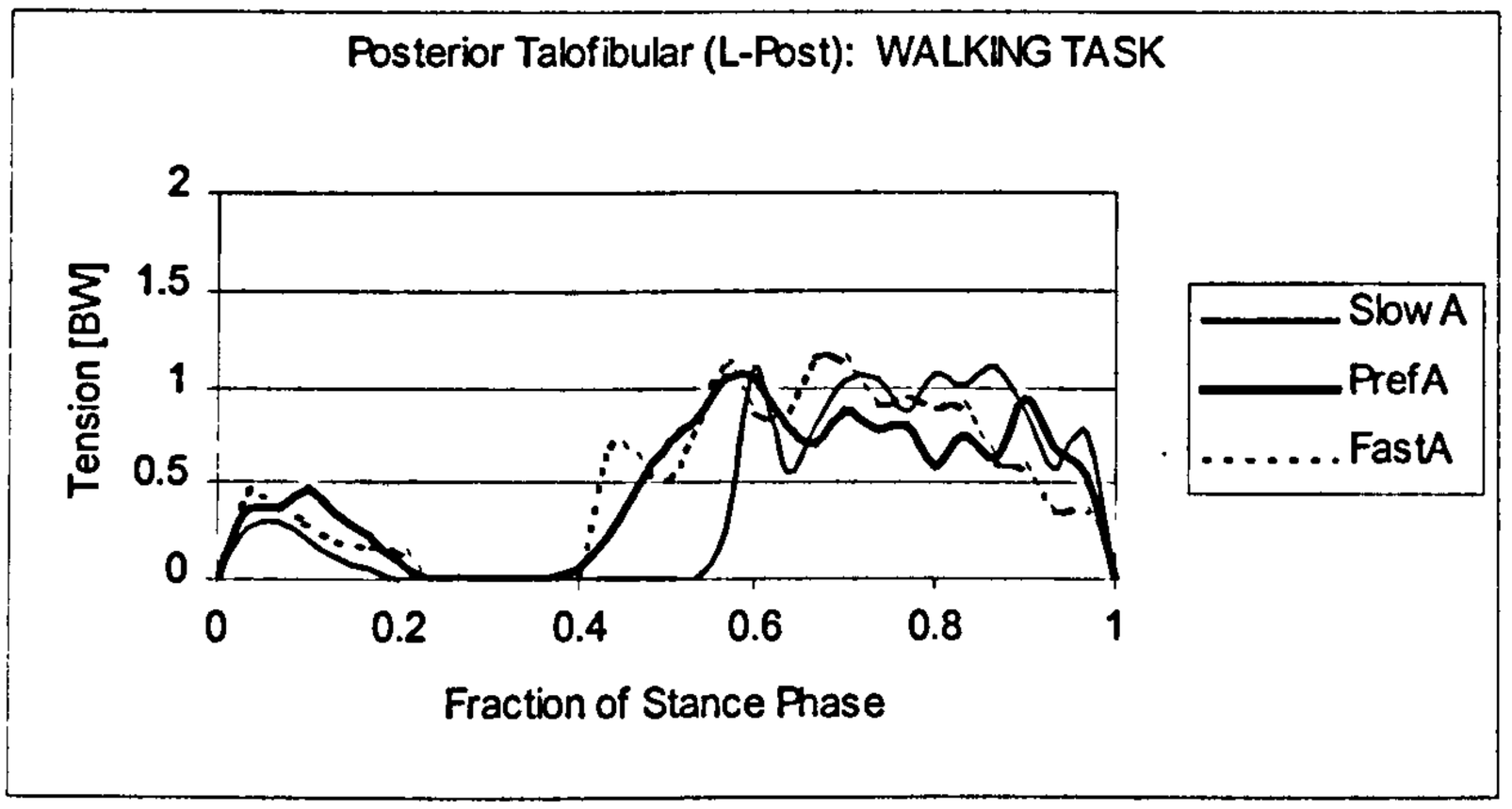

Figure 8.3-5 Comparing Speed differences in Lateral group Ligament Tensions for the Walking Task for Subjects A and B.

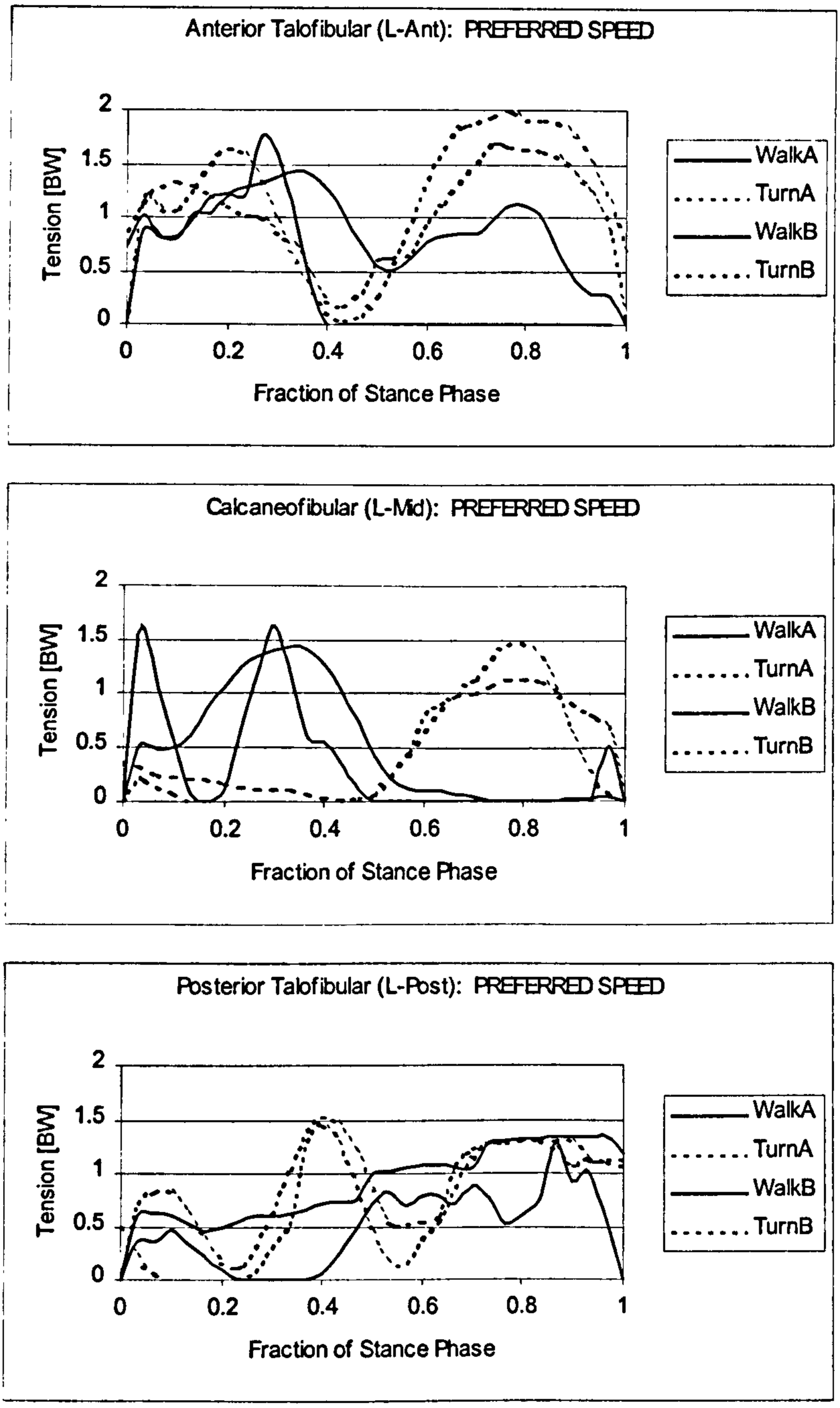

Figure 8.3-6 Comparing Task differences in Lateral group Ligament Tensions for Preferred Speed Walking and Turning for Subjects A and B.

8.3.2 Ligament Tension Discussion

The variability in the tensions of the ligaments, both between trials of the same subject and between subjects was unexpected given the repeatability of the external loading results and the muscle tension results. The variability in ligament tensions could be due to two things. First, this may be the physiological reality of ligament loading; that during repetitions of the same task at the same speed, the ligaments can be tensed in a variety of ways while producing the same constraint of the Ankle Complex. The second cause may not be physiological at all, but may be due to the Linear Optimisation method used to solve the system. The linear method of optimisation may be sensitive to small differences in the input muscle tensions or in the positions of the ligments in repetitions of the same trial. These small differences in input could have then been amplified into large differences between equilibrium solutions of similar trials. A sensitivity analysis of the Linear Optimisation method was not performed since, as will be seen in the next section, the same variability was not seen in the compression loads of the articular surfaces. Nonetheless, it would be useful in future to employ a more physiological, *non-linear* optimisation method within the Muscle Model Assisted Optimisation technique to see if this variability in ligament tensions reduces or disappears.

Despite the variability, an interesting result that can be drawn from the ligament tensions is that the ligaments seemed to be tensed in an *all-or-nothing* fashion. The ligaments seemed to have the same peaks in tension regardless of the speed of the task. This indicates that the ligament did not provide a graded constraint of the Ankle Complex, but were either tensed or not tensed. The difference in the tension patterns between the walking and turning tasks seemed to be confined to the *shape* and *timing* of the tensions in the lateral group of ligaments. During turning, a second peak in tension appeared in the three lateral ligaments. However the magnitude of these peaks was the same as the peaks seen during walking. Since the optimisation system was not constrained, and the ligaments were able to take on any tension assigned to them by the equilibrium solution, this result may indeed be physiological. Also, like tendon tissue, ligaments are stress-stiffening. Therefore for a small change in elongation, the tension in the ligament increases exponentially.

Ligaments therefore have a very small range of elongation by which they can be stretched before rupture. Therefore, ligaments are not suited to a graded constraint of joints, but to an all-or-nothing type of constraint.

8.4 ARTICULAR SURFACE COMPRESSION

8.4.1 Articular Surface Compression Results

Within the Ankle Complex there were seven separate surfaces defined. Four of these surface made up the Ankle Joint and three made up the Subtalar Joint. The Ankle Joint surfaces were the Lateral and Medial Malleolar surfaces (L-Mall and M-Mall) and the Lateral and Medial Mortice surfaces (L-Mort and M-Mort). The surfaces of the Subtalar Joint were the Posterior and Middle Talocalcaneal surfaces (Post and Mid) and the Socket of the Navicular (Socket).

Figures 8.4-1 and 8.4-2 shows the surface compression loads for the seven surfaces during preferred speed walking for *three* subjects, Subjects A and B as in the preceding section and Subject C. Subject C was a male of height 1.68 m and body mass 78 kg and aged 25 years. A third subject was introduced in this final section to demonstrate how little variability there was between subjects in the timing of surface compression and in the magnitudes of the peak compressions.

Figure 8.4-1 shows the compressions on the four Ankle Joint surfaces. Note that there was little variability between subjects, despite the differences in the three example subject body types. The lateral and medial Mortice surfaces, M-Mort and L-Mort, showed very similar compression curves. The compression showed two broad peaks, one in early stance and a second in late stance. The first peak was smaller than the second and was centred around 0.2 of stance phase with a magnitude of around 3.5×BW to 4.0×BW for the both surfaces and for all three subjects. The second peak was centred around 0.65 of stance phase and had a magnitude of around 5.0×BW. The division of the Mortice surface into medial and lateral halves, M-Mort and L-Mort, was an artificial step taken to aid in the optimisation process. It is therefore not surprising that the two surfaces bore such similar compressions. The

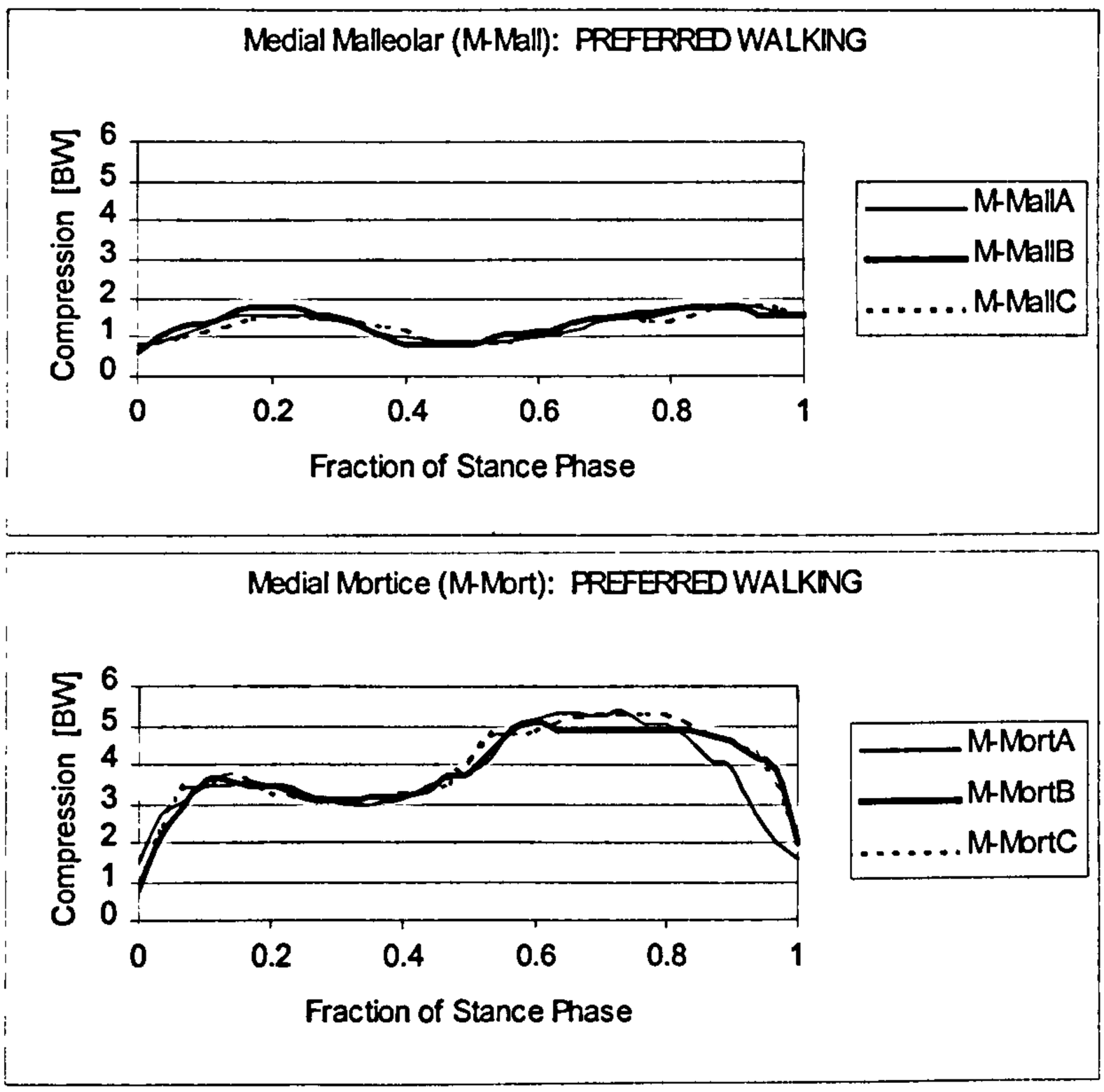

Figure 8.4-1 Ankle Joint Surface Compressions for Preferred Speed Walking for Subjects A and B.

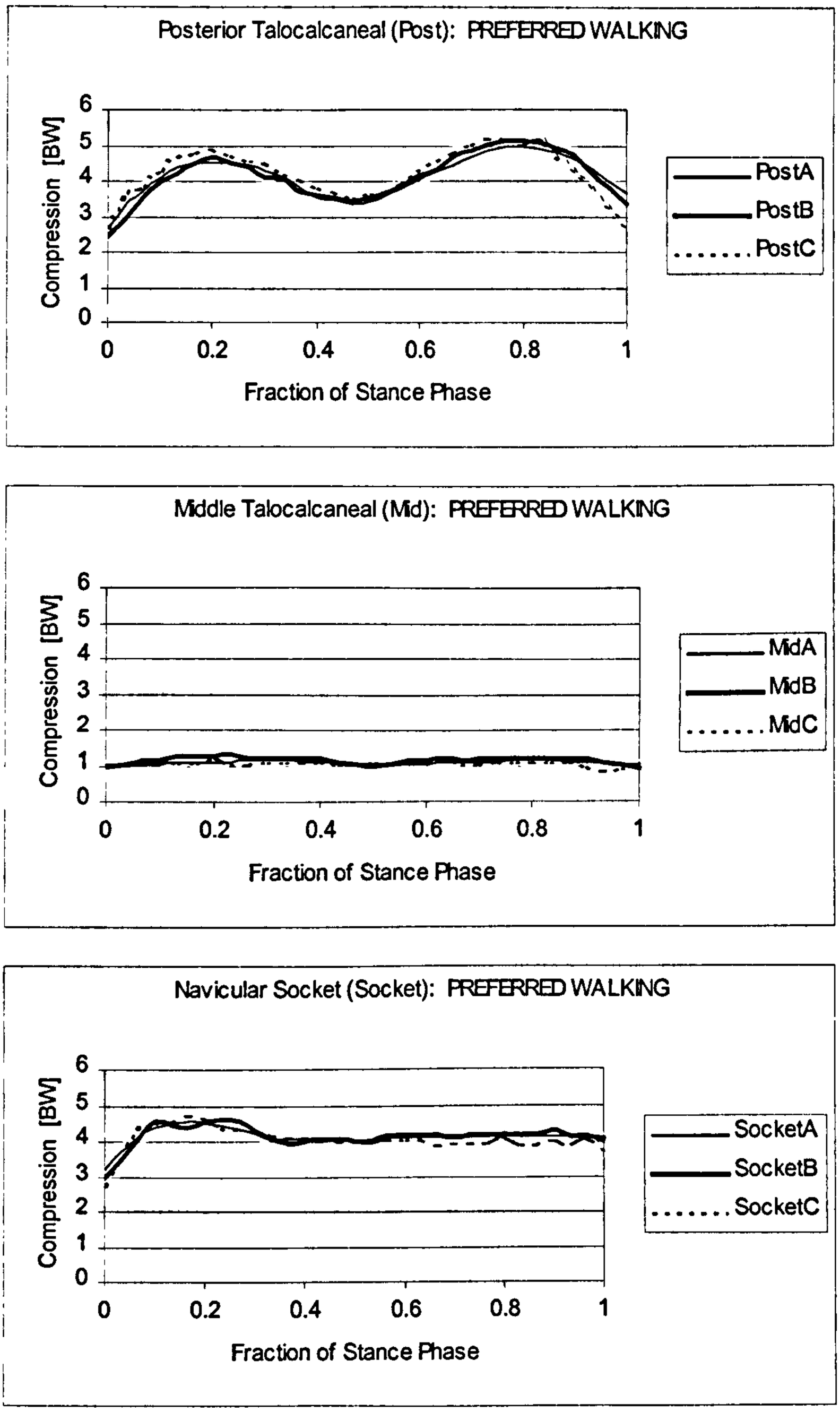

Figure 8.4-2 Ankle Joint Surface Compressions for Preferred Speed Walking for Subjects A and B.

one variation in loading occurred in the second peak of the L-Mort compression for Subject C which was larger than for A and B with a magnitude of 6.0×BW.

The M-Mall and L-Mall surfaces bore similar loading to each other. Both possessed two flat peaks for all three subjects, which were coincident with the peaks in L-Mort and M-Mort. The two peaks in M-Mall were around 1.5×BW and the late peak had a magnitude of 2.0×BW. The late peak for M-Mall was somewhat delayed with respect to the L-Mall and mortice surfaces, occurring at around 0.9 of stance phase with a magnitude of 1.8×BW.

Figure 8.4-2 plots the compressions on the three surfaces of the Subtalar Joint. The Mid surface bore a constant compression throughout stance phase with a magnitude of 1.2×BW. The Post surface compression possessed two peaks, one early at 0.18 of stance phase and the second at 0.8. The first peak was smaller than the second with magnitudes of 4.5×BW and 5.0×BW respectively. The Socket surface had a single early peak centred at 0.18 and then remained constant at 4.0×BW from 0.4 of stance phase until TO. The early peak of the Post surface and the early peak of the Socket surfaces were coincident.

8.4.2 Effective Joint Force Resultants

The articular surface compressions reported so far have been the individual resultant loads on each of the individual surface facets that made up the two Ankle Complex Joints. To give a better impression of the overall loading within each joint *effective* resultant compressive forces were calculated for the Ankle and Subtalar Joints.

The effective resultant for each joint was not a true resultant since the compression forces from each facet, which were the components of the effective resultant, did not have a common origin. Each facet resultant had an origin which lay on the rotational axis of the associated joint, but these origins were not necessarily the same point. Ignoring this, the facet resultants were assumed to possess a common origin and the vector sum of the facet resultants was taken for each joint. In the following plots the magnitudes of the effective resultants for the Ankle and Subtalar Joints are presented.

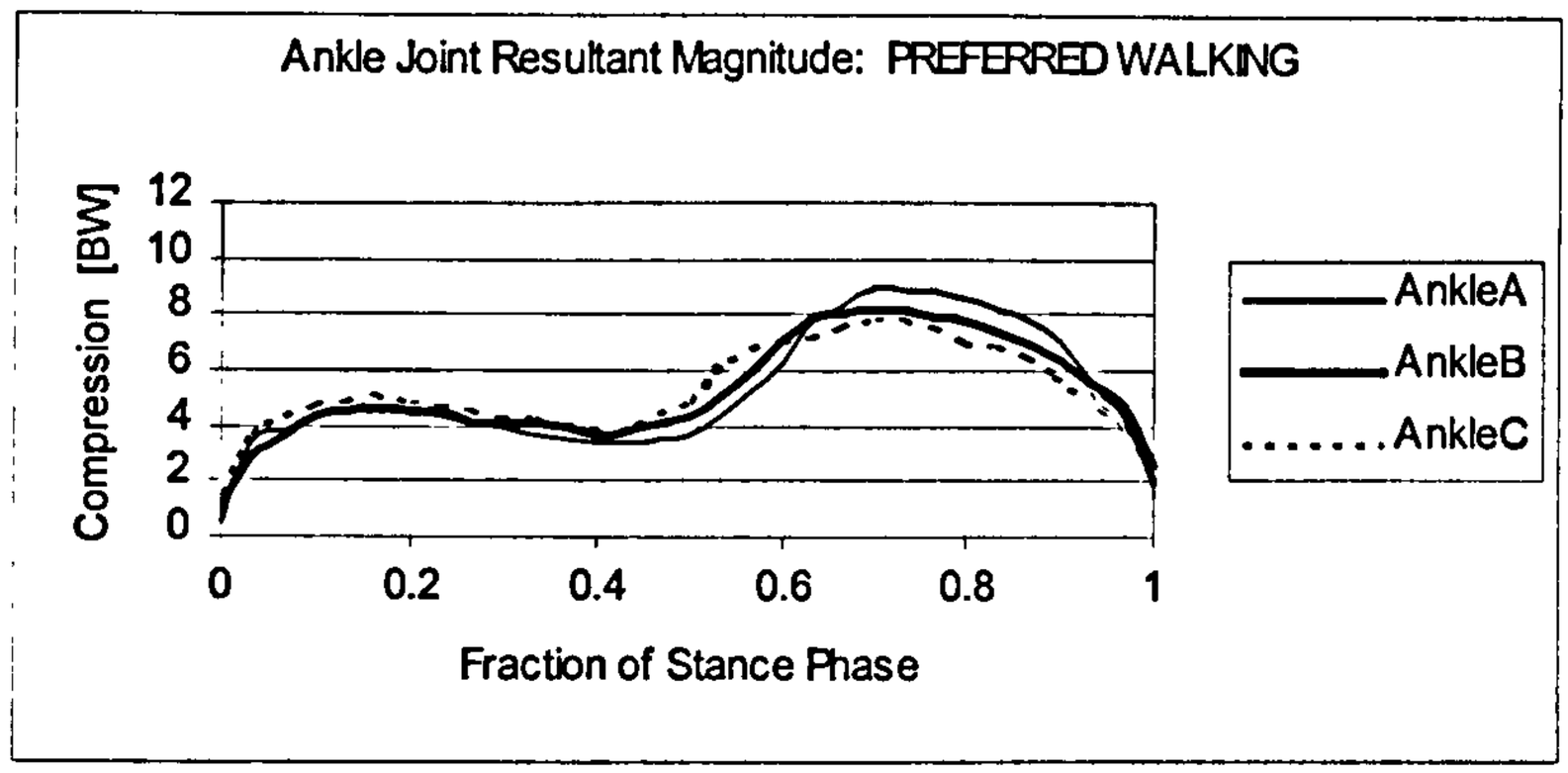

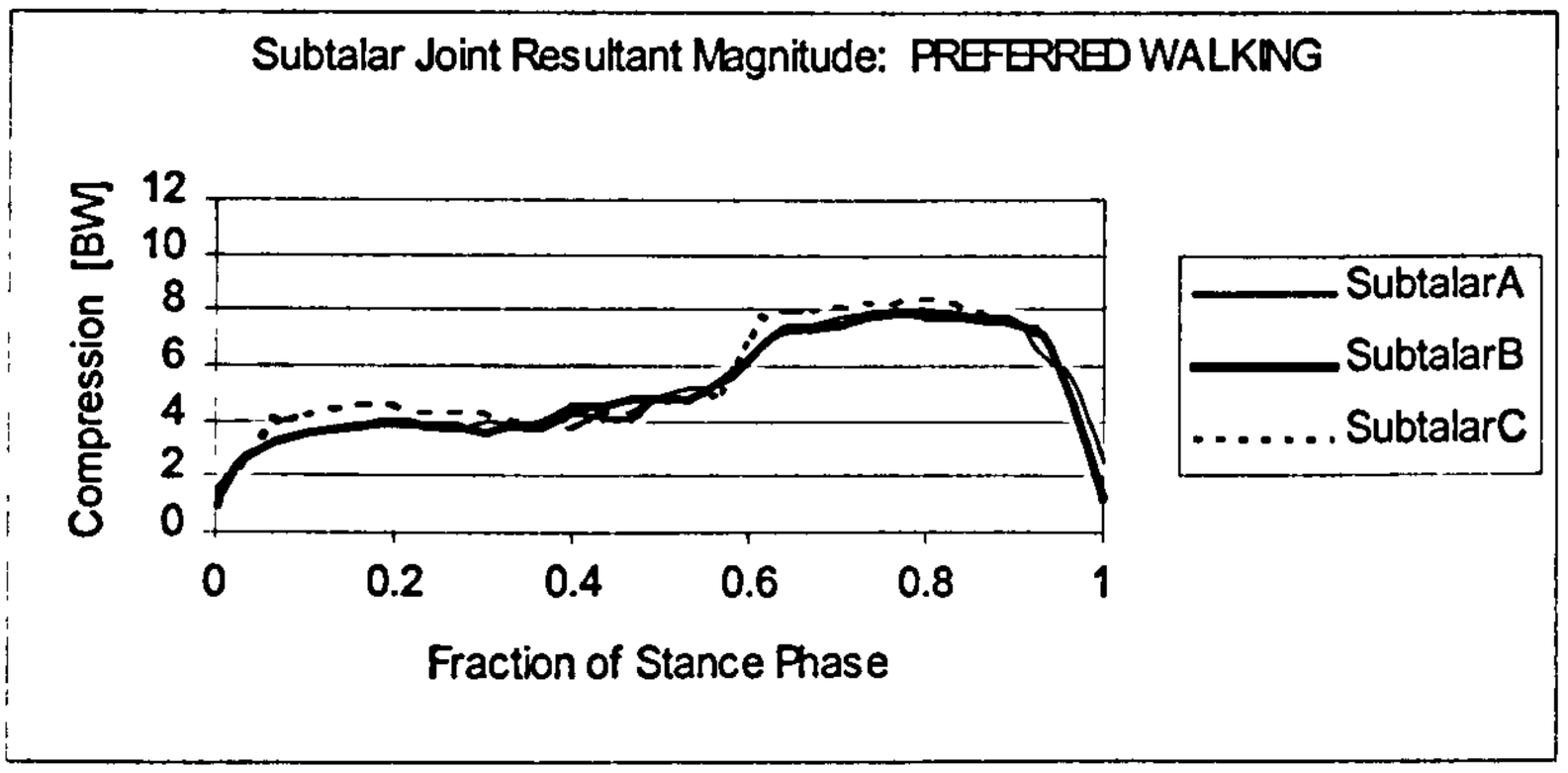

Figure 8.4-3 Effective Joint Force Resultants for the Ankle and Subtalar Joints during the Walking Task for Subjects A, B and C.

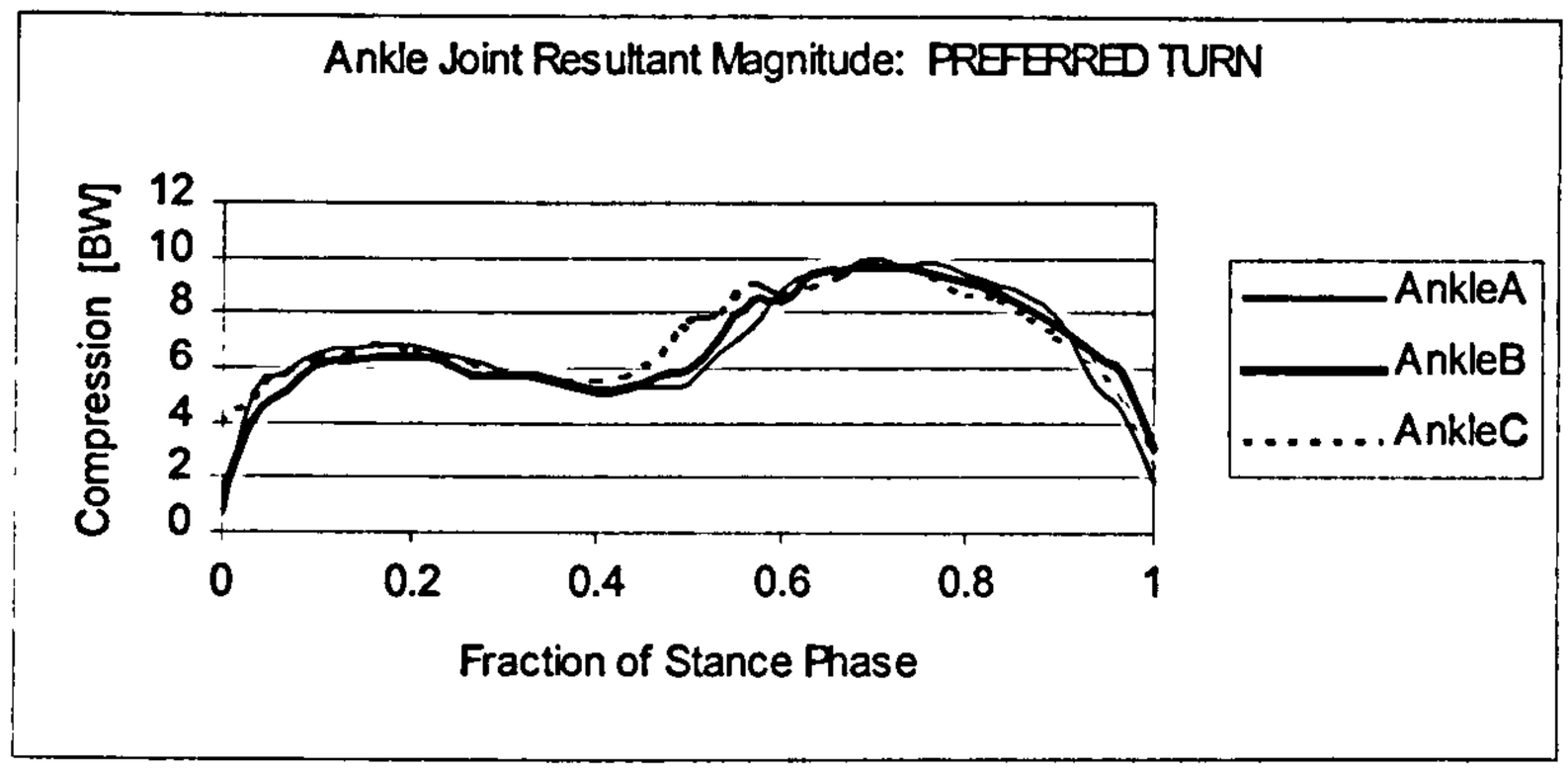

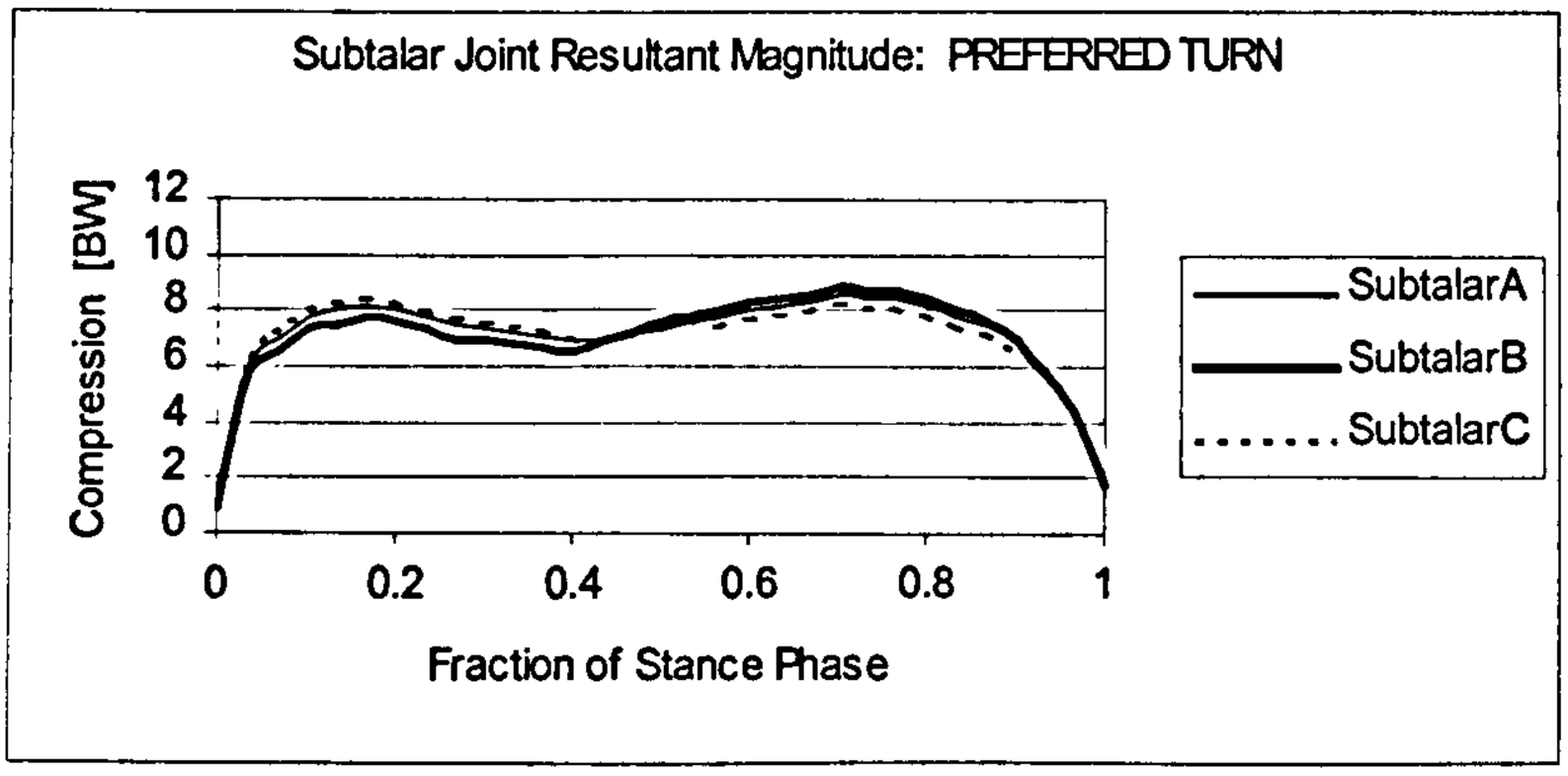

Figure 8.4-4 Effective Joint Force Resultants for the Ankle and Subtalar Joints during the Turning Task for Subjects A, B and C.

Figure 8.4-3 shows the effective resultants during walking for the Ankle and Subtalar Joints. Both joint resultants had a peak occurring at around 0.8 of stance phase. The Subtalar Joint resultants were similar for the three subjects with the peaks all having magnitudes of around 8.0×BW. For the Ankle Joint, Subject A had the most distinct peak with the peak having a magnitude of 8.5×BW. The late peak magnitudes for Subjects B and C were less than for A, at 7.8×BW.

Figure 8.4-4 shows the effective resultants for the Ankle and Subtalar Joints during the turning task. There was little variability between subjects in the resultants for the Subtalar Joint. This compression possessed two flat peaks at 0.2 and 0.8 of stance phase with magnitudes of 8.0×BW and 9.0×BW respectively. The Ankle Joint resultants also had two peaks, which were coincident with those in the Subtalar Joint. The early peak was similar for all three subjects at 6.5×BW. The second peak was largest for Subject B at a maximum of 9.5×BW with Subjects A and C at around 9.0×BW.

The differences in the effective resultants for the Ankle and Subtalar Joints between tasks are plotted in Figure 8.4-5 for preferred speed. The interesting result for the Ankle Joint was that the effective resultant had similar trends for the walking and turning tasks, but that the resultant was larger during the turning for all the subjects. The compression bore two peaks, the first smaller than the second peak in each case. The shape of the effective resultant curves for the Subtalar Joint was also somewhat changed between tasks. During walking, the early peak in compression was significantly smaller than the second, late peak (around 4.0×BW for early and 8.0×BW for the late peak). During turning, the early peak was increased to a similar magnitude as the late peak (around 8.0×BW for both). For all subjects, the loading in early stance was increased during turning from what it was during walking.

The differences between speeds in the effective resultants for Subject A during walking and turning are plotted in Figures 8.4-6 and 8.4-7. The resultants for the Ankle Joint during walking tended to increase in the magnitudes of its two peaks as speed increased from to slow to preferred. There was minimal difference

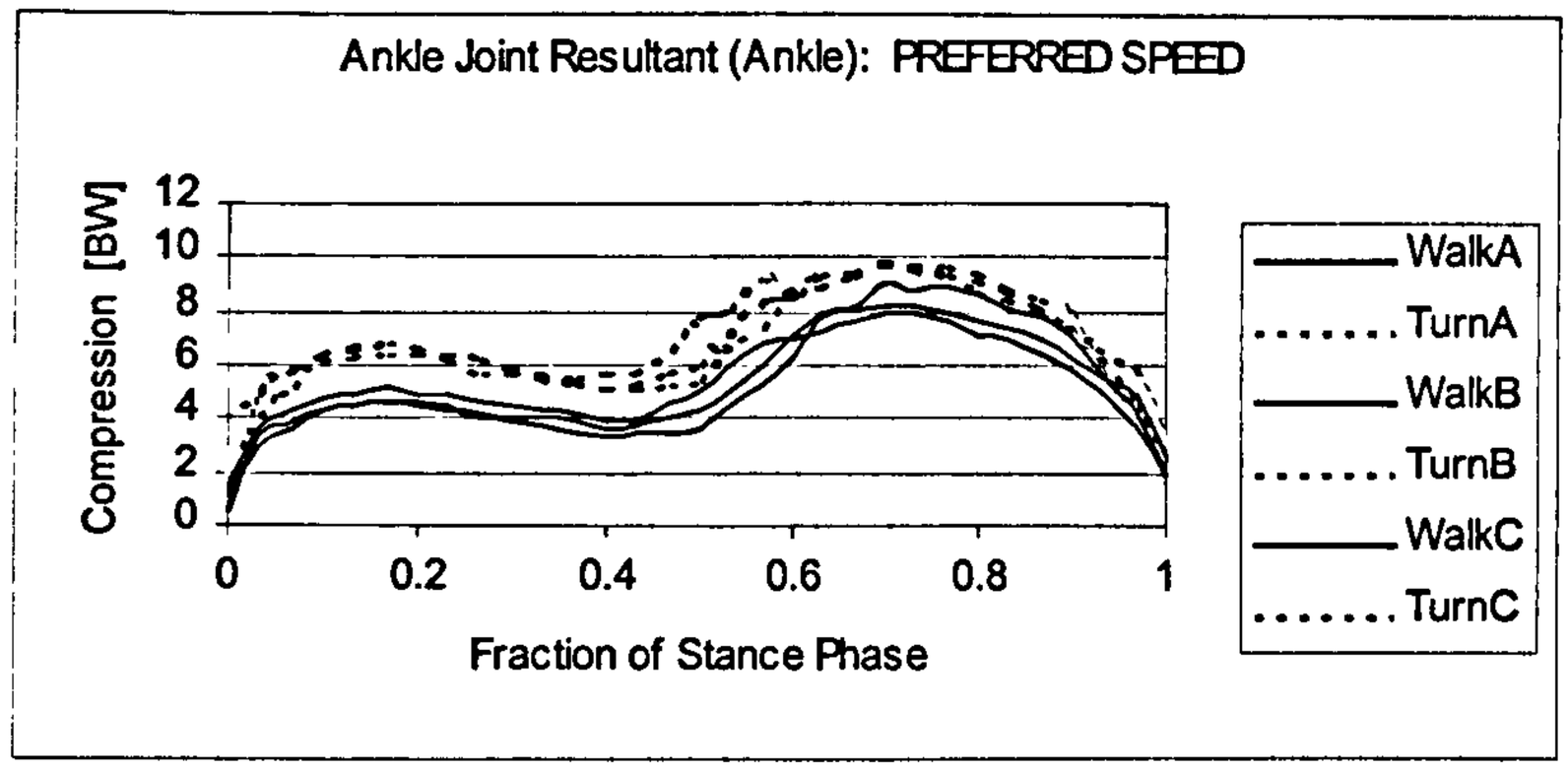

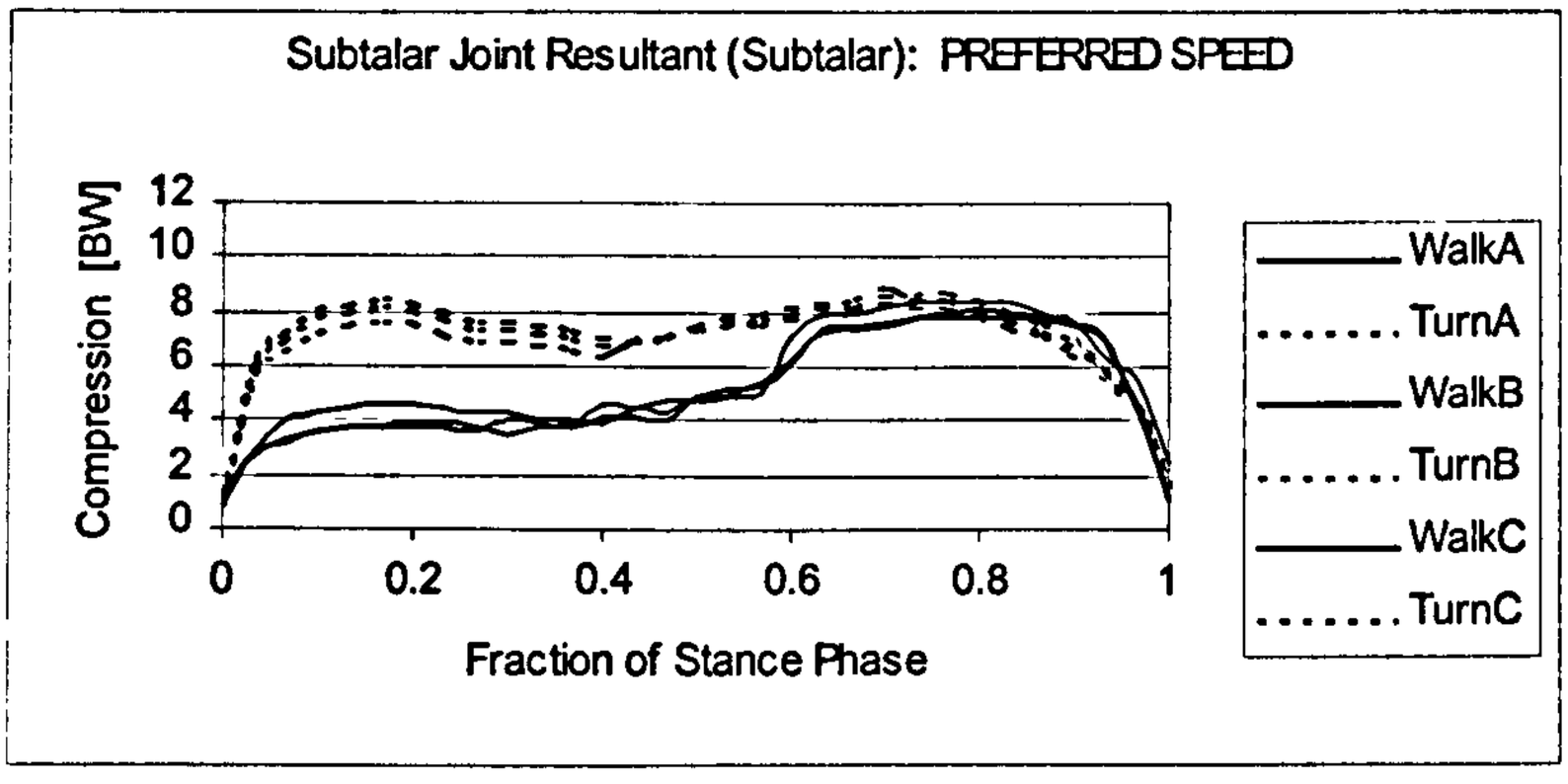

Figure 8.4-5 Comparing Task differences in Effective Resultants for the Ankle and Subtalar Joints during Preferred Speed for Subjects A, B and C.

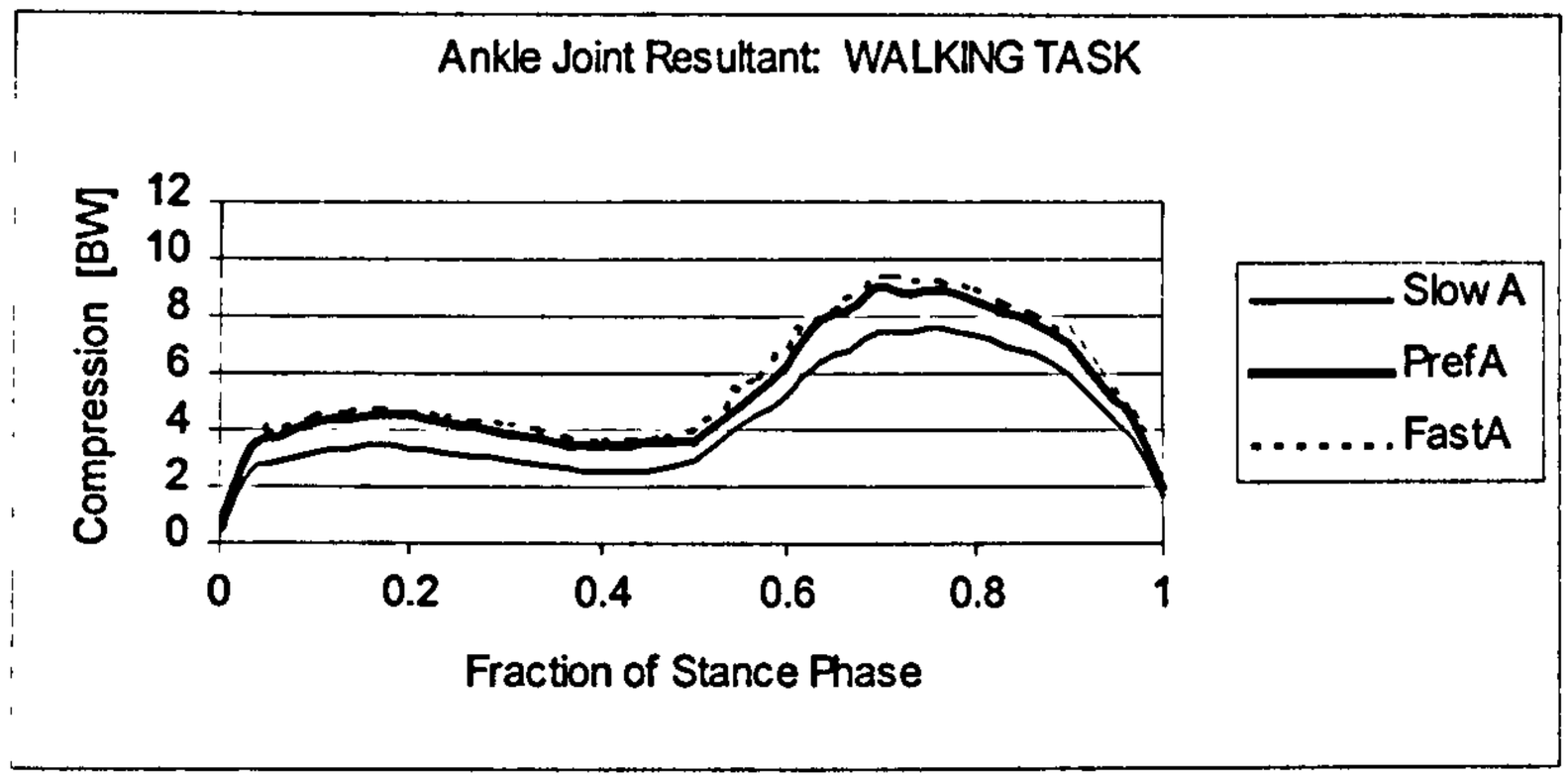

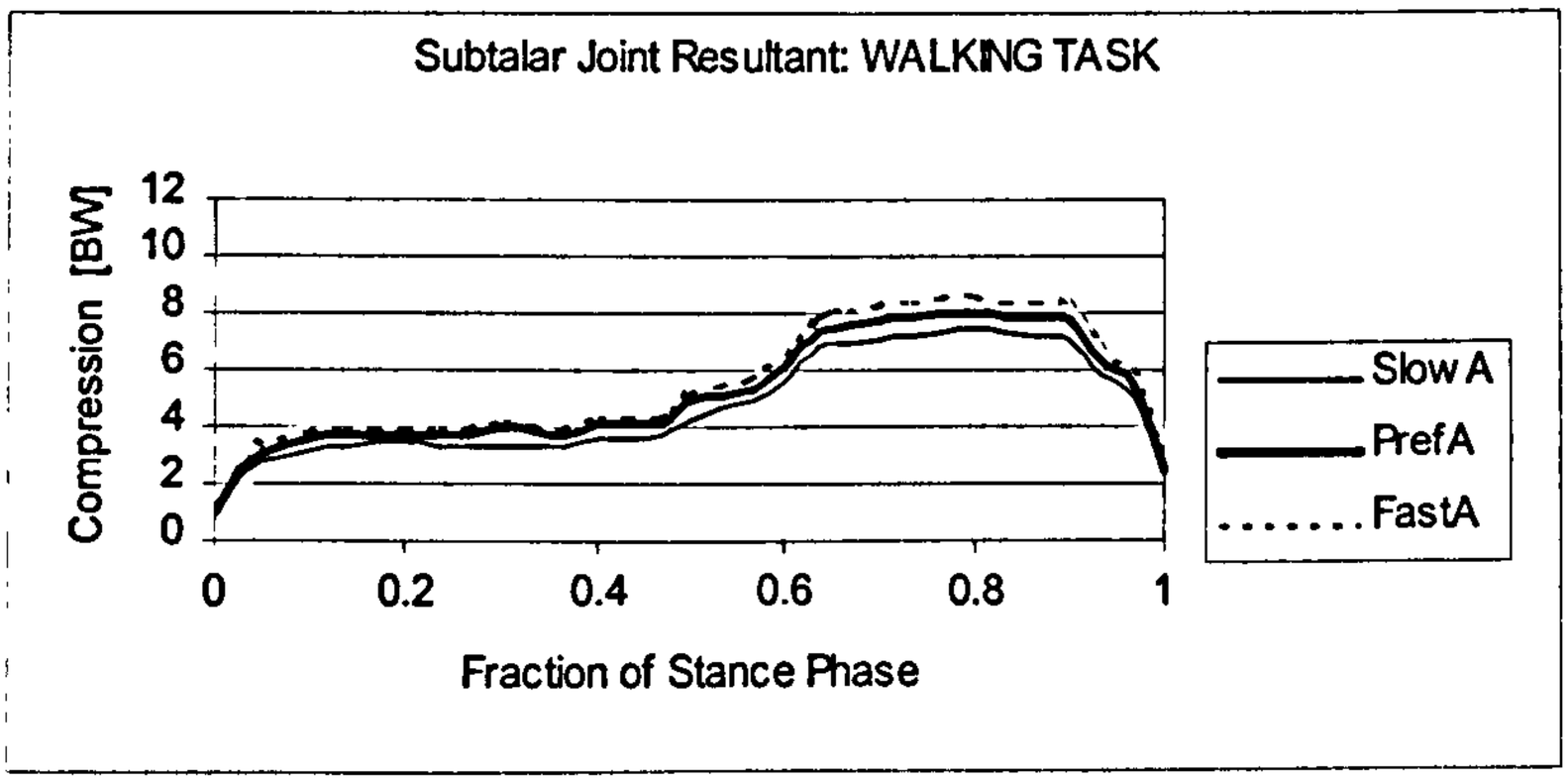

Figure 8.4-6 Comparing Speed differences in Effective Resultants during Walking for the Ankle and Subtalar Joints during Preferred Speed for Subjects A, B and C.

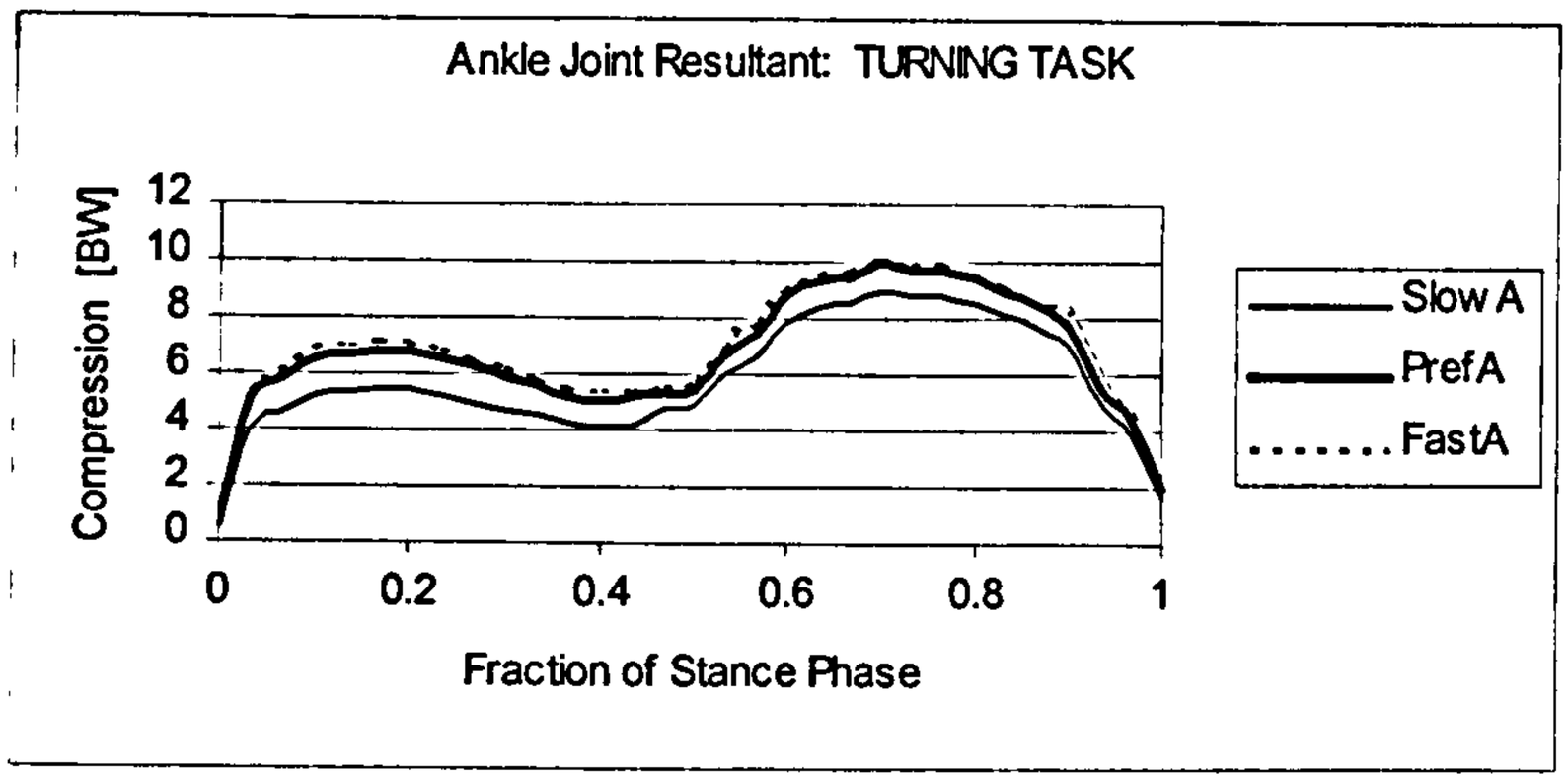

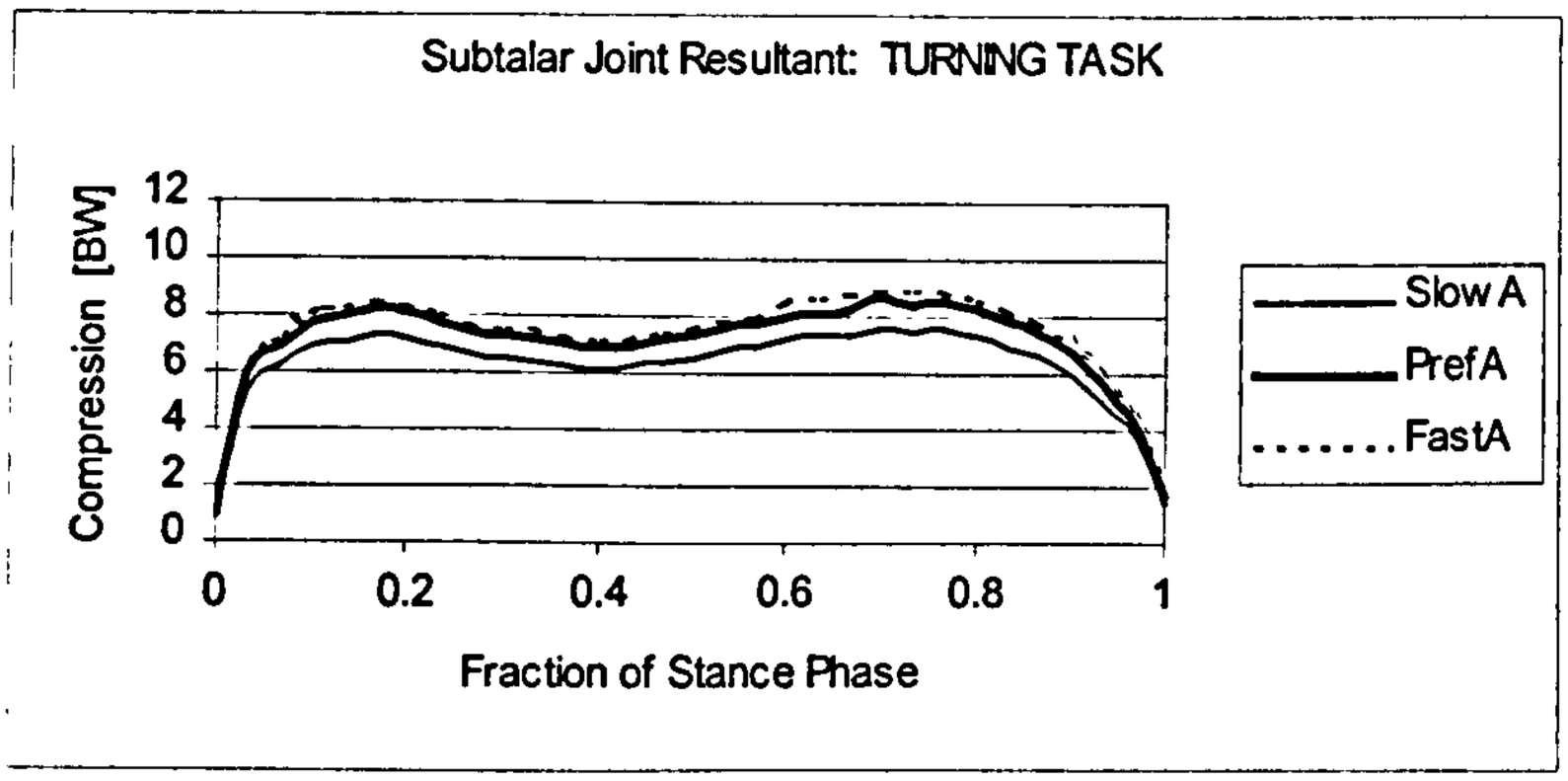

Figure 8.4-7 Comparing Speed differences in Effective Resultants during Walking Turn for the Ankle and Subtalar Joints during Preferred Speed for Subjects A, B and C.

between preferred and fast speeds. The magnitude of the early peaks increased from about 2.5×BW at slow speed to around 4.0×BW during preferred and fast speed. The compression at MS between the two peaks was about 2.0×BW for slow speeds and increased to 3.0×BW at preferred and fast speeds. The shape of the Subtalar Joint resultants was similar for all three speeds of walking but the overall magnitude of compression increased slightly as speed increased. The late peak magnitudes increased from 7.2×BW at slow speed to around 8.0×BW to 8.5×BW at fast speed. The same behaviour was seen during the changing speeds of turning. The peaks in the Ankle Joint resultants increased as speed increased from slow to preferred speed with the loading remaining the same for preferred and fast speeds. At preferred and fast speed, the MS compression increased that at slow speed from 4.0×BW to 5.3×BW. The shape of the Subtalar Joint resultants remained constant with changes in turning speed with the overall magnitude of compression increasing as speed increased. The largest change occurred between slow and preferred speeds with the peaks increasing from 7.0×BW at slow speed turning to 8.0×BW during fast speed.

8.4.3 Articular Surface Compression Discussion

The large second peaks seen in the effective joint compression resultants for both joints were all coincident with each other and with the second peak in vertical Ground Reaction Force and the tensions in the Triceps Surae muscles. This likely represents the portion of stance phase where the greatest compression occurs for the Ankle Joint specifically and for the Ankle Complex generally. The single peak in the compression of the medial Malleolar surface occurred *after* these peaks. Since the Trochlear surface of the Talus, which is held within the bimalleolar mortice of the lower leg, is wider anteriorly than it is posteriorly, it tends to wedge itself into the mortice during dorsi-flexion. Recall from the joint angle results in Section 3.2.2 that the Ankle Joint experienced its maximum dorsi-flexion (of nearly than 10°) just before TO. Therefore at TO, the Talus bone was securely wedged into the bimalleolar mortice of the lower leg. The late peak in the compression of the M-Mall surface therefore likely represents this wedging action, as the medial Malleolar surface of the Talus moves into contact with the corresponding Fibular surface in

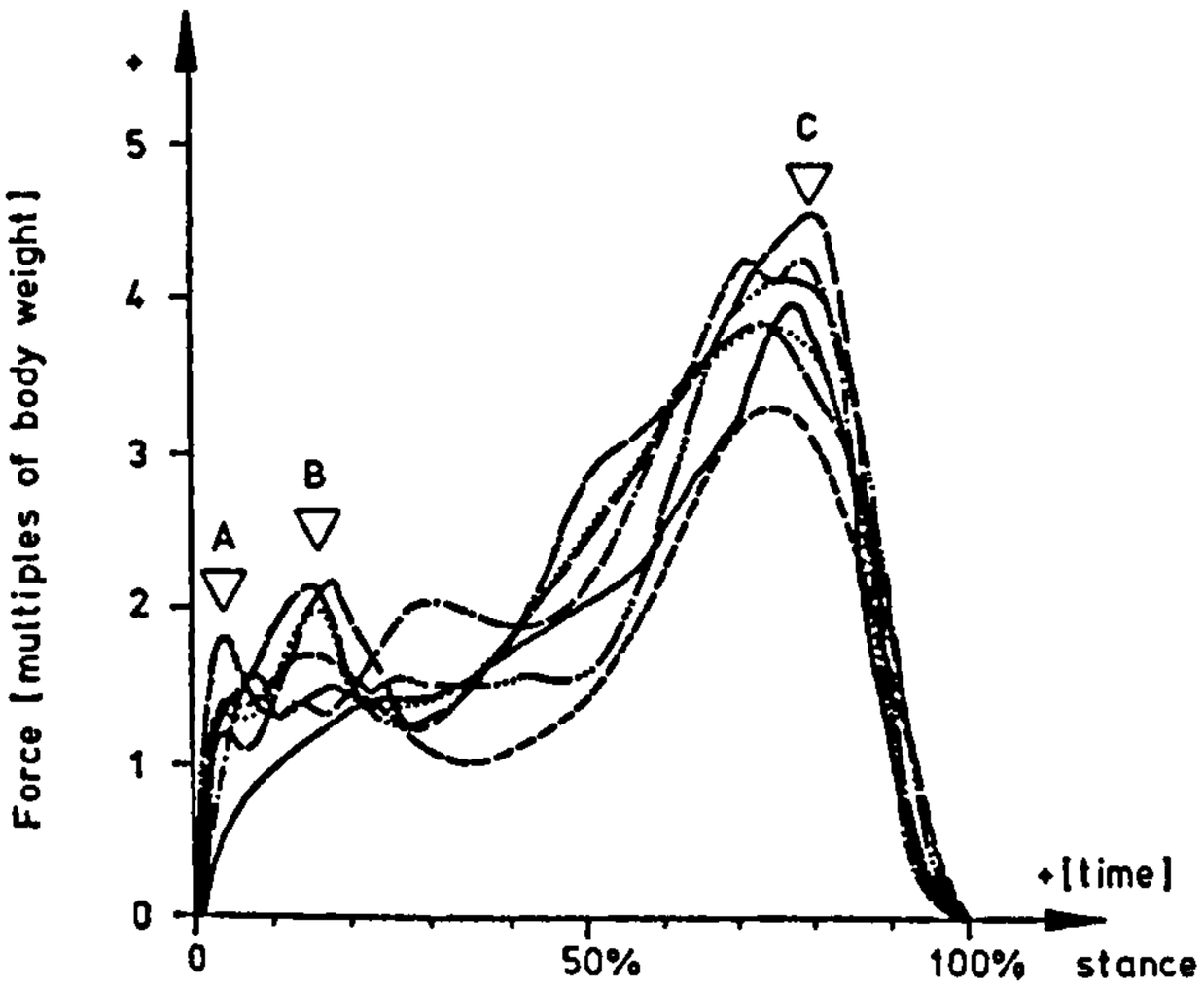

Figure 8.4-8 Joint compressive load in the ankle joint as calculated by Procter, 1980.

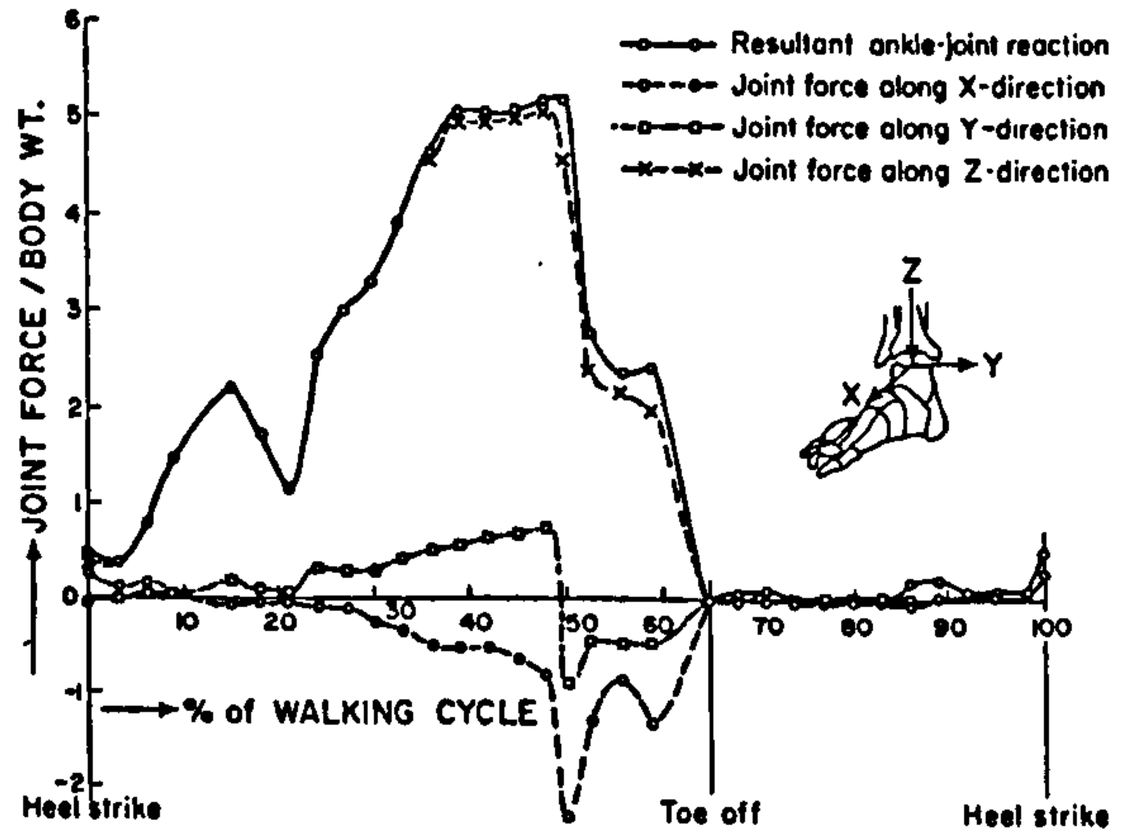

Figure 8.4-9 Joint compression force in the ankle joint as calculated by Seireg and Arvikar, 1975.

dorsi-flexion. Whereas with the foot in neutral and in plantar-flexion, the two surfaces were not in contact at all. The wedging action of the Talus into the Mortice tends to stabilise the Talus with respect to the leg during the acceleration portion of stance phase where the loading is greatest. This relieves the tension required of the ligaments to constrain the Ankle Joint from motion other than about the rotational axis.

Figures 8.4-8 and 8.4-9 show the ankle joint compression predicted by the Procter model (Procter, 1980) and the Seireg model (Seireg and Arvikar, 1975) as reported previously in Section 2.3. What should be noted from these plots is that there are similarities and differences between these results and the results from the current model (Figure 8.4-3). The results all show similar trends through stance phase. There are two peaks in loading, a smaller peak early in stance phase (around 0.2 stance) and a larger peak late in stance (around 0.8 stance). The greatest difference between the current model results and those from both Seireg and Procter is in the overall magnitude of the compressive loading. In both Seireg and Procter, the magnitudes of the two peaks are around 2.5×BW and 5.5×BW respectively. In the current model, the peaks are 4.5×BW and 8.0×BW.

Since the shapes of the compressive loading curves are so similar, it seems as though all three models are demonstrating the same mechanics of ankle joint use, with an early deceleration-related peak in compression and a later acceleration-related peak. The discrepancy in magnitude is probably due to the presence of antagonism in the ankle joint muscles that has been simulated by the current model. This gives rise to this increased compressive loading over that predicted by the Seireg and Procter models; both of which predict no antagonism about the joint.

Figure 8.4-10 shows the comparison of ankle joint loading from the Stauffer model (Stauffer, et al, 1977) between the preferred and fast pace walking. This can be compared to Figure 8.4-6 for the current model. Note that similarly for both models, the peak magnitudes for both preferred and fast speed, the articular compression is very similar. As already mentioned, the magnitude of the loading in the current model and the Stauffer model are different. The Stauffer results predicted compression of around 5.0×BW in late stance and the current results simulated

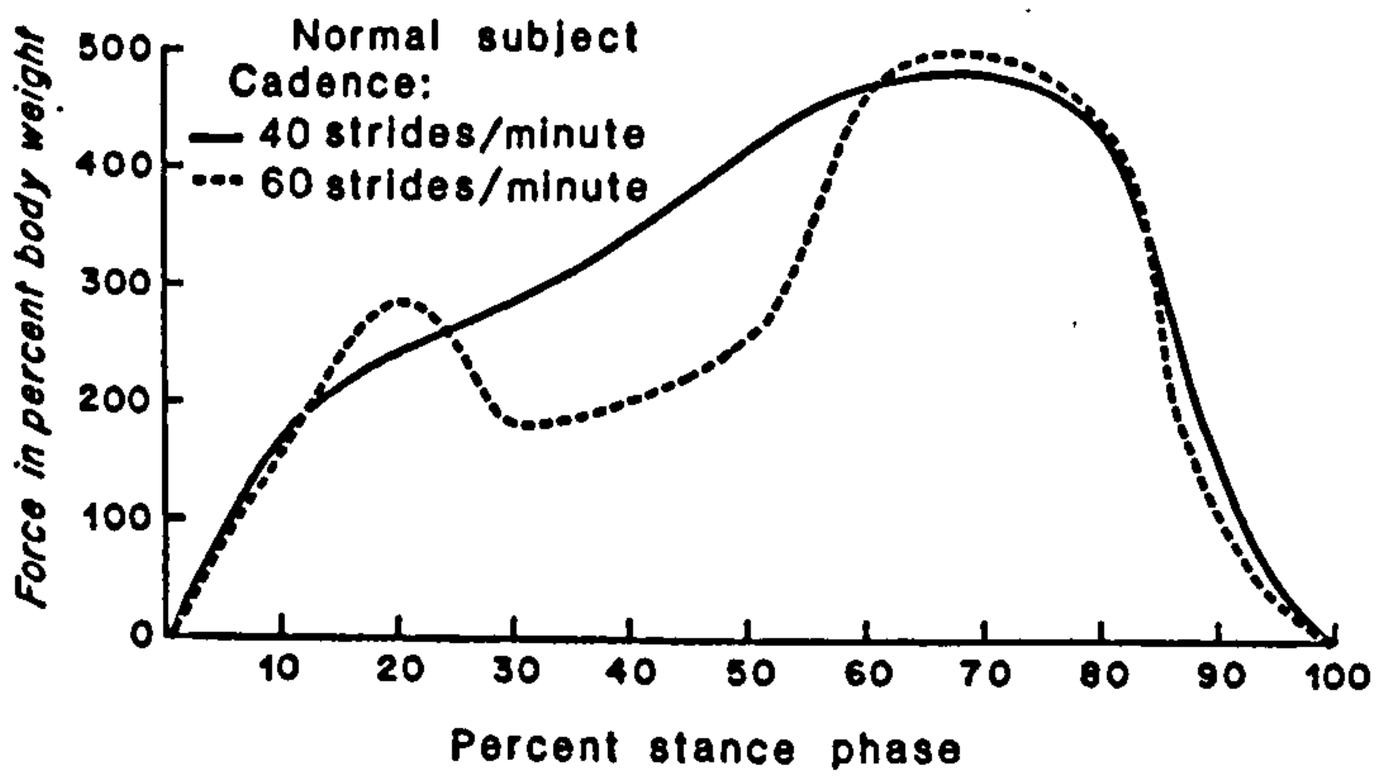

Figure 8.4-10 Joint compression forces for two difference walking speeds: 40 and 60 strides/minute as reported by Stauffer, et al, 1977.

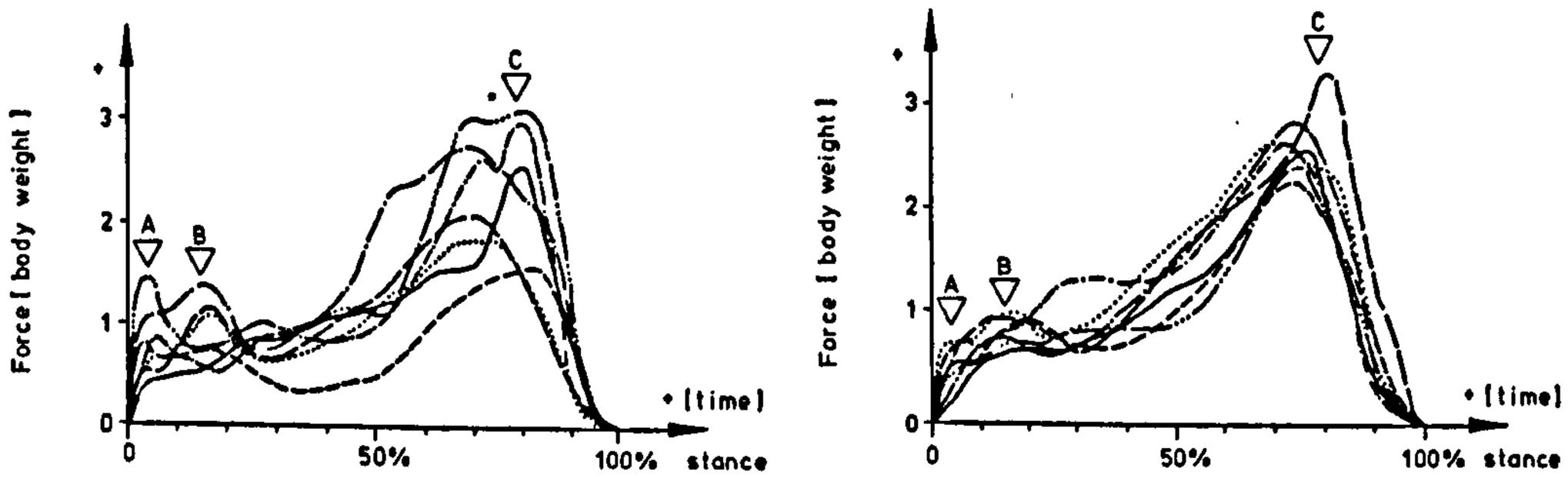

Figure 8.4-11 Joint compressive loading for two facets of the subtalar joint: anterior facet (left) and posterior facet (right), as determined by Procter, 1980.

8.5×BW. The main feature of the Stauffer results predicted that the compression at MS would decrease as walking speed decreased; from 4.0×BW at 60 strides/minute to 2.3×BW at 40 strides/minute. This dip in the MS compression was not simulated by the current model, perhaps due to the presence of muscle antagonism through the middle of stance phase.

Figure 8.4-11 plots the joint compression results predicted for the subtalar joint by the Procter model. These can be compared to the current results plotted in Figure 8.4-3. The results from Procter show the compression on two of the subtalar joint facets (anterior and posterior) separately, whereas the current results combine the loading from all three facets into a single joint resultant. Therefore the magnitudes of these results are not directly comparable. However, the trends in the curves for both models show similarities. As with the compression in the ankle joint, the subtalar loading shows a smaller, early peak (around 0.2 of stance phase) and a larger, late peak (around 0.8 stance). Notice that the peaks for the anterior facet from Figure 8.4-10 are broader than for the posterior facet. These are similar to the broad peaks displayed in Figure 8.4-3 and if the Procter results were combined into a single joint resultant for the subtalar joint, this resultant may possess a similar shape to the current results.

8.4.4 Articular Surface Pressures

Due to the antagonism simulated by the current model, the joint compression resultants reported are larger in magnitude than those predicted by Procter, 1980, and Seireg and Arvikar, 1975. This brings into question whether the large compressive loads, some as high as 9.0×BW during walking and 10.0×BW during the turning task, can be possible physiologically. The factor that limits the physiology of joint compression is the pressure that the articular cartilage is able to withstand repeatedly without damage. Discussing joint pressure is appropriate since this takes into account both the joint compressive force (which has thus far been presented) and the surface area over which this force is borne.

A comparison of joint pressures experienced at the other joints of the leg would also be instructive. Plotted in Figure 8.4-12 are the joint resultants for the hip

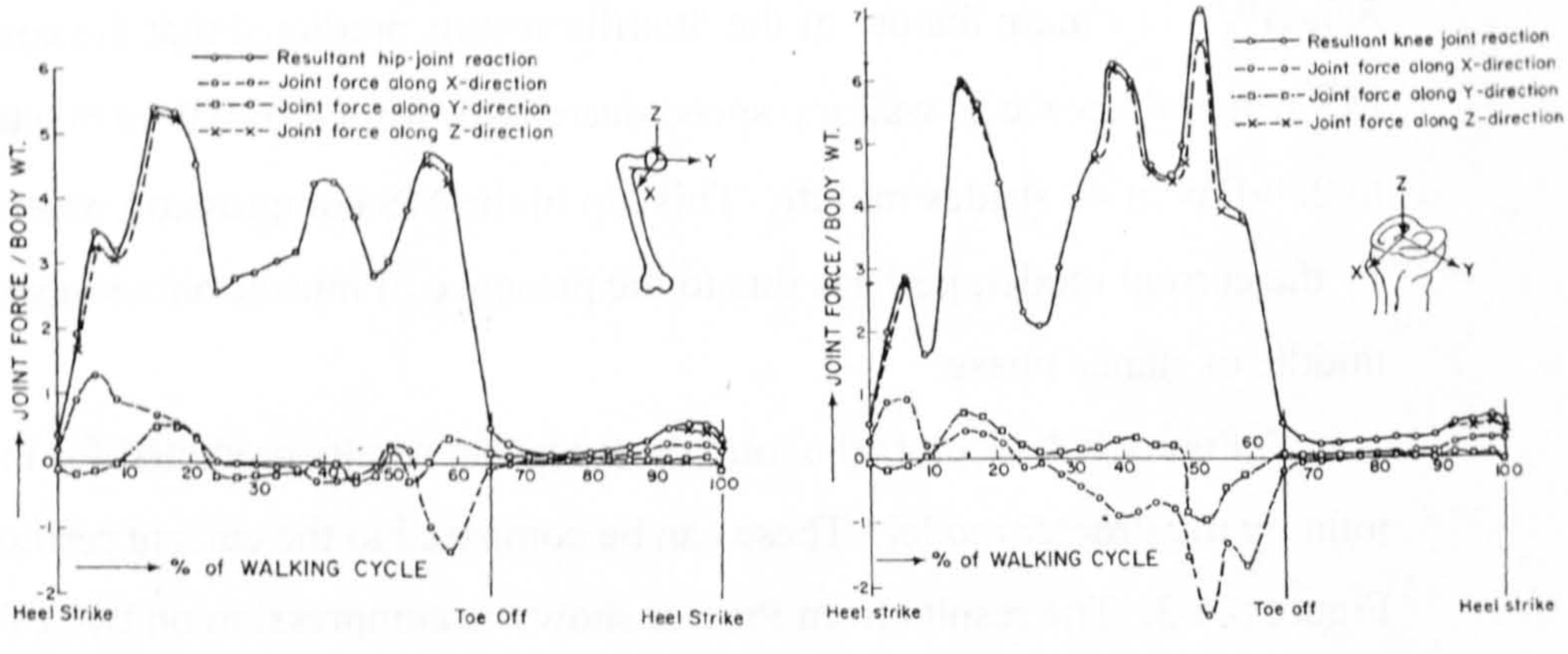

Figure 8.4-12 Joint compression force resultants for the hip (left) and the knee (right) as calculated by Seireg and Arvikar, 1975.

and the knee as reported by Seireg and Arvikar, 1975. Note that for these joints, during preferred pace, level walking, the compressive loading in the hip peaks at around 5.5×BW in early stance and at around 7.5×BW in late stance in the knee. It was the argument in Seireg that the loading as calculated in their model for the three joints showed the knee compression to be higher than the other two (7.5×BW as opposed to around 5.0×BW) since a large amount of antagonism was found acting about the knee. Seireg did not predict much antagonism about the ankle, but did suggest that the results presented in that paper would represent the minimum possible compression of the ankle. Should antagonism actually be present during walking, the compression would consequently be greater. In the study by Nisell, 1985, the compressive loading in the knee was modeled during lifting activities that included the full squat manoeuvre without load. Here the loading was estimated to be 9.0×BW.

From anatomical studies of cadaveric joints under physiological loading, the area of contact in the knee and ankle joints has been determined. Kura, Kitaoka, et al, 1998 demonstrated that under load, the contact area of the ankle was 719±264 mm^2. Kettlekamp et al, 1972 showed that contact area in a loaded knee at full extension was 762±220 mm^2 and 560±260 mm^2 at 30° flexion. A study by Hodge, et al, 1989, examined the contact pressures in the hip joint by direct measurement, in vivo, during various activities using an instrumented endoprosthesis. This study provided pressure measurement during walking, stair climbing and rising from a chair, among other activities.

Using the contact area measured for the knee and ankle and the compressive loading calculated for these joints by the current model, Seireg and Arvikar 1975 and Nisell, 1985, the pressures imposed on the articular cartilage of these joints could be calculated. The pressures measured directly in the Hodge, 1989 study supply the contact pressures for the hip joint. These are all listed in Table 8.4-1. The peak pressures for each of the three subjects in the current study during walking and walking turn are listed in Table 8.4-2. The specific body mass for each of the subjects of the current study were used in these tables whereas the surface contact areas for all the subjects were assumed to be the same, 719 mm^2 as reported in Kura,

1998. These maximum pressures from walking and from turning are reported in Table 8.4-1 as the ankle joint pressure results.

Joint	Activity	Compressive Force (×BW)	Contact Pressure (Mpa)	Source
Hip	Walking	-	5.4	Hodge, et al, 1989
	Stair climbing	-	10.7	" "
	Rising from chair	-	18.0	" "
Knee	Walking	7.3	7.05*	Seireg, et al, 1975
	Full squat	9.0	11.8*	Nisell, 1985
	*assuming body mass is 75 kg			
Ankle	Walking	9.0	8.3*	current model
	Turning	10.0	10.7^{+}	" "
	*for Subjects B,C $^{+}$for Subject C			

Table 8.4-1 Peak joint contact pressures for the hip, knee and ankle during various common activities.

Subject	Body Mass (kg)	Walking		Turning	
		Force (×BW)	Pressure (MPa)	Force (×BW)	Pressure (MPa)
A	53.5	9.0	6.59	10	7.32
B	76	8.0	8.32	10	10.40
C	78	7.8	8.32	10	10.67

Table 8.4-2 Peak ankle joint force and pressure for Subjects A, B and C during walking and turning at preferred speed.

For the pressures calculated at the knee during walking and the full squat, the body mass of the subject was assumed to be 75 kg (similar to Subject B in the current study). Since the Kettlekamp, 1972 study showed the knee contact area decreases with increasing knee flexion, the contact area during walking was taken to be 762 mm^2 and during squat to be 560 mm^2. This is really the area measured for 30° flexion as opposed to a full squat where the flexion of the knee is greater and the contact area consequently smaller. Therefore this pressure will underestimate the actual pressure.

What should be noted from the pressures in Table 8.4-1 is that despite the high compressive loads reported in the current model, the contact pressures resulting from this loading are well within the normal range reported for the knee and hip joints during the common movement tasks of walking, stair climbing and squating. The peak hip pressure was reported as 5.4 MPa in the elderly subject in the Hodge, 1989 study and this pressure could well be higher in an energetic young adult such as the three subjects in the current study. The pressure in the knee during walking was reported as 7.05 MPa. The pressures arising from the loading in the current study during walking (8.32 MPa) are slightly higher than those for the hip and knee, but not tremendously so.

The peak pressures in the ankle during the more demanding turning task were larger than during walking. For Subjects B and C the pressures were 10.40 and 10.67 MPa respectively. However, the pressures are comparable to the pressure in the knee during a full squat and the hip during a stair climb which are both tasks which are more demanding on these joints than walking. This range of pressure seems to be the pressure experienced in the joints of the leg during those tasks which are more demanding than walking.

The interesting pressure result was for the hip during a rise from a chair. The peak pressure reported was 18.0 MPa in an elderly subject. Clearly this pressure must be within the range of physiological pressures that can be repeatably withstood by articular cartilage without permanent damage. Therefore despite the large loading calculated for the ankle joint during walking and turning in the current, the pressures realised by the ankle cartilage falls well within physiological limits.

8.5 SIMPLIFIED EQUILIBRIUM SOLUTIONS

8.5.1 Simplified Model

The results for the muscle-tendon tensions, ligament tensions and effective joint surface resultants, as well as the joint angles and external joint moments were produced by a complex three-dimensional solution of quasi-static equilibrium that was, for the most part, opaque in its computation. To facilitate an understanding of how the broad range of results are interrelated and how they fit together to describe the loading of the Ankle Complex during walking and walking turns, a set of example calculations from a simplified Ankle Complex system are presented. The three-dimensional system of the current model has been simplified to a two segment, solid foot and shank system defined in a pair of two-dimensional planes: the sagittal and frontal planes. The sample calculations were done for Preferred Speed Walking and Turning for both Subjects A and B. Three points of interest were chosen from stance phase: 0.2, 0.5 and 0.8 of stance phase.

In the full MMAO model of the ankle joints, the line of action of the muscle tendons and their lever arms about the Ankle and Subtalar Joints were calculated at each instance of joint moment. These quantities would change as the relative positions of the rigid segments moved with respect to each other. The instantaneous lever arms and lines of action at 0.2, 0.5 and 0.8 of stance phase used in the simplified model were calculated in the full MMAO model. Table 8.5-1 lists the lever arms for the three simplified muscle groups: TS, DF and P.

The lever arm values for the DF group about the Ankle Joint are of the same order as the lever arms presented in the study by Maganaris, 2000 for the tibialis anterior throughout the ankle range of motion. That study reported the lever arm, measured using an MRI technique, as ranging from 4.5±0.4 cm in full dorsi-flexion to 3.0±0.3 cm in full plantarflexion while relaxed and from 6.0±0.4 cm (full dorsi-flexion) to 4.0±0.4 cm (full plantarflexion) during maximum voluntary contraction. During gait, the ankle joint angle begins slightly dorsi-flexed at heel strike and quickly moves to slight plantarflexion for the remainder of stance (from around 0.25 of stance to toe off) as discussed in Section 5.3. The ankle does not approach either extreme in its range of motion. The change

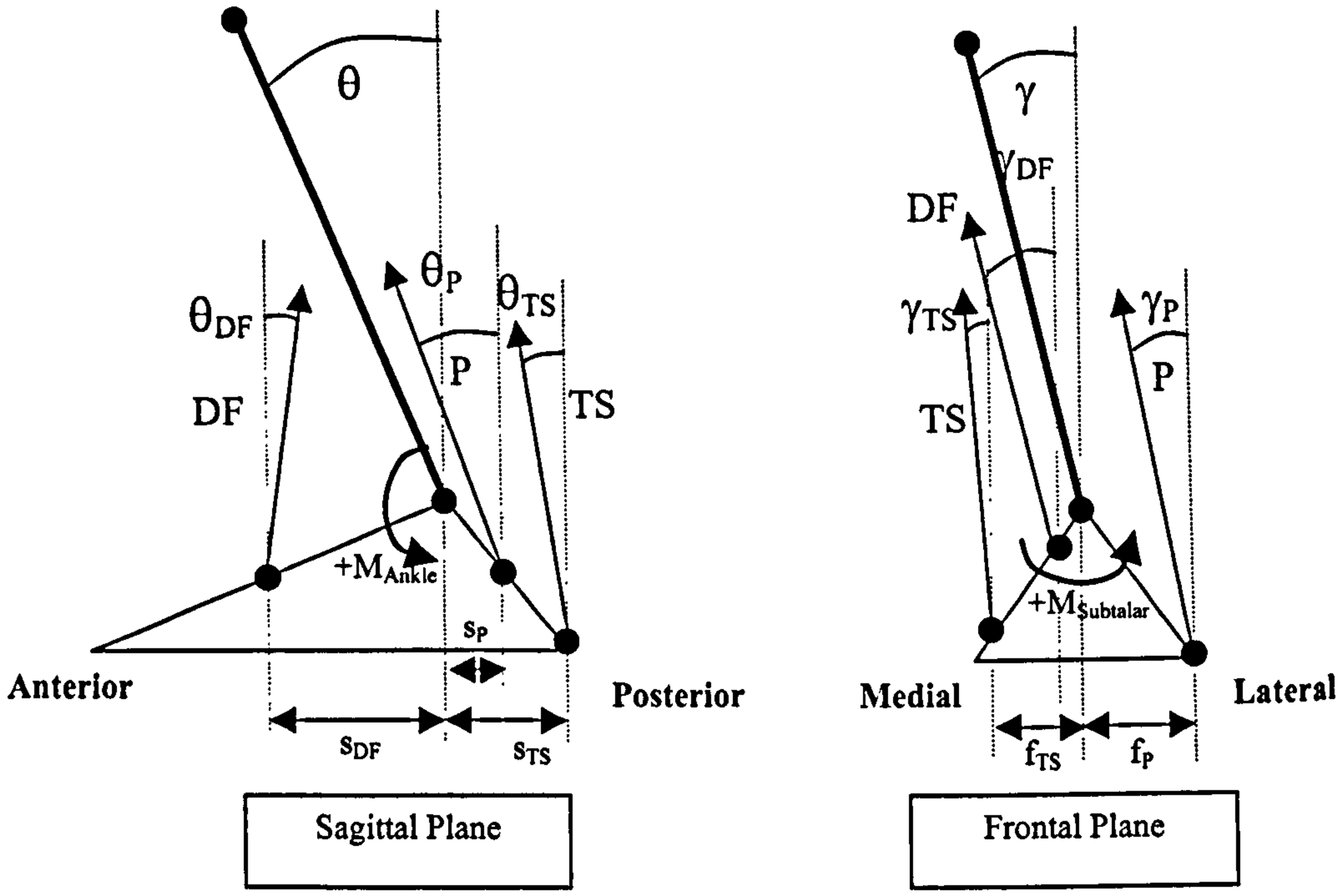

Figure 8.5-1 Simplified foot-shank, two-segment model shown in two planes: the Sagittal and Frontal Planes. Also shown are the three muscle groups: TS, P and DF.

in lever arm from longer at 0.2 of stance to shorter at 0.5 and 0.8 of stance reported in Table 8.5-1 is due to the behaviour of the Ankle Joint angle.

	[mm]	0.2 A	0.2 S	0.5 A	0.5 S	0.8 A	0.8 S
Walking	TS	-48	7	-46	5	-46	5
	DF	58	2	55	3	55	3
	P	-6	-25	-8	-25	-8	-24
Turning	TS	-48	5	-46	5	-46	5
	DF	58	3	56	3	55	4
	P	-6	-25	-8	-25	-8	-25

Table 8.5-1 Lever arms of the three simplified muscle groups (TS, DF and P) at the three points of interest in stance phase, as calculated from the full MMAO model.

The lever arms presented in Table 8.5-1 also compare well with the lever arms measured in the study by Klein, et al, 1996 for the three muscle groups about both the Ankle Joint and Subtalar Joint. The TS group lever arm was measured to be constant through its range of ankle joint motion with a value of around 52.8±5.1 mm. The lever arm presented in the current model falls within the Klein, et al variance. The peroneal muscles had a smaller, constant lever arm about the Ankle Joint as measured by Klein, et al of 9.9±2.4 mm. Again the lever arms for the peroneal muscles used in the current MMAO model fall within this variance. The peroneal lever arm about the Subtalar Joint was shown to be constant through the complete range of motion from inversion to eversion at 21.8±4.3 mm. The TS and DF Subtalar Joint lever arms are of similar size magnitude or smaller with means of 5.3±7.4 mm for TS and 3.8±4.4 mm for tibialis anterior.

Figure 8.5-1 shows the simplified foot-shank system in the sagittal and frontal planes and displays the general positioning of the three muscle groups

	Early Stance (0.2)	Midstance (0.5)	Late Stance (0.8)
SAGITTAL PLANE **WALK + TURN**	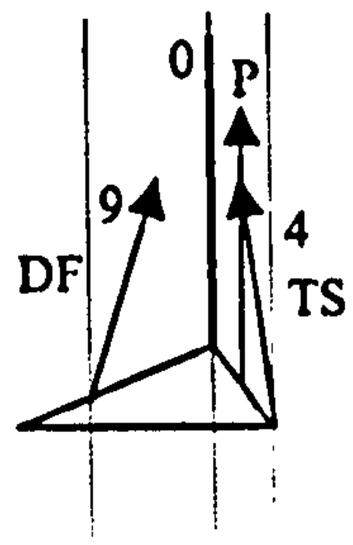	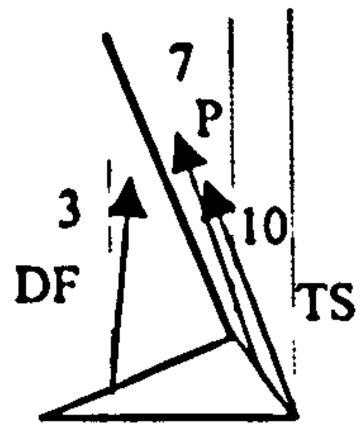 * P group follows shank	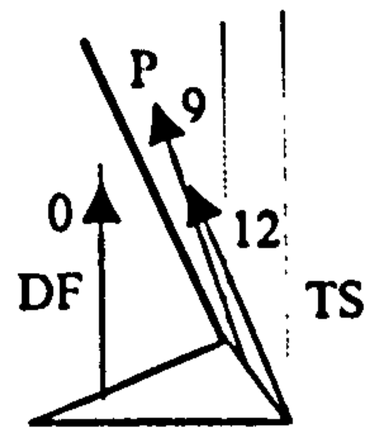
FRONTAL PLANE **WALK**	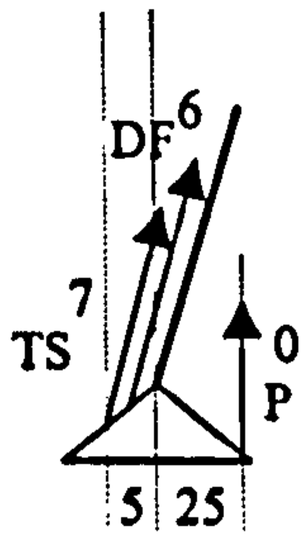	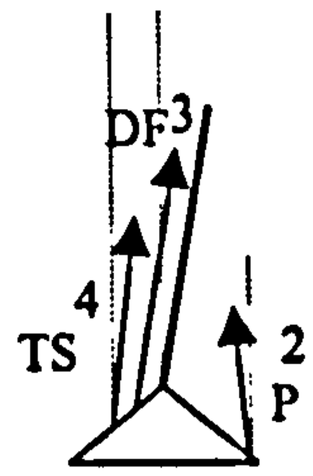 * DF group follows shank	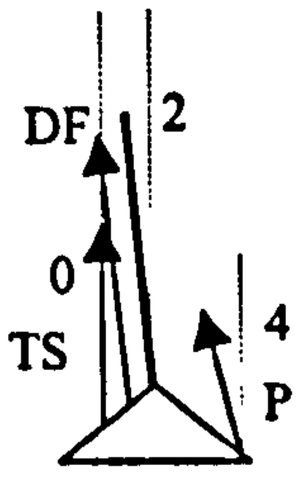
TURN	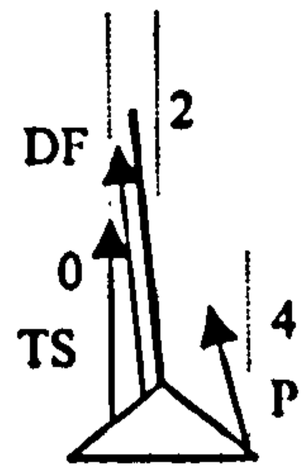	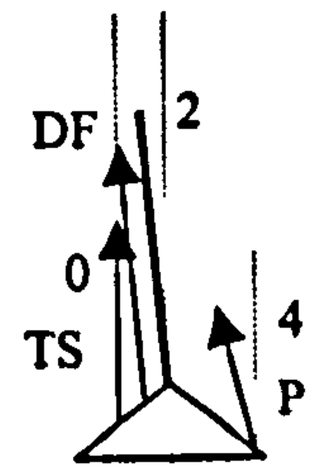	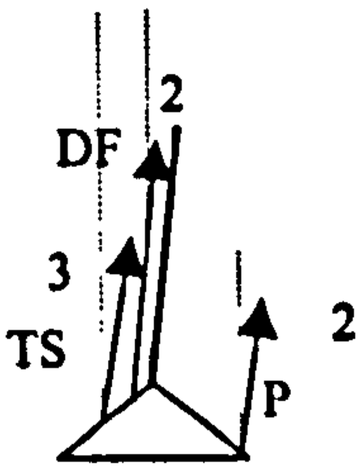

Figure 8.5-2 Positioning of the foot-shank segment system in the Sagittal and Frontal Planes for Subjects A and B during Walking and Turning at the three points in stance phase: 0.2, 0.5 and 0.8.

included in the system. Figure 8.5-2 shows the specific positioning of the simplified foot-shank system at the three stance phase points in the sagittal and frontal planes during walking and turning. As can be seen from Figures 5.3-1 and 5.3-2 in Chapter 5, the joint angles were nearly identical for Subjects A and B. Therefore the system positioning was assumed to be identical for the two subjects. The simplified muscle group positionings are also plotted in 8.5-2. The GaL, GaM and Sol muscles were combined into the Triceps Surae group (TS). The Peroneal group (P) was composed of the PeB and PeL and the Dorsi-flexor group (DF) was composed of TiA, EDL and EHL. This simplified model was unable to assign tensions individually to the muscles of each group. However, comparison with the current, MMAO model results is possible by summing the tensions of the muscles in each group from the results of Section 8.2.

The Ankle Joint is assumed to run perpendicular to the sagittal plane and the Subtalar Joint runs at 30° to perpendicular to the frontal plane directed upward anteriorly. Positive moments about the Ankle Joint are plantar-flexing and positive Subtalar Joint moments are everting. Positive forces run upward and medially in the sagittal and frontal planes respectively.

The equilibrium equations balance the moments and the forces in the two planes. The component of Subtalar Joint moment about the vertical axis is ignored in this simplified model since loading due to this mechanism was assumed to be borne by the malleolar articular surfaces and by the ligaments which have not been included in the simplified model. The equations of moment equilibrium are therefore,

$$\begin{aligned}\sum M_{sagittal} = 0 = {} & DF\cos\theta_{DF}\cos\delta_{DF}\times s_{DF} + TS\cos\theta_{TS}\cos\delta_{TS}\times s_{TS} \\ & + P\cos\theta_{P}\cos\delta_{P}\times s_{P} + M_{Ankle} \\ \sum M_{frontal} = 0 = {} & DF\cos\theta_{DF}\cos\delta_{DF}\times f_{DF} + TS\cos\theta_{TS}\cos\delta_{TS}\times f_{TS} \\ & + P\cos\theta_{P}\cos\delta_{P}\times f_{P} + M_{Subtalar}\end{aligned} \qquad (8.5\text{-}1)$$

The mortice of the tibia-fibula bones on the superior side of the Ankle Joint bears a significant curvature when viewed in the sagittal plane. This means that the joint is able to withstand anterior-posterior shearing forces with the joint compression resultant. The curvature extends approximately 20° anterior to the long

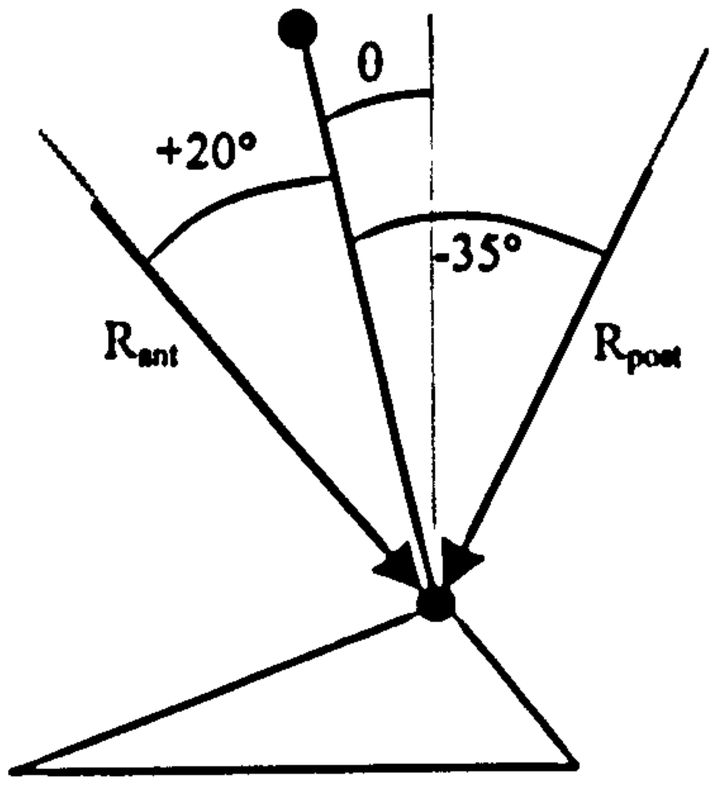

Sagittal Plane

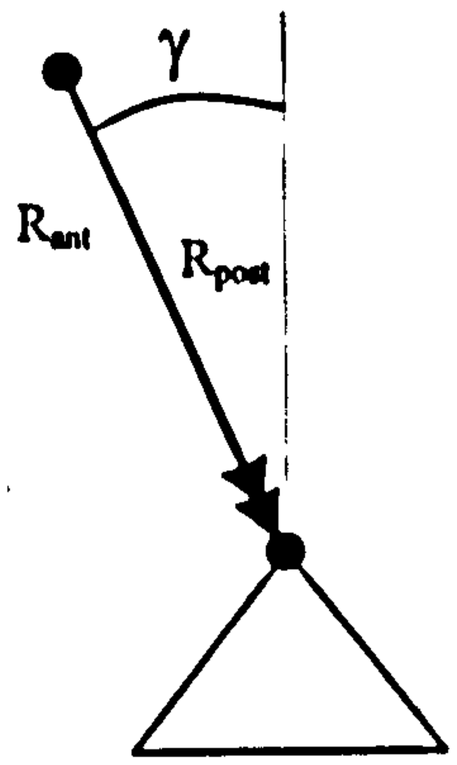

Frontal Plane

Figure 8.5-3 Orientations of the anterior and posterior components of the joint compression acting on the Ankle and Subtalar Joints in the sagittal and frontal planes respectively.

axis of the shank and 35° posterior. To include this shear-resisting action of the Ankle Joint surface, the joint compression force in the Ankle Joint is therefore modeled by two joint force components as shown in Figure 8.5-3. Note that these force components are not orthogonal. This is a simplified version of the method of resultant "confinement" used in the full MMAO model as described in Section 7.4.2. So long as the magnitudes of these components are positive, the resultant force vector will lie between these two components and therefore on the Ankle Joint surface.

The equations of force equilibrium are therefore,

$$\sum F_{sagittal} = 0 = DF\cos\theta_{DF}\cos\delta_{DF} + TS\cos\theta_{TS}\cos\delta_{TS} + P\cos\theta_{P}\cos\delta_{P}$$
$$- R_{ant}\cos(\theta+20)\cos\delta - R_{post}\cos(\theta-35)\cos\delta + F_{Vertical}$$
$$\sum F_{frontal} = 0 = DF\sin\theta_{DF}\cos\delta_{DF} + TS\sin\theta_{TS}\cos\delta_{TS} + P\sin\theta_{P}\cos\delta_{P} \qquad (8.5\text{-}2)$$
$$- R_{ant}\sin(\theta+20)\cos\delta - R_{post}\sin(\theta-35)\cos\delta + F_{A-P}$$

where the resultant joint compression will be,

$$\vec{R} = \begin{bmatrix} \cos(20) & \cos(-35) \\ \sin(20) & \sin(-35) \end{bmatrix} \begin{bmatrix} R_{ant} \\ R_{post} \end{bmatrix} \qquad (8.5\text{-}3)$$

which lies at an angle with respect to the shank long axis,

$$\theta_R = -\arctan\left[\frac{\hat{2}R}{\hat{1}R}\right] \qquad (8.5\text{-}4)$$

This gives four equations to solve for five variables. However, a determinate systems was not required since the purpose of the simplified model is to examine the results of the full current model and examine the effects of anatagonism. Therefore, the tension in DF was taken from the results in Section 8.2 and the remaining four unknowns were calculated and compared to the results from the MMAO model.

As an example, the simplified equilibrium solutions were calculated for preferred speed turning at 0.5 of stance phase for Subject B. The DF muscle tensions are summed from the results in Figure 8.2-6 and the external joint loading are taken from Figures 5.2-5 and 5.4-3. Plugging the values into Eqs. 8.5-1 yields,

$$\sum M_{sagittal} = 0 = (1.0)\cos(-3)\cos(2)\times(0.055) + TS\cos(10)\cos(0)\times(-0.046)$$
$$+ P\cos(7)\cos(4)\times(-0.008) + 0.10$$
$$\sum M_{frontal} = 0 = (1.0)\cos(-3)\cos(2)\times(0.003) + TS\cos(10)\cos(0)\times(0.005)$$
$$+ P\cos(7)\cos(4)\times(-0.025) + 0.02\cos(30)$$
$$DF = 1.0$$
$$P = 1.614$$
$$R = 3.464$$

These values are then inserted into Eq.s 8.5-2,

$$\sum F_{sagittal} = 0 = (1.0)\cos(-3)\cos(2) + (3.464)\cos(10)\cos(0) + (1.614)\cos(7)\cos(4)$$
$$- R_{ant}\cos(7+20)\cos(2) - R_{post}\cos(7-35)\cos(2) + 0.70$$
$$\sum F_{frontal} = 0 = (1.0)\sin(-3)\cos(2) + (3.464)\sin(10)\cos(0) + (1.614)\sin(7)\cos(4)$$
$$- R_{ant}\sin(7+20)\cos(2) - R_{post}\sin(7-35)\cos(2) + 0.0$$

$$R_{ant} = 4.650$$
$$R_{post} = 2.905$$

The joint compression resultant is put into a more informative form using Eq.s 8.5-3 and 8.5-4,

$$\vec{R} = \begin{bmatrix} \cos(20) & \cos(-35) \\ \sin(20) & \sin(-35) \end{bmatrix} \begin{bmatrix} 4.650 \\ 2.905 \end{bmatrix} = \begin{bmatrix} 6.750 \\ -0.08 \end{bmatrix}$$

Therefore,

$$|\vec{R}| = 6.75$$
$$\theta_R = 0.70\,\text{deg}$$

A summary of the simplified results are tabulated in Table 8.5-2. For comparison, the results from the three-dimensional MMAO model are also included. Note that the muscle group tensions are comparable to the summed results from the current model. The discrepancies between the two are due to the simplification and the lack of ligaments in the simplified model. Without ligaments, the constraint of the Ankle and Subtalar Joints then becomes the job of the muscles. Therefore one might expect the muscle loading from a model lacking ligaments to be larger than

one with ligaments included. This would also result in joint contact loading that was larger.

Also note in Table 8.5-1 that in most cases, although the values are close, there is a trend in the discrepancies between the simplified and the full MMAO models. The TS loading in the simplified model are generally lower than MMAO values and the joint compression is larger. In some cases the P muscle group loading is also larger in the simplified model than the MMAO model.

		Walk				**Turn**			
		Subject A		Subject B		Subject A		Subject B	
	DF	2.00	2.00	1.20	1.20	1.69	1.69	1.45	1.45
0.2	TS	4.22	5.30	1.45	2.35	4.02	5.00	3.72	4.2
	P	1.67	0.76	0.84	0.72	1.70	1.72	1.61	2.1
	R	9.18	7.91	4.81	4.00	8.69	8.11	8.06	7.92
	θ_P	2.63		5.83		1.87		1.90	
	DF	0.50	0.50	0.51	0.51	0.12	0.12	1.0	1.0
0.5	TS	3.37	3.55	3.38	3.75	3.05	3.6	3.464	4.2
	P	1.08	1.00	1.08	1.23	1.32	1.49	1.614	1.93
	R	5.67	5.12	5.70	5.20	5.18	5.67	6.75	6.81
	θ_P	-6.98		-6.97		-7.59		0.70	
	DF	0.26	0.26	1.36	1.36	0.36	0.36	1.10	1.10
0.8	TS	5.31	6.00	6.70	7.25	5.59	6.50	6.53	7.50
	P	2.05	1.52	2.47	2.27	2.57	2.61	2.87	3.43
	R	8.87	7.98	11.76	10.21	9.75	9.91	11.71	11.47
	θ_P	-11.88		-10.68		-11.03		-10.36	

Table 8.5-2 Summary of loading results from simplified model and from MMAO model (shaded) for Subjects A and B during Walking and Walking Turn.

The main characteristic of the resultant from the MMAO model and the simplified model is the amount of antagonism produced by the Dorsi-flexor (DF) group of muscles. With just a small relative tension in the DF group (mostly from the TiA muscle), a somewhat larger tension is required by the Triceps Surae (TS) muscles to balance both the externally applied joint loading about the Ankle Joint and the antagonistic DF tension. This increased TS muscle tension then requires that the Peroneal (P) group of muscles increase tension to balance the moments about the Subtalar Joint.

8.5.2 The Role of Antagonism

It should be noted from the results of this chapter that the current MMAO model predicts a large amount of antagonism between both the TS and DF groups and the TS and P groups. These results therefore differ from the results of previous models which predicted nearly no antagonism in either of these muscle group two pairings (recall Stauffer, et al, 1977, Seireg and Arvikar, 1975 and Procter and Paul, 1982 in Sections 2.3, 8.2 and 8.4). Therefore the results from the MMAO model, particularly the joint effective resultant forces, will be larger for the current model than for the previous models.

The influence of antagonism on the tension of the TS and P muscle groups and on the joint resultant, R, can be examined by the imposing DF=0 on the simplified model and solving for the remaining unknowns in Eqs. 8.5-1 and 8.5-2. Taking the previous example calculation of walking and turning at 0.5 of stance phase for Subject B and applying DF=0 and the same external loading, yields the following for the moment equilibrium,

$$\sum M_{sagittal} = 0 = (0)\cos(-3)\cos(2)\times(0.055) + TS\cos(10)\cos(0)\times(-0.046)$$
$$+ P\cos(7)\cos(4)\times(-0.008) + 0.10$$

$$\sum M_{frontal} = 0 = (0)\cos(-3)\cos(2)\times(0.003) + TS\cos(10)\cos(0)\times(0.005)$$
$$+ P\cos(7)\cos(4)\times(-0.025) + 0.02\cos(30)$$

$$TS = 2.18$$
$$P = 1.24$$
$$DF = 0.0$$

and for the force equilibrium,

$$\sum F_{sagittal} = 0 = (0)\cos(-3)\cos(2) + (2.18)\cos(10)\cos(0) + (1.24)\cos(7)\cos(4)$$
$$- R_{ant}\cos(7+20)\cos(2) - R_{post}\cos(7-35)\cos(2) + 0.70$$

$$\sum F_{frontal} = 0 = (1.0)\sin(-3)\cos(2) + (2.18)\sin(10)\cos(0) + (1.24)\sin(7)\cos(4)$$
$$- R_{ant}\sin(7+20)\cos(2) - R_{post}\sin(7-35)\cos(2) + 0.0$$

$$R_{ant} = 2.91$$
$$R_{post} = 1.68$$

which convert into the magnitude and direction of the joint force compression vector,

$$|\vec{R}| = 4.11$$
$$\theta_R = -0.431\,\text{deg}$$

Compare these values to the simplified solution results for Subjects A and B at 0.5 of stance phase walking that were calculated in the previous section. These are summarised in Table 8.5-3, along with the change in loading between the no antagonism solution and the two subject solutions.

Table 8.5-3 illustrates how antagonistic tension in the DF group causes an increase in the tensions of the TS and P groups of muscles and in the joint compression. The no antagonism results agree well with the results of the ankle models of Stauffer, et al,1977, Seireg and Arvikar, 1975 and Procter, 1980 (recall Sections 8.2.2 and 8.4.3).

The previous models of Stauffer, Seireg and Procter either assumed no antagonism or predicted very little based on the University of California (1953) EMG data set. The current MMAO model produces as much as 2.00×BW of antagonistic tension in the DF group of muscles based on subject-specific EMG data. This will therefore cause the internal joint compression results and the muscle-tendon tension results of this model to be larger than the previous models. However, since

		No antagonism	Subject A	Δ	Subject B	Δ
	DF	0	0.5	+0.50	0.51	+0.51
Walking	TS	2.74	3.37	+0.63	3.38	+0.64
0.5	P	0.89	1.08	+0.19	1.08	+0.19
	P	4.33	5.67	+1.34	5.70	+1.37
	θ_R	-7.68	-6.98	+0.70	-6.97	+0.69
	DF	0	0.12	+0.12	1.0	+1.0
Turning	TS	2.18	3.05	+0.87	3.64	+1.46
0.5	P	1.24	1.32	+0.08	1.61	+0.37
	P	4.11	5.18	+1.07	6.75	+2.64
	θ_R	-0.43	-7.59	-7.16	0.70	+0.74

Table 8.5-3 Comparing the case of no antagonism to the simplified solutions for Subjects A and B at 0.5 of stance phase during Preferred Speed Walking and Turning.

the current model used subject-specific EMG as input, a detailed anthropometric representation of the internal structure of the Ankle Complex, individual muscle tensions and twelve separate ligaments (which had been omitted from all previous models), the current model is much more sensitive to deviations from normal gait patterns in the individual subjects than the other, previous ankle models. In the EMG data presented and discussed in Section 8.2.3 and the free moment data calculated in Section 5.5, it seems likely that the subjects in the current study were using a more "guarded" or stiffer gait that their usual preferred walking pattern. This seems to have increased the amount of antagonism acting about the ankle complex and increased the resulting joint compression.

CHAPTER 9 RECOMMENDATIONS AND CONCLUSIONS

9.1 RECOMMENDATIONS FOR FUTURE DEVELOPMENT

The method of Muscle Model Assisted Optimisation (MMAO) used in the current study could be improved or expanded in a number of ways. The variability in the tensions of the ligaments of the Ankle Complex was an unexpected result given the repeatability of the muscle tension and the surface compression outputs. A possible source of this variability could be the use of a *linear* method of optimisation which was ill-suited to assigning tensions to the constraining ligaments, perhaps due to its sensitivity to small variations in the input. It is suggested then that a *non-linear* method of optimisation be tried as a part of the MMAO procedure, which may prove to be more robust when presented with perturbations in the input. A sensitivity analysis of the current linear optimisation method would also be useful to determine if this was the cause of output variability.

There was a weakness in the method used to calibrate the Muscle Model for each individual subject, as identified in Sections 6.5 and 7.3. This weakness rested in how the tensions were assigned to each of the muscles when solving for isometric equilibrium during the Muscle Model Calibration (MMC) trials. While the author can at present suggest no other method for assigning tensions to the individual muscles, the errors arising from the present method would be mitigated if more MMC trials were performed to calibrate the Muscle Model. Instead of two isometric trials for each of the recorded muscles, additional isometric trials over a large range of contraction strengths could be performed. Isokinetic trials could also be added to the calibration procedure either using commercial isokinetic machines or in-house designed devices of the sort used by Hof and Van den Berg (1981a-d).

It has been reported in the literature that surface EMG can be recorded from the deep muscles of the lower leg, such as the posterior tibial group of muscles, with the appropriate placement of electrodes. The Muscle Model could therefore be used to model more than the eight muscles of the present study. It would also be fruitful

to evaluate the relative presence of cross-talk between muscle EMGs in the muscles of the lower leg for a number of subjects.

EMG from the intrinsic muscles of the foot could also be included in Muscle Model. This would expand the Ankle Complex Model of the present study to include some joints of the foot, such as Lisfranc's Joint and the longitudinal and transverse. Such an expanded model could examine the coupling between the joints of the Talus and the joints of the foot.

The present MMAO method could be used to study more subjects than the twelve of the current study. Tasks other than walking and walking turn could also be examined, such as hopping, running, jumping or walking on sloped surfaces (similar to Procter, 1980). Examining other movement tasks would see if the current model would predict changes in the surface compression loading of the Ankle Complex due to changing task. The absence of such changes in the surface loading between the walking and walking turn tasks was an unexpected result and is a result that should be tested further.

It is also recommended that the current gait data be recollected for the walking trials since there appears to be a deviation of the subjects' gait pattern from their preferred pattern of normal walking. This deviation was exhibited in the EMG activity which, showed more antagonism than is commonly assumed to be present. The turning task should be reliable since this task was likely to show antagonism and since its kinematics were more demanding on the ankle complex. To the author's knowledge, there is no report of "normal" kinematics or EMG during a walking turn in the current literature with which these results can be compared.

By testing a wide range of subjects, the different muscle tension strategies employed by individuals in the normal population could be examined further. The prediction that individuals used differing strategies of muscle tensions to perform the same tasks was remarkable and perhaps the most important of this study. It would be very interesting to examine the range of strategies employed and perhaps question what mechanism was behind the choice of one over another.

Finally, it is recommended that the Muscle Model Assisted Optimisation method be used to solve for equilibrium about other joints. Since the method

requires surface EMG recordings from the muscle involved, some joints would not be suitable, such as the hip or the shoulder complex. The joints of the knee, elbow and wrist, however, could be modelled using the MMAO method. It would be of great interest to see whether individuals employed different muscle tension strategies at these joints, as was the case with the Ankle Complex.

9.2 CONCLUSIONS

A Muscle Model Assisted Optimisation Model (MMAO) was developed and was successfully applied to the biomechanics of the Ankle and Subtalar Joint during the stance phase of walking and turning. The Muscle Model was driven by surface EMG recorded from the muscles of the lower leg. The three-dimensional positions of the internal structures of the Ankle Complex were mapped using medical images.

The Ground Reaction Forces (GRF) and the Joint Angles for the tasks of walking and turning were very similar between subjects. The turning task introduced a large medially directed GRF component with a peak magnitude of 0.70×BW occurring in early stance phase.

Despite similar external loading, individuals employed *different muscle tension strategies* to produce equilibrium in the Ankle Complex. The Triceps Surae group of muscles produced the largest tensions. The maximum tension in the Achilles tendon during the walking task was 7.90×BW and during turning was 8.0×BW.

The Peroneus Brevis muscle was mostly involved in producing movement about the Subtalar Joint. The Peroneus Longus muscle often performed a more postural or stabilising role about the Subtalar Joint. There was a significant antagonistic activity between the Triceps Surae and the Dorsi-flexing muscle groups balancing moments about the Ankle Joint, and between the Triceps Surae and the Peroneal groups about the Subtalar Joint. This antagonism produced larger loading in the muscles and on the articular surfaces than those of previous Ankle Complex models.

Great variability was seen in the tension patterns of the ligaments of the Ankle Complex. The ligaments seemed to operate in an *all-or-nothing* manner, instead of providing a graded constraint of the joints. The maximum tension seen in any of the ligaments was 1.75×BW in the lateral group of ligaments of the Ankle Joint.

No difference in the compression loading of the articular surfaces of the Ankle Complex was seen between the tasks of walking and turning. The maximum surface compression in the Ankle Joint was 10.0×BW and in the Subtalar Joint was 8.0×BW.

It appeared that the subjects used a "guarded" or stiffer gait during the walking trials due perhaps to the awkwardness of the apparatus and the discomfort of a cold laboratory with a hard linoleum floor. This guarded gait manifested as a great deal of antagonism in the muscles of the ankle complex.

Alexander RMcN and Ker RF (1990). "The architecture of the leg muscles." in Winters JM and Woo SLY (eds.) Multiple muscle systems: Biomech. And Movem. Organisation. New York, Spring-Verlag pp. 568-577

Alexander RMcN and Vernon A (1975). "The dimensions of Knee and Ankle Muscles and the Forces they exert." J Human Mvmt Sci Vol. 1 pp. 115-123

An KN, Kwak BM, Chao EY and Morrey BF (1984). "Determination of muscle and joint forces: a new technique to solve the indeterminate problem." J Biomech Eng Vol. 106 pp. 364-367

An KN, Chao EY and Kaufman KR (1991). "Analysis of muscle and joint loads." Basic Orthop Biomech Vol. 10 pp. 1-50

Attarian DE, McCrackin HJ, DeVito DP, McElhaney JH and Garret WE. (1985) "Biomechanical characteristics of human ankle ligaments." Foot & Ankle Vol 6(2) pp. 54-58

Barnett CH, Napier JR (1952). "The axis of rotation at the ankle joint in man: Its influence upon the form of the talus and mobility of the fibula." Anat Vol. 86 (1) pp. 156

Bean JC, Chaffin DB, and Schultz, AB (1988). "Biomechanical model calculation of muscle contraction forces: double linear programming method." J Biomech Vol. 21 pp. 59-66

Brewster RC, Chao EY, and Stauffer RN (1974). "Force Analysis of the Ankle Joint during Stance Phase." Proc of the 27th ACEMB

Bogey RA, Perry J, Bontrager EL, Gronley JA (2000). "Comparison of across-subject EMG profiles using surface and multiple indwelling wire electrodes during gait." J Electromyo Kinesiol Vol. 10 pp. 255-259

Buchanan TS, Moniz, MJ, Dewald JPA and Rymer WZ (1993) " Estimation of muscle forces about the wrist joint during isometric tasks using an EMG coefficient method." J Biomech Vol. 26 (4-5) pp. 547-560

Bush AW (1992). Perturbation Methods for Engineers and Scientists. London, CRC Press pp. 248-298

Caldwell GE (1995). "Tendon elasticity and relative length: effects on the Hill two-component muscle model." J App Biomech Vol. 11 pp. 1-24

Cappozzo A, Catani F, Croce UD and Leardini A (1995). "Position and orientation in space of bones during movement: anatomical frame definition and determination." Clin Biomech Vol. 10 (4) pp. 171-178

Choi H and Vanderby R (1999). "Comparison of biomechanical human neck models: Muscle forces and spinal loads at C4/5 level." J App Biomech Vol. 15 (2) pp. 120-138

Cholewicki J, McGill SM, and Norman RW (1995). "Comparison of Muscle Forces and Joint Load from an optimization and EMG Assisted Lumbar spine model- towards a hybrid approach." J Biomech Vol. 28 (3) pp. 321-331

Cholewicki J and McGill SM (1994). "EMG Assisted Optimization- a Hybrid approach for estimating Muscle Forces in an Indeterminate Biomechanical Model." J Biomech Vol. 27 (10) pp. 1287-1289

Crago PE (1992). "Muscle input-output model: the static dependence of force on length, recruitment, and firing period." IEEE Trans BME Vol. 39 (8) pp. 871-874

Crowninshield RD (1978). "Use of optimisation techniques to predict muscle forces". J Biomech Vol. 100 pp. 88-92

Currier DP and Nelson RM (1992). Dynamics of Human Biologic Tissues. Philadelphia, FA Davis Co. pp. 1-23, 74-113.

Czerniecki JM (1988). "Foot and Ankle Biomechanics in Walking and Running." Am J Phys Med & Rehab Vol. 54 pp. 21-26

DeLuca CJ (1997). "The Use of Surface Electromyography in Biomechanics." J App Biomech Vol. 13 pp. 135-163

Durfee WK and Palmer KI (1994). "Estimation of force-activation, force-length and force-velocity properties in isolated, electrically stimulated muscle." IEEE Trans BME Vol. 41 (3) pp. 205-216

Edgerton VR, Roy RR, Gregor RJ and Rugg S (1986). "Morphology Basis of Skeletal Muscle Power Output." in Human Muscle Power. Champaign, IL, Human Kinetics Books pp. 43-64

Faulkner JA, Clatlin DR and McCully KK (1986). "Power Output of Fast and Slow Fibres from Human Skeletal Muscles." in Human Muscle Power. Champaign, IL Human Kinetics Books pp. 81-94

Fowler NK (1997). Biomechanics of the Rheumatoid Proximal Interphalageal Joint. PhD Thesis, Bioengineering Unit, University of Strathclyde, Glasgow, Scotland, UK

Garnett RAF, O'Donovan MJ, Stephens JA and Taylor A (1979). "Motor unit organisation of human medial gastrocnemius." J Physiol (London) Vol. 287 pp. 33-43

Glitsch U and Baumann W (1997). "The three-dimensional determination of internal loads in the lower extremity." J Biomech Vol. 30 (11-12) pp. 1123-1131

Goldspink G (1977). "Design of muscle in relation to locomotion." in Alexander RMcN and Goldspink G (1977). Mechanics and Energetic of Animal Locomotion. London, Chapman and Hall pp. 1-22

Gollnick PD, Sjodin B, Karlsson J, Jansson E and Saltin B (1974). "Human Soleus Muscle: a comparison of fiber composition and enzyme activity with other leg muscles." Pflugers Archiv Vol. 348 pp. 247-255

Gordon AM, Huxley AF and Julian FT (1966). "The variation in isometric tension With sarcomere length in vertebrate muscle fibers." J Physiol (Lond) Vol. 184 pp. 170-192 in Currier DP and Nelson RM (1992). Dynamics of Human Biologic Tissues. Philadelphia, FA Davis Co pp. 83

Green LS, Daub B, Houston ME, Thomson JA, Fraser I and Ranney D (1981). "Human vastus lateralis and gastrocnemius muscles. A comparative histochemical analysis." J Neurol Sci Vol. 52 pp. 200-201

Golub GH and Ortega JM (1992). Scientific Computing and Differential Equations. San Diego, CA, Academic Press, Ltd. pp. 187-193

Gosling JA, Harris FF, Humpherson JR, Whitmore I and Willan PLT (1993). Human Anatomy. 2nd ed. Hong Kong, Wolfe Co. pp 6.2-6.56

Happee R (1994). "Inverse dynamic optimisation including muscular dynamics, a new simulation method applied to goal directed movements." J Biomech Vol. 27 953-960

Happee R, and Van der Helm FT (1995). "The control of shoulder muscles during goal directed movements, an inverse dynamic analysis." J Biomech Vol. 28 pp. 1179-1191

Hatze H (1981). Myocybernetic control models of skeletal muscle. PhD Thesis University of South Africa, Pretoria

Hashimoto T and Inokuchi S (1997). "A kinematic study of ankle joint instability due to rupture of the lateral ligaments." Foot & Ankle Int Vol. 18 (11) pp. 729-734
Herzog W (1987a). "Considerations for predicting individual muscle forces in athletic movements". Int J Sport Biomech Vol. 3 pp. 128-141

Herzog W and Binding P (1993). "Co-contraction of pairs of antagonistic muscles: analytical solution for planar static nonlinear optimisation approaches." Math Biosci Vol. 118 pp. 83-95

Herzog W and Leonard TR (1991). "Validation of optimisation models that estimate the forces exerted by synergistic muscles." J Biomech Vol. 24 pp. 31-39

Hicks JH (1953). "Mechanics of the foot I: The joints" Anat Vol. 86 (1) pp. 345

Hill AV (1938). "The heat of shortening and the dynamic constants of muscle". Proc Royal Soc Vol. 126B pp. 136-195

Hodge WA, Carlson KL, Fijan RS, Burgess RG, Riley PO, Harris WH and Mann RW, (1989). "Contact pressures from an instrumented endoprosthesis". J Bone and Joint Surg Vol. 71-A (9) pp. 1378-1386

Hof AL and Van den Berg JW (1981a). "EMG to Force Processing I: An electrical analogue of the Hill Muscle Model". J Biomech Vol. 14 (11) pp. 747-758

Hof AL and Van den Berg JW (1981b). "EMG to Force Processing II: Estimation of Parameters of the Hill Muscle Model for the Human Triceps Surae by means of a Calfometer". J Biomech Vol. 14 (11) pp. 759-770

Hof AL and Van den Berg JW (1981c). "EMG to Force Processing III: Estimation of Model Parameters for the Human Triceps Surae Muscle and Assessment of the Accurcy by means of a Torque Plate". J Biomech Vol. 14 (11) pp. 771-785

Hof AL and Van den Berg JW (1981d). "EMG to Force Processing IV: Eccentric-Concentric Contractions on a Spring-Flywheel Set Up". J Biomech Vol. 14 (11) pp. 786-792

Houtz MS and Walsh FP (1959). "Electromyographic Analysis of the Function of the Muscles acting on the Ankle during Weight Bearing with Special Reference to the Triceps Surae." J Bone Joint Surg. Vol. 41A pp. 1469-1481

Huijing PA (1995). "Parameter interdependence and success of skeletal muscle modelling." Human Mvmt Sci Vol 14 pp. 443-486

Huson A (1961). Een Ontleedkundig-Functioneel Onderzoek van de Voetworte (An Anatomical and Functional Study of the Tarsal Joints). Drukkerij, Leiden. pp. 133-142

Huxley (1974). "Muscular contraction (review literature)." J Physiol (London) Vol. 243 pp. 1-43

Inman TV (1976). The Joints of the Ankle. Williams and Wilkins, Baltimore. pp. 19, 26-27, 31, 37, 70-73

Jacob HAC (1989). Biomechanics of the Forefoot. PhD Thesis, Bioengineering Unit, University of Strathclyde, Glasgow, Scotland, UK

Kaufman KR, An KN, Litchy W and Chao EYS (1991a). "Physiological prediction of muscle forces. I: Theoretical Formulation". Neuroscience Vol. 40 pp. 781-792

Kaufman KR, An KN, Litchy W and Chao EYS (1991b). "Physiological prediction of muscle forces. II: Application to isokinetic exercise". Neuroscience Vol. 40 pp. 793-804

Kin W and Voloshin AS (1995). "Role of Plantar Fascia in the Loading Bearing capacity of the Human Foot." J Biomech Vol. 28 (9) pp. 1025-1033

Kettlekamp DB and Jacobs AW (1972). "Tibiofemoral contact area- determination and implications." J Bone Joint Surg 54-A (2) pp. 349-356

King AI (1984). "A Review of Biomechanical Models." J Biomech Eng Vol. 106 pp. 97-105

Klein P, Mattys S, Rooze M (1996) "Moment Arm Length variations of selected muscles acting on Talocrural and Subtalar Joints during movement: an in vitro study." J Biomech Vol. 29 (1) pp. 21-30

Komi PV (1990). "Relevance of *In Vivo* Force Measurements to Human Biomechanics." J Biomech Vol. 23 (S1) pp. 23-34

Krylow AM and Sandercock TG (1997). "Dynamic Force Responses of Muscle involving Eccentric Contraction." J Biomech Vol. 30 (1) pp. 27-33

Kura H, Kitoaka H, Luo Z-P, An K-N (1998). "Measurement of surface contact area of the ankle joint." Clin Biomech Vol. 13 pp. 365-370

Leardini A, O'Connor JJ, Catani F and Giannini S (1999a). "A geometric model of the Human Ankle Joint." J Biomech Vol. 32 (6) pp. 585-591

Leardini A, O'Connor JJ, Catani F and Giannini S (1999b). "Kinematics of the Human Ankle Complex in passive flexion; a single degree of freedom system." J Biomech Vol. 32 (2) pp. 111-118

Lew WD and Lewis JL (1977). "An anthropometric scaling method with application to the knee joint." J Biomech Vol. 10 pp. 171-181

Lewis JL, Lew WD and Zimmerman JR (1980). "A nonhomogeneous anthropometric scaling method based on finite element principles." J Biomech Vol. 13 pp. 815-824

Lieber RL, Brown CG and Trestik CL (1992). "Model of muscle-tendon interactions during frog semitendonosis fixed-end contractions." J Biomech Vol. 25 pp. 421-428

Maganaris CN (2000). "In vivo measurement-based estimations of the moment arm in the human tibialis anterior muscle-tendon unit." J Biomech Vol. 33 pp. 375-379

Martini FH (1995). Fundamentals of Anatomy and Physiology. 3rd ed. Upper Saddle River, NJ, Prentice Hall pp. 246-253, 364-369

McComas AJ (1996). Skeletal Muscle. Form and Function. Leeds, Human Kinetics pp. 1-226

McGill SM and Norman RW (1986). "Partitioning of the L4-L5 dynamic moment Into disc, ligamentous and muscular components during lifting." Spine Vol. 11 pp. 666-678

McMahon TA (1984). Muscles, Reflexes and Locomotion. Princeton, NJ Princeton University Press pp. 3-26, 85-114, 189-233

Moore KL (1992). Clinically Oriented Anatomy. 3rd ed. Williams and Wilkins, Baltimore. pp. 373-500

Nigg BM, Skarvan G, Frank CB and Yeadon MR (1990). "Elongation and Forces of Ankle Ligaments in a Physiological Range of Motion." Foot & Ankle Vol. 11(1) pp. 30-40

Nisell R (1985). "Mechanics of the Knee. A study of joint and muscle load with clinical applications." Acta Orthop Scand Suppl., Vol. 216 pp. 1-42

Orfanidis SJ (1996). Introduction to Signal Processing. London, Prentice-Hall International (UK) Ltd. pp. 98-123, 388-461

Otten E (1988). "Concepts and models of functional architecture in skeletal muscle." Exercise Sport Sci Rev Vol. 16 pp. 89-139

Pankovich AM & Shivaram MS (1979). "Anatomical basis of variability in injuries of the medial malleolus and deltoid ligament: I. Anatomical Studies." Acta Orthop Scand Vol. 50 pp. 217

Pandy MG and Anderson FC (1999). "A dynamic optimization solution for one complete cycle of human gait." Proc of the 17th ISB Congress

Pandy MG, Zajac FE, Sim E and Levine WS (1990). "An optimal-control model for maximum-height human jumping." J Biomech Vol. 23 (12) pp. 1185-1198

Paul JP (1967). "Force transmitted by joints in the human body." Proc IMechE Vol. 181 Part 3J Paper 8

Perotto AO (1994). Anatomical Guide to the Electromyographer: Limbs and Truck. 3rd ed. Springfield, IL, Charles C Thomas Co pp. 142-171

Perry J (1983). "Anatomy and Biomechanics of the Hindfoot." Clin Orthop Rel Res No. 177 pp. 9-15

Press WH, Flannery BP, Teukolsky SA and Vetterling WT (1989). Numerical Recipes in Pascal. Cambridge, UK, Cambridge University Press pp. 351-365

Procter P (1980). Ankle Joint Biomechanics. PhD Thesis, Bioengineering Unit, University of Strathclyde, Glasgow, Scotland, UK

Procter P and Paul JP (1983). "Ankle Joint Biomechanics." J Biomech Vol. 15 pp. 627-634

Renstrom P, Wertz M, Incavo S, Pope M, Ostgaard HC, Arms S and Haugh L (1988). "Strain in the Lateral Ligaments of the Ankle." Foot & Ankle Vol. 9 (2) pp. 59-63

Sammarco GJ, Burstein AH, Frankel VH (1973). "Biomechanics of the ankle: A kinematic study." Orthop Clin North Am. Vol. 4 pp. 1-75

Sarrafian SK (1983). Anatomy of the Foot and Ankle: Descriptive, Topographical, Functional. J.B. Lippincott Company, Philadelphia. pp. 35-261, 375-426

Seireg A and Arvikar RJ (1973). "A mathematical model for evaluation of forces in lower extremities of the musculoskeletal system." J Biomech Vol. 6 pp. 313-326

Seireg A and Arvikar RJ (1975). "The prediction of muscular load-sharing and joint in the lower extremity during walking." J Biomech Vol. 8 pp. 89-102

Sharkey NA and Hamel AJ (1998). "A dynamic cadaver model of the stance phase of gait: performance characteristics and kinematic validation." Clin Biomech Vol. 13 (6) pp. 420-433

Sica REP and McComas AJ (1971). "Fast and Slow twitch units in a human muscle." J Neuro, Neurosurg, Psych Vol. 34 pp. 113-120

Sommer HJ (1982). "Three-dimensional osteometric scaling and normative modelling of skeletal segments." J Biomech Vol. 15 pp. 171-180

Sparto PJ, Parnianpour M, Marras M, Granata KP, Reinsel TE, and Simon S (1998). "Effect of electromyogram-force relationship and method of gain estimation on the prediction of an elecromyogram-driven model of spinal loading." Spine Vol. 23(4) pp. 423-429

Stauffer RN, Chao EY, and Brewster RC (1977). "Force and Motion Analysis of the Normal, Diseased and Prosthetic Ankle Joint." Clin Orthop Vol. 127 pp. 189-196

Thoma W, Scale D and Kurth A (1993). "Computerized analysis of the Kinematics of the Upper Ankle Joint." Zeitschrift fur Orthopadie und ihre Grenzgebiete Vol. 131 (1) pp. 14-17

Thordarson DB, Motamed S, Hedman T, Ebramzadeh E and Bakshian S (1997). "The effect of fibular malreduction on contact pressures in an ankle fracture malunion model." J Bone Joint Surg- Amer Vol. 79A (12) pp. 1809-1815

Tsirakos D, Baltzopoulos V and Bartlett R (1997). "Inverse Optimization: Functional and Physiological considerations related to the Force-sharing Problem." Crit Rev BME Vol. 25 (4-5) pp. 371-407

Udupa JK, Hirsch BE, Hillstrom HJ, Bauer GR and Kneeland JB (1999a). "Analysis of in vivo 3-D kinematics of the joints of the foot." IEEE Trans BME Vol. 45 (11) pp. 1387-1396

University of California (1953). "The Pattern of Muscle Activity in the Lower Extremity during Walking." Prosth Dev Res Proj Inst Engng Res U Calif Berkley Ser 11 Issue 25

Van Brocklin JD and Ellis DG (1965). "A study of the mechanical behaviour of toe extensor tendons under applied stress." Arch Phys Med Rehabil Vol. 46 pp. 369-370 in Currier DP and Nelson RM (1992). Dynamics of Human Biologic Tissues. Philadelphia, FA Davis Co pp. 13

Ward KA and Soames RW (1997). "Contact patterns of the tarsal joints." Clin Biomech Vol. 12 (7-8) pp. 496-507

Winters JM and Van der Helm FCT (1994). "A field-based musculoskeletal framework for studying human posture and manipulation in 3-D." Proc Symp on Modelling and Control of Biomed Sys, Intern Fed on Autom Control pp. 410-411

Van Zandwijk JP, Bobbert MF, Baan GC and Huijing PA (1990). "From twitch to tetanus: performance of excitation dynamics optimized for a twitch in predicting tetanic muscle forces." Biol Cybern Vol. 75 pp. 409-417

White DCS (1977). "Muscle Mechanics." in Alexander RMcN and Goldspink G (1977). Mechanics and Energetic of Animal Locomotion. London, Chapman and Hall pp. 23-56

White SC and Winter DA (1993). "Predicting muscle forces in gait from EMG signals and musculoskeletal kinematics." J EMG Kinesiol Vol. 2 (4) pp. 217-231

White SC, Yack HJ and Winter DA (1989). "A three-dimensional musculoskeletal model for gait analysis, anatomical variablility estimates." J Biomech Vol. 22 (8-9) pp. 885-893

Wickiewicz TL, Roy RR, Powell PL and Edgerton VR (1983). "Muscle Architecture of the Human Lower Limb." Clin Orthop Vol. 179 pp. 275-283

Wickiewicz TL, Roy RR, Powell PL, Perrine JJ and Edgerton VR (1984). "Muscle Architecture and force-velocity relationships in humans." J App Physiol Resp Env Ex Physiol Vol. 57 pp. 435-443

Wilkie DR (1950). "The relationship between force and velocity in human muscle." J Physiol Vol. 110 pp. 249-280

Winter DA (1990). Biomechanics and motor control of human movement. New York, John Wiley and Sons

Winters JM (1995). "How detailed should muscle models be to understand multi-joint movement co-ordination?". Human Mvmt Sci Vol. 14 pp. 401-442

Winters JM and Stark L (1985). "Analysis of fundamental human movement patterns through the use of in-depth anatagonistic muscle models." IEEE Trans BME-32 (10) pp. 826-839

Winters JM and Stark L (1987). "Muscle models: what is gained and what is lost by varying model complexity." Biol Cybern Vol. 55 pp. 403-420

Woltring (1986). "A FORTRAN package for generalised cross-validatory spline smoothing and differentiation." Adv in Eng Software Vol. 8 (2) pp. 104-106

Wynarsky GT and Greenwald AC (1983). "Mathematical Model of the Human Ankle Joint." J Biomech Vol. 16 pp. 241-252

Yamaguchi GT, Moran DW and Si J (1995). "A computationally efficient method for solving the redundant problem in biomechanics." J Biomech Vol. 28 (8) pp. 999-1005

Zajac FE (1992). "How musculotendon architecture and joint geometry affect the capacity of muscles to move and exert force on objects- a review with application to arm and forearm tendon transfer." J Hand Surg- Amer Vol. 17A (5) pp. 799-804

APPENDIX

	TiA	EDL	PeL	GaL	GaM	Sol	PeB	EHL	From
A	0.304	0.304	0.304	0.304	0.304	0.304	0.304	0.304	**4**
B	0.0527	0.0486	0.0258	0.0414	0.0276	0.0252	0.0234	0.0558	**4**
v_{max}[mm/s]	173.5	159.8	84.7	136.1	90.7	82.9	76.9	183.5	**4**
v_{trans}[mm/s]	8.48	7.82	4.14	6.66	4.44	4.05	3.76	8.9	**6**
PCSA [cm^2]	9.9	5.6	12.3	12.1	20.3	58.0	5.7	1.8	**2**
SF [N/ cm^2]	22.5	22.5	22.5	22.5	22.5	22.5	22.5	22.5	**1**
N_s*10^4	2.93	2.70	1.43	2.30	1.53	1.40	1.30	3.10	**2**
θ [°]	5	8	10	8	16	25	5	6	**2**
l_f [cm]	7.7	8.0	3.9	3.8	2.9	1.9	3.9	8.7	**2**
l_m [cm]	29.8	35.5	28.6	21.7	24.8	31.0	23	27.3	**2**
$l_{f[opt]}$[cm]	6.45	5.94	3.15	5.06	3.37	3.08	2.86	6.82	**2**
$v_{max[sarc]}*10^4$ [mm/s]	47	47	47	47	47	47	47	47	**4**
$l_{SE[rest]}$ [cm]	13.96	15.18	26.42	27.42	23.83	11.3	12.97	10.17	**2**
CSA_{SE}[cm^2]	0.206	0.134	0.189	0.585	0.585	0.585	0.13	0.091	**5**
$l_{m[opt]}$[mm]	437.63	506.84	550.18	491.20	486.30	421.30	359.72	374.69	**4**
fast/slow	48/52	70/30	60/40	51/49	45/55	20/80	60/40	70/30	**3**

Sources:
1 Faulkner, et al. (1986)
2 Wickiewicz, et al. (1983)
3 McComas (1996)
4 Wickiewicz, et al. (1984)
5 Procter (1980)
6 Jenkyn (original derivation)

Table A.1 Parameters defining the architecture of the eight muscle-tendons of the Muscle Model.

Subject	Body Mass [kg]	Height [m]	Age	Sex
A	53.5	1.63	23	F
B	76.0	1.88	25	M
C	78.0	1.68	25	M
D	67.5	1.82	26	M
E	67.0	1.79	29	M
F	53.0	1.64	26	F
G	74.5	1.88	40	M
H	65.0	1.62	25	F
I	57.5	1.66	22	F
J	52.0	1.68	29	F
K	56.0	1.70	30	F
L	64.0	1.79	24	M
Average	63.66	1.73	27	

Table A.2 Summary of Sex, Age, Body Mass and Height of the twelve subjects.

GRF Slow speed [units of BW]

Peak value plus timing of peak as fraction of stance phase in parentheses.

Subject	A-P		M-L		Vertical	
	Walk	Turn	Walk	Turn	Walk	Turn
A	0.26(0.10)	0.25(0.10)	-0.08(0.30)	-0.28(0.20)	1.11(0.78)	1.18(0.20)
B	0.19(0.21)	0.19(0.17)	-0.10(0.81)	-0.28(0.23)	1.10(0.80)	1.07(0.76)
C	0.21(0.11)	0.21(0.10)	-0.08(0.40)	-0.30(0.25)	1.09(0.80)	1.10(0.78)
D	0.20(0.15)	0.21(0.15)	-0.09(0.35)	-0.25(0.20)	1.10(0.81)	1.15(0.20)
E	0.16(0.16)	0.17(0.15)	-0.11(0.85)	-0.27(0.21)	1.08(0.81)	1.07(0.22)
F	0.27(0.12)	0.26(0.13)	-0.06(0.62)	-0.31(0.23)	1.10(0.78)	1.08(0.81)
G	0.25(0.12)	0.25(0.13)	-0.04(0.50)	-0.26(0.24)	1.10(0.78)	1.10(0.79)
H	0.22(0.22)	0.22(0.22)	-0.5(0.30)	-0.32(0.24)	1.11(0.72)	1.07(0.82)
I	0.17(0.16)	0.18(0.16)	-0.05(0.32)	-0.28(0.20)	1.10(0.80)	1.13(0.20)
J	0.21(0.18)	0.18(0.18)	-0.10(0.81)	-0.31(0.19)	1.08(0.79)	1.18(0.81)
K	0.18(0.20)	0.19(0.21)	-0.07(0.60)	-0.30(0.24)	1.09(0.82)	1.20(0.19)
L	0.21(0.22)	0.20(0.18)	-0.11(0.32)	-0.26(0.25)	1.10(0.81)	1.04(0.17)
Ave	0.21(0.18)	0.21(0.16)	-0.07(0.52)	-0.29(0.19)	1.10(0.79)	1.11(0.32)

Table A.3 Average magnitude and timing over three trials of the peaks in the Ground Reaction Force for all subjects at Slow Speed.

+ Posterior (A-P)/ Lateral (M-L)/ Upward (Vertical)
- Anterior (A-P)/ Medial (M-L)/ Downward (Vertical)

GRF Preferred speed [units of BW]

Peak value plus timing of peak as fraction of stance phase in parentheses.

Subject	A-P		M-L		Vertical	
	Walk	Turn	Walk	Turn	Walk	Turn
A	0.26(0.11)	0.26(0.10)	-0.15(0.81)	-0.38(0.20)	1.26(0.20)	1.30(0.20)
B	0.20(0.18)	0.20(0.20)	-0.15(0.81)	-0.43(0.20)	1.08(0.21)	1.28(0.20)
C	0.21(0.12)	0.22(0.10)	-0.18(0.80)	-0.40(0.18)	1.12(0.20)	1.31(0.20)
D	0.21(0.12)	0.21(0.11)	-0.12(0.78)	-0.41(0.20)	1.15(0.20)	1.27(0.18)
E	0.25(0.14)	0.26(0.16)	-0.15(0.81)	-0.37(0.21)	1.10(0.18)	1.25(0.19)
F	0.24(0.20)	0.23(0.21)	-0.13(0.83)	-0.38(0.17)	1.18(0.17)	1.28(0.20)
G	0.22(0.18)	0.18(0.17)	-0.12(0.82)	-0.40(0.19)	1.21(0.21)	1.27(0.21)
H	0.21(0.11)	0.21(0.10)	-0.12(0.79)	-0.41(0.22)	1.28(0.23)	1.26(0.20)
I	0.20(0.15)	0.21(0.17)	-0.13(0.75)	-0.42(0.20)	1.18(0.20)	1.20(0.21)
J	0.26(0.16)	0.26(0.18)	-0.14(0.81)	-0.39(0.21)	1.21(0.19)	1.21(0.18)
K	0.21(0.21)	0.21(0.20)	-0.15(0.83)	-0.37(0.18)	1.16(0.18)	1.30(0.19)
L	0.22(0.16)	0.21(0.15)	-0.10(0.79)	-0.36(0.20)	1.15(0.20)	1.27(0.20)
Ave	0.22(0.15)	0.22(0.15)	-0.14(0.80)	-0.39(0.20)	1.17(0.20)	1.27(0.20)

Table A.4 Average magnitude and timing over three trials of the peaks in the Ground Reaction Force for all subjects at Preferred Speed.

+ Posterior (A-P)/ Lateral (M-L)/ Upward (Vertical)
- Anterior (A-P)/ Medial (M-L)/ Downward (Vertical)

GRF Fast speed [units of BW]

Peak value plus timing of peak as fraction of stance phase in parentheses.

Subject	A-P		M-L		Vertical	
	Walk	Turn	Walk	Turn	Walk	Turn
A	0.41(0.11)	0.50(0.07)	-0.15(0.80)	-0.72(0.19)	1.42(0.20)	1.81(0.19)
B	0.32(0.20)	0.25(0.09)	-0.19(0.10)	-0.69(0.18)	1.42(0.22)	1.61(0.20)
C	0.40(0.20)	0.42(0.10)	-0.20(0.11)	-0.70(0.20)	1.40(0.20)	1.82(0.21)
D	0.38(0.18)	0.39(0.06)	-0.16(0.15)	-0.69(0.18)	1.45(0.25)	1.75(0.20)
E	0.31(0.12)	0.41(0.08)	-0.16(0.81)	-0.68(0.17)	1.42(0.19)	1.72(0.21)
F	0.37(0.15)	0.41(0.11)	-0.18(0.80)	-0.70(0.21)	1.43(0.21)	1.80(0.18)
G	0.41(0.20)	0.42(0.13)	-0.20(0.10)	-0.70(0.22)	1.42(0.20)	1.75(0.15)
H	0.37(0.22)	0.51(0.05)	-0.14(0.82)	-0.72(0.20)	1.45(0.24)	1.76(0.21)
I	0.36(0.18)	0.45(0.06)	-0.15(0.15)	-0.69(0.80)	1.40(0.23)	1.65(0.20)
J	0.40(0.17)	0.41(0.11)	-0.15(0.16)	-0.70(0.19)	1.39(0.24)	1.67(0.22)
K	0.39(0.21)	0.42(0.08)	-0.15(0.21)	-0.69(0.18)	1.40(0.21)	1.80(0.20)
L	0.32(0.19)	0.45(0.07)	-0.17(0.76)	-0.70(0.80)	1.41(0.19)	1.82(0.17)
Ave	0.37(0.18)	0.42(0.08)	-0.17(0.41)	-0.70(0.29)	1.42(0.22)	1.75(0.18)

Table A.5 Average magnitude and timing over three trials of the peaks in the Ground Reaction Force for all subjects at Fast Speed.

+ Posterior (A-P)/ Lateral (M-L)/ Upward (Vertical)
- Anterior (A-P)/ Medial (M-L)/ Downward (Vertical)

Joint Angles Slow speed [units of Degrees °]
Peak value plus timing of peak as fraction of stance phase in parentheses.

Subject	Ankle		Subtalar	
	Walk	Turn	Walk	Turn
A	8.9(0.79)	9.3(0.78)	-4.1(0.23)	1.8(0.21)
B	7.0(0.66)	8.9(0.60)	-4.8(0.31)	3.8(0.14)
C	8.2(0.80)	10.1(0.52)	-5.1(0.25)	4.1(0.20)
D	7.8(0.50)	9.1(0.61)	-6.0(0.26)	3.7(0.15)
E	7.6(0.62)	8.1(0.92)	-3.2(0.36)	1.1(0.17)
F	7.7(0.65)	6.2(0.75)	-9.6(0.15)	2.9(0.18)
G	8.1(0.71)	9.1(0.60)	-5.0(0.31)	3.2(0.21)
H	8.2(0.66)	9.0(0.79)	-6.0(0.30)	0.8(0.25)
I	8.7(0.90)	8.5(0.61)	-4.1(0.21)	1.9(0.17)
J	9.0(0.51)	8.6(0.80)	-4.0(0.26)	4.0(0.18)
K	7.5(0.62)	7.2(0.77)	-6.0(0.32)	3.1(0.33)
L	6.0(0.67)	6.5(0.62)	-3.0(0.15)	0.7(0.12)
Ave	7.9(0.67)	8.4(0.70)	-4.7(0.24)	2.6(0.19)

Table A.6 Average magnitude and timing over three trials of the peaks in the Joint Angles for all subjects at Slow Speed.

+ Dorsi-flexing (Ankle)/ Inverting (Subtalar)
- Plantar-flexing (Ankle)/ Everting (Subtalar)

Joint Angles Preferred speed [units of Degrees °]
Peak value plus timing of peak as fraction of stance phase in parentheses.

Subject	Ankle		Subtalar	
	Walk	Turn	Walk	Turn
A	8.58(0.81)	8.3(0.64)	6.8(1.0)	2.1(0.20)
B	7.1(0.69)	7.0(0.65)	6.1(1.0)	3.0(0.20)
C	9.0(0.50)	8.1(0.61)	6.7(1.0)	1.5(0.20)
D	8.2(0.72)	8.7(0.80)	6.0(1.0)	2.1(0.15)
E	7.0(0.81)	9.7(0.78)	9.1(1.0)	2.6(0.21)
F	7.3(0.79)	7.0(0.61)	8.1(1.0)	2.1(0.20)
G	8.6(0.63)	6.1(0.67)	8.0(1.0)	3.1(0.25)
H	7.3(0.71)	6.7(0.70)	6.2(1.0)	3.0(0.20)
I	6.1(0.83)	7.5(0.75)	6.1(1.0)	1.4(0.17)
J	8.6(0.65)	8.7(0.74)	8.0(1.0)	1.3(0.31)
K	7.3(0.80)	6.1(0.82)	7.2(1.0)	2.0(0.23)
L	6.2(0.52)	6.0(0.60)	6.1(1.0)	3.0(0.25)
Ave	7.6(0.71)	7.5(0.70)	7.0(1.0)	2.3(0.21)

Table A.7 Average magnitude and timing over three trials of the peaks in the Joint Angles for all subjects at Preferred Speed.

+ Dorsi-flexing (Ankle)/ Inverting (Subtalar)
- Plantar-flexing (Ankle)/ Everting (Subtalar)

Joint Angles Fast speed [units of Degrees °]
Peak value plus timing of peak as fraction of stance phase in parentheses.

Subject	Ankle		Subtalar	
	Walk	Turn	Walk	Turn
A	8.2(0.70)	8.2(0.81)	7.1(1.0)	3.8(0.20)
B	7.1(0.82)	7.0(0.82)	7.0(1.0)	2.1(0.20)
C	8.0(0.75)	8.3(0.75)	8.0(1.0)	2.4(0.21)
D	7.6(0.80)	8.0(0.79)	7.6(1.0)	2.0(0.20)
E	6.5(0.78)	6.1(0.81)	6.9(1.0)	3.1(0.20)
F	7.0(0.62)	6.9(0.85)	6.7(1.0)	1.6(0.18)
G	7.1(0.69)	7.8(0.80)	8.1(1.0)	1.8(0.21)
H	8.3(0.83)	7.1(0.80)	9.0(1.0)	3.1(0.21)
I	6.9(0.71)	7.0(0.78)	8.2(1.0)	3.5(0.32)
J	6.5(0.61)	6.2(0.61)	8.4(1.0)	2.4(0.15)
K	8.5(0.70)	(8.6)0.73	7.5(1.0)	2.0(0.21)
L	7.3(0.71)	6.0(0.81)	6.9(1.0)	2.3(0.18)
Ave	7.4(0.73)	7.3(0.78)	7.6(1.0)	2.5(0.21)

Table A.8 Average magnitude and timing over three trials of the peaks in the Joint Angles for all subjects at Fast Speed.

+ Dorsi-flexing (Ankle)/ Inverting (Subtalar)
- Plantar-flexing (Ankle)/ Everting (Subtalar)

External Joint Axis Moments Slow speed [units of BW-m or N-m/N]
Peak value plus timing of peak as fraction of stance phase in parentheses.

Subject	Ankle		Subtalar	
	Walk	Turn	Walk	Turn
A	0.140(0.77)	0.143(0.75)	0.030(0.81)	0.020(0.85)
B	0.113(0.80)	0.111(0.80)	0.040(0.80)	0.030(0.82)
C	0.120(0.80)	0.121(0.80)	0.021(0.80)	0.020(0.80)
D	0.131(0.78)	0.131(0.78)	0.033(0.81)	0.020(0.76)
E	0.118(0.75)	0.110(0.81)	0.030(0.78)	0.035(0.81)
F	0.120(0.82)	0.150(0.83)	0.036(0.80)	0.045(0.85)
G	0.125(0.71)	0.141(0.74)	0.049(0.81)	0.042(0.80)
H	0.130(0.80)	0.132(0.82)	0.021(0.76)	0.020(0.81)
I	0.131(0.81)	0.120(0.81)	0.030(0.85)	0.040(0.77)
J	0.140(0.79)	0.124(0.76)	0.023(0.83)	0.046(0.078)
K	0.121(0.85)	0.119(0.75)	0.022(0.80)	0.030(0.80)
L	0.110(0.81)	0.120(0.85)	0.021(0.81)	0.041(0.81)
Ave	0.125(0.79)	0.126(0.79)	0.028(0.81)	0.034(0.80)

Table A.9 Average magnitude and timing over three trials of the peaks in the External Joint Axis Moments for all subjects at Slow Speed.

+ Dorsi-flexing (Ankle)/ Inverting (Subtalar)
- Plantar-flexing (Ankle)/ Everting (Subtalar)

External Joint Axis Moments Preferred speed [units of BW-m or N-m/N]
Peak value plus timing of peak as fraction of stance phase in parentheses.

Subject	Ankle		Subtalar	
	Walk	Turn	Walk	Turn
A	0.140(0.79)	0.140(0.80)	0.023(0.87)	0.040(0.83)
B	0.100(0.78)	0.116(0.63)	0.037(0.81)	0.052(0.80)
C	0.120(0.80)	0.136(0.78)	0.021(0.80)	0.051(0.80)
D	0.131(0.81)	0.121(0.80)	0.026(0.78)	0.037(0.78)
E	0.140(0.76)	0.138(0.61)	0.035(0.80)	0.026(0.81)
F	0.136(0.75)	0.115(0.71)	0.040(0.80)	0.041(0.81)
G	0.128(0.85)	0.121(0.78)	0.022(0.76)	0.040(0.76)
H	0.110(0.83)	0.136(0.82)	0.030(0.87)	0.032(0.78)
I	0.108(0.76)	0.140(0.80)	0.033(0.81)	0.025(0.81)
J	0.139(0.80)	0.142(0.81)	0.028(0.80)	0.051(0.72)
K	0.126(0.81)	0.120(0.76)	0.041(0.85)	0.042(0.82)
L	0.113(0.87)	0.110(0.81)	0.030(0.79)	0.040(0.80)
Ave	0.124(0.80)	0.128(0.76)	0.031(0.81)	0.040(0.79)

Table A.10 Average magnitude and timing over three trials of the peaks in the External Joint Axis Moments for all subjects at Preferred Speed.

+ Dorsi-flexing (Ankle)/ Inverting (Subtalar)
- Plantar-flexing (Ankle)/ Everting (Subtalar)

External Joint Axis Moments Fast speed [units of BW-m or N-m/N]
Peak value plus timing of peak as fraction of stance phase in parentheses.

Subject	Ankle		Subtalar	
	Walk	Turn	Walk	Turn
A	0.130(0.79)	0.120(0.80)	0.030(0.86)	0.040(0.83)
B	0.110(0.78)	0.117(0.81)	0.047(0.84)	0.060(0.82)
C	0.130(0.81)	0.130(0.80)	0.031(0.89)	0.061(0.80)
D	0.126(0.80)	0.121(0.81)	0.036(0.81)	0.053(0.76)
E	0.121(0.85)	0.108(0.76)	0.041(0.76)	0.047(0.77)
F	0.118(0.70)	0.115(0.77)	0.029(0.77)	0.052(0.80)
G	0.132(0.76)	0.120(0.83)	0.043(0.80)	0.048(0.85)
H	0.138(0.80)	0.136(0.85)	0.040(0.81)	0.060(0.86)
I	0.119(0.80)	0.120(0.80)	0.037(0.85)	0.057(0.87)
J	0.141(0.83)	0.134(0.76)	0.034(0.80)	0.056(0.77)
K	0.138(0.76)	0.113(0.79)	0.030(0.76)	0.045(0.79)
L	0.120(0.80)	0.110(0.80)	0.027(0.72)	0.041(0.80)
Ave	0.127(0.79)	0.120(0.80)	0.035(0.82)	0.052(0.81)

Table A.11 Average magnitude and timing over three trials of the peaks in the External Joint Axis Moments for all subjects at Fast Speed.

+ Dorsi-flexing (Ankle)/ Inverting (Subtalar)
- Plantar-flexing (Ankle)/ Everting (Subtalar)

Muscle Tensions (Triceps Surae) Preferred speed [units of BW]
Peak value plus timing of peak as fraction of stance phase in parentheses.

Subject	GaL		GaM		Sol	
	Walk	Turn	Walk	Turn	Walk	Turn
A	1.2(0.23)	1.0(0.81)	1.9(0.23)	1.6(0.81)	3.6(0.80)	4.9(0.80)
B*	0.7(0.78)	0.4(0.75)	0.8(0.74)	1.2(0.72)	6.0(0.72)	7.0(0.70)
C	1.1(0.25)	1.2(0.80)	2.1(0.25)	1.7(0.81)	4.0(0.81)	5.0(0.80)
D	1.3(0.20)	1.4(0.75)	1.9(0.25)	1.8(0.82)	3.7(0.83)	4.0(0.81)
E*	0.5(0.75)	0.7(0.75)	1.1(0.75)	1.1(0.75)	5.6(0.75)	6.3(0.70)
F*	0.9(0.80)	1.1(0.75)	1.6(0.23)	1.0(0.73)	6.2(0.81)	7.1(0.73)
G	1.4(0.26)	0.7(0.83)	2.0(0.20)	1.2(0.84)	4.0(0.84)	4.7(0.83)
H	1.0(0.26)	1.0(0.78)	1.6(0.27)	1.5(0.75)	4.1(0.80)	5.2(0.81)
I*	1.1(0.73)	1.0(0.71)	0.9(0.70)	0.8(0.74)	5.8(0.73)	6.7(0.74)
J	1.3(0.25)	1.2(0.80)	2.0(0.20)	2.1(0.81)	4.1(0.81)	4.6(0.75)
K*	0.3(0.78)	0.3(0.77)	0.6(0.76)	2.1(0.79)	5.3(0.78)	5.1(0.80)
L	1.1(0.20)	1.3(0.81)	1.7(0.21)	1.2(0.81)	4.0(0.81)	3.9(0.75)
Ave	1.2(0.24)	1.1(0.79)	1.9(0.23)	1.6(0.81)	3.9(0.81)	4.6(0.79)
Ave*	0.70(0.77)	0.7(0.75)	1.0(0.64)	1.2(0.75)	5.8(0.76)	6.4(0.73)

Table A.12 Average magnitude and timing over three trials of the peaks in the Triceps Surae group of Muscle Tensions for all subjects at Preferred Speed.

*separate averages were taken of the peaks and timings for the two muscle tension strategies

Muscle Tensions (Peroneals) Preferred speed [units of BW]
Peak value plus timing of peak as fraction of stance phase in parentheses.

Subject	PeL		PeB	
	Walk	Turn	Walk	Turn
A	0.6(0.15)	0.6(0.16)	1.0(0.78)	2.3(0.80)
B*	0.7(0.78)	1.2(0.80)	1.5(0.70)	2.3(0.82)
C	0.6(0.15)	0.6(0.15)	1.1(0.77)	2.2(0.75)
D	0.55(0.77)	0.65(0.15)	1.0(0.80)	2.3(0.80)
E*	0.6(0.75)	1.2(0.79)	1.5(0.75)	2.4(0.80)
F*	0.7(0.80)	1.4(0.80)	1.6(0.70)	2.2(0.79)
G	0.6(0.13)	0.5(0.20)	0.95(0.80)	2.5(0.78)
H	0.5(0.14)	0.4(0.10)	1.0(0.75)	1.8(0.77)
I*	0.8(0.78)	1.1(0.80)	1.6(0.73)	2.3(0.80)
J	0.5(0.16)	0.55(0.15)	0.95(0.78)	1.6(0.76)
K*	0.6(0.76)	1.1(0.77)	1.5(0.70)	2.4(0.78)
L	0.4(0.17)	0.45(0.16)	1.0(0.77)	2.1(0.80)
Ave	0.5(0.15)	0.54(0.15)	1.0(0.78)	2.1(0.78)
Ave*	0.7(0.77)	1.2(0.79)	1.5(0.72)	2.3(0.80)

Table A.13 Average magnitude and timing over three trials of the peaks in the Peroneal group of Muscle Tensions for all subjects at Preferred Speed.

*separate averages were taken of the peaks and timings for the two muscle tension strategies

Muscle Tensions (Dorsi-flexors) Preferred speed [units of BW]
Peak value plus timing of peak as fraction of stance phase in parentheses.

Subject	TiA		EDL		EHL	
	Walk	Turn	Walk	Turn	Walk	Turn
A	1.0(0.13)	1.0(0.18)	0.54(0.36)	0.50(0.3)	0.50(0.30)	0.30(0.35)
B*	1.30(0.15)	1.20(0.09)	0.52(0.53)	0.20(0.47)	0.51(0.86)	0.01(0.07)
C	0.95(0.16)	1.01(0.20)	0.55(0.35)	0.60(0.40)	0.45(0.31)	0.30(0.35)
D	1.0(0.14)	1.1(0.18)	0.54(0.41)	0.70(0.38)	0.51(0.35)	0.28(0.37)
E*	1.0(0.14)	1.15(0.10)	0.51(0.51)	0.50(0.48)	0.51(0.85)	0.01(0.06)
F*	1.15(0.15)	1.20(0.11)	0.52(0.53)	0.56(0.50)	0.51(0.86)	0.01(0.10)
G	0.93(0.15)	1.0(0.19)	0.54(0.30)	0.35(0.31)	0.55(0.30)	0.29(0.40)
H	0.97(0.17)	0.98(0.17)	0.53(0.32)	0.41(0.33)	0.60(0.30)	0.31(0.35)
I*	1.21(0.14)	1.20(0.09)	0.51(0.53)	0.51(0.49)	0.52(0.85)	0.01(0.08)
J	1.11(0.18)	1.01(0.17)	0.55(0.34)	0.51(0.38)	0.51(0.32)	0.32(0.32)
K*	1.08(0.18)	1.30(0.12)	0.58(0.64)	0.58(0.50)	0.51(0.84)	0.01(0.07)
L	0.89(0.14)	1.1(0.15)	0.53(0.35)	0.53(0.41)	0.56(0.21)	0.30(0.33)
Ave	0.96(0.15)	1.03(0.18)	0.54(0.35)	0.53(0.36)	0.53(0.30)	0.30(0.35)
Ave*	1.11(0.15)	1.21(0.10)	0.53(0.53)	0.55(0.49)	0.51(0.85)	0.02(0.08)

Table A.14 Average magnitude and timing over three trials of the peaks in the Dorsi-flexors group of Muscle Tensions for all subjects at Preferred Speed.

*separate averages were taken of the peaks and timings for the two muscle tension strategies

Ligament Tensions (Lateral) Preferred speed [units of BW]
Peak value plus timing of peak as fraction of stance phase in parentheses.

Subject	L-Ant		L-Mid		L-Post	
	Walk	Turn	Walk	Turn	Walk	Turn
A	1.40(0.38)	1.65(0.80)	1.45(0.39)	1.10(0.30)	1.10(0.60)	1.50(0.40)
B	1.70(0.37)	1.20(0.80)	1.65(0.35)	1.50(0.40)	1.30(0.80)	1.50(0.40)
C	1.60(0.20)	1.63(0.80)	1.41(0.35)	1.20(0.35)	1.21(0.50)	1.45(0.40)
D	1.27(0.45)	1.45(0.45)	1.35(0.40)	1.31(0.40)	1.00(0.65)	1.51(0.80)
E	1.70(0.40)	1.75(0.91)	1.18(0.38)	1.45(0.38)	1.35(0.85)	1.32(0.75)
F	1.00(0.35)	1.15(0.81)	1.67(0.30)	1.10(0.39)	1.32(0.80)	1.40(0.41)
G	1.32(0.15)	1.42(0.83)	1.71(0.32)	1.40(0.35)	1.40(0.71)	1.42(0.30)
H	1.41(0.10)	1.51(0.32)	1.32(0.35)	1.37(0.32)	1.07(0.82)	1.30(0.35)
I	1.40(0.45)	1.49(0.85)	1.41(0.36)	1.27(0.36)	1.15(0.65)	1.47(0.36)
J	1.45(0.15)	1.31(0.89)	1.58(0.35)	1.05(0.35)	1.23(0.51)	1.21(0.71)
K	1.30(0.32)	1.40(0.87)	1.18(0.41)	1.07(0.32)	1.34(0.60)	1.06(0.45)
L	1.75(0.41)	1.72(0.91)	1.32(0.37)	1.42(0.35)	1.20(0.78)	1.41(0.40)
Ave	1.44(0.31)	1.47(0.77)	1.43(0.36)	1.27(0.36)	1.22(0.69)	1.38(0.48)

Table A.15 Average magnitude and timing over three trials of the peaks in the Lateral group of Ligament Tensions for all subjects at Preferred Speed.

Ligament Tensions (Medial) Preferred speed [units of BW]
Peak value plus timing of peak as fraction of stance phase in parentheses.

Subject	M-Ant		M-Mid		M-Post	
	Walk	Turn	Walk	Turn	Walk	Turn
A	1.20(0.30)	1.20(0.37)	0.70(0.0)	0.80(0.0)	0.60(0.70)	0.70(0.65)
B	1.30(0.40)	1.20(0.30)	0.65(0.08)	0.80(0.10)	0.65(0.75)	0.60(0.70)
C	1.00(0.35)	1.15(0.50)	0.50(0.07)	0.90(0.0)	0.61(0.75)	0.62(0.70)
D	1.40(0.50)	1.05(0.51)	0.60(0.0)	0.71(0.0)	0.58(0.81)	0.59(0.62)
E	1.15(0.42)	1.21(0.35)	0.61(0.01)	0.62(0.04)	0.50(0.70)	0.68(0.74)
F	1.20(0.51)	1.31(0.30)	0.70(0.09)	0.65(0.0)	0.60(0.70)	0.61(0.71)
G	1.31(0.30)	1.16(0.37)	0.65(0.0)	0.80(0.0)	0.62(0.70)	0.71(0.75)
H	1.25(0.32)	1.20(0.41)	0.50(0.10)	0.76(0.0)	0.64(0.74)	0.60(0.80)
I	1.26(0.41)	1.31(0.50)	0.53(0.05)	0.71(0.10)	0.51(0.76)	0.55(0.76)
J	1.30(0.40)	1.26(0.30)	0.61(0.0)	0.80(0.08)	0.40(0.80)	0.61(0.75)
K	1.07(0.32)	1.10(0.36)	0.52(0.0)	0.60(0.10)	0.59(0.75)	0.52(0.80)
L	1.41(0.38)	1.31(0.41)	0.50(0.04)	0.55(0.0)	0.62(0.75)	0.60(0.82)
Ave	1.24(0.38)	1.21(0.39)	0.59(0.04)	0.73(0.04)	0.58(0.73)	0.62(0.73)

Table A.16 Average magnitude and timing over three trials of the peaks in the Medial group of Ligament Tensions for all subjects at Preferred Speed.

Ligament Tensions (M-Nav + Outer Subtalar) Preferred speed [units of BW]
Peak value plus timing of peak as fraction of stance phase in parentheses.

Subject	M-Nav		M-Tc		P-Tc	
	Walk	Turn	Walk	Turn	Walk	Turn
A	1.20(0.65)	1.30(0.40)	1.00(0.21)	0.90(0.20)	0.80(0.30)	0.80(0.30)
B	1.40(0.40)	1.30(0.35)	1.30(0.26)	1.30(0.30)	0.80(0.20)	0.70(0.80)
C	1.30(0.50)	1.21(0.35)	1.05(0.25)	0.95(0.25)	0.81(0.20)	0.75(0.42)
D	1.32(0.41)	1.29(0.55)	1.21(0.30)	1.06(0.30)	0.76(0.21)	0.74(0.35)
E	1.40(0.45)	1.34(0.41)	1.25(0.25)	1.29(0.21)	0.75(0.31)	0.69(0.34)
F	1.25(0.60)	1.06(0.30)	1.30(0.25)	1.17(0.25)	0.81(0.25)	0.75(0.85)
G	1.21(0.62)	1.27(0.34)	1.21(0.20)	1.20(0.31)	0.69(0.30)	0.80(0.79)
H	1.40(0.55)	1.32(0.37)	1.07(0.22)	1.02(0.25)	0.65(0.21)	0.91(0.30)
I	1.35(0.32)	1.19(0.41)	1.16(0.28)	0.97(0.26)	0.73(0.26)	0.70(0.81)
J	1.31(0.44)	1.28(0.40)	1.25(0.30)	1.25(0.26)	0.78(0.31)	0.63(0.35)
K	1.27(0.45)	1.25(0.50)	1.17(0.21)	1.16(0.21)	0.75(0.38)	0.71(0.34)
L	1.32(0.54)	1.31(0.30)	1.05(0.27)	1.02(0.20)	0.80(0.20)	0.73(0.67)
Ave	1.31(0.49)	1.26(0.39)	1.17(0.25)	1.11(0.25)	0.76(0.26)	0.74(0.53)

Table A.17 Average magnitude and timing over three trials of the peaks in the M-Nav plus Outer Subtalar group of Ligament Tensions for all subjects at Preferred Speed.

Ligament Tensions (Inner Subtalar) Preferred speed [units of BW]
Peak value plus timing of peak as fraction of stance phase in parentheses.

Subject	Cerv		M-IO		L-IO	
	Walk	Turn	Walk	Turn	Walk	Turn
A	0.71(0.20)	0.60(0.15)	0.70(0.30)	0.70(0.35)	1.20(0.80)	1.30(0.90)
B	0.73(0.25)	0.80(0.30)	0.90(0.18)	0.90(0.22)	1.40(0.90)	1.50(0.85)
C	0.65(0.25)	0.71(0.21)	0.80(0.18)	0.45(0.30)	1.31(0.85)	1.49(0.86)
D	0.68(0.23)	0.80(0.23)	0.91(0.31)	0.91(0.22)	1.42(0.91)	1.50(0.87)
E	0.75(0.35)	0.83(0.18)	0.73(0.28)	0.81(0.35)	1.06(0.85)	1.32(0.90)
F	0.52(0.30)	0.61(0.15)	0.62(0.32)	0.75(0.40)	1.21(0.85)	1.37(0.75)
G	0.71(0.32)	0.65(0.31)	0.71(0.25)	0.82(0.26)	1.38(0.87)	1.42(0.79)
H	0.77(0.20)	0.71(0.28)	0.75(0.20)	0.60(0.38)	1.35(0.80)	1.50(0.80)
I	0.68(0.21)	0.73(0.25)	0.81(0.18)	0.71(0.15)	1.30(0.89)	1.31(0.81)
J	0.52(0.24)	0.80(0.25)	0.84(0.15)	0.76(0.17)	1.32(0.90)	1.28(0.90)
K	0.79(0.27)	0.71(0.10)	0.72(0.19)	0.83(0.21)	1.41(0.91)	1.27(0.87)
L	0.57(0.32)	0.63(0.32)	0.63(0.25)	0.91(0.28)	1.28(0.87)	1.30(0.78)
Ave	0.67(0.26)	0.72(0.23)	0.76(0.23)	0.76(0.27)	1.30(0.87)	1.38(0.84)

Table A.18 Average magnitude and timing over three trials of the peaks in the Inner Subtalar group of Ligament Tensions for all subjects at Preferred Speed.

Surface Compressions (Medial Ankle) Preferred speed [units of BW]
Peak value plus timing of peak as fraction of stance phase in parentheses.

Subject	M-Mall		M-Mort	
	Walk	Turn	Walk	Turn
A	1.50(0.85)	1.40(0.80)	5.81(0.65)	6.01(0.67)
B	1.00(0.90)	1.00(0.95)	5.86(0.60)	5.82(0.60)
C	0.60(1.0)	0.50(0.98)	5.83(0.80)	5.95(0.77)
D	0.75(1.0)	1.15(0.84)	5.71(0.80)	6.07(0.78)
E	1.05(0.95)	1.23(0.96)	5.62(0.65)	6.00(0.67)
F	1.37(0.93)	1.01(0.82)	5.81(0.77)	5.85(0.72)
G	1.42(0.84)	0.71(0.98)	5.52(0.80)	5.91(0.75)
H	1.09(1.0)	0.91(0.81)	5.31(0.61)	5.91(0.81)
I	0.85(0.95)	1.36(0.85)	5.87(0.63)	5.73(0.61)
J	0.96(0.95)	1.41(0.92)	5.42(0.77)	5.52(0.67)
K	1.42(0.88)	0.87(0.92)	5.72(0.77)	5.95(0.75)
L	1.30(0.87)	0.61(0.94)	5.50(0.82)	6.05(0.82)
Ave	1.11(0.93)	1.01(0.90)	5.67(0.72)	5.90(0.72)

Table A.19 Average magnitude and timing over three trials of the peaks in the Medial Ankle Surface Compressions for all subjects at Preferred Speed.

Surface Compressions (Lateral Ankle) Preferred speed [units of BW]
Peak value plus timing of peak as fraction of stance phase in parentheses.

Subject	L-Mort		L-Mall	
	Walk	Turn	Walk	Turn
A	6.00(0.57)	6.10(0.60)	2.10(0.66)	2.00(0.68)
B	6.10(0.73)	6.10(0.75)	2.00(0.73)	2.00(0.74)
C	6.00(0.70)	6.00(0.72)	2.00(0.70)	2.10(0.71)
D	5.81(0.70)	5.90(0.75)	1.95(0.70)	1.95(0.73)
E	5.90(0.61)	5.95(0.70)	2.06(0.76)	2.05(0.70)
F	6.05(0.58)	6.10(0.65)	2.15(0.75)	2.02(0.67)
G	6.10(0.80)	6.11(0.62)	2.06(0.62)	2.07(0.74)
H	6.06(0.76)	6.02(0.80)	2.00(0.67)	1.95(0.77)
I	6.00(0.75)	5.96(0.78)	1.90(0.73)	1.98(0.70)
J	5.96(0.62)	5.90(0.69)	1.97(0.78)	1.85(0.73)
K	5.82(0.70)	5.80(0.67)	1.94(0.77)	1.87(0.65)
L	5.99(0.69)	5.95(0.75)	2.06(0.72)	2.07(0.69)
Ave	5.98(0.68)	5.99(0.71)	2.02(0.72)	1.99(0.71)

Table A.20 Average magnitude and timing over three trials of the peaks in the Lateral Ankle Surface Compressions for all subjects at Preferred Speed.

Surface Compressions (Subtalar) Preferred speed [units of BW]
Peak value plus timing of peak as fraction of stance phase in parentheses.

Subject	Post		Mid		Socket	
	Walk	Turn	Walk	Turn	Walk	Turn
A	4.92(0.30)	4.98(0.78)	1.47(0.78)	1.35(0.80)	4.40(0.20)	4.54(0.20)
B	5.00(0.80)	5.01(0.75)	1.43(0.78)	1.40(0.80)	4.30(0.10)	4.50(0.13)
C	4.63(0.75)	4.50(0.80)	1.41(0.78)	1.43(0.82)	4.80(0.08)	4.92(0.12)
D	5.02(0.80)	5.04(0.81)	1.02(0.75)	1.07(0.75)	4.65(0.20)	4.81(0.15)
E	4.95(0.75)	4.62(0.75)	0.91(0.76)	1.11(0.77)	4.42(0.21)	4.72(0.16)
F	4.71(0.76)	4.81(0.76)	1.47(0.80)	1.50(0.81)	4.61(0.11)	4.51(0.16)
G	4.87(0.80)	4.97(0.61)	1.53(0.74)	1.30(0.80)	4.80(0.17)	4.90(0.21)
H	4.62(0.70)	4.71(0.79)	1.12(0.70)	1.18(0.81)	4.71(0.21)	4.67(0.12)
I	5.08(0.72)	5.18(0.81)	1.21(0.78)	1.28(0.70)	4.60(0.02)	4.74(0.21)
J	5.00(0.78)	4.90(0.80)	1.28(0.80)	1.33(0.75)	4.51(0.11)	4.81(0.20)
K	4.82(0.82)	4.81(0.81)	1.02(0.75)	1.12(0.76)	4.40(0.02)	4.90(0.12)
L	4.71(0.81)	4.77(0.89)	1.40(0.75)	1.31(0.80)	4.57(0.27)	4.60(0.14)
Ave	4.86(0.77)	4.86(0.78)	1.26(0.76)	1.28(0.78)	4.56(0.4)	4.71(0.16)

Table A.21 Average magnitude and timing over three trials of the peaks in the Subtalar Surface Compression for all subjects at Preferred Speed.

Surface Compressions Resultants Preferred speed [units of BW]
Peak value plus timing of peak as fraction of stance phase in parentheses.

Subject	Ankle		Subtalar	
	Walk	Turn	Walk	Turn
A	9.00(0.67)	10.10(0.60)	8.00(0.76)	9.00(0.78)
B	8.00(0.83)	9.70(0.75)	8.00(0.83)	9.00(0.84)
C	7.90(0.80)	9.80(0.72)	7.90(0.80)	9.10(0.81)
D	8.81(0.80)	9.90(0.75)	7.95(0.80)	8.95(0.83)
E	7.90(0.71)	8.95(0.70)	7.06(0.86)	9.05(0.80)
F	9.00(0.68)	10.00(0.65)	7.15(0.85)	9.02(0.77)
G	8.10(0.90)	10.11(0.62)	8.06(0.72)	9.07(0.84)
H	9.06(0.86)	9.02(0.80)	8.00(0.77)	8.95(0.87)
I	9.00(0.85)	8.96(0.78)	7.90(0.83)	8.98(0.80)
J	8.96(0.72)	9.90(0.69)	6.97(0.88)	8.85(0.83)
K	7.82(0.80)	8.80(0.67)	6.94(0.87)	8.87(0.75)
L	8.99(0.79)	9.55(0.75)	8.06(0.82)	9.07(0.89)
Ave	8.55(0.78)	9.56(0.71)	7.67(0.82)	8.99(0.81)

Table A.22 Average magnitude and timing over three trials of the peaks in the Joint Compressions Resultants for all subjects at Preferred Speed.

A.23 Sample calculation of Inferior Extensor Retinacula loading (from Section 8.2.4)

For Subject A walking at 0.2 of stance phase, the landmarks of interest are:

$$\underline{i}_{EDL} = \begin{bmatrix} 50.8 \\ -19.05 \\ 31.75 \end{bmatrix},\ \underline{o}_{EDL} = \begin{bmatrix} -50.8 \\ -190.05 \\ 38.1 \end{bmatrix},\ \underline{p}_{EDL} = \begin{bmatrix} -26.99 \\ 4.76 \\ 25.4 \end{bmatrix}$$

$$\underline{i}_{EHL} = \begin{bmatrix} 69.85 \\ -23.81 \\ -6.35 \end{bmatrix},\ \underline{o}_{EHL} = \begin{bmatrix} -52.0 \\ 180.0 \\ 34.0 \end{bmatrix},\ \underline{p}_{EHL} = \begin{bmatrix} -23.8 \\ 12.7 \\ 9.525 \end{bmatrix}$$

$$\underline{p}_{MedM} = \begin{bmatrix} -49.21 \\ 11.11 \\ -19.05 \end{bmatrix},\ \underline{p}_{Navic} = \begin{bmatrix} 0 \\ 0 \\ 0 \end{bmatrix},\ \underline{p}_{Calc} = \begin{bmatrix} -36.51 \\ -9.525 \\ 39.69 \end{bmatrix}$$

were the units are mm and the landmarks are defined in the foot frame of reference where: $\hat{1}$ is anterior, $\hat{2}$ is dorsal (proximal on shank) and $\hat{3}$ is to the subject's right.

From Eq. 8.2-1,

$$\vec{a}_{EDL} = \begin{bmatrix} -23.81 \\ 185.74 \\ 12.7 \end{bmatrix} \Rightarrow \hat{a}_{EDL} = \begin{bmatrix} -0.127 \\ 0.990 \\ 0.0667 \end{bmatrix};\ \vec{b}_{EDL} = \begin{bmatrix} 77.79 \\ -23.81 \\ 6.35 \end{bmatrix} \Rightarrow \hat{b}_{EDL} = \begin{bmatrix} 0.953 \\ -0.292 \\ 0.0778 \end{bmatrix}$$

$$\vec{a}_{EHL} = \begin{bmatrix} -28.3 \\ 167.30 \\ 24.48 \end{bmatrix} \Rightarrow \hat{a}_{EHL} = \begin{bmatrix} -0.165 \\ 0.976 \\ 0.143 \end{bmatrix};\ \vec{b}_{EHL} = \begin{bmatrix} 93.65 \\ -36.51 \\ -15.88 \end{bmatrix} \Rightarrow \hat{b}_{EHL} = \begin{bmatrix} 0.920 \\ -0.359 \\ -0.156 \end{bmatrix}$$

From Eq. 8.2-2, the resultant force directions are,

$$\vec{f}_{EDL} = \begin{bmatrix} 0.826 \\ 0.698 \\ 0.146 \end{bmatrix} \Rightarrow \hat{f}_{EDL} = \begin{bmatrix} 0.757 \\ 0.640 \\ 0.134 \end{bmatrix}$$

$$\vec{f}_{EHL} = \begin{bmatrix} 0.755 \\ 0.617 \\ -0.013 \end{bmatrix} \Rightarrow \hat{f}_{EHL} = \begin{bmatrix} 0.774 \\ 0.633 \\ -0.013 \end{bmatrix}$$

From Eq. 8.2-3, the resultant force magnitudes are,

$$T_{EDL} = 0.555 \times BW \text{ and } F_{EDL} = 0.555 \times (0.547) + 0.555 \times (0.547) = 0.6072$$

$$T_{EHL} = 0.507 \times BW \text{ and } F_{EDL} = 0.507 \times (0.488) + 0.507 \times (0.488) = 0.4950$$

From Eq. 8.2-5, the opposing IER vectors are,

$$\vec{c}_{EDL} = \begin{bmatrix} -22.22 \\ 6.35 \\ -44.45 \end{bmatrix} \Rightarrow \hat{c}_{EDL} = \begin{bmatrix} -0.444 \\ 0.127 \\ -0.887 \end{bmatrix}; \quad \vec{d}_{EDL} = \begin{bmatrix} -9.52 \\ -14.29 \\ 14.29 \end{bmatrix} \Rightarrow \hat{d}_{EDL} = \begin{bmatrix} -0.426 \\ -0.640 \\ 0.640 \end{bmatrix}$$

$$\vec{c}_{EHL} = \begin{bmatrix} -25.41 \\ -1.59 \\ -28.58 \end{bmatrix} \Rightarrow \hat{c}_{EHL} = \begin{bmatrix} -0.664 \\ -0.042 \\ -0.745 \end{bmatrix}; \quad \vec{d}_{EHL} = \begin{bmatrix} -12.71 \\ -22.23 \\ 30.165 \end{bmatrix} \Rightarrow \hat{d}_{EHL} = \begin{bmatrix} -0.331 \\ -0.579 \\ 0.745 \end{bmatrix}$$

Therefore the equilibria for the two muscles are written as follows from Eq. 8.2-7,

$$\text{EDL: } -0.6072 \begin{bmatrix} 0.757 \\ 0.640 \end{bmatrix} = \begin{bmatrix} -0.444 & -0.426 \\ 0.127 & -0.640 \end{bmatrix} \begin{bmatrix} T_{c_{EDL}} \\ T_{d_{EDL}} \end{bmatrix}$$

$$\text{EHL: } -0.4950 \begin{bmatrix} 0.774 \\ 0.633 \end{bmatrix} = \begin{bmatrix} -0.664 & -0.331 \\ -0.042 & -0.579 \end{bmatrix} \begin{bmatrix} T_{c_{EHL}} \\ T_{d_{EHL}} \end{bmatrix}$$

which solves to become,

$$\begin{bmatrix} T_{c_{EDL}} \\ T_{d_{EDL}} \end{bmatrix} = \begin{bmatrix} 0.380 \\ 0.683 \end{bmatrix} \text{ and } \begin{bmatrix} T_{c_{EHL}} \\ T_{d_{EHL}} \end{bmatrix} = \begin{bmatrix} 0.319 \\ 0.518 \end{bmatrix}$$

The total loads in the A-P and P-D directions acting on the medial malleolus are therefore (from Eq. 8.2-9),

$$\begin{bmatrix} F_{A-P_{MedM}} \\ F_{P-D_{MedM}} \end{bmatrix} = -0.380 \begin{bmatrix} -0.444 \\ 0.127 \end{bmatrix} - 0.319 \begin{bmatrix} -0.664 \\ -0.042 \end{bmatrix} = \begin{bmatrix} 0.381 \\ -0.035 \end{bmatrix} \times BW$$

which means 0.38×BW acting anteriorly and 0.035×BW acting distally.